

AD-A273 270



①

**PROCEEDINGS**

**1992 U.S. WORKSHOP  
ON THE PHYSICS AND CHEMISTRY  
OF MERCURY CADMIUM TELLURIDE  
AND OTHER IR MATERIALS**

**S** DTIC  
ELECTE  
NOV 30 1993  
**A**

**Edited by  
J.R. Waterman and R.P. Ruth**

**1993**

**TMS**

Minerals • Metals • Materials

This document has been approved  
for public release and sale; its  
distribution is unlimited

93

26

024

**93-28982**



**93 11 26 024**

**Proceedings of the  
1992 U.S. Workshop on the  
Physics and Chemistry  
of Mercury Cadmium Telluride  
and Other IR Materials**

**13-15 October 1992  
Danvers, Massachusetts**

Special Editors for the Proceedings:

**James R. Waterman and Ralph P. Ruth**

This book is a reprint of Volume 22, No. 8  
of the *Journal of Electronic Materials*.  
Hence, the pagination begins on page 800  
rather than the customary page 1.

Published for the American Vacuum Society  
by The Minerals, Metals & Materials Society,  
Warrendale, PA 1993

DTIC QUALITY INSPECTED 8

|                    |                      |
|--------------------|----------------------|
| Accession For      |                      |
| NTIS               | CRA&I                |
| DTIC               | TAB                  |
| Unannounced        |                      |
| Justification      |                      |
| By                 |                      |
| Distribution /     |                      |
| Availability Codes |                      |
| Dist               | Avail and/or Special |
| A-1                |                      |

**Proceedings of the  
1992 U.S. Workshop on the  
Physics and Chemistry  
of Mercury Cadmium Telluride  
and Other IR Materials**



**A Publication of The Minerals, Metals & Materials Society**  
420 Commonwealth Drive  
Warrendale, Pennsylvania 15086  
(412) 776-9000

The Minerals, Metals & Materials Society is not responsible for statements or opinions and is absolved of liability due to misuse of information contained in this publication.

Printed in the United States of America  
Library of Congress Catalog Number 93-86220  
ISBN Number 0-87339-254-X

Authorization to photocopy items for internal or personal use, or the internal or personal use of specific clients, is granted by The Minerals, Metals & Materials Society for users registered with the Copyright Clearance Center (CCC) Transactional Reporting Service, provided that the base fee of \$3.00 per copy is paid directly to Copyright Clearance Center, 27 Congress Street, Salem, Massachusetts 01970. For those organizations that have been granted a photocopy license by Copyright Clearance Center, a separate system of payment has been arranged.

**TMS**  
Minerals • Metals • Materials

© 1993

If you are interested in purchasing a copy of this book, or if you would like to receive the latest TMS publications catalog, please telephone 1-800-759-4867.

# **Proceedings of the 1992 U.S. Workshop on the Physics and Chemistry of Mercury Cadmium Telluride and Other II-VI Compounds**

|  |            |
|--|------------|
| <b>Foreword .....</b>                      | <b>801</b> |
| <i>James R. Waterman and Ralph P. Ruth</i> |            |

## **MATERIALS**

|  |            |
|--|------------|
| <b>Growth Kinetics and Properties of Heteroepitaxial (Cd,Zn)Te Films Prepared<br/>by Metalorganic Molecular Beam Epitaxy .....</b>   | <b>803</b> |
| <i>D. Rajavel and J.J. Zinck</i>   |            |
| <b>Growth of HgSe and Hg<sub>1-x</sub>Cd<sub>x</sub>Se Thin Films by Molecular Beam Epitaxy .....</b>  | <b>809</b> |
| <i>Y. Lansari, J.W. Cook, Jr., and J.F. Schetzina</i>  |            |
| <b>CdTe and HgTe Surface Growth Kinetics for Molecular<br/>and Metalorganic Molecular Beam Epitaxy .....</b>   | <b>815</b> |
| <i>R.G. Benz, II, B.K. Wagner, A. Conte, and C.J. Summers</i>  |            |
| <b>Growth and Characterization of Hot-Wall Epitaxial CdTe on (111) HgCdTe<br/>and CdZnTe Substrates .....</b>  | <b>821</b> |
| <i>J.H. Tregilgas, C.-F. Wan, and H.-Y. Liu</i>  |            |
| <b>Substrate Issues for the Growth of Mercury Cadmium Telluride .....</b>  | <b>827</b> |
| <i>R. Triboulet, A. Tromson-Carli, D. Lorans, and T. Nguyen Duy</i>  |            |
| <b>MOCVD Grown CdZnTe/GaAs/Si Substrates for Large-Area HgCdTe IRFPAs .....</b>  | <b>835</b> |
| <i>S.M. Johnson, J.A. Vigil, J.B. James, C.A. Cockrum, W.H. Konkel, M.H. Kalisher,<br/>R.F. Risser, T. Tung, W.J. Hamilton, W.L. Ahlgren, and J.M. Myrosznyk</i>   |            |
| <b>Comparison of In<sub>1-x</sub>Tl<sub>x</sub>Sb and Hg<sub>1-x</sub>Cd<sub>x</sub>Te as Long Wavelength Infrared Materials .....</b>   | <b>843</b> |
| <i>A.-B. Chen, M. van Schilfgaarde, and A. Sher</i>  |            |
| <b>Comparison of Spatial Compositional Uniformity and Dislocation Density<br/>for Organometallic Vapor Phase Epitaxial Hg<sub>1-x</sub>Cd<sub>x</sub>Te Grown by the Direct Alloy<br/>and Interdiffused Growth Processes .....</b> | <b>847</b> |
| <i>D.D. Edwall</i>   |            |
| <b>Indium Doping of HgCdTe Grown by Metalorganic Chemical Vapor<br/>Deposition-Direct Alloy Growth Using Trisopropylindium and Diisopropyltellurium<br/>Trisopropylindium Adduct .....</b>   | <b>853</b> |
| <i>R. Korenstein, P.H. Hallock, D.L. Lee, E. Sullivan, R.W. Gedridge, Jr., and K.T. Higa</i>   |            |
| <b>A New n-Type Doping Precursor for MOCVD-IMP Growth of Detector Quality MCT .....</b>  | <b>859</b> |
| <i>S.J.C. Irvine, J. Bajaj, L.O. Bubulac, W.P. Lin, R.W. Gedridge, Jr., and K.T. Higa</i>  |            |
| <b>Effects of Growth Rate and Mercury Partial Pressure on Twin Formation<br/>in HgCdTe (111) Layers Grown by Metalorganic Chemical Vapor Deposition .....</b>  | <b>865</b> |
| <i>K. Shigenaka, L. Sugiura, F. Nakata, and K. Hirahara</i>  |            |

(Continued)

|   |            |
|---|------------|
| <b>Improved CdTe Layers on GaAs and Si Using Atomic Layer Epitaxy .....</b>         | <b>873</b> |
| <i>Wen-Sheng Wang, Hassan Ehsani, and Ishwara Bhat</i>                              |            |
| <b>The Effect of Substrate Tilt on MOCVD Growth of {100}CdTe on {100}GaAs .....</b> | <b>879</b> |
| <i>W.J. Hamilton, J.A. Vigil, W.H. Konkel, V.B. Harper, and S.M. Johnson</i>        |            |

## CHARACTERIZATION

|   |            |
|---|------------|
| <b>Use of Ellipsometry to Characterize the Surface of HgCdTe .....</b>  | <b>887</b> |
| <i>David R. Rhiger</i>  |            |
| <b>Modelling of In Situ Monitored Laser Reflectance During MOCVD Growth of HgCdTe .....</b>   | <b>899</b> |
| <i>J. Bajaj, S.J.C. Irvine, H. O. Sankur, and Spyros A. Svoronos</i>  |            |
| <b>Hall Effect Characterization of LPE HgCdTe p/n Heterojunctions .....</b>   | <b>907</b> |
| <i>S.P. Tobin, G.N. Pultz, E. E. Krueger, M. Kestigian, K.-K. Wong, and P. W. Norton</i>  |            |
| <b>Assessment of Electrical Inhomogeneity of Undoped and Doped Hg<sub>1-x</sub>Cd<sub>x</sub>Te MOVPE (IMP) Layers by Variable Magnetic Field Hall Profile Measurements .....</b> | <b>915</b> |
| <i>M.L. Young, J. Giess, and J.S. Gough</i>   |            |
| <b>Characterization of Hg<sub>1-x</sub>Cd<sub>x</sub>Te Heterostructures by Thermoelectric Measurements .....</b>   | <b>923</b> |
| <i>J. Baars, D. Brink, D.D. Edwall, and L.O. Bubulac</i>  |            |
| <b>Photo-Induced Excess Low Frequency Noise in HgCdTe Photodiodes .....</b>   | <b>931</b> |
| <i>G.M. Williams, R.E. DeWames, J. Bajaj, and E.R. Blazejewski</i>  |            |
| <b>Synchrotron White Beam X-Ray Topography Analysis of MBE Grown CdTe/CdTe (111)B .....</b>   | <b>943</b> |
| <i>T. Fanning, M.B. Lee, L.G. Casagrande, D. DiMarzio, and M. Dudley</i>  |            |
| <b>Structure of CdTe (111)B Grown by MBE on Misoriented Si(001) .....</b>   | <b>951</b> |
| <i>Y.P. Chen, S. Sivananthan, and J. P. Faurie</i>  |            |
| <b>X-Ray Diffraction Characterization of LPE HgCdTe Heterojunction Photodiode Material .....</b>  | <b>959</b> |
| <i>S.P. Tobin, E.E. Krueger, G.N. Pultz, M. Kestigian, K.-K. Wong, and P.W. Norton</i>  |            |
| <b>Growth Method, Composition, and Defect Structure Dependence of Mercury Diffusion in Cd<sub>x</sub>Hg<sub>1-x</sub>Te .....</b>   | <b>967</b> |
| <i>N.A. Archer, H.D. Palfrey, and A.F.W. Willoughby</i>   |            |

## SURFACES AND INTERFACES

|   |            |
|---|------------|
| <b>Integrated Heterostructure Devices Based on II-VI Compound Semiconductors .....</b>  | <b>973</b> |
| <i>J. Ren, Y. Lansari, Z. Yu, J.W. Cook, Jr., and J.F. Schetzina</i>  |            |
| <b>UV Photon Assisted Control of Interface Charge Between CdTe Substrates and Metalorganic Chemical Vapor Deposition CdTe Epilayers .....</b> | <b>977</b> |
| <i>Y. Nemirovsky, A. Ruzin, and A. Bezingier</i>  |            |
| <b>Heavily Accumulated Surfaces of Mercury Cadmium Telluride Detectors: Theory and Experiment .....</b>                                       | <b>985</b> |
| <i>J.R. Lowney, D.G. Seiler, W.R. Thurber, Z. Yu, X.N. Song, and C.L. Littler</i>   |            |
| <b>The Role of the Insulator in Determining 1/f Noise in Hg<sub>1-x</sub>Cd<sub>x</sub>Te Integrating MIS Devices .....</b>                   | <b>993</b> |
| <i>José L. Meléndez and Jeff Beck</i>   |            |

(Continued)

## DEFECTS

|   |             |
|---|-------------|
| <b>Process Modeling of Point Defect Effects In <math>\text{Hg}_{1-x}\text{Cd}_x\text{Te}</math> .....</b>                       | <b>999</b>  |
| <i>José L. Meléndez and C. R. Helms</i>   |             |
| <b><math>\text{Hg}_{0.8}\text{Cd}_{0.2}\text{Te}</math> Native Defects: Densities and Dopant Properties .....</b>               | <b>1005</b> |
| <i>M.A. Berding, M. van Schilfhaarde, and A. Sher</i>   |             |
| <b>Observation of Indium-Vacancy and Indium-Hydrogen Interactions In <math>\text{Hg}_{1-x}\text{Cd}_x\text{Te}</math> .....</b> | <b>1011</b> |
| <i>Wm. C. Hughes, M.L. Swanson, and J.C. Austin</i>   |             |
| <b>Electrical Effects of Dislocations and Other Crystallographic Defects</b>  |             |
| <b>In <math>\text{Hg}_{0.78}\text{Cd}_{0.22}\text{Te}</math> n-on-p Photodiodes .....</b>                                       | <b>1017</b> |
| <i>R.S. List</i>  |             |

## DEVICES

|  |             |
|--|-------------|
| <b>Large Improvement In HgCdTe Photovoltaic Detector Performances at LETI .....</b>  | <b>1027</b> |
| <i>G. Destefanis and J.P. Chamonal</i>   |             |
| <b>Influence of Hg Pressure on Diffusion Coefficient of As In HgCdTe .....</b>   | <b>1033</b> |
| <i>D. Chandra, M.W. Goodwin, M.C. Chen, and J.A. Dodge</i>   |             |
| <b>Annealing Effect on the p-Type Carrier Concentration in Low-Temperature Processed Arsenic-Doped HgCdTe .....</b>                                      | <b>1039</b> |
| <i>S.H. Shin, J.M. Arias, M. Zandian, J.G. Pasko, L.O. Bubulac, and R.E. DeWames</i>   |             |
| <b>MBE HgCdTe Heterostructure p-on-n Planar Infrared Photodiodes .....</b>   | <b>1049</b> |
| <i>J.M. Arias, J.G. Pasko, M. Zandian, S.H. Shin, G.M. Williams, L.O. Bubulac, R.E. DeWames, and W.E. Tennant</i>  |             |
| <b>Nanometer Fabrication In Mercury Cadmium Telluride by Electron Cyclotron Resonance Microwave Plasma Reactive Ion Etching .....</b>                    | <b>1055</b> |
| <i>C.R. Eddy, Jr., C.A. Hoffman, J.R. Meyer, and E.Z. Dobisz</i>   |             |
| <b>Low Threshold Injection Laser in HgCdTe .....</b>   | <b>1061</b> |
| <i>Ph. Bouchut, G. Destefanis, A. Million, T. Colin, and J. Bablet</i>   |             |
| <b>Vapor Phase Equilibria In the <math>\text{Cd}_{1-x}\text{Zn}_x\text{Te}</math> Alloy System .....</b>   | <b>1067</b> |
| <i>H.H. Vydyanath, J.A. Ellsworth, R.F. Fisher, J.J. Kennedy, C.J. Johnson, and G.T. Neugebauer</i>  |             |
| <b>Thermomigration of Te Precipitates and Improvement of (Cd,Zn)Te Substrate Characteristics for the Fabrication of LWIR (Hg,Cd)Te Photodiodes .....</b> | <b>1073</b> |
| <i>H.R. Vydyanath, J.A. Ellsworth, J.B. Parkinson, J.J. Kennedy, B. Dean, C.J. Johnson, G.T. Neugebauer, J. Sepich, and Pok-Kai Liao</i>                 |             |
| <b>Evidence for 1/f Noise In Diffusion Current Due to Insulator Trapping and Surface Recombination Velocity Fluctuations .....</b>                       | <b>1081</b> |
| <i>R.A. Schabel, D. Blanks, D. Bartholomew, and M.A. Kinch</i>   |             |

## SUPERLATTICES

|  |             |
|--|-------------|
| <b>Properties of InAs/(Ga,In)Sb Strained Layer Superlattices Grown on the {111} Orientations .....</b> | <b>1087</b> |
| <i>J.A. Dura, J.T. Zborowski, T.D. Golding, D. Donnelly, and W. Covington</i>                          |             |
| <b>Auger Lifetimes In Ideal InGaSb/InAs Superlattices .....</b>  | <b>1093</b> |
| <i>C.H. Grein, P.M. Young, H. Ehrenreich, and T.C. McGill</i>  |             |

(Continued)

|   |             |
|---|-------------|
| <b>In-Situ Ellipsometric Measurements of the MBE Growth of CdTe/HgTe<br/>and CdTe/ZnTe Superlattices .....</b>  | <b>1097</b> |
| <i>M.A. Folkard, G. Shen, V. Kumar, T.A. Steele, D. Rees, I.K. Varga, D. Carr,<br/>K. Fueloep, B.A. Johnson, P.J. Orders, R.H. Hartley, H. Buskes, and M. Gal</i> |             |
| <b>States Confined in the Barriers of Type-III HgTe/CdTe Superlattices .....</b>  | <b>1103</b> |
| <i>H. Luo, L.R. Ram-Mohan, G.L. Yang, Y. Xuan, and J.K. Furdyna</i>   |             |
| <b>Band Gap Uniformity and Layer Stability of HgTe-CdTe Superlattices Grown<br/>by Photon-Assisted Molecular Beam Epitaxy.....</b>                                | <b>1107</b> |
| <i>R.W. Yanka, K.A. Harris, L.M. Mohnkern, A.R. Reisinger, T.H. Myers, and N. Otsuka</i>  |             |

## Foreword

The 1992 U.S. Workshop on the Physics and Chemistry of Mercury Cadmium Telluride and Other IR Materials was held in Danvers, Massachusetts, on October 13–15, 1992. This workshop was the eleventh in a series which began in October 1981. Over that time, it has become the preeminent forum for open interdisciplinary discussion of scientific and technological issues concerning HgCdTe. Its scope includes the discussion of other materials which are important to the development of technology based on HgCdTe, e.g., CdZnTe substrates for epitaxial growth and other materials addressing applications for which HgCdTe is the leading contender, e.g., III-V strained-layer superlattices and quantum wells for infrared detectors.

Subject areas discussed at the 1992 workshop include material growth processes, electronic and physical characterization, surfaces and interfaces, defects, devices, and superlattices. This special issue is arranged by topical area, as presented at the workshop. Forty-five of the 57 papers presented at the workshop appear in this publication. The editors thank the referees for their careful and prompt review of the manuscripts and the program committee for having selected such high-quality work for presentation.

The program committee members were S.K. Ghandhi (Rensselaer Polytechnic Institute), P.W. Norton (Loral IR and Imaging Systems), R.L. Aggarwal (Massachusetts Institute of Technology), R. Balcerak (Advanced Research Projects Agency), J.P. Faurie (University of Illinois at Chicago), J.K. Furdyna (Notre Dame University), E.R. Gertner (Rockwell International), C.R. Helms (Stanford University), S.M. Johnson (Santa Barbara Research Center), M. Martinka (CECOM Night Vision and Electronic Sensors Directorate), P.R. Norton (Santa Barbara Research Center), H.F. Schaake (Texas Instruments), J.F. Schetzina (North Carolina State University), D.G. Seiler (National Institute of Standards and Technology), A. Sher (SRI International), C.J. Summers (Georgia Institute of Technology), J.R. Swenson (SDIO), and J.R. Waterman (Naval Research Laboratory). Special thanks go to Sorab Ghandhi and Peter Norton, co-chairmen of the workshop, and Jay Morreale (Palisades Institute for Research Services, Inc.), workshop coordinator.

The workshop was cosponsored by the U.S. Office of Naval Technology, the U.S. Air Force Wright Laboratory, and the U.S. Army CECOM Night Vision and Electronic Sensors Directorate.

The proceedings of nearly all of the past workshops have been published under the auspices of the American Vacuum Society (AVS), Electronic Materials and Processing Division, through the American Institute of Physics in the *Journal of Vacuum Science and Technology (JVST)*. The support of those organizations over the years is widely recognized and is gratefully acknowledged by the present workshop committee.

Following publication of the 1991 workshop proceedings in *JVST* in mid-1992, it was learned that the AVS would not be able to continue publishing the proceedings in *JVST*. Although the Institute would have published the proceedings in its Conference Proceedings Series, members of the workshop committee preferred that the proceedings continue to have the wider coverage and availability offered by an archival journal.

Out of that situation came the present arrangement, in which papers from the workshop are being published for the first time in the *Journal of Electronic Materials* (*JEM*). Plans were proposed and adopted in a very short time, between distribution of the 1992 Workshop Advance Program and the actual meeting dates, so that authors of papers knew in advance that their work would be published in *JEM*—subject to the existing refereeing policies of this journal.

The editors are grateful to Theodore C. Harman, editor of *JEM*, to Robert Makowski, Director of Publishing Services of The Minerals, Metals, and Materials Society, and to members of the *JEM* Editorial Oversight Committee for their cooperation in facilitating this shift of publication plans on such short notice. We are pleased to report that plans are already in place for the 1993 workshop papers also to be published in *JEM*; it is anticipated that this association will be a long and successful one—as was the case for so many years with *JVST*.

James R. Waterman  
Naval Research Laboratory  
Washington, DC

Ralph P. Ruth  
Santa Barbara Research Center  
Goleta, CA

Special Issue Editors

# Growth Kinetics and Properties of Heteroepitaxial (Cd,Zn)Te Films Prepared by Metalorganic Molecular Beam Epitaxy

D. RAJAVEL and J.J. ZINCK

Hughes Research Laboratories, Malibu, CA 90265

Thermally precracked diethylzinc, dimethylcadmium, and diethyltelluride were used for the metalorganic molecular beam epitaxial growth of (001) ZnTe, CdTe, and CdZnTe films on GaAs substrates. Measurements of the growth rate as a function of the substrate temperature and the II/VI ratio were used to determine the growth kinetics of (001) ZnTe and CdTe. (001) CdTe, ZnTe, and CdZnTe films were deposited under near-stoichiometric growth conditions, as determined from the growth kinetics. The best heteroepitaxial films exhibited x-ray rocking curve full widths at half maximum of 200–210 arc-s. The photoluminescence spectra of the binary and ternary films at 5K were dominated by features associated with bound and free excitons. Secondary ion mass spectrometry measurements showed that the films were free of carbon and oxygen. A new mercury precursor, divinylmercury, was used for HgTe growth. Preliminary results indicated that divinylmercury is a viable mercury source for metalorganic molecular beam epitaxial growth when it is precracked.

**Key words:** CdZnTe/GaAs, divinylmercury, MOMBE

## INTRODUCTION

The high degree of flux control obtained with gas phase source materials coupled with a high-vacuum growth environment has made metalorganic molecular beam epitaxy (MOMBE) an attractive growth technique.<sup>1,2</sup> To date, studies of the fundamental growth processes and developments in MOMBE technology have been largely pursued in III-V materials. Studies of the dependence of growth rate on substrate temperature and the reactant ratio can provide important information concerning incorporation coefficients (defined as the ratio of atoms of a constituent incorporated in the lattice to its incident flux), activation energies for desorption, and film stoichiometry, which is necessary for material optimization. Knowledge of the growth kinetics and an understanding of the effects of the growth conditions on material properties is therefore crucial for the production of high quality films. However, relatively few studies which are relevant to the MOMBE growth of II-VI compounds have been reported, and in particular little is known about (Hg,Cd,Zn)Te alloys. This family of alloys constitutes an important class of infrared detector materials.<sup>3</sup> In addition, CdTe and ZnTe find

applications in optical modulators,<sup>4</sup> and the ternary alloy  $\text{Cd}_{1-x}\text{Zn}_x\text{Te}$  is used as a buffer layer for the lattice matched growth of mercury-based infrared detector materials.<sup>5</sup>

In this paper, we present the MOMBE growth kinetics and properties of (001) CdTe and ZnTe films deposited on GaAs substrates. Growth rates measured in-situ from reflection high energy electron diffraction (RHEED) intensity oscillations were used to determine the growth kinetics. (001) CdTe and ZnTe films were deposited under near-stoichiometric growth conditions, as determined from the growth kinetics. In addition, we report the first MOMBE growth of  $\text{Cd}_{1-x}\text{Zn}_x\text{Te}$  ( $x \approx 0.04$ ) alloys. The heteroepitaxial (Cd,Zn)Te films were characterized by RHEED, x-ray double crystal rocking curve, photoluminescence (PL), and secondary ion mass spectrometry (SIMS) measurements. Results of these comprehensive characterization studies indicate that films grown by MOMBE compare favorably with the best films grown by other vapor phase techniques. We also report preliminary results of HgTe growth using a new mercury precursor, divinylmercury (DVHg).

## EXPERIMENTAL

The growth experiments were conducted in a Vacuum Generators MOMBE system. The growth

(Received October 30, 1992; revised January 13, 1993)



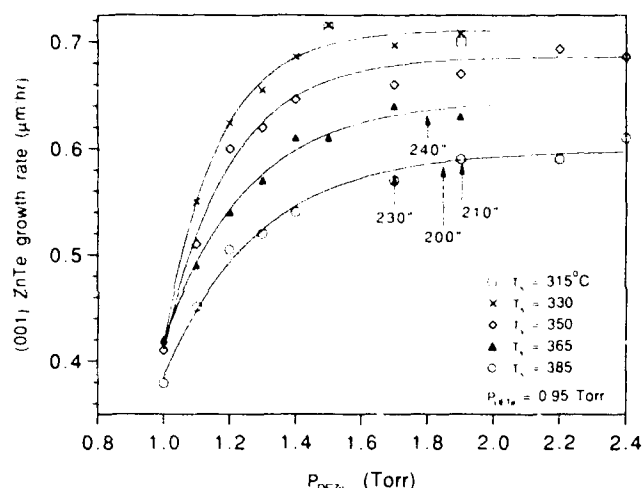


Fig. 1. (001) ZnTe growth rate as a function of DEZn upstream pressure and substrate temperature. The points represent growth rates determined from RHEED intensity oscillations. The lines serve as an aid to the eye. The numbers associated with arrows are the x-ray FWHMs of the (001) ZnTe/GaAs layers.

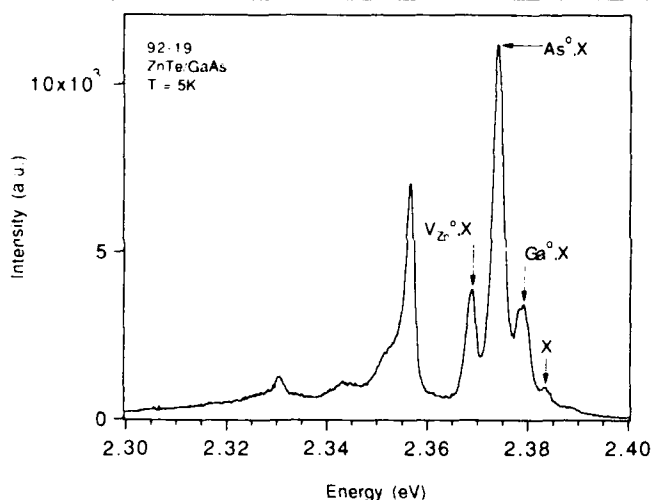


Fig. 2. 5K near-band-edge PL spectrum of a 3  $\mu\text{m}$  thick (001) ZnTe/GaAs sample.

chamber was equipped with liquid-nitrogen cooled panels and evacuated with a Balzers 2200 l/s turbomolecular pump. The base pressure was  $2 \times 10^{-10}$  Torr and the pressure during growth was  $\approx 5 \times 10^{-5}$  Torr. Electronic grade dimethylcadmium (DMCd), diethylzinc (DEZn), and diethyltelluride (DETe) source materials were obtained from Morton International, Inc. The mercury precursor, DVHg, was obtained from a custom synthesis performed both in our laboratory and at STREM chemicals. All the precursors were contained in temperature controlled baths, and were incident on the substrate after passing through high temperature Vacuum Generators cracker cells. DMCd and DEZn were delivered to the same tantalum-based cracker cell where they were pyrolyzed, and DVHg was delivered to a separate tantalum-based cracker cell. Due to the corrosive nature of tellurium, a modified quartz-based cracker cell was used to pyrolyze DETe. The required flow rate of a

source material was obtained by regulating the pressure on the upstream side of an orifice which was attached to the entry port of each cracker cell. This pressure regulation was performed by a solenoid valve with a capacitance manometer feedback assembly. A quadrupole mass analyzer (Extranuclear Labs.) mounted on a translation stage could be moved to the substrate position to determine the pyrolysis by-products produced in the cracker cells. The system was also equipped with RHEED capability.

The optimum operating temperatures of the cracker cells were determined by examining the temperature dependence of the species produced in the cracker cells using quadrupole mass spectrometry. At 800°C, DMCd and DEZn decomposed completely producing the group II elements and hydrocarbon by-products. However, at the operating temperature of 700°C, the pyrolysis of DETe produced tellurium,  $\text{Te}_2$ , partially alkylated tellurium compounds (collectively referred to as the tellurium species), and hydrocarbon by-products. Depending on whether precracking was desired, the DVHg cracker cell was operated at 50 or 500°C. GaAs substrates of the (001) orientation were used for this study, and were used as received. The substrate temperature was calibrated using the melting points of indium and tin in reference to the substrate thermocouple. The heteroepitaxial growth of (001) (Cd,Zn)Te layers was accomplished by nucleating (001) ZnTe films on GaAs substrates prior to the growth of CdTe or  $\text{Cd}_{1-x}\text{Zn}_x\text{Te}$  films.

## RESULTS AND DISCUSSION

### Growth Kinetics and Properties of (001) ZnTe

We have recently reported on the MOMBE growth kinetics of ZnTe and some of the key results are included here.<sup>6</sup> The (001) ZnTe films were grown on (001) GaAs substrates using thermally precracked DEZn and DETe. ZnTe growth rates were determined from RHEED intensity oscillations and the dependence of growth rate on II/VI ratio for substrate temperatures between 315–385°C is shown in Fig. 1. The points represent experimental data and the lines serve to guide the eye. The flow rate of DETe was kept constant, corresponding to an upstream pressure of 0.95 Torr. The upstream pressure of DEZn,  $P_{\text{DEZn}}$ , was varied between 1.0–2.4 Torr. As shown in Fig. 1, RHEED intensity oscillations were observed for a wide range of II/VI ratios and substrate temperatures. However, the more intense oscillations were observed around the knee of the growth rate curve. For a fixed tellurium flux, the growth rate increased monotonically with increasing  $P_{\text{DEZn}}$ , and then saturated to a maximum value at each substrate temperature. The saturated maximum growth rate was dictated by the temperature dependent incorporation coefficient of the tellurium species for zinc-rich growth conditions. At 385°C, the maximum tellurium-limited growth rate was 0.61  $\mu\text{m/hr}$ , and increased with decreasing substrate temperature to a maximum of 0.71  $\mu\text{m/hr}$  at 330°C. Within the limits of error of the

growth rate measurement, the tellurium-limited growth rates at 330°C and 315°C were equal, with a value of 0.71  $\mu\text{m/hr}$ . These results indicate that the incorporation coefficient of the tellurium species under zinc-saturated growth conditions is nearly unity at 330°C and below, but is less than unity at higher temperatures. Past the knee of the curve, with further increase in  $P_{\text{DETe}}$ , the RHEED pattern exhibited the  $(2 \times 2)$  reconstruction coexisting with the  $(2 \times 1)$  reconstruction, indicative of zinc-rich growth conditions.<sup>7</sup> X-ray rocking curve measurements were performed using  $\text{Cu}_{K\alpha}$  radiation to assess the crystalline quality of the ZnTe/GaAs films. The full widths at half maximum (FWHM) of the (004) diffraction peaks for 2–3  $\mu\text{m}$  (001) ZnTe films are also shown in Fig. 1. The growth conditions for each film are indicated by an arrow. Films with the best crystalline quality exhibited rocking curves between 200–240 arc-s.

Photoluminescence measurements were performed at 5K in a continuous flow helium cryostat to determine the optical properties of the films. The samples were excited with 476.5 nm argon-ion laser radiation at a power density of 1 W/cm<sup>2</sup>. The luminescence from the sample was dispersed by a Spex double grating diffractometer and the signal measured by a photomultiplier tube. The PL spectra of the ZnTe/GaAs samples were dominated by strong near band edge emissions. A representative near-band-edge spectrum is shown in Fig. 2. Strong bound excitonic recombinations associated with gallium donors (2.379 eV) and arsenic and zinc vacancy ( $V_{\text{zn}}$ ) acceptors were observed at 2.374 and 2.368 eV, respectively.<sup>6</sup> However, in the absence of PL excitation data, these assignments are tentative. The strongest bound excitonic feature was the arsenic bound excitonic transition which had a FWHM of 3 meV. Despite extensive reabsorption, the free excitonic recombination was observed at 2.382 eV. Features repeating at 26 meV below the free excitonic peak were observed at 2.356 and 2.330 eV, and may be attributed to the phonon replicas of the free exciton.<sup>7</sup> However, Dean et al. have interpreted the feature at 2.356 eV to the recombination of an exciton at a silicon double acceptor system.<sup>8</sup> Therefore, the precise origin of this feature has not been confirmed. The transition at 2.235 eV attributed to  $V_{\text{zn}}$  complexes and features at 1.986 eV associated with oxygen<sup>10</sup> contamination were absent. In addition, there was no deep level emission in the 1.6–2.0 eV range from the MOMBE grown layers.<sup>6</sup> Films grown under different II/IV ratios exhibited the same features, however, the relative intensities of the excitonic features varied. These results demonstrate that the structural and optical properties of the MOMBE grown ZnTe films are on par with the best films prepared by other epitaxial growth techniques.

### Growth Kinetics and Properties of (001) CdTe

(001) ZnTe films deposited on (001) GaAs substrates were employed as buffer layers for the subsequent growth of (001) CdTe layers. The ZnTe buffer layer was used to ensure CdTe growth along the (001)

direction.<sup>11</sup> The source materials DETe and DMCD were precracked. After nucleation on a ZnTe surface, the growth of CdTe proceeded by two-dimensional layer-by-layer growth as inferred from the streaked RHEED pattern of the nucleating film. The growth rate of CdTe measured as a function of the substrate temperature and the II/VI ratio is shown in Fig. 3. The upstream pressure of DETe was controlled at 1.0 Torr, while DMCD pressure was varied from 1.0–2.2 Torr for substrate temperatures between 215–280°C. The dependence of the CdTe growth rate on the II/VI ratio, shown in Fig. 3, is similar to that observed by Benz et al. when DMCD and diisopropyltelluride were used as the source materials.<sup>12</sup> For a fixed temperature, the growth rate increased monotonically with increasing II/VI ratio and then saturated to a maximum growth rate similar to that observed for ZnTe growth.<sup>6</sup> At a growth temperature of 280°C, the maximum tellurium-limited growth rate was 0.88  $\mu\text{m/hr}$  and increased systematically with decreasing growth temperature to 0.92  $\mu\text{m/hr}$  at 215°C. These results indicate that the incorporation coefficient of the tellurium species on CdTe surfaces is less than unity at a growth temperatures above 260°C. On the other hand, the incorporation coefficient of the tellurium species on ZnTe surfaces is nearly unity even at 330°C. This difference is attributed to the different bond strengths of CdTe and ZnTe.

The near-stoichiometric CdTe growth conditions corresponding to the knee of the curve were identified from the growth rate dependence on the II/VI ratio shown in Fig. 3. Heteroepitaxial (001) CdTe films of 2–3  $\mu\text{m}$  thickness were grown on 0.2  $\mu\text{m}$  (001) ZnTe buffer layers deposited on GaAs substrates. The growth conditions of these films are indicated by arrows and the x-ray rocking curve FWHMs are shown in parenthesis in Fig. 3. These heteroepitaxial films exhibited

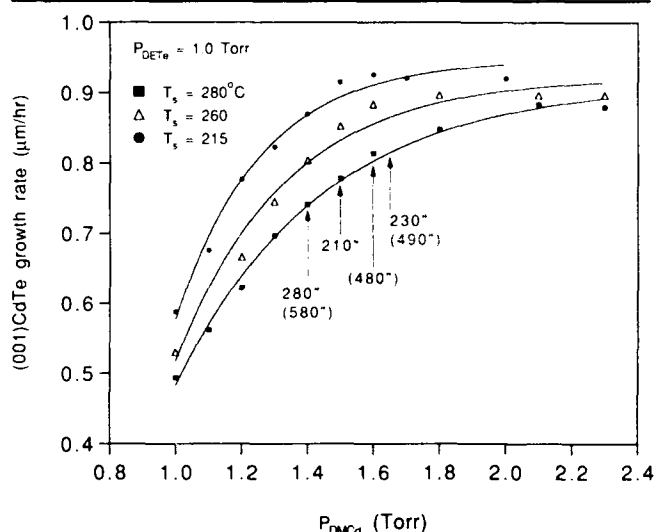


Fig. 3. (001) CdTe growth rate as a function of DMCD upstream pressure and substrate temperature. The points represent growth rates determined from RHEED intensity oscillations. Numbers enclosed in parenthesis represent x-ray FWHMs for 2–3  $\mu\text{m}$  thick CdTe/GaAs films and those without parenthesis are values for 6–7  $\mu\text{m}$  thick films.

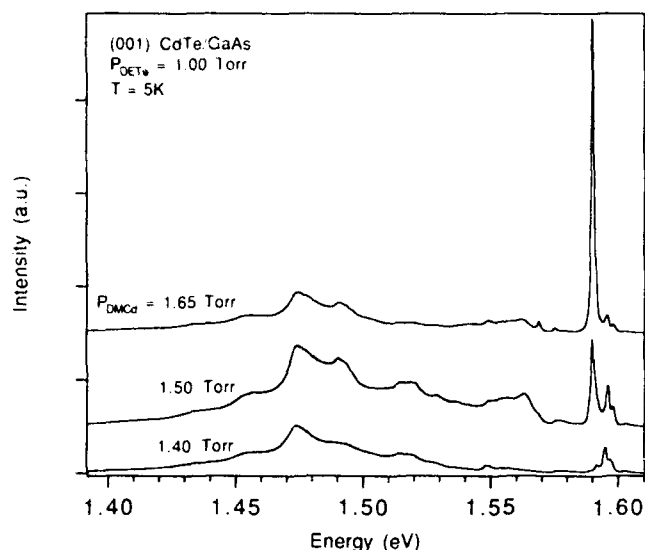


Fig. 4. 5K PL spectra of CdTe/GaAs films grown at 280°C under different II/VI ratios.

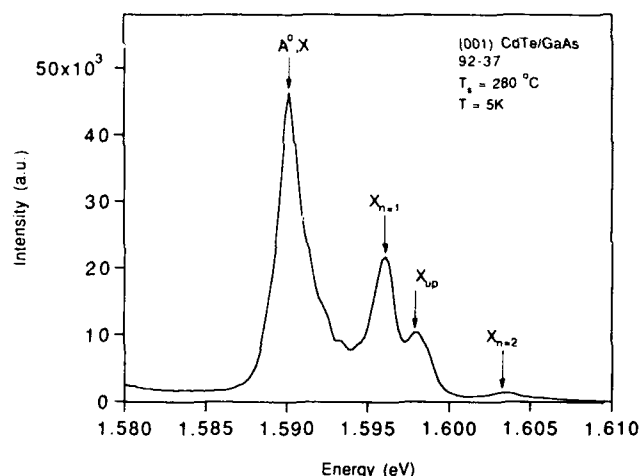


Fig. 5. 5K near-band edge PL spectrum of a 6.1  $\mu\text{m}$  thick (001) CdTe/GaAs sample which exhibited an x-ray FWHM of 210 arc-s.

x-ray rocking curve FWHMs of 480–580 arc-s. For the same growth conditions, 6–7  $\mu\text{m}$  thick films exhibited higher crystalline perfection, due to the presence of a smaller dislocation density.<sup>13</sup> Consequently, the x-ray rocking curve FWHMs were narrower and these values are indicated in Fig. 3 by numbers that are not enclosed in parenthesis. The best films exhibited x-ray rocking curve FWHMs of 210–230 arc-s. The crystalline quality of the films was strongly dependent on the II/VI ratio, with the FWHMs increasing sharply for growth conditions deviating from those indicated by arrows in Fig. 3.

Photoluminescence measurements were performed (excitation with 476.5 nm at 1 W/cm<sup>2</sup>) to assess the optical properties of the CdTe films. Three (001) CdTe films of 6–7  $\mu\text{m}$  thickness grown at 280°C with varying II/VI ratios were analyzed by PL. The x-ray rocking curve FWHMs of these films were between 280–210 arc-s. For these films, the tellurium flux was constant and  $P_{\text{DMCD}}$  was varied from 1.40–1.65 Torr.

The dependence of the PL properties on the II/VI ratio is shown in Fig. 4. The radiative defect density, defined as the ratio of the defect band intensity to the intensity of the principle bound exciton,<sup>14</sup> decreased by over an order of magnitude with increasing II/VI ratio. Similarly, the absolute intensity of the principal bound exciton also increased by an order of magnitude with increasing II/VI ratio over the same range. A high energy feature at 1.595 eV was observed for the film grown with the smallest II/VI ratio. It appears that this feature is not associated with a simple donor, but is instead a donor-like bound excitonic feature associated with a point-defect-impurity complex. A similar feature has been observed by at 1.593 eV by Feng et al. in MBE grown CdTe.<sup>15</sup> The near-band-edge PL spectrum of the CdTe sample that exhibited an x-ray FWHM of 210 arc-s is shown in Fig. 5. A sharp (FWHM = 1 meV) and intense bound excitonic feature was observed at 1.590 eV and is attributed to excitons bound to arsenic acceptors.<sup>16</sup> The free excitonic peak was strong and was observed at 1.596 eV. We also observe the upper branch of the polariton of the free exciton and the recombination of the  $n = 2$  excited state of the free exciton at 1.598 and 1.603 eV, respectively.<sup>15</sup> These three free excitonic features attest to the high quality of the MOMBE grown (001) CdTe/GaAs films.

### Growth Kinetics and Properties of (001) CdZnTe

The (001)  $\text{Cd}_{1-x}\text{Zn}_x\text{Te}$  ( $x \approx 0.04$ ) films were grown at 320°C on 0.2  $\mu\text{m}$  thick (001) ZnTe films deposited on (001) GaAs substrates. The DETe pressure was fixed and the DEZn and DMCD pressures were adjusted such that the growth rate of  $\text{Cd}_{1-x}\text{Zn}_x\text{Te}$  was always limited by the tellurium flux. Thus, the films were grown under group II rich growth conditions. The alloy compositions of the layers were determined by the Bond x-ray diffraction technique<sup>5</sup> and correlated with PL measurements performed at 5K.<sup>17</sup> The agreement between the two techniques was better than 1.5% of zinc content. The properties of the films are listed in Table I. Film thicknesses were estimated from RHEED intensity oscillation measurements. Films of 8–9  $\mu\text{m}$  thickness exhibited x-ray FWHMs of 210–250 arc-s and 3  $\mu\text{m}$  thick films had FWHMs of 400–450 arc-s.

Photoluminescence measurements were performed on the  $\text{Cd}_{1-x}\text{Zn}_x\text{Te}$  alloys under the same excitation conditions used for CdTe and ZnTe films. The PL spectrum of a representative  $\text{Cd}_{0.96}\text{Zn}_{0.04}\text{Te}$  film is shown in Fig. 6. The near band-edge region of the PL spectrum was dominated by bound excitonic features associated with acceptors and donors at 1.615 and 1.619 eV, respectively. The recombination of the free exciton was observed at 1.622 eV. The donor acceptor pair (DAP) recombination was observed at 1.5686 eV, and two orders of the phonon replicas of the DAP with a spacing of 0.021 eV were also observed.<sup>18</sup> A weak defect related band appeared at 1.494 eV. The surface morphology of the (Cd,Zn)Te films prepared under

near-stoichiometric growth conditions were smooth and nearly featureless as determined by Nomarski contrast microscopy. However, an estimate of the etch pit density in these films is presently not available.

Secondary ion mass spectrometry measurements were performed to determine the level of impurities present in the MOMBE grown films. Secondary ion mass spectrometry analysis for the ZnTe films has been reported elsewhere.<sup>6</sup> A summary of the SIMS evaluation of a  $\text{Cd}_{0.96}\text{Zn}_{0.04}\text{Te}/\text{GaAs}$  film is given in Table II. With the exception of indium, the concentration of the impurities in both CdTe and  $\text{Cd}_{1-x}\text{Zn}_x\text{Te}$  films were approximately equal. Oxygen and carbon were measured at levels of  $2 \times 10^{17}$  and  $2 \times 10^{16} \text{ cm}^{-3}$ , respectively, which were at the limit of sensitivity of the measurement due to the presence of these elements in the SIMS ambient. Due to the nature of the SIMS measurement, it was not possible to quantify the absolute concentration of gallium and arsenic in the  $\text{Cd}_{1-x}\text{Zn}_x\text{Te}/\text{GaAs}$  films. However, the concentrations of both gallium and arsenic were approximately  $1 \times 10^{15} \text{ cm}^{-3}$  in the ZnTe/GaAs films, and appeared to originate from the substrate.<sup>6</sup> Silicon was present at  $3 \times 10^{16} \text{ cm}^{-3}$  and was traced to the DEZn source material. The concentration of indium was  $1 \times 10^{16} \text{ cm}^{-3}$  and was traced to the In-Ga alloy used to mount the substrate to the molybdenum holder, as the CdTe samples which were mounted with a colloidal graphite suspension had an indium concentration of less than  $1 \times 10^{14} \text{ cm}^{-3}$ . Sodium and chlorine were present at concentrations of  $5 \times 10^{15}$  and  $1 \times 10^{15} \text{ cm}^{-3}$ , respectively, and are attributed to sample handling before and after growth. The concentrations of aluminum and bromine in the film were both  $2 \times 10^{14} \text{ cm}^{-3}$ . In summary, the structural and optical properties of the films are among the best grown by any epitaxial technique.

### HgTe Growth Using Divinylmercury

We have performed preliminary growth experiments with DVHg to investigate its efficacy as a precursor for the MOMBE growth of mercury containing II-VI infrared detector materials. This compound has a vapor pressure of 2.5 Torr at 25°C. Unlike diethyl or dimethylmercury, DVHg has a strong odor and, therefore, good warning properties. Differential scanning calorimetry measurements performed in our laboratory showed that the onset of thermal decomposition for DVHg occurs at 195°C.<sup>19</sup>

Consequently, the feasibility of using DVHg for HgTe growth in both the uncracked and thermally precracked modes was studied. (001) CdTe deposited on GaAs substrates were used as a buffer layer. Little or no growth was observed by monitoring the RHEED specular spot intensity when HgTe growth was attempted using uncracked DVHg and precracked DETe at growth temperatures from 150–200°C. Furthermore, the RHEED pattern indicated the formation of tellurium precipitates when the tellurium flux was initiated. However, successful growth of single crystalline (001) HgTe was achieved at 150°C when both

DVHg and the DETe were precracked. Reflection high energy electron diffraction oscillations were observed during HgTe growth which indicated a growth rate of  $0.5 \mu\text{m/hr}$ .

### SUMMARY

Heteroepitaxial (001) ZnTe, CdTe, and  $\text{Cd}_{1-x}\text{Zn}_x\text{Te}$  ( $x \approx 0.04$ ) were grown on GaAs substrates by MOMBE using thermally precracked DEZn, DMCd, and DETe. Reflection high energy electron diffraction intensity oscillations were observed during the growth of the films and were used to measure the growth rate. The growth rate dependence on the II/VI ratio and the substrate temperature was used to determine the growth kinetics of (001) ZnTe and CdTe. For a fixed tellurium flux, the growth rates increased monotonically with increasing II/VI ratio and saturated to a maximum value corresponding to tellurium-limited growth conditions. The maximum tellurium-limited growth rate was dependent on the substrate temperature which determines the incorporation coefficient of the tellurium species. The (Cd,Zn)Te films were grown under near stoichiometric growth conditions, as determined from their growth kinetics. The properties of the MOMBE grown films were characterized by double crystal rocking curve x-ray diffraction, PL

Table I. Properties of (001)  $\text{Cd}_{1-x}\text{Zn}_x\text{Te}$  Films Grown on GaAs Substrates

| Sample No. | Thickness ( $\mu\text{m}$ ) | % Zinc | X-Ray FWHM (arc-s) |
|------------|-----------------------------|--------|--------------------|
| 92-68      | 8.7                         | 5.2    | 250                |
| 92-77      | 9.1                         | 3.9    | 210                |
| 92-78      | 8.9                         | 5.1    | 240                |
| 92-72      | 3.0                         | 4.5    | 450                |
| 92-75      | 3.1                         | 3.7    | 400                |

Note: The alloy compositions were determined by the bond x-ray diffraction technique.

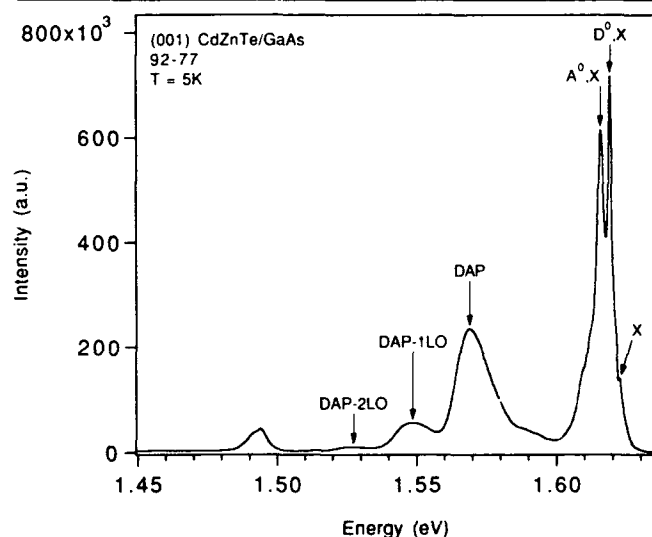


Fig. 6. 5K PL spectrum of a  $9.1 \mu\text{m}$  thick  $\text{Cd}_{0.96}\text{Zn}_{0.04}\text{Te}/\text{GaAs}$  sample which exhibited an x-ray FWHM of 210 arc-s.

**Table II. Results of the SIMS Analysis of a (001)  $\text{Cd}_{.96}\text{Zn}_{.04}\text{Te/GaAs}$  Sample**

| Element  | Concentration ( $\text{cm}^{-3}$ ) |
|----------|------------------------------------|
| Oxygen   | $2 \times 10^{17}$                 |
| Carbon   | $3 \times 10^{16}$                 |
| Silicon  | $3 \times 10^{16}$                 |
| Indium   | $1 \times 10^{16}$                 |
| Sodium   | $5 \times 10^{15}$                 |
| Chlorine | $1 \times 10^{15}$                 |
| Aluminum | $2 \times 10^{14}$                 |
| Bromine  | $2 \times 10^{14}$                 |

Note: The PL spectrum of this sample is shown in Fig. 6.

measurements at 5K, and SIMS. The crystalline quality was strongly dependent on the II/VI ratio, and x-ray FWHMs of 200–210 arc-s were measured for the heteroepitaxial ZnTe, CdTe, and  $\text{Cd}_{1-x}\text{Zn}_x\text{Te}$  ( $x \approx 0.04$ ) films. The optical properties of ZnTe determined by PL measurements were relatively independent of the II/VI ratio. However, the PL properties of the CdTe films were strongly dependent on the II/VI ratio, with cadmium-rich growth conditions significantly enhancing the optical properties. All the films exhibited intense bound excitonic transitions, and a well resolved free excitonic peak. In addition, the CdTe/GaAs films also exhibited the  $X_{\text{up}}$  and  $X_{\text{n=2}}$  states of the free exciton. Secondary ion mass spectrometry measurements were performed to assess the purity of the films, and carbon and oxygen were below the SIMS detectivity limit. These results demonstrate that the quality of the MOMBE grown (001) (Cd,Zn)Te/GaAs films were on par with the best films grown by other vapor phase techniques. In addition, we have investigated the use of a new metalorganic mercury compound, divinylmercury. A preliminary investigation indicated that divinylmercury is a useful mercury precursor for MOMBE growth when it is precracked.

## ACKNOWLEDGMENT

The authors acknowledge R.G. Wilson for assistance with the SIMS analysis, C. LeBeau for technical support, and L.D. Warren and C.D. Haeussler for assistance with sample characterization.

## REFERENCES

1. W.T. Tsang, *J. Cryst. Growth* 120, 1 (1992).
2. B.K. Wagner, D. Rajavel, R.G. Benz, II and C.J. Summers, *J. Vac. Sci. Technol.* B9, 1656 (1991).
3. D.A. Scribner, M.R. Kruer and J.M. Killiany, *Proc. IEEE* 79, 66 (1991).
4. R.D. Feldman, D. Lee, A. Partovi, R.P. Stanley, A.M. Johnson, J.E. Zucker, A.M. Glass and J. Hegarty, *Critical Rev. Solid State Mater. Sci.* 17, 477 (1992).
5. S.M. Johnson, S. Sen, W.H. Konkel and M.H. Kalisher, *J. Vac. Sci. Technol.* B9, 1897 (1991).
6. D. Rajavel and J.J. Zinck, *Appl. Phys. Lett.* 61, 1534 (1992).
7. R.D. Feldman, R.F. Austin, F.M. Bridenbaugh, A.M. Johnson, W.M. Simpson, B.A. Wilson and C.E. Bonner, *J. Appl. Phys.* 64, 1191 (1988).
8. P. J. Dean, M. J. Kaue, N. Magnea, F. de Maigret, L.S. Dang, A. Nahmani, R. Romestain and M. S. Skolnick, *J. Phys. C* 18, 6185 (1985).
9. B.A. Wilson, C.E. Bonner, R.D. Feldman, R.F. Austin, D.W. Kisker, J.J. Krajewski and P.M. Bridenbaugh, *J. Appl. Phys.* 64, 3210 (1988).
10. M. Ekawa, Y. Kawakami, T. Taguchi and A. Hiraki, *J. Cryst. Growth* 93, 667 (1988).
11. R.D. Feldman, R.F. Austin, P.H. Fuoss, A.H. Dayhem, E. H. Westerwick, S. Nakahara, T. Boone, J. Menendez, A. Pinczuk, J.P. Valladares and S. Brennan, *J. Vac. Sci. Technol.* B5, 690 (1997).
12. R.G. Benz, II, B.K. Wagner, A. Conte and C.J. Summers, to be published in *J. Electron. Mater.*
13. R.N. Bicknell, R.W. Yanka, N.C. Giles, J.F. Schetzina, T.J. Magee, C. Leung and H. Kawayoshi, *Appl. Phys. Lett.* 44, 313 (1984).
14. Z.C. Feng, A. Mascarenhas and W.J. Choyke, *J. Lumin.* 35, 329 (1986).
15. Z.C. Feng, M.G. Burke and W.J. Choyke, *Appl. Phys. Lett.* 53, 128 (1988).
16. E. Molva, J.L. Pautrat, K. Saminadayar, G. Milchberg and N. Magnea, *Phys. Rev. B* 30, 3344 (1984).
17. D.J. Olego, J.P. Faurie, S. Sivananthan and P.M. Raccach, *Appl. Phys. Lett.* 47, 1172 (1985).
18. W.M. Duncan, R.J. Koestner, J.H. Tregilgas, H.-Y. Li and M.-C. Chen, *Mater. Res. Soc. Sym. Proc.* 161, 39 (1990).
19. L.W. Tutt, unpublished results.

# Growth of HgSe and $\text{Hg}_{1-x}\text{Cd}_x\text{Se}$ Thin Films by Molecular Beam Epitaxy

Y. LANSARI, J.W. COOK, JR., and J.F. SCHETZINA

Department of Physics, North Carolina State University, Raleigh, NC 27695-8202

Thin epitaxial films of HgSe and  $\text{Hg}_{1-x}\text{Cd}_x\text{Se}$  ( $x \leq 0.34$ ) were successfully grown for the first time by molecular beam epitaxy. Film growth parameters are discussed, and results of structural, electrical, and optical studies are reported.

**Key words:** Characteristics of thin films, HgSe, HgCdSe, MBE, semimetals

## INTRODUCTION

The binary II-VI compound HgSe is a semimetallic material, characterized by a symmetry-induced band structure inversion at the center of the Brillouin zone.<sup>1</sup> This characteristic is shared with HgTe, resulting in many similar physical properties and potential applications for the two compounds. In particular, both of these materials are suitable for infrared (IR) applications when alloyed or layered with compatible wide band gap II-VI compounds (i.e. CdTe for HgTe and CdSe for HgSe). It is, therefore, surprising to note that, while molecular beam epitaxy (MBE) growth of thin epitaxial HgTe and HgTe-based solid solutions such as HgCdTe has been studied for over a decade,<sup>2</sup> there has been no report to date of MBE-grown HgSe thin films or related alloys. In this paper, we report the first epitaxial growth of HgSe and  $\text{Hg}_{1-x}\text{Cd}_x\text{Se}$  thin films by MBE. Optical, electrical, and structural properties of the MBE-grown layers were studied and will also be reported.

## EXPERIMENTAL DETAILS

Growth of HgSe and  $\text{Hg}_{1-x}\text{Cd}_x\text{Se}$  ( $x \leq 0.34$ ) epilayers was carried out in a mercury-compatible MBE system<sup>3</sup> equipped with an externally replenishable, barometer-type mercury source and two-zone Knudsen effusion cells containing elemental selenium and cad-

mium. Substrate materials used in the film growth experiments included (100) and (211)B ZnTe and  $\text{Cd}_{0.96}\text{Zn}_{0.04}\text{Te}$  single crystals. Each substrate was chemimechanically polished in a 1:25:25 solution of bromine-methanol-ethylene glycol and degreased in trichloroethylene, acetone, and methanol. The substrate was then etched in a 1:1 solution of HCl in deionized water immediately before loading into the MBE chamber. Once in place in the MBE system, the substrate was maintained at a temperature of 325°C for 10 min. This process promotes the desorption of tellurium-rich surface layers and allows epilayer nucleation on a bare substrate surface. The substrate was then cooled to the growth temperature and film growth was initiated.

The structural properties of the MBE-grown layers were studied by means of Nomarski interference-contrast microscopy and double-crystal x-ray diffraction. Reflectance/transmittance measurements were completed to assess the optical properties of the epilayers. Electrical properties were studied by means of Van der Pauw Hall effect measurements.

## RESULTS AND DISCUSSION

### Film Growth Experiments

Optimum MBE-growth conditions for HgSe thin films were determined based on the results of preliminary deposition experiments in which film growth parameters such as substrate temperature, mercury

flux, selenium flux, and the Hg/Se flux ratio were systematically varied. The substrate temperature range investigated in these initial experiments was between 80–150°C. The mercury and selenium beam equivalent pressures (BEPs) were varied in the range from  $0.4\text{--}1.5 \times 10^{-4}$  Torr and from  $0.6\text{--}1 \times 10^{-6}$  Torr, respectively.

For HgSe, it was found that there was no appreciable condensation (e.g. very low growth rate) for substrate temperatures above 125°C. At a substrate temperature of ~80°C, the films exhibited poor structural quality and uniformly rough surfaces. In the range 80–150°C, for given mercury and selenium BEPs, the growth rate was found to increase with decreasing temperature. It was also found that, at a given growth temperature, the mercury to selenium BEP ratio has a definite effect on the growth rate. For instance, at a growth temperature of 100°C, and for Hg/Se BEP ratios between 90 and 130, the growth rate is controlled by the selenium flux and increases when the selenium BEP is increased. Below a Hg/Se BEP ratio of 90, on the other hand, film growth becomes mercury-flux limited and the growth rate decreases even when a high selenium flux is present at the substrate surface. This behavior is a direct

consequence of the well-documented<sup>4</sup> low sticking coefficient of mercury.

For Hg/Se BEP ratios higher than 130 (e.g. 130–180), a decrease of the growth rate was also observed. This may be due to a gas-phase beam interaction effect, which results in part of the selenium flux being deflected by the high density of mercury atoms and prevented from reaching the substrate surface. From a morphological and structural quality viewpoint, it was found that the best results were obtained for a BEP ratio in the range of 90–100, for a growth temperature of 100°C.

Based on the above results, in all subsequent HgSe growth experiments, a substrate temperature of 100°C was used along with a Hg/Se BEP ratio of ~100 (mercury and selenium BEPs of  $\sim 1 \times 10^{-4}$  Torr and  $\sim 1 \times 10^{-6}$  Torr, respectively). These conditions resulted in a film growth rate of  $\sim 1.1 \text{ Å/s}$ . Note that this growth rate is still quite low compared to that of HgTe grown under similar conditions. This may be related to the higher evaporation rate of the HgSe compound at low temperatures.<sup>5</sup>

The  $\text{Hg}_{1-x}\text{Cd}_x\text{Se}$  solid solution is a pseudo-binary alloy of the two compounds HgSe and CdSe. In bulk form, HgSe crystallizes in the zincblende cubic structure with lattice constant  $a = 6.084 \text{ Å}$ .<sup>6</sup> However, bulk CdSe crystallizes in the wurtzite hexagonal structure. The formation of the cubic phase for small CdSe mole fractions ( $x < 0.57$ ), or of the hexagonal phase for large CdSe mole fractions ( $x > 0.57$ ), is, therefore, expected and is observed in bulk growth of  $\text{Hg}_{1-x}\text{Cd}_x\text{Se}$ .<sup>7</sup> However, it has recently been demonstrated that stable cubic-phase growth of CdSe occurs for MBE-growth of CdSe films on (100) GaAs substrates.<sup>8</sup> Based on this result, MBE growth of cubic  $\text{Hg}_{1-x}\text{Cd}_x\text{Se}$  epilayers should be possible over the entire composition range. The compositions of interest for most infrared (IR) applications, however, fall within the bulk-growth cubic phase range. For this reason,  $\text{Hg}_{1-x}\text{Cd}_x\text{Se}$  epilayers with concentrations  $x \leq 0.34$  were grown in the present study. Based on the results obtained for growth of HgSe thin films, a growth temperature of 100°C was selected for growth of all  $\text{Hg}_{1-x}\text{Cd}_x\text{Se}$  layers, along with a mercury flux BEP of  $\sim 1 \times 10^{-4}$  Torr. The selenium and cadmium flux BEPs were in the range  $8.2\text{--}9.2 \times 10^{-7}$  Torr, and  $1.5\text{--}0.3 \times 10^{-7}$  Torr, respectively. Film growth rates of 0.7 to  $0.9 \text{ Å/s}$  were obtained using these growth parameters.

### Structural Properties

The surfaces of all MBE-grown layers were examined using a Nomarski interference-contrast microscope. High concentrations ( $\geq 10^6 \text{ cm}^{-2}$ ) of rectangular pyramidal hillocks were found for HgSe and  $\text{Hg}_{1-x}\text{Cd}_x\text{Se}$  films grown at 100°C on both (100) CdZnTe and (100) ZnTe substrates. By contrast, layers grown at the same temperature on (211)B CdZnTe and (211)B ZnTe substrates exhibited hillock-free, specular surfaces. This behavior parallels that of HgTe and  $\text{Hg}_{1-x}\text{Cd}_x\text{Te}$  epilayers grown by MBE,<sup>9–11</sup> which indicates that similar processes are involved in the nucle-

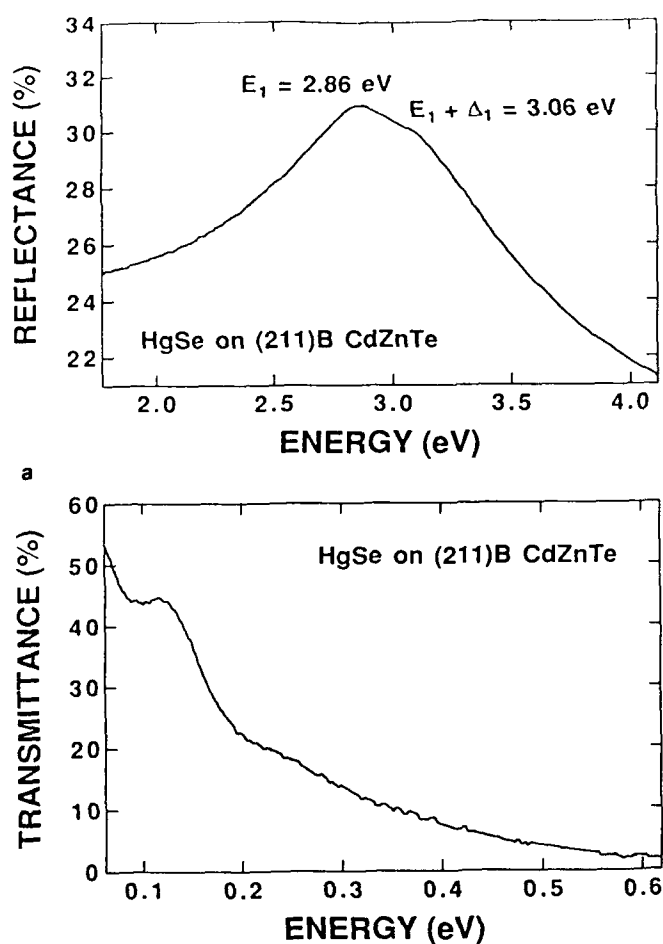


Fig. 1. Room temperature (a) reflectance and (b) transmittance of a 1 μm-thick HgSe layer.

ation of pyramidal hillocks for both the mercury-based selenides and tellurides.

Double-crystal x-ray rocking curve measurements were performed on all the epilayers included in this study. The full width at half maximum (FWHM) of the (400) or (422) diffraction peak served as a measure of structural perfection of the layer, depending on the substrate orientation employed. In the case of HgSe layers 1–1.5  $\mu\text{m}$  thick grown at 100°C, FWHMs in the range 370–740 arc-s, 370–560 arc-s, and 270–320 arc-s, were measured for films grown on (100) CdZnTe, (100) ZnTe, and (211)B CdZnTe, respectively. All of the above FWHMs values correspond to single film peaks, confirming the epitaxial nature of these layers. The smallest FWHMs were obtained for the (211)-oriented films. The same trend holds true for Hg<sub>1-x</sub>Cd<sub>x</sub>Se thin films grown at 100°C, with FWHMs of (211)-oriented layers being at least a factor of two smaller than those of (100)-oriented layers. For Hg<sub>1-x</sub>Cd<sub>x</sub>Se layers with x-values ranging from 0.12 to 0.34, FWHMs of the (422) diffraction peak were between 350 and 400 arc-s.

### Optical Properties

Room temperature transmittance and reflectance measurements from 2–20  $\mu\text{m}$  (0.62–0.062 eV) and 0.3–0.7  $\mu\text{m}$  (4.13–1.77 eV), respectively, were performed on the HgSe and Hg<sub>1-x</sub>Cd<sub>x</sub>Se epilayers. As the cadmium concentration x is varied from 0 to 0.34 in Hg<sub>1-x</sub>Cd<sub>x</sub>Se crystals, the band structure at the  $\Gamma$ -point changes from that of a perfect semimetal to that of a direct-gap semiconductor. In bulk Hg<sub>1-x</sub>Cd<sub>x</sub>Se, the transitional composition was reported to occur at x = 0.11 at 4.2K.<sup>12</sup> In addition, higher order transitions (i.e. E<sub>1</sub> and E<sub>1</sub> +  $\Delta_1$ ) shift to higher energies with increasing x-value. As a consequence, optical measurements of this type can provide a convenient and nondestructive way to determine cadmium concentrations in Hg<sub>1-x</sub>Cd<sub>x</sub>Se samples.

Figure 1 shows reflectance and transmittance spectra obtained for a 1  $\mu\text{m}$ -thick HgSe layer grown at 100°C on a (211)B CdZnTe substrate. In Fig. 1a, a broad reflectance peak, associated with the E<sub>1</sub> interband transition along the L direction of the Brillouin zone, is observed at 2.863 eV. On the high energy side of the spectrum, a slight shoulder attrib-

uted to the E<sub>1</sub> +  $\Delta_1$  transition is seen at 3.06 eV. No other features are present in the room temperature spectrum, and no evidence of the e<sub>1</sub> +  $\Delta_1$  ( $\approx$ 2.75 eV) or A ( $\approx$ 2.40 eV) transitions, observed by Borisov et al.<sup>13</sup> in reflectance spectra of bulk HgSe (x  $\leq$  0.4), was found. The energy position of the E<sub>1</sub> transition found in the present study is in good agreement with the value of 2.85 eV determined by Borisov et al., although it is somewhat higher than the value obtained by Kumazaki<sup>14</sup> through ellipsometric measurements performed on Bridgman-grown samples (2.797 eV). On the other hand, our value of the E<sub>1</sub> +  $\Delta_1$  transition falls below that of both Refs. 13 (3.17 eV) and 14 (3.159 eV). These differences may be related to residual strain effects associated with nonlattice-matched

Table I. E<sub>1</sub> Reflectance Peak Energies for  
MBE-Grown Hg<sub>1-x</sub>Cd<sub>x</sub>Se (x = 0–0.34)

| Sample | E <sub>1</sub> Peak Energy (eV) | X-Value |
|--------|---------------------------------|---------|
| A      | 3.159                           | 0.34    |
| B      | 3.088                           | 0.27    |
| C      | 2.985                           | 0.17    |
| D      | 2.921                           | 0.11    |
| E      | 2.863                           | 0.00    |

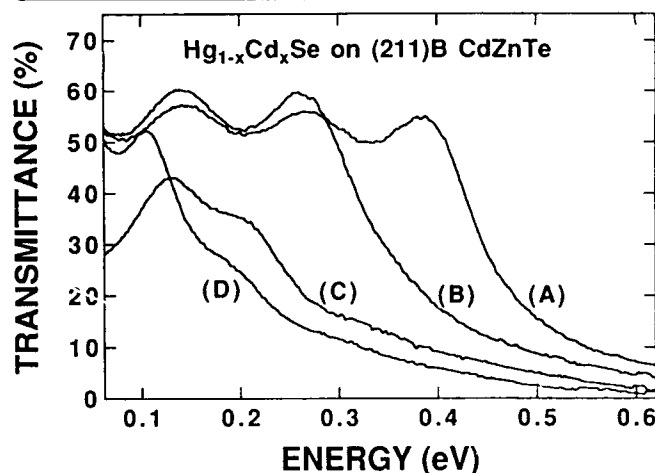


Fig. 2. Room temperature transmittance of Hg<sub>1-x</sub>Cd<sub>x</sub>Se thin films with x-values of (A) 0.34, (B) 0.27, (C) 0.17, and (D) 0.11.

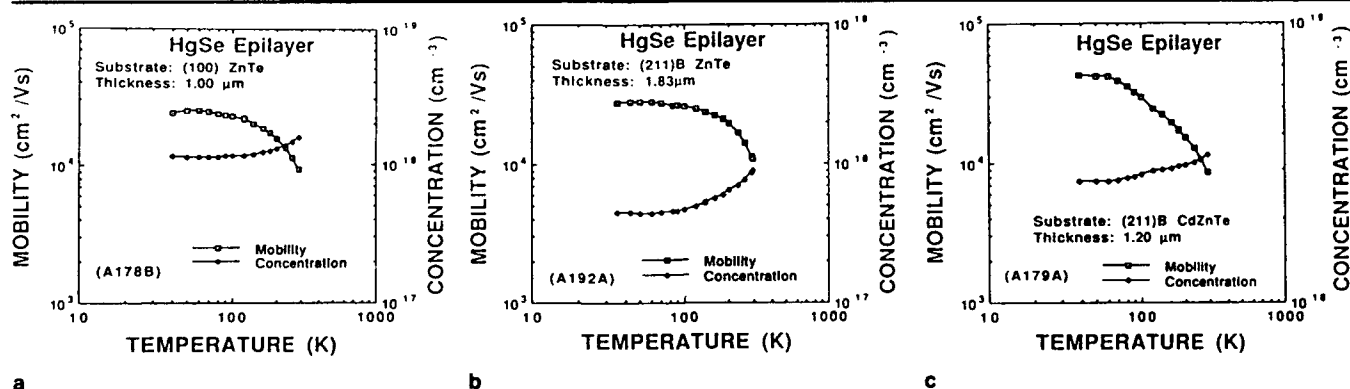


Fig. 3. Hall data for HgSe epilayers grown on (a) (100) ZnTe, (b) (211)B ZnTe, and (c) (211)B CdZnTe substrates.



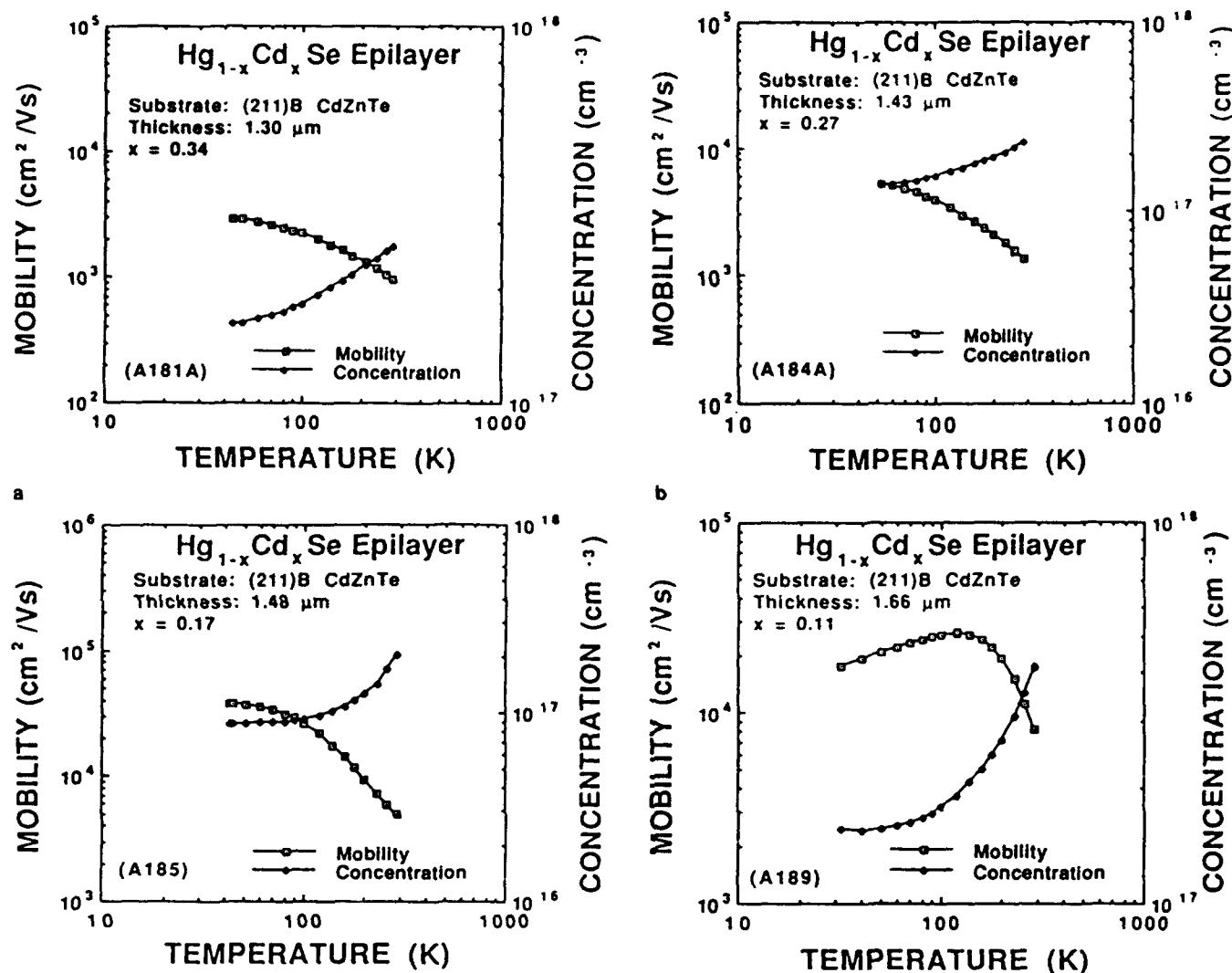


Fig. 4. Hall data for  $\text{Hg}_{1-x}\text{Cd}_x\text{Se}$  samples with  $x$ -values of (a) 0.34, (b) 0.27, (c) 0.17, and (d) 0.11.

heteroepitaxy. An IR transmittance spectrum of this HgSe film is shown in Fig. 1b. Note that absorption occurs over the entire IR region, reflecting the semi-metallic nature of HgSe. Features in the spectrum are due to thin film interference effects associated with heteroepitaxy, and do not reflect optical properties of MBE-grown HgSe layer.

Reflectance spectra of a series of  $\text{Hg}_{1-x}\text{Cd}_x\text{Se}$  samples of varying  $x$ -values grown at  $100^\circ\text{C}$  on (211)B CdZnTe substrates were also measured. The peak position of the  $E_1$  transition shifts toward higher energies with increasing cadmium content. The cadmium concentrations of the epilayers were determined using a quadratic fit of the  $E_1$  reflectance peak position as a function of  $x$ -value based on the work of Borisov et al.<sup>13</sup> for bulk  $\text{Hg}_{1-x}\text{Cd}_x\text{Se}$  samples:

$$E_1 \text{ (eV)} = 0.8x^2 + 0.71x + 2.85 \quad (1)$$

The  $x$ -value results are summarized in Table I.

Room-temperature transmittance measurements were also performed on the same series of  $\text{Hg}_{1-x}\text{Cd}_x\text{Se}$  samples (A, B, C, and D) in order to probe the funda-

mental absorption edge region of these epilayers. The transmittance vs energy spectra obtained are shown in Fig. 2. As expected, a shift in the absorption edges toward lower energies occurs with decreasing cadmium concentration ( $x$ -value).

### Electrical Properties

Van der Pauw Hall effect measurements were performed between 30 and 300K using an applied magnetic field of 0.3 T. All of the HgSe and  $\text{Hg}_{1-x}\text{Cd}_x\text{Se}$  epilayers studied exhibited n-type conduction over the entire temperature range. Figure 3 shows the electron concentration and mobility curves as a function of temperature for HgSe thin films grown on (100) ZnTe (a), (211)B ZnTe (b), and (211)B CdZnTe (c) substrates. For these layers, the low temperature (30K) carrier concentrations are in the range  $0.45\text{--}2.7 \times 10^{18} \text{ cm}^{-3}$ , and increase with increasing temperature, reaching  $0.9\text{--}3.5 \times 10^{18} \text{ cm}^{-3}$  at 300K. Low temperature mobilities range from  $2.5\text{--}4.2 \times 10^4 \text{ cm}^2/\text{Vs}$  and decrease to values of  $0.9\text{--}1.2 \times 10^4 \text{ cm}^2/\text{Vs}$  at room temperature. All three samples show deviations from

intrinsic behavior, with carrier concentrations being virtually independent of temperature below 100K. In addition, fairly large variations are observed in the values of the low temperature mobility and carrier concentration measured for different samples. Similar observations have been reported by Lehoczky et al.<sup>15</sup> for bulk samples grown by the traveling molten-zone technique. Based on the results of a Hall effect data analysis conducted on several as-grown and annealed samples, they attribute the observed large mobility and carrier concentration variations to high densities of stable neutral defects as well as ionized donors nucleated during the growth process. On the other hand, Kumazaki et al.<sup>16</sup> conducted a thermodynamic analysis of data obtained on bulk HgSe samples annealed under varying conditions of mercury and selenium vapor pressures. They concluded that the dominant electrically active point defects in HgSe are doubly ionized mercury interstitials (which act as donor impurities). Other electrically active impurities identified in Ref. 16 include ionized selenium vacancies (donors) and ionized mercury vacancies (acceptors). In our study, we also observed a clear correlation between the growth conditions of the HgSe layers and their electrical properties. In particular, the low temperature electron concentration of these layers tends to increase as the Hg/Se ratio is increased, in agreement with the previously cited studies.<sup>15,16</sup> This is illustrated in Figs. 3b and c for two (211)-oriented HgSe films, A179A and A192A, grown at 100°C with Hg/Se ratios of 180 and 120, respectively.

Figure 4 shows the mobility and carrier concentration vs temperature curves for  $\text{Hg}_{1-x}\text{Cd}_x\text{Se}$  layers grown on (211)B CdZnTe substrates at 100°C. The x-values for these samples, measured by the reflectance technique described above, were 0.34 (a), 0.27 (b), 0.17 (c), and 0.11 (d). All four samples were found to be n-type over the entire temperature range investigated. Low temperature carrier concentrations were in the range  $0.9\text{--}1.5 \times 10^{17} \text{ cm}^{-3}$  and increased to  $1.5\text{--}4.0 \times 10^{17} \text{ cm}^{-3}$  at room temperature. Note that the low temperature carrier concentrations fall within a rather narrow range for all four samples, consistent with a small variation in the Hg/Se ratio used during the growth of these layers (120–130).

Room temperature mobilities were within the range  $1\text{--}8 \times 10^3 \text{ cm}^2/\text{Vs}$ , and decreased as the cadmium concentration (x-value) increased. This behavior is qualitatively consistent with the expected increase of compositional-disorder scattering at room temperature as the x-value of  $\text{Hg}_{1-x}\text{Cd}_x\text{Se}$  becomes larger.<sup>6</sup> At low temperatures, the mobility of these samples ranged within  $3 \times 10^3$  and  $4 \times 10^4 \text{ cm}^2/\text{Vs}$ . In this temperature

range, neutral and ionized impurity scattering have a predominant effect on the carrier mobility.<sup>6</sup>

## SUMMARY

We have reported the first epitaxial HgSe and  $\text{Hg}_{1-x}\text{Cd}_x\text{Se}$  thin films grown by MBE. The structural, optical, and electrical properties of the epilayers were investigated. Results comparable to those of bulk-grown single crystals were obtained. Correlations between growth parameters, such as growth rate, growth temperature and Hg/Se flux ratio, and the layers physical properties were also discussed. Controlled doping studies were not attempted. Such studies, coupled with improvements in structural quality, would constitute the next logical step in the development of these materials for IR applications, particularly if p-type doping were to be achieved.

## ACKNOWLEDGMENTS

The authors wish to thank J. Matthews for help with MBE system maintenance and Z. Yang for help with some of the Hall effect measurements. This work was supported by U.S. Office of Naval Research grant N00014-92-J-1644.

## REFERENCES

1. T.C. Harman, W.H. Kleiner, A.J. Strauss, G.B. Wright, J.G. Mavroides, J.M. Honig and D.H. Dickey, *Solid State Commun.* 2, 305 (1964).
2. J.P. Faurie and A. Million, *J. Cryst. Growth* 54, 582 (1981).
3. J.W. Cook, Jr., K.A. Harris and J.F. Schetzina, *Mater. Res. Soc. Symp. Proc.* 90, 419 (1987).
4. J.P. Faurie, A. Million, R. Boch and J. L. Tissot, *J. Vac. Sci. Tech. A* 1, 1593 (1983).
5. Z.A. Munir, D.J. Meschi and G.M. Pound, *J. Cryst. Growth* 15, 263 (1972).
6. C.R. Whitsett, J.G. Broerman and C.J. Summers, *Semiconductors and Semimetals*, eds. R. K. Willardson and A. C. Beer (Academic, New York, 1981), Vol. 16. (Editor note: This reference is the entire book).
7. D.A. Nelson, J.G. Broerman, C.J. Summers and C.R. Whitsett, *Phys. Rev. B* 18, 1658 (1978).
8. N. Samarth, H. Luo, J.K. Furdyna, S.B. Qadri, Y.R. Lee, A.K. Ramdas and N. Otsuka, *J. Electron. Mater.* 19, 543 (1990).
9. R.J. Koestner and H.F. Schaaake, *J. Vac. Sci. Technol.* A6, 2834 (1988).
10. K.A. Harris, T.H. Myers, R.W. Yanka, L.M. Mohnkern, R. W. Green and N. Otsuka, *J. Vac. Sci. Technol.* A8, 1013 (1990).
11. Y. Lansari, Z. Yang, S. Hwang, F.E. Reed, A.T. Sowers, J.W. Cook, Jr. and J.F. Schetzina, *J. Cryst. Growth* 111, 720 (1991).
12. J. Stankiewicz, *Phys. Status Solidi* (b) 93, 113 (1979).
13. I.N. Borisov, P.S. Kireev, V.M. Mikhailin and V. M. Bezborodova, *Sov. Phys. Semicond.* 5, 734 (1971).
14. K. Kumazaki, *J. Cryst. Growth* 101, 687 (1990).
15. S.L. Lehoczky, J.G. Broerman, D.A. Nelson and C.R. Whitsett, *Phys. Rev. B* 9, 1598 (1974).
16. K. Kumazaki, E. Matsushima and A. Odajima, *Phys. Status Solidi* (a) 37, 579 (1976).

# CdTe and HgTe Surface Growth Kinetics for Molecular and Metalorganic Molecular Beam Epitaxy

R.G. BENZ, II, B.K. WAGNER, A. CONTE, and C.J. SUMMERS

Electro-Optics and Physical Sciences Laboratory, Georgia Tech Research Institute, Atlanta, GA 30332

The surface growth kinetics of CdTe and HgTe have been investigated during molecular and metalorganic molecular beam epitaxy. The surface growth kinetics was studied through in-situ measurements of the growth rate as a function of flux ratio and substrate temperature on the (001), (111)B, and (211)B CdTe surface orientations. For the (001) and (111)B CdTe growth kinetics, the existence of low binding energy surface precursor sites was proposed for both molecular and atomic growth species before lattice incorporation. Intensity oscillations were observed during HgTe growth on misoriented (111)B surfaces and during CdTe growth on the (211)B orientation. The (211)B surface reconstructions displayed both vicinal and singular surface characteristics, depending on the growth flux ratio.

**Key words:** CdTe, HgTe, MBE, MOMBE, surface growth kinetics, substrate orientation effects

## INTRODUCTION

An understanding of the fundamental mechanisms involved in HgCdTe epitaxial growth is necessary for the production of material for advanced infrared applications. With knowledge of the growth processes, the variation in material properties with growth conditions can be predicted and hence optimized. In addition, advanced device concepts which rely on high quality heterojunction interfaces, such as superlattices, will benefit from increased knowledge of the growth kinetics as applied to interface abruptness and stoichiometry. Metalorganic molecular beam epitaxy (MOMBE) is especially applicable to studies of the surface growth kinetics because of the control offered over the chemical growth species, along with its ability for rapid, accurate, and reproducible control of the growth fluxes. In addition, MOMBE has already demonstrated high quality HgCdTe ( $x = 0.1-0.3$ )<sup>1</sup> growth and iodine doping of CdTe.<sup>2</sup>

This paper describes a study of the surface kinetics that controls the growth of CdTe and HgTe. The surface growth kinetics was studied by measurements of the growth rate as a function of the substrate temperature and flux ratio for different surface orientations. The growth rates were evaluated in-situ

using reflection high energy electron diffraction (RHEED) intensity oscillation measurements. The measurements to be presented were made possible because of the exceptional growth flux control and reproducibility offered by the MOMBE system, coupled with the rapid and highly accurate in-situ growth rate measurements by RHEED intensity oscillations. After a description of the experimental procedures, the results of the growth kinetics studies on the (001), (111)B, and (211)B surfaces are presented, followed by a discussion of the experimental data.

## EXPERIMENTAL PROCEDURES

The MOMBE system used for these studies has been described previously.<sup>3,4</sup> It consists of a Varian GEN II MBE which was modified by the addition of gas handling systems for constituent and doping gases, specially designed gas injectors, a mercury pressure controlled vapor source (Hg-PCVS) for highly accurate mercury flux control,<sup>5</sup> and a special pumping system. The gas flow rates were controlled by MKS Instruments 1150B pressure-based flow controllers. The tellurium organometallic source was diisopropyltelluride (DipTe) and the cadmium source was either diethylcadmium (DeCd) or dimethylcadmium (DmCd), supplied by Air Products, Inc. The MOMBE system also has conventional MBE solid sources for CdTe, cadmium, and tellurium. The pumping system con-

(Received October 12, 1992; revised January 15, 1993)

sists of a Varian cryopump and a Balzers MBE series turbomolecular pump for handling the high gas loads. This combination gave a background pressure of  $10^{-6}$  to  $10^{-5}$  Torr during MOMBE CdTe growth.

The organometallic source gases were decomposed in separate high temperature injectors to remove any cracking dependence on substrate temperature. The operating temperatures of the gas injectors were optimized through quadrupole mass spectrometry studies and in-situ growth rate measurements as a function of the injector temperatures.<sup>6</sup> The group VI injector was operated at 650°C. Quadrupole mass spectrometry studies showed complete decomposition of DipTe into monomer tellurium and organic by-products, with negligible dimer tellurium formation. Similarly, the group II injector was operated at 1100°C for DmCd and at various constant temperatures between 500–800°C for DeCd. These conditions produced complete DmCd decomposition and partial DeCd decomposition into cadmium and organic by-products.<sup>6</sup> DeCd was used in the initial experiments, but its use was discontinued because of room temperature DeCd decomposition in the organometallic bubbler. This effect resulted in a mixture of low pressure DeCd and high pressure organic gases in the bubbler, a condition which made proper operation of the pressure-based flow controller impossible and, therefore, prevented determination of the optimum operating conditions for DeCd cracking. No such problems were observed for DmCd. Experiments performed originally with DeCd were repeated using DmCd. Identical results for the tellurium surface kinetics experiments were observed when using DmCd compared to DeCd, however, reproducible cadmium surface kinetics experiments were only obtained with DmCd. Dimer tellurium was provided by the tellurium solid source.

Chemo-mechanically polished CdTe substrates were obtained from Johnson Matthey, Texas Instruments, and II-VI, Inc. Substrates whose morphology showed minimum orange peel were used. These substrates were degreased and then given an additional chemo-

mechanical polish in a low concentration bromine:ethylene glycol solution before loading into the growth chamber and annealing under a monomer tellurium flux at temperatures between 300–320°C. This procedure yielded high quality surfaces at the atomic scale, and no buffer layer growth was required before the RHEED experiments.<sup>6</sup> The substrate temperature was calibrated using the tellurium-condensation technique.<sup>7</sup>

The RHEED system consisted of an electron gun, video camera, and a computer equipped with a digitizing board and software for RHEED analysis. The video signal was fed into a 386 IBM-compatible computer where the diffraction pattern was analyzed by a RHEED Data Acquisition System developed by Epitaxial Growth Systems.<sup>8</sup> An Imaging Technology PC Vision Plus framegrabber board was used with Image Pro Plus software for acquiring eight-bit greyscale images of the RHEED diffraction patterns.

The uncertainty in the growth rate from intensity oscillation measurements was estimated to be  $\pm 3\%$ . Low growth rates ( $<1$  ML/s) were used to minimize surface degradation and to allow rapid surface recovery after growth. The surfaces were kept under a monomer or dimer tellurium flux at substrate temperatures greater than 250°C to prevent surface degradation. In addition, flux transients were prevented by not shuttering the solid tellurium furnace. Because the MKS 1150 flow controllers are based on pressure control, their calibration is sensitive to the downstream conductance. Therefore, the growth flux vs apparent flow rate was calibrated using in-situ growth rate measurements at the growth conditions which yielded unity incorporation for monomer tellurium, dimer tellurium, and cadmium.

## RESULTS

### (001) CdTe Surface

The CdTe growth rate at a set cadmium flux was measured as a function of the monomer tellurium flux at different substrate temperatures. Figure 1 shows the (001) CdTe growth rate for a cadmium flux of 0.6 ML/s at substrate temperatures between 200–320°C. Also included in the figure are the growth conditions, defined by the ratio of the growth fluxes, and the growth regimes, which are defined by the derivative of the growth rate with respect to monomer tellurium flux,  $dR_{Te}$ . At low monomer tellurium fluxes, the growth rate increased linearly with increasing monomer tellurium flux ( $dR_{Te} = 1$ ) and did not increase with increasing cadmium flux. For these growth conditions, the cadmium-stabilized  $c(2 \times 2)$  surface reconstruction was observed.<sup>9</sup> Because the growth rate was independent of the cadmium flux, these growth conditions defined the tellurium-limited, saturated growth regime, where the temperature dependence of the growth rate in this regime is representative of the tellurium species surface kinetics. From Fig. 1, the tellurium-limited, saturated growth rate was independent of temperature below 300°C.

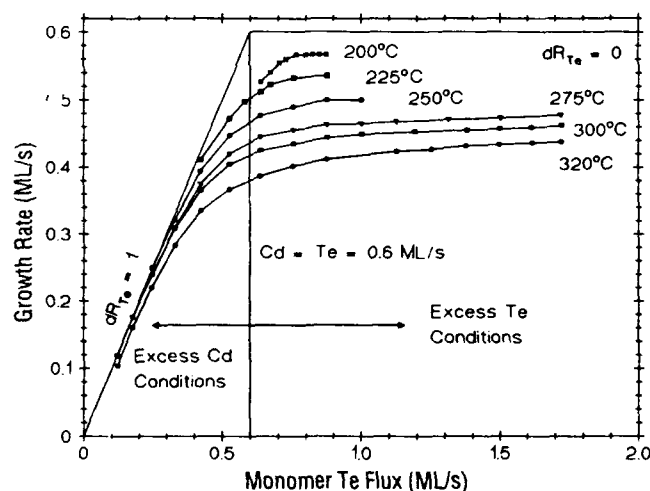


Fig. 1: (001) CdTe growth rate for a constant cadmium flux as a function of monomer tellurium flux for substrate temperatures between 200–320°C.

At large tellurium fluxes, the growth rate was constant ( $dR_{Te} = 0$ ) and independent of the tellurium flux. Although the experiment depicted in the figure corresponded to a set cadmium flux, the growth rate was found to vary linearly with the cadmium flux in this regime. The surface reconstruction under these growth conditions was the tellurium-stabilized ( $2 \times 1$ ).<sup>9</sup> Because the growth rate was independent of the tellurium flux, these growth conditions defined the cadmium-limited, saturated growth regime, where the temperature dependence of the growth rate in this regime is representative of the cadmium species surface kinetics. The cadmium-limited, saturated growth rate decreased with increasing temperature for all temperatures studied, in contrast to tellurium-limited growth. Therefore, complete cadmium incorporation did not occur over this temperature range. The growth rate data displayed Arrhenius type behavior, with an activation energy of 51 meV.

Because the tellurium-limited, saturated growth rate was independent of temperature below 300°C, measurements were performed at higher substrate temperatures. Figure 2 shows the tellurium-limited growth rate as a function of reciprocal temperature from 275–400°C for two different tellurium fluxes. The growth rate data was divided into three temperature regions. Below 305°C, the growth rate was constant with temperature, indicating complete incorporation of all incident tellurium atoms. The growth rate decreased between 305°C and 360°C with an activation energy of 0.15 eV. The growth rate decreased rapidly at substrate temperatures greater than 360°C, which resulted from insufficient cadmium flux to insure saturated growth conditions and prevent sublimation. The activation energy in this regime was 1.9 eV, in agreement with the CdTe sublimation energy measured by Arias et al.<sup>10</sup> Measurements were also performed with dimer tellurium and the data were qualitatively similar to the case when monomer tellurium was used. Below 300°C, the growth rate was constant with temperature and all incident dimer tellurium molecules were incorporated. At temperatures between 300°C and 350°C, the growth rate decreased with an activation energy of 85 meV, approximately half of the monomer tellurium activation energy. For substrate temperatures greater than 350°C, the growth rate decreased rapidly due to CdTe sublimation with an activation energy of 1.9 eV.

### (111)B CdTe Surface

Metalorganic molecular beam epitaxy growth of CdTe on the (111)B surface was also investigated. The substrates were unintentionally misoriented by approximately 0.3°, as assessed by RHEED measurements. Long lasting intensity oscillations with rapid surface recovery [compared to the (001) surface] were observed on the (111)B surface for temperatures as low as 190°C. The (111)B growth rate at a set cadmium flux was studied as a function of the tellurium flux for substrate temperatures from 200°C to 300°C, in analogy to the experiment depicted in Fig. 1. The

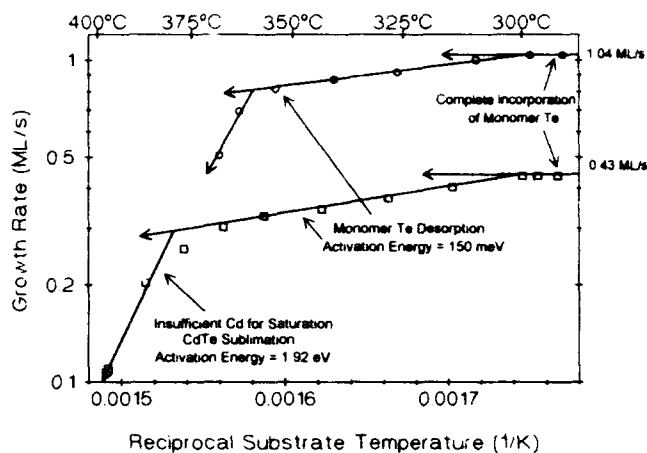


Fig. 2. (001)CdTe growth rate as a function of reciprocal substrate temperature under tellurium-limited, saturated growth conditions for two different monomer tellurium fluxes.

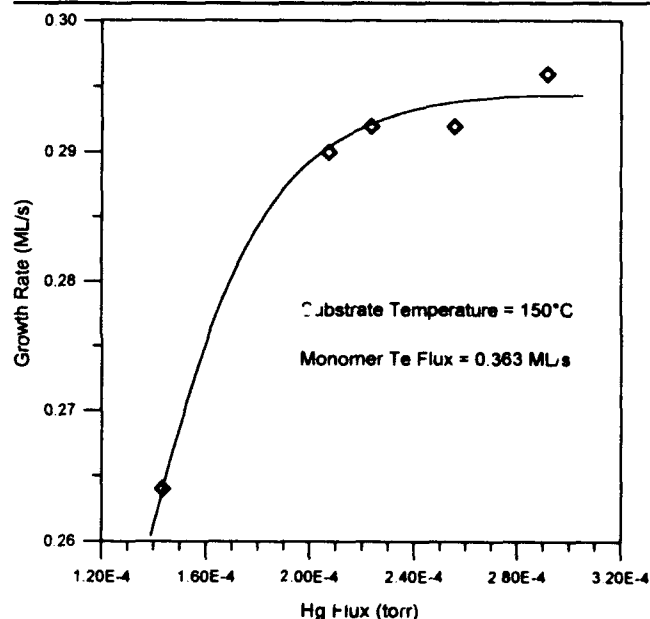


Fig. 3. HgTe growth rate on the (111)B surface at 150°C as a function of mercury flux for a set monomer tellurium flux.

surface kinetics on the (111)Te and the (001) were qualitatively identical. However, the cadmium-limited, saturated growth rate decreased with temperature with an activation energy of 0.12 eV, compared to 51 meV on the (001) surface.

Metalorganic molecular beam epitaxy growth of HgTe was also studied on the slightly misoriented (111)B surface. For temperatures greater than 170°C, intensity oscillations were not observed, presumably because the tellurium adatom mobility was sufficient for step flow growth.<sup>11</sup> Intensity oscillations with up to 28 periods were observed for substrate temperatures between 165–110°C, indicating a smooth atomic growth front during (111)B HgTe growth. Figure 3 shows the HgTe growth rate at 150°C, as a function of the mercury flux for a set monomer tellurium flux of 0.363 ML/s. As shown, the growth rate initially increases with increasing mercury flux, and then pla-

tenus to a constant value for mercury fluxes  $> 2.6 \times 10^{-4}$  Torr. Notice that the tellurium-limited, saturated growth rate at 150°C was 0.294 ML/s, 19% less than the incident tellurium flux. In addition, this unexpected decrease in the saturated HgTe growth rate was not a result of scattering of the tellurium beam by the large mercury flux, because the maximum tellurium-limited, saturated growth rates for CdTe and HgTe (which were obtained at the lowest growth temperatures for each material) were equal.<sup>12</sup>

### (211)B CdTe Surface

Recently, RHEED studies were initiated on the (211)B CdTe surface. This orientation is favored for HgCdTe growth because of the small mercury fluxes required and the lower twin density on the (211)B compared to the (111)B and (001) surfaces.<sup>13</sup> This bulk surface termination can be visualized as a vicinal surface composed of three atomic wide (111)B terraces in the  $\langle 111 \rangle$  direction, with step edges parallel to the  $\langle 011 \rangle$  direction. Two different surface structures were observed during growth of CdTe and HgCdTe by MOMBE. A cadmium-stabilized surface was observed during CdTe barrier layer growth in a HgCdTe/CdTe superlattice structure. The diffraction pattern in the  $\langle 011 \rangle$  direction was similar to that observed for a vicinal surface, which implies a bulk termination for the cadmium-stabilized surface. However, during HgCdTe growth and tellurium annealing of the CdTe surface at 300°C, the diffraction pattern from the surface was different from that during CdTe growth and was characteristic of a singular, step free surface. This observation implies that (211)B HgCdTe growth occurs on the tellurium-stabilized surface, as opposed to (001) growth which occurs on the cadmium-stabilized surface. Intensity oscillations were observed on the (211)B surface. Figure 4 shows the intensity

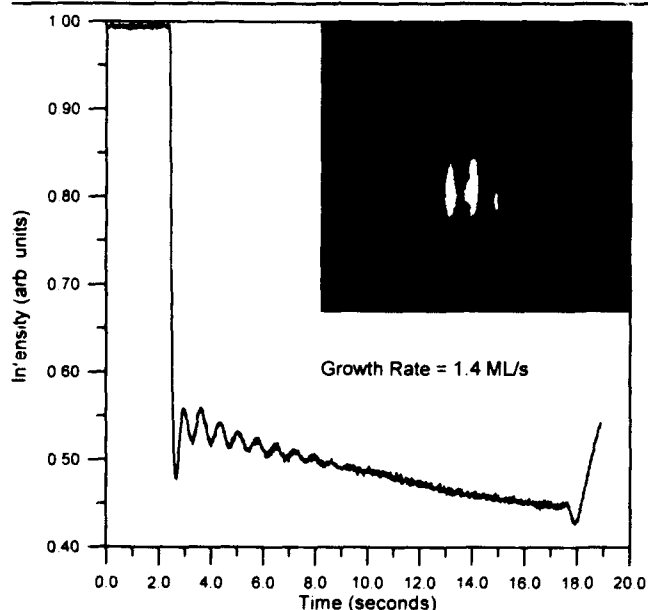


Fig. 4. Reflection high energy electron diffraction intensity oscillations during MOMBE growth of CdTe at 310°C on the (211)B CdTe surface. Inset shows the RHEED diffraction pattern in the  $\langle 011 \rangle$  direction.

oscillations during MOMBE growth of CdTe at 310°C, with an inset picture of the diffraction pattern in the  $\langle 011 \rangle$  direction. The growth rate was 1.4 ML/s and the surface was tellurium-stabilized during growth.

### DISCUSSION

The growth rates measured under saturated conditions decreased with increasing temperature and displayed Arrhenius type behavior on the (001) surface. The growth rate decrease with temperature is postulated to result from desorption of the limiting species from the surface. However, the desorption activation energies were very small for all the growth species. For comparison, the heat of vaporization is ~1 eV for elemental cadmium and tellurium and the CdTe sublimation energy is 1.92 eV, as measured by Arias et al.<sup>10</sup> In addition, the desorption activation energies measured by Benson et al. for chemisorbed surface species on a static CdTe surface were 5.1 eV and 1.9 eV for cadmium and tellurium, respectively.<sup>14</sup> The desorption activation energies measured in this study and those referenced in this work are summarized in Table I. Examination of the data from MBE CdTe growth shows a similar temperature dependence for the MBE growth rate,<sup>10,11</sup> which confirms that the small activation energies measured in this work are not unique to MOMBE growth, or result from the interaction of organic species with the surface, but rather are intrinsic to the CdTe surface processes.

An explanation for the small desorption activation energies is that the growth species, whether atomic or molecular, adsorb into weakly bound precursor states on the surface. From these precursor states the growth species can either desorb from the surface or incorporate into the CdTe lattice. The explanation that the small desorption activation energies result from precursor state adsorption is supported by results from GaAs growth kinetic studies, which show that the molecular arsenic species exist in a low binding energy precursor state before GaAs incorporation.<sup>15</sup> However, the small desorption activation energies are quite unexpected for the atomic cadmium and tellurium species, because atomic species are expected to directly chemisorb onto a surface, with precursor states usually occurring only for the adsorption of molecular species or inert gas atoms.<sup>16</sup> Therefore, these results suggest that a different surface kinetic effect is operative during the MBE growth of II-VI compounds as compared to III-V materials.

The observation that the monomer and dimer tellurium desorption activation energies were not equal strongly suggests that dimer tellurium molecules must exist as dimers on the surface, rather than dissociating into monomers after adsorption and that, similarly, monomer tellurium must exist on the surface and desorb as a monomer. If dimer tellurium did desorb from the surface during growth using monomer tellurium, no difference would be expected in the desorption activation energies measured for monomer and dimer tellurium-limited growth. Therefore, it is

**Table I. CdTe and HgTe Surface Growth Kinetics for Molecular and Metalorganic Molecular Beam Epitaxy**

| Growth Species | Surface Processes                             |  |                                |   |
|----------------|---|--|--------------------------------|---|
|                | Desorption of Growth Species (this work) (eV) | Thermal Desorption from Static Surface <sup>9</sup> (eV) | Sublimation <sup>10</sup> (eV) | He-Ne Laser Illumination <sup>17</sup> (T<300°C) (eV) |
| Monomer Te     | 0.15  | —  | —                              | 0.15  |
| Dimer Te       | 0.085   | 1.9  | 1.92                           | —   |
| Cd             | 0.051 (001)<br>0.12 (111)B                    | 5.1  | 1.92                           | 4.3   |

Note: Summary of experimental activation energies are for CdTe growth processes on the (001) surface, unless otherwise noted.

concluded that for either monomer or dimer tellurium growth both species adsorb, exist separately on the surface, and also desorb as monomers or dimers, respectively. This behavior suggests that the material properties of HgCdTe will be affected by the different tellurium incorporation processes into the crystal. However, this hypothesis remains to be verified through the correlation of material properties of HgCdTe grown with the different tellurium species. Notice that the small desorption activation energies measured during growth should not be directly compared to those measured on a static surface by Benson et al.,<sup>9</sup> which corresponds to the loss of chemisorbed tellurium from a tellurium-stabilized surface. In the study presented here, the tellurium growth species desorb principally from a cadmium-stabilized surface because of the large cadmium flux required to maintain tellurium-limited, saturated growth conditions.

The 150 meV monomer tellurium desorption activation energy is also equal to the tellurium desorption energy under He-Ne laser illumination, as measured by Benson, et al.<sup>17</sup> In those experiments, the time required for a static tellurium-stabilized surface to convert to a static cadmium-stabilized surface was measured as a function of substrate temperature under He-Ne laser illumination, to yield the tellurium desorption activation energy. Since no growth occurred, the change in surface reconstruction is associated with the desorption of the outer chemisorbed tellurium layer from the surface. This technique was used to determine the tellurium and cadmium thermal desorption activation energies described in the previous paragraph.<sup>9</sup> Pure thermal desorption of tellurium has an activation energy of 1.9 eV, with the desorption species assumed to be the dimer molecule. With He-Ne laser illumination at a photon energy of 1.96 eV, which is approximately resonant with the pure thermal tellurium desorption energy, a photo-assisted tellurium desorption energy of 150 meV was measured. This result implies that laser excitation breaks the surface tellurium dimer bonds and promotes the tellurium atoms into the proposed precursor state, from which they desorbed as the monomer rather than the dimer. This supposition remains to be verified by determination of the

desorbing tellurium species under laser illumination using a technique such as mass spectrometry.

Notice that despite the factor of two difference in desorption activation energies for dimer tellurium compared to monomer tellurium, both species were completely incorporated at saturated conditions under 300°C. In contrast, complete cadmium incorporation under saturated conditions was not observed, despite similar energies for cadmium (51 meV) and dimer tellurium (85 meV). This behavior suggests a kinetic limitation to cadmium incorporation and shows that the cadmium and tellurium incorporation kinetics are not simply related to the precursor state binding energy. A possible explanation for the cadmium data is that cadmium incorporation is controlled by adatom incorporation at surface steps and not by nucleation on the terraces. This phenomenon has been observed by RHEED intensity oscillation measurements during GaAs MBE growth.<sup>11</sup>

The surface kinetics during MOMBE growth on the (111)B surface parallels those on the (001). The difference in the cadmium desorption activation energies implies that cadmium exists in a more tightly bonded site on the (111)Te surface, compared to the (001) surface, which agrees with observations for mercury incorporation during HgCdTe growth on the (111)Te.<sup>18</sup> The HgTe results are more difficult to interpret. An important observation is that the HgTe intensity oscillations disappear at temperatures greater than 170°C on the 0.3° misoriented surface. Therefore, the surface diffusion length is approximately 714 Å for monomer tellurium and shows that excellent heterointerfaces are possible with MOMBE. These measurements indicate that monomer tellurium desorption occurs from the (111)B surface for temperatures greater than 115°C. This conclusion is supported by the measurements of Myers et al.,<sup>19</sup> where a 10–40% enhancement in the (111)B HgCdTe growth rate was observed under laser illumination. Since the incident, growth rate controlling tellurium flux is constant irrespective of laser illumination, the HgCdTe growth rate can only increase under laser illumination if additional tellurium flux, which normally desorbs from the surface, is incorporated. However, another possible explanation for these results has been advanced recently, where the apparent

growth rate decrease on a vicinal surface results from the loss, by incorporation at the step edges, of the growth species which normally nucleate on the terraces.<sup>11</sup> Which mechanism is operative must be verified by ex-situ measurements of layer thicknesses. As opposed to the HgTe results, CdTe growth on misoriented (111)B and the (001) surfaces yielded intensity oscillations, which suggest decreased adatom mobility for CdTe relative to HgTe. Further research of MOMBE growth kinetics on vicinal surfaces is currently under way.

### CONCLUSIONS

This research has examined the surface growth kinetics for CdTe and HgTe during MOMBE and MBE growth. It is apparent that the kinetics differ significantly from those observed during III-V growth, and therefore III-V results must be applied with caution to CdTe and HgTe growth. These differences also point to the need for additional investigations of the surface growth kinetics, for further improvement in HgCdTe material properties. This argument is highlighted by the rapid progress made in III-V and silicon-based IR detectors, which have benefited from the increased understanding of the surface growth kinetics for these materials.<sup>20, 21</sup>

This research has also demonstrated experimentally the importance of steps on the growth of CdTe and HgCdTe. This is especially true for the (211)B surface. Although the (211)B surface yields high quality material, little quantitative research on the surface growth kinetics has been performed. Progress in this area has been hampered by a lack of in-situ growth characterization techniques. Therefore, the observation of intensity oscillations is an important step toward characterizing the surface processes on the (211)B surface. To this end, research on the adatom surface mobility is currently being pursued to determine the optimum growth conditions for (211)B superlattice structures.

### ACKNOWLEDGMENTS

The authors thank Johnson Matthey, Texas Instruments, and II-VI, Inc. for providing substrate material and Professor Tom Myers of West Virginia

University for assistance with the (211)B measurements. This research was supported by the Wright Research Development Center under contract no. F33615-89-C-1066, and by the Internal Research Program of the Georgia Tech Research Institute.

### REFERENCES

1. B.K. Wagner, D. Rajavel, R.G. Benz, II and C.J. Summers, *J. Vac. Sci. Technol.* B 9, 1656 (1991).
2. D. Rajavel and C.J. Summers, *Appl. Phys. Lett.* 60, 2231 (1992).
3. R.G. Benz II, B.K. Wagner and C.J. Summers, *J. Vac. Sci. Technol.* A8, 1020 (1990).
4. R.G. Benz II, B.K. Wagner, D. Rajavel and C.J. Summers, *J. Cryst. Growth* 111, 725 (1991).
5. B.K. Wagner, R.G. Benz and C.J. Summers, *J. Vac. Sci. Technol.* A7, 295 (1989).
6. R.G. Benz, II, "Surface Growth Kinetics in Molecular Beam Epitaxy and Gas Source Molecular Beam Epitaxy of CdTe," Ph.D. Dissertation, Georgia Institute of Technology, 1992.
7. D. Rajavel, F. Mueller, J.D. Benson, B.K. Wagner, R.G. Benz II and C.J. Summers, *J. Vac. Sci. Technol.* A8, 1002 (1990).
8. J.S. Resh, K.D. Jamison, J. Strozier and A. Ignatiev, *Rev. Sci. Instrum.* 61, 771 (1990).
9. J.D. Benson, B.K. Wagner, A. Torabi and C.J. Summers, *Appl. Phys. Lett.* 49, 1034 (1986).
10. J.M. Arias and G. Sullivan, *J. Vac. Sci. Technol.* A5, 3143 (1987).
11. B.A. Joyce, J. Zhang, T. Shitara, J.H. Neave, A. Taylor, S. Armstrong, M.E. Pemble and C.T. Foxon, *J. Cryst. Growth* 115, 338 (1991).
12. A. Million, L. DiCioccio, J.P. Gailliard and J. Piagnet, *J. Vac. Sci. Technol.* A6, 2813 (1988).
13. R.J. Koestner and H.F. Schaafe, *J. Vac. Sci. Technol.* A6, 2834 (1988).
14. L. Ulmer, H. Mariette, N. Nagnea and P. Gentile, *J. Cryst. Growth* 111, 711 (1991).
15. C.T. Foxon and B.A. Joyce, *Surf Sci.* 64, 293 (1977).
16. H.J. Kreuzer and Z.W. Gortel, *Physisorption Kinetics*, Berlin: Springer Verlag (1986).
17. J.D. Benson, D. Rajavel, B.K. Wagner, R. Benz II and C.J. Summers, *J. Cryst. Growth* 95, 543 (1989).
18. S. Sivananthan, X. Chu, J. Reno and J.P. Faurie, *J. Appl. Phys.* 60, 1359 (1986).
19. T.H. Myers, R.W. Yanka, K.A. Harris, A.R. Reisinger, J. Han, S. Hwang, Z. Yang, N.C. Giles, J.W. Cook, Jr., J.F. Schetzina, R.W. Green and S. McDevitt, *J. Vac. Sci. Technol.* A7, 300 (1989).
20. R. People, J.C. Bean, C.G. Bethea, S.K. Sputz and L.J. Peticolas, *Appl. Phys. Lett.* 61, 1122 (1992).
21. S.R. Kurtz, A. Katz, R.M. Biefeld, R.L. Gunshor and R.J. Malik, *MRS Symp. Proc.* 216, 163 (1991).



# Growth and Characterization of Hot-Wall Epitaxial CdTe on (111) HgCdTe and CdZnTe Substrates

J.H. TREGILGAS, C.-F. WAN, and H.-Y. LIU

Central Research Laboratories, Texas Instruments, Inc., Dallas, TX 75265

Thin CdTe films were deposited by hot-wall epitaxy (HWE) on (111) HgCdTe and CdZnTe substrates at temperatures from about 140 to 335°C. X-ray rocking curves were used to show that crystal quality of the CdTe (111)B films improved as substrate temperature increased from 140 to about 250°C. Rocking curve values for full width at half maximum (FWHM) decreased from 2–4 degrees at 140–150°C to less than 100 arc-s at 250°C, and a FWHM of 59 arc-s was the lowest value observed near 250°C. The FWHM of the HWE CdTe was found to be insensitive to growth rate below about 400 Å/min, but increased to four degrees at 1250 Å/min. X-ray diffraction confirmed that films grown on the B-face at higher temperatures were epitaxial, but contained a significant volume fraction, 35% to 50%, of rotational in-plane twins. Electron microscopy confirmed a coarse twin density, and photoluminescence spectra showed an absence of excitonic emission in the HWE films. Simultaneous growth on two (111) HgCdTe substrates with different surface polarities between 230°C and 335°C showed that deposition rate on the A-face decreased relative to that on the B-face as temperature increased. Films grown on the B-face exhibited better surface morphologies than those grown on the A-face.

**Key words:** CdTe, CdZnTe, HgCdTe, hot-wall epitaxy, twinning in thin films

## INTRODUCTION

Deposition of CdTe layers on HgCdTe surfaces has become increasingly more important as a method for passivating surfaces of photodiodes.<sup>1–3</sup> Presence of this CdTe layer can reduce surface leakage and improve diode performance, especially at longer wavelengths. Detectors passivated with ZnS can be limited by a high interface recombination, but epitaxial CdTe reduces the number of dangling bonds which contribute to generation centers, recombination centers, and traps at the interface.

CdTe can be deposited by a variety of techniques, but deposition by hot-wall epitaxy<sup>4</sup> (HWE) is especially well suited for CdTe since it congruently evaporates over a range of temperatures,<sup>5</sup> and can produce high quality layers at a relatively low cost. Hot-wall epitaxy has been used to grow heteroepitaxial CdTe on a variety of substrates, including GaAs,<sup>6–9</sup> silicon,<sup>9</sup> and fluoride substrates,<sup>10–12</sup> and more recently, has been used to grow high quality homo-

epitaxial CdTe films on (111)B CdTe surfaces.<sup>13</sup> Our work was aimed at understanding some of the factors which can influence the quality of HWE CdTe films deposited on HgCdTe and CdZnTe (111) surfaces. Most films were grown on tellurium-rich (111)B substrates, but growth on the cadmium-rich (111)A substrates was also examined. X-ray diffraction techniques were used to establish the crystalline quality of the as-grown HWE films as a function of growth temperature and substrate surface polarity.

## EXPERIMENTAL PROCEDURES

CdTe HWE films were grown in a dynamically pumped quartz tube using a stoichiometric polycrystalline CdTe source between 590°C and 605°C with the substrates held at temperatures between about 140°C and 335°C. Substrates were either Hg<sub>(1-x)</sub>Cd<sub>x</sub>Te ( $x = 0.23$ ) grown by liquid phase epitaxy (LPE) or CdZnTe with about a 0.05 mole fraction of ZnTe. The (111)B substrate face was typically used, but some films were grown on the (111)A face for comparison. All substrates were prepared by pad polishing with Br-methanol solutions, followed by

(Received October 12, 1992; revised January 15, 1993)

either spray or static etching with Br-methanol, and rinsing. Samples were loaded in the vertical position with a backfilled inert gas ambient of either hydrogen or nitrogen to aid thermal equilibration. Deposition on the substrate was initiated by pumping on the growth tube with a cryopump, and vacuum levels improved during growth to about  $10^{-5}$  Torr. Vacuum levels better than about  $10^{-4}$  Torr are necessary to increase the mean free path and achieve deposition on the substrate located about 30 cm from the CdTe source. Growth rates as high as 1250 Å/min were examined, but typical growth rates were about 100–350 Å/min. Film thicknesses were generally in the 1000–4000 Å range, but films as thick as 7.5  $\mu\text{m}$  were also produced. Thicknesses were measured with either a Dektak, ellipsometry, or by counting colored interference fringes when a portion of the LPE substrate

was masked.

Films were characterized by a variety of techniques, including x-ray powder diffraction and single crystal diffraction techniques for obtaining x-ray rocking curves. Rocking curves were performed with copper  $K\alpha$  radiation using the symmetric (111) reflection to measure crystal quality and with the asymmetric (224) reflections to confirm epitaxial growth and measure in-plane twinning. The rocking curve full width at half maximum (FWHM), peak position and peak intensities were determined using Jandel Scientific's Peakfit Program. Photoluminescence (PL) characterization was performed at 4.2K using a 0.1 W/cm<sup>2</sup> argon laser (514.5 nm). Bright field and dark field optical microscopy were also performed both before and after annealing, and transmission electron microscopy (TEM) was used to examine an annealed HWE film.

## RESULTS AND DISCUSSION

The CdTe films were, initially, grown on (111)B CdZnTe and HgCdTe substrates at about 150°C and were characterized by both optical and x-ray techniques. Surface morphologies were generally specular, but some films exhibited a slight surface haze, possibly due to surface preparation. A typical x-ray powder diffraction scan, shown in Fig. 1, revealed a strong (111) reflection from both the film and underlying substrate. No additional peaks were observed indicating the absence of both polycrystalline CdTe and second-phase tellurium. Single-crystal diffraction confirmed the 150°C deposited CdTe layers were either epitaxial or highly textured film, and values of the full width at half maximum (FWHM) from x-ray rocking curves were found to be in the two to four degree range.

Two CdTe films were grown on (111)A CdZnTe substrates at 150°C for comparison to growth on the B-face. Single crystal diffraction of the first film, which was about 1  $\mu\text{m}$  thick, failed to show a reflected peak intensity from the CdTe layer, thereby suggesting that the CdTe was not epitaxial and did not have a strong (111) texture. Powder diffraction of the second film, which was 0.6  $\mu\text{m}$  thick, showed a strong (111) reflection, but small secondary peaks indicating some CdTe polycrystallinity in this film were also observed. An x-ray rocking curve from this second sample had a FWHM of about 1.1 degrees. Surface morphology of these two A-faced samples produced a much heavier haze compared to the B-face samples. Under dark-field optical microscopy, the CdTe films grown on the A-face, shown in Fig. 2, had a granular appearance, in contrast to featureless films on the B-face.

Subsequent growth on (111)B substrates was performed using higher substrate temperatures. Characteristics from several films grown on CdZnTe substrates at 270–300°C are presented in Table I. This table shows that much lower FWHM values were achieved by using higher substrate temperatures, but that high growth rates can also affect the FWHM, as sample #21 indicates. The measured four degree

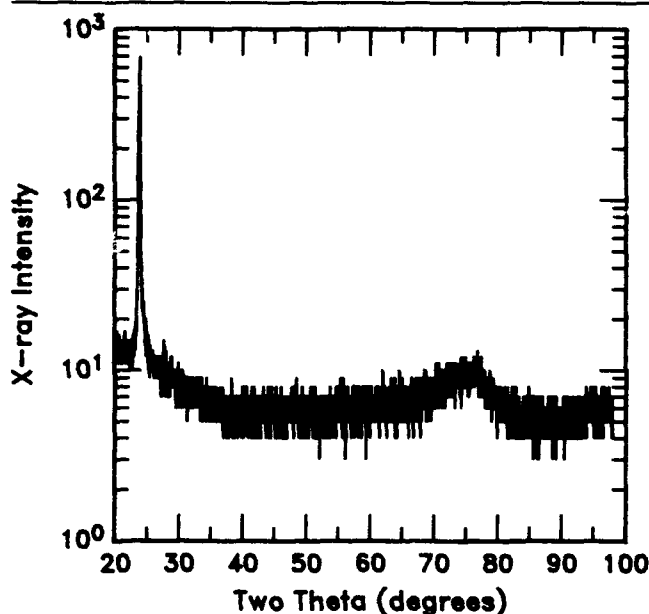


Fig. 1. X-ray powder diffraction of 150°C HWE CdTe film after annealing at 400°C for 1 h showing (111) reflection (left) from both the CdTe and underlying substrate and a broad (333) reflection (right).



Fig. 2. Dark-field optical micrograph of HWE CdTe film grown on (111)A surface showing granular texture (400X).

**Table I. High Temperature Growth on (111)B CdZnTe**

| Spl. | Growth Temp. °C | Growth Thick. $\mu\text{m}$ | Rate $\text{\AA}/\text{min}$ | FWHM deg. | FWHM (arc-s) |
|------|-----------------|-----------------------------|------------------------------|-----------|--------------|
| 32   | 300             | 1.2                         | 167                          | 0.058     | (209")       |
| 20   | 300             | 2.4                         | 393                          | 0.130     | (468")       |
| 21   | 271             | 7.5                         | 1250                         | 4         | (14400")     |

**Table II. High Temperature Growth on (111)B HgCdTe**

| Spl. | Growth Temp. °C | Thick. $\text{\AA}$ | Growth Rate $\text{\AA}/\text{min}$ | FWHM deg. | FWHM (arc-s) |
|------|-----------------|---------------------|-------------------------------------|-----------|--------------|
| 46   | 247             | 18000               | 300                                 | 0.094     | (338")       |
| 48   | 247             | 4200                | 167                                 | 0.016*    | (59")*       |
| 48   | 247             | 4200                | 167                                 | 0.091*    | (327")*      |
| 59   | 202             | 2524                | 393                                 | 0.072*    | (262")*      |
| 59   | 202             | 2524                | 393                                 | 0.492*    | (1771")*     |
| 71   | 250             | 2500                | 167                                 | 0.021     | (74")*       |
| 71   | 250             | 2500                | 167                                 | 0.144     | (520")*      |
| 75-1 | 230             | 1250                | 125                                 | 0.045     | (162")       |
| 75-2 | 230             | 1250                | 125                                 | 0.048     | (172")       |
| 79   | 295             | 2565                | 122                                 | 0.022     | (79")        |
| 117  | 300             | N.M.                | N.M.                                | 0.012*    | (43")*       |
| 117  | 300             | N.M.                | N.M.                                | 0.021*    | (76")*       |
| 120  | 297             | 2200                | 147                                 | 0.023     | (84")        |

\*Denotes 2 peaks fitted to the HWE CdTe rocking curve.

FWHM for this 271°C film is in the same range as values measured on 150°C films produced at much lower growth rates. Although samples #32 and #20 show that FWHM increased slightly with growth rate, this difference has not been shown to be significant.

Based on the above CdZnTe results, higher growth temperatures were evaluated on HgCdTe substrates using growth rates below 400 $\text{\AA}/\text{min}$ . Characteristics from some films grown on HgCdTe substrates are shown in Table II. This table shows that higher growth temperatures produced significantly lower values for FWHM compared to the two to four degrees observed for films grown at 150°C. Rocking curve data for sample #48 in Table II is shown in Fig. 3. The FWHM for this CdTe film is 59 arc-s compared to about 53 arc-s for the HgCdTe substrate. Secondly, to achieve the best curve fit to the epitaxial film an additional broad peak with a FWHM of 327 arc-s has been added. The double FWHM values for samples #48, #59, #71, and #117 in Table II reflect this additional fit to a broad peak. Presence of this second fitted peak implies possible grading in some CdTe films, but other samples (i.e. #46, #75-1, #75-2, #79, and #120 in Table II) needed only a single peak to obtain the best fit of the epitaxial CdTe layer. A comparison of two samples, #46 and #48, from the Table II shows that thick film (#46), which did not allow x-ray penetration to the interface, had a single

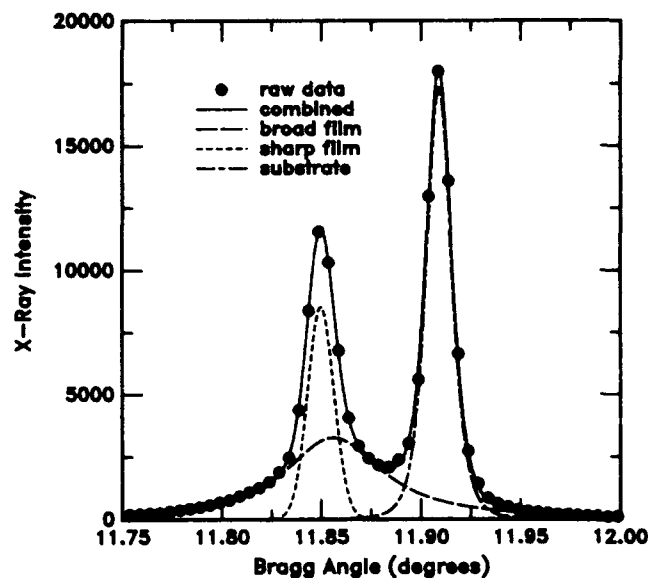


Fig. 3. Rocking curve for 247°C HWE CdTe film showing a FWHM of 59" (left), 53" for the HgCdTe substrate (right), and a broad second peak fitted to the CdTe with a FWHM of 327".

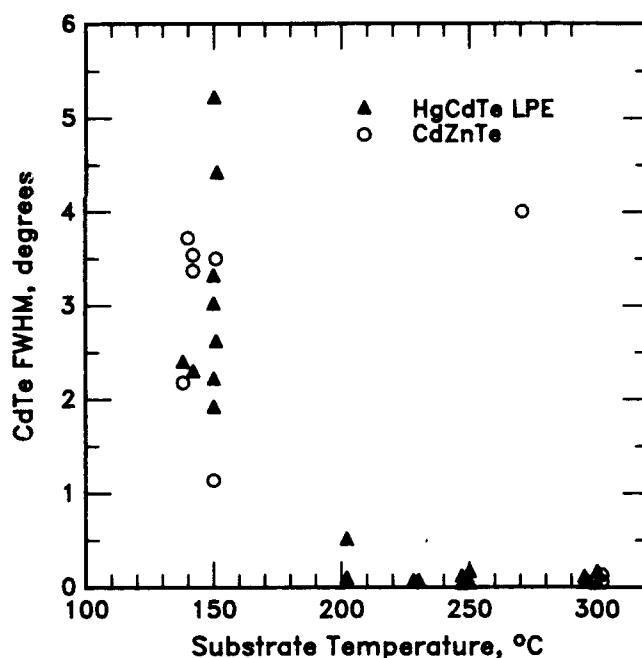


Fig. 4. Full width at half maximum of HWE CdTe as a function of substrate temperature for both CdZnTe and HgCdTe (111)B substrates. Growth rates were below 400 $\text{\AA}/\text{min}$  except for the lone data point in the upper right which was at 1250 $\text{\AA}/\text{min}$ .

FWHM value of 338 arc-s which is close to the second FWHM value of 327 arc-s fitted to thinner sample (#48). This observation suggests that, for samples which have been fitted by two peaks, the fraction of the epitaxial CdTe producing the smallest FWHM value occurs at the interface adjacent to the substrate. In addition, it implies that films may become more defective as thickness increases, and other thick films, such as those in Table I, may have lower FWHM values at the CdTe-substrate interface.

Collectively, data for growth on both CdZnTe and

HgCdTe substrates as a function of temperature are summarized in Fig. 4. This data shows that quality of deposited CdTe layers, as measured by the decrease in the value of FWHM, improves significantly when the substrate temperature increases from 150 to 200°C. Heating substrates above 200°C produces only a slight additional improvement in crystal quality, and no additional improvement is observed with substrate temperatures above 250°C.

The influence of substrate polarity on growth rate was determined for different growth temperatures by simultaneously growing on both the A and B (111) faces of LPE substrates during the same growth run. These results are summarized in Table III. The

**Table III. CdTe Growth vs (111) Face Polarity**

| Substrate Temp. °C | (111)A Thick. Å | (111)B Thick. Å | A-Face/B-Face Thick. Ratio |
|--------------------|-----------------|-----------------|----------------------------|
| 230                | 2252            | 2348            | 0.96                       |
| 250                | 2130            | 2577            | 0.83                       |
| 295                | 767             | 2565            | 0.30                       |
| 335                | 0-300*          | 3950            | <0.08                      |

\*Visual estimate; thickness could not be accurately measured.



Fig. 5. Transmission electron micrograph of 3000Å CdTe HWE film grown on HgCdTe at 150°C and annealed at 350°C for 1 h showing coarse rotational in-plane twinning.

decrease in thickness with increasing substrate temperature for the cadmium-rich A-face suggests that the cadmium sticking coefficient on this face decreases with temperature above about 230°C. X-ray rocking curves taken on both samples grown at 295°C were fitted to single peaks having FWHM values of 79 arc-s and 306 arc-s for the B-face and A-face films, respectively. Again, surface morphologies of the A-face films were hazy and had a granular texture, such as shown in Fig. 1, but the films on the B-faces were specular and did not show granularity.

Rocking curves from B-face CdTe films obtained with the asymmetric (224) reflections have confirmed that high temperature films are epitaxial and contain in-plane twins. The ratio of rocking curve intensities taken on a sample before and after rotation by 180 degrees about the [111] provides a measure of the in-plane twins.<sup>14</sup> The volume fraction of the in-plane twin in HWE CdTe films ranged from about 0.35 to 0.50; however, this does not provide a measure of the twin size. Transmission electron microscopy (TEM) was performed on a (250°C) HWE sample after annealing for an hour at 350°C in nitrogen. The TEM micrograph in Fig. 5 shows twins were coarse grained, which may result during the HWE growth process. Particles characteristic of second-phase tellurium appear to be absent in this sample. Variations in twin density have been observed within the films examined by TEM. The density of twins in this sample was much lower than in both heavily twinned (111)B CdTe grown by MBE on bulk CdTe substrates<sup>15</sup> and in (111) CdTe grown by MOCVD on GaAs.<sup>16</sup>

Hall measurements of as-grown HWE CdTe were employed to investigate the stoichiometry of the as-deposited CdTe films. Several attempts to characterize thick 150°C CdTe deposits on p-type CdZnTe substrates were unsuccessful due to contacting problems, but measurements at both room temperature and 77K were obtained on a 9000Å CdTe film on a  $2 \times 10^{15}$  p-type HgCdTe LPE substrate. This CdTe film showed n-type behavior with a carrier density in the  $2-5 \times 10^{18} \text{ cm}^{-3}$  range at both temperatures, and Hall mobilities of -864 and -2200  $\text{cm}^2/\text{v-sec}$  were measured at room temperature and 77K, respectively. The absence of a large change in carrier concentration upon cooling from room temperature to liquid nitrogen

**Table IV. Hall Measurements of Annealed HWE CdTe/HgCdTe Samples\***

| Sample # | Anneal Temp. °C | Anneal Ambient | 77K Hall Carrier Density, $\text{cm}^{-3}$ | Hall Mobility 77K, $\text{cm}^2/\text{V-s}$ |
|----------|-----------------|----------------|--|---|
| 254-1    | 250             | N <sub>2</sub> | $5.4 \times 10^{15}$ p                     | 639   |
| 86-1     | 300             | N <sub>2</sub> | $2.1 \times 10^{16}$ p                     | 503   |
| 254-4    | 300             | N <sub>2</sub> | $2.3 \times 10^{16}$ p                     | 583   |
| 86-2     | 350             | N <sub>2</sub> | $1.0 \times 10^{17}$ p                     | 405   |
| 254-1    | 400             | N <sub>2</sub> | $1.3 \times 10^{17}$ p                     | 324   |
| 86-3     | 300/250         | Hg             | $-2.4 \times 10^{14}$ n                    | -24900                                      |
| 93-1     | 300/250         | Hg             | $7.9 \times 10^{16}$ p                     | 289   |

\*HWE CdTe grown at either 200°C (254-1, -4) or 240-250°C, and CdTe thickness ranged between 1400-3000Å.

temperatures implies the p-type LPE substrate is not dominating conduction. The strong n-type behavior does not persist with post-deposition annealing, thereby, suggesting the stoichiometry of the as-grown HWE films may be dominated by defects produced during deposition. The as-grown CdTe thin-film result is drastically different from tellurium-rich bulk grown CdTe crystals which can be p-type due to excess metal vacancy concentrations, and which can become lightly n-type after high temperature annealing in a cadmium-rich atmosphere. The occurrence of n-type as-deposited HWE CdTe films also suggests that these films might be more cadmium-rich than as-grown bulk CdTe crystals.

CdTe capped LPE films have, also, been characterized by Hall after being annealed in either nitrogen or a saturated mercury atmosphere. Hall measurements from these samples are shown in Table IV. After annealing at 250–400°C in nitrogen for 1–4 h, samples were p-type, and acceptor concentrations were determined by the annealing temperature. Conduction in these annealed CdTe capped HgCdTe samples was dominated by much thicker HgCdTe layer rather than the thin CdTe layer after annealing, even when contacts are made directly to the CdTe layer. Samples annealed in a mercury ambient at 300°C for one hour followed by 250°C for 16 h were found to be either n-type or p-type. The occurrence of the compensated n-type sample (86–3) after the mercury anneal suggests excess tellurium in the HWE CdTe cap layer for this film is either very low or absent (since excess tellurium pins the HgCdTe to the high vacancy p-type side of the phase diagram), and mercury in-diffusion has reduced the intrinsic vacancy concentration of the HgCdTe LPE. The p-type sample (93–1) exhibits a higher acceptor concentration than expected from intrinsic metal vacancies which suggests a higher residual (extrinsic) acceptor density in the LPE film, or possible problems diffusing mercury through the CdTe layer. Others have used CdTe masks to make diodes with selective mercury in-diffusion,<sup>17</sup> but low mercury permeability of the CdTe may be related to excess tellurium within the film.

Surface morphologies of 150°C HWE CdTe on HgCdTe were examined before and after one hour anneals at 250–400°C in nitrogen by optical microscopy. Examination by dark field microscopy showed no change in surface quality for samples annealed at 250, 300, and 350°C. Samples annealed at 400°C, however, developed a granular surface appearance like that shown in Fig. 2. These results suggest that HWE CdTe films are stable below 350°C, but may undergo changes at higher temperatures possibly as the result of regrowth or interdiffusion.

Photoluminescence (PL) spectra from 4000 Å CdTe films deposited at different temperatures on (111)B HgCdTe LPE substrates were measured at 4.2 K and are shown in Figs. 6a and 6b. Deposition at 150°C, Fig. 6a, produced a broad deep level PL emission band at about 0.85 eV range with a relative peak intensity of 0.015, and near band transitions were absent. The

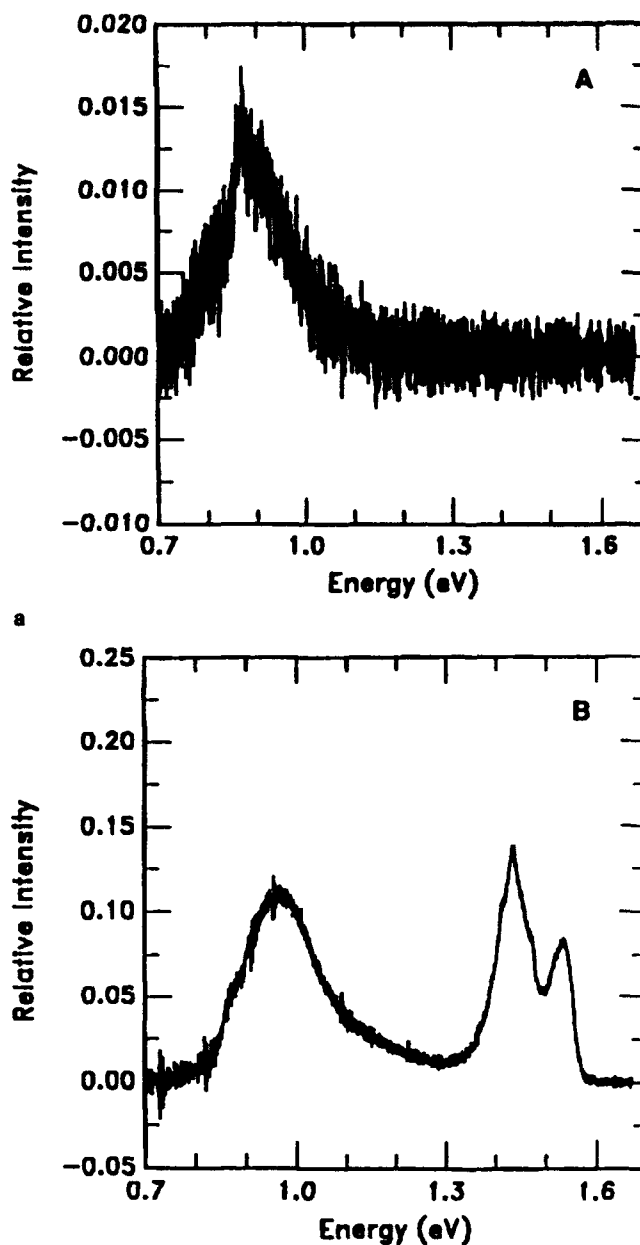


Fig. 6. Two 4.2 K PL spectra showing HWE CdTe films deposited on HgCdTe LPE substrates at different growth temperatures; (a) grown at 150°C, and (b) grown at 250°C.

low relative intensity for this band indicates a low quantum efficiency in this sample. Higher temperature deposition at 250°C, in Fig. 6b, shows both a broad deep level band at about 0.95 eV with a relative peak intensity of 0.12 and near band transitions at both 1.4 eV and 1.5 eV. Near band transitions at these energies are usually attributed to acceptor-donor complexes and free to bound transitions.<sup>18–20</sup> Excitonic transitions are still absent in Fig. 6b, but this sample shows much higher quantum efficiencies than the low temperature sample in Fig. 6a. The general broad spectral features observed in these as-deposited films tend to persist with further annealing; however, some sharpening and shifting of the peak maxima have

been observed. After annealing at 250°C for an hour in nitrogen, the relative intensity of the peak in Fig. 6a increased by a factor of three, while the peaks in Fig. 6b decreased as much as 27% to 36%. Higher temperature annealing of another 150°C HWE film for an hour at either 300 or 350°C in nitrogen introduced a broad emission band in the PL spectra at about 1.41 eV. The relative intensity of this band was higher after the 350°C anneal, but the overall quantum efficiency of this sample decreased upon annealing at 400°C. The absence of excitonic emissions in all the HWE CdTe thin films measured implies that they exhibit much higher defect densities than bulk CdTe crystals grown from the melt which show some excitonic emissions.<sup>19</sup>

### SUMMARY

The crystalline quality of epitaxial CdTe films grown by HWE on both CdZnTe and HgCdTe (111)B substrates has been observed to vary with substrate temperature. From x-ray rocking curves, values of FWHM for thin films grown at 140–150°C ranged from about two to four degrees; but above about 250°C, the FWHM decreased to less than 100 arc-s. The best CdTe film exhibited a FWHM of 59 arc-s compared to 53 arc-s for the HgCdTe substrate. X-ray measurements also showed that the CdTe films were epitaxial, but contained in-plane twinning rotated by 180 degrees within the films. The amount of in-plane twins measured was found to vary between 35 and 50% of the film. Transmission electron microscopy confirmed a coarse twin density, and the absence of excitonic emission in PL spectra implies much higher defect densities than typically observed in bulk CdTe crystals grown from melts. Simultaneous growth on A and B faces of (111) HgCdTe substrates between 230 and 335°C showed a decreasing thickness of films on the metal-rich A-face with higher substrate temperatures compared to those grown on the tellurium-rich B-face. Films grown on (111)B substrates were specular while those grown on the (111)A surfaces exhibited more surface haze and appeared granular with dark-field optical microscopy.

The microstructure of HWE CdTe films grown on (111) substrates is quite similar to those grown by both MOCVD and MBE. We believe that these epitaxial films may be superior to polycrystalline CdTe

deposited by evaporation or sputtering. In future investigations of HWE CdTe, films should be grown on other substrate orientations to reduce twin densities, and device measurements should be examined to assess the quality of the passivation interface.

### ACKNOWLEDGMENT

The authors would like to thank Dave C. Smith, Quinn Montague and Larry Presley for help with film characterization, Doris Hess and Dave Smith for sample preparation and film growth, and both Herb Schaaake and Walter Duncan for helpful discussions.

### REFERENCES

1. J.H.P. Maille and Andre Salaville, U.S. Pat. No. 4,132,999 (1979).
2. G. Sarusi, G. Cinader, A. Zemel, D. Eger and Y. Shapira, *J. Appl. Phys.* 73, 5070 (1992).
3. M.R. Krueger, E.E. Krueger, P.H. Zimmermann, M. Kestigian and M.H. Weiler, *Proc. IRIS Detector Specialty Conf.*, Aug. 1991.
4. A. Lopez-Otero, *Thin Solid Films* 49, 3 (1978).
5. A.J. Strauss, in *Proc. Int. Symp. Cadmium Telluride Mater. Gamma-Ray Detect.*, Strasbourg, France, 1971, Eds. P. Siffert and A. Cornet, (Strasbourg, France: Center de Recherches Nucleaires, 1971), pp. 1–31.
6. H. Sitter, K. Lischka, W. Faschinger, J. Wolfrum, H. Pascher, and J.L. Pautrat, *J. Cryst. Growth* 86, 377 (1988).
7. D. Schikora, H. Sitter, J. Humenberger and K. Lischka, *Appl. Phys. Lett.* 48, 1276 (1986).
8. K. Lischka, E.J. Fantner, T.W. Ryan and H. Sitter, *Appl. Phys. Lett.* 55, 1309 (1989).
9. R. Korenstein, P. Madison and P. Hallock, *J. Vac. Sci. Technol. B* 10, 1370 (1992).
10. J. Humenberger, H. Sitter, W. Huber, N.C. Sharma and A. Lopez-Otero, *Thin Solid Films* 90, 101 (1982).
11. H. Sitter, J. Humenberger, W. Huber and A. Lopez-Otero, *Solar Energy Mater.* 9, 199 (1983).
12. A. Lopez-Otero and W. Huber, *J. Cryst. Growth* 45, 214 (1978).
13. H. Tatsuoka, H. Kuwabara, Y. Nakanishi and H. Fujiyasu, *J. Appl. Phys.* 69, 6472 (1991).
14. R. Koestner, V. Lopes, R. Korenstein, S. Oguz, V. Kreismanis, H. Ehsani and I. Bhat, *J. Vac. Sci. Technol. B* 10, 1643 (1992).
15. H.F. Schaaake and R.J. Koestner, *J. Cryst. Growth* 86, 452 (1988).
16. J.E. Hails, E.J. Russel, A.W. Brinkman and J. Woods, *J. Cryst. Growth* 79, 940 (1986).
17. K.K. Parat, H. Ehsani, I.B. Bhat and S.K. Ghandi, *J. Vac. Sci. Technol. B* 9, 1625 (1991).
18. J.L. Pautrat, J.M. Francou, N. Magnea, E. Molva and K. Saminadayar, *J. Cryst. Growth* 72, 194 (1985).
19. D.E. Cooper, J. Bajaj and P.R. Newman, *J. Cryst. Growth* 86, 544 (1988).
20. W.M. Duncan, R.J. Koestner, J.H. Tregilgas, H.-Y. Liu and M.-C. Chen, *Mat. Res. Soc. Symp. Proc.* 161, 39 (1990).

# Substrate Issues for the Growth of Mercury Cadmium Telluride

R. TRIBOULET and A. TROMSON-CARLI

C.N.R.S., Laboratoire de Physique des Solides de Bellevue, 1, Place A. Briand,  
F-92195 Meudon-Cedex, France

D. LORANS and T. NGUYEN DUY

Société Anonyme de Télécommunications, 41, rue Cantagrel, F-75631 Paris  
Cedex 13, France

Close lattice matching and lattice compatibility with mercury cadmium telluride (MCT) make CdTe and related alloys ideal substrate materials for growth of MCT layers for the purpose of making high-performance second-generation infrared detectors. However, the limitations in the properties of CdTe and the difficulties in its bulk growth have prompted extensive research in the area of alternative substrates. Some basic relevant characteristics of substrates such as sapphire, GaAs, and silicon are compared and the possibilities and problems associated with each material are analyzed in the light of the most recent results in the field.

**Key words:** Alternative substrates, CdTe, epitaxy, GaAs, growth substrates, HgCdTe, infrared detector, sapphire, silicon

## INTRODUCTION

It is well known that the properties of mercury cadmium telluride (MCT) epitaxial layers, the possible architecture of subsequently fabricated devices, and their performance depend strongly on the characteristics of the substrates used. These include their chemical nature; their mechanical, thermal, optical, electrical, and crystallographic properties; and also their surface crystallographic orientation, purity, their surface state after cutting and subsequent surface treatment; and the sizes required. The epitaxial growth technique to be used and the kind of layer or structure to be grown are also among the questions to be taken into account, as well as the availability and price of the substrates. The choice of substrates is thus a complex multiparameter problem.

Close lattice match and lattice compatibility with MCT make CdTe an ideal substrate for growth of MCT layers for high-performance second-generation infrared detectors. However, the current lack of availability of high-quality, large-area CdTe sub-

strates is generally recognized as a main limitation on an efficient MCT detector technology and has prompted extensive research in the area of alternative substrates for epitaxial growth of MCT. Composite substrates such as CdTe/GaAs, CdTe/sapphire, CdTe/GaAs/Si, and more recently, CdTe/Si can now be viewed as prime candidates to replace bulk CdTe.

Some basic properties of these different materials, relative to their use as substrates, will be compared before analyzing the possibilities and problems of each material in the light of the most recent results.

## COMPARISON OF SOME BASIC PROPERTIES OF SUBSTRATES FOR MCT GROWTH

Several relevant characteristics of the materials have to be taken into account: lattice mismatch with MCT; chemical compatibility, in view of possible contamination from the substrate elements; transparency in the two optical IR windows in case of backside illumination; mechanical and thermal properties; and the possibility of monolithic electronic integration, are some of the factors to be considered in making the choice.

Table I. Comparison of Relevant Characteristics of Materials Used as MCT Substrates

|   | Materials       |                 |                                |                 |           |
|---|-----------------|-----------------|--------------------------------|-----------------|-----------|
|   | CdTe            | (Cd,Zn) Te4% Zn | Al <sub>2</sub> O <sub>3</sub> | GaAs            | Silicon   |
| Melting Point (°C)  | 1092            | 1088            | —                              | 1237            | 1412      |
| Thermal Conductivity (mWcm <sup>-1</sup> K <sup>-1</sup> )        | 55              | 55              | 419                            | 500             | 1235      |
| Vickers Hardness at 300K (kg mm <sup>-2</sup> )                   | 40              | 60              | 2500–3000                      | 360             | 1150–1330 |
| Lattice Constant (Å)  | 6.482           | 6.466           | —                              | 5.6532          | 5.4307    |
| Structure   | zincblende      | zincblende      | hexagonal                      | zincblende      | diamond   |
| Etch Pit Density (cm <sup>-2</sup> )                              | 10 <sup>5</sup> | 10 <sup>4</sup> | 4 × 10 <sup>3</sup>            | 10 <sup>3</sup> | 0         |
| Rocking Curve Width (arc-s)                                       | 60              | 20              | <60                            | 14              | 7         |
| Thermal Expansion Coefficient (10 <sup>-6</sup> K <sup>-1</sup> ) | 5.31            | —               | 5.0                            | 6.7             | 2.6       |
| Available Sizes (diam in)   | 2               | 2               | 2,3                            | 2,3             | 5         |

Some basic properties of the materials conventionally used as substrates for MCT are displayed in Table I (from Ref. 1). It stems from this comparison that from the mechanical, thermal, and crystallographic point of view (among the main criteria of choice of a substrate), the quality of CdTe is very poor. The improvement of its mechanical properties due to the incorporation of zinc, although significant, leaves it nonetheless far behind the other materials.

#### CdTe AND RELATED ALLOYS

Several reasons make CdTe an attractive substrate for MCT. The addition of a slight amount of zinc or selenium to CdTe not only allows a perfect lattice match to any Hg<sub>1-x</sub>Cd<sub>x</sub>Te composition by adjusting the Cd/Zn or Se/Te ratios but has been shown to reduce the density of dislocations and subgrain boundaries<sup>2,3</sup> and to improve the mechanical properties.<sup>4,5</sup> This improvement has been studied theoretically by means of a solution hardening model.<sup>4</sup> The transparency of CdTe in the two classical IR windows, 8–12 and 3–5  $\mu$ m, allows backside illumination and thus reduction of the noise of IR detectors and maximization of their quantum efficiency. The similarity in thermal expansion coefficients between the MCT layer and the CdTe substrate gives excellent resistance to thermal cycling. In addition, the chemical compatibility is a primary advantage. If auto-doping from the substrate takes place during epitaxial growth, the diffusing element is at least isoelectronic and does not alter the carrier concentration. The best high-performance IR devices, working at low temperature, have been obtained using good (Cd,Zn)Te substrates, whatever the epitaxial growth technique used.

These advantages are unfortunately balanced by severe drawbacks. In addition to the poor CdTe properties mentioned above, large CdTe crystals of high quality are extremely difficult to obtain routinely, although there has been much effort to improve CdTe crystal growth. This stems from several basic reasons:

- The low CdTe thermal conductivity makes it difficult to control the solid-liquid interface shape.
- The presence of Cd-Te pairs ("associates") in the liquid phase, coupled with a high degree of supercooling, makes the duality of overheating-super-

cooling difficult to solve and prevents the use of growth seeds.<sup>6</sup> In the case of large overheating, the seed is easily dissolved, while weak overheating will favor the presence of Cd-Te pairs in large density, making single-crystal growth difficult.

- Because of the high ionicity of the Cd-Te bond, it has been shown that the CdTe crystallographic structure could easily oscillate between hexagonal and cubic structures near the CdTe melting point, making CdTe very easily twinned when grown from the melt.<sup>1</sup>
- A cooperative alignment of certain dislocation components can give rise to tilts and rotations of the lattice, also inducing twinning.<sup>7</sup>

Additional problems that have to be taken into account include the following:

- The stoichiometry of the melt requires control of the cadmium vapor pressure—achieved by the modified Bridgman technique—to avoid the presence of tellurium precipitates. The Cd/Zn partial pressure has to be controlled in order to avoid not only tellurium but also zinc precipitates in the (Cd,Zn)Te alloys.
- In the case of the (Cd,Zn)Te or Cd(Te,Se) alloys, the zinc or selenium segregation along the growth direction leads to a gradual lattice constant change, preventing perfect lattice matching to MCT. This problem has been solved either by zinc and selenium co-doping,<sup>8</sup> taking advantage of the differences in effective segregation coefficients of zinc (1.35) and Se (0.9), or, in the case of (Cd,Zn)Te, by control of the Cd/Zn partial pressure.<sup>9</sup>
- The purity of the substrates is also of prime importance. It has been recently shown that electrical properties of MCT layers grown by MBE on commercially available CdTe and (Cd,Zn)Te substrates are controlled by impurities diffusing from the substrate.<sup>10</sup>
- Monolithic electronic integration cannot be envisaged with CdTe, although CdTe MESFETs have been successfully fabricated by photoassisted MBE.<sup>11</sup>
- Fast and significant characterization of CdTe substrates has been frequently stressed as difficult to achieve. A plethora of characterization



techniques has been applied to specify the properties of CdTe substrates, but have proved to be inadequate to consistently predict the performance of the IR devices grown on them. Three optical techniques have been recently proposed<sup>12</sup> for a fast electronic and structural assessment of CdTe substrates: room temperature IR transmission allows a fast evaluation of  $(N_D - N_A)$ , while light scattering IR tomography and scanning photoluminescence give images providing clear information on structural perfection.

The assessment of the properties of MCT layers, or of the devices made on the MCT layers grown on the CdTe substrates, remains the most significant and unquestioned procedure of substrate characterization, although extremely time consuming.

As a result of all these limitations and problems, CdTe substrates are very expensive. Their uncertain availability, due to poor reproducibility of the growth processes, their lack of uniformity, and their price are considered the major limitations to their use in industrial production.

However, actual breakthroughs have been achieved recently in the bulk crystal growth of CdTe. From a high-pressure Bridgman method (HPB), very large (diam. 10 cm, several kg) undoped semi-insulating ( $> 10^{11}$  ohm-cm)  $\text{Cd}_{1-x}\text{Zn}_x\text{Te}$  crystals ( $x = 0, 0.04$ , and  $0.20$ ) of high crystallographic quality (DCRC FWHM in the 10–15 arc-s range) and uniformity have been obtained by Aurora Technologies.<sup>13</sup> A seeded physical vapor transport (SPVT) method is used by Eagle Picher<sup>14</sup> to reliably produce single-crystal boules that have about 2 in diam and weigh as much as 320 g. The growth axis is  $\langle 111 \rangle$ ; typical DCRC FWHM values lie in the range 8.6–20 arc-s and are reported to be more uniform over the surface of the crystal when compared with Bridgman material. Real improvements have been also achieved in several laboratories in the horizontal Bridgman growth of CdTe.

Let us now consider typical results of epitaxial growth on these substrates.

The crystallographic properties of CdTe and (Cd,Zn)Te substrates can be achieved in homoepitaxial layers of sufficient thickness grown either by MBE,<sup>15,16</sup> by pulsed laser epitaxy,<sup>17</sup> or by LPE.<sup>18</sup> The same occurs for the MOVPE growth above 400°C of

MCT layers on lattice-matched CdSeTe and CdZnTe substrates, as reported by Bevan et al.<sup>19</sup> with DCRC widths comparable to the substrate (typically 25 arc-s, for MCT films deposited on CdZnTe substrates of 21 arc-s, which is the lowest value reported so far). Some degradation occurs more generally when growing CdTe or MCT layers by MOVPE on such substrates at lower temperature: DCRC FWHM of 67 arc-s for MCT on CdTe substrates<sup>20</sup> and 47 arc-s for MCT on lattice-matched Cd(Te,Se) substrates<sup>21</sup> have been reported, although the narrowest values lie generally in the range 70–80 arc-s.

## SAPPHIRE

Sapphire has been proposed and used as an alternative substrate for the growth of device-quality MCT layers for about a decade. It is an attractive candidate because of its high crystalline quality, low cost, robustness, availability in large areas, high electrical resistivity, high thermal conductivity, thermal expansion mismatch to silicon less than that of CdTe, and transparency in the infrared out to about 6  $\mu\text{m}$ . Moreover, the great uniformity in the dislocation distribution (with uniform high density of small dislocations) in CdTe layers grown on sapphire allows a very uniform junction depth to be prepared by ion implantation, leading to devices exhibiting a very high uniformity compared with those made in MCT/CdTe.<sup>22</sup> {111} CdTe layers on {0001} sapphire basal planes have been reported as deposited either by MBE<sup>23</sup> or by MOVPE,<sup>24–29</sup> or by a combination MOVPE/LPE.<sup>30,31</sup> Microtwins have been pointed out as common defects in the {111}Te face of CdTe grown by MOCVD on {0001} sapphire. Their density is reported to be reduced to be much less than 1% volume fraction by proper choice of operating conditions, and they are completely eliminated by annealing in the vicinity of 600°C.<sup>32</sup> The subsequent LPE step, in the case of a combination MOVPE-LPE, greatly improves the crystal quality and morphology of the layer.<sup>30</sup> The CdTe films grown by MBE are reported to be smooth and mirrorlike, with a featureless surface.<sup>23</sup>

Some characteristics of CdTe and MCT layers grown on sapphire substrates by MOVPE and LPE are displayed in Table II. The MOVPE layers exhibit 77K electron concentration significantly higher than those

Table II. Characteristics of MCT Layers Grown on CdTe/Sapphire Substrates by MOVPE and LPE

| $x_{\text{Cd}}$<br>( $\text{Hg}_{1-x}\text{Cd}_x\text{Te}$ ) | Growth<br>Tech.     | Thick.<br>( $\mu\text{m}$ ) | Uniformity<br>$\Delta x$ over 2 in<br>diam area | Epd<br>( $\text{cm}^{-2}$ ) | DCRC<br>FWHM<br>(arc-s) | $\mu_{77\text{K}}^*$ | $\mu_{300\text{K}}^*$ | $(N_D - N_A)_{77\text{K}}$<br>( $\text{cm}^{-3}$ ) | $(N_D - N_A)_{300\text{K}}$<br>( $\text{cm}^{-3}$ ) |
|--|---------------------|-----------------------------|---|-----------------------------|-------------------------|----------------------|-----------------------|--|---|
| 1  | MOVPE <sup>27</sup> | 8.9                         | —   | —                           | 56                      | —                    | —                     | —  | —   |
| 1  | MOVPE <sup>26</sup> | 8.4                         | —   | —                           | —                       | 1600                 | 950                   | —  | —   |
| 0.22   | MOVPE <sup>25</sup> | 13                          | —   | —                           | —                       | 47000                | —                     | $4 \times 10^{15}$                                 | $4 \times 10^{16}$                                  |
| 0.2  | MOVPE <sup>28</sup> | 1–14                        | —   | —                           | 96–330                  | —                    | $(5-800)10^2$         | —  | $10^{15}-10^{16}$                                   |
| 0.3  | MOVPE <sup>29</sup> | 10–12                       | 0.02  | —                           | —                       | 23000                | —                     | $(1-5)10^{15}$                                     | —   |
| 0.3  | LPE <sup>29</sup>   | 10–12                       | 0.002   | —                           | 60–108                  | 32000                | —                     | $5 \times 10^{14}$                                 | —   |
| 0.31   | LPE <sup>33</sup>   | 12–15                       | —   | $(5-9)10^5$                 | 43–66                   | 51000                | —                     | —  | —   |

\* $\text{cm}^2\text{V}^{-1}\text{s}^{-1}$

observed for the LPE layers, and a uniformity over a 2 in diam area about one order of magnitude poorer than that of LPE layers. The MCT layers ( $x = 0.31$ ) grown by LPE on 2 in CdTe/sapphire substrates at Rockwell, using a new low temperature ( $420^{\circ}\text{C}$ ) tellurium-melt process, exhibit excellent electronic as well as structural properties, just a little poorer than those observed on CdTe substrates.<sup>33</sup> Reliable, high-performance  $256 \times 256$  hybrid MCT FPAs have been reported to be produced at the same laboratory.<sup>34</sup> The authors state that the key to producing these large hybrid arrays is the use of sapphire to reduce the thermal expansion mismatch with the silicon readout circuit.

Sapphire substrates do present some limitations and drawbacks: they are not transparent in the 8–12



Fig. 1. Surface morphology of CdTe layers grown on (211)A GaAs substrates.

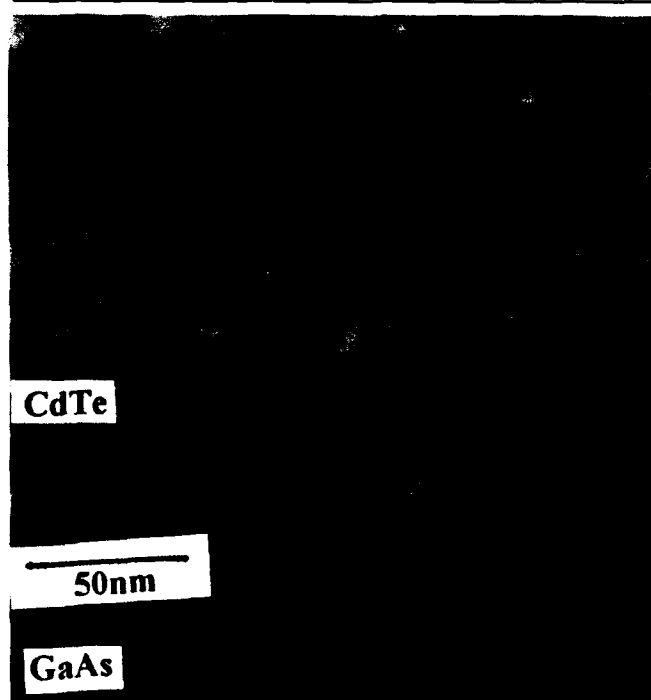


Fig. 2. Transmission electron cross-section micrograph of a CdTe layer grown on a (211)A GaAs substrate.

$\mu\text{m}$  window; their thinning, cutting, and polishing technology is delicate; and they are "passive" substrates, thus preventing monolithic integration.

### GaAs

The capability of growing good-quality MCT layers directly onto GaAs substrates, despite a very large lattice mismatch of 13.6%, was demonstrated by Mullin et al.<sup>35</sup> in 1981. The growth of CdTe on GaAs is at the origin of spectacular progress in the understating of heteroepitaxy. In order to account for {100} and/or {111} oriented heteroepitaxial growth of CdTe on {100} GaAs, Cohen-Solal et al.<sup>36</sup> developed a model based on the formation, during the early stage of the growth, of stable clusters of chemically bound tellurium atoms. According to this model, two types of cluster configurations are obtained, depending on the atomic structure of the {100} GaAs surface: the first one, made up of tetrahedral unit cells, is formed on an arsenic-deficient surface and leads to a {111} orientation, whereas the second one, formed by twin tetrahedral structures developed on an arsenic- or gallium-stabilized surface, gives rise to a {100} orientation.

The use of GaAs substrates has been restricted to epitaxial growth techniques in the vapor phase, such as MOVPE, MBE, and HWE. Despite the very large lattice mismatch, similar DCRC widths have been measured for MCT growth on GaAs to those on CdTe, while much lower FWHM values have been obtained in layers grown on lattice-matched substrates.<sup>19</sup> Layers of MOVPE-grown MCT/CdTe/GaAs{100} $2^{\circ} \rightarrow$  {110} can give DCRC FWHM values as low as 55 arc-s, with values of less than 84 arc-s over an  $8 \times 8 \text{ mm}^2$  area.<sup>37</sup> Typical values lying in the same range ( $\sim 1.0 \text{ arc-min}$ ) have been reported for MBE-grown MCT/CdTe/(211)B GaAs layers.<sup>38</sup>

Several problems arise from the use of GaAs substrates:

- The out-diffusion of gallium and arsenic from the substrate into the layer has been stressed as a factor affecting the purity of the epitaxial layer. The use of CdTe buffer layers of less than  $1 \mu\text{m}$  thickness<sup>39</sup> and at least  $0.5 \mu\text{m}$  thickness<sup>40</sup> has been shown to reduce significantly the gallium penetration into the MCT layers, which can be brought back to background detection levels by growing a sufficiently thick buffer layer ( $8 \mu\text{m}$ )<sup>41</sup> or by the use of CdTe/ZnTe superlattice buffer layers and nucleation on near-atomically planar GaAs surfaces.<sup>42</sup> Nonetheless, the presence of extended defects in the layers<sup>42,43</sup> and the use of specific orientations, such as (111)B,<sup>44</sup> have been reported to enhance gallium diffusion. Moreover, it has been suggested that gallium and arsenic can be transported in the reactor through mechanisms probably involving chemical reaction of the organometallics at the rear surface of the GaAs substrates.<sup>43–45</sup>
- Although in a preliminary study, the possibility of integration of an interdigitated photoconductor



Fig. 1. Cross section of CdTe grown on GaAs substrate at 500°C.

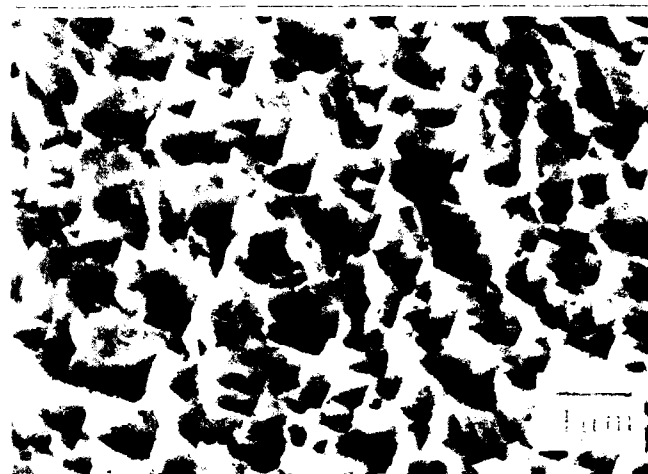


Fig. 2. Cross section of CdTe grown on GaAs substrate at 500°C.

CdTe, as a first step, with an AlGaAs FET has been demonstrated; the monolithic electronic integration in the GaAs substrate is yet an unsolved question, however.

- A worrisome problem is the presence of pyramidal defects, namely the so-called "hillocks," which develop on the surface of (100)-MCT/(100)-GaAs heterostructures and can impede the detector technology.

Several solutions have been proposed to overcome this last problem:

- The use of alternative buffer layer strategies, such as combinations of discrete CdTe and HgTe layers,  $\text{Al}_x\text{Ga}_{1-x}\text{As}$  or graded buffer layers, from ZnTe to CdTe, together with growth interruption during the MPT deposition.
- A tilt of 3–4° from the (100) orientation toward the (111)B face.
- The use of various (111)A or B GaAs orientations. Pan et al.<sup>11</sup> found that MCT growth on (111), (111), and (111) GaAs substrates of both A and B polarity yielded layers of superior morphology when compared with layers grown either on (100)

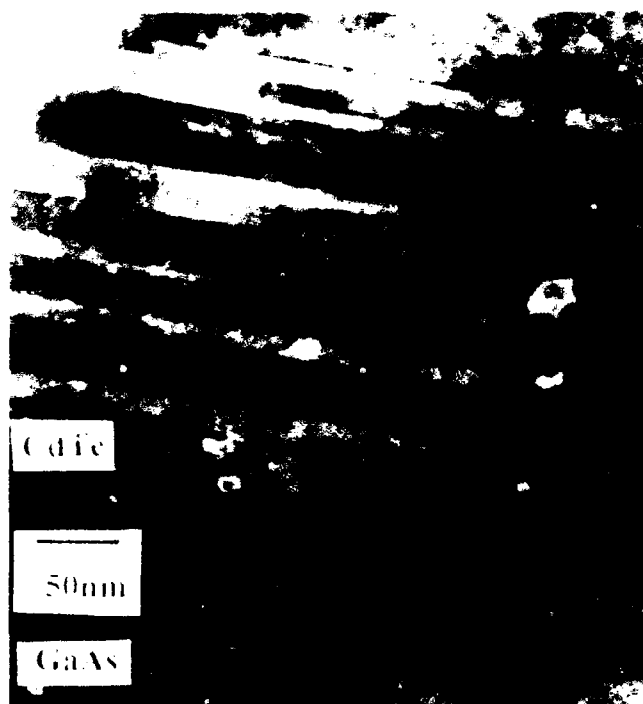


Fig. 3. Cross section of CdTe grown on GaAs substrate at 500°C.

or (100)2° vs. (111) GaAs substrates. The best results were obtained for the (111)B orientation, where they measured DCRC FWHM of 150–200 arc s. Broader values (>500 arc s) were obtained for the (111) or (111) orientations. Lange et al.<sup>12</sup> have reported on the MBE growth of both (211) and (311) CdTe layers on (211)B GaAs substrates. High crystal quality was obtained for both orientations, especially for the (311). As indicated above, Arias et al.<sup>13</sup> have measured typical DCRC FWHM values of 1.0 arc min for MCT/CdTe layers on (211)B GaAs, while Yano et al.<sup>14</sup> have measured good electrical properties on the same heterostructure with  $x = 0.36$ .

In order to solve the hillock problem, we have performed a systematic investigation of the (111) GaAs substrate orientation and polarity on the structural and electronic properties and surface morphology of CdTe and MCT/CdTe layers grown by MOVPE. The surface polarity of the (111) GaAs substrates was determined without ambiguity by electron microscopy. The structural quality of the CdTe and MCT layers was assessed by double crystal x-ray diffraction (DCXRD), electron channeling pattern (ECP) analysis, and cross-sectional transmission electron microscopy (TEM).

Let us consider as an example the results obtained for (211) surfaces. On the A face, the surface morphology is not very smooth but regularly faceted without polycrystalline defects (Fig. 1). No twinning is seen in TEM cross section micrographs, however, numerous dislocations, about  $10^4/\text{cm}^2$ , extend from the interface through the buffer layer (Fig. 2). The electron channeling pattern (ECP) displays a tilt of 4°

(Fig. 3). The orientation of the surface is between (211)A and (311)B due to some rotation around  $\langle 111 \rangle$ . This asymmetry is verified using DCXRD measurements in two orthogonal directions. The narrowest DCRC FWHM (180 arc-s) occurs when the measurement axis is parallel to the cleavage plane.

On the B face, the surface is rough, as shown by the poorly defined pseudo-Kikuchi lines of Fig. 4, which give a layer misorientation of  $4^\circ$  around the  $\langle 011 \rangle$  axis, as for the A face. The rocking curve widths are larger than those measured on the (211)A layer. The TEM cross section micrograph indicates that twinning occurs at the interface (Fig. 5).

The atomic structures of ideal A and B (211) surfaces projected on the {011} plane are presented in Figs. 6a and b. Ideal (211)A and B surfaces possess an equal number of gallium and arsenic atoms, but the bonds are not identical. Gallium atoms, as shown by several authors, are preferentially removed by chemical etching from GaAs surfaces, leaving arsenic-rich surfaces. On the (211)A surface, the remaining arsenic atoms with double dangling bonds are able to induce epitaxy without twinning, while the remaining

arsenic atoms on the B face present single dangling bonds that may induce twins, which are visible in the TEM micrograph (Fig. 5).

The same kind of considerations hold for the (311) and (511) orientations. The presence of single dangling bonds on the (311) and (511)A faces, after chemical etching, is the origin of twinning; the double dangling bonds on the (311) and (511)B faces prevent twinning, as experimentally verified and explained in detail in Ref. 54. It is thus demonstrated that the (211)A, (311)B, and (511)B surfaces have a polarity suitable to avoid twinning.

10- $\mu$ m-thick MCT layers ( $x = 0.3$ ) have been deposited on these CdTe/GaAs hybrid substrates by MOVPE by the interdiffused multilayer process (IMP).<sup>45</sup> The DCRC FWHM values measured on these layers are given in Table III.

Photoconductors have been made at the laboratories of the Société Anonyme de Télécommunications on these layers. Their detectivities at 300K as a function of their cut-off wavelength are presented in Fig. 7. Particularly good results are obtained on (311)B orientations, demonstrating the importance of twin-free layers, as confirmed by lifetimes greater than 600 nsec at 150K measured for us by transient-wave reflectance (TMR) at LTV Aerospace and Defense Company.<sup>55</sup>

All these results demonstrate that GaAs is a viable alternative to CdTe substrates for some applications. Nonetheless, it has been shown from optical studies that layers deposited by MOVPE on CdTe substrates exhibit significantly better properties than those deposited on GaAs.<sup>56</sup>

## SILICON

One ultimate goal of present IR focal-plane array development is large arrays with the charge storage and signal multiplexing performed monolithically on the same silicon chip.

Epitaxial buffers such as  $(\text{Ca,Ba})\text{F}_2$ ,<sup>57</sup> GaAs,<sup>58,59\*</sup> or ZnTe<sup>60</sup> have been used by several groups to overcome the difficulties resulting from the very large lattice mismatch between CdTe and silicon (19%). More recently, the direct growth of CdTe on silicon has been shown possible despite this large mismatch. This direct growth is the most attractive, since a simple growth chamber is available and less contamination is expected. From a theoretical model of heteroepitaxial growth, Bailly et al.<sup>61</sup> have shown that the growth direction of CdTe on  $\langle 100 \rangle$  silicon ought to be  $\langle 111 \rangle$ , as is indeed experimentally observed. The epitaxial relationship  $\langle 111 \rangle$  CdTe/ $\langle 100 \rangle$  silicon brings the lattice mismatch down to 3.4% along the  $\langle 211 \rangle$  CdTe axis.

Direct growth of CdTe on silicon has been reported by MOCVD,<sup>62-64</sup> by hot wall epitaxy (HWE),<sup>65</sup> and by MBE.<sup>10,66</sup> Typical DCRC FWHM values are displayed in Table IV.

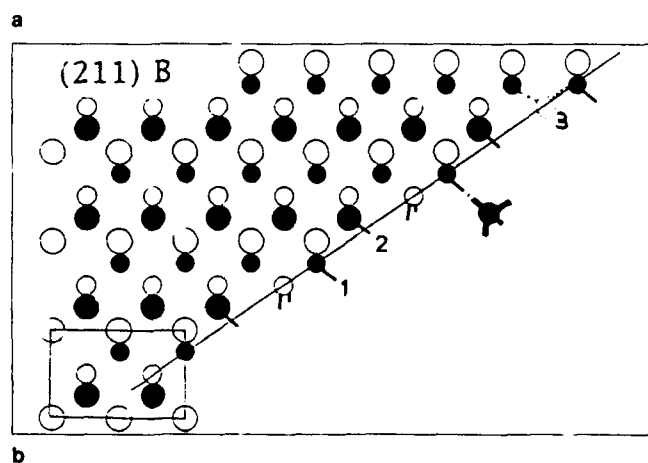
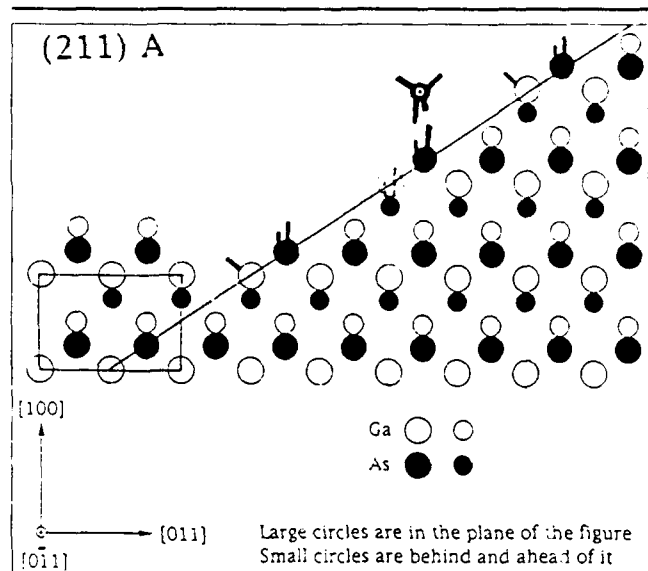


Fig. 6a and b. Atomic structure of (a) an ideal (211)A GaAs surface and (b) an ideal (211)B GaAs surface.

\*GaAs/Si substrates are available, for example, from Kopin Corp. (Taunton, MA).

**Table III. DCRC FWHM of MCT Layers Grown on GaAs Substrates of Various (h11) Orientations and Polarities**

| Orientation | DCRC FWHM (arc-s) |
|-------------|-------------------|
| {100}       | 150               |
| (211)A      | 320               |
| (211)B      | 320               |
| (311)A      | 200               |
| (311)B      | 220               |
| (511)A      | 250               |
| (511)B      | 380               |

Twinning was reported to be suppressed using {111} silicon substrates misoriented toward {110},<sup>63</sup> while twin-free single-domain films were obtained by MBE on slightly misoriented {100} substrates, up to 5 in diam, with very good thickness uniformity.<sup>10</sup>

As in the case of GaAs, the growth of CdTe on more exotic orientations than {100} or {111} could be extremely promising. The risk of cracking or peeling of the device during its operation due to temperature changes remains an open question. The CdTe/Si heterostructure will bend upon cooling because of the thermal expansion coefficient difference, making it difficult to attach cold fingers over large areas. Reticulation technologies will be necessary.

### CONCLUSION

Despite fundamental reasons for difficulties in CdTe bulk crystal growth, actual progress has been achieved recently in this domain. Nonetheless, the poor physical properties of CdTe for use as an epitaxial substrate, its lack of availability and uniformity, and its price have prompted extensive research in the area of alternative substrates. Good MCT/CdTe/sapphire layers can be obtained either by MOVPE<sup>24-29</sup> or by a combination MOVPE/LPE,<sup>30,31</sup> improving the crystal quality and morphology of the layer. Microtwinning has been reported to be completely eliminated by annealing under proper conditions.<sup>32</sup> Reliable high performance 256 × 256 hybrid MCT FPAs have been reported to be produced on sapphire substrates owing to a reduced thermal expansion mismatch to the silicon readout circuit.<sup>34</sup> The interest in sapphire is tempered by its lack of transparency in the 8–12 μm IR window, its difficult "mechanical" technology, and the fact that it is a passive substrate. The growth of CdTe layers on GaAs substrates, despite a considerable lattice mismatch, is at the origin of spectacular progress in the understanding of heteroepitaxy. Twinning on some {h11} GaAs surfaces can be explained in terms of dangling bond characteristics; (211)A, (311)B, and (511)B surfaces present characteristics suitable to avoid twinning, as confirmed by the performance of MCT photoconductors made on these surfaces. Twin-free single-domain CdTe films have been reported by MBE directly on large-area silicon substrates with remarkable crystallographic properties and thickness uniformity.<sup>10</sup> Some difficulties resulting from the great thermal expansion mis-

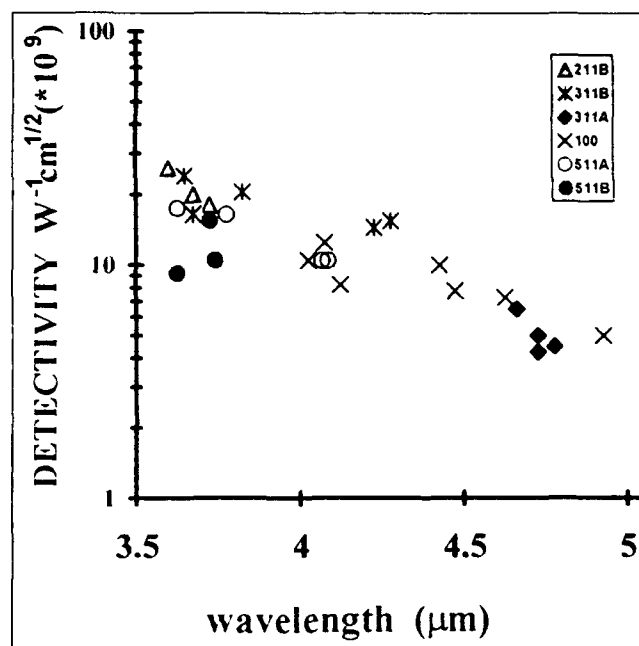


Fig. 7. Detectivity at 300 K and 10 kHz of photoconductors made on MCT layers grown on GaAs substrates of various orientations and polarities.

**Table IV. Typical DCRC FWHM Values for CdTe Layers Grown on Silicon Substrates**

| Growth Tech.        | Thick. (μm) | DCRC FWHM (arc-s) | Growth Temp. (°C) | Substrate Orientation |
|---------------------|-------------|-------------------|-------------------|-----------------------|
| MOVPE <sup>64</sup> | 1           | 400               | 400               | {111}                 |
| HWE <sup>65</sup>   | 5.5         | 315               | —                 | {100}                 |
| MBE <sup>10</sup>   | —           | 140               | —                 | {100}                 |

match between CdTe and silicon are foreseeable.

The domain of alternative substrates for MCT appears extremely active and quite topical. Break-throughs have been achieved using heteroepitaxial growth. Several valuable alternatives are now possible for realizing good-quality MCT layers. Each particular problem can find an advantageous particular solution; it is difficult to suggest a unique solution to all the problems. Nonetheless, several remarks have to be kept in mind: The structural properties of MCT layers grown by vapor-phase techniques depend more on their own nature than on the characteristics of the substrates. Lattice matching remains the key to obtaining high-performance devices. The detectors of highest performance are obtained on (Cd,Zn)Te substrates, while the detector arrays of lowest price and largest area are on GaAs and sapphire substrates. Silicon substrates could become "unbeatable" if some technological problems resulting from their lattice and expansion coefficient mismatch with CdTe are solved.

### ACKNOWLEDGMENT

The authors would like to thank Dr. L.O. Bubulac for kindly providing extensive literature on sapphire

substrates, and Dr. P. Mitra for lifetime measurements.

## REFERENCES

1. R. Triboulet, *Mater. Forum* 15, 30 (1991).
2. A. Sher, A.B. Shen and W.E. Spicer, *J. Vac. Sci. Technol.* A3, 105 (1985).
3. S.L. Bell and S. Sen, *J. Vac. Sci. Technol.* A3, 112 (1985).
4. K. Guergouri, R. Triboulet, A. Tromson-Carli and Y. Marfaing, *J. Cryst. Growth* 8, 61 (1988).
5. D. Imhoff, A. Zozime and R. Triboulet, *J. Phys. III*, France 1, 1841 (1981).
6. P. Rudolph and M. Muhlberg, *Mater. Sci. and Eng. B* 16, 8 (1993).
7. K. Durose, A. Turnbull and P. Brown, *Mater. Sci. and Eng. B* 16, 96 (1993).
8. A. Tanaka, Y. Masa, S. Seto and T. Tawasaki, *J. Cryst. Growth* 94, 166 (1989).
9. M. Azoulay, S. Rotter, G. Gafni, R. Tenne and M. Roth, *J. Cryst. Growth* 117, 276 (1992).
10. J.P. Faurie, R. Sporken, Y.P. Chen, M.D. Lange and S. Sivananthan, *Mater. Sci. Eng. B* 16, 51 (1993).
11. D.L. Dreifus, R.M. Kolbas, J.R. Tassitino, R.L. Harper, R.N. Bicknell and J.F. Schetzina, *J. Vac. Sci. Technol.* A6, 2722 (1988).
12. R. Triboulet, A. Durand, P. Gall, J. Bonnafe, J.P. Fillard and S.K. Krawczyk, *J. Cryst. Growth* 117, 227 (1992).
13. J.F. Butler, F.P. Doty, B. Apotovsky, J. Lajzerowicz and L. Verger, *Mater. Sci. Eng. B* 16, 291 (1993).
14. B.A. Foreman, J.L. Boone, G. Cantwell, W.C. Harsch and J.E. Thomas, unpublished work.
15. L. Di Ciocco, A. Million, J. Piagnet, G. Rolland, G. Lentz, N. Magnea and H. Mariette, *J. Cryst. Growth* 95, 552 (1989).
16. K. Harris, T. Meyers, R. Yanka, L. Mohnkern, R. Green and N. Otsuka, *J. Vac. Sci. Technol.* A8, 1013 (1990).
17. C. Coutal, J.C. Roustan, A. Azema, A. Gilabert, P. Gaucherel and R. Triboulet, *Mater. Sci. Eng. B* 16, 64 (1993).
18. G.L. Destefanis, *Semicond. Sci. Technol.* 6, C 88 (1991).
19. M.J. Bevan, N.J. Doyle, J. Gregg and D. Snyder, *J. Vac. Sci. Technol.* A8, 1049, (1990).
20. S.J.C. Irvine, J.S. Gough, J. Giess, M.J. Gibbs, A. Royle, C.A. Taylor, G.T. Brown, A.M. Keir and J.B. Mullin, *J. Vac. Sci. Technol.* A7, 285 (1989).
21. S.K. Ghandhi, I.B. Bhat and H. Fardi, *Appl. Phys. Lett.* 52, 392 (1988).
22. L. Bubulac, *Appl. Phys. Lett.* 46, 976 (1985).
23. T.H. Myers, Y. Lo, R.N. Bicknell and J.F. Schetzina, *Appl. Phys. Lett.* 42, 247 (1983).
24. H.M. Manasevit and W.I. Simpson, *J. Electrochem. Soc.* 118, 644 (1971).
25. J.B. Mullin, S.J.C. Irvine and D.J. Ashen, *J. Cryst. Growth* 55, 92 (1981).
26. H.S. Cole, H.H. Woodbury and J.F. Schetzina, *J. Appl. Phys.* 55, 3166 (1984).
27. W.E. Hoke, R. Traczewski, V.G. Kreismanis, R. Korenstein and J.L. Lemonias, *Appl. Phys. Lett.* 47, 276 (1985).
28. J. Thompson, K.T. Woodhouse and C. Dineen, *J. Cryst. Growth* 77, 452 (1986).
29. D.D. Edwall, E.R. Gertner and L.O. Bubulac, *J. Cryst. Growth* 86, 240 (1988).
30. R.A. Reidel, E.R. Gertner, D.D. Edwall and W.E. Tennant, *Appl. Phys. Lett.* 46, 64 (1985).
31. E.R. Gertner, W.E. Tennant, J.D. Blackwell and J.P. Rode, *J. Cryst. Growth* 72, 462 (1985).
32. H.L. Glass, M.R. Appleby Woods, M.C. Buehnerkemper, D.L. Varnum and T.P. Weismuller, *J. Cryst. Growth* 128, 617 (1993).
33. S. Johnston, E.R. Blazejewski, J. Bajaj, J.S. Chen, L. Bubulac and G. Williams, *J. Vac. Sci. Technol.* B9, 1661 (1991).
34. R.B. Bailey, L.J. Kozlowski, J. Chen, D.Q. Bui, K. Vural, D.D. Edwall, R.V. Gil, A. Ben Vanderwyck, E.R. Gertner and M.B. Gubala, *IEEE Trans. on Electr. Devices* 38, 1104 (1991).
35. J.B. Mullin, S.J.C. Irvine and D.J. Ashen, *J. Cryst. Growth* 55, 92 (1981).
36. G. Cohen-Solal, F. Bailly and M. Barbe, *Appl. Phys. Lett.* 49, 1519 (1986).
37. S.J.C. Irvine, J.S. Gough, J. Giess, M.J. Gibbs, A. Royle, C.A. Taylor, G.T. Brown, A.M. Keir and J.B. Mullin, *J. Vac. Sci. Technol.* A7, 285 (1989).
38. J. Arias, M. Zandian, J.G. Pasko, S.H. Shin, L.O. Bubulac, R.E. De Wames and W.E. Tennant, *J. Appl. Phys.* 69, 2143 (1991).
39. J. Giess, J.S. Gough, S.J.C. Irvine, J.B. Mullin and G.W. Blackmore, *Mater. Res. Soc. Symp. Proc.* 90, 389 (1987).
40. I.B. Bhat, N.R. Taskar, K. Patel, J.E. Ayers, S.K. Ghandhi, J. Petruzello and D. Olego, *SPIE Proceedings* 796, 194 (1987).
41. J. Giess, J.S. Gough, S.J.C. Irvine, G.W. Blackmore, J.B. Mullin and A. Royle, *J. Cryst. Growth* 72, 120 (1985).
42. B.K. Wagner, J.D. Oakes and C.J. Summers, *J. Cryst. Growth* 86, 296 (1988).
43. G. Patriarche, R. Triboulet, Y. Marfaing and J. Castaing, *J. Cryst. Growth* 129, 375 (1993).
44. R. Korenstein, P. Hallock, B. Macleod, W. Hoke and S. Oguz, *J. Vac. Sci. Technol.* A8, 1039 (1990).
45. R. Druilhe, F. Desjonqueres, A. Katty, A. Tromson-Carli, D. Lorans, L. Svob, A. Heurtel, Y. Marfaing and R. Triboulet, *J. Cryst. Growth* 101, 73 (1990).
46. J.L. Filippozzi, F. Therez, D. Esteve, M. Fallahi, D. Kendil, M. Da Silva, M. Barbe and G. Cohen-Solal, *J. Cryst. Growth* 101, 1013 (1990).
47. J.B. Mullin, S.J.C. Irvine, J. Giers, J.S. Gough, A. Royle and M.C.L. Ward, *SPIE Proceedings* 1106, 17 (1989).
48. L.M. Smith, C.F. Byrne, D. Patel, P. Knowles, J. Thompson, G.T. Jenkin, T. Nguyen Duy, A. Durand and M. Bourdillot, *J. Vac. Sci. Technol.* A8, 1078 (1990).
49. D.W. Snyder, S. Mahajan, M. Brazil, E.I. Ko, P.J. Sides and R.E. Nahory, *Appl. Phys. Lett.* 58, 848 (1991).
50. G.N. Pain, C. Sandford, G.K.G. Smith, A.W. Stevenson, D. Gao, L.S. Wielunski, S.P. Russo, G.K. Reeves and R. Elliman, *J. Cryst. Growth* 107, 610 (1991).
51. M.D. Lange, R. Sporken, K.K. Mahavadi, J.P. Faurie, Y. Nakamura and N. Otsuka, *Appl. Phys. Lett.* 58, 1988 (1991).
52. S. Yuan, Li He, J. Yu, M. Yu, Y. Qiao and J. Zhu, *Appl. Phys. Lett.* 58, 914 (1991).
53. P.D. Brown, A. Tromson-Carli, R. Druilhe, R. Triboulet and Y. Marfaing, *Proc. of the Xth European Congress on Electron Microscopy (EUREM 92)*.
54. A. Tromson-Carli, G. Patriarche, R. Druilhe, Y. Marfaing, R. Triboulet, P.D. Brown and A. Brinkman, *Mater. Sci. Eng. B* 16, 145 (1993).
55. P. Mitra, private communication.
56. R. Druilhe, F. Desjonqueres, A. Tromson-Carli, A. Lusson, E. Rzepka, A. Katty, Y. Marfaing and R. Triboulet, *Semicond. Sci. Technol.* 6, C22 (1991).
57. H. Zogg and S. Blunier, *Appl. Surf. Sci.* 30, 402 (1987).
58. J.M. Arias, S.H. Shin, M. Zandian, W.V. McLevige, J.G. Pasko and R.E. de Wames, *J. Vac. Sci. Technol.* B9, 1646 (1991).
59. J.W. Lee, J.P. Salerno, R.P. Gale and J.C.C. Fan, *Mater. Res. Soc. Symp. Proc.* 91, 33 (1987).
60. R. Sporken, S. Sivananthan, K.K. Mahavadi, G. Monfroy, M. Boukerche and J.P. Faurie, *Appl. Phys. Lett.* 55, 1879 (1989).
61. F. Bailly, M. Barbe and G. Cohen-Solal, *SPIE Proceedings* 944, 40 (1988).
62. A. Nouhi, G. Radhakrishnan, J. Katz and K. Koliwad, *Appl. Phys. Lett.* 52, 2028 (1988).
63. R.L. Chou, M.S. Lin and K.S. Chou, *Appl. Phys. Lett.* 48, 523 (1986).
64. H. Ebe and H. Takigawa, *Mater. Sci. Eng. B* 16, 57 (1993).
65. R. Korenstein, P. Madison and P. Hallock, *J. Vac. Sci. Technol.* B10, 1370 (1992).
66. Y. Lo, R.N. Bicknell, T.H. Myers, J.F. Schetzina and H. Stadelmeier, *J. Appl. Phys.* 54, 4238 (1983).

# MOCVD Grown CdZnTe/GaAs/Si Substrates for Large-Area HgCdTe IRFPAs

S.M. JOHNSON, J.A. VIGIL, J.B. JAMES, C.A. COCKRUM, W.H. KONKEL, M.H. KALISHER, R.F. RISSE, T. TUNG, W.J. HAMILTON, W.L. AHLGREN, and J.M. MYROSZNYK

Santa Barbara Research Center, Goleta, CA 93117

Large-area HgCdTe  $480 \times 640$  thermal-expansion-matched hybrid focal plane arrays were achieved by substituting metalorganic chemical vapor deposition (MOCVD)-grown CdZnTe/GaAs/Si alternative substrate in place of bulk CdZnTe substrates for the growth of HgCdTe p-on-n double-layer heterojunctions by controllably-doped mercury-melt liquid phase epitaxy (LPE). (100) CdZnTe was grown by MOCVD on GaAs/Si using a vertical-flow high-speed rotating disk reactor which incorporates up to three two-inch diameter substrates. Layers having specular surface morphology, good crystalline structure, and surface macro defect densities  $< 50 \text{ cm}^{-2}$  are routinely achieved and both the composition uniformity and run-to-run reproducibility were very good. As the composition of the CdZnTe layers increases, the x-ray full width at half maximum (FWHM) increases; this is a characteristic of CdZnTe grown by VPE techniques and is apparently associated with phase separation. Despite a broader x-ray FWHM for the ternary CdZnTe, the FWHM of HgCdTe grown by LPE on these substrates decreases, particularly for [ZnTe] compositions near the lattice matching condition to HgCdTe. An additional benefit of the ternary CdZnTe is an improved surface morphology of the HgCdTe layers. Using these silicon-based substrates, we have demonstrated 78K high-performance LWIR HgCdTe  $480 \times 640$  arrays and find that their performance is comparable to similar arrays fabricated on bulk CdZnTe substrates for temperatures exceeding approximately 78K. The performance at lower temperatures is apparently limited by the dislocation density which is typically in the low-mid  $10^6 \text{ cm}^{-2}$  range for these heteroepitaxial materials.

**Key words:** CdZnTe/GaAs/Si substrates, focal-plane arrays, HgCdTe, LPE, MOCVD

## INTRODUCTION

As the size of HgCdTe hybrid focal plane arrays (FPA) increases it becomes more important to provide a detector array that is thermal-expansion-matched to the silicon readout to ensure long-term thermal cycle reliability. This cannot be realized using either sapphire or GaAs substrates because of their poor thermal expansion match to silicon. We have achieved a thermal-expansion-matched FPA by substituting a metalorganic chemical vapor deposition (MOCVD)-grown CdZnTe/GaAs/Si alternative substrate in place of bulk CdZnTe substrates for the growth of HgCdTe p-on-n double-layer heterojunction structures by

controllably doped mercury-melt liquid phase epitaxy (LPE). This approach allows us to realize the benefits of a silicon-based substrate grown by vapor-phase epitaxy together with a mature LPE-based HgCdTe high-performance photovoltaic array technology. Additional benefits of a silicon-based substrate include lower cost, increased strength, and larger dimensions than bulk CdZnTe substrates which are the present industry standard.

In order to realize a silicon-based substrate for HgCdTe growth, most efforts have utilized GaAs/Si as a starting material since it is relatively easy to get epitaxial growth of CdTe or CdZnTe on a GaAs surface (as opposed to directly on a silicon surface) by a wide variety of techniques. Epitaxial CdTe has been grown on GaAs/Si by congruent evaporation,<sup>1</sup> MOCVD,<sup>2-8</sup>

(Received October 29, 1992; revised January 15, 1993)

MBE,<sup>9,10</sup> hot-wall epitaxy<sup>11</sup> and atomic layer epitaxy (ALE);<sup>12</sup> CdZnTe/GaAs/Si has primarily been grown using MOCVD<sup>4,13-15</sup> and more recently MOMBE.<sup>16</sup> HgCdTe has been grown on these composite substrates using closed-spaced vapor phase epitaxy,<sup>1</sup> LPE,<sup>4,13-15</sup> MOCVD,<sup>3,5-8,11</sup> and molecular beam epitaxy (MBE).<sup>9,10</sup> MWIR HgCdTe detectors on silicon-based substrates were first demonstrated in 1987 by Kay et al.<sup>1</sup> using CdTe grown on GaAs/Si by congruent evaporation and HgCdTe grown by closed-spaced vapor phase epitaxy. We demonstrated the first HgCdTe MWIR<sup>13</sup> and LWIR<sup>15</sup> 128 × 128 arrays in 1989 and 1990, respectively, using MOCVD-grown CdZnTe/GaAs/Si together with Hg-melt LPE p-on-n diode technology. LWIR p-on-n detectors have also been demonstrated using arsenic ion implantation in HgCdTe grown on GaAs by MOCVD.<sup>17</sup> Epitaxial growth of CdTe directly on silicon has been achieved by MBE,<sup>18-24</sup> MOCVD,<sup>12,25,26</sup> hot-wall epitaxy (HWE),<sup>11</sup> and indirectly using CaF<sub>2</sub>/BaF<sub>2</sub> buffer layers;<sup>27,28</sup> however, no HgCdTe detector results have yet been reported for these materials.

This work describes the material characteristics of both MOCVD-grown CdZnTe/GaAs/Si substrates and LWIR HgCdTe grown on these substrates by LPE. Results are then given for the first LWIR HgCdTe 480 × 640 arrays using these silicon-based substrates.

### MATERIAL GROWTH

CdZnTe epitaxial layers were grown on GaAs/Si substrates by MOCVD using a vertical-flow, high-speed rotating disk reactor that was designed and built at SBRC. The reactor has a 5 in diam susceptor which accommodates up to three 2 in diam substrates per run. CdZnTe layers were grown at temperatures between 350–380°C and had a nominal thickness of 8 μm. Metalorganic chemical vapor deposition-grown GaAs/Si substrates were supplied by Kopin Corp.

with a (100)3.5° toward <111> orientation.

The (100) substrate orientation was maintained in the CdZnTe epitaxial layers using a thin nucleation layer of ZnTe on the GaAs surface.<sup>29</sup> Some of our earlier work focused on (111)CdZnTe/(100)GaAs/Si, but we found that it was difficult to reproducibly suppress twinning in (111)CdZnTe.<sup>15</sup> We have also investigated growth of CdZnTe on (211)GaAs/Si and found that CdZnTe layers had either a (211) or a (552) first order twin orientation.<sup>15,30</sup> This twin orientation was also observed for CdTe grown on (211)GaAs substrates by MBE.<sup>31,32</sup> For MBE-grown HgCdTe, which is generally grown on (211), this twinning will need to be suppressed to allow successful use of (211) silicon-based substrates.

The HgCdTe double-layer heterojunction detectors were grown by vertical liquid phase epitaxy (VLPE) from infinite melt mercury-rich solutions. The n-type base layer was doped with indium and the p-type wider bandgap capping layer was doped with arsenic. Several excellent reviews describing this technology have been published.<sup>33-35</sup>

### MATERIAL CHARACTERISTICS

The thickness uniformity of the CdZnTe layers was determined from the spacing of interference fringes in the transmission vs wavenumber spectrum measured at room temperature using a Fourier transform infrared spectrometer (FTIR). X-ray rocking curve full-width at half-maximum measurements were determined from symmetric (400) reflections. Absolute CdZnTe composition measurements were determined from lattice constant measurements and using Vegard's Law. Lattice constant measurements were made at the center of each wafer with the Bond technique<sup>36</sup> using a high-resolution x-ray diffractometer having a silicon four-crystal monochromator to produce CuKα<sub>1</sub> radiation and having an optically

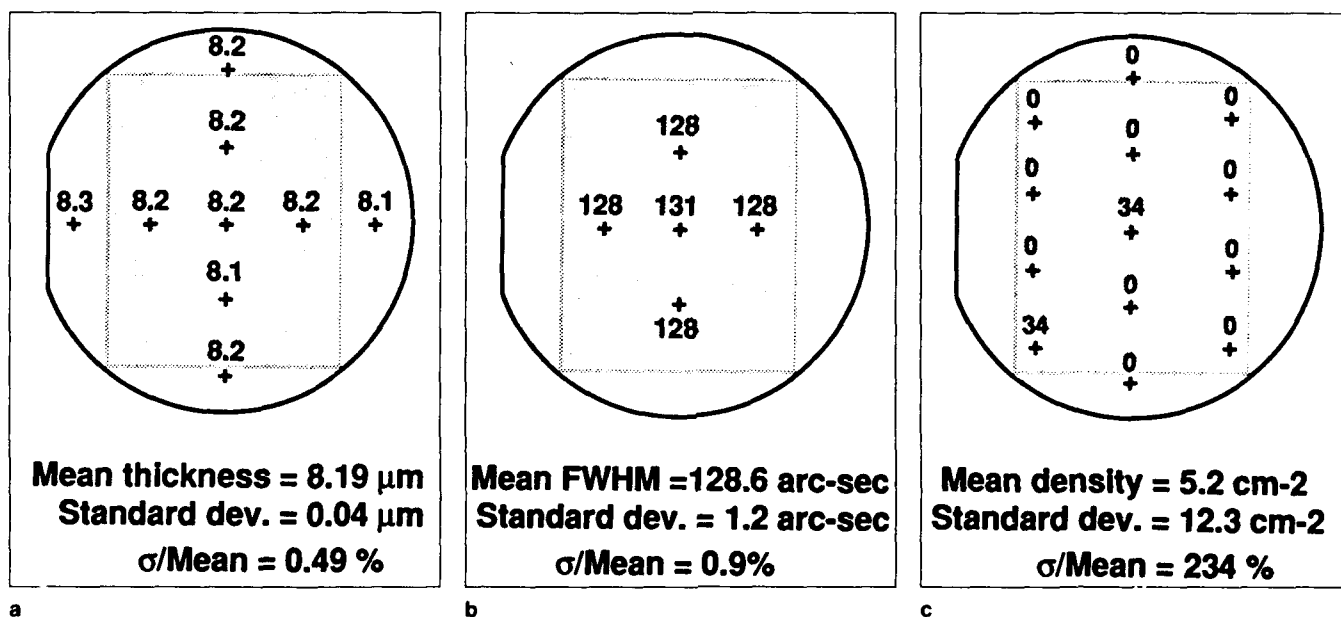


Fig. 1. Plots of the spatial uniformity of the a) thickness, b) x-ray FWHM, and c) hillock density of a single 2 in diam CdTe/GaAs/Si layer.



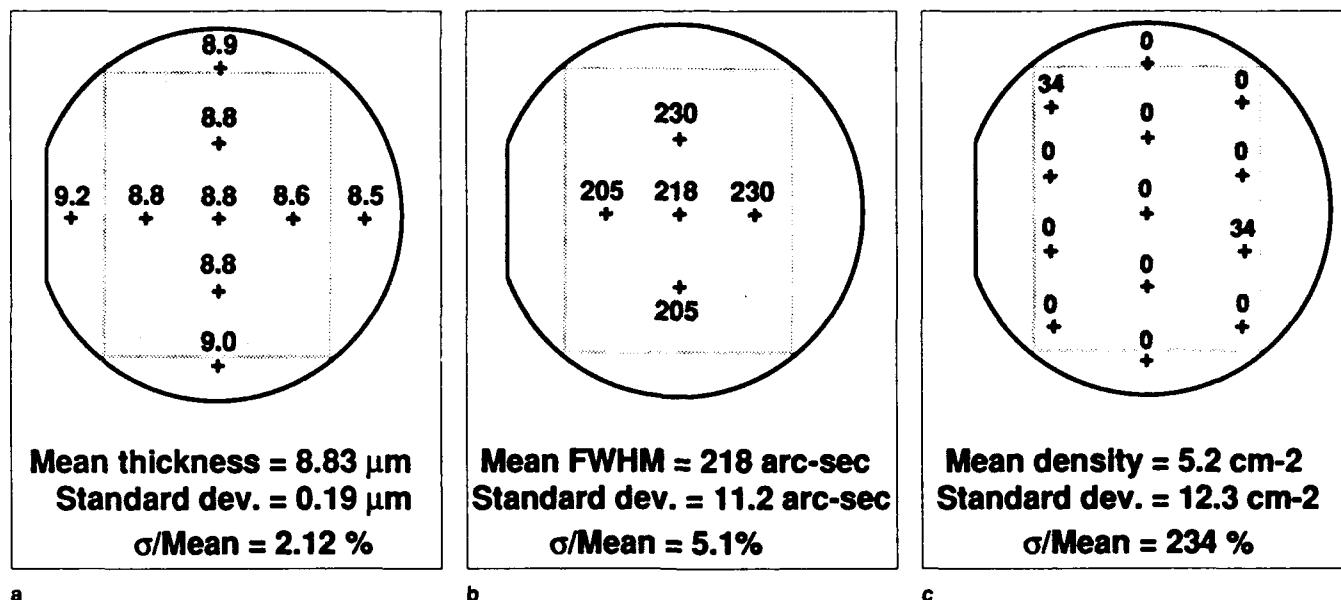


Fig. 2. Plots of the spatial uniformity of the a) thickness, b) x-ray FWHM, and c) hillock density of a single 2 in diam  $\text{Cd}_{0.96}\text{Zn}_{0.04}\text{Te/GaAs/Si}$  layer.

encoded angular readout for precise angle measurements. Composition uniformity across a wafer was determined from 77K photoluminescence (PL) measurements.<sup>37</sup> The average density of hillocks, or macrodefects, on the surface was determined using 100 $\times$  optical microscopy at 13 different locations across the wafer surface.

Figures 1a, b, and c summarize the spatial uniformity of the thickness, x-ray FWHM, and hillock density, respectively, of a single CdTe/GaAs/Si layer. The thickness uniformity is excellent and has a standard deviation/mean of 0.5%. The average x-ray FWHM is 129 arc-s which is quite good for CdTe grown on a silicon-based substrate. X-ray FWHM values of 70–80 arc-s have been reported for (111)CdTe grown on (100)GaAs/Si by HWE for CdTe layer thicknesses exceeding approximately 10  $\mu\text{m}$  with the best reported value of 59 arc-s.<sup>11</sup> The hillock density is very low and this is attributed to a reduction in particulates in the reactor which can nucleate these type of macrodefects.<sup>38</sup>

The ternary CdZnTe is more difficult to grow and Figures 2a, b, and c summarize the spatial uniformity of the thickness, x-ray FWHM, and hillock density, respectively, of a single  $\text{Cd}_{0.96}\text{Zn}_{0.04}\text{Te/GaAs/Si}$  layer. The thickness uniformity is still very good with a standard deviation/mean of 2.1% but is noticeably different than that of CdTe. The average x-ray FWHM is now 218 arc-s which is larger than that of CdTe and will be discussed later in more detail. The hillock density is again very low and is the same as that of the CdTe layer. A series of eight CdZnTe runs was done with the same conditions to determine the reproducibility of the process and Fig. 3 shows a plot of the average hillock density vs the run number. Six of these runs had three wafers, one had two wafers, and one had a single wafer. Figure 3 shows that the average hillock density is generally  $<50\text{ cm}^{-2}$ . We have

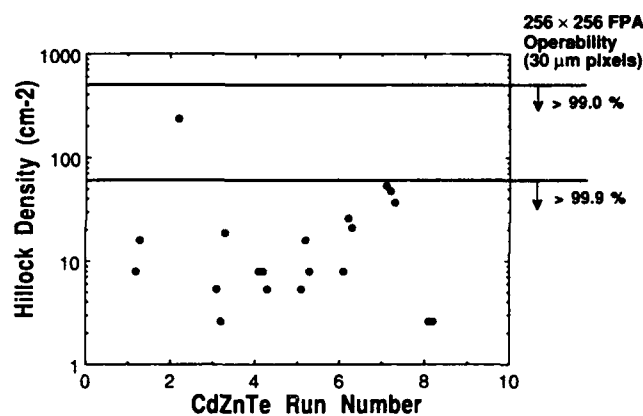


Fig. 3. Average hillock density vs the run number for a series of eight runs of CdZnTe grown under the same conditions.

previously made a one-to-one correlation relating a hillock to a poor pixel in 128  $\times$  128 arrays so it is important to minimize the density of these macrodefects.<sup>13</sup> The projected array operability (associated with hillock defects only) of a 256  $\times$  256 array (30  $\mu\text{m}$  pixels) will exceed 99.9% for hillock densities  $<50\text{ cm}^{-2}$ .

Figure 4a shows a plot of the [ZnTe] composition determined from 77K PL measured across the diameter of a  $\text{Cd}_{0.96}\text{Zn}_{0.04}\text{Te/GaAs/Si}$  layer. Measurements were made in the radial and tangential directions across the diameter as shown in the schematic of the susceptor in Fig. 4b. The uniformity is quite good with the largest variation in composition occurring in the radial direction which shows a depletion of [ZnTe] near the outside edges of the susceptor. The composition tangential direction is more uniform as would be expected for a rotating susceptor. We generally observe that the composition of CdZnTe grown on GaAs/Si measured by 77K PL is lower by  $\Delta y \approx 0.005$  to 0.01 than the composition determined from lattice constant measurements; this may be associated with strain but this has not yet been resolved. Figure 5

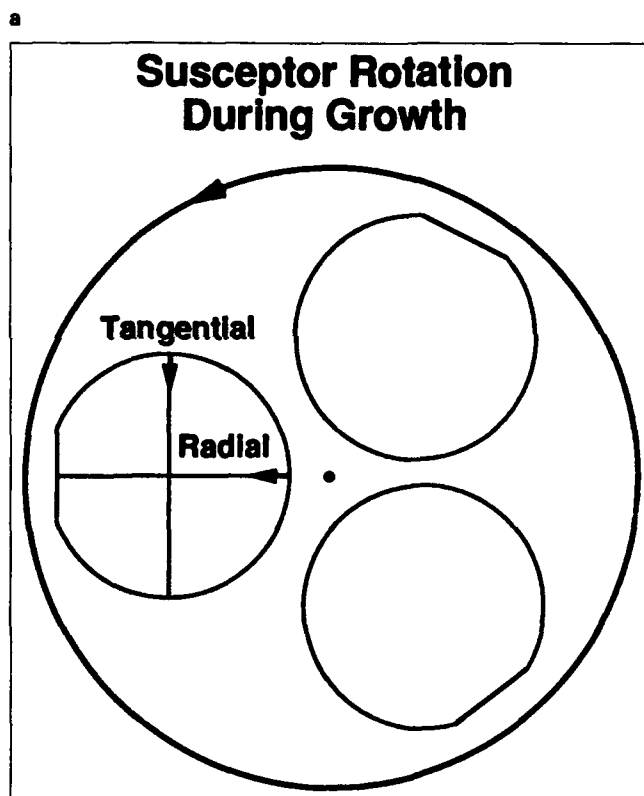
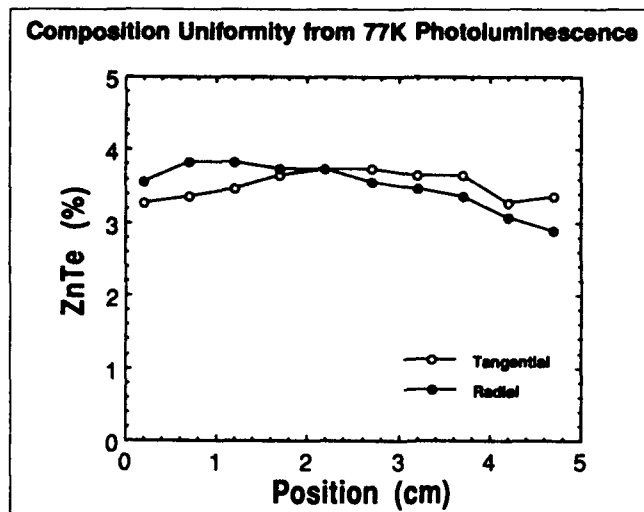


Fig. 4. a) Plot of the [ZnTe] composition determined from 77K PL measured across the diameter of a  $\text{Cd}_{0.96}\text{Zn}_{0.04}\text{Te}/\text{GaAs}/\text{Si}$  layer and b) schematic of the susceptor showing radial and tangential measurement directions.

show the run-to-run reproducibility in  $\text{Cd}_{1-y}\text{Zn}_y\text{Te}$  composition (determined from lattice constant measurements) for a series of eight runs containing multiple wafers per run (corresponding to the same runs shown in Fig. 3) and shows that the reproducibility is approximately  $\Delta y = \pm 0.005$ .

Figure 6 shows a plot of the x-ray FWHM of a large number of  $\text{Cd}_{1-y}\text{Zn}_y\text{Te}$  layers grown on GaAs/Si vs  $y = [\text{ZnTe}]$  composition determined from lattice constant measurements. The data shows that the FWHM in-

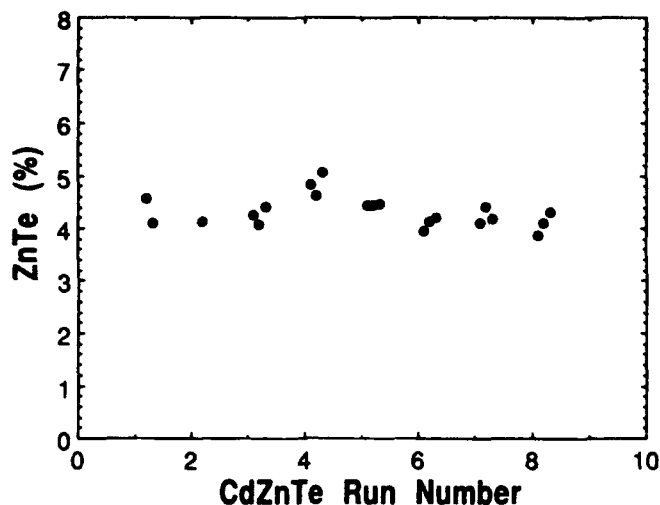


Fig. 5. Run-to-run reproducibility in  $\text{Cd}_{1-y}\text{Zn}_y\text{Te}$  composition (determined from lattice constant measurements) for a series of eight runs showing the reproducibility is approximately  $\Delta y = \pm 0.005$ .

creases as the composition increases. This FWHM broadening is a characteristic that is peculiar to ternary  $\text{CdZnTe}$  alloys (but not the  $\text{CdTe}$  or  $\text{ZnTe}$  binary compounds) grown by vapor phase epitaxy (VPE) and has been observed for  $\text{CdZnTe}/\text{GaAs}$  grown by MBE,<sup>39-41</sup> MOCVD,<sup>42</sup> and MOMBE.<sup>16</sup> A broadening in x-ray FWHM with composition was also seen for  $\text{CdZnTe}$  grown on InSb substrates by MBE but was interpreted to be associated with lattice mismatch.<sup>43</sup> The increase in x-ray FWHM with composition for the ternary  $\text{CdZnTe}$  has been attributed to phase separation<sup>39</sup> and this has been experimentally observed using both x-ray scattering<sup>40</sup> and transmission electron microscopy (TEM).<sup>40,44</sup> It is interesting to note that bulk  $\text{CdZnTe}$  grown by the vertical modified-Bridgman technique does not show a degradation in x-ray FWHM with increased composition and FWHM values as low as 11 arc-s have been reported for  $\text{Cd}_{0.84}\text{Zn}_{0.16}\text{Te}$ .<sup>45</sup> More work is needed to both fundamentally understand the reasons for the occurrence of phase separation in  $\text{CdZnTe}$  grown by VPE and to modify the growth techniques to improve the material quality.

Despite the broader x-ray FWHM for ternary  $\text{CdZnTe}/\text{GaAs}/\text{Si}$ , an improvement in the FWHM of LPE-grown  $\text{HgCdTe}$  grown on these substrates is found. Figure 7 is a plot of the x-ray FWHM of LPE-grown LWIR  $\text{Hg}_{0.77}\text{Cd}_{0.23}\text{Te}$  layers vs the FWHM of the  $\text{CdZnTe}/\text{GaAs}/\text{Si}$  substrates and shows that, with the exception of one layer, FWHM of the  $\text{HgCdTe}$  is always less than that of the  $\text{Cd}_{1-y}\text{Zn}_y\text{Te}$  buffer layer. As shown in Fig. 7, a larger improvement is seen for ternary  $\text{CdZnTe}$  buffer layers compared with  $\text{CdTe}$  buffer layers. This improvement in x-ray FWHM has been widely observed for  $\text{HgCdTe}$  grown by a variety of techniques on heteroepitaxial substrates which have primarily used  $\text{CdTe}$  as opposed to  $\text{CdZnTe}$  buffer layers. This FWHM reduction is attributed to dislocation annihilation which occurs both as the thickness of the  $\text{CdZnTe}$  and  $\text{HgCdTe}$  layers increase

and to thermal annealing, which increases the mobility of dislocations, during the HgCdTe layer growth.<sup>14,46</sup>

The reduction in x-ray FWHM in the LPE-grown HgCdTe layers is also related to the composition of the CdZnTe/GaAs/Si substrates as shown in Fig. 8. Figure 8 is a plot of the x-ray FWHM of HgCdTe layers vs the composition of the CdZnTe substrate and shows that the use of ternary  $\text{Cd}_{1-y}\text{Zn}_y\text{Te/GaAs/Si}$  substrates, particularly  $y \approx 0.03$ – $0.05$ , results in a smaller x-ray FWHM in the HgCdTe layer. The most obvious explanation is to attribute this effect to closer lattice-matching of the CdZnTe buffer layer to the HgCdTe layer but it is interesting to observe that this near lattice matching results in a lower x-ray FWHM in the HgCdTe despite the fact that the ternary CdZnTe layers have much a broader x-ray FWHM compared with CdTe.

A further benefit of using the ternary CdZnTe buffer layers is seen by an improvement in the surface morphology of HgCdTe grown by LPE on these substrates. Figures 9a and b compare the surface morphology, accentuated using Nomarski optical micrographs, of MOCVD-grown CdTe/GaAs/Si and  $\text{Hg}_{0.77}\text{Cd}_{0.23}\text{Te}$  grown on CdTe/GaAs/Si while Figs. 9c and d compare the surface morphology of MOCVD-grown  $\text{Cd}_{0.96}\text{Zn}_{0.04}\text{Te/GaAs/Si}$  and  $\text{Hg}_{0.77}\text{Cd}_{0.23}\text{Te}$  grown on  $\text{Cd}_{0.96}\text{Zn}_{0.04}\text{Te/GaAs/Si}$ . Using a surface profilometer, the peak-to-peak roughness of the CdTe buffer layer (Fig. 9a) is approximately  $0.05\text{ }\mu\text{m}$  while that of the HgCdTe (Fig. 9b) grown on a CdTe buffer layer is approximately  $1.5\text{ }\mu\text{m}$ . Figure 9b also shows the fourfold symmetry of the morphology related to the (100) surface orientation. By contrast, the peak-to-peak roughness of the  $\text{Cd}_{0.96}\text{Zn}_{0.04}\text{Te}$  buffer layer (Fig. 9c) is approximately  $0.1\text{ }\mu\text{m}$  while that of the HgCdTe (Fig. 9d) grown on a  $\text{Cd}_{0.96}\text{Zn}_{0.04}\text{Te}$  buffer layer is approximately  $0.25\text{ }\mu\text{m}$  which shows that the morphology of the HgCdTe surface is more dependent on the composition rather than the morphology of the CdZnTe buffer layer. This HgCdTe surface morphol-

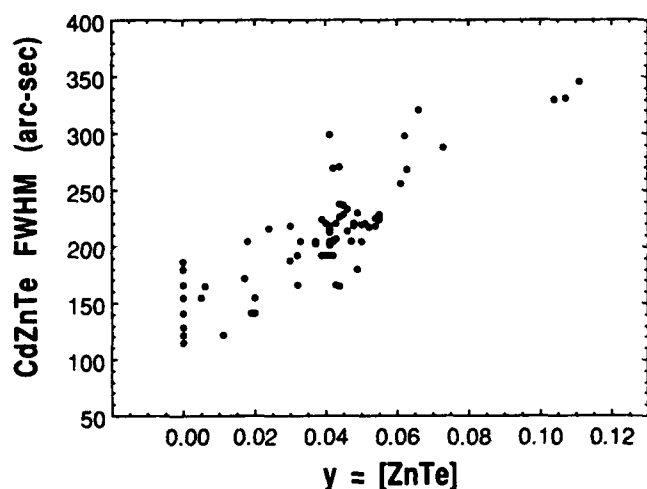


Fig. 6. Plot of the x-ray FWHM of a large number of  $\text{Cd}_{1-y}\text{Zn}_y\text{Te}$  layers grown on GaAs/Si vs  $y = [\text{ZnTe}]$  composition determined from lattice constant measurements.

ogy is adequate to fabricate high-density LWIR arrays as discussed in the next section.

### LWIR HgCdTe $480 \times 640$ ARRAYS ON Si-BASED SUBSTRATES

Large area  $480 \times 640$  HgCdTe hybrid arrays were fabricated from p-on-n double-layer heterojunctions grown by LPE on CdZnTe/GaAs/Si substrates by defining and etching mesas to isolate the individual detectors; the center-to-center spacing of the individual elements was  $20\text{ }\mu\text{m}$ . Figure 10a shows a histogram of the resistance-area product at zero bias ( $R_0A_0$ ; optical area,  $A_0 = 4 \times 10^{-6}\text{ cm}^2$ ) of 36 diodes in an array, accessed from a fanout, measured at  $T = 78\text{ K}$  under an  $f/2$  FOV (300K) background and Fig. 10b shows the spectral response of three of these detectors measured at zero bias at  $T = 78\text{ K}$ . The mean  $R_0A_0$  product is  $1.78 \times 10^3\text{ ohm-cm}^2$  for detectors having a cutoff wavelength of  $9.0\text{ }\mu\text{m}$  which demonstrates that high-quality large-area LWIR HgCdTe focal plane arrays can be fabricated on these heteroepitaxial silicon-based substrate materials.

To determine the mechanisms that limit the performance of these detectors the  $R_0A_0$  product (junction

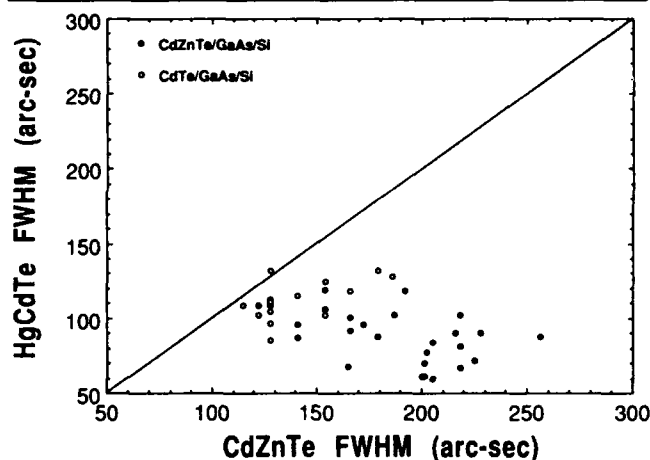


Fig. 7. X-ray FWHM of LPE-grown LWIR  $\text{Hg}_{0.77}\text{Cd}_{0.23}\text{Te}$  layers vs the FWHM of the CdZnTe/GaAs/Si substrates.

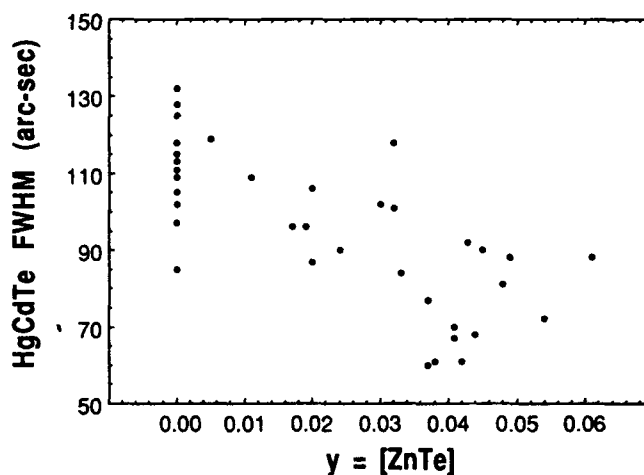


Fig. 8. X-ray FWHM of LPE-grown LWIR  $\text{Hg}_{0.77}\text{Cd}_{0.23}\text{Te}$  layers vs the composition of the  $\text{Cd}_{1-y}\text{Zn}_y\text{Te/GaAs/Si}$  substrates.

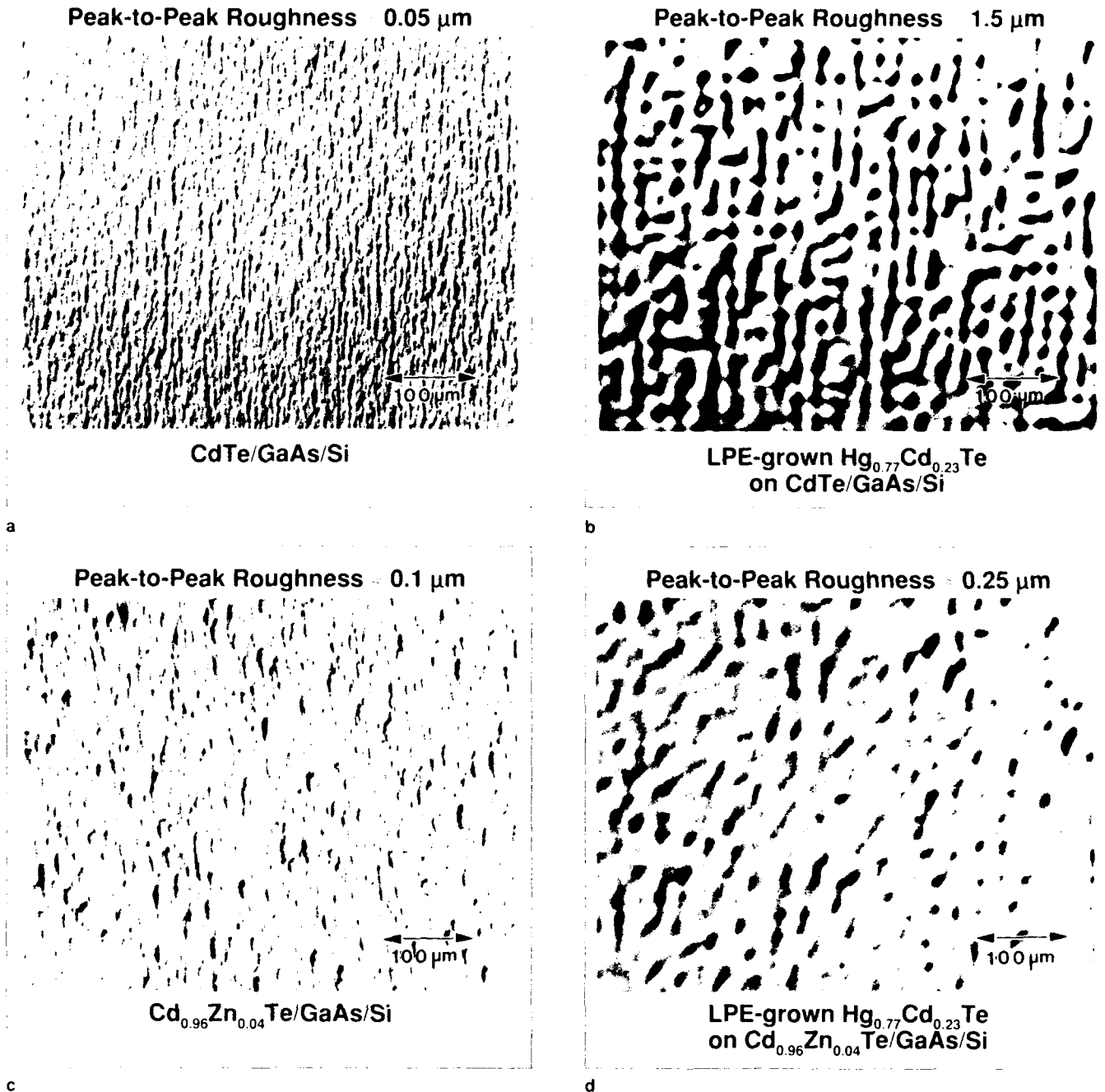


Fig. 9. Nomarski micrographs comparing surface morphology of a) CdTe/GaAs/Si and b)  $\text{Hg}_{0.77}\text{Cd}_{0.23}\text{Te}$  grown on CdTe/GaAs/Si. c)  $\text{Cd}_{0.96}\text{Zn}_{0.04}\text{Te}$ /GaAs/Si and d)  $\text{Hg}_{0.77}\text{Cd}_{0.23}\text{Te}$  grown on  $\text{Cd}_{0.96}\text{Zn}_{0.04}\text{Te}$ /GaAs/Si.

area,  $A_d = 2 \times 10^{-4} \text{ cm}^2$ ) was measured as a function of temperature at zero FOV for one of these array diodes. Figure 11 compares the  $RA_d$  product vs inverse temperature for an array diode fabricated on CdZnTe/GaAs/Si with a diode from another  $480 \times 640$  array having a cutoff wavelength of 9.1  $\mu\text{m}$  at  $T = 78\text{K}$  that was fabricated on a bulk CdZnTe substrate. For temperatures above approximately 78K both diodes have nearly identical  $RA_d$  products, while at lower temperatures the diode on the silicon-based substrate is limited by tunneling currents. The  $RA_d$  data at low temperature for the diode fabricated on bulk CdZnTe

is noisy because the  $R_d$  of detector is near  $10^{12}$  ohms and is difficult to reliably measure.

We have previously reported similar effects comparing the low-temperature  $RA_d$  product of MWIR HgCdTe arrays fabricated on CdZnTe/GaAs/Si and bulk CdZnTe and attributed these differences to an increased dislocation density in the heteroepitaxial substrates.<sup>13</sup> In a recent study of the effects of dislocations on the electrical and optical properties of LWIR HgCdTe detectors, we found that an increased dislocation density only weakly affects the high-temperature diffusion component of the leakage current

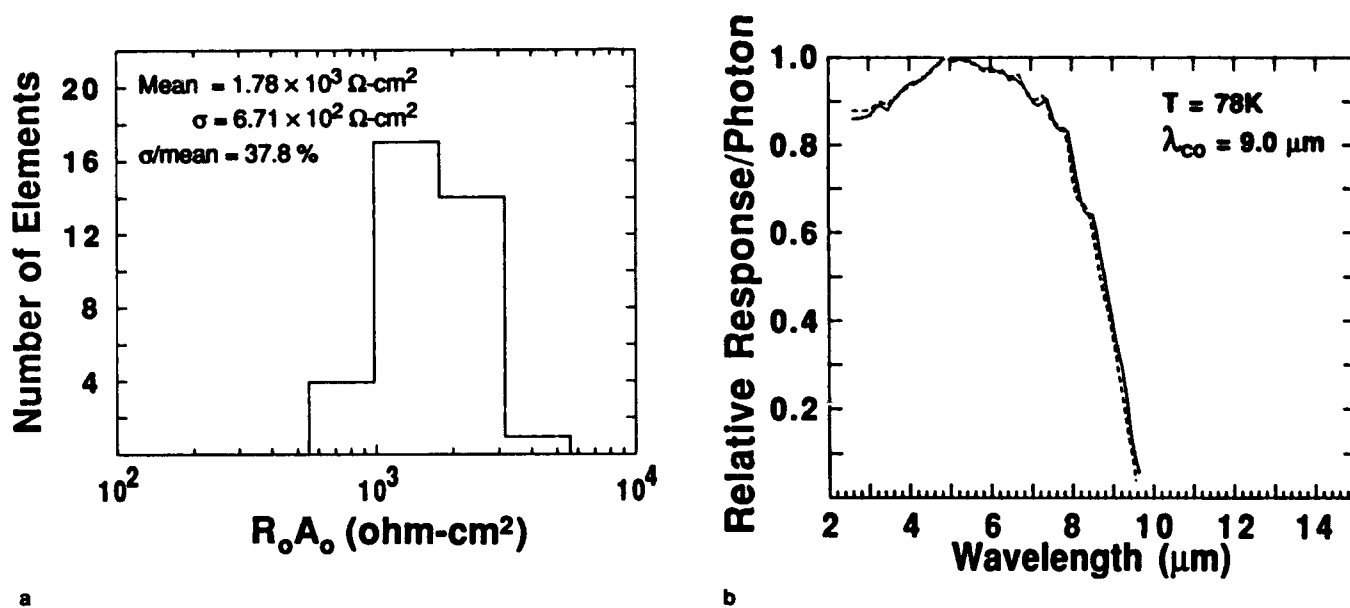


Fig. 10. a)  $R_o A_o$  histogram of 36 diodes in a  $480 \times 640$  HgCdTe array fabricated on CdZnTe/GaAs/Si measured at  $T = 78K$  under an  $1/2$  FOV (300 K) background and b) spectral response of three of these detectors measured at zero bias at  $T = 78K$ .

while the low temperature leakage current is dominated by tunneling.<sup>47</sup> This is identical to the results shown in Fig. 11. Since HgCdTe grown by LPE on CdZnTe/GaAs/Si has dislocation densities of low-mid  $10^6 \text{ cm}^{-2}$  while HgCdTe grown on bulk CdZnTe substrates has dislocation densities in the low  $10^5 \text{ cm}^{-2}$  range we believe that the differences in performance for detectors fabricated on both types of substrates can be attributed to their differences in dislocation density. These results show that CdZnTe/GaAs/Si alternative substrates are suitable for fabricating high-performance large-area arrays for 78K applications but a decrease in the dislocation density is needed both to increase the performance margin at 78K and to achieve higher performance for lower temperature applications.

### SUMMARY AND CONCLUSIONS

Large-area HgCdTe hybrid focal plane arrays need a silicon-based substrate that is thermal-expansion-matched to the silicon readout to ensure long-term cycle reliability; additional benefits of a silicon-based substrate include lower cost, increased strength, and larger dimensions than bulk CdZnTe substrates which are the present industry standard. We have achieved a thermal-expansion-matched FPA by substituting an MOCVD-grown CdZnTe/GaAs/Si alternative substrate in place of bulk CdZnTe substrates for the growth of HgCdTe p-on-n double-layer heterojunctions by controllably doped mercury-melt LPE. This approach allows us to realize the benefits of a silicon-based substrate grown by vapor-phase epitaxy together with a mature LPE-based HgCdTe high-performance photovoltaic array technology.

(100) CdZnTe layers were grown by MOCVD on GaAs/Si using a vertical-flow high-speed rotating disk reactor. Three 2-in diam substrates can be grown per run using a 5-in diam susceptor. Layers having

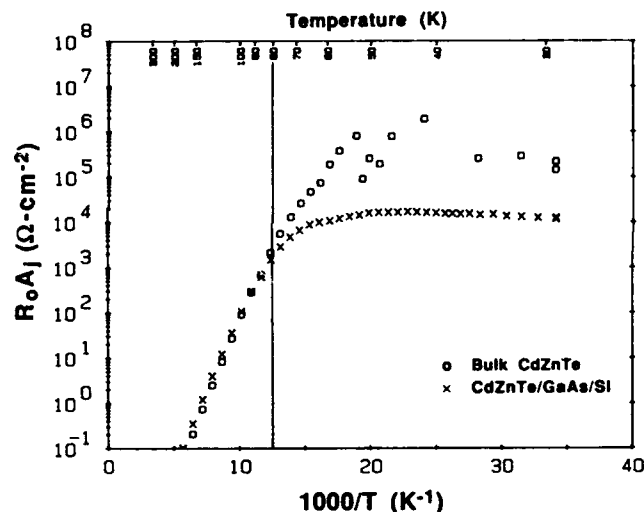


Fig. 11.  $R_o A_o$  product at zero FOV vs inverse temperature comparing  $480 \times 640$  array diodes fabricated on CdZnTe/GaAs/Si and bulk CdZnTe substrates.

specular surface morphology, good crystalline structure, and surface macro defect densities  $< 50 \text{ cm}^{-2}$  are routinely achieved and both the composition uniformity and run-to-run reproducibility were very good. As the composition of the CdZnTe layers increases the x-ray FWHM increases; this is a characteristic of CdZnTe grown by VPE techniques and is apparently associated with phase separation. Despite a broader x-ray FWHM for the ternary CdZnTe, the FWHM of HgCdTe grown by LPE on these substrates decreases, particularly for [ZnTe] compositions near the lattice matching condition to HgCdTe. An additional benefit of the ternary CdZnTe is an improved surface morphology of the HgCdTe layers.

Using these silicon-based substrates, we have demonstrated 78K high-performance LWIR HgCdTe  $480 \times 640$  arrays and find that their performance is

comparable to similar arrays fabricated on bulk CdZnTe substrates for temperatures exceeding approximately 78K. The performance at lower temperatures is apparently limited by the dislocation density which is typically in the low-mid  $10^6 \text{ cm}^{-2}$  range for these heteroepitaxial materials. These results show that CdZnTe/GaAs/Si alternative substrates are suitable for fabricating high-performance large-area arrays for 78K applications but a decrease in the dislocation density is needed both to increase the performance margin at 78K and to achieve higher performance for lower temperature applications.

### ACKNOWLEDGMENT

The authors thank V.L. Liguori, J.M. Peterson, V.B. Harper, G.M. Venzor, and D.A. Olson for materials characterization and B.A. Baumgratz and F.I. Gesswein for sample preparation and processing.

### REFERENCES

1. R. Kay, R. Bean, K. Zanio, C. Ito and D. McIntyre, *Appl. Phys. Lett.* 51, 2211 (1987).
2. A. Nouhi, G. Radhakrishnan, J. Katz and K. Koliwad, *Appl. Phys. Lett.* 52, 2028 (1988).
3. N.W. Cody, U. Sudarsan and R. Solanki, *J. Appl. Phys.* 66, 449 (1989).
4. W.L. Ahlgren, S.M. Johnson, E.J. Smith, R.P. Ruth, B.C. Johnston, M.H. Kalisher, C.A. Cockrum, T.W. James, D.L. Arney, C.K. Ziegler and W. Lick, *J. Vac. Sci. Technol. A* 7, 331 (1989).
5. D.D. Edwall, J. Bajaj and E.R. Gertner, *J. Vac. Sci. Technol. A* 8, 1054 (1990).
6. K. Zanio, R. Bean, R. Matson, P. Vu, S. Taylor, D. McIntyre, C. Ito and M. Chu, *Appl. Phys. Lett.* 56, 1207 (1990).
7. L.O. Bubulac, D.D. Edwall and C.R. Viswanathan, *J. Vac. Sci. Technol. B* 9, 1695 (1991).
8. S.J.C. Irvine, D.D. Edwall, L.O. Bubulac, R.V. Gil and E.R. Gertner, *J. Vac. Sci. Technol. B* 10, 1392 (1992).
9. J.M. Arias, M. Zandian, S.H. Shin, W.V. McLevige, J.G. Pasko and R.E. DeWames, *J. Vac. Sci. Technol. B* 9, 1646 (1991).
10. S.H. Shin, J.M. Arias, D.D. Edwall, M. Zandian, J.G. Pasko and R.E. DeWames, *J. Vac. Sci. Technol. B* 10, 1492 (1992).
11. R. Korenstein, P. Madison and P. Hallock, *J. Vac. Sci. Technol. B* 10, 1370 (1992).
12. W.-S. Wang, H. Ehsani and I.B. Bhat, these proceedings.
13. S.M. Johnson, M.H. Kalisher, W.L. Ahlgren, J.B. James and C.A. Cockrum, *Appl. Phys. Lett.* 56, 946 (1990).
14. S.M. Johnson, W.L. Ahlgren, M.H. Kalisher, J.B. James and W.J. Hamilton, *Properties of II-VI Semiconductors: Bulk Crystals, Epitaxial Films, Quantum Well Structures, and Dilute Magnetic Systems*, Mater. Res. Soc. Symp. Proc., eds. F.J. Bartoli, H.F. Schaake and J.F. Schetzina (Mater. Res. Soc., Pittsburgh, PA, 1990), Vol. 161, p. 351.
15. S.M. Johnson, J.B. James, W.L. Ahlgren, W.J. Hamilton, M. Ray and G.S. Tompa, *Long-Wavelength Semiconductor Devices, Materials, and Processes*, Mater. Res. Soc. Symp. Proc., eds. A. Katz, R.M. Biefeld, R.L. Gunshor and R.J. Malik (Mater. Res. Soc., Pittsburgh, PA, 1991), Vol. 216, p. 141.
16. D. Rajavel and J.J. Zinck, these proceedings.
17. L.O. Bubulac, D.D. Edwall and C.R. Viswanathan, *J. Vac. Sci. Technol. B* 9, 1695 (1991).
18. Y. Lo, R.N. Bicknell, T.H. Myers and J.F. Schetzina, *J. Appl. Phys.* 54, 4238 (1983).
19. R. Sporken, S. Sivananthan, K.K. Mahavadi, G. Monfroy, M. Boukerch and J.P. Faurie, *Appl. Phys. Lett.* 55, 1879 (1989).
20. R. Sporken, M. D. Lange, C. Massetand J.P. Faurie, *Appl. Phys. Lett.* 57, 1449 (1990).
21. R. Sporken, M.D. Lange and J.P. Faurie, *J. Vac. Sci. Technol. B* 9, 1651 (1991).
22. R. Sporken, M.D. Lange, S. Sivananthan and J.P. Faurie, *Appl. Phys. Lett.* 59, 81 (1991).
23. R. Sporken, Y.P. Chen, S. Sivananthan, M.D. Lange and J.P. Faurie, *J. Vac. Sci. Technol. B* 10, 1405 (1992).
24. Y.P. Chen, S. Sivananthan and J.P. Faurie, these proceedings.
25. R.L. Chou, M.S. Lin and K.S. Chou, *Appl. Phys. Lett.* 48, 523 (1986).
26. M.S. Lin, R.L. Chou and K.S. Chou, *J. Cryst. Growth* 77, 475 (1986).
27. H. Zogg and S. Blunier, *Appl. Phys. Lett.* 49, 1531 (1986).
28. A.N. Tiwari, W. Floeder, S. Blunier, H. Zogg and H. Weibel, *Appl. Phys. Lett.* 57, 1108 (1990).
29. H. Shtrikman, M. Oron, A. Raizman and G. Cinader, *J. Electron. Mater.* 17, 105 (1988).
30. S.M. Johnson, J.B. James, W.L. Ahlgren, W.J. Hamilton and M. Ray, *Appl. Phys. Lett.* 59, 2055 (1991).
31. M.D. Lange, R. Sporken, K.K. Mahavadi, J.P. Faurie, Y. Nakamura and N. Otsuka, *Appl. Phys. Lett.* 58, 1988 (1991).
32. T. Sasaki, M. Tomono and N. Oda, *J. Vac. Sci. Technol. B* 10, 1399 (1992).
33. T. Tung, M.H. Kalisher, A.P. Stevens and P.E. Herning, *Materials for Infrared Detectors and Sources*, Mater. Res. Soc. Symp. Proc., eds. R.F.C. Farrow, J.F. Schetzina and J.T. Cheung (Mater. Res. Soc., Pittsburgh, PA, 1987), Vol. 90, p. 321.
34. T. Tung, *J. Cryst. Growth* 86, 161 (1988).
35. T. Tung, L.V. DeArmond, R.F. Herald, P.E. Herning, M.H. Kalisher, D.A. Olson, R.F. Risser, A.P. Stevens and S.J. Tighe, (Soc. Phot. Opt. Inst. Eng. 1735, Bellingham, WA 1992), in print.
36. W.L. Bond, *Acta. Cryst.* 13, 814 (1960).
37. S.M. Johnson, S. Sen, W.H. Konkel and M.H. Kalisher, *J. Vac. Sci. Technol. B* 9, 1897 (1991).
38. W.J. Hamilton, S.M. Johnson and W.L. Ahlgren, *J. Vac. Sci. Technol. B* 10, 1543 (1992).
39. R.D. Feldman, R.F. Austin, A.H. Dayem and E.H. Westerwick, *Appl. Phys. Lett.* 49, 797 (1986).
40. R.D. Feldman, R.F. Austin, P.H. Fuoss, A.H. Dayem, E.H. Westerwick, S. Nakahara, T. Boone, H. Menéndez, A. Pinczuk, H.P. Valladares and S. Brennan, *J. Vac. Sci. Technol. B* 5, 690 (1987).
41. C.J. Summers, A. Torabi, B.K. Wagner, J.D. Benson, S.R. Stock and P.C. Huang, *Materials Technologies for IR Detectors*, eds. J. Besson (Soc. Phot. Opt. Inst. Eng. 659, Bellingham, WA 1986), p. 153.
42. S.M. Johnson, W.L. Ahlgren, M.T. Smith, B.C. Johnston and S. Sen, *Advances in Materials, Processing, and Devices in III-V Compound Semiconductors*, Mater. Res. Soc. Symp. Proc., eds. D.K. Sadana, L.E. Eastman and R. Dupuis (Mater. Res. Soc., Pittsburgh, PA, 1989), Vol. 144, p. 121.
43. S.B. Qadri and J.H. Dinan, *Appl. Phys. Lett.* 47, 1066 (1985).
44. A. Marbeuf, R. Druilhe, R. Triboulet and G. Patriarche, *J. Cryst. Growth* 117, 10 (1992).
45. E.A. Patten, M.H. Kalisher, G.R. Chapman, J.M. Fulton, C.Y. Huang, P.R. Norton, M. Ray and S. Sen, *J. Vac. Sci. Technol. B* 9, 1746 (1991).
46. H.-J. Kleebe, W.H. Hamilton, W.L. Ahlgren, S.M. Johnson and M. Rühle, *Properties of II-VI Semiconductors: Bulk Crystals, Epitaxial Films, Quantum Well Structures, and Dilute Magnetic Systems*, Mater. Res. Soc. Symp. Proc., eds. F.J. Bartoli, H.F. Schaake and J.F. Schetzina (Mater. Res. Soc., Pittsburgh, PA, 1990), Vol. 161, p. 63.
47. S.M. Johnson, D.R. Rhiger, J.P. Rosbeck, J.M. Peterson, S.M. Taylor and M.E. Boyd, *J. Vac. Sci. Technol. B* 10, 1499 (1992).

# Comparison of $\text{In}_{1-x}\text{Tl}_x\text{Sb}$ and $\text{Hg}_{1-x}\text{Cd}_x\text{Te}$ as Long Wavelength Infrared Materials

A.-B. CHEN

Physics Department, Auburn University, AL 36849

M. VAN SCHILFGAARDE and A. SHER

SRI International, Menlo Park, CA 94025

Cohesive energies, elastic constants, band structures, and phase diagram are calculated to evaluate the  $\text{In}_{1-x}\text{Tl}_x\text{Sb}$  alloy (ITA) as a long-wavelength infrared (LWIR) material compared to  $\text{Hg}_{1-x}\text{Cd}_x\text{Te}$  (MCT). To obtain a 0.1 eV gap at zero temperature, the  $x$  value for ITA is estimated to be  $x = 0.083$  as compared to  $x = 0.222$  for MCT. At this gap, ITA is more robust than MCT because the cohesive energies order as  $\text{InSb} > \text{TlSb} > \text{CdTe} > \text{HgTe}$ , and ITA has the stronger bonding InSb as the majority component. Although TlSb is found to favor the CsCl structure, ITA is a stable alloy in the zincblende structure for low  $x$  values. However, our phase diagram indicates that it is difficult to grow the 0.1 eV gap ITA from the melt, because above the eutectic the liquidus curve is flat, and the solidus drops rapidly. Moreover, the width of the stable concentration range of the zincblende solid phase shrinks at low temperatures due to the presence of the CsCl structure.

**Key words:** Elastic constants, InTlSb, HgCdTe, long-wavelength infrared materials, phase diagram

## INTRODUCTION

As growth technology continues to progress, researchers are always in pursuit of better semiconductors. In the area of long-wavelength infrared (LWIR) semiconductors, efforts have been directed into three fronts: refinement of the  $\text{Hg}_{1-x}\text{Cd}_x\text{Te}$  (MCT) technology, search for alternative semiconductors, and use of superlattices and quantum-well structures.<sup>1</sup> Among alternative LWIR semiconductors, obvious III-V candidates are alloys of InSb with TlSb or InBi. An energy-assisted epitaxial growth technique<sup>2</sup> has been used to obtain the  $\text{InSb}_{1-x}\text{Bi}_x$  alloy with a gap in the LWIR range (8 to 12  $\mu$ ), but that method has never evolved into a practical device technology. Thus it is interesting to examine the prospects of the  $\text{In}_{1-x}\text{Tl}_x\text{Sb}$  (ITA) alloy.

We have calculated<sup>3</sup> the structural properties, band structures, and phase diagram to evaluate ITA as an infrared (IR) material as compared to MCT. At the same gap for LWIR application, the band structure of ITA is similar to that of MCT, but ITA is a more robust

material. The phase diagram of ITA is more complicated than MCT, because of the presence of a stable CsCl structure in TlSb. Our phase diagram indicates that it is difficult to grow ITA from the melt. However, the zincblende solid solution of ITA is stable at low thallium compositions, which may permit the growth of ITA at the desired concentration using epitaxial growth methods. These studies show that ITA is a potential but challenging IR material deserving more attention.

## LATTICE CONSTANT, COHESIVE ENERGY, AND ELASTICITY

Table I shows the cohesive energies, atomic volumes, and some elastic constants of CdTe, HgTe, InSb, and TlSb calculated<sup>3</sup> from the full-potential linear muffin-tin orbital method<sup>4</sup> (FP-LMTO) within the local density approximation (LDA). The calculated atomic volumes and elastic constants are in good agreement with available experimental values. The calculated cohesive energies are consistently larger than the experimental values by about 0.9 eV, which is typical in LDA owing mainly to errors in the free atom. However, the relative cohesive energies

(Received October 12, 1992; revised January 13, 1993)

**Table I. Calculated vs Experimental Values of Atomic Volume (V), Cohesive Energy (E), Shear Modulus ( $c_{11}-c_{12}$ ), and Bulk Modulus (B)**

|   | CdTe |      | HgTe |      | InSb |      |       | TlSb |       |
|---|------|------|------|------|------|------|-------|------|-------|
|   | ZB*  | Expt | ZB*  | Expt | ZB   | Expt | CsCl† | ZB   | CsCl† |
| V ( $\text{\AA}^3$ )                              | 33.4 | 34.2 | 34.2 | 33.4 | 34.1 | 33.8 | 25.6  | 36.4 | 27.1  |
| E (eV/pr. of atoms)                               | 5.28 | 4.40 | 4.24 | 3.24 | 6.46 | 5.60 | 6.08  | 5.70 | 5.79  |
| $c_{11}-c_{12}$ ( $10^{12}$ erg/cm <sup>3</sup> ) | 0.20 | 0.17 | 0.19 | 0.18 | 0.31 | 0.31 | —     | 0.17 | —     |
| B ( $10^{12}$ erg/cm <sup>3</sup> )               | 0.44 | 0.42 | 0.44 | 0.47 | 0.45 | 0.48 | 0.72  | 0.38 | 0.49  |

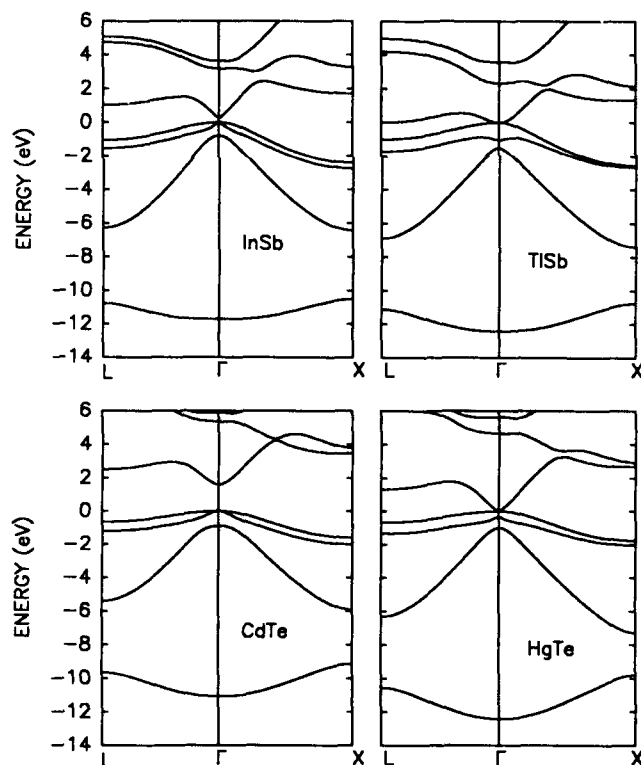
\*zincblende structure

†CsCl structure

**Table II. Direct Band Gaps (in eV) of Several Semiconductors Calculated in the Local Density Approximation (LDA) and Comparison with Experimental Gaps (Expt)**

|           | CdTe | GaAs | InP  | InAs  | InSb  | HgTe  | TlSb    |
|-----------|------|------|------|-------|-------|-------|---------|
| LDA       | 0.54 | 0.44 | 0.47 | -0.39 | -0.46 | -0.95 | -2.20   |
| LDA-SO    | 0.23 | 0.32 | 0.42 | -0.53 | -0.73 | -1.28 | (-2.50) |
| Expt      | 1.60 | 1.52 | 1.42 | 0.42  | 0.26  | -0.31 | (-1.52) |
| Underest. | 1.37 | 1.20 | 1.00 | 0.95  | 0.99  | 0.97  | (0.98)  |

Note: Systematic LDA errors are used to deduce the bandgap for TlSb. The numbers inside the parentheses are the estimated values.

**Fig. 1.** The parametrized band structures for InSb, TlSb, CdTe, and HgTe along the  $\Delta$  ( $\Gamma$ -L) and  $\Delta$  ( $\Gamma$ -X) directions.

are reliable. Our result shows that TlSb slightly favors the CsCl over the zincblende structure at zero temperature. In the zincblende structure, the cohesive energy magnitudes order as  $\text{InSb} > \text{TlSb} > \text{CdTe} > \text{HgTe}$ . Although TlSb has a weaker shear modulus than either HgTe or CdTe, InSb is stronger than both. As will be shown later, InSb is the majority com-

ponent in ITA for LWIR applications. These results combined imply that ITA is more robust structurally than MCT as a LWIR material.

### BAND STRUCTURE

Although LDA is known to produce band gaps for semiconductors that are too small, the gap for TlSb can be deduced by exploiting the systematic nature of LDA errors as shown in Table II. The first row shows the band gaps calculated from LDA for several direct-gap semiconductors. These values do not include the spin-orbit coupling. The second row shows the LDA values with the spin-orbit (SO) correction added. The third row lists the available experimental values. The fourth row lists the underestimated values, ranging from 0.95 to 1.37 eV, in LDA. CdTe, and to a certain extent GaAs, has a larger underestimate owing to its smaller dielectric constant. TlSb should have a dielectric constant close to InSb and HgTe, so an average of the underestimates of the two, i.e. 0.98 eV, can be used for TlSb to obtain an energy gap of -1.52 eV.

This inversion to a negative gap can also be estimated and understood in terms of tight-binding concepts. Firstly, due to a stronger scalar relativistic potential, the s-level of thallium is about 1.4 eV deeper than that of indium, which lowers the conduction minimum of TlSb. Secondly, the valence d-level of thallium is higher than that of indium by about 3 eV, and is only 10 eV below the top of the valence band. In the crystal, the cation d-level interacts with the neighboring p-state of antimony to push up the valence band maximum (VBM). This p-d repulsion raises the VBM in TlSb by 0.3 eV higher than that in InSb. Starting with a 0.25 eV gap for InSb, we subtract from this value the 0.3 eV from the p-d interaction, the 1.4 eV of the s-shift, and 0.05 eV due to a larger spin-orbit



coupling to arrive at a gap of  $-1.5$  eV for  $\text{TlSb}$ . This p-d interaction plus the spin-orbit coupling also produces a  $0.35$  eV valence band offset between  $\text{TlSb}$  and  $\text{InSb}$ . The same mechanism is also responsible for the band inversion and valence band offset between  $\text{HgTe}$  and  $\text{CdTe}$ .

To obtain more details, we have used a hybrid pseudopotential tight-binding method<sup>5</sup> to parametrize the band structures for the hosts and calculate the band structures for the alloys. The band structures for the four hosts along  $\Lambda$  ( $\Gamma$ -L) and  $\Delta$  ( $\Gamma$ -X) directions are plotted in Fig. 1. The gaps for these band structures are  $0.25$ ,  $-1.50$ ,  $1.60$ , and  $-0.31$  eV, respectively, for  $\text{InSb}$ ,  $\text{TlSb}$ ,  $\text{CdTe}$ , and  $\text{HgTe}$ . Based on a scaled-virtual crystal approximation (SVCA),<sup>5</sup> the calculated band gaps for both MCT and ITA at zero temperature are plotted in Fig. 2 as a function of the alloy concentration  $x$ . The predicted  $x$  values for the  $0.1$  eV gap at zero temperature are  $x = 0.083$  for ITA and, in close agreement with experiment,  $x = 0.222$  for MCT. The band structures in the vicinity of the band gap for ITA and MCT at the  $0.1$  eV gap are compared in Fig. 3. We can see these two alloys have very similar band structures at the band gap. This result implies that ITA has electrical and optical properties similar to MCT for LWIR applications.

### PI: ASE DIAGRAM

The phase diagram of  $\text{Hg}_{1-x}\text{Cd}_x\text{Te}$  is very simple;<sup>6</sup> one in which the liquidus-solidus curves have a simple lens shape and the zincblende solid solution is completely miscible except at very low temperatures. The presence of a stable CsCl solid phase in  $\text{TlSb}$  considerably complicates the phase diagram of  $\text{In}_{1-x}\text{Tl}_x\text{Sb}$ . Because of the small lattice mismatch between  $\text{InSb}$  and  $\text{TlSb}$ , the free energies of the solid solutions in both zincblende and CsCl structures can be approximated by a regular solution model given by  $F(x) = E(x) + kT[x \ln x + (1-x) \ln (1-x)]$ , and the internal energy can be written as  $E(x) = (1-x)E(0) + xE(1) + x(1-x)\Omega$ . The end point energies are given in Table I. The mixing enthalpies  $\Omega$  are calculated within LDA using quasi-random structures<sup>7</sup> and the results<sup>3</sup> give  $\Omega_{\text{ZB}} =$

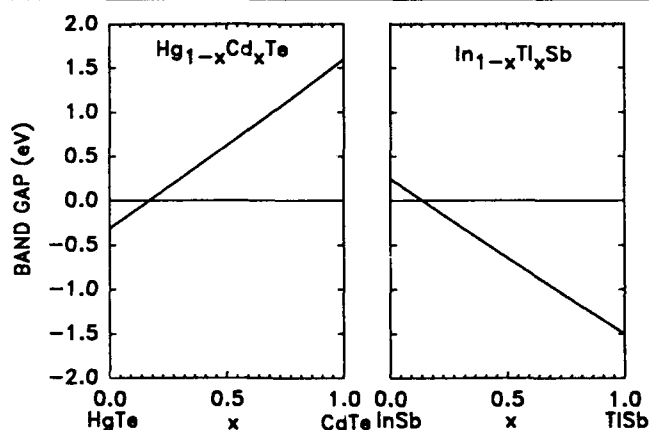


Fig. 2. Calculated band gaps as a function of alloy concentration  $x$  for  $\text{Hg}_{1-x}\text{Cd}_x\text{Te}$  and  $\text{In}_{1-x}\text{Tl}_x\text{Sb}$  at zero temperature.

$32$  meV per two atoms for the zincblende structure and  $\Omega_{\text{CC}} = -4$  meV for the CsCl structure. These two free energy functions produce a large miscibility gap separating the zincblende (ZB) alloy from the nearly pure  $\text{TlSb}$  crystal in the CsCl structure as shown in Fig. 4. Also shown are the solidus-liquidus curves calculated from the regular solution model. In addition to the above data for the solid solution, the following data were adopted for the liquid phase: mixing enthalpy  $\Omega = -1000$  cal/mole, melting temperatures of  $808$  and  $558$  K, and enthalpies of melting of  $11878$  and  $8629$  cal/mole respectively for  $\text{InSb}$  and  $\text{TlSb}$ . The  $\Omega$  value is taken to be the value previously used for MCT,<sup>8</sup> and the other values for the ZB  $\text{TlSb}$  are extrapolated from those of  $\text{InSb}$ <sup>9</sup> assuming they scale as  $Q(\text{TlSb})/Q(\text{InSb}) = Q(\text{HgTe})/Q(\text{CdTe})$ . Our phase diagram shows that it is very difficult to grow the  $0.1$  eV ( $x = 0.083$ ) ITA from the melt, because above the eutectic the liquidus curve is rather flat, and the solidus drops rapidly. Moreover, the width of the stable concentration range of the zincblende solid

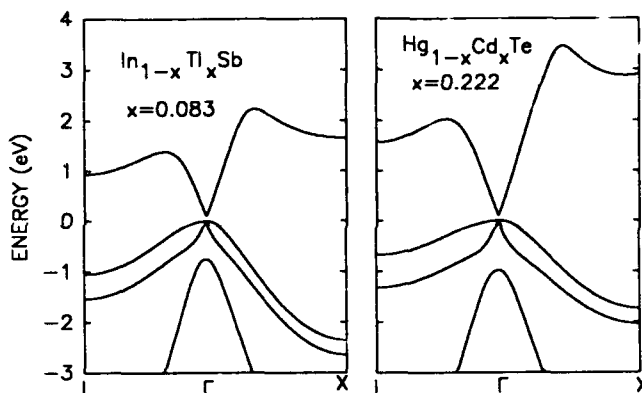


Fig. 3. Comparison of band structures around the band gap for  $\text{In}_{1-x}\text{Tl}_x\text{Sb}$  and  $\text{Hg}_{1-x}\text{Cd}_x\text{Te}$  at the  $0.1$  eV gap.

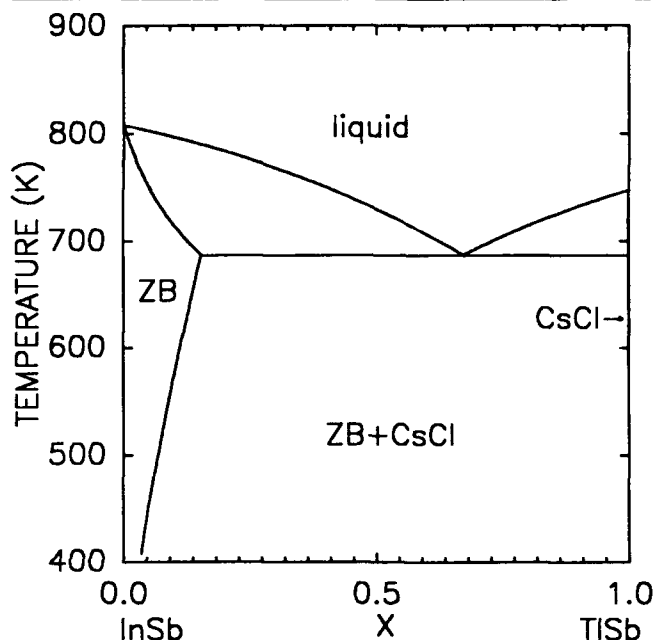


Fig. 4. Phase diagram of  $\text{In}_{1-x}\text{Tl}_x\text{Sb}$  alloy.

phase shrinks at low temperatures due to the presence of the CsCl structure. However, the ZB solid ITA solution is stable at low  $x$  values and moderate temperatures. A metastable alloy at the desired concentration may be obtained using epitaxial growth techniques.

### CONCLUSION AND DISCUSSION

Several properties of ITA have been studied. Our results show that, when compared to MCT as LWIR material, ITA is superior in structural bonding, comparable in electrical and optical properties, but more difficult to grow. However, our work represents the first reasonable materials evaluation. The predicted phase diagram depends heavily on the accuracy of the energy difference between the CsCl and the zincblende structures of both InSb and TlSb, and to a less extent, on the other parameters used. Further studies are called for to test these suggestions and to explore the potential of this LWIR material.

### ACKNOWLEDGMENT

We wish to thank J.M. MacCallum, G. Cinader, A. Sanjurjo, and M.A. Berding for their helpful suggestions. The support by ONR Contract N00014-89K-0132 and NASA Contract NAS1-18226 is gratefully acknowledged.

### REFERENCES

1. B.J. Levine, C.G. Bethea, K.G. Glogovsky, J.W. Stayt and R.E. Leibenguth, *Semicond. Sci. Technol.* 6, C114 (1991).
2. J. Zilko and J.E. Green, *Appl. Phys. Lett.* 33, 254 (1978); *J. Appl. Phys.* 51, 1549 (1980).
3. M. van Schilfgaarde, A. Sher and A.-B. Chen, submitted for publication.
4. M. Methfessel and M. van Schilfgaarde, unpublished.
5. A.-B. Chen and A. Sher, *Phys. Rev.* B23, 5360 (1981).
6. R.S. Patrick, A.-B. Chen, A. Sher and M.A. Berding, *J. Vac. Sci. Technol. A* 6(4), 2643 (1988) and references therein.
7. S.-H. Wei, L.G. Ferreira, J.E. Bernard and A. Zunger, *Phys. Rev.* B42, 9622 (1990).
8. F.R. Szofran and S.L. Lohoczky, *J. Electron. Mater.* 10, 1131 (1981).
9. G.B. Stringfellow and P.E. Green, *J. Phys. Chem. Solids* 30, 1779 (1969).

# Comparison of Spatial Compositional Uniformity and Dislocation Density for Organometallic Vapor Phase Epitaxial $\text{Hg}_{1-x}\text{Cd}_x\text{Te}$ Grown by the Direct Alloy and Interdiffused Growth Processes

D.D. EDWALL

Rockwell International Science Center, Thousand Oaks, CA 91360

Etch pit density and spatial compositional uniformity data are presented for organometallic vapor phase epitaxial  $\text{Hg}_{1-x}\text{Cd}_x\text{Te}$  grown by the direct alloy and interdiffused growth methods. For alloy growth, composition variation is as low as  $\Delta x = 0.004$  and  $0.02$  over 2- and 3-in diam areas, respectively; while for growth on  $\text{CdZnTe}$  substrates, etch pit density values lower than  $2 \times 10^5 \text{ cm}^{-2}$  have been achieved. For interdiffused growth on  $\text{CdZnTe}$ , etch pit density values lower than  $5 \times 10^5 \text{ cm}^{-2}$  have been obtained, while the composition variation is usually  $\Delta x \leq 0.004$  and  $0.014$  over 2- and 3-in diam areas, respectively. Data demonstrate that the choice of particular  $\text{CdZnTe}$  substrate strongly affects the subsequent etch pit density measured in the layer. Reasonably uniform n-type doping over 3-in diam area using the source triethylgallium is also reported for both growth methods.

**Key words:** Dislocation density,  $\text{HgCdTe}$ , OMVPE

## INTRODUCTION

$\text{Hg}_{1-x}\text{Cd}_x\text{Te}$  (MCT), a useful infrared (IR) detection semiconductor, can be grown by organometallic vapor phase epitaxy (OMVPE) in two ways: by the interdiffused multilayer process<sup>1</sup> (IMP, alternating thin layers of  $\text{CdTe}$  and  $\text{HgTe}$  which interdiffuse completely to form MCT) or by direct growth of the alloy. Historically, the major disadvantage of alloy growth has been poor spatial compositional uniformity due to the very different energies of formation of  $\text{CdTe}$  and  $\text{HgTe}$  using the commonly available organometallic precursors (dimethylcadmium and diisopropyltelluride). In interdiffused growth, this problem is circumvented by separate growth of the binaries, each under nearly optimized conditions, leading to much better compositional uniformity. Figure 1 shows the trend of compositional uniformity vs area, comparing IMP and alloy growth, using values reported in the literature. With the exception of recent data from Murakami et al.<sup>2</sup> where the alloy growth method was used using a multinozzle injection, for larger areas there has been a clear uniformity advantage using the IMP growth method.

However, a potential drawback of the IMP method is the growth interruptions, with subsequent nucle-

ation of one binary on the other, which might cause higher dislocation density. In fact, until recently, we have measured significantly higher dislocation densities (by chemical defect etching) for interdiffused compared with alloy growth on  $\text{CdZnTe}$ ,  $\text{GaAs}$ , and  $\text{GaAs/Si}$  substrates (Fig. 2). Although relatively low dislocation density material grown by the alloy method has been reported,<sup>2-4</sup> we have been able to do so with greatly improved compositional uniformity. In addition, based on a report by Bevan et al.<sup>5</sup> showing apparently low dislocation density IMP (100) MCT grown on  $\text{CdZnTe}$  (measured by transmission electron microscopy, TEM), we further studied growth of this material and have demonstrated lower dislocation density values than previously (Fig. 2) and similar to those obtained using alloy growth. Accordingly, results on alloy and IMP growth will be treated separately below.

## EXPERIMENTAL

The general growth conditions have been reported<sup>6,7</sup> and will not be repeated here. Extrinsic gallium doping using the source triethylgallium was used to create n-type conduction. Both alloy and interdiffused MCT layers were grown in the same commercial reactor (Crystal Specialties, Inc.) using the same horizontal flow chamber. Growth temperatures were also identical ( $>350^\circ\text{C}$ ) so that the only differences

(Received October 12, 1992; revised January 13, 1993)

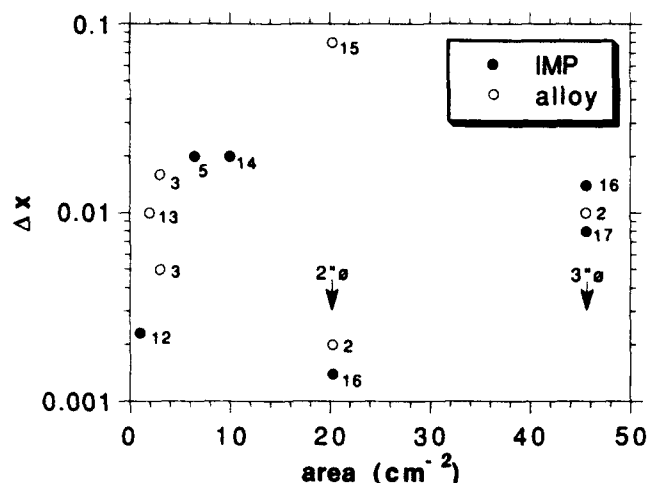


Fig. 1. Compositional uniformity vs area for IMP and alloy growth, using values reported in the literature. Symbol numbers refer to the references.

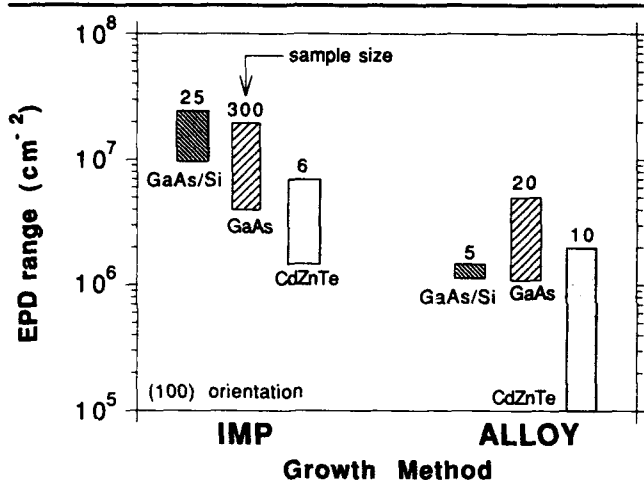


Fig. 2. Initial data showing ranges of EPD for OMVPE MCT grown by the IMP and alloy methods on CdZnTe, GaAs, and GaAs/Si substrates ( $x$  in range 0.2–0.3). Lower EPD values obtained for alloy vs IMP growth and for CdZnTe vs alternate substrates.

were alkyl and  $H_2$  carrier gas flows. The primary substrates used in the work described below for etch pit density (EPD) studies were (100) CdZnTe from two different vendors, misoriented  $10^\circ$  toward (111). Preliminary data are also reported for layers grown on (211)B oriented substrates. All of these substrates were not prescreened for quality such as zinc content (affecting lattice matching), dislocation density, or x-ray diffraction curve half-width. Because these substrates were not available in large areas, the  $x$  uniformity studies were carried out using 2- and 3-in diam (100) GaAs wafers. Substrates were rotated during growth ( $\sim 2$  rpm) to improve uniformity.

Layer characterization techniques included room-temperature infrared transmission to determine composition  $x$  and layer thickness, Hall effect measurements at 77K to determine doping concentration and carrier mobility, and chemical defect etching using a potassium dichromate solution<sup>8</sup> to determine EPD. Samples for EPD analysis have been etched both in an

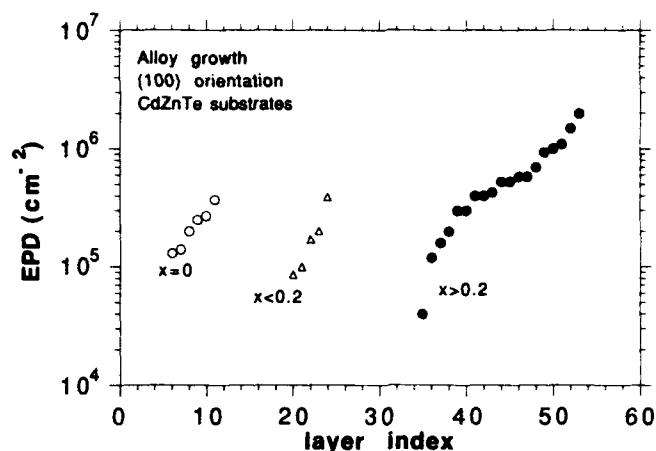


Fig. 3. Etch pit density distribution for alloy-grown MCT/CdZnTe for different ranges of  $x$  value. Different growth conditions and substrates.

as-grown state and following light etching ( $\sim 0.5$ – $1.0$   $\mu\text{m}$ ) in a bromine-methanol solution to remove the top region of the layers; both methods result in similar, consistent EPD results. No attempt has been made to correlate these EPD measurements and absolute dislocation density. Hall samples were annealed at  $250^\circ\text{C}$  in mercury vapor prior to measurement to remove mercury vacancy acceptors.

## RESULTS

### Alloy Growth

Figure 3 shows the EPD distribution for alloy-grown MCT/CdZnTe for different ranges of  $x$  value. Three groups of data are shown corresponding to  $x = 0$  (HgTe),  $x$  in the range 0.15–0.20, and 0.2–0.35. In this figure and in others to follow, each layer is given an arbitrary index number so that, in most cases, EPD values are arranged in ascending order. We have observed a weak dependence of increasing EPD with composition  $x$ . The data were generated using different substrates and growth conditions during a time when other aspects of the growth process, such as layer morphology, composition, and compositional uniformity, were being optimized. This may partially explain the variations. However, since it will be shown below that for interdiffused growth the choice of substrate strongly affects the EPD of the layer, it is likely that many of the EPD variations in Fig. 3 are due to uncontrolled differences in substrate material characteristics. The lower EPD values in Fig. 3 are similar to those reported by other groups.<sup>4,9</sup>

Using reasonably optimized growth conditions, Table I shows compositional uniformity data for two alloy layers grown on 3-in diam GaAs substrates. Maximum  $\Delta x$  values measured were 0.004 and 0.009 for the interior 2-in diam areas and 0.02 for the full 3-in diam areas. As will be seen below, the uniformity over the interior 2-in diam areas is similar to what we typically measure for interdiffused-grown layers, although the uniformity near the wafer edge is somewhat poorer by comparison. Comparing with the Fig. 1 data, these results represent a significant improve-

**Table I. Spatial Compositional Uniformity Data for Two 3-In Diam MCT Layers Grown by the Direct Alloy Growth Process on GaAs Substrates**

| Layer | Composition $x$ |        |       |       | Max $\Delta x$ |         |                          | 77 K Hall                        |                              |       |
|-------|-----------------|--------|-------|-------|----------------|---------|--------------------------|----------------------------------|------------------------------|-------|
|       | Center          | C+0.5" | C+1"  | Edge  | 2" diam        | 3" diam | EPD ( $\text{cm}^{-2}$ ) | $n(\text{cm}^{-3})$              | $\mu(\text{cm}^2/\text{Vs})$ | $x$   |
| 724   | 0.288           | 0.291  | 0.287 | 0.271 | 0.004          | 0.020   | $1.7 \times 10^6$        | $4.0 \times 10^{15}$<br>(center) | 43059                        | 0.288 |
|       |                 |        |       |       |                |         |                          | $4.6 \times 10^{15}$<br>(edge)   | 48693                        | 0.271 |
|       |                 |        |       |       |                |         |                          | $1.3 \times 10^{15}$             | 62728                        | 0.26  |
| 742   | 0.260           | 0.259  | 0.251 | 0.239 | 0.009          | 0.021   | $2.5 \times 10^6$        |                                  |                              |       |

Note: Data also included for EPD and 77K Hall effect measurements.

ment in composition uniformity for OMVPE MCT grown using the direct alloy growth method without the complication of multinozzle injection. This improvement is believed to result primarily from an increased width of the reaction cell (4.75 in) compared with the previous width (3 in) used in the Ref. 15 work.

Data are also included in Table I for EPD and 77K Hall effect characteristics. The EPD values, higher than usually observed for growth onto CdZnTe substrates due to lattice mismatch (14.5%), are consistent with those reported by other groups.<sup>2,3</sup> The Hall effect data show spatially uniform doping over 3-in diam area and high electron mobilities consistent with the  $x$  values. Undoped layers typically show mixed conduction after mercury-rich annealing (high resistivities and mobility values intermediate between those normally measured for good n- and p-type material).

### Interdiffused Growth

Despite the improved compositional uniformity demonstrated above for alloy growth, interdiffused growth retains relative advantages of easier p-type doping,<sup>6</sup> greater versatility of optical in situ monitoring of the growth process,<sup>10,11</sup> and greater understanding of the alkyl chemistry with potentially improved reproducibility. However, these advantages are irrelevant if IMP cannot produce MCT with similarly low dislocation density as for alloy-grown material.

Figure 4 shows the EPD distribution for IMP (100) MCT/CdZnTe grown on two different wafer lots from Vendor A and another lot from Vendor B (solid symbols). As for alloy growth (Fig. 3), the growth conditions were not constant, and the EPD distributions cover a wide range. Shown for comparison in open symbols are preliminary results for (211)B orientation growth where the growth conditions were constant except for minor changes to composition. Despite essentially same intended growth conditions, there is still a wide variation in EPD values. While at least some of this variation may be due to small, uncontrolled differences in growth (for example, substrate surface condition and growth nucleation), it has been shown that substrate effects play an important role. This is illustrated in Fig. 5, where results are shown for two different wafer lots in the same growth runs. Often very different EPDs are obtained for different substrates (prepared nominally identi-

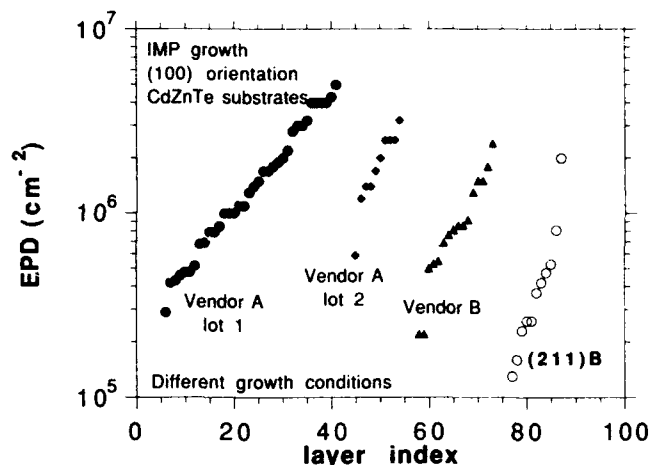


Fig. 4. Etch pit density distribution for IMP-grown (100) MCT/CdZnTe grown on wafers from different lots and from two different vendors (solid symbols). Different growth conditions within each set. Shown in open symbols are similar data for (211)B layers all grown using the same growth conditions except for minor adjustments to composition. All layers have  $x$  in range 0.2–0.3.

cally) exposed to the same growth conditions. Statistically, the Vendor B wafers have resulted in lower EPD values than the Vendor A, Lot 1 wafers. Due to these substrate effects, concluding from the Fig. 4 data that the (211)B orientation tends to result in lower EPD than (100) is unwarranted at this time.

These lower EPD values for IMP-grown layers, compared with the initial data shown in Fig. 2, have probably resulted, in part, from a much larger data set, but continued optimization of all aspects of the growth process may also be partly responsible. A systematic investigation of this issue has not yet been started.

Some of the above data would be expected to be consistent with the low dislocation density results reported by Bevan et al.<sup>5</sup> Although TEM was used in this work, unfortunately, no comparisons with EPD results were reported. Although there was, in one sample, a uniform distribution of small dislocation loops with a periodicity similar to the CdTe/HgTe multilayers, in another sample no dislocations or other defects were apparent in a sampled region extending from the surface to within  $\sim 1000\text{\AA}$  of the interface. This material would be expected to have low EPD (low- $10^5 \text{ cm}^{-2}$  or less) if characterized using the method used here.

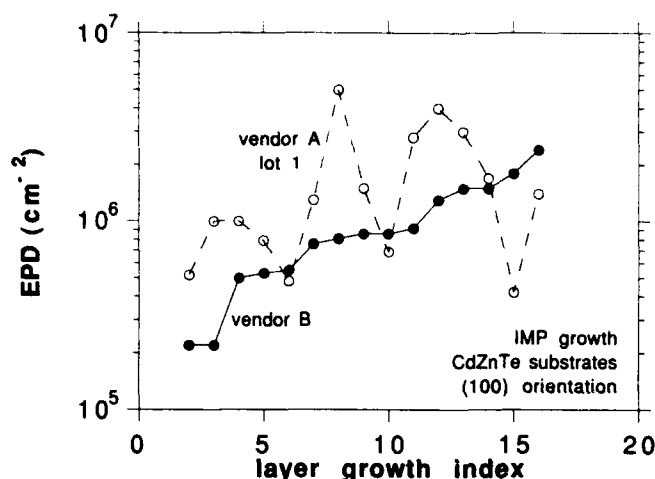


Fig. 5. Etch pit density comparison for IMP-grown MCT grown on two different lots of CdZnTe wafers in the same growth runs ( $x$  in range 0.2–0.3). The growth runs are arranged so that the EPD values corresponding to the Vendor B wafers are in ascending order.

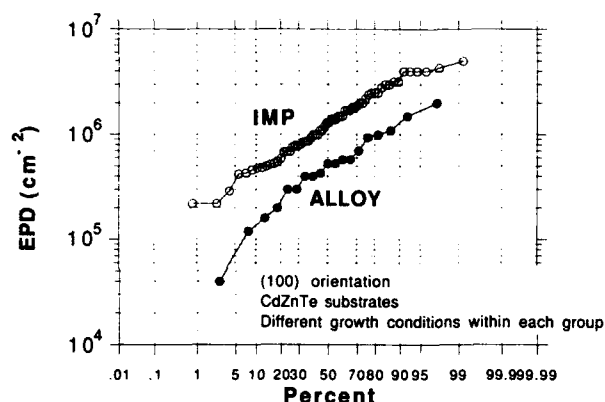


Fig. 6. Comparison of IMP and alloy MCT EPD distributions using the Fig. 3 data for  $x > 0.2$  and combined Fig. 4 data.

To more easily compare the EPD distributions for alloy- and IMP-grown layers, Fig. 6 shows a cumulative distribution plot of the Fig. 3 data (for  $x > 0.2$ ) with combined data from Fig. 4. Statistically, at present, alloy growth can be expected to result in somewhat lower EPD, but the difference in the two methods is not as large as previously believed. This result for layers grown on CdZnTe substrates is consistent with those for growth on the alternate substrates GaAs and GaAs/Si (Fig. 2). This initial data base is only a modest beginning toward identification of structural differences between layers grown by the two methods. Further improvements from both methods are likely with further growth optimization and careful attention to the choice of substrate.

Figure 7 shows the spatial compositional uniformity for a series of 29 3-in diam IMP layers grown on GaAs substrates ( $x$  in the range 0.22–0.24). The  $x$  variations from the center to 1-in from the center and from the center to the edge are plotted. For most layers the composition variation is  $\Delta x \leq 0.004$  and 0.014 over 2- and 3-in diam areas, respectively. The data show that OMVPE is capable of producing compositionally uni-

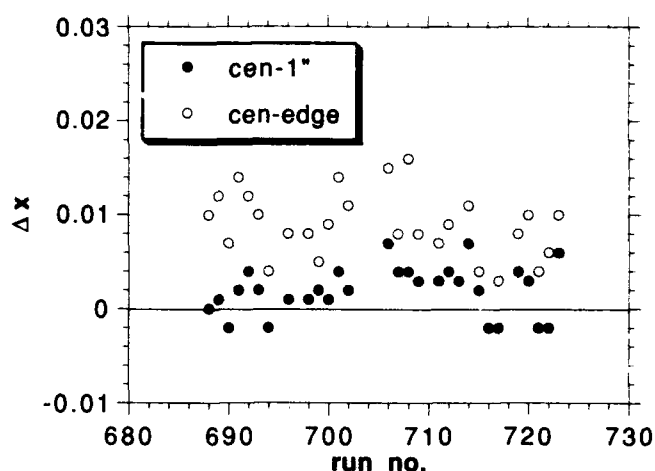


Fig. 7. Spatial compositional uniformity for a series of 29 3-in diam IMP layers grown on GaAs substrates ( $x$  in range 0.22–0.24). Uniformity is expressed as maximum  $x$  variation over the interior 2-in diam area and for the entire 3-in diam area. The variation is defined relative to the center value; in most layers the  $x$  value is highest at the center.

Table II. Doping Uniformity Over 3-in Diam Areas for IMP Growth Using Triethylgallium

| Layer | 77K Carrier Conc. ( $\times 10^{15} \text{ cm}^{-3}$ ) |      |
|-------|--|------|
|       | Center   | Edge |
| 822   | 5.7  | 5.9  |
| 823   | 1.5  | 1.2  |

form MCT over 2-in diam areas.

The n-type doping level is quite uniform over the 3-in diam area. Two recently grown layers that were measured showed excellent doping uniformity (See Table II).

## SUMMARY

At our laboratory, alloy growth has improved such that spatial compositional uniformity is approaching IMP standards, while IMP growth on CdZnTe substrates has improved such that EPD is approaching alloy standards. While alloy growth retains the advantage of producing the lowest EPD OMVPE MCT and IMP growth the most compositionally uniform material, the material characteristics of layers grown using the two methods are now more similar than previously. In future work, correlation with substrate material characteristics and details of the growth process will identify the requirements for consistently obtaining low EPD MCT. To our knowledge, this is the first report of low dislocation density IMP MCT measured by chemical defect etching. This development is of great importance to OMVPE MCT growth technology due to IMP's relative advantages of greater versatility and less complex growth kinetics.

## ACKNOWLEDGMENTS

This work was supported by SDIO under U.S. Air Force contract No. F33615-89-C5557 managed by Wright Laboratory (Lyn Brown Technical Monitor), and Rockwell IR&D funds.

## REFERENCES

1. J. Tunnicliffe, S.J.C. Irvine, O.D. Dosser and J.B. Mullin, *J. Cryst. Growth* 66, 245 (1984).
2. S. Murakami, Y. Sakachi, H. Nishino, T. Saito, K. Shinohara, and H. Takigawa, *J. Vac. Sci. Technol.* B10, 1380 (1992).
3. R. Korenstein, P. Hallock and B. MacLeod, *J. Vac. Sci. Technol.* B9, 1630 (1991).
4. R. Koestner, V. Lopes, R. Korenstein, S. Oguz, V. Kreismanis, H. Ehsani and I. Bhat, *J. Vac. Sci. Technol.* B10, 1643 (1992).
5. M.J. Bevan, J. Gregg and N.J. Doyle, *J. Mater. Res.* 5, 1475 (1990).
6. D.D. Edwall, L.O. Bubulac and E.R. Gertner, *J. Vac. Sci. Technol.* B10, 1423 (1992).
7. D.D. Edwall, J.-S. Chen and L.O. Bubulac, *J. Vac. Sci. Technol.* B9, 1691 (1991).
8. J.-S. Chen, United States Patent No. 4897152.
9. S. Murakami, private communication.
10. S.J.C. Irvine, J. Bajaj and H.O. Sankur, *J. Cryst. Growth* (in press).
11. J. Bajaj, S.J.C. Irvine and H.O. Sankur, "Modeling of In Situ Monitored Laser Reflectance During MOCVD Growth of  $\text{HgCdTe}$ ," 1992 U.S. Workshop on the Phys. and Chem. of Mercury Cadmium Telluride and Other IR Mater., Boston, MA (1992), *J. Electron. Mater.* 22, 899 (1993).
12. J. Thompson, P. Mackett and L.M. Smith, *J. Cryst. Growth* 86, 233 (1988).
13. S.K. Ghandhi, I.B. Bhat and H. Fardi, *Appl. Phys. Lett.* 52, 392 (1988).
14. R. Druilhe, F. Desjonqueres, A. Katty, A. Tromson-Carli, D. Lorans, L. Svob, A. Heurtel, Y. Marfaing and R. Triboulet, *J. Cryst. Growth* 101, 73 (1990).
15. D.D. Edwall, E.R. Gertner and L.O. Bubulac, *J. Cryst. Growth* 86, 240 (1988).
16. D.D. Edwall, J. Bajaj and E.R. Gertner, *J. Vac. Sci. Technol.* A8, 1045 (1990).
17. D.D. Edwall, J.-S. Chen, J. Bajaj and E.R. Gertner, *Semicond. Sci. Technol.* 5, S221 (1990).

# Indium Doping of HgCdTe Grown by Metalorganic Chemical Vapor Deposition-Direct Alloy Growth Using Triisopropylindium and Diisopropyltellurium•Triisopropylindium Adduct

R. KORENSTEIN, P.H. HALLOCK, D.L. LEE, and E. SULLIVAN

Raytheon Company, Research Division, Lexington, MA 02173

R.W. GEDRIDGE, JR., and K.T. HIGA

Research Department, Naval Air Warfare Center Weapons Division, China Lake, CA 93555

A new indium source, triisopropylindium, was used to dope HgCdTe layers grown by metalorganic chemical vapor deposition n-type with carrier concentrations,  $n_H$ , in the range between low  $10^{15}$  and low  $10^{17}$   $\text{cm}^{-3}$  at 77K. The reproducibility of carrier concentration was found to be excellent for  $n_H < 3 \times 10^{15}$   $\text{cm}^{-3}$ . High electron mobilities and minority carrier lifetime comparable to published values indicate that indium doping produces high quality n-type HgCdTe material. State-of-the-art photodiodes were obtained by growing a p-type HgCdTe layer by liquid phase epitaxy on an indium doped layer. In addition, an adduct compound formed between diisopropyltellurium (DIPTe) and triisopropylindium (TIPIIn): DIPTe-InTIP, was also found to be a viable n-type dopant for HgCdTe especially at concentrations in the low  $10^{15}$   $\text{cm}^{-3}$  or less.

**Key words:** DIPTe, HgCdTe, MOCVD-DAG, TIPIIn

## INTRODUCTION

Advanced infrared (IR) photovoltaic detectors fabricated from epitaxial HgCdTe (MCT) will require controlled extrinsic doping of both p- and n-type material. Whereas good progress has been made in the metalorganic chemical vapor deposition (MOCVD) of p-type MCT doped with arsenic using both arsine<sup>1</sup> and tertiarybutylarsine,<sup>2</sup> n-type doping remains more of a problem. Not only must the extrinsic n-type doping be controllable and reproducible, but for p/n heterostructures, the carrier concentration of the n-type layer should be in the low  $10^{15}$   $\text{cm}^{-3}$  or less.

Indium is the dopant of choice for producing n-type material due to its slow diffusion in MCT compared to other n-type dopants.<sup>3</sup> It has been used to produce n-type MCT grown by MOCVD using both IMP<sup>4</sup> and direct alloy growth (DAG).<sup>5</sup> Most of the work to date has utilized trimethylindium (TMIn) as the indium precursor.<sup>4-7</sup> However, TMIn is not a suitable precursor for doping HgCdTe n-type at low concentrations.

Because of its relatively high vapor pressure, the lowest doping achieved to date with TMIn is in the mid  $10^{16}$   $\text{cm}^{-3}$ .<sup>5</sup> Significant "memory" doping, has also been reported with this compound.<sup>6,7</sup> In addition, indium is introduced from a solid TMIn source which may be less desirable than a liquid source. An indium precursor is required that is a liquid which can provide a constant quantity of indium and has a very low vapor pressure at reasonable temperatures to allow doping at low carrier concentrations. Here we show controllable n-type doping in the range between low  $10^{15}$  and low  $10^{18}$   $\text{cm}^{-3}$  using two new indium compounds triisopropylindium (TIPIIn) and an adduct compound formed between TIPIIn and diisopropyltellurium (DIPTe):DIPTe-InTIP.

## EXPERIMENTAL

MCT was grown on both (111)B and (100) CdTe substrates by the MOCVD DAG (direct alloy growth) process in a horizontal reactor<sup>8</sup> at 360°C using diisopropyltellurium, dimethylcadmium, and elemental mercury. Both TIPIIn and DIPTe-InTIP, synthesized at the Naval Air Warfare Center, were used as

(Received October 13, 1992; revised January 13, 1993)



Table I. Material Characteristics of In-doped HgCdTe (MCT) Using TIPIIn

| Sample | x     | $n_H^{77K}$<br>( $\text{cm}^{-3}$ ) | $\mu_H^{77K}$<br>( $\text{cm}^2/\text{V-s}$ ) | SIMS In<br>( $\text{cm}^{-3}$ )(Surface) | SIMS In<br>( $\text{cm}^{-3}$ )(Interface) |
|--------|-------|-------------------------------------|---|--|--|
| 1525   | 0.206 | $2.5 \times 10^{15}$                | $2.0 \times 10^5$                             | $1.0 \times 10^{15}$                     | $4.0 \times 10^{15}$                       |
| 1559   | 0.212 | $2.6 \times 10^{15}$                | $9.0 \times 10^4$                             | $2.0 \times 10^{15}$                     | $3.0 \times 10^{15}$                       |
| 1548   | 0.203 | $5.3 \times 10^{16}$                | $9.0 \times 10^4$                             | $1.0 \times 10^{16}$                     | $2.0 \times 10^{17}$                       |
| 1544   | 0.222 | $2.1 \times 10^{17}$                | $4.5 \times 10^4$                             | $7.0 \times 10^{16}$                     | $7.0 \times 10^{17}$                       |

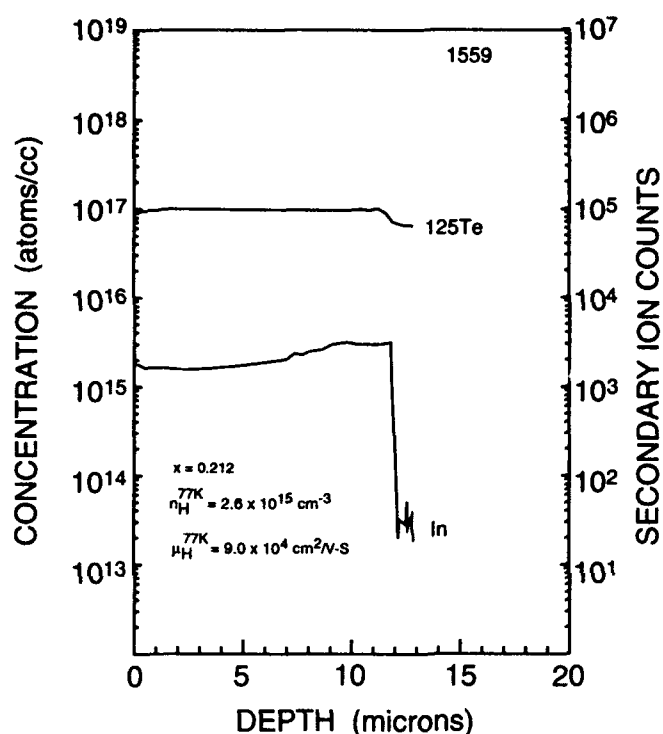


Fig. 1. Secondary ion mass spectroscopy profile of the In concentration as a function of depth in a 15  $\mu\text{m}$  thick epilayer doped with TIPIIn. The carrier concentration determined from Hall effect was  $2.6 \times 10^{15} \text{ cm}^{-3}$ .

indium precursors and each was contained in a standard cylinder operated in the conventional bubbler mode. The composition of the grown layers was determined from infrared transmission and thickness measurements. Samples were annealed at 220°C for 15 h in a Hg ambient to eliminate Hg vacancies. Carrier concentration and mobility were determined from van der Pauw measurements performed at room temperature and 77K. Indium concentrations were obtained from secondary ion mass spectroscopy (SIMS) measurements performed at Charles Evans and Associates. The data was quantified using relative sensitivity factors determined from ion implant standards of known dose into HgCdTe and should be accurate to within a factor of two.

## RESULTS AND DISCUSSION

The work in this study primarily involved the investigation of TIPIIn as an n-type dopant for MCT. In addition, the adduct compound DIPTe-InTIP was also examined as an n-type dopant for MCT.

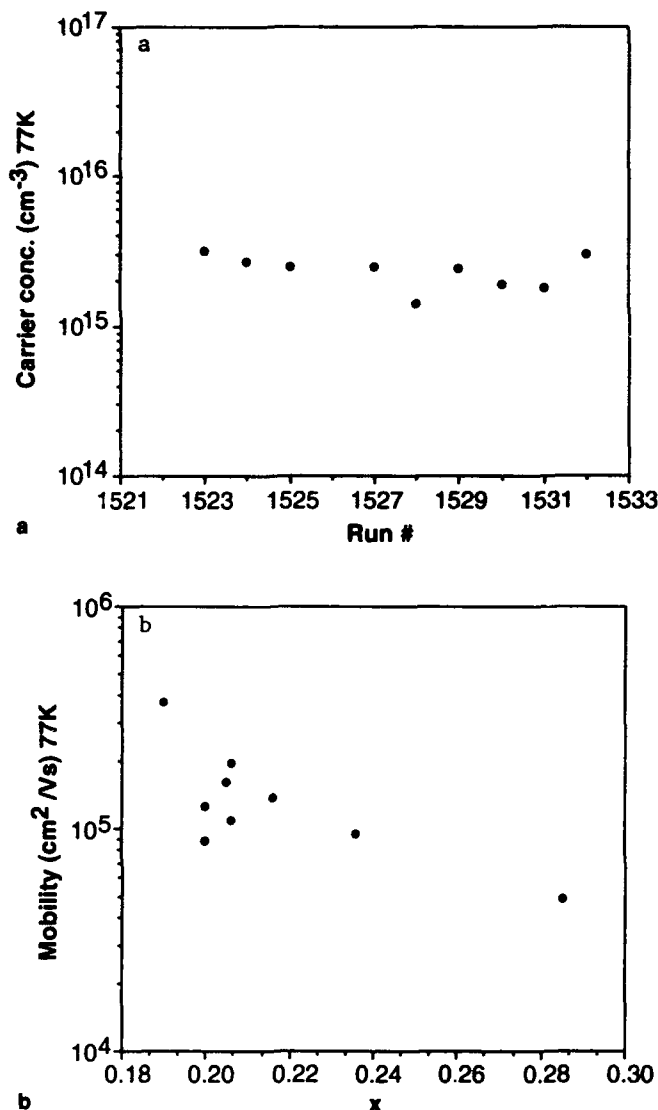


Fig. 2. a) Reproducibility of carrier concentration for ten consecutive growth runs, b) electron mobility (77K) as a function of composition, x, for the epilayers shown in a).

## N-type Doping Using TIPIIn

For this part of the work, MCT was grown onto (111)B CdTe substrates. Epilayers grown in the reactor prior to indium doping exhibited anomalous Hall effect behavior indicative of a parallel conduction process in low p-type material.<sup>8</sup> Doping was accomplished by introducing TIPIIn into the reactor simultaneously with the other reactants. The TIPIIn was not mixed with any other precursor prior to injection

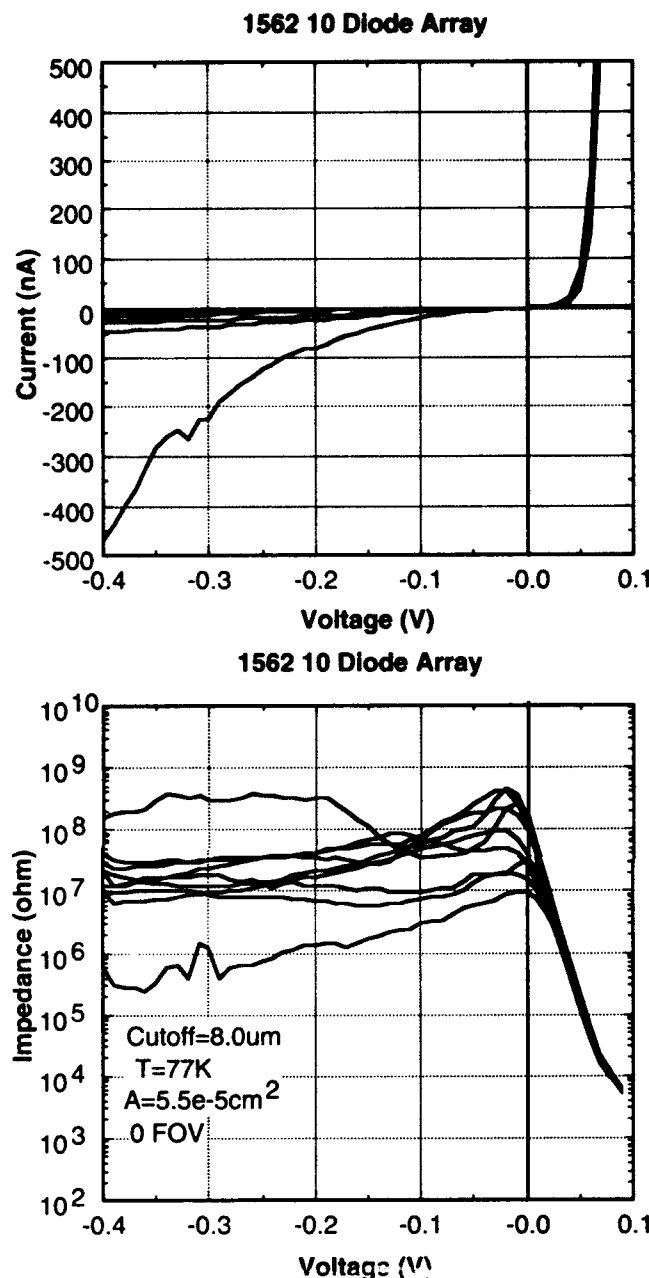


Fig. 3. I-V and R-V curves for diodes within an array fabricated by depositing a p-type layer grown by LPE on an In doped layer.

into the growth chamber. For most of the experiments, TIPIn was maintained at  $-15.0^{\circ}\text{C}$  where the compound is a liquid with a vapor pressure of 0.039 Torr.

Table I below lists the material characteristics for some of the epilayers grown in this study. As can be seen, the MCT carrier concentration,  $n_H$ , could be varied between low  $10^{15}\text{ cm}^{-3}$  and low  $10^{17}\text{ cm}^{-3}$ . This was accomplished by increasing the flow of hydrogen through the TIPIn bubbler. The material is n-type with electron mobilities consistent with the composition.<sup>9</sup> For the highest doped layer (1544), the reduced mobility can be attributed to ionized impurity scattering. Figure 1 is a SIMS profile of the indium atomic

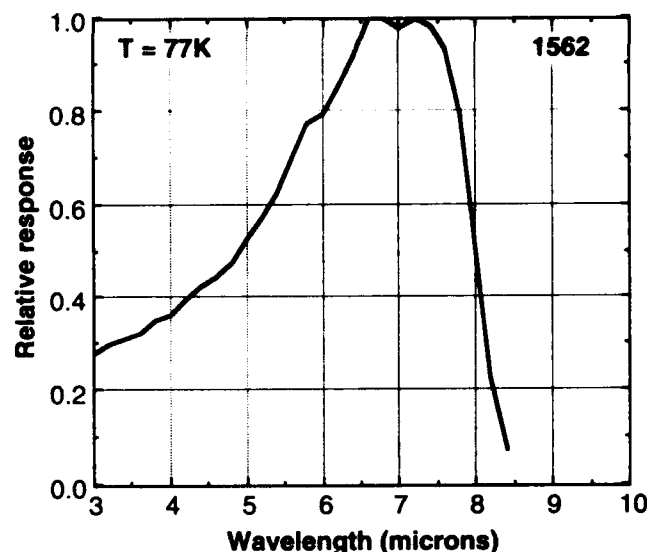


Fig. 4. Spectral response ( $\text{watt}^{-1}$ ) of one of the diodes in Fig. 3.

concentration as a function of depth in a  $15\text{ }\mu\text{m}$  thick layer (1559). Except for an increase near the substrate interface, the indium concentration is fairly uniform at a value of  $2 \times 10^{15}\text{ atoms cm}^{-3}$  and agrees fairly well with the excess carrier concentration listed in Table I indicating near 100% indium activation at this doping concentration. For the higher doped layers 1548 and 1544 listed in Table I, SIMS profiles indicate a grading in the indium concentration with the indium being highest at the substrate interface and decreasing gradually toward the epilayer/air interface. The Hall carrier concentration,  $n_H$ , for these layers falls somewhere between the surface and interface indium concentrations determined by SIMS. This would indicate that both the indium at the surface and the indium at the interface is electrically active n-type. The nonuniformity of indium incorporation at high doping ( $> 10^{16}\text{ cm}^{-3}$ ) may be indicative of an indium memory effect.<sup>10</sup> However, this may not be important since we are primarily interested in doping at low concentrations ( $1\text{--}3 \times 10^{15}\text{ cm}^{-3}$ ). In this range, indium incorporates very uniformly throughout the epilayer (Fig. 1).

The run-to-run reproducibility of n-type doping at low carrier concentrations was examined and the results are displayed in Fig. 2. Ten consecutive runs were made at a constant TIPIn partial pressure of  $5.1 \times 10^{-8}\text{ atm}$ . Figure 2a shows that the run-to-run reproducibility is very good. The 77K electron mobilities (Fig. 2b) for the epilayers shown in Fig. 2a are consistent with their x value<sup>9</sup> and indicate that indium doping produces high quality n-type material. The dependence of indium incorporation on x value was not examined in this work.

Additional testing of the indium doped MCT was obtained by performing minority carrier lifetime measurements and by fabricating and characterizing mesa diodes. The minority carrier lifetime was measured by the photoconductive decay technique using a GaAs laser operating at  $0.85\text{ }\mu\text{m}$ . Sample 1559

Table II. Material Characteristics of In-doped HgCdTe (MCT) Using DiPTE-InTIP

| Sample | $\times$ | $n_H^{77K}$<br>( $\text{cm}^{-3}$ ) | $\mu_H^{77K}$<br>( $\text{cm}^2/\text{V}\cdot\text{s}$ ) | SIMS In<br>( $\text{cm}^{-3}$ )(Surface) | SIMS In<br>( $\text{cm}^{-3}$ )Interface |
|--------|----------|-------------------------------------|--|--|--|
| 1697   | 0.271    | $3.7 \times 10^{14}$                | $7.3 \times 10^4$  | $4.0 \times 10^{14}$                     | $4.0 \times 10^{14}$                     |
| 1685   | 0.243    | $3.0 \times 10^{15}$                | $7.3 \times 10^4$  | $4.0 \times 10^{15}$                     | $4.0 \times 10^{15}$                     |
| 1683   | 0.235    | $2.7 \times 10^{16}$                | $7.1 \times 10^4$  | —  | —  |
| 1680   | 0.295    | $2.0 \times 10^{18}$                | $1.0 \times 10^4$  | $4.0 \times 10^{18}$                     | $1.0 \times 10^{17}$                     |

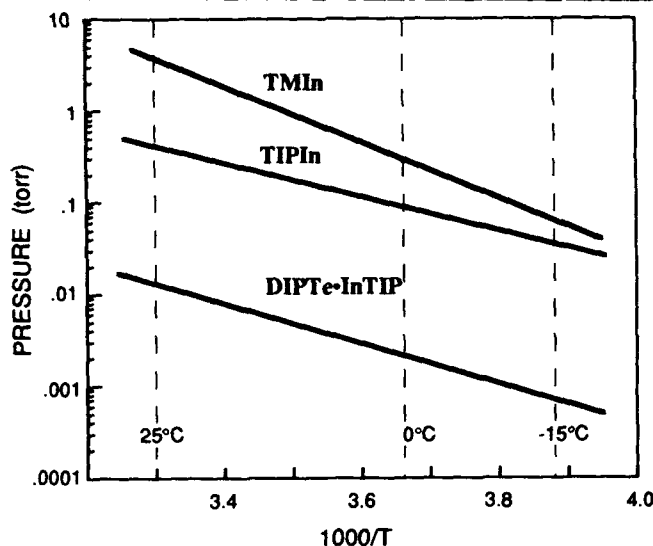


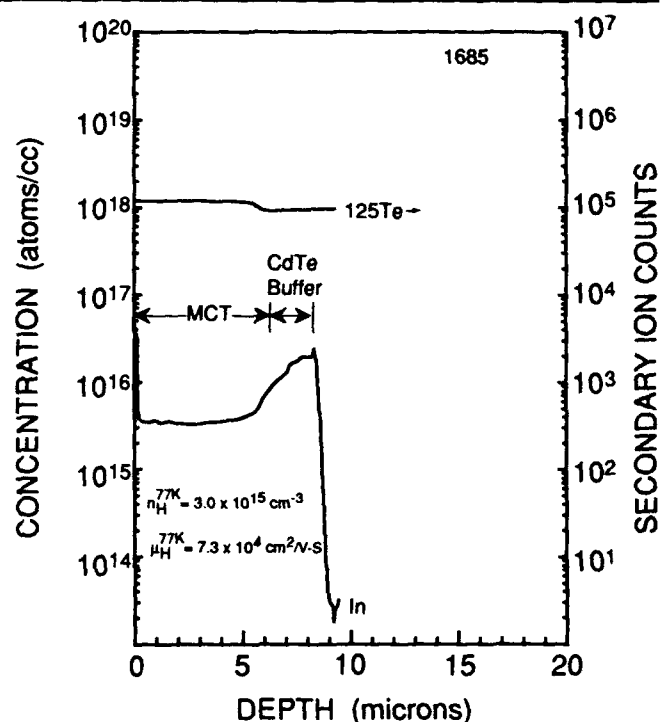
Fig. 5. Vapor pressure of TMIn, TIPIn, and DiPTE-InTIP as a function of temperature.

(doped at  $2.6 \times 10^{15} \text{ cm}^{-3}$  with a 77K cut-off wavelength of  $10.8 \mu\text{m}$ ) had a lifetime of 180 ns at 77K. This value is comparable to the lifetime measured for MCT grown on GaAs by MOCVD<sup>11</sup> and is within a factor of two of the lifetime measured for indium-doped MCT grown by liquid phase epitaxy (LPE).<sup>12</sup>

Wider bandgap p-type MCT was grown on our indium doped MCT by LPE at Fermionics. Mesa diodes were then fabricated and tested. I-V and R-V curves for a ten element array fabricated from wafer 1562 is shown in Fig. 3. An RoA value of  $5500 \text{ ohm}\cdot\text{cm}^2$  was measured at 77K for a diode with a cut-off wavelength of  $8.0 \mu\text{m}$  (Fig. 4). This diode performance is comparable to published data on diodes fabricated from LPE-grown MCT.<sup>13</sup> This result indicates that indium doped MCT grown by MOCVD-DAG is capable of producing state-of-the-art photovoltaic detectors.

### N-type Doping Using DiPTE-InTIP

The adduct indium precursor DiPTE-InTIP has a significantly lower vapor pressure than either TMIn or TIPIn. This can be seen in Fig. 5 where the vapor pressures of TMIn, TIPIn, and DiPTE-InTIP are plotted as a function of bubbler temperature. The vapor pressure of TMIn is approximately ten times higher at room temperature than that of TIPIn but is comparable at  $-15^\circ\text{C}$ . The advantage of using TIPIn instead of TMIn at low temperatures is that it is a liquid compared to solid TMIn. On the other hand, the vapor

Fig. 6. Secondary ion mass spectroscopy profile of the In concentration as a function of depth in a  $6 \mu\text{m}$  thick epilayer doped with DiPTE-InTIP. The carrier concentration determined from Hall effect was  $3.0 \times 10^{15} \text{ cm}^{-3}$ .

pressure of DiPTE-InTIP is at least 10x lower at  $-15^\circ\text{C}$  and it is still a liquid. Therefore, the adduct may be the better choice for doping MCT n-type at low concentrations. Because of its lower vapor pressure, the bubbler can be kept at or near room temperature thus simplifying its use. In addition, the lower vapor pressure allows one to use larger hydrogen flow rates through the bubbler which is important in the control of low carrier concentrations.

DiPTE-InTIP was introduced into the reactor in the same stainless steel manifold as the DMCD compound and the bubbler was maintained at  $22.0^\circ\text{C}$ . For this part of the study, MCT was grown onto (100) CdTe substrates misoriented four degrees toward (110) and a CdTe buffer layer was first grown by MOCVD on the substrate prior to MCT deposition. Table II lists some of the material characteristics of MCT doped with the adduct compound. The epilayers are n-type and could be doped from mid  $10^{14}$  to low  $10^{18} \text{ cm}^{-3}$ . There is good agreement between  $n_H$  determined from Hall measurements and indium determined from SIMS indicating near 100% indium activation in these layers.

Figure 6 is a SIMS profile of the atomic indium concentration through a 6  $\mu\text{m}$  thick layer (1685). As can be seen indium is very uniform through the layer. Indium is also present in the 3  $\mu\text{m}$  CdTe buffer layer. At present it is not known why indium diffuses into the CdTe layer but it may be due to the poor crystallinity of the CdTe layer which was not optimized for this work. Similarly to results obtained with TIPIn, the indium concentration as a function of depth is very uniform for low doping ( $<10^{16} \text{ cm}^{-3}$ ) (Table II) but becomes less uniform at higher concentrations. Finally, layer 1697 is a good example of the kind of low doping that is possible with this indium precursor. The value of  $4 \times 10^{14}$  indium atoms  $\text{cm}^{-3}$  is well above the detection limit of  $1 \times 10^{13} \text{ cm}^{-3}$  for indium SIMS analysis (Figs. 1 and 6).

These results indicate that DIPTe-InTIP is a viable n-type dopant for MCT. Because of its very low vapor pressure, it should be possible to reproducibly dope MCT n-type in the low  $10^{15} \text{ cm}^{-3}$  or less with this compound.

### CONCLUSION

We have shown that TIPIn is a suitable indium precursor for producing n-type MCT epilayers with carrier concentrations in the  $1\text{--}3 \times 10^{15} \text{ cm}^{-3}$  range. The run-to-run doping repeatability was found to be excellent. Comparison between SIMS and Hall effect measurements indicate near 100% activation of indium at low doping concentrations ( $1\text{--}3 \times 10^{15} \text{ atom cm}^{-3}$ ). Minority carrier lifetime measurements and diode characterization confirm that doping with indium using TIPIn results in excellent n-type MCT capable of producing state-of-the-art detectors.

Preliminary results using the adduct compound DIPTe-InTIP indicate that it is also a viable n-type dopant for MCT. Its very low vapor pressure makes it an attractive indium precursor for doping MCT at concentrations in the low  $10^{15} \text{ cm}^{-3}$  or less.

### ACKNOWLEDGMENT

The authors would like to thank C.C. Wang of Fermionics Corporation for growing the p-type MCT layer on the MOCVD grown n-type layer. One of the authors (R.W.G.) acknowledges the support of the Office of Naval Research and the Office of Naval Technology.

### REFERENCES

1. S.K. Ghandhi, N.R. Taskar, K.K. Parat, D. Terry and I.B. Bhat, *Appl. Phys. Lett.* 53, 1641 (1988).
2. D.D. Edwall, J.-S. Chen and L.O. Bubulac, *J. Vac. Sci. Technol. B*, 1691 (1991).
3. M. Brown and A.F. Willoughby, *J. Cryst. Growth* 59, 27 (1982).
4. J.S. Whiteley, P. Koppel, V.L. Conger and R.E. Owens, *J. Vac. Sci. Technol. A* 6, 2804 (1988).
5. S.K. Ghandhi, N.R. Taskar, K.K. Parat and I.B. Bhat, *Appl. Phys. Lett.* 57, 252 (1990).
6. B.C. Easton, C.D. Maxey, P.A.C. Whiffin, J.A. Roberts, I.G. Gale, F. Grainger and P. Capper, *J. Vac. Sci. Technol. B*, 1682 (1991).
7. J.S. Gough, M.R. Houlton, S.J.C. Irvine, N. Shaw, M.L. Young and M.G. Astles, *ibid.*, 1687 (1991).
8. R. Korenstein, P. Hallock, B. MacLeod, W. Hoke and S. Oguz, *J. Vac. Sci. Technol. A* 8, 1039 (1990).
9. W.M. Higgins, G.N. Pultz, R.G. Roy, R.A. Lancaster and J.L. Schmit, *J. Vac. Sci. Technol. A* 7, 271 (1989).
10. S.J.C. Irvine, J. Bajaj, L.O. Bubulac, W.P. Lin, R.W. Gedridge and K.T. Higa, *this issue*.
11. R. Zucca, D.D. Edwall, J.S. Chen, S.L. Johnston and C. R. Younger, *J. Vac. Sci. Technol. B* 9, 1823 (1991).
12. M.C. Chen and L. Colombo, *J. Appl. Phys.* 72, 4761 (1992).
13. C.C. Wang, *J. Vac. Sci. Technol. B* 9, 1740 (1991).

# A New N-Type Doping Precursor for MOCVD-IMP Growth of Detector Quality MCT

S.J.C. IRVINE, J. BAJAJ, L.O. BUBULAC, and W.P. LIN

Rockwell International Science Center, 1049 Camino Dos Rios, Thousand Oaks, CA 91360

R.W. GEDRIDGE, JR., and K.T. HIGA

Naval Air Warfare Center Weapons Division, China Lake, CA 93555

A new indium precursor, triisopropyl indium (TIPIIn), has been used for doping MCT at low carrier concentrations. Previous attempts using indium organometallics resulted in a strong memory effect where residual doping would persist for many growth runs. Introducing TIPIIn on the tellurium inject line resulted in a similarly strong memory doping but this was not observed when feeding the dopant in on the cadmium injection line. The TIPIIn is believed to have been forming a low volatility adduct with diisopropyl tellurium (DIPTe) in the feed line and to have continued to evaporate at a low but significant rate. By keeping the TIPIIn and DIPTe precursors separate until they entered the reactor, the desired low  $10^{15} \text{ cm}^{-3}$  carrier concentration and flat indium profiles could be achieved with good reproducibility. Good electrical characteristics were measured for these layers with Auger limited lifetime  $>1 \mu\text{s}$  at 77K.

**Key words:** Detector quality, HgCdTe, LPE, MOCVD-IMP growth, n-type doping

## INTRODUCTION

A variety of approaches have been used to control the doping of n-type MCT grown by metalorganic chemical vapor deposition (MOCVD).<sup>1</sup> These include group III doping onto the group II site using Al,<sup>2</sup> Ga,<sup>3</sup> and In<sup>4,5</sup> and group VII doping onto the group VI site using I.<sup>6</sup> A common problem with the precursors developed for III-V MOCVD is that the saturated vapor pressures are too high to be handled conveniently as dopant precursors. Lower dopant concentrations can be obtained from an effuser source but there is less flexibility in the range of concentrations from vapor pressure simply controlled by the source temperature. A potentially more serious problem is unwanted reaction processes that cause a memory effect where doping will persist for a number of growth runs following its introduction. Of the group III precursors, Al reacted strongly with residual carbon and oxygen resulting in low activity, Ga is a

relatively fast diffuser and may getter during subsequent annealing, and indium has a strong memory effect. Easton et al.<sup>6</sup> showed iodine to be successful in doping MCT down to  $2 \times 10^{15} \text{ cm}^{-3}$  but its introduction from a solid source may be less desirable than a liquid source. Three different groups<sup>3,5,6</sup> used trimethyl indium (TMIn) and all found that the doping concentrations were difficult to control at high concentrations ( $>1 \times 10^{17} \text{ cm}^{-3}$ ) and low concentrations could be achieved only from the memory effect. Edwall et al.<sup>7</sup> observed similar effects for ethyldimethyl indium. In all cases, the incorporation efficiency was high, particularly in HgTe layers and, as far as could be determined, activation was 100%. Therefore, indications are that indium is potentially a good dopant provided a suitable precursor can be controlled at low carrier concentrations without memory effects.

This paper presents results on the doping of MCT using a new precursor triisopropyl indium (TIPIIn). Results are presented on the method of dopant introduction, memory effect, activation, and electrical quality of the MCT layers.

(Received October 14, 1992; revised January 15, 1993)

## EXPERIMENTAL

MCT layers were grown using the interdiffused multilayer process (IMP)<sup>8</sup> where alternate layers of HgTe and CdTe are grown and allowed to interdiffuse during the total growth cycle. Each HgTe/CdTe cycle is approximately 1500 Å thick where the individual thicknesses are chosen to yield the required composition (*x*) in the homogenized layer. These doping experiments were carried out in a horizontal reactor cell operating at atmospheric pressure. The substrate holder was rotated and heated to 380°C using a pyrolytic boron nitride heater situated underneath the holder. An internal liquid mercury source was used to evaporate mercury into the hydrogen stream and was held at 210°C. The growth process was continuously monitored by laser reflectance which gave layer thickness, growth rate, and morphology.<sup>9</sup>

These growth experiments were carried out on 3-inch GaAs substrates oriented (100)10°→(110) and were supplied by Show Adenko. Before loading into the reactor, substrates were etched for one min in 5:1:1, H<sub>2</sub>SO<sub>4</sub>:H<sub>2</sub>O<sub>2</sub>:H<sub>2</sub>O, rinsed in deionized water followed by a final rinse in sodium free high purity methanol.

The epitaxial MCT layers were isothermally annealed in mercury vapor at 250°C to remove metal vacancies prior to making the Hall measurements.

The TIPIn dopant, synthesized at Naval Air War-

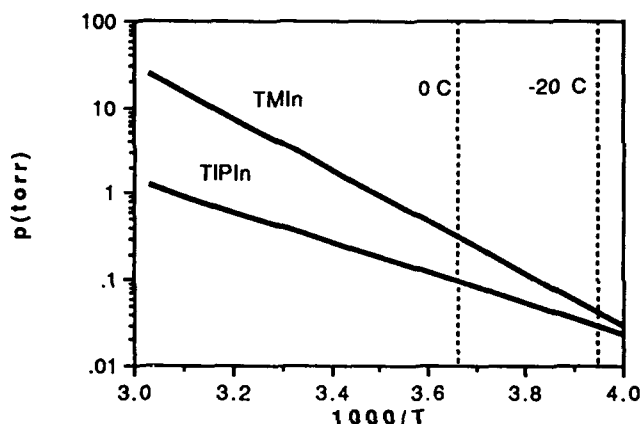


Fig. 1. Saturated vapor pressures for TMIn and TIPIn.

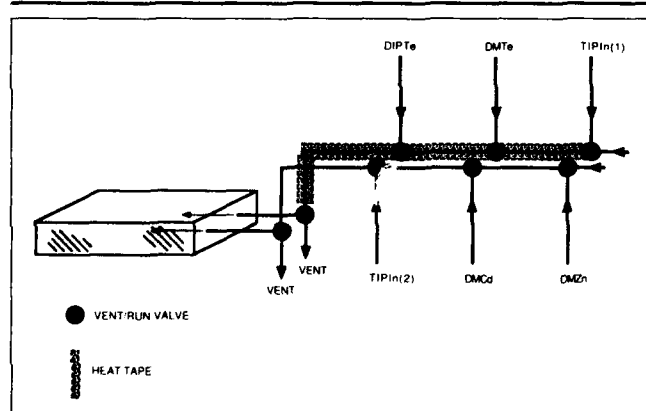


Fig. 2. Schematic of reactor layout showing routing of organometallics.

fare Center Weapons Division, China Lake, was cooled to -20°C where the saturated vapor pressure was 0.03 Torr. The vapor pressures for TIPIn as a function of bubbler temperature are shown in Fig. 1 and can be compared with the saturated vapor pressures for TMIn. Although the vapor pressures for TIPIn at higher temperatures are about a factor of ten smaller than for TMIn, at -20°C, they are much closer. The advantage of TIPIn is that at -20°C it is still a liquid and will give a steady vapor pressure whereas TMIn is a solid. Easton et al.<sup>6</sup> have shown that indium incorporates between 10 and 100 times more efficiently in HgTe than in CdTe but for IMP thicknesses of CdTe and HgTe will diffuse fast enough to yield a uniform concentration. Utilizing the flexibility of IMP, we can introduce the TIPIn dopant only during the HgTe growth cycle, thus minimizing the molar concentration of TIPIn needed to dope to the desired concentration. Minimizing the TIPIn concentration will reduce the risk of any doping memory effects.

## DOPING RESULTS

Three different configurations were used to investigate the doping and memory mechanisms using TIPIn. The schematic of the gas flow layout shown in Fig. 2, reveals that this reactor is configured with two independent organometallic manifolds feeding into injector assemblies inside the reactor cell. Mixing of these gas flows inside the reactor (combined with an internal Hg source) is assisted with a third flow, not shown, which purges the whole reactor cell space. Each organometallic line is fed into the cadmium or tellurium gas manifolds via vent/run valves. Vent/run valves are also used to direct these manifold gas mixtures into the reactor cell injectors. The first series of experiments used the TIPIn feed on the tellurium manifold [indicated as TIPIn(1)], and used a continuous feed into the reactor cell during the MCT growth. A second series of experiments used a heat tape to bake the tellurium manifold at approximately 100°C between runs and only injected TIPIn into the reactor cell during the HgTe IMP cycle, as described

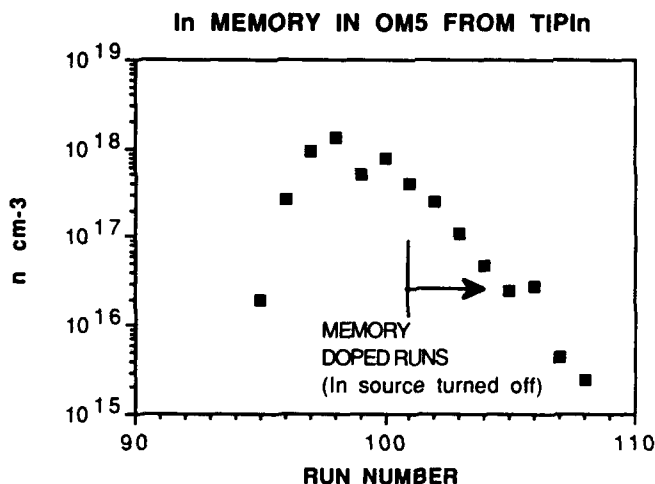


Fig. 3. 77K Hall carrier concentration as a function of run number for TIPIn on tellurium inject line.

above. The third series used the TIPIIn feed on the cadmium manifold and injection of TIPIIn only during the HgTe cycle.

### TIPIIn on Tellurium Manifold

A TIPIIn concentration (defined as moles of TIPIIn/moles of hydrogen) ranging between  $1.3 \times 10^{-8}$  and  $1.3 \times 10^{-7}$  was used as compared with a DIPTe concentration of  $4.8 \times 10^{-4}$  for the HgTe IMP cycle. The measured Hall carrier concentration at 77 K is shown in Fig. 3 vs wafer run number which runs consecutively. The first six layers were grown with intentional doping and resulted in the carrier concentration going from  $2 \times 10^{16}$  to  $1.5 \times 10^{18} \text{ cm}^{-3}$  over the first four runs, with no change in growth conditions. This increase is due to a memory effect and indicates an accumulation in TIPIIn concentration or some byproduct in the system. No further TIPIIn was intentionally introduced into the reactor from runs 101 to 108 and Fig. 3 shows a steady decrease in carrier concentration to a level of  $2 \times 10^{15} \text{ cm}^{-3}$ . Each of these layers was analyzed for their indium concentration by secondary ion mass spectroscopy (SIMS) using a Cameca IMS 3F at Charles Evans and Associates, which gives a depth profile of dopant concentration as shown in Fig. 4. This profile was calibrated using indium doped standards. Layer number 104 was memory doped and displays a distinct peak at the CdTe buffer/MCT interface, increasing to  $4 \times 10^{17} \text{ cm}^{-3}$ . The Hall carrier concentration for this layer was  $5 \times 10^{16} \text{ cm}^{-3}$ , in good agreement with the bulk indium concentration of  $4 \times 10^{16} \text{ cm}^{-3}$ . The peak is associated with memory doping and was observed by Gough et al.<sup>4</sup> using TMIn to dope MCT. The mechanism we propose for this effect is that the residual TIPIIn concentration in the gas phase must be present during the CdTe buffer layer but is not at a sufficiently high concentration to incorporate into the layer. It is proposed that the indium will accumulate on the surface until the first HgTe IMP layer is grown when this high surface concentration will be incorporated into the layer, hence giving rise to the peak.

The presence of this strong indium memory could be partly attributed to the continuous flow of indium during the MCT growth but this cannot explain the persistence of indium over many runs. The reactor cell was baked at  $850^\circ\text{C}$  between runs, so it was unlikely that dopant would remain in the reactor cell. All parts of the system were flushed with hydrogen between runs, so that volatile precursors should be adequately removed from the pipework. A more likely explanation was that the TIPIIn was reacting with another organometallic to form a relatively involatile product which would persist in the lines. Experiments with DIPTe and TIPIIn at Naval Air Warfare Center Weapons Division, China Lake, were successful in isolating the DIPTe:TIPIIn adduct. It is a 1:1 liquid adduct and remains liquid down to  $-78^\circ\text{C}$ . While DIPTe is not released under dynamic vacuum at room temperature, around  $50\text{--}60^\circ\text{C}$  the adduct slowly loses DIPTe under vacuum. This suggested

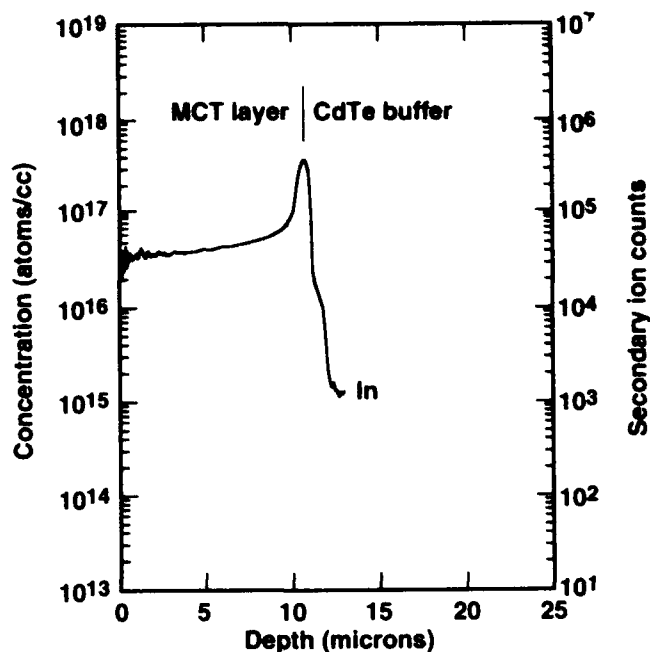


Fig. 4. Secondary ion mass spectroscopy depth profile for indium concentration in layer 104, showing memory effect.

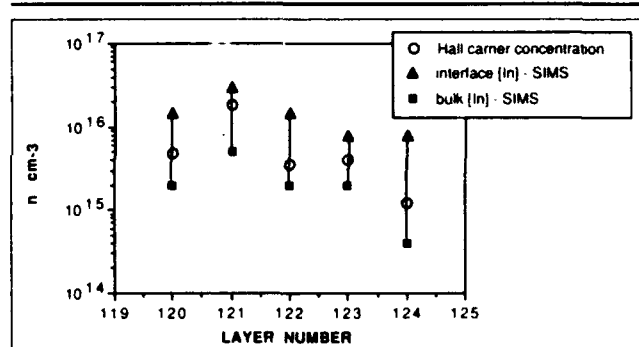


Fig. 5. 77K Hall carrier concentration and indium concentrations for consecutive runs where the tellurium inject line was baked between runs.

that the use of TIPIIn will not form the adduct in the reactor cell since the walls are kept at around  $200^\circ\text{C}$ . However, this adduct forms at room temperature, which can clearly explain the memory effect down the DIPTe feed line where the transit time between bubbler and reactor cell is about 20 s. Once formed, the adduct has a vapor pressure about a factor of 30 below that of TIPIIn and slowly evaporates to continue the doping long after the TIPIIn flow has been turned off. However, the adduct would be a suitable low volatility dopant as it would not react further in the feed lines and is generally less reactive than TIPIIn. To verify that this adduct was accumulating in the common inject manifold, carrying both the DIPTe and TIPIIn flows, a heat tape was used to bake the line between runs, at approximately  $100^\circ\text{C}$ , and dissociate the adduct.

### Tellurium Manifold Bake

The heat tape shown in Fig. 2 heated the inject manifold line between the TIPIIn vent/run valve and

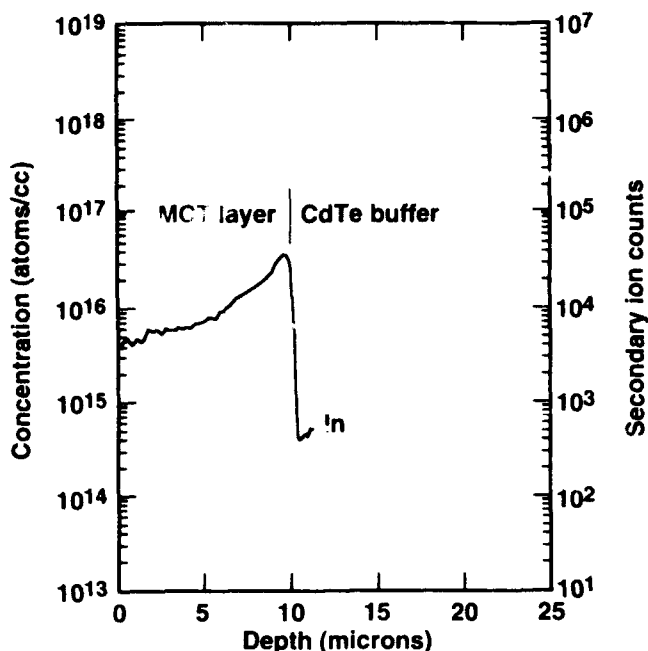


Fig. 6. Indium SIMS profile for layer 121 taken from the series of growths shown in Fig. 5.

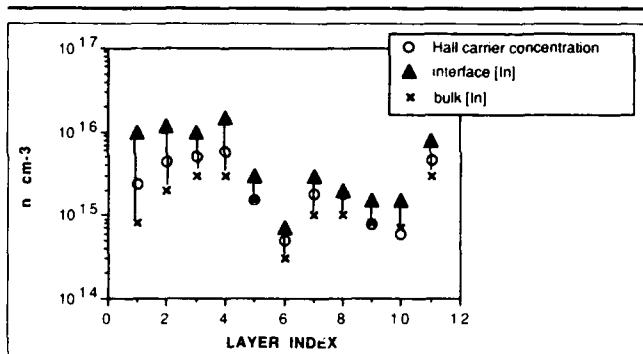


Fig. 7. 77K Hall carrier concentration and indium concentrations for layers grown with TIPIn on the cadmium inject line.

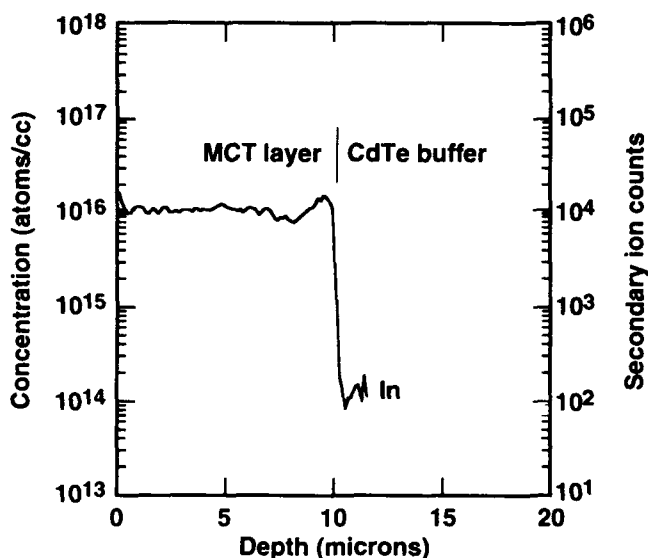


Fig. 8. Indium SIMS profile for layer doped with TIPIn on the cadmium inject line, taken from the series shown in Fig. 7.

the vent/run valve in front of the injector. This covers most of the common line where DIPTe and TIPIn can mix. The mode of doping in this series of experiments was injecting TIPIn just in the HgTe IMP phase which reduced the total dose of TIPIn going through the system by approximately a factor of two. The Hall carrier concentrations together with the SIMS analysis for indium content are shown in Fig. 5. Over five consecutive runs, there was no net increase in indium concentration and the results were mostly in the desired range of low  $10^{15} \text{ cm}^{-3}$ . Because the indium depth profiles still have an interface peak with some grading in the layer, these results have been represented in Fig. 5 as the bulk value (lowest) and the peak value (highest). The Hall carrier concentrations are in between these values, averaging the indium profile. This indicates that both the peak and bulk indium contents are electrically active n-type. A typical SIMS profile (Fig. 6) clearly shows the interface peak but is less prominent than in Fig. 4. The presence of the peak confirms that there is still some residual memory of indium segregating to the surface during the CdTe growth. This is not surprising as 100% line baking is difficult to achieve, but these results support the hypothesis of a nonvolatile adduct forming in the tellurium inject line.

#### TIPIn on Cd Manifold

Mixing of the TIPIn and DIPTe organometallic vapors was avoided until entry into the reactor by introducing the TIPIn flow into the Cd inject manifold. No similar adduct reaction was expected between TIPIn and group II organometallics. The carrier concentration and SIMS analysis for indium concentrations are shown in Fig. 7. This chart is plotted with layer index as it groups together three different sets of consecutive experiments. Some residual memory from the tellurium line was present for the first three to four runs as can be seen by a narrowing of the peak and bulk indium concentrations. The remaining layers have a much tighter spread in indium concentrations and can be contrasted with the spread in Fig. 5. Again, the SIMS and Hall measurements show remarkably good agreement indicating 100% activation. Most of these layers have carrier concentrations close to the target value of  $2 \times 10^{15} \text{ cm}^{-3}$  which shows good dopant control. A SIMS profile for indium concentration for layer index number 9 on Fig. 7 is shown in Fig. 8. The profile is now flat with no discernible interface peak and can be contrasted with the profiles in Figs. 4 and 6. In all these examples, the intentional concentration going into the reactor is the same; the differences are in the mode of introduction which is crucial in achieving good dopant control.

#### Indium Activation and Dynamic Range

The results presented in Figs. 5 and 7 show that for low indium concentrations, the activation of indium is 100%. All these layers had received a standard  $250^\circ\text{C}$  Hg rich anneal to remove metal vacancies. Young et



al.<sup>10</sup> showed that if the vacancies were not removed then the apparent activation of indium doping from TMIn was about 33%, but after annealing 100% activation was observed between  $1 \times 10^{15}$  to  $1 \times 10^{18}$  cm<sup>-3</sup>. Above  $10^{18}$  cm<sup>-3</sup>, the activation was about 40%. Figure 9 is an activation curve for TIPIIn doping between  $1.5 \times 10^{14}$  and  $1 \times 10^{18}$  cm<sup>-3</sup>. These results are a mixture of memory and nonmemory doping. The memory doped layers have greater variations in indium concentration with depth which introduces larger errors in the determination of activation. However, there appears to be no difference in activation efficiency for the two doping modes. Within experimental error, there appears to be 100% activation over this entire range. Note that memory doped layers have a significant variation in the indium concentration in the layer which can easily cause variations of up to a factor of two in accurately estimating the average concentration.

### MINORITY CARRIER LIFETIME IN TIPIIn DOPED MCT

Minority carrier lifetime was measured between room temperature and 77K using the photoconductive decay technique on vacancy annealed Hall samples. This ensured that the carrier concentration for that sample had been measured accurately. Samples were selected over a range of carrier concentrations from  $8 \times 10^{15}$  to  $4 \times 10^{16}$  cm<sup>-3</sup>, the upper end of this range being the limit of measurement of the photoconductive decay electronics.

An example of the lifetime as a function of temperature is shown in Fig. 10 for a layer with  $N_d$  of  $2.5 \times 10^{15}$  cm<sup>-3</sup> and mobility of 81763 cm<sup>2</sup>/V-s. The 77K lifetime is 350 ns with a peak lifetime of 700 ns at 143K. The theoretical Auger lifetime curve, calculated using the independently measured  $N_d$  and  $x$ , and overlap integral of 0.3, is also plotted and shows very good agreement with the experimental data. The 77K lifetimes for all the TIPIIn doped layers measured are plotted against electron concentration in Fig. 11. The trend follows the expected  $1/n^2$  dependence for Auger limited lifetime, increasing to  $>1 \mu$ s at  $1 \times 10^{15}$  cm<sup>-3</sup>. A few of these layers did show a significantly lower lifetime (up to a factor of two) than predicted by the Auger mechanism. Most of the samples showed very good agreement indicating that the electrical properties of these layers are dominated by the shallow indium donors at 77K. P/n arsenic implanted and diffused diodes have been fabricated from these layers and have excellent performance at 77K. The forward bias ideality factors range from 1 to 1.3 which means that the better diodes are dominated by diffusion currents and have  $R_0A$  values comparable with good quality LPE p/n junctions.<sup>11-13</sup> The nondiffusion component, for diodes where  $n > 1$ , could be generation-recombination in nature due to defects propagating from the lattice mismatched substrate. The  $R_0A$  of these diodes would not be simply determined by the donor doping concentration. Further experiments will be carried out in lower dislocation density ( $<1 \times 10^6$  cm<sup>-2</sup>) MCT to

### ACTIVATION FOR TIPIIn DOPING

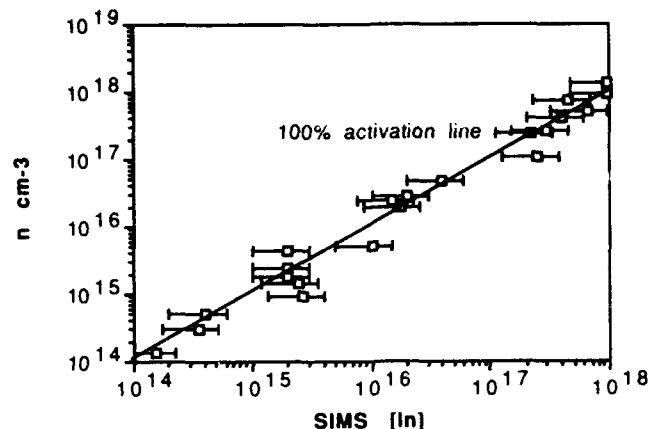


Fig. 9. Activation line for MCT doped with indium from TIPIIn, error bars represent the accuracy of indium concentration measurement using SIMS.

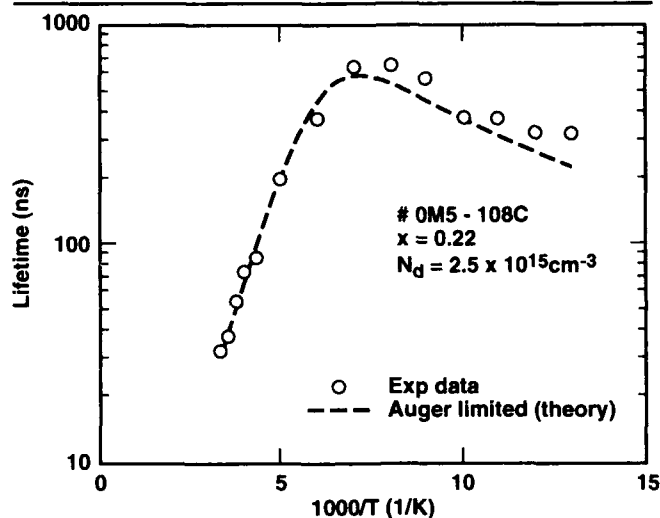


Fig. 10. Minority carrier lifetime as a function of temperature for layer 108, the Auger lifetime was calculated using the following value for the overlap integral  $|F_1 F_2|^2 = 0.3$ .

study the relationships between doping concentration, lifetime and diode  $R_0A$ .

### CONCLUSION

A new dopant precursor, TIPIIn, has been used to dope MCT n-type at low carrier concentrations, suitable for p/n detectors. TIPIIn is a liquid at the bubbler temperature of  $-20^\circ\text{C}$  and has a low enough vapor pressure to operate in the bubbler mode and achieve carrier concentrations down to  $1 \times 10^{15}$  cm<sup>-3</sup>, thus giving greater control over the dopant concentration. Strong memory effects were observed when feeding the dopant into the reactor on the tellurium line. This has been attributed to the formation of a low volatility adduct with DIPTe. No memory doping was observed for TIPIIn introduction on the cadmium inject line. Reproducible doping at the low  $10^{15}$  cm<sup>-3</sup> concentration level has been demonstrated with 100% activation and most of these layers have Auger limited minority carrier lifetime at 77K.

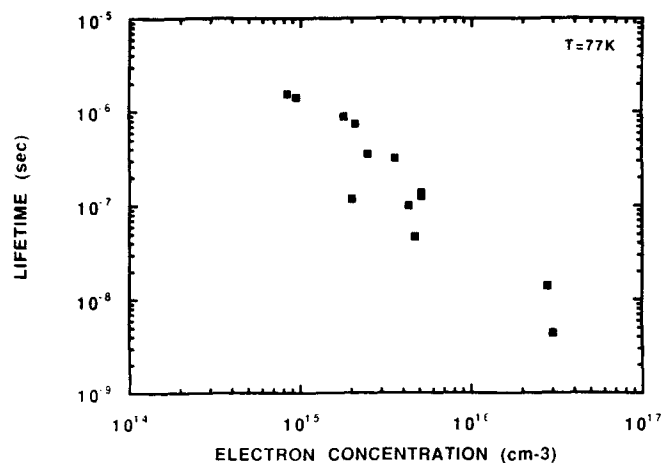


Fig. 11. 77K minority carrier lifetime as a function of electron concentration for TIPIIn doped MCT layers.

### ACKNOWLEDGMENT

This work was partially supported by DARPA Contract MDA 972-91C-0047, and monitored by L. Brown, Wright Laboratories/MLPO. R.W.G. and K.T.H. from the Naval Air Warfare Center acknowledge funding from the Office of Naval Research and the Office of Naval Technology.

### REFERENCES

1. P. Capper, *J. Vac. Sci. Technol.* B9, 1667 (1991).
2. J.S. Gough, M.R. Houlton, S.J.C. Irvine, N. Shaw, M.L. Young and A. Royle, *Mater. Lett.* 10, 1393 (1991).
3. D.D. Edwall (personal communication).
4. J.S. Gough, M.R. Houlton, S.J.C. Irvine, N. Shaw, M.L. Young and M.G. Astles, *J. Vac. Sci. Technol.* B9, 1687 (1992).
5. J.S. Whiteley, P. Koppel, V.L. Conger and K.E. Owens, *J. Vac. Sci. Technol.* A6, 2804 (1988).
6. B.C. Easton, C.D. Maxey, P.A.C. Whiffin, J.A. Roberts, I.G. Gale, F. Grainger and P. Capper, *J. Vac. Sci. Technol.* B9, 1682 (1991).
7. D.D. Edwall, and L.O. Bubulac, *Ext. Abstracts, 1990 US Workshop on the Phys. and Chem. of MCT*, p. 51.
8. J. Tunnicliffe, S.J.C. Irvine, O.D. Dosser and J.B. Mullin, *J. Cryst. Growth* 68, 245 (1984).
9. S.J.C. Irvine, J. Bajaj and H.O. Sankur, *J. Cryst. Growth* 124, 654 (1992).
10. M.L. Young, M.G. Astles, J.S. Gough, M.R. Houlton and N. Shaw, *Semicond. Sci. Technol.* 6, C31 (1991).
11. S.J.C. Irvine, *SPIE Symp. on Adv. Detectors and Systems*, San Diego 1735, 92 (1992).
12. L.O. Bubulac, S.J.C. Irvine, E.R. Gertner, J. Bajaj, W.P. Lin and R. Zucca, *Int. Conf. on Narrow Gap Semicond.*, Southampton, UK, 19-23 July 1992.
13. P.R. Norton, *Opt. Eng.* 30, 1651 (1991).

# Effects of Growth Rate and Mercury Partial Pressure on Twin Formation in HgCdTe (111) Layers Grown by Metalorganic Chemical Vapor Deposition

K. SHIGENAKA, L. SUGIURA, F. NAKATA,\* and K. HIRAHARA

Research and Development Center, Toshiba Corporation, 1, Komukai  
Toshiba-cho, Saiwai-ku, Kawasaki, 210, Japan

The relationship between twin formation and the growth conditions for (111) HgCdTe epitaxial layers grown by metalorganic chemical vapor deposition was investigated. The existence of twins was confirmed by x-ray diffraction and cross-sectional transmission electron microscopy. The x-ray diffraction intensity of the 180° rotated 422 asymmetric reflection with that of the 422 asymmetric reflection was compared to detect the presence of twins. The layer obtained using a low growth rate and a low Hg partial pressure showed double-positioning (DP) twins. The twins became lamellar as the growth rate increased. Twin-free HgCdTe epitaxial layers were obtained under a high growth rate and a high Hg partial pressure. These results suggest a model for twin formation based on the difference in the growth mechanism of HgTe and CdTe. Twin-free (111) HgCdTe epitaxial layers were reproducibly obtained without using inclined substrates by optimizing the growth conditions by using this model.

**Key words:** CdTe, HgCdTe, MOVPE, TEM, twin formation

## INTRODUCTION

The reduction of twins is a significant problem in {111}-oriented  $\text{Hg}_{1-x}\text{Cd}_x\text{Te}$  epitaxial layers. Many researchers have tried to reduce twins and have investigated their origin.<sup>1-3</sup> The orientation of the substrate is a most sensitive factor for twin formation. Some researchers have obtained twin-free layers grown on 3–18° inclined (111) substrates<sup>2,4</sup> and (211) substrates,<sup>5-7</sup> which were 19° inclined from (111). Twin-free layers have also been obtained on (100) substrates.<sup>7,8</sup> Increasing inclination of substrates from (111) is supposed to extend growth condition in which twin-free HgCdTe layers are obtained. Improper growth conditions, however, would make twinned layers even if the inclined substrates were used.

The other approach to reduce twins is to modify the growth process. A twin may also arise due to a variation in the alloy composition or a fluctuation of the surface

temperature during growth. L. Di Cioccio et al.<sup>9</sup> and K.A. Harris et al.<sup>10</sup> have obtained twin-free HgCdTe layers by stabilizing the cell temperature of the mercury source using molecular beam epitaxy (MBE). R.W. Yanka et al.<sup>11</sup> have also obtained twin-free layers by adopting the compositionally modulated structure, which is an alternate CdTe and HgTe thin film growth method. The result of our previous experiments<sup>12</sup> was that twins were observed in CdTe layers but not in HgTe layers. However, a HgCdTe layer grown by the low-mercury partial pressure direct alloy growth (LMP-DAG) method, which eliminates variations in alloy composition, included lamellar twins.<sup>13</sup> HgTe layers grown by MBE often include lamellar twins, which originate from voids in the HgTe layer.<sup>14</sup> However, HgTe layers grown by metalorganic chemical vapor deposition (MOCVD) under a low Hg partial pressure include no twins.<sup>12</sup> A higher density of Hg vacancy was assumed to be in these MOCVD grown HgTe layers than in the MBE grown layers, because of the higher growth temperature of MOCVD (380°C) than that of MBE (180°C).

Based on this, it appears that the formation of twins

(Received October 12, 1992; revised January 22, 1993)

\*On attachment to the R&D Center from Komukai Works, Toshiba Corporation 1, Komukai Toshiba-cho, Saiwai-ku, Kawasaki, 210, Japan.

depends on the growth conditions such as the growth rate and the Hg partial pressure. In the present work, the relationship between twin formation and the MOCVD growth rate has been clarified and a twin formation model is proposed.

### EXPERIMENT

The MOCVD system used in these experiments consisted of flow controllers for the metalorganic precursors, an external mercury reservoir, an induction coil for susceptor heating and a horizontal reactor. The external mercury reservoir could achieve

a precise Hg partial pressure in the reactor. The grown layers accordingly exhibited good compositional uniformity with depth.<sup>13</sup> The fluctuation of the susceptor temperature was maintained within 0.1°C during growth. The growth of HgCdTe was performed by minimizing the variation of the alloy composition. The epitaxial layers were grown on Cd<sub>1-y</sub>Zn<sub>y</sub>Te ( $y = 0.03$ ) (111)B substrates using diisopropyltelluride (DIPTe), dimethylcadmium (DMCd), and elemental mercury (Hg). The partial pressures were varied from  $1 \times 10^{-3}$  to  $1.2 \times 10^{-3}$  atm for DIPTe, from  $1.9 \times 10^{-4}$  to  $2.3 \times 10^{-4}$  atm for DMCd, and from  $6 \times 10^{-3}$  to  $7.3 \times 10^{-3}$  atm for Hg, respectively. The Hg partial pressure was determined by measuring the weight of the mercury reservoir before and after growth. The high Hg partial pressure specimen was grown under a partial pressure of  $1.5 \times 10^{-2}$  atm of Hg.

The HgCdTe growth rate was varied by altering the partial pressures of all the precursors. The Hg and DMCd partial pressures were varied with a constant ratio of the DIPTe partial pressure to the DMCd partial pressure to obtain an equal alloy composition ( $x = 0.23$ ) except for the high Hg partial pressure specimen. This growth method, presented as LMP-DAG in a previous paper,<sup>13</sup> minimizes the variation of the alloy composition in the HgCdTe layer.

The characterization of twins in these HgCdTe layers was carried out by x-ray diffraction, using the technique described by Oron et al.,<sup>15</sup> scanning electron microscopy (SEM), and transmission electron microscopy (TEM). The CuK $\alpha$  line reflected by a four-crystal

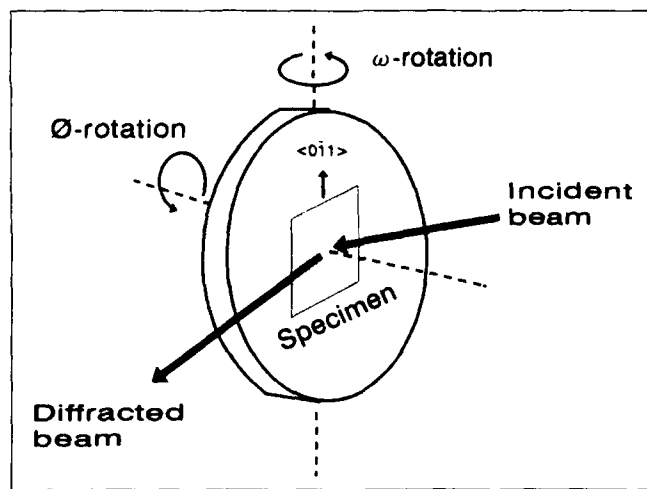


Fig. 1. A schematic view of the x-ray diffraction arrangement.

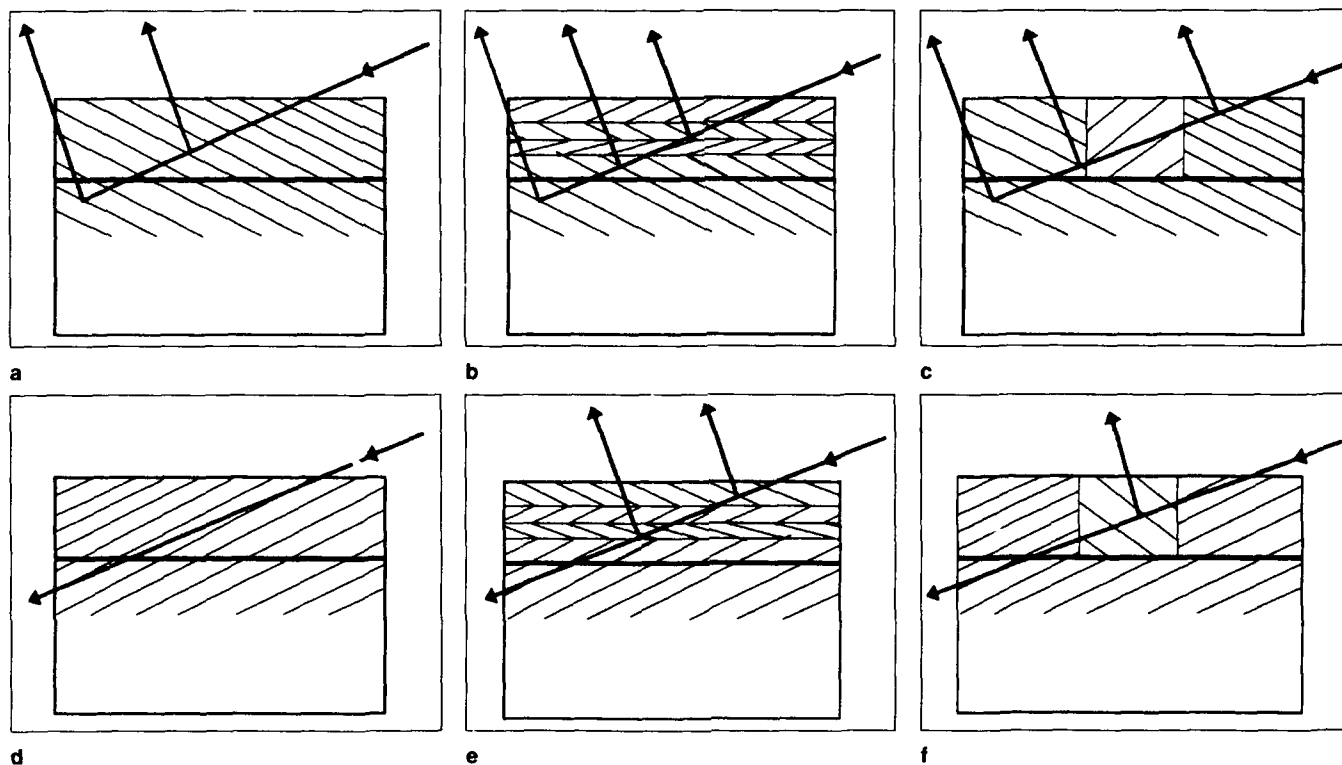


Fig. 2. Schematic diagrams of the x-ray 422 asymmetric reflection from (a) a twin-free layer, (b) a lamellar twinned layer, and (c) a DP twinned layer; and schematic diagrams of the x-ray 180° rotated 422 asymmetric reflection from (d) a twin-free layer, (e) a lamellar twinned layer and (f) a DP twinned layer.

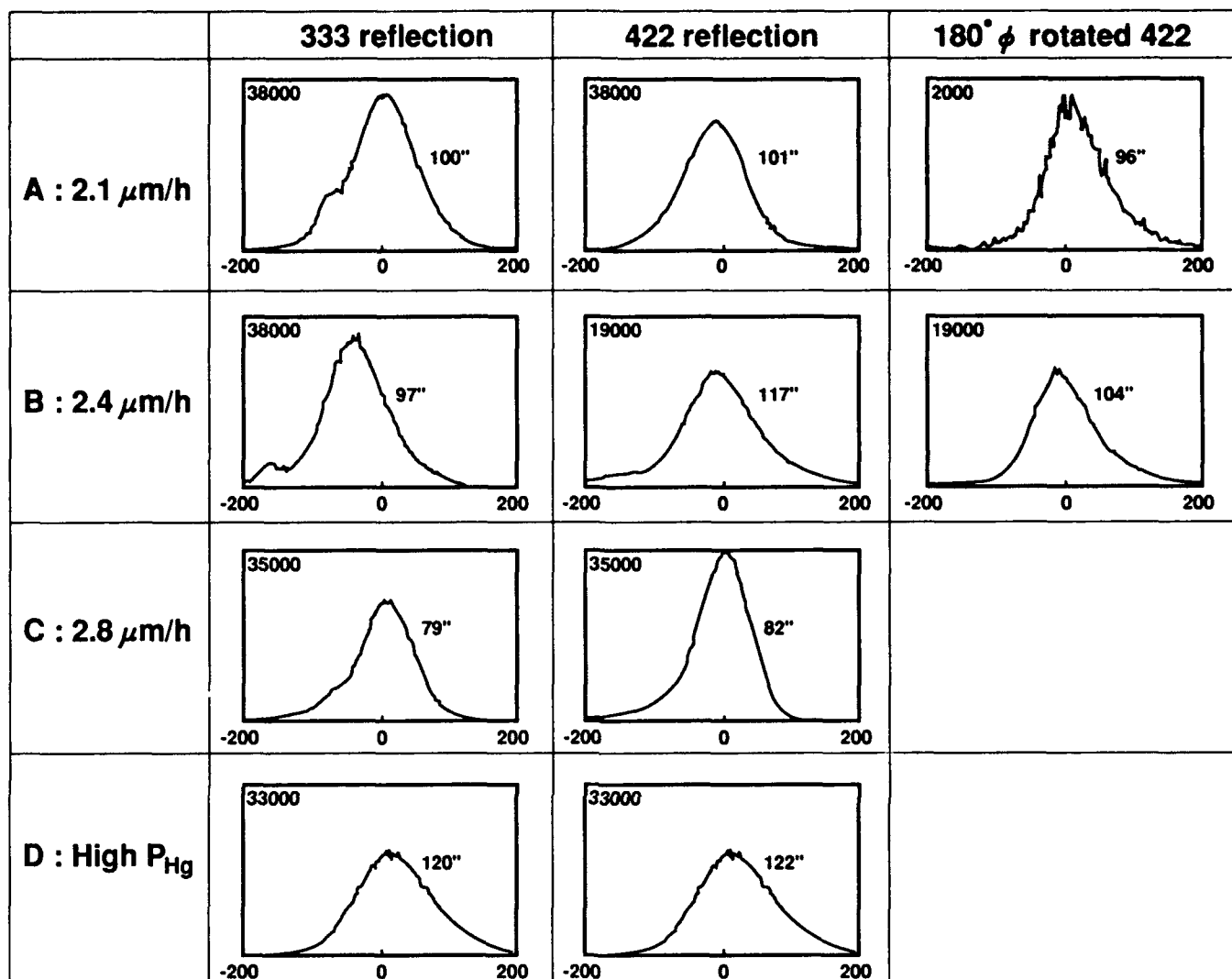


Fig. 3. Rocking curves measured for (a) the 422 asymmetric reflection, (b) the 180°  $\phi$  rotated 422 asymmetric reflection and (c) the 333 symmetric reflection. Numerical values on the upper left hand corner of the each figure and on the right hand site of the each peak represent the peaks' integrated intensities and FWHMs, respectively.

monochromator (Ge 440) was used as the incident beam. Comparing the x-ray diffraction intensity of the 180°  $\phi$  rotated 422 asymmetric reflection to that of the 422 asymmetric reflection can lead to an estimate of the density of twins in a macroscopic area. Transmission electron microscopy observation enables confirmation of the existence twins in a microscopic area.

Figure 1 shows the arrangement of this x-ray diffraction measurement. Figures 2a, b, and c schematically show the x-ray 422 asymmetric reflection from a twin-free layer, a lamellar twin included layer, and a double-positioning (DP) twin included layer, respectively. A lamellar twin was defined as a twin for which the symmetry operator is parallel to the twin boundary and which is completely spread over the surface. On the other hand, a DP twin was defined as a twin for which the symmetry operator is perpendicular to the boundary and which appear in a limited area surrounded by a twin boundary. Figures 2d, e, and f schematically show the 180°  $\phi$  rotated 422 reflection from these layers. Oron et al.<sup>15</sup> have shown that the

full width at half-maximum value (FWHM) of the 422 asymmetric diffraction peak is greater than that of the 333 symmetric diffraction peak in a lamellar twin included layer. However, they found that the FWHM of the 422 asymmetric diffraction peak and the 333 symmetric diffraction peak were equal in a DP twin included layer. It was difficult to completely distinguish these two kinds of twin by these x-ray diffraction measurements because lamellar twins often accompanied DP twins. The twin configuration was finally confirmed by TEM observation and by SEM observation because a groove (showing a twin boundary) on the surface accompanied a DP twin<sup>16</sup> allowing it to be distinguished from a lamellar twin.

Transmission electron microscopy observation was carried out in the [011] projection at 400 keV to observe the twins directly. The specimens for TEM were prepared by Ar<sup>+</sup> ion beam milling at 3 kV. In the final procedure of preparing specimens, the ion beam milling was performed at less than 1 kV with liquid nitrogen cooling to minimize ion milling damage.

## RESULTS AND DISCUSSION

### Influence of the Growth Rate

Table I lists the growth rates, alloy compositions, Hg partial pressures, and Te partial pressures for the specimens studied. The growth rates of the first three layers were 2.1 (specimen A), 2.4 (specimen B), and 2.8 (specimen C)  $\mu\text{m/h}$ , respectively, while the growth rate of the specimen grown under a high Hg partial pressure (specimen D) was 2.4  $\mu\text{m/h}$ . The alloy compositions (x) of all the specimens were within 0.004 of 0.235. Dramatic differences in the twin configuration were found, though the differences in growth rate were small. Figure 3 shows the x-ray rocking curves

**Table I. A List of the Growth Rate, Alloy Composition, Hg Partial Pressure, and Te Partial Pressure for the Specimens Studied**

|   | Growth Rate<br>( $\mu\text{m/h}$ ) | Alloy Comp. | Hg Press.<br>(atm.) | Te Press.<br>(atm.) |
|---|------------------------------------|-------------|---------------------|---------------------|
| A | 2.1                                | 0.237       | 6.0E-03             | 1.0E-03             |
| B | 2.4                                | 0.232       | 6.5E-03             | 1.1E-03             |
| C | 2.8                                | 0.230       | 7.3E-03             | 1.2E-03             |
| D | 2.4                                | 0.239       | 1.5E-02             | 3.0E-04             |



2.5  $\mu\text{m}$

Fig. 4. A groove showing a twin boundary on the surface of specimen A observed by a scanning electron microscope. The triangular pits on the surface are of opposite orientation on either side of the groove.

of the 333 symmetric reflection, 422 asymmetric reflection, and  $180^\circ$  rotated 422 asymmetric reflection for each specimen. The numerical value written in the upper left hand corner of the each figure is the integrated intensity of reflection peak. The twin volume ratio is determined by the ratio of the integrated intensity of the  $180^\circ$  rotated reflection to the total integrated intensity, which is the sum of the integrated intensity of 422 reflection and that of  $180^\circ$  rotated 422 reflection. The numerical values on the right hand side of each peak show the diffraction FWHM.

The intensity of  $180^\circ$  rotated 422 reflection was lower than that of the 422 reflection at a 2.1  $\mu\text{m/h}$  growth rate (A), which was the lowest growth rate. The integrated intensity of the  $180^\circ$  rotated 422 reflection was 2000 counts per sec (cps) compared to 38000 cps for the 422 reflection. The twin volume ratio was evaluated to be 5%. The FWHM of 422 asymmetric reflection (101 arc-s) was almost equal to that of 333 symmetric reflection (100 arc-s). The existence of DP twins was confirmed by SEM from the grooves observed on this layer surface, shown in Fig. 4. In the 2.4  $\mu\text{m/h}$  growth rate (B) case, the intensity of the  $180^\circ$  rotated 422 reflection (19000 cps) was almost equal to that of the 422 reflection (19000 cps). The twin volume ratio was determined to be 50%. Full width at half maximum broadening of the 422 reflection (117 arc-s) compared to the 333 reflection (97 arc-s) was observed and grooves on the surface were not observed by SEM. Therefore, the layer can be said to include lamellar twins but no DP twins. A twin-free layer was obtained at the 2.8  $\mu\text{m/h}$  growth rate (C). Similarly, a twin-free layer was obtained for growth under a high Hg partial pressure with a 2.4  $\mu\text{m/h}$  growth rate (D). The  $180^\circ$  rotated 422 reflection peak was not observed in these layers.

Figures 5a, b, c, and d show images of cross-sectional TEM observation for the 2.1, 2.4, 2.8  $\mu\text{m/h}$  growth rate, and high Hg partial pressure specimens, respectively. A twin boundary could not be observed in the TEM image of the 2.1  $\mu\text{m/h}$  growth rate specimen (A) due to the small, less than 5% volume ratio of the twin domains (Fig. 5a). A twin boundary parallel to the interface was visible in the TEM image of the 2.4  $\mu\text{m/h}$  growth rate specimen (B) shown in Fig. 5b. The contrast in this picture was opposite across the twin boundary. The high resolution TEM image of the twin boundary in Fig. 5b shows  $\{111\}$ -plane arrangements rotated  $180^\circ$  around the  $[111]$  axis. Figures 5c and d show twin-free layers for the 2.8  $\mu\text{m/h}$  growth rate (C) and the high mercury partial pressure (D) specimens. The cracks visible in Figs. 5a and c were introduced during the ion beam milling process. Figure 6 is a schematic showing the relationship of the twin configuration with the growth rate and the Hg partial pressure. The twin configuration in grown layers changed from a DP twin to a lamellar twin as the growth rate increased. Twin-free layers were obtained at a high growth rate and under a high Hg partial pressure.

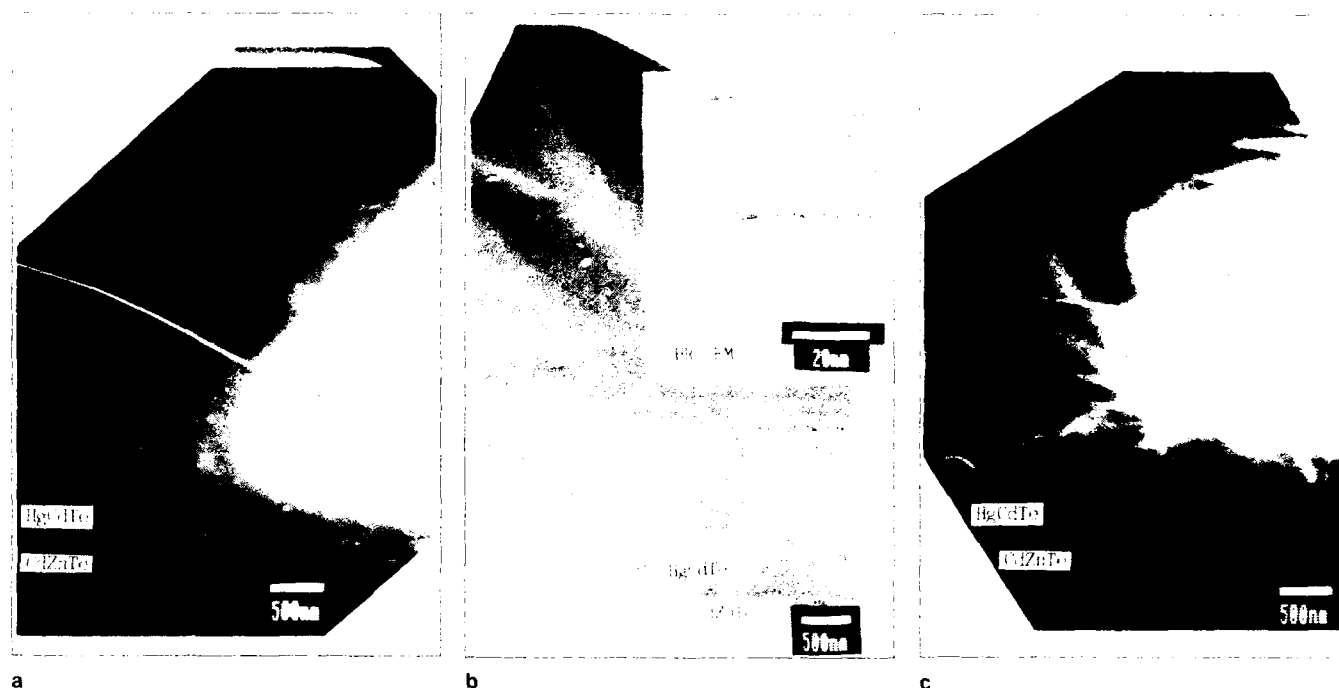


Fig. 5. Bright field cross sectional transmission electron microscope (TEM) images of (a) A: 2.1, (b) B: 2.4, (c) C: 2.8  $\mu\text{m/h}$  growth rate, and (d) D: high Hg partial pressure ( $1.5 \times 10^{-3}$  atm) specimens. A high resolution image of a lamellar twin boundary is seen in the upper right hand corner of (b). The cracks in the specimen in (c) and (d) were introduced during the ion milling process.

### Twin Formation Model

According to these results, a twin formation model in (111)B oriented layers is proposed. The model was based on the following characteristics supposed of the individual elements: A Hg atom helps layer-by-layer growth. A Cd atom on a Te atom easily rotates. Tellurium atoms prevent a group II atom rotating around the [111] axis by terminating unconnected bonds.

The binding distances in the tetrahedra, which are supposed to correspond to depths of the potential energy wells,<sup>17</sup> of Hg-Te and Cd-Te are 2.80 and 2.79 Å,<sup>18</sup> respectively. The covalent radii, which are supposed to correspond to widths of the potential energy wells, of Hg and Cd are 1.49 and 1.48 Å, respectively, supposed to correspond to widths of their potential energy wells. The potential energy of a Hg atom on a Te atom is a shallow, wide well as shown in Fig. 7a. The potential energy of a Cd atom on a Te atom is a deep, narrow well as shown in Fig. 7b. The Hg-Te binding distance in the tetrahedron (2.80 Å) is longer than that calculated for sphalerite HgTe (2.79 Å). The Cd-Te binding distance in the tetrahedron (2.79 Å) is shorter than that calculated for sphalerite CdTe (2.80 Å). Hg-Te binding is strengthened by binding to other Te atoms at adjacent upper anion sites. Mercury atoms accordingly do not subsequently move around or rotate, but Cd atoms continue to be easily rotated.

Figures 8a, b, and c show atomic scale growth models for the individual growth rates. Considering

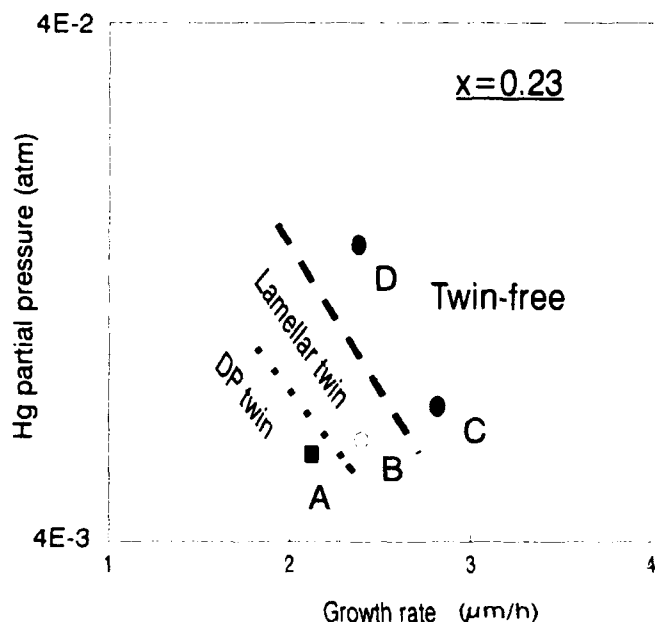


Fig. 6. Schematic diagram showing the relationship of the twin configuration with growth rate and Hg partial pressure.

the potential energy shape of a Hg atom on a Te atom, a Hg atom on a Te atom moves around easily, allowing layer-by-layer growth. When the Te partial pressure is low, as shown in Fig. 8b, a Hg atom often rotates around the  $[111]$  axis. Other Hg atoms can gather around the rotated Hg atom to form a twin nucleus thereby resulting in lamellar twin formation. When the Te partial pressure is high, as shown in Fig. 8a, Te atoms prevent a Hg atom rotating around the  $[111]$  axis. A twin-free layer therefore is obtained.

A Cd atom on a Te atom seldom moves but easily rotates around the  $[111]$  axis, considering the potential energy shape of Cd on Te. The difficulty of a Cd atom moving around enables multinucleation, as shown in Fig. 8c. The ease with which a Cd atom can rotate allows the formation of a side-by-side twin configuration leading to a DP twin. This model approximately corresponds to a previous study<sup>19</sup> in which it was concluded from a calculation of the surface energy that Cd atoms on the (111)B surface preferred to nucleate new layers rather than to complete partially grown layers.

Two other experimental results support this model: One is that HgTe layers grown on (111)A substrates include DP twins under the same growth conditions as twin-free HgTe layers grown on (111)B substrates.<sup>1</sup>

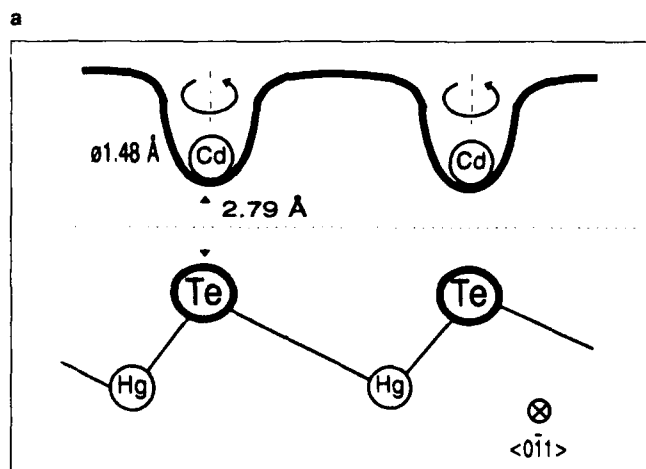
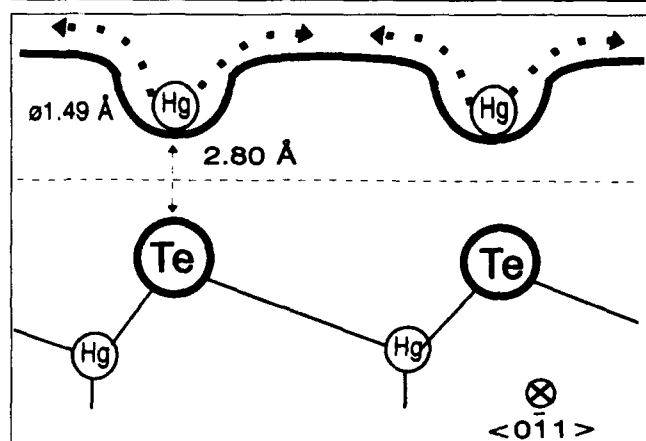


Fig. 7. Schematic diagrams of the potential energy well of (a) Hg on Te and (b) Cd on Te.

The other is that HgTe layers grown by MBE on (111)B substrates include lamellar twins.<sup>14</sup> The former result is interpreted as being the opposite case to that of HgTe layers grown on (111)B substrates. The potential energy of Te on Hg is a well narrower than that of Hg on Te because the covalent radius of Te is 1.36 Å. Therefore, a Te atom on a Hg atom rotates around the  $[111]$  axis more easily than Hg on Te. Hence, HgTe layers grown on (111)A substrates include DP twins. CdTe layers grown on (111)A substrates are also more susceptible to twinning than are layers grown on (111)B substrates. The latter result, that MBE grown HgTe layers included many twins, was interpreted as being due to the influence of growth temperature. The temperature for HgTe growth by MBE was lower than 200°C. The energy of this temperature is equivalent to about two-thirds that of the growth temperature (380°C) for MOCVD. At such low temperatures, Hg atoms cannot easily move on a Te surface but are easily rotated around the  $[111]$  axis. Therefore, the HgTe layers grown on (111)B substrates by MBE include many twins.

## CONCLUSION

The growth rate and Hg partial pressure significantly affect twin formation in HgCdTe MOCVD layers. The primary origin of twin formation is the difference in the growth mechanisms of CdTe and

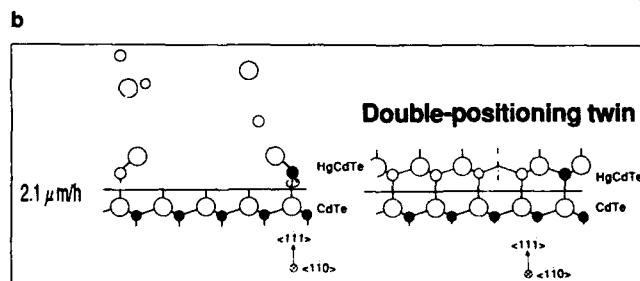
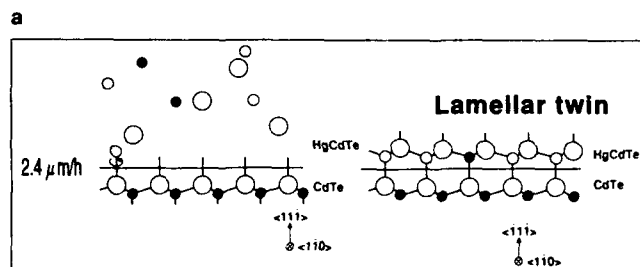
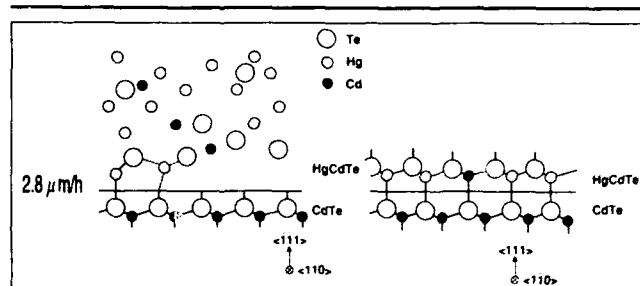


Fig. 8. Atomic scale growth models for the (a) C: 2.8 μm/h, (b) B: 2.4 μm/h, and (c) A: 2.1 μm/h growth rate specimens.



HgTe. Twins will arise from variation in the alloy composition unless the partial pressure of precursors is precisely controlled. Even if precise control of the precursors is achieved, improper growth conditions (an improper growth rate or improper Hg partial pressure) will cause twin formation. Lamellar twins can occur under a layer-by-layer growth, DP twins occur under a multinucleated growth. Increasing the Hg partial pressure accelerates layer-by-layer growth. Layers grown under a Hg-rich condition include lamellar twins when the Te partial pressure is low. Increasing the Te partial pressure accelerates the reduction of lamellar twins in the layer.

These results prove that it is possible to produce twin-free (111) HgCdTe layers without using inclined substrates.

### ACKNOWLEDGMENT

The authors thank Dr. T. Uemoto for the transmission electron microscope observations and Mr. M. Azuma and Dr. T. Beppu for their encouragement and support.

### REFERENCES

1. G. Cinader, A. Raizman and M. Oron, *J. Cryst. Growth* 101, 167 (1990).
2. P. Capper, C.D. Maxey, P.A.C. Whiffin and B.C. Easton, *J. Cryst. Growth* 96, 519 (1989).
3. J.P. Faurie, R. Sporken, S. Sivananthan and M.D. Lange, *J. Cryst. Growth* 111, 698 (1991).
4. G. Cinader, A. Raizman and A. Sher, *J. Vac. Sci. Technol. B* 9, 1634 (1991).
5. R.J. Koestner and H.F. Schaaake, *J. Vac. Sci. Technol. A* 6, 2834 (1988).
6. M.J. Bevan, N.J. Doyle and T.A. Temofonte, *J. Appl. Phys.* 71, 204 (1992).
7. I.B. Bhat and S.K. Ghandhi, *J. Cryst. Growth* 75, 241 (1986).
8. J.M. Arias, S.H. Shin, J.T. Cheung, J.S. Chen, S. Sivananthan, J. Reno and J.P. Faurie, *J. Vac. Sci. Technol. A* 5, 3133 (1987).
9. L. Di Cioccio, A. Million, J. Piagnet, G. Rolland, G. Lentz, N. Magnea and H. Mariette, *J. Cryst. Growth* 95, 552 (1989).
10. K.A. Harris, T.H. Myers, R.W. Yanka, L.M. Mohnkern, R.W. Green and N. Otsuka, *J. Vac. Sci. Technol. A* 8, 1013 (1990).
11. R.W. Yanka, K.A. Harris, L.M. Mohnkern and T.H. Myers, *J. Cryst. Growth* 111, 715 (1991).
12. K. Shigenaka, T. Kanno, M. Saga, T. Uemoto, L. Sugiura, K. Ichizono and K. Hirahara, *J. Cryst. Growth* 117, 49 (1992).
13. K. Shigenaka, T. Uemoto, L. Sugiura, K. Ichizono, K. Hirahara, T. Kanno and M. Saga, *J. Cryst. Growth* 117, 37 (1992).
14. H.F. Schaaake and R.J. Koestner, *J. Cryst. Growth* 86, 452 (1988).
15. M. Oron, A. Raizman, H. Shtrikman and G. Cinader, *Appl. Phys. Lett.* 52, 1059 (1988).
16. J.E. Hails, G.J. Russell, P.D. Brown, A.W. Brinkman and J. Woods, *J. Cryst. Growth* 86, 516 (1988).
17. J.C. Phillips, *Bonds and Bands in Semiconductors*, Academic Press, New York, 1973.
18. B. Ray, *II-VI Compounds*, 1st Ed., Pergamon Press, Oxford, 1969.
19. M.A. Berding, S. Krishnamurthy and A. Sher, *J. Vac. Sci. Technol. B* 9, 1858 (1991).

# Improved CdTe Layers on GaAs and Si Using Atomic Layer Epitaxy

WEN-SHENG WANG, HASSAN EHSANI, and ISHWARA BHAT

Electrical, Computer and Systems Engineering Department, Rensselaer Polytechnic Institute, Troy, New York 12180

In this paper, we report on the atomic layer epitaxy (ALE) of CdTe on GaAs and Si by the organometallic vapor phase epitaxial process at atmospheric pressure. Self-limiting growth at one monolayer was obtained over the temperature range from 250°C to 320°C, under a wide range of reactant pressure conditions. A study of growth mechanism indicates that DMCD decomposes into Cd on the surface and the Te precursors react catalytically on the Cd covered surface. We have used this ALE grown layer to improve the crystal quality and the morphology of conventionally grown CdTe on GaAs. Improvement in the crystal quality was also observed when ALE CdTe nucleation was carried out on Si pretreated with DETe at 420°C. Atomic layer epitaxy grown ZnTe was used to obtain (100) oriented CdTe on (100) silicon.

**Key words:** Atomic layer epitaxy, CdTe/GaAs, CdTe/Si, OMVPE, ZnTe

## INTRODUCTION

The use of large area substrates such as GaAs and Si for the heteroepitaxial growth of CdTe has been a subject of study in many recent articles because of its suitability as a substrate material for subsequent HgCdTe growth. However, many problems have to be addressed before this heteroepitaxial layer will be suitable for high quality HgCdTe growth. Growth of CdTe on alternative substrates generally results in a large number of macro defects which appear as hill-ocks on the surface.<sup>1-4</sup> This is especially true when (100) oriented CdTe is grown. Even though specular films of (111) oriented films can be obtained, it is preferred to have (100) oriented layers for subsequent HgCdTe growth. One reason for this is the fact that it is easier to control the dopant incorporation in the (100) orientation. Also, formation of lamellar twins on (111) oriented wafers is another problem. Hence, it is important to control the growth at the initial phase of (100) growth so that no mixed phase will be obtained when thicker layers are grown.

One solution to the above problem is to grow a thin layer of ZnTe on GaAs or Si prior to CdTe growth.<sup>5</sup> This has resulted in superior CdTe morphology on GaAs compared to direct growth of CdTe. In addition, the crystal quality of CdTe was found to be better. However, the quality of CdTe is very much dependent on the thickness and the growth temperature of ZnTe.<sup>5,7</sup> A better control of ZnTe growth is essential in order to optimize the CdTe growth. The effect of ZnTe layer thickness on the CdTe layer quality is shown in Table I. The atomic layer epitaxy (ALE) method is an ideal choice for controlling this thickness. In ALE, the crystal is grown by sending reactants in sequential pulses over the substrates, usually separated by a flush step of hydrogen.<sup>6</sup> Growth occurs in layer-by-layer form so that excellent control on the thickness can be achieved. In addition, this method provides control of the initial nucleation condition at the monolayer level.

Once the initial few monolayers are deposited by ALE, subsequent thicker layers of CdTe can be deposited by conventional methods in order to get the complete layer in a reasonable amount of time. In this paper, we study this approach to grow CdTe on both

**Table I. FWHM Values of X-Ray Diffraction Peak of CdTe Layers Grown on (100) GaAs Substrates for Various ZnTe Buffer Layer Thicknesses**

| ZnTe Layer Thickn.                                | 0Å                               | 50Å  | 150Å | 300Å |
|---|----------------------------------|------|------|------|
| CdTe Layer Thickness (μm)                         | 5.6                              | 4.6  | 4.5  | 4.7  |
| FWHM of (400) peak (arc-s)                        | 530                              | 195  | 204  | 365  |
| Max. Variation of FWHM with azimuth angle (arc-s) | ±70                              | ±12  | ±12  | ±12  |
| Morphology pyramidal (hillock/cm <sup>2</sup> )   | 10 <sup>3</sup> –10 <sup>4</sup> | <500 | <500 | <500 |

Note: Both CdTe and ZnTe layers were at 370°C on (100) 10° → (110)GaAs substrates.

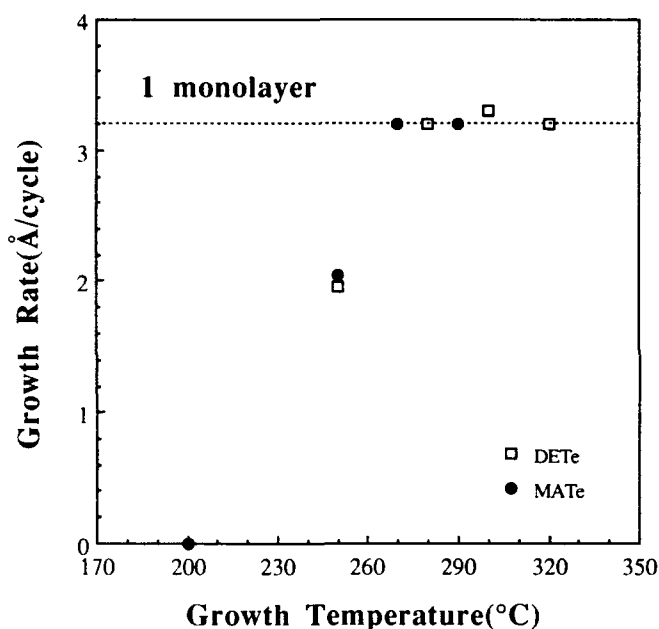


Fig. 1. Growth rate of ALE-CdTe as a function of temperature. (□)DMTc =  $6.5 \times 10^{-4}$  atm; DMTc =  $2.5 \times 10^{-4}$  atm; (●)DMTc =  $2 \times 10^{-4}$  atm; MATe =  $1 \times 10^{-4}$  atm.

GaAs and Si substrates. This is the first time that a detailed study of CdTe growth on Si was carried out using an atmospheric pressure OMVPE system.

### EXPERIMENT

The ALE experiments were carried out at atmospheric pressure in a horizontal vapor phase epitaxial reactor, equipped with a fast switching manifold. Dimethylcadmium (DMCd) and dimethylzinc (DMZn) were used as the Cd and Zn sources respectively and diethyltelluride (DETe) or methylallyltelluride (MATe) were used as Te precursors. The total hydrogen flow was 4 to 6 l/min, and the reactor diameter was approximately 45 mm, so that it took less than 2 s to flush out the gases in front of the susceptor. Separate ALE experiments at 320°C with variable flushing period indicated that 6 s of flushing period is necessary to completely eliminate intermixing when

4 l/min total flow was used. In order to eliminate any chance of intermixing of the reactant gases, we kept the ALE flush cycle at 8 s. Some runs were repeated with 12 s flush period with no changes in the resultant film thickness. A typical ALE cycle consists of 4 s of DMCd or DMZn with hydrogen flow, 8 s of hydrogen purge, 4 s of MATe or DETe with hydrogen flow followed by 8 s of hydrogen purge.

(100) oriented GaAs substrates which were mis-oriented 10° toward the nearest (110) direction were cleaned in organic solvents and etched in Caro's etch (5:1:1 of H<sub>2</sub>SO<sub>4</sub>:H<sub>2</sub>O<sub>2</sub>:H<sub>2</sub>O by volume) to remove about 5 μm thick GaAs. Prior to loading into the reactor, the substrates were dipped in NH<sub>4</sub>OH to remove any residual oxide. Silicon wafers were cleaned in organic solvents and immersed into H<sub>2</sub>O<sub>2</sub>:HCl:H<sub>2</sub>O (1:1:4 by volume) for 10 min at 70°C. The wafers were then dipped in HF:methanol (1:1 by volume) solution for a few seconds prior to loading into the reactor. We have used (100) misoriented by four degrees toward (110), and (111) ± 1/2 degree oriented Si wafers in this study.

The film thickness on GaAs was determined either by measuring the weight change or by using an optical interferometer. For this, a small piece of GaAs was placed on the substrate wafer to serve as a mask. Atomic layer epitaxy growth rate on Si was measured by etching part of the wafer using a mask and then measuring the thickness by interferometer or alpha step profiler. When conventional growth of CdTe was carried out on ALE grown CdTe, the thickness was measured from the interference fringe spacings using infrared reflectance. The crystal quality of the films was measured using both single and double crystal x-ray diffraction.

## RESULTS AND DISCUSSION

### CdTe Growth On GaAs

We have reported on our initial results of ALE-CdTe growth on GaAs.<sup>7,8</sup> A one monolayer (ML) per cycle growth rate is obtained for a temperature range from 270 to 320°C. This is shown in Fig. 1 for a variety of reactor conditions. Growth rate at 250°C was less than one ML per cycle for the data in Fig. 1, but this could be increased to one ML level by increasing the DMCd and MATe flow rates. The growth rate at higher than 320°C shows less than a ML per cycle indicating increased desorption of Cd during the purge period. By reducing this period, it may be possible to extend the growth rate plateau beyond 320°C. Growth at higher than 390°C resulted in greater than a ML per cycle indicating increased gas phase mixing. Hence, most of our studies were carried out below this temperature. Some of the experiments at 280 to 320°C were repeated under various DMCd and DETe flow rates, but in each case the growth rate was one ML per cycle indicating self-limiting behavior.

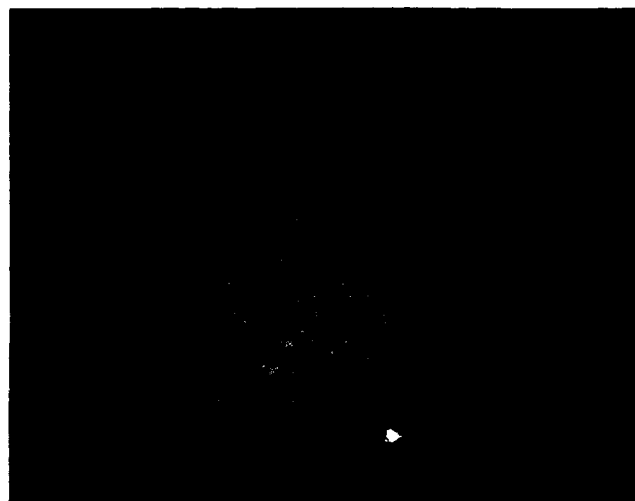
It is well known that DETe is very stable at temperatures below 350°C,<sup>9</sup> and does not decompose into Te. However, we have observed CdTe growth even at 250°C, even when they are kept from mixing with one

another in the gas phase. This gives credence to our earlier theory<sup>10</sup> that CdTe growth takes place first by the decomposition of DMCd into Cd, followed by the catalytic reaction of DETe or MATe with the surface-adsorbed elemental Cd. Hence, the results are similar whether DETe or MATe is used for the growth.

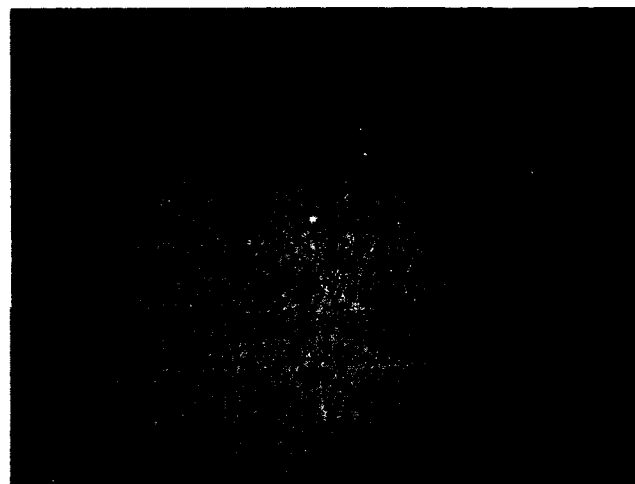
To confirm this hypothesis, we conducted the decomposition study of DMCd in our reactor under the flow conditions used for ALE growth. The reactor wall was kept at 300°C and the sample surface was kept at 150°C while the DMCd flow was maintained for 30 min. The amount of Cd deposited on the substrate corresponded to a growth rate of 0.24  $\mu\text{m/h}$ . Nonuniform Cd deposits could be observed at lower temperatures as well. The experiments were repeated with other reactants namely, DETe and MATe. No deposition of Te was observed in the above experiments, unless the reactor wall was increased to 400°C. From these results, it is clear that the decomposition of dimethylcadmium into Cd is responsible for CdTe growth at low temperatures.

The ALE grown CdTe at the interface can be used to improve the quality of conventionally grown CdTe on GaAs. When CdTe is grown on GaAs by the conventional method, either (100) or (111) CdTe results, depending on the initial phases of the growth. For example, we have observed that growth initiation with DETe at 370°C will result in (111) CdTe if a DETe to DMCd ratio of three is maintained. On the other hand, growth initiation with DETe at 350°C will result in (100) growth. It is safe to say that at either temperature, the possibility of having a small percentage of the unwanted phase is extremely high. This is a part of the problem in obtaining hillock free CdTe on GaAs. One solution to this problem is a controlled initiation of (100) growth using ZnTe, as shown in Table I. However, the quality and the morphology of the CdTe is very much dependent on the thickness of the initial ZnTe layer, which is difficult to control in the conventional growth process. Atomic layer epitaxy nucleation at low temperature will be advantageous here since the results will be more reproducible.

We have used the ALE growth method described here to improve the epilayer morphology and crystal quality. A 320Å thick layer of CdTe was grown at 300°C using the ALE method. The sample temperature was then increased to 360°C and CdTe grown by the conventional methods. Figure 2 shows the surface morphology of CdTe on GaAs, grown by the process described above. Figure 2a shows the morphology of the layer grown without ALE nucleation and Fig. 2b shows for the case when ALE nucleation was used. Significant improvement in the layer morphology is observed when the ALE nucleation layer is used. An improvement in morphology can be obtained using ZnTe nucleation by conventional means, which suggests that the mechanism responsible for improved morphology may be similar. In both cases, it appears that a forced (100) nucleation completely eliminates any (111) phases at the initial phase of growth.



a



b

Fig. 2. Morphology of 5  $\mu\text{m}$  thick CdTe layers grown on GaAs with (a) no ALE nucleation and (b) with 300 cycles of ALE CdTe.

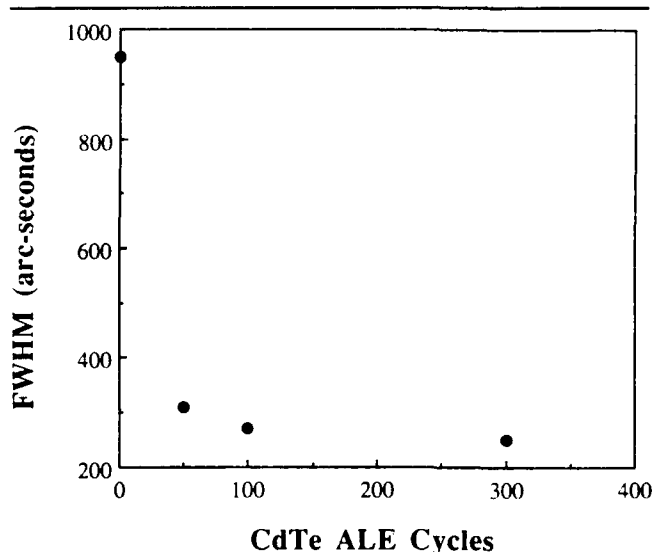


Fig. 3. Full width at half maximum of x-ray diffraction (400) peak of 5  $\mu\text{m}$  thick CdTe as a function of ALE layer thickness.

**Table II. Growth Conditions and Single Crystal X-Ray Diffraction Intensity (%) Results of CdTe Layers Grown on (100) 4° Si**

| Run No. | ALE CdTe | Te Pre-Clean | (111) | (220) | (311) | (400) | (331) | (422) | (333) |
|---------|----------|--------------|-------|-------|-------|-------|-------|-------|-------|
| 196     | No       | No           | 100   | 30    | 145   | 0     | 10    | 27.8  | 13.2  |
| 216     | 300°C*   | No           | 100   | 2.2   | 5.6   | 0     | 0     | 3.5   | 2.7   |
| 221     | 360°C*   | No           | 100   | 0     | 1.4   | 0     | 1.2   | 3.7   | 3.5   |
| 198     | No       | Yes          | 100   | 0     | 3     | 0     | 0     | 9.5   | 3.8   |
| 200     | 300°C*   | Yes          | 100   | 0     | 5.5   | 0     | 0     | 5     | 6.5   |
| 224     | 330°C*   | Yes          | 100   | 0     | 3.1   | 0     | 0     | 5.4   | 3.1   |
| 222     | 360°C*   | Yes          | 100   | 0     | 1(?)  | 0     | 0     | 0     | 2.3   |

\*100 cycles

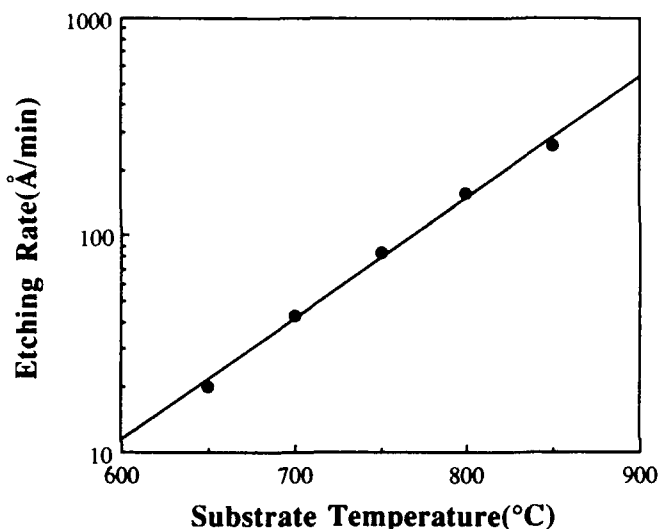


Fig. 4. Etch rate of Si as a function of temperature. The DETe partial pressure was maintained at  $1 \times 10^{-4}$  atm.



Fig. 5. The morphology of Si wafer after etching with DETe at 850°C, 30 min. Marker represents 25 microns.

width at half maximum (FWHM) of about 800 arcs whereas the FWHM is about 250 arc-s when ALE nucleation was used. However, increasing the thickness of the ALE layer beyond a few hundred angstroms does not decrease the FWHM further. This is expected because the main reason for the improvement in the quality is the controlled two dimensional nucleation in the (100) orientation. Hence, ALE grown CdTe is thus an important interfacial layer for optimizing the heteroepitaxial growth of CdTe on GaAs.

#### CdTe Growth on Si

All prior CdTe growth studies on Si were carried out either using molecular beam epitaxial system or ultra high vacuum (UHV) chemical vapor phase epitaxial system.<sup>1,2,11</sup> Low pressure OMVPE was used in one study, but no details on the substrate preparation are available.<sup>12</sup> The layers were generally degassed for many hours overnight and deoxidized at 850–900°C for about 30 min. We first carried out CdTe growth on Si substrates after the deoxidation step at 850°C for 30 min under a hydrogen flow. Growth of CdTe was carried out at 360°C on Si directly without any ALE layers. This resulted in polycrystalline layers as expected which are poorly adherent to the wafers, probably because the high temperature deoxidation step may actually contaminate the surface with oxides and carbides since the system is not equipped with a load lock. Hence, this deoxidation step was not used further. Direct growth of CdTe on Si without the deoxidation step also resulted in polycrystalline layers.

We repeated the ALE growth experiments on Si substrates in order to control the initial phase of nucleation. The growth conditions were the same as before, except that ALE growth was kept constant at 50 cycles. This was followed by conventional CdTe growth at 360°C. In some cases, pre-annealing of ALE CdTe at the growth temperature was carried out prior to conventional CdTe growth. In all cases, the layer obtained was (111) oriented CdTe with a small percentage of mixed phases, as shown in Table II (samples 196, 216, and 221). Crystallization of this layer at high temperature is difficult because the layer will decompose if proper over pressure of the constituent elements is not maintained. This is unlike the GaAs system where thin amorphous layer of GaAs grown at

Improvement in the crystal quality can also be achieved by ALE nucleation. Figure 3 shows the double crystal x-ray diffraction data for CdTe grown with and without ALE nucleation. The conventional CdTe was grown under the same condition. CdTe layers grown without ALE nucleation have a full

low temperature can be crystallized at 700°C under an overpressure of arsine without resulting GaAs decomposition or GaAs growth.

In the case of CdTe, crystallization is difficult because overpressure of both Cd and Te has to be maintained without growing any CdTe. The poor quality of CdTe is probably due to the presence of a sub-monolayer of oxygen on Si. The presence of a strong Si-H bond can also be responsible for the poor quality of CdTe.

In-situ etching of Si will be a significant step, if it can be carried out at low temperatures. We used Te vapors derived from DETe for this purpose. Etching of Si was performed at various temperatures from 600 to 850°C, under DETe and hydrogen flow. The DETe partial pressure was kept at 1E-4 atm for all the runs. We have found that above 600°C, it is possible to etch Si using DETe vapors.

Figure 4 shows the etch rate of Si as a function of temperature when 1E-4 atm of DETe was used. It should be noted that the etch rate was estimated by measuring the weight change so that it is an average value. The morphology of the Si wafers after the etching contained numerous etch pits as shown in Fig. 5, and hence not suitable for epitaxial growth. Based on the phase diagram,<sup>13</sup> Te-Si<sub>2</sub>Te<sub>3</sub> has an eutectic point at 407°C and hence we used 420°C as the optimum temperature for Si pre-clean using Te. We can also expect a significant amount of DETe pyrolysis, yielding Te at this temperature.

We have used DETe etching at low temperature to grow CdTe layers on Si. The wafers were kept at 420°C and DETe was passed for 10 min prior to CdTe growth. The temperature and time used, is by no means, optimum. However, all such layers were considerably superior to layers grown without this Te pre-clean step. Preferentially (111) oriented layers were obtained when this process was used (compare samples 196 and 198 in Table II). Conventional growth was carried out at 360°C, and Te cleaning was at 420°C for 10 min and the layer thicknesses were about 1 µm for all the samples tabulated here. Since (100) four degree misoriented toward (110) wafers were used, the Si peak was not observed in the x-ray diffraction spectra. Atomic layer epitaxy nucleation layers were used prior to conventional CdTe growth on these Te-cleaned surfaces. The x-ray diffraction data on these layers show only (111) and (333) peaks indicating single crystal (111) CdTe layers on (100) Si wafers.

Effect of Te pre-clean was also demonstrated when (111) Si wafers were used. Figure 6 shows the conventional CdTe grown directly on (111) oriented Si, showing polycrystalline behavior. When the layer was grown on Te pre-cleaned surface (420°C for 10 min), the layer was single crystal with (111) orientation. This was shown in Fig. 6b. Optimization of this Te etching is necessary to fully utilize this technique.

In all the above cases, (111) oriented CdTe layer was obtained irrespective of the orientation of the substrate. In order to grow (100) oriented CdTe on Si,

ZnTe interfacial layer was grown prior to CdTe growth. Atomic layer epitaxy growth of ZnTe on Si was carried out at temperatures in the range 330 to 390°C, using 6 l/min hydrogen flow. Growth rate was higher than 1 ML at 390°C, but about 1 ML per cycle was obtained at 360°C. We have used this interfacial layer grown at 360°C, followed by the CdTe growth at 420°C. It was found that (100) oriented single crystal CdTe can be obtained by this growth process as shown in Fig. 7. The FWHM value for this 0.6 µm thick CdTe was ~4200 arc-s.

It is interesting to note that single crystal CdTe can be grown on Si wafers with a ZnTe ALE layer, without using a Te cleaning process. On the other hand, the Te cleaning process is essential if the ZnTe layer was not used. At present it is not clear what role Zn or Te play, but we believe, in the ZnTe case, ZnO (or Zn-O-Si) forms at the interface which will be single crystal. ZnO has hexagonal lattice structure, but when grown on cubic Si substrate, it may grow in cubic form for the first monolayer. ZnTe growth on such an interfacial layer will result in single crystal growth. On the other hand, Cd and Te oxides are less stable above 300°C, and their formation is less likely on Si. Studies using surface analytical techniques will be required to fully support the above argument.

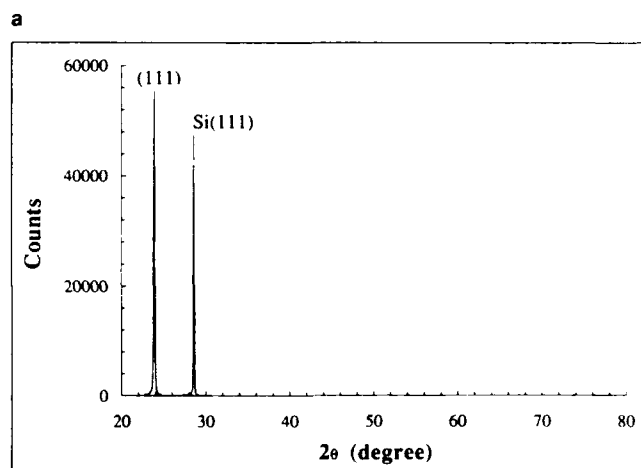
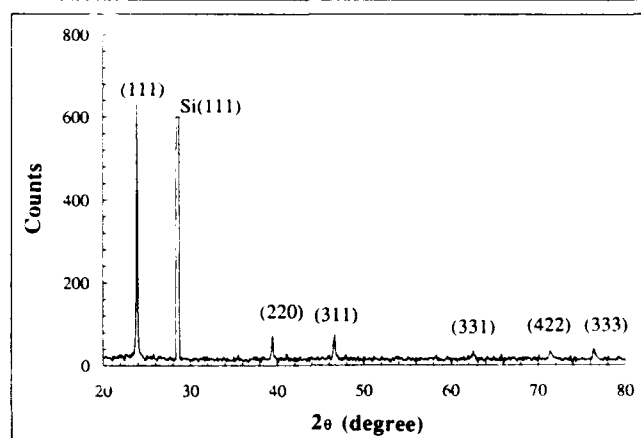


Fig. 6. X-ray diffraction curve of CdTe layer grown on (a)(111)Si, (b)(111)Si with Te pre-clean. Layer thickness ~ 0.6 µm.

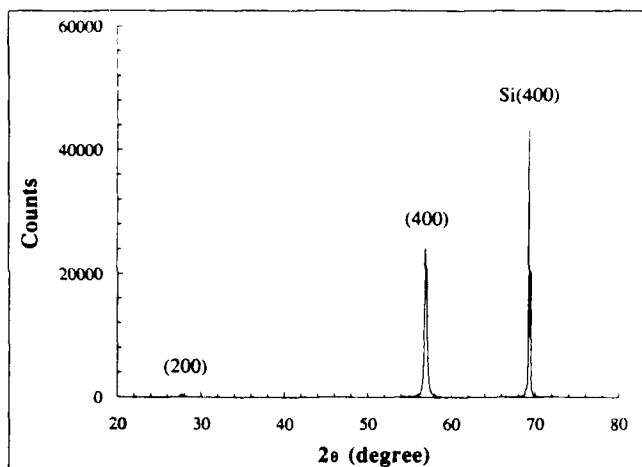


Fig. 7. X-ray diffraction curve of CdTe layer grown on (100)Si using ALE nucleated ZnTe layer. Layer thickness  $\approx 0.6 \mu\text{m}$ .

### CONCLUSION

We have shown that CdTe can be grown by the ALE method over a wide range of temperatures, from 250 to 320°C. This study shows that the growth mechanism involves the decomposition of DMCD into Cd, which reacts with undecomposed DETe and MATe so that exactly one ML per growth occurs over a wide range of temperature. We have shown that the ALE nucleation layer followed by conventional CdTe growth improves the layer morphology and crystal quality. Atomic layer epitaxy nucleation also helps in improving the quality of CdTe grown on Si. Complete removal of surface oxides is essential to fully utilize the advantage of ALE nucleation. Preliminary studies show that Te vapors can be used to etch Si at high temperatures, but this process results in etch pits. A low temperature cleaning process at 420°C followed by ALE nucleation resulted in single crystal CdTe without using the high temperature deoxidation step.

Further optimization in this process is necessary to improve the CdTe layer quality. To get (100) CdTe, ZnTe was grown by ALE prior to CdTe growth. In conclusion, ALE grown layers are shown to be useful for obtaining controlled nucleation for hetero-epitaxial growth.

### ACKNOWLEDGMENT

The authors would like to thank J. Barthel for technical assistance and P. Magilligan for manuscript preparation. This work was supported in part by Spire Corp. (Contract No. 117975) through a subcontract to Rockwell (Contract No. BQK210170) for DARPA. Partial support was provided by grants from the Raytheon Corp., and Texas Instruments. These supports are gratefully acknowledged. We also want to thank Professor S.K. Ghandi for many hours of fruitful discussions on this subject.

### REFERENCES

1. R. Korenstein, P. Madison and P. Hallock, *J. Vac. Sci. Technol.* B10, 1370 (1992).
2. R. Sporken, Y.P. Chen, S. Sivananthan, M.D. Lange and J.P. Faurie, *J. Vac. Sci. Technol.* B10, 1405 (1992).
3. J.M. Arias, M. Zandian, S.H. Shin, W.V. McLevige, J.G. Pasko and R.E. Dewames, *J. Vac. Sci. Technol.* B9, 1646, (1991).
4. S.J.C. Irvine, D.D. Edwall, L.O. Bubulac, R.V. Gil and E.R. Gertner, *J. Vac. Sci. Technol.* B10, 1392 (1992).
5. H. Shtrikman, M. Oron, A. Raisman and G. Cinader, *J. Electron. Mater.* 17, 105 (1988).
6. C. Goodman and M.V. Pessa, *J. Appl. Phys.* 60, R65 (1986).
7. I.B. Bhat, H. Ehsani, W.S. Wang, S.K. Ghandi and N.H. Karam, *J. Vac. Sci. Technol.* B10, 1376 (1992).
8. W.S. Wang, H. Ehsani and I.B. Bhat, to appear in *J. Cryst. Growth* (1992).
9. J.B. Mullin and S.J.C. Irvine, *J. Vac. Sci. Technol.* 21, 178 (1982).
10. B. Bhat and S.K. Ghandi, *J. Electrochem. Soc.* 134, 195 (1987).
11. Y. Lo, R.N. Bicknell, T.H. Myers, J.F. Schetzina and H.H. Stadelmeier, *J. Appl. Phys.* 54, 4238 (1983).
12. R.L. Chow, M.S. Lin and K.S. Chou, *J. Cryst. Growth* 94, 551 (1989).
13. T.G. Davey and E.H. Baker, *J. Mater. Sci. Lett.* 15, 1601 (1980).

# The Effect of Substrate Tilt On MOCVD Growth of {100}CdTe on {100}GaAs

W.J. HAMILTON, J.A. VIGIL, W.H. KONKEL, V.B. HARPER, and S.M. JOHNSON

Santa Barbara Research Center, 75 Coromar Dr., Goleta, California 93117

Epitaxial layers of CdTe were grown by metalorganic chemical vapor deposition on surfaces of single crystal, {100} GaAs which had been ground, polished, and etched to a spherically shaped dome. This dome-shaped surface allowed the morphological and structural properties of the epitaxial CdTe layers to be determined for all 360° of azimuth and up to 15° of polar angle from the [100] axis within a single growth experiment. At two growth temperatures, approximately 275 and 375°C, the results show distinct twofold rotational symmetry in both morphology and crystal perfection as determined by x-ray rocking curve measurement. Surface morphology is superior at azimuths near tilts toward the <111>A pole. Four-sided pyramidal hillocks appear at other azimuths and at 0° tilt; the symmetry of the hillocks diminishes as the tilt increases. The orientations for growth which simultaneously minimize the surface defects and rocking curve full-width half-maximum appear to be at locations on the surface where the surface normal is tilted 3–4° toward the <111>A or <111>B, depending on the temperature regime chosen. Epitaxial layers grown on planar wafers of {100}GaAs tilted toward <111>Ga and <111>As show surface morphology essentially identical to the dome at these orientations. The surface morphology of CdTe grown on GaAs/Si wafers suggests that these layers are tilted toward the <111>B.

**Key words:** CdTe/GaAs, hillocks, MOCVD, substrate tilt

## INTRODUCTION

GaAs wafers and thin films of GaAs on silicon are increasingly being used as substrates for epitaxial growth of HgCdTe layers for infrared detectors.<sup>1,2,3</sup> The development effort on Si-based substrates has been motivated by effects of the large mismatch in thermal expansion coefficients between the conventional CdZnTe substrates of the infrared hybrid focal-plane arrays and the silicon integrated circuit readout chips. The hybrid array is formed by pressure cold-welding of the detector chip to the readout chip through indium-bump vias. Fabrication at room temperature with repeated cycling to cryogenic operating temperatures causes stress due to the thermal expansion mismatch. However, testing to several thousand cycles in our facilities has indicated that the thermal cycle life of silicon-based hybrid detector arrays is virtually limitless.

Growth of II-VI materials directly on silicon is

difficult,<sup>4</sup> so most workers have used GaAs wafers or MOCVD-grown GaAs on silicon wafers as starting substrates.<sup>2,5</sup> Because Ga and As atoms dope HgCdTe active layers, an intermediate buffer layer of CdTe or, preferably, Cd<sub>1-y</sub>Zn<sub>y</sub>Te is grown. The value of y is chosen to provide a lattice match for the HgCdTe base layer.

Two issues have been central in the development of usable CdZnTe buffer layers:

- achievement of greater crystal perfection as determined by x-ray rocking curve (XRC) full-width half-maximum (FWHM) measurements, estimates of "twin volume fraction" by x-ray measurements, and dislocation etch-pit density (EPD) measurements; and
- reduction and elimination of defects on the growth surface, commonly called "hillocks."

Crystal perfection, defined by x-ray rocking curve determination, can be quite good for {111}CdZnTe grown on {111} or {100} GaAs and on {111}Si, but at present these epitaxial layers are heavily twinned. The twins propagate into the active HgCdTe layers,<sup>3</sup>



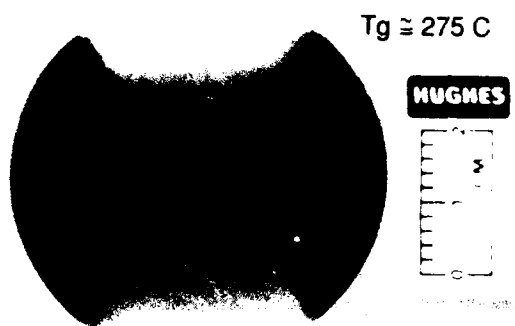


Fig. 1. Photograph (top view) of CdTe growth at 275 C on a GaAs dome. Twofold rotational symmetry is visible. Lighter area is due to nonspecular reflection from areas of rougher surface.

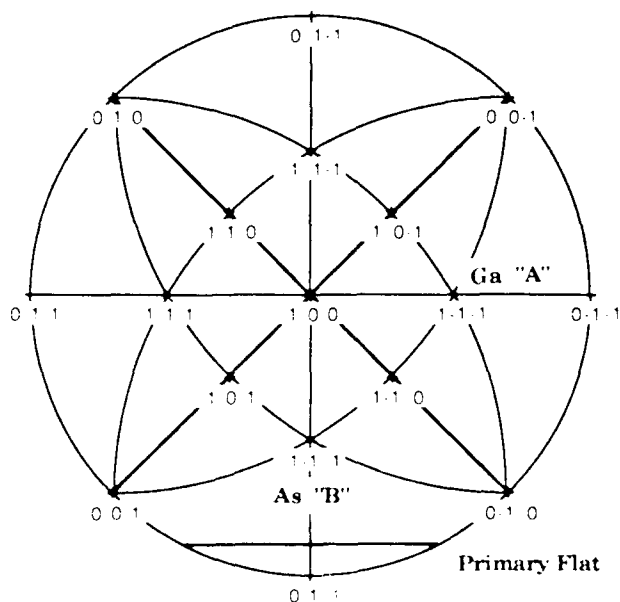


Fig. 2. Stereographic projection of the  $\langle 100 \rangle$  zone axis aligned as is the wafer in Figs. 1 and 3. The  $\langle 111 \rangle$ A and  $\langle 111 \rangle$ B axes are marked and the location of the primary wafer flat is shown symbolically at the bottom to correspond with the photographs.

and it is widely believed that this twinning results in poor device performance. Twinning is reduced in  $\{211\}$  CdTe grown on  $\{211\}$  GaAs, but the  $\{522\}$  twin can also occur and stacking faults propagate from the substrate interface to the surface. Twinning does not generally occur in  $\{100\}$  CdTe and CdZnTe epitaxial layers. The  $\{100\}$  surface seems to be optimal for MOCVD growth of the buffer layers of CdTe or CdZnTe. For this orientation, however, the achievement of good crystal structure simultaneously with an acceptable surface defect density has been the major research focus. Previous studies have determined that surface morphology may be optimized by appropriate tilt of the surface normal of the substrate away from the low index axis.<sup>2</sup> Most investigators have found that a small angle tilt of the surface normal away from

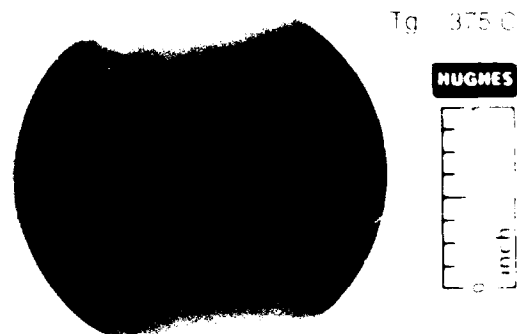


Fig. 3. Photograph (top view) of CdTe growth at 375 C on a GaAs dome. Twofold rotational symmetry again is visible.

the  $\langle 100 \rangle$  axis results in growth of higher quality material. Tilts toward the nearest  $\langle 011 \rangle$ , toward the  $\langle 111 \rangle$ , or other low index orientations have been reported.

Full optimization of the magnitude and direction of the tilt-angle which will provide the best epitaxial quality using planar wafers could require a large number of growth runs on a large number of varying tilt-angles. Our approach in this study has been to present all surface tilt vectors simultaneously in a single substrate by using a spherically polished dome of GaAs. The radius of curvature of the surface was chosen to reveal all azimuths around the  $\langle 100 \rangle$  axis to a maximum polar angle of  $15^\circ$ . The experiment is similar to the previous homoeptaxy experiments conducted with a polished CdTe dome.<sup>1</sup>

## EXPERIMENTAL METHODS

Wafers of single-crystal GaAs<sup>11</sup> were cut into disks of 50.8 mm diameter and approximately 14 mm thickness, with a  $\{100\}$  crystallographic orientation of the flat surface. Edge flats were ground on the  $\{011\}$  plane and a minute scratch placed on the  $\{100\}$  surface to assure internal consistency of crystallographic orientation. The  $\{100\}$  surfaces were ground and polished to a radius of curvature of 99.85 mm with the center of the radius on the wafer axis, and given a chemical polish using bromine-methanol etch.<sup>12</sup> The spherical surfaces were specular and optically perfect. At magnifications above about 200X, surface roughness became visible using Nomarski light microscopy which was greater than that for high quality planar wafers.

CdTe was deposited by conventional pyrolytic metalorganic chemical vapor deposition (MOCVD) in a downward-flow, high-speed rotating-disk reactor with growth methods similar to those described previously.<sup>13</sup> Growth of the  $\{100\}$  CdTe was insured by a thin nucleation layer of ZnTe.<sup>14</sup> The dome was mounted centrosymmetrically on the susceptor to avoid artifacts created by eddy currents due to asymmetric flow.

The temperature of GaAs dome at the growing epitaxial surface was estimated by calibrating a ther-

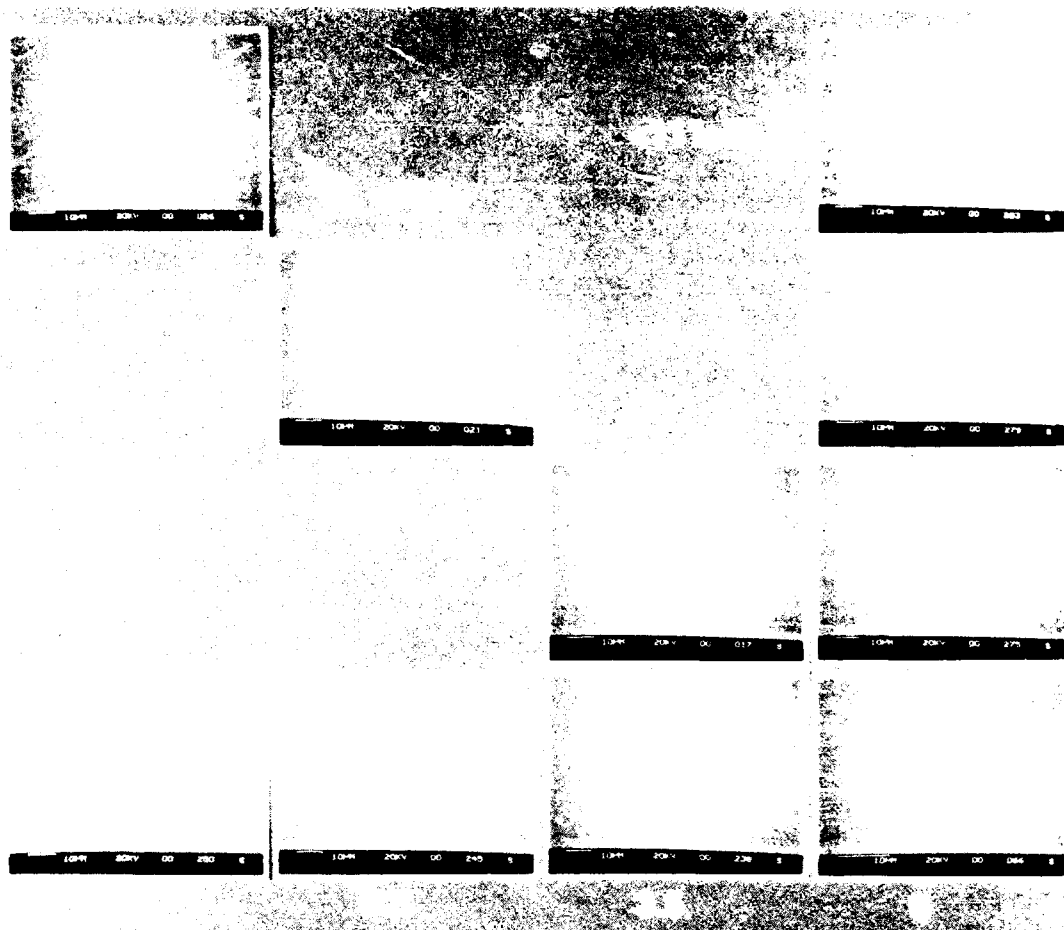


Fig. 4. Montage of SEM micrographs at angles and directions shown of the CdTe layer grown on the GaAs dome at 275 °C. Optimum surface is 3.5° toward  $\langle 111 \rangle$ A.

thermocouple in direct contact with the surface vs the heater controller temperature setpoint. During the calibration the total carrier gas flow rate was identical to that used for the growth runs. No attempt was made to rotate the sample during the thermocouple calibration, however, so that boundary layer conditions for the flow near the surface will be somewhat different from rotating conditions. Therefore, the stated growth temperatures should be considered approximate. Temperatures calibrated to be 275 and 375 °C were chosen for the deposition experiments.

CdTe was also deposited on planar wafers of GaAs and GaAs Si at 375 °C. The surface normal of single-crystal GaAs wafers was tilted 4° away from the  $\langle 100 \rangle$  axis toward either the  $\langle 111 \rangle$ A or the  $\langle 100 \rangle$ B (that is, either  $\langle 111 \rangle$ Ga or  $\langle 111 \rangle$ As, respectively). Wafers of  $\langle 100 \rangle$  GaAs on silicon were tilted 3–4° toward a silicon  $\langle 111 \rangle$  axis. The nominal thickness of the layers reported here was 8 μm.

Surface morphology was examined using Nomarski optical microscopy and scanning electron microscopy (SEM). Thickness of the epitaxial layer was determined using reflection Fourier-transform infrared interference (FTIR) measurement. Crystal quality was estimated using double-crystal x-ray rocking curve measurement determined from symmetric  $\langle 400 \rangle$

reflections. A special fixture was constructed to allow appropriate positioning of the curved surface for the x-ray measurement.

## RESULTS

The result of the growth of epitaxial CdTe on the GaAs dome at 275 °C is shown in an optical photo in Fig. 1. The  $\{100\}$  stereographic projection in Fig. 2 is aligned with the crystallographic orientation of the wafer. Growth on a second dome is shown in Fig. 3 at the same orientation. Fourier-transform infrared interference measurement shows the nominal thickness of both of these layers is approximately 6 μm.

For deposition at both 275 and 375 °C, a twofold rotational symmetry about the  $\langle 100 \rangle$  axis is clearly evident in the surface patterns. Large hazy areas occur at both temperatures in regions with azimuths close to the  $\langle 111 \rangle$ B from near zero tilt to the edge of the dome (15°). At tilt directions near the  $\langle 111 \rangle$ A azimuth, the surface is significantly more smooth and specular with some hazy areas apparent on the 275 °C sample surface.

Scanning electron microscope images were obtained at a series of four tilt angles (0°, 3.5°, 6.5°, 9.5°) and azimuths (toward the  $\langle 111 \rangle$ A,  $\langle 011 \rangle$ , and the  $\langle 111 \rangle$ B axes). Composites of these images are presented in

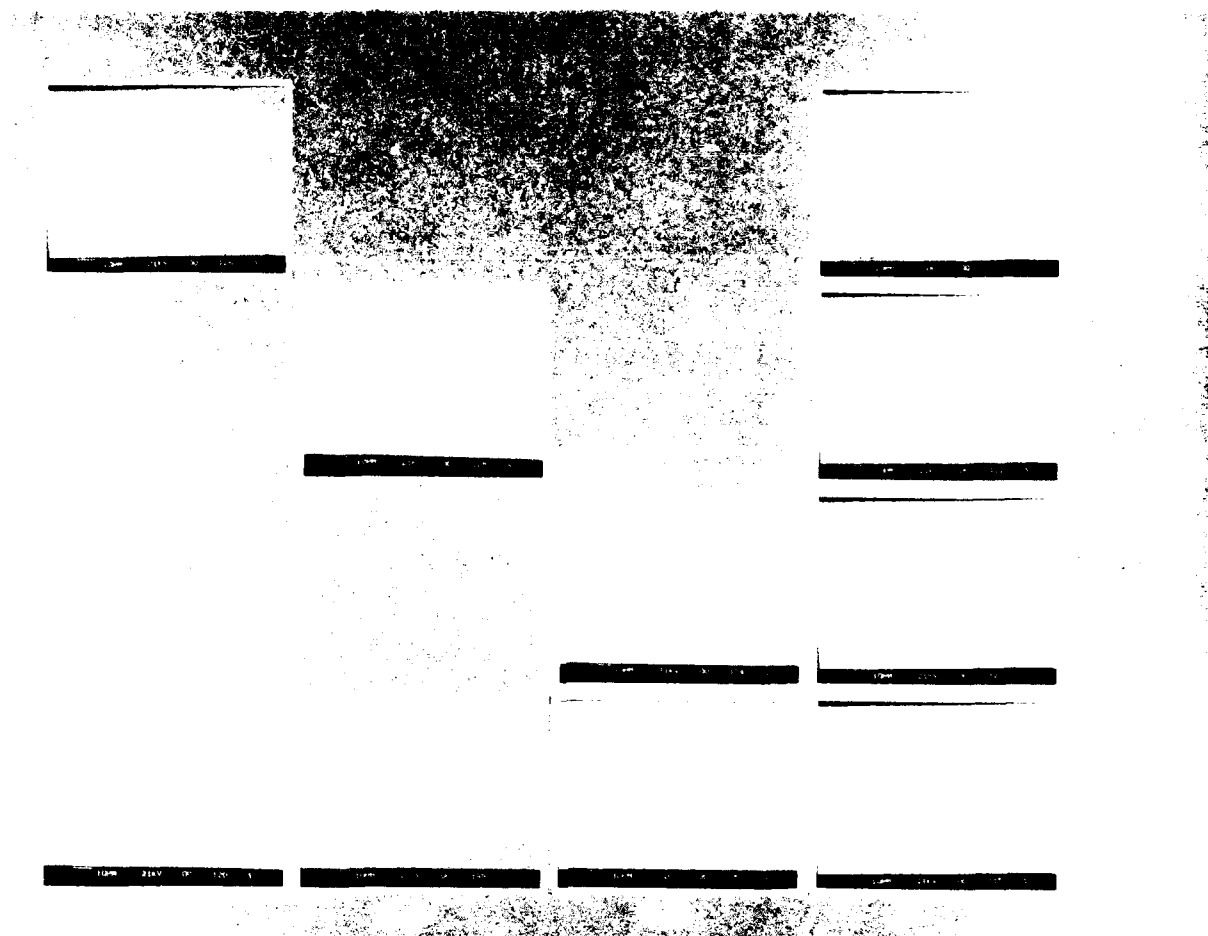


Fig. 4. Micrographs of the four faces of a single CdTe layer grown on the (100) surface of GaAs. Epitaxial growth on the (111)A, (111)B, (110), and (100) surfaces are relatively smooth.

#### X-RAY ROCKING-CURVE MEASUREMENT (FWHM- arc sec)

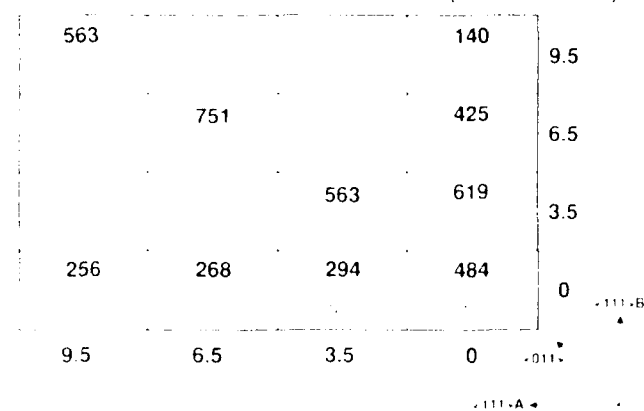


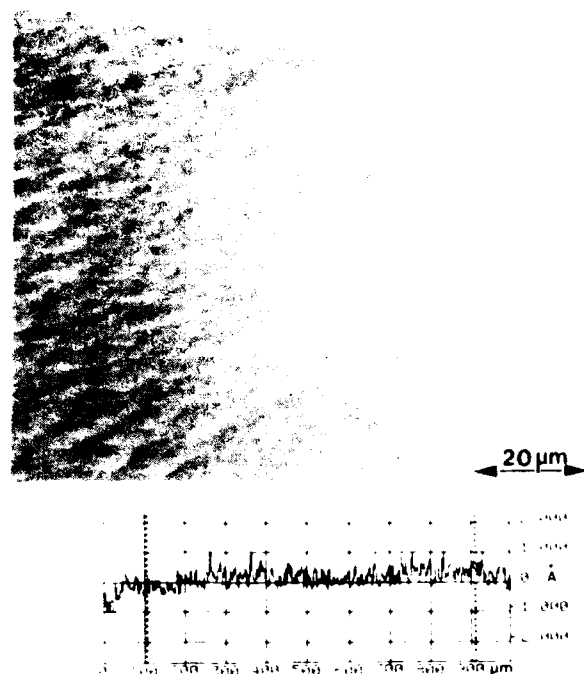
Fig. 5. X-ray rocking curve measurement of the epitaxial CdTe layer grown on the (100) surface of GaAs. The growth temperatures are 275, 375, 475, and 575°C. The curves show the dependence of the rocking curve on the tilt angle. The curves are measured at the same time as the micrographs shown in Fig. 4. The curves show that the epitaxial layer is of high quality and that the growth process is well controlled.

Figs. 4 and 5 for  $T = 275$  and  $375^\circ\text{C}$ , respectively. At both growth temperatures, SEM micrographs demonstrate that the nonspecular areas result from four-sided pyramidal hillocks commonly seen in (100)

CdTe vapor phase epitaxy. Directly on the (100) surface (that is, near zero tilt), the hillocks show twofold symmetry. The hillocks become progressively more distended in one axis as the tilt angle increases in the  $\langle 111 \rangle$ B and the  $\langle 110 \rangle$  directions. Surfaces with tilts toward the  $\langle 111 \rangle$ A show little surface texture in SEM images. Nomarski light microscopy is required to demonstrate that these surfaces are textured as well.

Small imperfections appearing over the whole spherical surface as white dots in the  $275^\circ\text{C}$  growth were seen at higher magnification to be small pits. These were traced to overetching during pregrowth cleaning of the surface in both the dome and in planar wafers and were eliminated from subsequent growth runs. They do not appear in the  $375^\circ\text{C}$  grown surface.

X-ray rocking curve measurements also show variations in crystal perfection of the epitaxial layer with tilt direction and azimuth. Table I summarizes a typical XRC data set obtained on both domes. The higher temperature data are shown in solid numbers and the lower temperature data are shown in an outline font. It is clear from the pattern of XRC values obtained that there is a clear dependence of the results on the growth temperature. At  $275^\circ\text{C}$ , lower rocking curve values are obtained with tilts toward

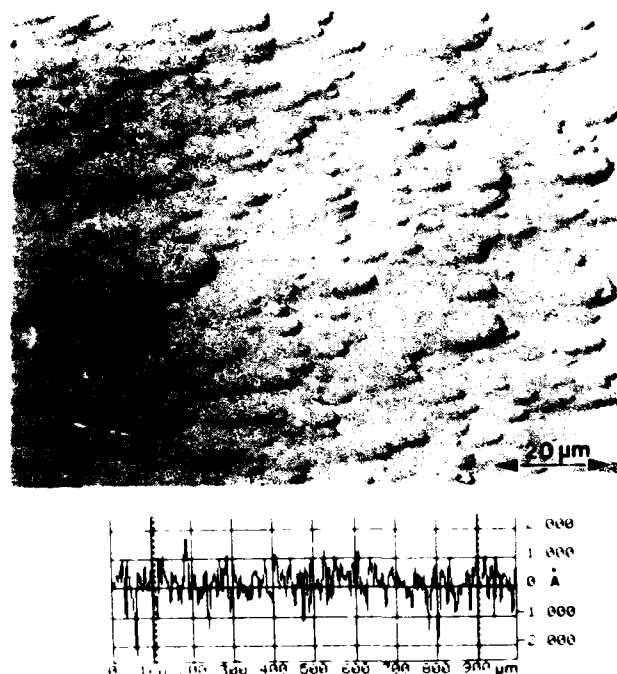


**{100} 4° TOWARD <111> A**  
**XRC FWHM = 140 - 147 "**

Fig. 6. Nomarski optical micrograph of CdTe grown at 375 °C on planar substrates of (100) GaAs tilted 4° toward <111>A. A profilometer trace over 1 mm of this surface is shown below.

the <111>B, whereas at 375 °C, lower values are obtained at tilts toward the <111>A. The low value at 9.5° toward the <111>B at 375 °C was consistently higher in repeated measurements. The largest rocking curves measured were at azimuths near the <011>, and in particular, at higher tilt angles for growths at both temperatures.

CdTe was grown under similar conditions on a limited number of (100) GaAs planar substrates with tilts toward the <111>A and <111>B. Figures 6 and 7 show Nomarski light microscope images of the surface morphology of samples of CdTe deposited at 375 °C under conditions identical to the dome experiments above. The elongated shape of the pyramidal hillocks is clearly visible in the sample tilted toward the <111>B. The images of both the A and B orientations on the flat surfaces reflect in detail the images obtained at 3.5° tilt on the dome's surface. The surface profilometry measurement shown in Figs. 6 and 7 indicates that the range of excursion of the surface roughness is approximately twice as great for the <111>B orientation (≈ 200 nm) as the <111>A orientation (≈ 100 nm). The x-ray rocking curves measurements are somewhat better for growths on substrates tilted toward the <111>B. This observation was consistent over a number of growth runs. The better rocking curve values on the planar wafers compared to the same orientation on the domes can probably be ascribed to a combination of the smoother substrate surfaces of the flat wafers and cleaner



**{100} 4° TOWARD <111> B**  
**XRC FWHM = 134 - 150 "**

Fig. 7. Nomarski optical micrograph of CdTe grown at 375 °C on planar substrates of (100) GaAs tilted 4° toward <111>B. A profilometer trace over 1 mm of this surface shows approximately twice the roughness of the <111>A sample in Fig. 6.

starting surfaces of the flats due to the relative difficulty of handling the heavy and bulky domes during pregrowth steps, and somewhat thicker layers on the flat wafers.

The surface morphology of an epitaxial layer of CdTe grown at 375 °C on (100) GaAs-Si tilted 3.5° toward the <111> is shown in Fig. 8. The elongated pyramidal geometry characteristic of growth on the single crystal GaAs tilted toward the <111>B are typical of surfaces grown on this composite substrate. Based on this surface structure, one may hypothesize that the orientation of the CdTe is most probably tilted toward the <111>B axis.

## DISCUSSION

The use of a spherically polished dome of single-crystal GaAs has allowed the MOCVD deposition of an epitaxial layer of CdTe over all azimuths and all polar angles up to 15° about the (100) axis. These results have indicated how the surface tilt of a planar wafer can be orientated for simultaneous optimization of crystal quality and surface morphology on planar wafers under well defined growth conditions. Under the conditions of these growths, it was clear that small tilt angles resulted in superior surface morphology when compared to either no tilt or large tilts. In all cases, the best surfaces were seen in tilts toward the <111>A axis. Crystal quality at a given orientation, as indicated by the x-ray rocking curve

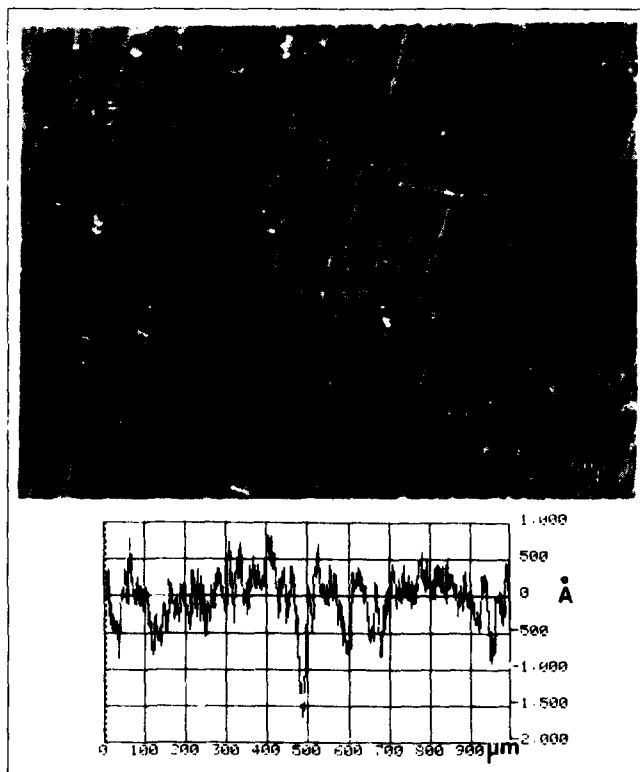


Fig. 8. Nomarski optical micrograph of CdTe grown at 375°C on planar substrates of {100} GaAs on Si tilted approximately 3.5° toward  $\langle 111 \rangle$ . A profilometer trace over 1 mm of this surface shows approximately the same roughness as the  $\langle 111 \rangle$ -B sample in Fig. 7.

data, was a function of growth temperature. Optimization can then be achieved within a range of temperature defined by other considerations such as growth rate and economic use of materials.

The validity of the technique for process optimization is supported by the observation of the growth of CdTe epitaxial layers on planar wafers. Growths on planar wafers with tilt angles determined to be optimal in these dome experiments produced high quality epitaxial layers. The morphology of these layers was nearly identical to the morphology of areas at the same azimuth and tilt angle on the dome. It is unlikely that this coincidence is accidental.

It is likely, however, as indicated by the difference in the results with variation in temperature, that the specific optimization for growth of CdTe on GaAs will depend on a number of growth parameters such as II/VI ratio, total pressure, total flow, and so forth. There is some validity in an argument that optimum growth conditions could be found for any tilt angle. However, the simultaneous optimization of surface morphology, surface defect density, crystal quality, growth rate, efficiency in raw material usage, etc. may favor growth parameters which then determine an optimal orientation.

One result that was independent of temperature was the consistent occurrence of the hazy, hillock covered surfaces at azimuths between the  $\langle 111 \rangle$ -B and  $\langle 011 \rangle$  directions. Surfaces with tilts having azimuth angles near the  $\langle 111 \rangle$ -A were more nearly

specular at both temperatures. Tilts toward the  $\langle 111 \rangle$ -A will expose Ga atoms at the step edges,  $\langle 111 \rangle$ -B will expose As atoms at the step edges and tilts toward the  $\langle 011 \rangle$  will expose both Ga and As. These observations suggest that an excess of Ga may be critical in nucleation of growth when excess Te reagent is present in the gas flow as was the case in these experiments.

On the other hand, the fact that optimal growth of {100} GaAs on {100} silicon substrates occurs at 3° to 4° tilt toward the  $\langle 111 \rangle$  axis<sup>14</sup> may not be coincidental. Perhaps there is a common mechanism of defect suppression at growth initiation at small tilt angles from the  $\langle 100 \rangle$  axis. We have not devised a simple model which would explain a preference for the tilt angles observed. Nor do we have sufficient data on bond angles and energies due to tilting of crystal planes<sup>8</sup> at the interfaces to model the interface with elastic theory. Snyder et al.<sup>10</sup> observe an optimal tilt of 3–4° toward the  $\langle 111 \rangle$ -B axis for homoepitaxial growth of CdTe on a CdTe hemispherical dome. They propose that this tilt is optimal because each Te atom on the steps in this orientation have four unpaired electrons which putatively results in preferential reaction with the impinging Cd atoms and a reduction in the formation of Te clusters, which they believe to have a causal relation in the formation of dislocations and stacking faults required for hillock formation. We have noted previously,<sup>6</sup> however, an anticorrelation between the incidence of crystal defects and hillock formation, and have not observed evidence of Te precipitates in TEM investigations of the GaAs/CdTe interface.

Several factors would indicate that differences would be expected between the results of homoepitaxial growth initiation as observed by Snyder et al.<sup>10</sup> and heteroepitaxial growth on GaAs demonstrated in this study. Snyder et al. achieve the best x-ray rocking curves at 0° or tilts toward the  $\langle 111 \rangle$ -B with values seen in the range of 10–30 arc-s over all angles. The heteroepitaxial values in this study of 200–300 arc-s, while significantly larger than the homoepitaxial values, are commensurate with state-of-the-art values achieved on planar substrates (at the given layer thickness) in this<sup>15</sup> and other laboratories.<sup>16</sup> The direct lattice matching of the homoepitaxial growth compared to the 14.7% lattice mismatch of the heteroepitaxial growth results in considerably more defect generation at the nucleating interface and concomitantly larger x-ray rocking curve measurements. Other results such as the distinct twofold symmetry in the surface morphology of heteroepitaxial growth on the dome compared to a symmetry very nearly fourfold symmetry of homoepitaxial growth may be due to differences in the atomic properties of Cd and Ga, and Te and As at the interface such as electronegativity, bond ionicities, atomic size, and so forth. One would expect that these properties will considerably effect differences in the process of nucleation of epitaxial growth.

Silicon substrates with a {100} surface have four-

fold symmetry and exhibit no A or B polarity in tilts toward  $\langle 111 \rangle$  directions. The orientation of GaAs grown on a surface tilted toward a Si  $\langle 111 \rangle$  axis must have a single polarity if it is a single crystal. Elimination of anti-phase domains resulting from growth in both polarities on a single surface was the critical issue in GaAs epitaxy at an early stage in its development. The great similarity of the CdTe growth on bulk GaAs and GaAs/Si surfaces (compare Figs. 7 and 8) has suggested to us that the CdTe and the GaAs below it are oriented with tilts toward the  $\langle 111 \rangle$ B. The orientation of the GaAs epitaxial layers used in these experiments has not been determined unequivocally.<sup>17</sup>

## CONCLUSIONS

A spherically ground and polished dome of GaAs was used as a substrate for the growth of epitaxial CdTe by MOCVD. The dome presented all azimuths around the  $\langle 100 \rangle$  axis and polar (tilt) angles up to  $15^\circ$ . Observation of the surface morphology and x-ray rocking curves as a measure of crystal quality, show an orientation of  $3\text{--}4^\circ$  toward the  $\langle 111 \rangle$ A or B to be optimal for the growth conditions used, with a surface smoothness advantage toward the  $\langle 111 \rangle$ A. Comparison of the surfaces of CdTe grown on GaAs {100} tilted  $4^\circ$  toward the  $\langle 111 \rangle$ B and CdTe grown on GaAs on Si {100} tilted  $3\text{--}4^\circ$  toward the  $\langle 111 \rangle$  suggested that the orientation of the GaAs on silicon and the epitaxial CdTe layer were {100} tilted toward  $\langle 111 \rangle$ B.

## REFERENCES

1. W.L. Ahlgren, M.H. Kalisher, C.A. Cockrum, T.W. James, D.J. Arney, C.K. Ziegler and W. Lick, *J. Vac. Sci. Technol.* A7, 331 (1989).
2. S.M. Johnson, M.H. Kalisher, W.L. Ahlgren, J.B. James and C.A. Cockrum, *Appl. Phys. Lett.* 56, 946 (1990).
3. S.M. Johnson, J.B. James, W.L. Ahlgren, W.J. Hamilton, M. Ray and G.S. Tompa, *Long-Wavelength Semiconductor Devices, Materials, and Processes*, Mater. Res. Soc. Symp. Proc., eds. A. Katz, R.M. Biefeld, R.L. Gunshor and R.J. Malik (Mater. Res. Soc., Pittsburgh, PA 1991) Vol. 216, p. 141.
4. R. Sporken, M.D. Lange, C. Masset and J.P. Faurie, *Appl. Phys. Lett.* 57, 1449 (1990).
5. R. Bean, K. Zanio and J. Ziegler, *J. Vac. Sci. Technol.* A7, 343 (1989).
6. W.J. Hamilton, S.M. Johnson and W.L. Ahlgren, *J. Vac. Sci. Technol.* B10, 1543 (1992).
7. D.D. Edwall, J. Bajaj and E.R. Gertner, *J. Vac. Sci. Technol.* A8, 1045 (1990).
8. S.M. Johnson, W.L. Ahlgren, M.H. Kalisher, J.B. James and W.J. Hamilton, *Properties of II-VI Semiconductors: Bulk Crystals, Epitaxial Films, Quantum Well Structures, and Dilute Magnetic Systems*, Mater. Res. Soc. Symp. Proc., eds. F.J. Bartoli, H.F. Schaake and J.F. Schetzina (Mater. Res. Soc., Pittsburgh, PA 1990) Vol. 161, p. 351.
9. W.L. Ahlgren, S.M. Johnson, E.J. Smith, R.P. Ruth, B.C. Johnston, M.H. Kalisher, C.A. Cockrum, T.W. James and D.L. Arney, *J. Vac. Sci. Technol.* A7, 331 (1989).
10. D.W. Snyder, S. Mahajan, E.I. Ko and P.J. Sides, *Appl. Phys. Lett.* 58, 848 (1991).
11. Crystal Specialties, Inc., Colorado Springs, Co.
12. II-VI Inc., Saxonburg, PA.
13. H. Shtrikman, M. Oron, A. Raizman and G. Cinader, *J. Electron. Mater.* 17, 105 (1988).
14. H. Morkoç, H. Unlu, H. Azbel and N. Otsuka, *Solid State Technol.* March 71 (1988).
15. S.M. Johnson, J.A. Vigil, J.B. James, C.A. Cockrum, W.H. Konkel, M.H. Kalisher, R.F. Risser, T. Tung, W.J. Hamilton, W.L. Ahlgren and J.M. Myrosznyk, presented at the U.S. Workshop on the Phys. and Chem. of HgCdTe, Oct. 1992, Danvers, Mass., *J. Electron. Mater.* 22, 835 (1993).
16. W.S. Wang, H.E. Ehsani and I.B. Bhat, presented at the U.S. Workshop on the Phys. and Chem. of HgCdTe, Oct. 1992, Danvers, Mass., *J. Electron. Mater.* 22, 873 (1993).
17. Private communication, Kopin Corp., 1992.

# Use of Ellipsometry to Characterize the Surface of HgCdTe

DAVID R. RHIGER

Santa Barbara Research Center, 75 Coromar Dr., Goleta, CA 93117

Ellipsometry is a sensitive, rapid, and nondestructive optical technique for characterizing materials, especially surfaces and films. By measuring the change in the state of polarization of a light beam reflecting from the sample, one may infer certain characteristics of the sample. We present a review of the applications of ellipsometry to HgCdTe and related materials. The fundamentals of the technique are discussed briefly and the optical parameters at the wavelength 6328Å for several materials of interest to infrared technology are listed. The emphasis of this paper is on the interpretation of the ellipsometric data, expressed in terms of the usual parameters  $\psi$  and  $\Delta$  obtained at a single wavelength. Methods and limitations of the analysis of single films, both nonabsorbing and absorbing, are discussed. Examples of an acceptance window for process monitoring are presented. The ellipsometric signatures of amorphous Te films and microroughness are described, along with a graphical method for interpreting the readings from very thin films. Spectroscopic applications and in situ monitoring of molecular beam epitaxial growth processes are briefly reviewed.

**Key words:** Characterization of surfaces, ellipsometry, HgCdTe

## INTRODUCTION

Ellipsometry is a highly sensitive optical technique for characterizing surfaces, thin films, and materials. It is widely used to monitor processes such as surface cleaning, deposition and removal of films, and the growth of epitaxial layers. It is also an important tool for fundamental investigations of the physics and chemistry of materials and surfaces, particularly for semiconductors. The sensitivity of ellipsometry is such that it can detect changes in film thickness as small as 1Å. It is nondestructive and noninvasive, and instrumentation is available to make measurements rapidly and automatically.

The objective of this paper is to review the applications of ellipsometry to HgCdTe and related materials. The emphasis will be on the methods of interpretation of the measurement, for the purpose of determining the characteristics of the sample. Only introductory comments will be made concerning the instrumentation and the theory of the optical interac-

tion with the sample. For a thorough discussion of the theory of ellipsometry and a review of the instrumentation, the reader may consult Azzam and Bashara.<sup>1</sup> A brief description of the theory has been given by Spanier,<sup>2</sup> while Kutko<sup>3</sup> has given a qualitative description of simple applications. Optical parameters of many materials plus reviews of the theory and methods for several optical techniques including ellipsometry can be found in two volumes edited by Palik.<sup>4,5</sup> Aspnes has reviewed the theory both in detail<sup>6,7</sup> and qualitatively<sup>8</sup> with several examples of applications to various materials. A great many references exist describing specific applications to Si and GaAs, but published applications to HgCdTe number fewer than 20.

We summarize the principles of the ellipsometric measurement and briefly describe the common null ellipsometer in the sections on ellipsometric measurement and the ellipsometer. Optical parameters of materials are defined in the following section with values given for several materials of interest in infrared technology. In the section on quantitative applications to bare substrates and single films, we

(Received November 14, 1992)

describe quantitative approaches to the analysis of single wavelength ellipsometric data. In Qualitative Interpretations of Ellipsometric Data, we discuss methods of qualitative and semi-quantitative interpretation of the data. The perspective is broadened to spectroscopic and in-situ applications in the last section before our conclusion. Throughout the paper, references on Si and GaAs, which illustrate concepts applicable to HgCdTe, have been selected for mention.

### THE ELLIPSOMETRIC MEASUREMENT

Ellipsometry involves the reflection of elliptically polarized light from the surface of a sample, causing a change in the state of polarization. By measuring this change, one may infer certain characteristics of

the sample. Figure 1 illustrates the geometry and optical electric field components for the simple case of a semi-infinite substrate with no film. The incident beam propagates along the vector  $q$  and the reflected beam along  $q'$ . The two paths define the plane of incidence, which is perpendicular to the sample surface. A third beam is transmitted into the substrate along the vector  $q''$  and is eventually absorbed. The angle of incidence  $\phi$  is the angle between the incident beam and a line normal to the surface.

The electric field of the incident light wave can be resolved into two orthogonal components, both of which are perpendicular to  $q$ .  $E_p$  is parallel to the plane of incidence and  $E_s$  is perpendicular to the plane of incidence. The vector sum of  $E_p$  and  $E_s$ , when viewed in a fixed plane perpendicular to  $q$  traces out, in general, an ellipse as a function of time. The reflected and transmitted beams can be similarly resolved into components. Each electric field component can be written in the general form

$$E(z, t) = E_0 \exp[i(\omega t - 2\pi \tilde{n} z / \lambda + \delta)] \quad (1)$$

where  $z$  is the distance along the direction of propagation,  $t$  is the time,  $E_0$  is a constant amplitude,  $\omega$  is the angular frequency,  $\tilde{n}$  is the complex refractive index of the medium of propagation,  $\lambda$  is the vacuum wavelength,  $\delta$  is the phase of the component, and  $i = \sqrt{-1}$ .

The effect of the sample can be described in terms of two complex reflectance coefficients

$$r_p = E'_p / E_p \quad (2)$$

$$r_s = E'_s / E_s \quad (3)$$

These are combined to give the complex reflectance ratio  $\rho$

$$\rho = r_p / r_s = \tan \psi \exp i \Delta \quad (4)$$

which has been cast here in terms of the usual

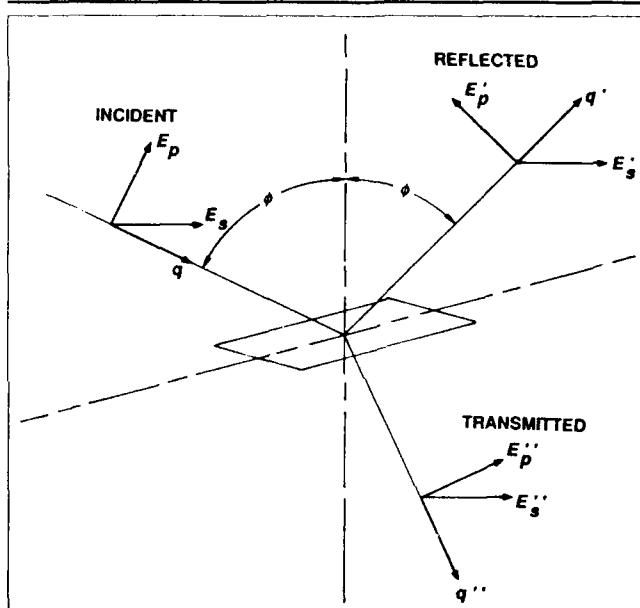


Fig. 1. Beam geometry and components of the optical electric field.

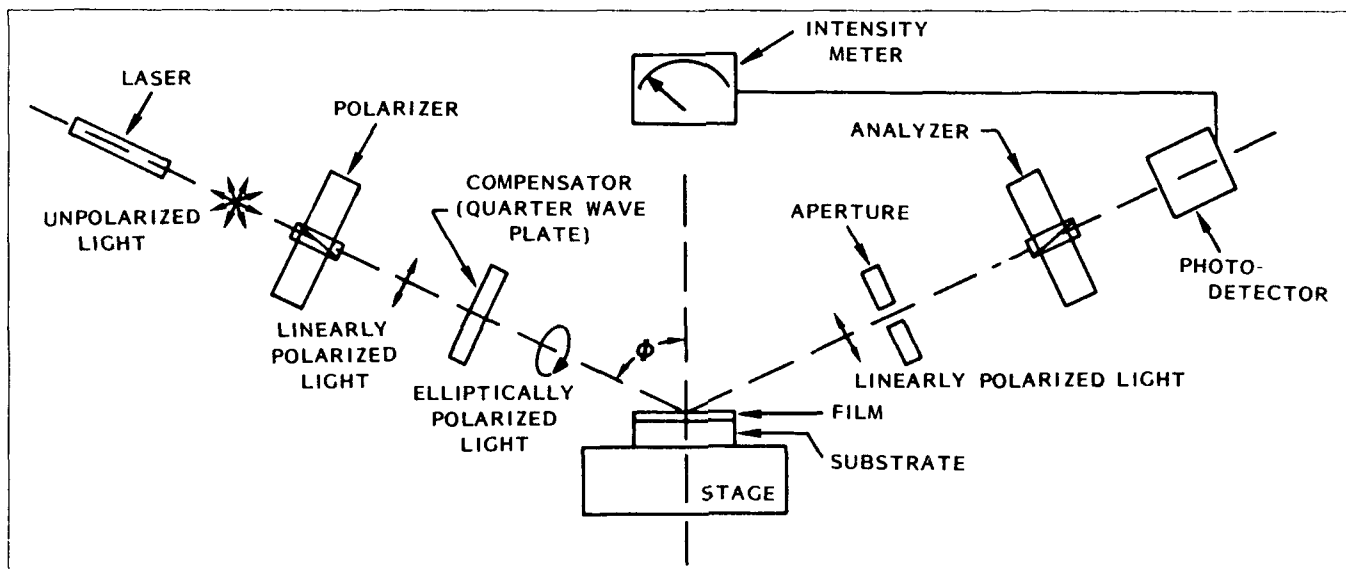


Fig. 2. Diagram of a single wavelength null ellipsometer.



ellipsometric parameters  $\psi$  and  $\Delta$ . Physically,  $\tan \psi$  is the factor by which the ratio of the p-component amplitude to the s-component amplitude changes upon reflection, and  $\Delta$  is the change in the phase difference between the two components upon reflection.

Every conventional ellipsometric reading of a sample can be expressed in terms of  $\psi$  and  $\Delta$ . (Equivalently, one may use the real and imaginary parts of  $\rho$ .) This is true regardless of the numbers and kinds of layers comprising the sample. The full allowed ranges are  $0^\circ \leq \psi \leq 90^\circ$  and  $0^\circ \leq \Delta \leq 360^\circ$ .

The great sensitivity of ellipsometry arises from the fact that polarization angles rather than light intensities are measured. In the latter case, the minimum film thickness measurable by an interferometric technique is somewhat smaller than about one quarter of the probing wavelength divided by the refractive index. A typical value would be greater than 100Å. For ellipsometry, however, the sensitivity is generally determined by the measurement of the polarization angles which in common commercial instruments are typically accurate to the nearest  $0.01^\circ$  or better. Scaled in proportion to the wavelength of visible light, this corresponds to film thickness differences of less than 1Å.

### THE ELLIPSOMETER

A basic ellipsometer is diagrammed in Fig. 2. This is a single wavelength nulling instrument of the most common configuration. Unpolarized light from the source enters the polarizer and emerges in a linearly polarized state. The compensator, usually a quarter wave plate, converts it to an elliptical state, after which it reflects from the sample. The light then passes through the aperture and the analyzer, and enters the photodetector. Readings are taken by means of a nulling operation whereby the polarizer and analyzer orientation angles are adjusted to minimize the photodetector signal. This occurs when the incident state of elliptical polarization is such that reflection from the sample converts it to linear, as indicated in Fig. 2. Instruments are available in which the nulling operation is performed manually or automatically. Other instruments make use of a continuously rotating analyzer.<sup>9</sup> The reading is expressed in terms of the parameters  $\psi$  and  $\Delta$ , which can be displayed and printed by the automatic instruments.

Under typical standard conditions, the light source is a HeNe laser with a wavelength  $\lambda$  of 6328Å, corresponding to a photon energy of 1.9592 eV. The angle of incidence  $\phi$  is most often set at  $70^\circ$ . These conditions will be assumed throughout this paper unless stated otherwise.

The most common usage of an ellipsometer in the processing of compound semiconductors is *ex situ*. Samples are carried from a processing station and placed on the stage of the ellipsometer for characterization. Alternatively, for *in situ* measurements, the two arms of the ellipsometer can be mounted on separate ports of a chamber in which a sample is being grown or processed. Also, for either *ex situ* or *in situ*

applications, the single wavelength source may be replaced with a white light plus a monochromator for spectroscopic measurements.

### MATERIAL PARAMETERS

#### General Expressions

The optical properties of any isotropic material can be expressed in terms of the complex refractive index

$$\tilde{n} = n - ik \quad (5)$$

where  $n$  is the ordinary refractive index and  $k$  is the extinction coefficient. Both  $n$  and  $k$  are positive real numbers and depend on the wavelength of the light, but are independent of the angle of incidence. When appropriate, we attach the following subscripts to  $n$  and  $k$ :  $a$  for the ambient medium,  $f$  for a film, and  $s$  for a substrate. The extinction coefficient is a measure of how rapidly the optical energy is absorbed in the material. The intensity falls as  $\exp(-\alpha z)$ , in which

$$\alpha = 4\pi k/\lambda \quad (6)$$

where  $\alpha$  is the absorption parameter, and  $\lambda$  is the vacuum wavelength. An equivalent description of the optical properties can be given in terms of the complex dielectric function  $\epsilon$

$$\epsilon = \epsilon_1 - i\epsilon_2 \quad (7)$$

where  $\epsilon_1$  is the real part and  $\epsilon_2$  is the imaginary part. The relationship to  $\tilde{n}$  is

$$\epsilon = \tilde{n}^2 \quad (8)$$

It can be shown that  $\epsilon_2$  is always nonnegative, but  $\epsilon_1$  can have either sign.

**Table I. Refractive Index  $n$  and Extinction Coefficient  $k$  for Several Materials of Interest in Infrared Technology**

| Material                               | $n$   | $k$   |
|--|-------|-------|
| CdTe                                   | 3.018 | 0.253 |
| Hg <sub>0.4</sub> Cd <sub>0.6</sub> Te | 3.38  | 0.46  |
| Hg <sub>0.7</sub> Cd <sub>0.3</sub> Te | 3.653 | 0.755 |
| Hg <sub>0.8</sub> Cd <sub>0.2</sub> Te | 3.742 | 0.880 |
| HgTe                                   | 3.926 | 1.194 |
| ZnTe                                   | 2.989 | 0.01  |
| GaAs                                   | 3.857 | 0.198 |
| InSb                                   | 4.189 | 1.763 |
| Si                                     | 3.882 | 0.019 |
| a-Te                                   | 4.1   | 1.7   |
| SiO <sub>2</sub>                       | 1.46  | 0.0   |
| Al <sub>2</sub> O <sub>3</sub>         | 1.76  | 0.0   |
| TeO <sub>2</sub>                       | 2.31  | 0.0   |
| Au                                     | 0.183 | 3.10  |
| Cr                                     | 3.58  | 4.36  |
| Hg                                     | 2.05  | 5.18  |
| In                                     | 1.07  | 6.17  |
| Ni                                     | 1.97  | 3.72  |
| Pd                                     | 1.77  | 4.29  |

Note: Wavelength of 6328Å and room temperature. References are given in the text.

For nonabsorbing materials such as insulators, we have  $k = 0$  (thus  $\alpha = 0$  and  $\epsilon_2 = 0$ ). Examples would be  $\text{SiO}_2$  and  $\text{TeO}_2$  at 6328Å. For the ambient medium, we normally assume  $n_a = 1$  and  $k_a = 0$ , which is appropriate for air,  $\text{N}_2$ , and vacuum, and is a good approximation to the atmosphere in a metalorganic chemical vapor deposition (MOCVD) reactor. For semiconductors and metals  $k > 0$ .

A brief note about sign conventions is necessary. We adhere to the optics convention, which establishes a positive sign in front of the  $i$  in the exponent of Eq. 1 and leads to a negative sign for the imaginary terms in Eqs. 5 and 7, as shown. This is the most common choice in the ellipsometry literature. The physics convention, on the other hand, reverses these signs but is equally valid. Conventions have been discussed by Hauge et al.<sup>10</sup> and by Holm.<sup>11</sup>

### Values For Selected Materials

To interpret or model ellipsometric data, it is necessary to know the values of  $n$  and  $k$  for some or all the materials comprising the sample. Table I lists several materials of interest in infrared technology. The values apply at 6328Å and room temperature. For CdTe and for  $\text{Hg}_{1-x}\text{Cd}_x\text{Te}$  with  $x = 0.2$  and  $0.3$ , we have taken values from Ref. 12. The CdTe data were obtained on samples that were cleaved and measured in a dry  $\text{N}_2$  environment.<sup>12</sup> For  $x = 0.6$ , we have made an interpolation as a function of  $x$ . Additionally, both Arwin and Aspnes<sup>13</sup> and Viña et al.<sup>14</sup> report spectroscopic measurements of the optical parameters for several  $\text{Hg}_{1-x}\text{Cd}_x\text{Te}$  compositions.

The HgTe data in Table I are from Ref. 13. Measurements at 6328Å for several  $x$  values were reported by Korsak et al.<sup>15</sup> but are not included in the Table I because of lower accuracy. The  $n$  of ZnTe is from the review by Li,<sup>16</sup> while its small  $k$  is from the estimate of Bajaj.<sup>17</sup> For both CdTe and ZnTe, Bajaj<sup>17</sup> has found that  $n = 3.04$  for MOCVD samples monitored in situ at about 380°C. This is slightly higher than the values listed in Table I, but the difference is probably due to the elevated temperature, because a corresponding increase in  $n$  is reported by Li<sup>16</sup> for ZnSe over a similar

temperature difference. The values for GaAs were found in the tables of Aspnes et al.<sup>18</sup> For InSb we believe that the best data are from Baumgratz,<sup>19</sup> who cleaved and measured samples in dry  $\text{N}_2$ . The  $n$  and  $k$  of Si are from Edwards.<sup>20</sup> For amorphous Te (a-Te) we have taken  $k$  from Keller and Stuke<sup>21</sup> and  $\epsilon_2$  from Stuke,<sup>22</sup> from which  $n$  was found according to Eqs. 5, 7, and 8. Among the nonabsorbing oxides,  $\text{SiO}_2$  and sapphire are well known, while the  $n$  for polycrystalline  $\text{TeO}_2$  is taken as a weighted average of the anisotropic values reported by Uchida<sup>23</sup> and Singh et al.<sup>24</sup> To complete the table, the metals included are Au,<sup>25</sup> Cr,<sup>26</sup> Hg,<sup>12</sup> In,<sup>27</sup> Ni,<sup>25</sup> and Pd.<sup>28</sup> Throughout Table I, the third digit after the decimal point may not be significant. When any of these materials is used as a substrate for an unknown film, the substrate parameters are needed in solving for the film parameters. Also, when any material in Table I occurs as a film, the measured  $n_f$  and  $k_f$  can be compared against the tabulated values for verification.

### QUANTITATIVE APPLICATIONS TO BARE SUBSTRATES AND SINGLE FILMS

#### Bare Substrates

Applications of ellipsometry to a bare substrate include

- Measuring the optical parameters  $n_s$  and  $k_s$  of the material,
- Identifying an unknown material,
- Measuring the composition of an alloy, as explained below for  $\text{Hg}_{1-x}\text{Cd}_x\text{Te}$ , and
- Verifying that the substrate is indeed free of a film, a procedure that is described below in the section on qualitative interpretations of ellipsometric data.

We describe here the connection between the ellipsometric reading on a bare substrate and the optical parameters of the material.

When the sample does in fact consist of a substrate with no film, the numerical analysis of the ellipsometric data is particularly simple. (In this case, the substrate must also be free of microroughness, which itself can be treated as a film, as discussed in the following section.) The complex refractive index  $\tilde{n}_s$  of the substrate is given by

$$\tilde{n}_s = \tilde{n}_a \tan \phi \left[ 1 - \frac{4\rho \sin^2 \phi}{(\rho + 1)^2} \right]^{1/2} \quad (9)$$

where  $\tilde{n}_a$  is the refractive index of the ambient medium (usually  $\tilde{n}_a = 1 - i0$ ),  $\phi$  is the angle of incidence, and  $\rho$  represents  $\psi$  and  $\Delta$  according to Eq. 4. The values of  $n_s$  and  $k_s$  for several of the materials in Table I have been determined by applying Eq. 9 to their measured  $\psi$  and  $\Delta$ . Conversely, when  $n_s$  and  $k_s$  are known, one may calculate  $\psi$  and  $\Delta$  for a given angle of incidence according to

$$\rho = -1 + 2y \pm \sqrt{4(y^2 - y)} \quad (10)$$

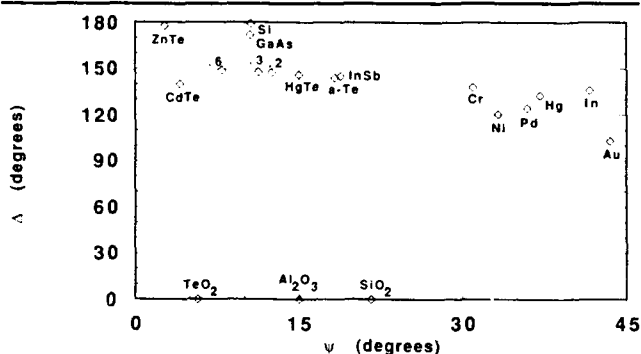


Fig. 3. Ellipsometry readings for a variety of materials assuming they are bare substrates. For each material the  $\psi$  and  $\Delta$  have been calculated according to the  $n$  and  $k$  listed in Table I. The wavelength is 6328Å and the angle of incidence is 70°. The  $\text{Hg}_{1-x}\text{Cd}_x\text{Te}$  alloy series lies between the points for CdTe and HgTe, with the points for  $x = 0.6, 0.3, 0.2$  being shown.

where

$$y = \frac{-\sin^2 \phi}{\bar{n}_s^2 - 1} \quad (11)$$

which has been obtained by inverting Eq. 9 with  $\bar{n}_a = 1 - i0$ . The sign on the square root must be chosen so that  $|\rho| \leq 1$ . Coverage of the sample by a very thin film, even as small as 5Å, can introduce errors in the determination of  $\bar{n}_s$  and  $k_s$ . This is why cleaving or growth, followed by measurement, in an inert atmosphere is advantageous. Methods of detecting contaminant films on various substrates and estimating the resulting errors have been discussed by Burge and Bennett<sup>29</sup> and by Aspnes.<sup>7</sup>

It is instructive to compare the ideal bare-substrate ellipsometry readings for all of the materials in Table I. Applying Eq. 10 with  $\phi = 70^\circ$ , we have generated the plot in Fig. 3. For bare substrates, the allowed parameter ranges are  $0^\circ \leq \psi \leq 45^\circ$  and  $0^\circ \leq \Delta \leq 180^\circ$ . Clustering of the materials into three groups is immediately evident. The insulators, which are nonabsorbing with a relatively low refractive index, lie at  $\Delta = 0^\circ$ . The semiconductors, having higher values of  $\bar{n}_s$  and moderate absorption, are distributed toward the upper left. In contrast, the metals, which are very strongly absorbing, are clustered at high values of  $\psi$ . If we imagine a sequence of samples having  $k_s = 0$  with  $\bar{n}_s$  increasing, the representative point for low  $\bar{n}_s$  in Fig. 3 will lie on the  $\psi$  axis ( $\Delta = 0^\circ$ ) with decreasing values of  $\psi$ , as illustrated by the three insulators. When  $\bar{n}_s = \tan \phi = 2.7475$ , then  $\psi$  reaches  $0^\circ$ . At this condition, the refractive index is such that the Brewster angle is equal to the angle of incidence,  $70^\circ$ . As  $\bar{n}_s$  becomes larger than  $\tan \phi$ , the phase of the reflected p-component jumps by  $180^\circ$ , causing  $\Delta$  to equal  $180^\circ$ . For further increases in  $\bar{n}_s$ , the representative point will move along the line of  $\Delta = 180^\circ$  with increasing  $\psi$ . The latter result is manifested, approximately, in the positions of ZnTe and Si (having  $\bar{n}_s > \tan \phi$ ), which are close to this line because of their very small extinction coefficients.

### Measuring Alloy Composition

For  $\text{Hg}_{1-x}\text{Cd}_x\text{Te}$  alloys, the ellipsometric readings in Fig. 3 lie on an arc joining the two end compounds. In the Hg-rich range, the composition varies mainly as a function of  $\psi$ . Making use of this, McLevige et al.<sup>30</sup> have developed the application of ellipsometry to the measurement of composition. They examined a set of samples in the range  $0.2 < x < 0.35$ , in which  $x$  had been calibrated by photovoltaic device cutoff wavelength. Cleanliness of the surface was established by requiring that  $146^\circ \leq \Delta \leq 148^\circ$ , according to the relationships described below in the section on qualitative interpretation of ellipsometric data. A fit to the data gave

$$\psi(x) = 14.73 - 12.96x + 2.726x^2 \quad (12)$$

A graph of this function was shown to run parallel to the data of Rhiger and Kvaas,<sup>12</sup> but  $\psi$  was shifted downward by approximately  $0.2^\circ$  at each  $x$ . The accuracy of this technique was estimated to be generally within  $\pm 0.01$  in  $x$  value.

Compositional profiling was performed<sup>30</sup> on samples grown by molecular beam epitaxy (MBE) and MOCVD. Ellipsometric measurements were alternated with the chemical removal of small amounts of material. A correlation with composition measurements made by energy dispersive x-ray (EDX) analysis was demonstrated. The abruptness of a CdTe/HgCdTe interface was characterized before and after annealing.<sup>31</sup>

### Single Nonabsorbing Films

A very important application of ellipsometry is the analysis of a single film on a known substrate. Two basic assumptions are that the materials are of uniform composition, and that both interfaces of the film are perfectly sharp. Often the film is assumed to be nonabsorbing ( $k_f = 0$ ), and the thickness  $d$  and ordinary refractive index  $n_f$  of the film are sought. The assumption of  $k_f = 0$  applies, for example, to a film of  $\text{SiO}_2$  on any semiconductor and for various native oxide films on HgCdTe. Layers formed by oxidizing the surface of HgCdTe by several methods have been shown to be nonabsorbing by spectroscopic ellipsometry.<sup>32,33</sup> (However, one would expect that  $k_f \neq 0$  for anodic oxides much thicker than 700Å because of the HgTe inclusions that occur.)<sup>34</sup> It is also likely that  $k_f = 0$  for films of  $\text{Si}_3\text{N}_4$  and ZnS.

To illustrate typical relationships between the ellipsometry reading and the film parameters, calculated plots in the  $\psi$ - $\Delta$  plane are shown as a function of film thickness in Fig. 4 for nonabsorbing films. The point labeled 0 represents the film-free substrate. Trajectories are displayed for two values of  $n_f$  with  $d$  indicated in angstroms at several points on each. The substrate is assumed to be  $\text{Hg}_{0.7}\text{Cd}_{0.3}\text{Te}$  which lies at  $\psi = 11.3^\circ$  and  $\Delta = 148.0^\circ$  (where  $d = 0$ ). The two assumed cases are  $n_f = 1.46$  and  $2.20$ , which represent  $\text{SiO}_2$  and anodically grown HgCdTe native oxide, respectively. In each case, the trajectory makes a loop, coming back to the starting point when  $d$  reaches the thickness period  $D$ , as defined below. When the loop for  $n = 2.20$  hits the bottom of the graph at  $\Delta = 0^\circ$ , it reenters at  $\Delta = 360^\circ$ , which is the same point because  $\Delta$  is an angle. Analogous plots have been presented, for example by Archer<sup>35</sup> and by Smith et al.<sup>36</sup> for silicon oxide films on Si, and by McDevitt and Baun<sup>37</sup> for various films on GaAs. The thickness period is given by

$$D = \frac{\lambda}{2\sqrt{n_f^2 - \sin^2 \phi}} \quad (13)$$

assuming  $\bar{n}_a = 1$ . For the two cases of  $n_f = 1.46$  and  $2.20$ , we have  $D = 2832\text{Å}$  and  $1591\text{Å}$ , respectively. When thickness increases beyond  $D$ , the readings retrace the same loop. The quantity  $d/D$  rounded down to the nearest integer is called the number of period mul-

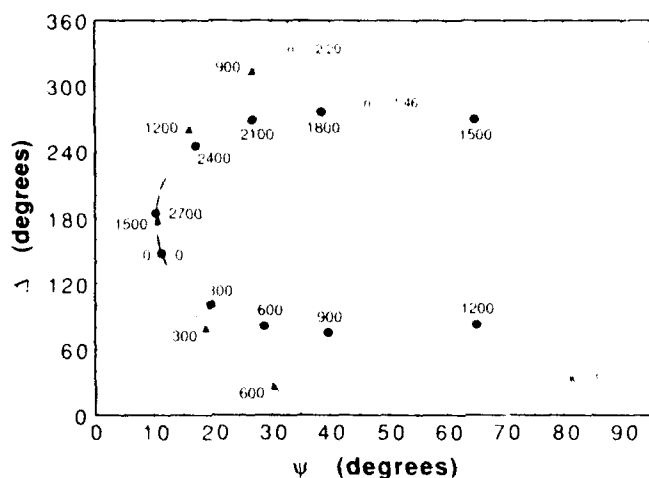


Fig. 4 Calculated full-cycle plots of the ellipsometry readings for nonabsorbing films ( $k_f = 0$ ) of varying thickness on HgCdTe. The two film materials are assumed to be  $\text{SiO}_2$  ( $n_f = 1.46$ ) and anodic oxide ( $n_f = 2.20$ ). Film thickness  $d$  is indicated in angstroms at several points on each curve. The wavelength is 6328Å and the angle of incidence is 70°.

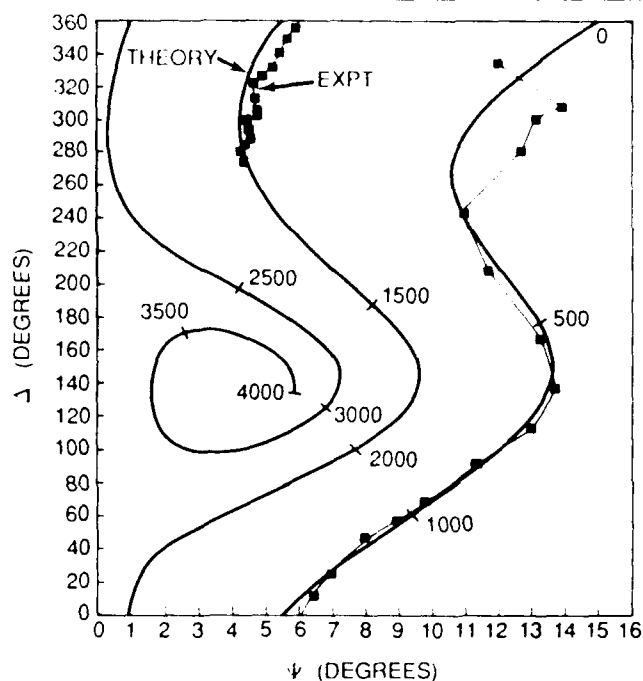


Fig. 5. Ellipsometry of CdTe ( $k_f > 0$ ) on sapphire. The smooth curve is the calculated trajectory of the ellipsometric readings for a film of varying thickness, which is indicated at 500Å intervals. The squares connected by line segments represent the experimental readings taken at 127  $\mu\text{m}$  intervals across a tapered region of MOCVD CdTe film grown on sapphire.

tiples. The cyclical behavior in Fig. 4 is a consequence of the interference processes that occur between the multiply-reflected beams within the layer, and applies in its exact form only when  $k_f = 0$ .

The general problem of characterizing an unknown film on a known substrate involves a fundamental ambiguity, in that only two conditions of the film,  $\psi$  and  $\Delta$ , are measured, but four parameters,  $n_f$ ,  $k_f$ ,  $d$ , and the number of period multiples, are unknown.

Although the ambiguities can be resolved by performing spectroscopic ellipsometry, and in some cases by holding the wavelength constant and varying the angle of incidence, we choose to emphasize single wavelength ellipsometry at a fixed angle of incidence because this is the kind of measurement that is most readily performed with common commercial instruments. In the current context, we are assuming that  $k_f = 0$ , a value that applies to most dielectrics used on HgCdTe. To find the number of period multiples, the approximate thickness must be determined by some auxiliary method, such as a knowledge of the growth rate, or etching and profilometry. In the majority of cases of films on HgCdTe of practical interest, it turns out that the number of period multiples is zero ( $d < D$ ). Therefore, this leaves only two unknowns,  $n_f$  and  $d$ , to be determined.

The general equations for  $\rho$  (or  $\psi$  and  $\Delta$ ) for any film on any substrate involve the Fresnel reflection coefficients at the interfaces and take into account the interference effects of multiple reflections. They have been presented by several authors<sup>1,2,4,8,9</sup> and will not be reproduced here. Given a set of ellipsometric data, the equations are solved numerically by appropriate software to determine the parameters of the sample. A versatile program capable of handling single or multiple films with commensurate quantities of input data has been written by Marchiando.<sup>10</sup> The configuration that we are now considering, however, consists of a single film on a known substrate with the simplifying assumptions that  $k_f = 0$  and  $d < D$ . In this case, given a single  $\psi$ - $\Delta$  reading, the equations can be solved in a routine manner on a small computer connected to the ellipsometer.<sup>10,11</sup> Conceptually, the procedure can be viewed as finding which trajectory (specified by  $n_f$ ) in the  $\psi$ - $\Delta$  plane the measured point lies on, and then determining how far (specified by  $d$ ) along this trajectory the point lies from the bare substrate point.

The accuracy of the analysis depends on the film thickness. For  $d$  less than about 100Å, the relative error in  $d$  and  $n_f$  becomes significant because trajectories in the  $\psi$ - $\Delta$  plane for different values of  $n_f$  (of which two have been shown in Fig. 4) converge at the bare substrate point ( $d = 0$ ). For small thicknesses, the point representing  $\psi$ - $\Delta$  reading lies in a region where a small error can displace the point to a trajectory belonging to a substantially different  $n_f$ . Estimates of the sensitivity to errors have been made by Rhiger and Kvaas.<sup>12</sup> They showed that for an 80Å thick native oxide film on  $\text{Hg}_{0.7}\text{Cd}_{0.3}\text{Te}$ , an increase of  $\psi$  by 0.2° will cause  $n_f$  to drop by about 0.10. When the native oxide is only 30Å thick, then the same increase of  $\psi$  will cause  $n_f$  to drop by about 0.30. Also for both thicknesses, an increase of  $\Delta$  by 1.0° will cause  $d$  to drop by about 3.5Å.

Errors in the single-wavelength ellipsometric measurements of  $\text{SiO}_2$  films on Si substrates have been analyzed by several authors.<sup>3,5,42-44</sup> When  $d < 200$ Å, uncertainties can be a severe problem because of the extreme sensitivity of  $n_f$  to  $\psi$ . This is a consequence of

the small extinction coefficient of Si. This effect is much less pronounced on HgCdTe because of its relatively high extinction coefficient, which contrasts strongly with that of the nonabsorbing films.

### Absorbing Films

It is sometimes necessary to analyze an absorbing film on a known substrate, but when  $k_f \neq 0$ , it is not possible to determine the three parameters  $n_f$ ,  $k_f$ , and  $d$  from a single  $\psi$ - $\Delta$  reading. In special cases, one of the three may be known so that the other two may be determined directly. However, in general, when using single wavelength ellipsometry, a typical approach is to consider several readings on a set of systematically varied samples. This can be done graphically, comparing the readings with a theoretical  $\psi$ - $\Delta$  trajectory. Such data can also be analyzed numerically with the more advanced software.<sup>38</sup>

We present an example of the graphical method relevant to HgCdTe.<sup>45</sup> A layer of polycrystalline CdTe was grown by MOCVD on a sapphire substrate at 300°C. The thickness was uniform over most of the area but tapered at the edges due the shadowing effect of a mechanical mask that was present during growth. The CdTe was characterized by ellipsometric profiling across the tapered region with no etching involved. Ex situ readings were taken at 127  $\mu$ m intervals along a line extending from the outer region of zero thickness to the central region of uniform thickness. The data are displayed in Fig. 5, along with the theoretical plot based upon values from Table I for CdTe of varying thicknesses on sapphire. We first discuss the theoretical plot, along which the thickness is indicated at 500Å intervals. Because  $k_f \neq 0$ , the trajectory does not return to the starting point, in contrast with the trajectories of Fig. 4. (It is unimportant that  $k_s = 0$  for the sapphire substrate.) A form of periodicity is evident, however, for the three cycles shown.

Eventually, the trajectory spirals to the point representing infinitely thick CdTe at  $\psi = 4.1^\circ$ ,  $\Delta = 140.0^\circ$ . There is excellent agreement between experiment and theory. Thus, the optical parameters of the MOCVD CdTe must be very close to those of bulk CdTe, suggesting that the MOCVD material has close to the proper stoichiometry. The cluster of points around  $\psi = 4.5^\circ$  and  $\Delta = 280^\circ$  represent the uniform region of the film. By matching to the theoretical trajectory, the thickness of the film except at the edges is 1260Å. In summary, we have obtained evidence that the optical parameters of the MOCVD CdTe match those of ideal material, indicating good stoichiometry, and we have measured the thickness of the film along a lateral profile.

Single wavelength ellipsometry has been applied to absorbing films on Si substrates. Layers of Si that have been rendered amorphous by ion implantation have been analyzed<sup>46-49</sup> for thickness and recrystallization on annealing. Polycrystalline silicon films have also been analyzed graphically in comparison to theoretical trajectories.<sup>50</sup>

## QUALITATIVE INTERPRETATIONS OF ELLIPSOMETRIC DATA

### Acceptance Window For Process Monitoring

Because of its high sensitivity to very thin films and rapid, nondestructive nature, ellipsometry is well suited to monitoring the condition of surfaces at many stages of semiconductor processing. Surface cleanliness is most often emphasized, but other parameters such as film thickness or surface  $\chi$  value may also be monitored. After a process has been developed, the desired  $\psi$ - $\Delta$  reading at each stage is known and the measured reading can be compared. For simplicity, one can set an acceptance window in the  $\psi$ - $\Delta$  plane so that a reading lying outside would indicate a wafer that must be set aside or reworked. The basis for this approach is described below.

Figure 6 shows theoretical trajectories for very thin nonabsorbing films on a substrate of  $\text{Hg}_{0.7}\text{Cd}_{0.3}\text{Te}$  for several refractive index values of  $n_f$ . Notice that  $\Delta$  drops with increasing film thickness for every reasonable index. Native oxides that typically occur on the surface have  $2.0 \leq n_f \leq 2.5$ , while surface organic residues are roughly estimated to have the same index as polyethylene,<sup>51</sup> which is 1.48. Hence  $\Delta$  is a convenient measure of surface cleanliness. Although the clean-surface value of  $\Delta$  does vary moderately

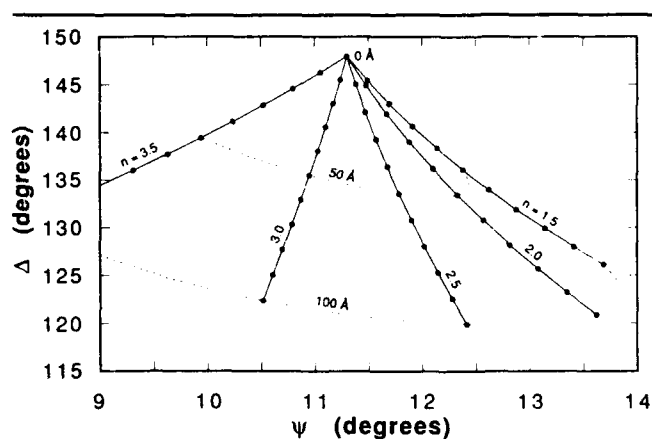


Fig. 6. Calculated  $\psi$ - $\Delta$  relation for thin nonabsorbing films on  $\text{Hg}_{0.7}\text{Cd}_{0.3}\text{Te}$  at 6328Å wavelength and  $70^\circ$  angle of incidence. On each trajectory, the dots lie at 10Å intervals.

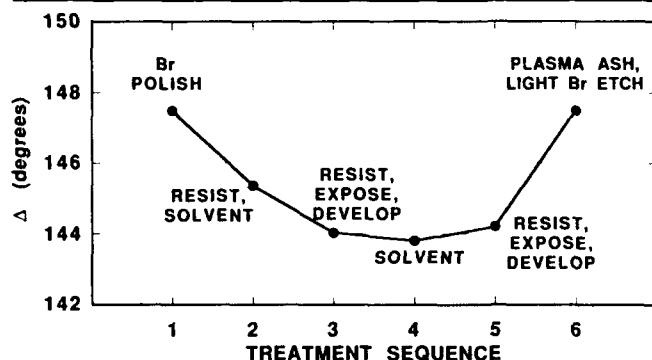


Fig. 7. Variation of  $\Delta$  on a wafer of  $\text{Hg}_{0.7}\text{Cd}_{0.3}\text{Te}$  with a sequence of simulated process steps.

with  $x$ , as shown in Fig. 3, the approximate shapes and sizes of the trajectories in Fig. 6 are almost independent of  $x$ . Consequently, a rule of thumb is that 3.5Å of surface film are present for every degree of drop in  $\Delta$  below the point of zero thickness.

An example<sup>12</sup> of the monitoring of a sample through a sequence of simulated process steps is illustrated in Fig. 7. A sample of  $\text{Hg}_{0.7}\text{Cd}_{0.3}\text{Te}$  was first cleaned by chemomechanically polishing in Br/dimethylformamide solution leaving a clean surface with  $\Delta$  near 148°. A layer of photoresist was then applied and removed with solvent. Further combinations of photoresist and developer or solvents were applied, with the final step being a plasma ash in oxygen followed by a dilute spray etch in Br/ethylene glycol. We observe that photoresist leaves a residue on the surface that is not removed by solvents or developer, bringing  $\Delta$  down near 144° or 145°. Auger electron

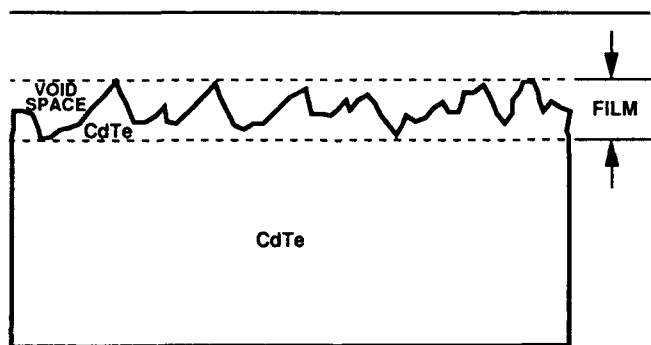


Fig. 8. Schematic of a rough surface. The rough region can be treated as a film having its own optical parameters, determined by averaging the parameters of the solid material with the parameters of the void spaces according to the effective medium approximation. The solid in this illustration is CdTe.

spectroscopy on other samples at this stage has shown carbon to be the majority surface element. The plasma ashing process removes the carbon as well as growing a native oxide of about 20Å (not shown), while the subsequent light Br etch removes the oxide and restores the clean condition. Other samples showed that without the plasma ash, the light Br etch actually causes  $\Delta$  to fall about 10° farther. At each process step, when a clean surface is expected, care must be taken to check that  $\psi$  remains near the value appropriate for the known HgCdTe composition. In summary, one could set an acceptance window such as  $147^\circ < \Delta < 149^\circ$  and  $11.1^\circ < \psi < 11.5^\circ$ .

An example of this approach to verify surface cleanliness of HgCdTe prior to deposition of  $\text{SiO}_2$  passivation was reported by Wilson et al.<sup>52</sup> A similar approach has been applied by Twu<sup>53</sup> for surface cleaning for GaAs, GaP, and related ternary compounds. In the fabrication of photovoltaic HgCdTe arrays, Poksheva et al.<sup>54</sup> have demonstrated a clear correlation between the  $\psi$ - $\Delta$  reading after the pre-passivation etch and the subsequent zero bias resistance  $R_0$  of the devices.

### Effective Medium Approximation and Microroughness

It is necessary to consider films consisting of mixtures of materials. One example would be a partially oxidized tellurium layer containing both Te and  $\text{TeO}_2$ . Another important case is microroughness, as illustrated in Fig. 8 for a CdTe surface. The rough region can be treated as a film consisting of a mixture of two materials, the CdTe and the void spaces. We define microroughness as roughness on a scale that is small compared to the wavelength of the probing light. Ellipsometry is not very sensitive to roughness on a

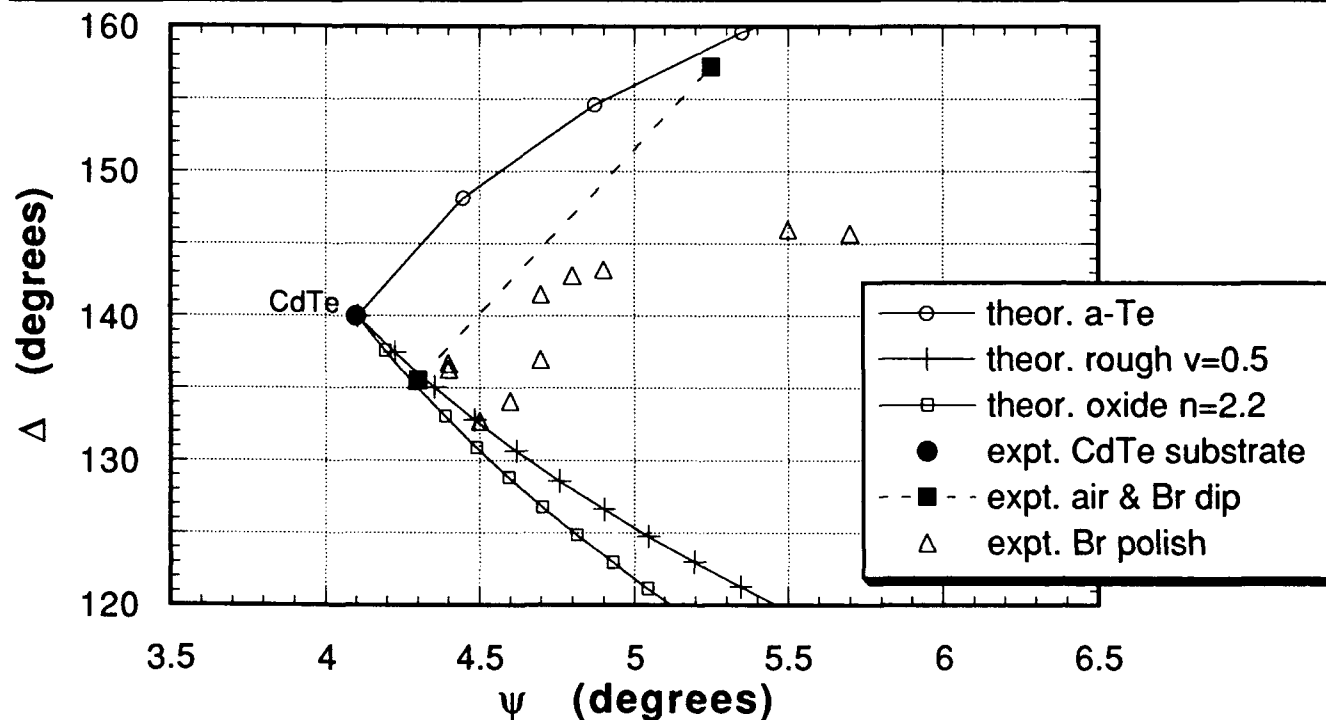


Fig. 9. Theoretical and experimental ellipsometry readings for very thin films on CdTe. Points on the theoretical curves are at 5Å intervals.

coarse scale, because light that is scattered out of the beam is undetected, but microroughness affects the polarization rather than scattering the beam.

The approach is to estimate an average dielectric function for the mixture so that it can be treated as a uniform medium. The best approximation is the Bruggeman effective medium approximation,<sup>7,55</sup> which can be applied in general to any number of constituent materials. When only two materials are present, it can be written as<sup>12</sup>

$$\epsilon_m = p\epsilon_j + q\epsilon_k + \sqrt{(p\epsilon_j + q\epsilon_k)^2 + \frac{1}{2}\epsilon_j\epsilon_k} \quad (14)$$

where  $\epsilon_m$  is the complex dielectric function of the effective medium,  $\epsilon_j$  and  $\epsilon_k$  are the complex dielectric functions of the constituent materials, and

$$p = \frac{2-u}{4(1+u)} \quad (15)$$

$$q = \frac{2u-1}{4(1+u)}$$

The ratio of volume fractions is

$$u = \frac{v_k}{v_j} = \frac{v_k}{1-v_k} \quad (16)$$

where  $v_j$  and  $v_k$  are the volume fractions of materials  $j$  and  $k$ , respectively. By definition  $v_j + v_k = 1$ . Equation 14 is easily shown to be symmetric in  $\epsilon_j$  and  $\epsilon_k$ . The complex refractive index of the effective medium is obtained from  $\epsilon_m$  with the help of Eq. 8. The usual assumption of uniform film composition from top to bottom does not hold strictly for microroughness, because, as seen in Fig. 8, the mountain-like shapes provide more solid material at the lower part of the film and more void spaces at the top of the film. Thus, the treatment of roughness as a single film is only an approximation, and any  $\psi$ - $\Delta$  plot derived on the basis of such a model can be interpreted semi-quantitatively at best. The effective medium approximation applied to microroughness has been used by Rhiger and Kvaas<sup>12</sup> for CdTe and HgCdTe, and by Strong and Smith<sup>56</sup> for ZnS films on HgCdTe and Si.

### Very Thin Films Interpreted Graphically

Figure 9 shows theoretical and experimental ellipsometric readings for CdTe with a variety of surface films. The point at  $\psi = 4.1^\circ$ ,  $\Delta = 140.0^\circ$  for the smooth bare substrate is indicated. To discuss the theoretical curves, we first observe the trajectory for amorphous Te, which rises strongly, reaching  $\Delta = 160^\circ$  for only 15Å. This contrasts with the trajectory for the oxide ( $n_f = 2.2$ ), which is very similar to some of the nonabsorbing films in Fig. 6.

The trajectory for microroughness, assuming a void fraction of 0.5, turns out to be very close to that of the oxide. For other values of the void fraction,<sup>12</sup> the trajectories lie very close to that for 0.5 when  $\Delta > 120^\circ$ , adding further to the difficulty in deriving any quan-

titative measure of microroughness for such small thicknesses ( $< 50\text{\AA}$ ).

In addition, it is unfortunate that the trajectories for oxides and microroughness are not better separated. A likely consequence is that sometimes a wafer of CdTe or HgCdTe may be thought from ellipsometry to have an oxide film when in fact it may have microroughness with negligible oxide. This question can be resolved by rinsing the sample in very dilute

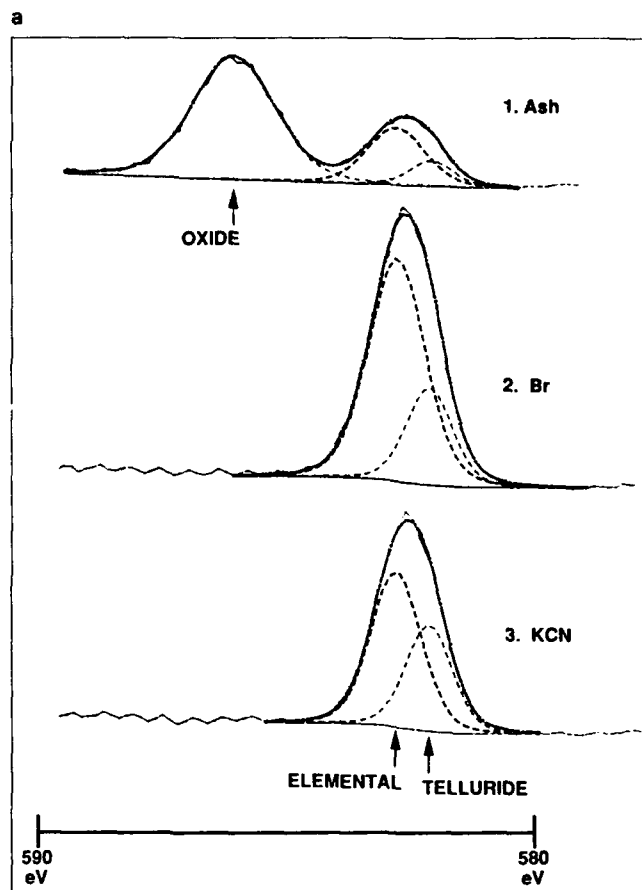
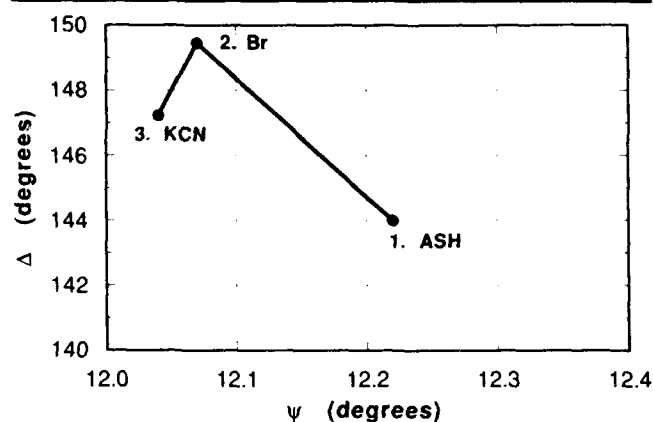


Fig. 10. Qualitative agreement between ellipsometry and XPS in monitoring the surface of  $\text{Hg}_{1-x}\text{Cd}_x\text{Te}$  ( $x = 0.236$ ) through a sequence of treatments: (a) Ellipsometry readings and (b) XPS spectra of the Te 3d3/2 line. Three different chemical shifts of Te are seen, corresponding to oxide (+4 oxidation state), elemental (0), and telluride (-2).

HCl, which readily dissolves native oxides, and taking another reading.

The experimental data in Fig. 9 can be interpreted in terms of the theoretical curves. A cleaved sample of CdTe was first measured in dry N<sub>2</sub> giving a reading at the substrate point in this figure. It was then exposed to room air for five minutes, giving the reading indicated by the solid square near 136°. Finally, it was dipped briefly in a Br etchant, rinsed, and dried, to give the other square point at about 157°. The air exposure produced an oxide of about 10Å, and the Br etch left a Te film almost 15Å thick. The latter is a familiar result.

Several authors have shown that Te films occur on CdTe and HgCdTe surfaces after etching.<sup>12,32,57-62</sup> The triangles in Fig. 9 represent several CdTe samples that were chemomechanically polished with Br/dimethylformamide. Those with  $140^\circ < \Delta < 150^\circ$  correspond to a film of rough amorphous Te (trajectory not shown) having a void fraction approximately between 0.2 and 0.4 and a thickness of 10 to 40Å. Finally, other CdTe samples<sup>12</sup> (not shown) that were polished with a 500Å grit gave readings near  $\psi = 6^\circ$ ,  $\Delta = 110^\circ$  that are consistent with microroughness.

For other HgCdTe compositions the trajectories for a-Te, microroughness, and native oxides have approximately the same shape and scale as those in Fig. 9, but they are translated in the  $\psi$ - $\Delta$  plane to start at a different bare substrate point. Whenever a semi-quantitative graphical method is applied to very thin films, a reliable interpretation requires an understanding of HgCdTe surface chemistry and a knowledge of the sample history.

### Comparison of XPS and Ellipsometry on HgCdTe

A set of HgCdTe samples from a wafer with  $x = 0.236$  was given a sequence of surface treatments and characterized by both ellipsometry and x-ray photoelectron spectroscopy (XPS).<sup>63</sup> Results are shown in Fig. 10. A ultraviolet (UV)-ozone ashing process was applied to an already clean surface, leaving  $\Delta = 144^\circ$ . The XPS spectrum at this stage shows that a majority of the surface Te is in the +4 oxidation state, corresponding to TeO<sub>2</sub> or CdTeO<sub>3</sub>. On a sample that received the UV-ozone ash plus a dilute Br/ethylene glycol spray etch, the  $\Delta$  is about 149.5°, indicating about 5Å of amorphous Te. The XPS at this stage shows the removal of all oxidized Te and the presence of a very strong elemental Te peak.

The third sample received both of the previous treatments plus a soak in KCN solution, which has been demonstrated<sup>64</sup> to remove Te layers from HgCdTe. In this case, the XPS shows a removal of much of the elemental Te, as expected. The change of the ellipsometric reading at this step is consistent with moving down the a-Te trajectory (which for  $x = 0.236$  resembles that of  $x = 1.0$  in Fig. 9). Thus, there is a very good qualitative agreement between the two highly surface-sensitive techniques, ellipsometry and XPS.

### SPECTROSCOPIC AND IN SITU APPLICATIONS

When the wavelength is allowed to vary, there is a great increase in the amount of information acquired in the ellipsometric characterization of a sample.<sup>6</sup> Despite the added cost of instrumentation and the complexity of the data reduction compared to single wavelength ellipsometry, the spectroscopic approach has proven to be extremely useful in the advancing understanding of the physics and chemistry of surfaces. It has also been applied to the characterization of multilayer and graded-layer samples that are otherwise not decipherable. In the spectroscopic technique, the complex dielectric function of a bare substrate, or the pseudodielectric function of a layered sample, is acquired, over a typical photon energy range of 1.5 to 6 eV.

For HgCdTe, Aspnes et al.<sup>32,33,57,65</sup> have investigated surface cleaning, Te film formation, the characteristics of oxide films, and other issues of surface chemistry. They also found no evidence of damage to the semiconductor attributable to the surface chemical treatments. Viña et al.<sup>66</sup> used spectroscopic ellipsometry to study the composition dependence of the electronic interband transitions in HgCdTe, and Raccach et al.<sup>67</sup> carried out a study showing that spectroscopic ellipsometry is less sensitive to defects in HgCdTe than the technique of electrolyte electroreflectance. For materials other than HgCdTe, spectroscopic ellipsometry has been employed to optimize surface cleaning processes<sup>68</sup> and to perform multiparameter analyses of multilayer and graded-layer samples.<sup>55,69-71</sup>

For monitoring growth processes, ellipsometry offers great sensitivity with real-time presentation of the data. The MBE growth of HgCdTe layers was monitored spectroscopically by Demay et al.<sup>72,73</sup> with a system that made use of a mirror inside of the growth chamber, forming a window-sample-mirror-sample-window optical path within the chamber so that only a single window of the chamber was needed. Modeling of the ellipsometric reading at  $\lambda = 6328\text{Å}$  vs thickness was performed by Rzhanozov et al.<sup>74</sup> for a HgTe/CdTe superlattice. A  $\psi$ - $\Delta$  trajectory was generated that changes direction as each layer begins. This was compared with the spiral that represents growth of an alloy having the same average composition. Recent work by Hartley et al.<sup>75-77</sup> has demonstrated the versatility and sensitivity of single wavelength ellipsometry at 6328Å as an in situ technique for monitoring the MBE growth of HgTe/CdTe superlattices and HgCdTe alloys. By ellipsometry, the authors were able to estimate the amount of Hg incorporated in the CdTe layers and its temperature dependence, and to detect growth-front roughening of the CdTe layers. Interdiffusion of the layers during post-growth annealing was monitored. Observed growth rates were in agreement with measurements by other techniques. Roughening of the surface during alloy growth was also detected. Finally, single wavelength ellip-



sometry has been used for in situ monitoring of the deposition of  $\text{SiO}_2$  films on HgCdTe by a photochemical process.<sup>7a</sup>

## CONCLUSIONS

Ellipsometry has proven to be very useful for the characterization of surfaces and films on HgCdTe and related materials. Existing instruments allow measurements to be performed routinely. Available choices of the technique include single wavelength vs spectroscopic, and ex situ vs in situ. We have emphasized the single wavelength, ex situ approach, which is the simplest and most common. We have discussed a variety of methods of interpreting the data, while giving examples and describing limitations.

With a small computer connected to the ellipsometer, it is easy to determine the refractive index  $n_f$  and thickness  $d$  of a nonabsorbing ( $k_f = 0$ ) film on the surface of a known substrate. For an absorbing film, the single wavelength method requires data from a systematic set of samples. The optical parameters of a material can be measured directly by ellipsometry if the sample surface is free of films and roughness. To monitor HgCdTe device fabrication processes, one can take an ellipsometry reading on the wafer at various times, and compare with a preset window in the  $\psi$ - $\Delta$  plane for acceptance or rejection.

Qualitative evaluations, made by graphically comparing the data with a set of theoretical curves for known film materials, provide an insightful method of characterizing very thin films. Often the user can obtain quick answers as to the condition of a surface. To interpret the data correctly requires some understanding of HgCdTe surface chemistry and a knowledge of the sample history. In general, ellipsometry can be a powerful complement to other surface analytical techniques. Agreement has been demonstrated between ellipsometry and XPS for qualitatively characterizing HgCdTe surfaces after various chemical treatments.

Some specific conclusions for HgCdTe, based upon measurements at the standard wavelength of 6328Å, are:

- The highest  $\Delta$  usually represents the cleanest surface.
- An exception is a layer of amorphous Te, which causes  $\Delta$  to rise above its bare substrate value.
- For very thin oxides and contaminants, a drop of  $\Delta$  by one degree represents about 3.5Å of film thickness.
- Microroughness can cause  $\Delta$  to drop even if the surface is chemically clean.
- There is an unfortunate near-coincidence between the trajectories for a typical native oxide and a thin layer of microroughness, but the two can be distinguished by the solubility of native oxides in very dilute HCl.
- When the surface is clean, the value of  $\psi$  is a reasonable estimator of the composition.
- In situ measurements have proven to be very revealing of the real-time process behavior in

the MBE growth of HgCdTe alloys and HgTe/CdTe superlattices.

The science and technology of HgCdTe will certainly benefit from the increased application of ellipsometry. The routine use of ellipsometry as a tool in the development of device fabrication processes has been helped by improvements in the methods of interpreting the data.

## ACKNOWLEDGMENTS

The author acknowledges helpful discussions with, or laboratory assistance from, B.A. Baumgratz, H.P. Bevens, F.I. Gesswein, S.M. Johnson, R.E. Kvaas, M.S. Langell, T.M. Lawton, J.D. Parsons, J.M. Peterson, J.A. Peyton, H.N. Rogers, and J.A. Vigil.

## REFERENCES

1. R.M.A. Azzam and N.M. Bashara, *Ellipsometry and Polarized Light*, North-Holland, Amsterdam (1977).
2. R.F. Spanier, *Industrial Research* 17, (9) 73 (1975).
3. R.J. Kutko, *Solid State Technol.* 21, (2) 43 (1978).
4. E.D. Palik, ed., *Handbook of Optical Constants of Solids*, Academic Press, Orlando (1985).
5. E.D. Palik, ed., *Handbook of Optical Constants of Solids II*, Academic Press, Orlando (1991).
6. D.E. Aspnes, *Optical Properties: New Developments*, ed. B.O. Seraphin, North-Holland, Amsterdam (1976).
7. D.E. Aspnes, in Ref. 4.
8. D.E. Aspnes, *Surf. Sci.* 101, 84 (1980).
9. R.W. Collins, *Rev. Sci. Instr.* 61, 2029 (1990).
10. P.S. Hauge, R.H. Muller and C.G. Smith, *Surf. Sci.* 96, 81 (1980).
11. R.T. Holm, in Ref. 5.
12. D.R. Rhiger and R.E. Kvaas, Final Report AFWAL-TR-86-4009, Contract F33615-80-C-5084 (1986).
13. P.M. Amirtharaj, in Ref. 5. Numerical table obtained from H. Arwin and D.E. Aspnes, *J. Vac. Sci. Technol.* A2, 1316 (1984).
14. P.M. Amirtharaj, in Ref. 5. Numerical table obtained from L. Viña, C. Umbach, M. Cardona and L. Vodopyanov, *Phys. Rev. B* 29, 6752 (1984).
15. T.E. Korsak, N.P. Syosoeva, B.M. Ayupov, V.V. Antonov, A.V. Voltsekhovskii and E.F. Tivota, *Sov. Phys. Semicond.* 19, 222 (1985).
16. H.H. Li, *J. Phys. Chem. Ref. Data* 13, 103 (1984).
17. J. Bajaj, S.J.C. Irvine, H.O. Sankur and S.A. Svoronos, these proceedings.
18. D.E. Aspnes, S.M. Kelso, R.A. Logan and R. Bhat, *J. Appl. Phys.* 60, 754 (1986).
19. B.A. Baumgratz, M.S. Thesis, University of California at Santa Barbara (1988).
20. D.F. Edwards, in Ref. 4.
21. H. Keller and J. Stuke, *Phys. Status Solidi* 8, 831 (1965).
22. J. Stuke, *J. Non-Cryst. Solids* 4, 1 (1970).
23. N. Uchida, *Phys. Rev. B* 4, 3736 (1971).
24. S. Singh, W.A. Bonner and L.G. van Uitert, *Phys. Lett.* 38A, 407 (1972).
25. D.W. Lynch and W.R. Hunter, in Ref. 4.
26. D.W. Lynch and W.R. Hunter, in Ref. 5.
27. R.Y. Koyama, N.V. Smith and W.E. Spicer, *Phys. Rev. B* 8, 2426 (1973).
28. A. Borghesi and A. Piaggi, in Ref. 5.
29. D.K. Burge and H.E. Bennett, *J. Opt. Soc. Amer.* 54, 1428 (1964).
30. W.V. McLevige, J.M. Arias, D.D. Edwall and S.L. Johnston, *J. Vac. Sci. Technol.* B 9, 2483 (1991).
31. J.M. Arias, M. Zandian, S.H. Shin, W.V. McLevige, J.G. Pasko and R.E. DeWames, *J. Vac. Sci. Technol.* B 9, 1646 (1991).
32. H. Arwin, D.E. Aspnes and D.R. Rhiger, *J. Appl. Phys.* 54, 7132 (1983).

33. H. Arwin and D.E. Aspnes, *J. Vac. Sci. Technol. A* 2, 1316 (1984).
34. C.M. Stahle, C.R. Helms, H.F. Schaake, R.L. Strong, A. Simmons, J.B. Pallix and C.H. Becker, *J. Vac. Sci. Technol. A* 7, 474 (1989). See also the erratum in *J. Vac. Sci. Technol. A* 8, 3373 (1990).
35. R.J. Archer, *J. Opt. Soc. Amer.* 52, 970 (1962).
36. N.V. Smith, Y. Komiya and R.H. Weissman, *Solid-State Electron.* 12, 765 (1969).
37. N.T. McDevitt and W.L. Baun, USAF report no. AFWAL-TR-83-4034 (NTIS:ADA131844), (1983).
38. J.F. Marchiando, *A Software Program for Aiding the Analysis of Ellipsometric Measurements, Simple Models*, National Institute of Standards and Technology, Special Publication No. 400-83 (1989).
39. F.L. McCrackin, E. Passaglia, R.R. Stromberg and H.L. Steinberg, *J. Res. Nat. Bur. Standards* 67A, 363 (1963).
40. Rudolph Research, P.O. Box 1000, Flanders, NJ 07836.
41. Gaertner Scientific Corp., 1201 Wrightwood Ave., Chicago, IL 60614.
42. D. Chandler-Horowitz and G.A. Candela, *J. Physique* 44 (Colloque C10), Page C10-23 (1983).
43. J.H. Ho, C.L. Lee, C.W. Jen and T.F. Lei, *Solid-State Electron.* 30, 973 (1987).
44. J.H. Ho, C.L. Lee and T.F. Lei, *Solid-State Electron.* 31, 1321 (1988).
45. D.R. Rhiger and J.D. Parsons (unpublished).
46. M. Delfino and R.R. Razouk, *J. Electrochem. Soc.* 129, 606 (1982).
47. K. Watanabe, T. Motooka, N. Hashimoto and T. Tokuyama, *Appl. Phys. Lett.* 36, 451 (1980).
48. T. Motooka and K. Watanabe, *J. Appl. Phys.* 51, 4125 (1980).
49. T. Lohner, G. Mezey, E. Kotai, F. Paszti, A. Manuaba and J. Gyulai, *Nucl. Instr. Meth. Phys. Res.* 209-210, 615 (1983).
50. E.A. Irene and D.W. Dong, *J. Electrochem. Soc.* 129, 1347 (1982).
51. J. Ashok, P.L.H. Varaprasad and J.R. Birch, in Ref. 5.
52. J.A. Wilson, V.A. Cotton, J. Silberman, D. Laser, W.E. Spicer and P. Morgen, *J. Vac. Sci. Technol. A* 1, 1719 (1983).
53. B. Twu, *J. Electrochem. Soc.* 126, 1589 (1979).
54. J. Poksheva, Y. Juravel, A. Wong, A. Childs, S. West and T. Heim, Final Report WL-TR-91-8054, Contract F33615-87-C-5218.
55. D.E. Aspnes, J.B. Theeten and F. Hottier, *Phys. Rev. B* 8, 3292 (1979).
56. R.L. Strong and P.B. Smith, *J. Vac. Sci. Technol. A* 8, 1544 (1990).
57. D.E. Aspnes and H. Arwin, *J. Vac. Sci. Technol. A* 2, 1309 (1984).
58. R. N. Zitter, *Surf. Sci.* 28, 335 (1971).
59. J.-P. Haring, J.G. Werthen, R.H. Bube, L. Gulbrandsen, W. Jansen and P. Luscher, *J. Vac. Sci. Technol. A* 1, 1469 (1983).
60. J.P. Ponpon, *Solid-State Electron.* 28, 689 (1985).
61. U. Solzbach and H.J. Richter, *Surf. Sci.* 97, 191 (1980).
62. D.R. Rhiger and R.E. Kvaas, *J. Vac. Sci. Technol.* 21, 168 (1982).
63. J.M. Peterson and D.R. Rhiger (unpublished).
64. R. Tenne, R. Brener and R. Triboulet, *J. Vac. Sci. Technol. A* 7, 2570 (1989).
65. D.E. Aspnes and H. Arwin, *J. Vac. Sci. Technol. A* 2, 600 (1984).
66. L. Viña, C. Umbach, M. Cardona and L. Vodopyanov, *Phys. Rev. B* 29, 6752 (1984).
67. P.M. Raccach, J.W. Garland, Z. Zhang, U. Lee, D.Z. Xue, L.L. Abels, S. Ugur and W. Wilinsky, *Phys. Rev. Lett.* 53, 1958 (1984).
68. D.E. Aspnes and A.A. Studna, *SPIE Proc.* 276, 227 (1981).
69. K. Vedam, S.Y. Kim, L. D'Aries and A.H. Guenther, *Optics Lett.* 12, 456 (1987).
70. J.L. Freeouf, *Appl. Phys. Lett.* 53, 2426 (1988).
71. S. Logothetidis, *J. Appl. Phys.* 65, 2416 (1989).
72. Y. Demay, J.P. Gailliard and P. Medina, *J. Cryst. Growth* 81, 97 (1987).
73. Y. Demay, D. Arnoult, J.P. Gailliard and P. Medina, *J. Vac. Sci. Technol. A* 5, 3139 (1987).
74. A.V. Rzhaznov, K.K. Svtashev, A.S. Mardezhov and V.A. Shvets, *Sov. Phys. Dokl.* 32, 930 (1987).
75. R.H. Hartley, M.A. Folkard, D. Carr, P.J. Orders, D. Rees, I.K. Varga, V. Kumar, G. Shen, T.A. Steele, H. Buskes and J.B. Lee, *J. Cryst. Growth* 117 166 (1992).
76. R.H. Hartley, M.A. Folkard, D. Carr, P.J. Orders, D. Rees, I.K. Varga, V. Kumar, G. Shen, T.A. Steele, H. Buskes and J.B. Lee, *J. Vac. Sci. Technol. B* 10, 1410 (1992).
77. M.A. Folkard, G. Shen, V. Kumar, T.A. Steele, D. Rees, I.K. Varga, D. Carr, K. Fueleop, B.A. Johnson, P.J. Orders, R.H. Hartley, H. Buskes and M. Gal, these proceedings.
78. B.W. Abshire, A.R. Davis, K.A. Kormos, R.E. Kvaas, D.R. Rhiger, R.P. Ruth, K.D. Treese and R.E. Welt, Final Report AFWAL-TR-85-4147, Contract F33615-84-C-5083.

# Modeling of In Situ Monitored Laser Reflectance During MOCVD Growth of HgCdTe

J. BAJAJ, S.J.C. IRVINE, and H. O. SANKUR

Rockwell International Science Center, Thousand Oaks, CA 91360

SPYROS A. SVORONOS

University of Florida, Department of Chemical Engineering, Gainesville, FL 32611

An effective way to in situ monitor the metalorganic chemical vapor deposition (MOCVD) of HgCdTe/CdTe/ZnTe on GaAs or GaAs/Si substrates is presented. Specular He-Ne laser reflectance was used to in situ monitor the growth rates, layer thickness, and morphology for each layer in the grown multilayer structure. In situ monitoring has enabled precise measurements of ZnTe nucleation and CdTe buffer layer thicknesses. Monitoring the constancy of reflectance during the thicker CdTe buffer growth where absorption in the CdTe reduces reflectance to just the surface component has led to optimum buffer growth ensuring good quality of subsequently grown HgCdTe. During the interdiffused multilayer process (IMP) HgCdTe growth, because multiple interfaces are present within the absorption length, a periodic reflectance signal is maintained throughout this growth cycle. A theoretical model was developed to extract IMP layer thicknesses from in situ recorded experimental data. For structures that required the growth of a larger band gap HgCdTe cap layer on top of a smaller band gap active layer, in situ monitored reflectance data allowed determination of alloy composition in the cap layer as well. Continuous monitoring of IMP parameters established the stability of growth conditions, translating into depth uniformity of the grown material, and allowed diagnosis of growth rate instabilities in terms of changes in the HgTe and CdTe parts of the IMP cycle. A unique advantage of in situ laser monitoring is the opportunity to perform "interactive" crystal growth, a development that is a key to real time MOCVD HgCdTe feedback growth control.

**Key words:** HgCdTe, in situ monitoring of growth, laser reflectance, MOCVD

## INTRODUCTION

Crystal growth by metalorganic chemical vapor deposition (MOCVD) has traditionally lacked in situ growth monitoring. This put MOCVD at a disadvantage compared to growth by molecular beam epitaxy (MBE)<sup>1</sup> which has enjoyed the strength of being able to incorporate in situ diagnostic tools. The MBE tools typically utilize electron and ion beams. The near atmospheric pressure in an MOCVD reactor does not allow use of these probes, leaving optical techniques as most suitable for monitoring MOCVD growth, although x-ray diffraction has been explored as a potential diagnostic tool.<sup>2</sup> Ellipsometric techniques

have been reported in literature for metalorganic chemical vapor deposition growth monitoring.<sup>3,4</sup> More recently, laser reflectance was demonstrated as a powerful way to monitor MOCVD growth of II-VI<sup>5,6</sup> and III-V<sup>7</sup> compound semiconductors.

The focus of this report is detailed theoretical modeling of in situ measured laser reflectance during each phase of a MOCVD grown multilayer structure consisting of CdTe (passivation layer)/IMP-Hg<sub>1-x</sub>Cd<sub>x</sub>Te (x ~ 0.3) cap layer/IMP-Hg<sub>1-x</sub>Cd<sub>x</sub>Te (x ~ 0.23) active layer/CdTe buffer-layer/ZnTe nucleation layer/GaAs or GaAs-on-Si substrate. Theoretical modeling and analysis of in situ monitored reflectance data has provided, in real time, information related to growth rate, thickness, and morphology of each component of the grown structure. In situ monitoring has enabled pre-

(Received October 12, 1992; revised January 15, 1993)

cise measurements of ZnTe nucleation and CdTe buffer layer thicknesses. The thickness of ZnTe nucleation layer has<sup>5</sup> been shown to impact the structural quality of the grown structure. Following the approach discussed previously,<sup>6</sup> monitoring constancy of the reflectance during the CdTe buffer layer growth where absorption in the thicker (>1 mm) CdTe reduces reflectance to just the surface component, has led to optimum buffer growth on GaAs/Si substrates ensuring good quality of subsequently grown HgCdTe.

The HgCdTe layers were grown by an interdiffused multilayer process (IMP)<sup>9,10</sup> which involves growing alternating films of HgTe and CdTe that interdiffuse during the growth period and a subsequent annealing phase resulting in a uniform  $\text{Hg}_{1-x}\text{Cd}_x\text{Te}$  alloy. The thicknesses of CdTe and HgTe determine the total thickness and composition of both the active HgCdTe layer and the cap layer. The reflectance profile for each interdiffused multilayer process period contains information on the thicknesses and growth rates for both HgTe and CdTe. Theoretical modeling of this profile is not straightforward because the IMP layers are interdiffusing at the growth temperature. This interdiffusion, as well as growth during the pause (flush) phases between the alternating layers of HgTe and CdTe, must be incorporated in the modeling to accurately explain the in situ monitored reflectance data. A dynamic model has been developed which predicts the time evolution of reflectance during IMP growth of HgCdTe. This model predicts the reflectance as a function of time for given parameters such as the duration of the CdTe and HgTe growth phases, duration of flush phases and growth temperature.

### EXPERIMENTAL DETAILS

A horizontal rectangular duct silica reactor was modified with a 2 cm diam optical window, mounted in a turret approximately 3 cm above the reactor top wall to allow optical access to the sample. The optical

window was flushed with helium gas and no deposit on the window was observed during growth. As has been reported earlier,<sup>5</sup> these reactor modifications did not affect the temperature and the gas flow conditions over the substrate, thereby maintaining the growth rate and lateral uniformity. The wafer holder, connected to the reactor end flange and extending to the middle of the reactor was made of graphite. This sample holder could hold a 3 in diam substrate and had rotational capability.

Dimethyl zinc (DMZn) plus dimethyl tellurium (DMTe) were used for the ZnTe nucleation layer which was typically 1000Å thick. Dimethyl cadmium (DMCd) plus DMTe or di-isopropyl tellurium (DIPTe) were used for the CdTe buffer which was typically 6 µm thick. HgCdTe layers were grown using the interdiffused multilayer process, where DMCd plus DIPTe and DIPTe plus mercury vapor were used for CdTe and HgTe parts of the IMP cycles, respectively. Liquid mercury was placed in a boat at the entrance zone of the reactor and heated to 210°C. The substrate temperature was typically 380°C obtained by heating with a pyrolytic boron nitride (PBN) resistance heater placed directly below the substrate.

A schematic of the experimental arrangement is shown in Fig. 1. The reflected light from a chopped He-Ne laser (2 mW at 0.6328 µm), incident at near normal incidence angle, was measured as a function of time, using a silicon detector (#1) and standard phase sensitive detection techniques. The incident laser power was measured using a beam splitter and a second detector (#2).

In addition, diffused scattered light was monitored using an additional detector (not shown in the figure). All signals, typically measured every 0.5 s, were fed into an IBM personal computer installed with a menu driven software package (LabTech Notebook) for data acquisition, real-time graphic display of data, data storage/retrieval and data analysis.

The bulk 2 or 3 in diam GaAs or GaAs/Si substrates were commercially purchased, typically with a (100) 10° off toward (110) crystallographic orientation. Prior to loading in the reactor, these substrates were etched in a 5:1:1 mixture of  $\text{H}_2\text{SO}_4:\text{H}_2\text{O}:\text{H}_2\text{O}_2$ .

### THEORETICAL FRAMEWORK FOR CALCULATING REFLECTANCE FROM SINGLE AND MULTIPLE LAYERS

This section contains the theoretical expressions used to calculate reflectance from a stack of thin films with varying optical indices. The simplest case is a single layer of thickness ' $d_1$ ' and complex refractive index  $N_1$  grown on a substrate with complex refractive index  $N_s$  (the complex refractive index  $N = n - ik$ ). In this case, two interfaces result in a number of reflected beams due to successive reflections, and the total reflectance is a summation of these beams. Following the matrix formulation of Macleod,<sup>11</sup> the total reflectance (for a nonabsorbing incident medium) can be written as:

$$R = rr^*$$

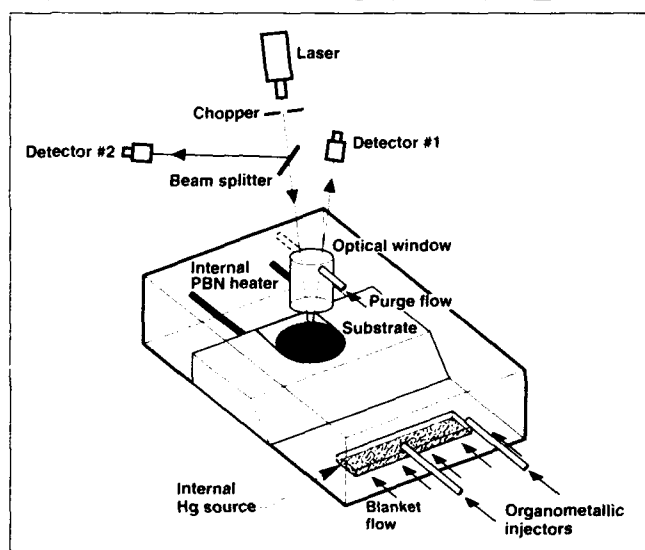


Fig. 1. A schematic of modified MOCVD reactor cell with in situ laser reflectance monitoring.

where

$$r = \frac{n_0 - Y}{n_0 + Y}$$

$n_0$  is the refractive index of the incident medium ( $= 1$  for air).  $Y = B/C$  with  $B$  and  $C$  defined by the matrix:

$$\begin{bmatrix} B \\ C \end{bmatrix} = \begin{bmatrix} \cos \delta_i & \frac{i \sin \delta_i}{N_i} \\ i N_i \sin \delta_i & \cos \delta_i \end{bmatrix} \begin{bmatrix} 1 \\ N_i \end{bmatrix}$$

The  $2 \times 2$  matrix in above expression is referred to as the characteristic matrix of the layer.  $\delta_i$  is the phase factor defined, for normal incidence, as:

$$\delta_i = \frac{2\pi N_i d_i}{\lambda}$$

This result can be extended to the general case of an assembly of  $m$  layers, with a characteristic matrix that is a product of the individual characteristic matrices taken in the correct order:

$$\begin{bmatrix} B \\ C \end{bmatrix} = \begin{bmatrix} m \\ \prod_{j=1}^m \begin{bmatrix} \cos \delta_j & \frac{i \sin \delta_j}{N_j} \\ i N_j \sin \delta_j & \cos \delta_j \end{bmatrix} \end{bmatrix} \begin{bmatrix} 1 \\ N_s \end{bmatrix}$$

This expression is the basis of all the theoretical calculations presented in this paper for a stack of layers with abrupt interfaces.

## EXPERIMENTAL DATA AND MODELING

Figure 2a shows a typical multilayer structure grown on bulk GaAs or GaAs/Si substrates. The corresponding complete in situ monitored laser reflectance (arbitrary units) profile is shown in Fig. 2b for different stages of growth. The in situ monitored laser power was constant throughout the growth run.

For convenience of discussion, the growth sequence is divided into four phases:

1. ZnTe nucleation and CdTe buffer layer growth,
2. IMP grown long wavelength infrared (LWIR) HgCdTe,
3. IMP grown mid wavelength infrared (MWIR) HgCdTe cap layer,
4. CdTe passivation layer.

A detailed description, analysis and theoretical modeling of each of these phases follows.

### ZnTe Nucleation and CdTe Buffer Layer Growth

Figure 3 shows the early stages of growth on a GaAs substrate. This stage contains a thin ZnTe nucleation layer followed by a thick CdTe buffer layer. The reflectance values on the y-axis were derived by normalizing the experimental data so that the measured reflectance of GaAs is equal to its theoretical reflectance calculated for refractive index  $n = 3.876$  and extinction coefficient  $k = 0.3$ . Using the multilayer reflectance model described above, a theoretical

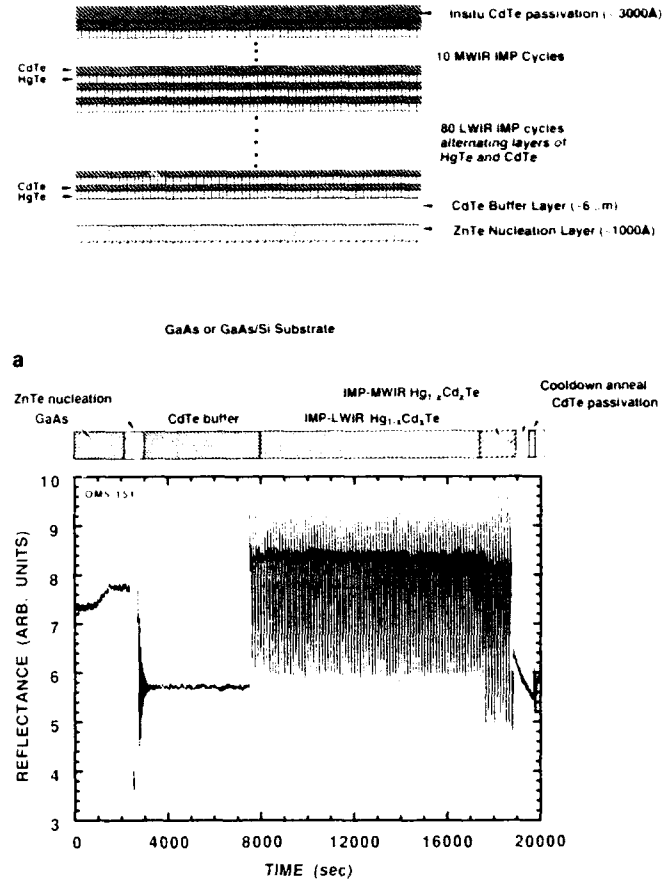


Fig. 2. (a) A typical multilayer structure grown by MOCVD on GaAs/Si substrates, and (b) complete in situ monitored laser reflectance profile corresponding to the multilayer structure in (a).

fit to the data in Fig. 3 was obtained using (3.04, 0.01) and (3.04, 0.253) as the  $(n, k)$  values for ZnTe and CdTe, respectively. The extinction coefficient of ZnTe was chosen as an arbitrary low number owing to its large band gap compared to the laser photon energy. The reflectance data from a statistically large number of growth runs consistently yielded the same values of  $n, k$  for CdTe and ZnTe. These values are close to the room temperature values of 3.018, 0.253 from ellipsometric measurements by Rhiger.<sup>12</sup>

Interference effects were utilized to determine the thicknesses of ZnTe and CdTe. For normal incidence, the thickness corresponding to each period of oscillation is given by  $0.6328/2n$ , where  $n$  is the real part of the refractive index. For both ZnTe and CdTe, therefore, each period of oscillation corresponds to 1041Å. This number divided by the time (in Fig. 3) corresponding to one oscillation yields the growth rate. For ZnTe, the time corresponding to 1/2 oscillation and for CdTe time corresponding to a few oscillations was used to calculate the growth rates. Knowing the growth rate and growth time yielded the thickness for each layer. For sample #OM5-151, these thicknesses were calculated to be 920Å and 6.9 µm for ZnTe and CdTe, respectively.

For CdTe, the oscillations are damped due to ab-

sorption; the constant reflectance for the rest of its growth duration is an indication of smooth morphology. Rough morphology due to faceting was found to reduce the magnitude of the reflectance. Figure 4 shows the reflectance profiles during ZnTe nucleation onto GaAs/Si substrate and CdTe buffer growth for three different growth conditions. Figure 4a shows the CdTe reflectance dropping off after a few cycles indicating rough morphology confirmed by the optical micrograph. The growth conditions of Fig. 4a always yielded smooth morphology on bulk GaAs substrates.

With conditions changed as shown in Fig. 4b, the reflectance of CdTe was monitored to determine the thickness at which roughening starts and to terminate buffer growth before serious surface deterioration occurred. As shown in Fig. 4b, the CdTe buffer growth was stopped very soon after the reflectance dropped and growth continued with HgCdTe, the surface of which was faceted as shown in the optical micrograph. Substituting DIPTe for DMTe and using Te rich conditions yielded smooth morphology for the CdTe buffer layer as shown in Fig. 4c. Even though the ratio of Cd to Te source partial pressures was kept the same in Fig. 4b and 4c, the speculation is that higher thermal stability of DMTe as compared to DIPTe prevented Te rich conditions at the substrate surface with DMTe being realized.

### IMP Grown LWIR HgCdTe Active Layer

The interdiffusion of HgTe/CdTe IMP layers is not instantaneous and accordingly the reflectance at any instant is representative of reflectance from a multi-layer stack consisting of HgTe and CdTe, and partially interdiffused HgCdTe. Therefore, the periodicity of the IMP results in periodicity of the in situ monitored laser reflectance. This is evident in Fig. 2 and is presented in detail later in this section. The interdiffusion needs to be incorporated in the theoretical modeling of reflectance data. Further complications arise as growth continues during the flush phases. The flush phases are introduced to allow changes in gas flow rates (HgTe and CdTe growths require different flow conditions) to stabilize prior to growth.

A dynamic model has been developed which predicts the time evolution of reflectance during IMP

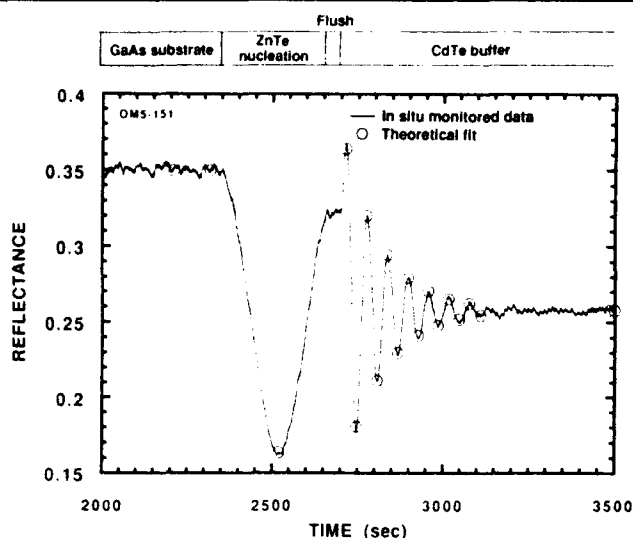


Fig. 3. In situ reflectance corresponding to the first phase of the complete growth sequence in Fig. 2, detailing ZnTe nucleation and CdTe buffer growth. Solid line is the experimental data and open circles are a theoretical fit to the data using  $n$ ,  $k$  values of 3.04, .01 and 3.04, .253 for ZnTe and CdTe, respectively.

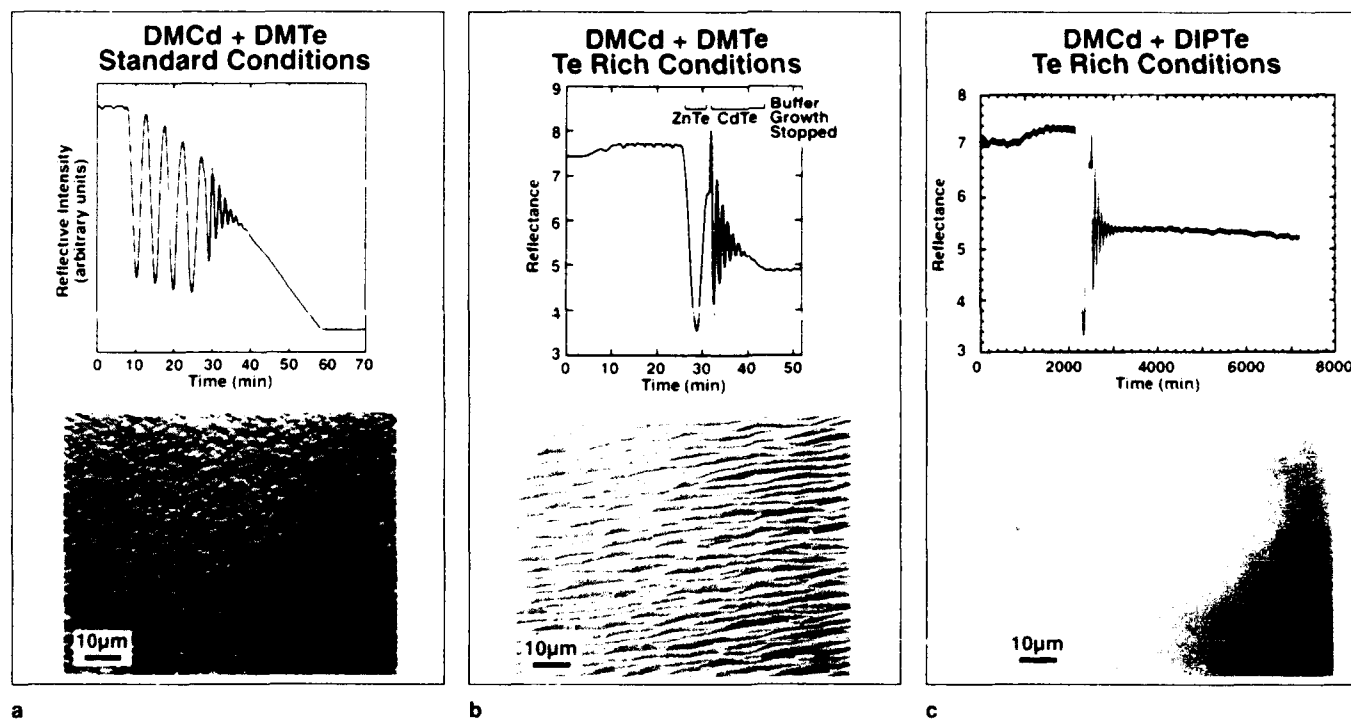


Fig. 4. In situ monitored reflectance profile detailing ZnTe nucleation and CdTe buffer growth under different conditions on GaAs/Si substrates.

growth of HgCdTe. This model relates the in situ monitored reflectance to manipulatable growth parameters. The model incorporates growth during flush phases as well as in-growth. Interdiffusion between layers. The modeling process was decomposed into two tasks. The first task was to develop a differential equation model, i.e. a mass balance derived model that gives the Cd composition  $x(z,t)$  as a function of depth 'z' at any instant 't' during IMP growth (the Cd composition will vary with depth because of interdiffusion). The interdiffusion was incorporated using the diffusivity expression from Tang and Stevenson:<sup>13,14</sup>

$$D(x,T) = 10^8 \cdot \exp(-17555 + 5918x/T)$$

where  $T$  (°K) is the growth temperature, which is 380°C for the present experiments. The growth rate during growth and flush phases was modeled as shown in Fig. 5. Two extreme conditions for modeling the precursor dilution were considered. One is a plug flow (Fig. 5a) which corresponds to zero longitudinal gas diffusivity and results in pure transportation lags. The other is a perfectly mixed tank (Fig. 5b) which corresponds to infinite gas diffusivity and results in instantaneous change according to an exponential function. The real situation was modeled as somewhere between the two extremes as shown in Fig. 5c. The time constant corresponding to the exponential part was calculated so that the total growth is identical to what it would be for the case of pure transportation lags (plug flow) shown by dashed line in Fig 5a. The fraction  $\Delta'/\Delta$  of the maximum transportation lag  $\Delta$  can be treated as a variable. The second task was to develop equations that utilize the theoretical framework discussed in the section entitled Theoretical Framework for Calculating Reflectance from Single and Multiple Layers and relate reflectance  $R(t)$  as a function of the composition profile  $x(z,t)$ . Detailed description of the two tasks will be published elsewhere.<sup>15</sup>

The application of the model to data requires accurate values of the refractive index 'n' and extinction coefficient 'k' for both HgTe and CdTe. The n,k values for CdTe were obtained from fitting the experimental data to theory as discussed in the section on Zn nucleation and CdTe buffer layer growth. A similar procedure used for HgTe is discussed next. The HgTe layer in the first IMP cycle, grown on the CdTe buffer, was used since it does not have the complications arising from the underlying multilayer structure. Figure 6 shows the HgTe part of the first IMP cycle following the buffer growth. As this layer is thin (approximately 1020Å for the present growth), only one maximum and one minimum are observed in reflectance. The result of the modeling described above yielded a good fit to data with n,k values of 4.0, 1.18. These n, k values are again close to 3.9, 1.179 values obtained by Rhiger<sup>12</sup> from room temperature ellipsometric measurements. A theoretical reflectance profile which assumed that no interdiffusion takes place between HgTe and CdTe during the growth time of HgTe could not reproduce the experimental

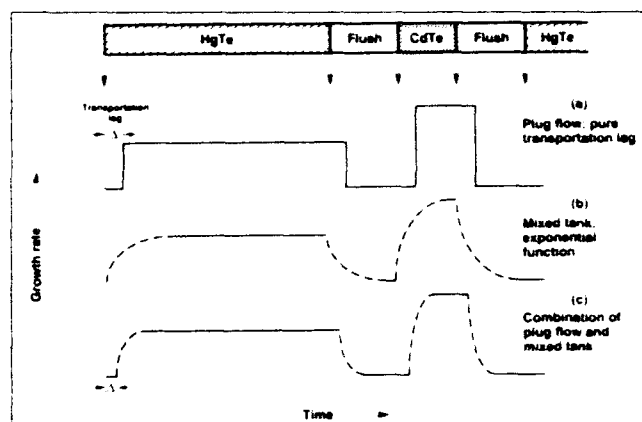


Fig. 5. Modeled growth rates for growth and flush phases during IMP cycles. The dashed line shows the case where growth during flush phases is solely due to transportation lags. Arrows indicate the switching times for different phases.

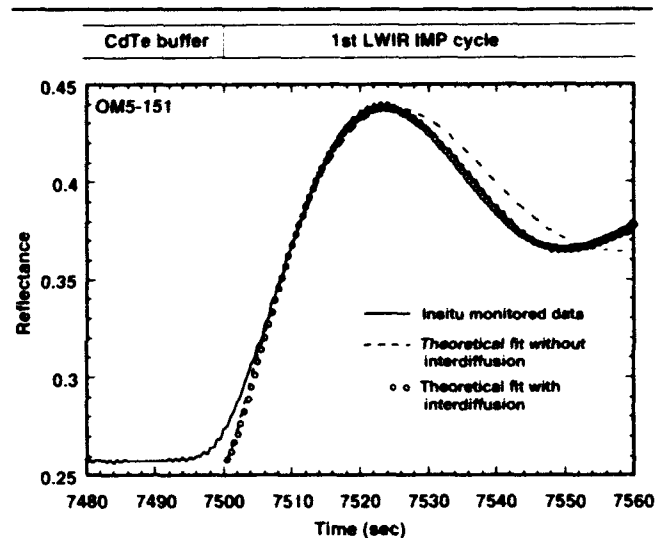


Fig. 6. In situ monitored reflectance profile for HgTe growth during the first IMP cycle following CdTe buffer growth. The solid line is the experimental data and the open circles are a theoretical fit obtained with  $n,k = 4.0, 1.18$  and using the model described in the text. The dashed line is the theoretical profile obtained by assuming no interdiffusion between HgTe and CdTe buffer during growth time of HgTe and  $n,k = 3.6, 1.45$ .

data. The magnitude of reflectance at the maxima and the minima could be matched with n,k values of 3.6, 1.45 but could not reproduce the entire profile.

An example of the application of the model to experimental data, acquired in situ during IMP cycles, is shown in Fig. 7. The solid line is the experimental data shown for a few successive IMP cycles. For this growth run, the HgTe and CdTe growth times were 60.8 s and 19.0 s, respectively. A 20 s flush phase followed the CdTe deposition and a 20 s flush phase followed the HgTe deposition. The theoretical reflectance profile is shown as the dashed line. The n,k values of 3.04, 0.253 and 4.0, 1.18 were used for CdTe and HgTe, respectively. The input thicknesses of HgTe and CdTe were calculated from the Cd composition derived from the ex situ measured infrared transmission spectra. For the example in Fig. 7, these values were 735Å and 250Å for HgTe and CdTe,

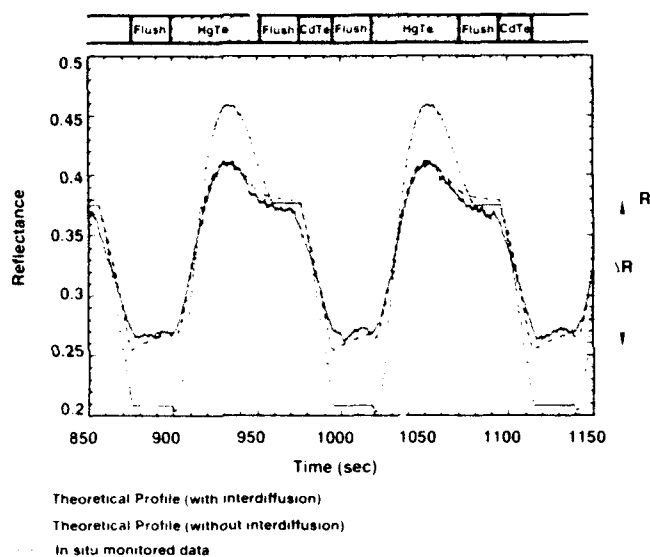


Fig. 7 Details of in situ monitored reflectance during one IMP period. The solid line is the experimental data and the dashed line is a theoretical fit with no fitted parameters. The dots represent theoretical profile assuming no interdiffusion between CdTe and HgTe.

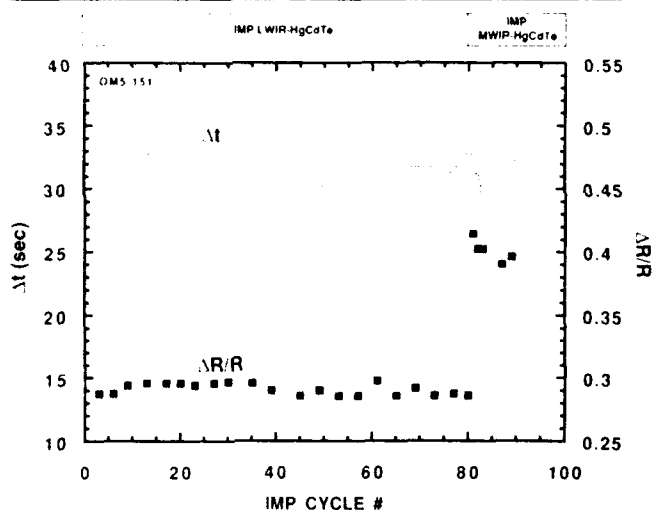


Fig. 8. Measures of CdTe thickness ( $\Delta R/R$ ) and HgTe growth rate ( $\Delta t$ ) during one IMP period plotted as a function of IMP cycle number, for the growth run described in Fig. 2.

respectively. Also the ratio  $\Delta t/\Delta$  described in Fig. 5 was set equal to 1 corresponding to pure transportation lags.

The agreement between in situ monitored reflectance data and theoretical model calculations is remarkable; several possibilities that might explain the slight discrepancy in the CdTe part of the cycle are being examined. The demonstration that the reflectance profile recorded in situ during IMP cycles can be reproduced theoretically without any fitted parameters implies that the modeling can be utilized in a 'predictive mode' to derive the IMP thicknesses of CdTe and HgTe, and hence the composition  $x$  in the interdiffused  $Hg_{1-x}Cd_xTe$  alloy. All other parameters are either constants ( $n, k$ ) or are selected (growth and flush phase durations, flow rates, temperature, etc.) prior to growth.

Figure 7 also demonstrates the importance of incorporating interdiffusion between CdTe and HgTe during growth in the theoretical model. The dots represent the theoretical reflectance profile assuming the same parameters as used in generating the dashed line but with the interdiffusion turned off. Clearly, the data cannot be explained with abrupt interfaces between CdTe and HgTe.

It has been discussed earlier<sup>5</sup> that a measure of the HgTe thickness in the IMP cycle is the valley to peak time difference ( $\Delta t$ ) during HgTe growth since this time difference depends on the growth rate. For the CdTe part of the IMP cycle, the thickness is not enough to give even half an oscillation in reflectance; therefore, the difference in reflectance from beginning to end of CdTe growth, denoted by  $\Delta R$ , was used as a measure of CdTe thickness. Qualitative monitoring of  $\Delta t$  and  $\Delta R$  as the IMP cycles progress determines the time stability of growth conditions. For the present case, discussed in Fig. 2, a plot of  $\Delta t$  and normalized reflectance  $\Delta R/R$  ( $R$  is the reflectance at the beginning of CdTe growth) against the IMP cycle # is shown in Fig. 8. For this run, the growth conditions were clearly very stable. In certain growth runs, instabilities occurred during the IMP growth leading to poor depth uniformity. For such growths, plots of  $\Delta t$  and  $\Delta R$  similar to Fig. 8 revealed whether the instabilities occurred in the HgTe or the CdTe part of IMP cycles. The source of the problem could then be identified. Ex situ diagnostics of such problems would be difficult.

Modeling of in situ monitored reflectance data discussed above allows an exact relationship between  $\Delta R$ ,  $\Delta t$  and CdTe, HgTe thicknesses during the IMP cycles.

### IMP Grown MWIR Cap Layer

The active HgCdTe LWIR layer was capped with an approximately  $1.5 \mu m$  of MWIR HgCdTe layer. This cap was also grown by IMP; therefore, the discussion in the section on IMP grown LWIR HgCdTe active layer is equally valid here. The only difference between the active LWIR and cap MWIR layers was the relative ratio of the HgTe to CdTe thicknesses in the IMP cycles. This change is reflected in the reflectance profile as seen in Fig. 9 and is also evident in the  $\Delta R/R$  plot in Fig. 8.

Separate ex situ secondary ion mass spectroscopy (SIMS) measurements confirmed the change in Cd composition in going from the active layer to the cap layer. This is seen clearly in the SIMS depth profiles in Fig. 10, where the  $^{125}Te$  secondary electronegative ion yield<sup>16</sup> is a measure of the Cd composition  $x$  in  $Hg_{1-x}Cd_xTe$ .

### CdTe Passivation Layer

A thin CdTe film was deposited in situ following the growth of MWIR HgCdTe cap layer. This thin film serves as a passivation to the grown structure. Knowledge of the CdTe passivation thickness is necessary for successful implementation of device processing



steps. Once again, the thickness accuracy of less than a hundred angstroms could be determined using the reflectance data. Ex situ determination of this thickness, to the same precision, would be difficult.

In situ reflectance data corresponding to this phase of the growth is shown in Fig. 11. The thickness of CdTe in the last IMP cycle was increased by increasing its growth duration. Then the IMP layers were allowed to interdiffuse during the anneal segment. This was followed by growth of approximately 2000Å more CdTe before cooldown. The reflectance data displays distinct features associated with each segment. The presence of the CdTe passivation layer is also clearly seen in the SIMS depth profile shown in Fig. 10.

### SUMMARY AND CONCLUSIONS

In situ measured laser reflectance has been demonstrated as an effective way to monitor and analyze MOCVD growth during each phase of a multilayer structure consisting of CdTe/Hg<sub>1-x</sub>Cd<sub>x</sub>Te ( $x \sim 0.3$ )/Hg<sub>1-x</sub>Cd<sub>x</sub>Te ( $x \sim 0.23$ )/CdTe/ZnTe/GaAs or GaAs-on-Si. The constituents of this multilayer structure have widely varying refractive indices at 0.6328  $\mu$ m wavelength, making this material system well suited for thin film interference monitoring. Theoretical modeling and analysis of in situ monitored reflectance data has provided, in real time, information related to growth rate, thickness and morphology of each component of the grown structure.

In situ monitoring has enabled measurements on the thickness of the ZnTe nucleation layer which has earlier been shown to impact the crystallinity of the CdTe buffer and subsequently grown HgCdTe layers. By in situ monitoring, the magnitude of reflectance during the thicker CdTe buffer growth where absorption in the CdTe reduces reflectance to just the surface component, the influence of growth conditions on surface roughness could be studied. This led to optimum buffer growth on GaAs/Si substrates ensuring good quality of subsequently grown HgCdTe.

During the IMP HgCdTe growth, because multiple interfaces are present within the absorption length, a periodic reflectance signal is maintained throughout this growth phase. Qualitative monitoring of the reflectance profile established the stability of growth conditions translating into depth uniformity of the grown material. For quantitative analysis, a dynamic model, which combines a multilayer optical model with in-growth interdiffusion of the IMP structure, has been developed which predicts the time evolution of reflectance during IMP growth of HgCdTe. This model also incorporates growth during flush phases. The modeled expressions relate the in situ monitored reflectance to adjustable parameters such as duration of CdTe and HgTe growth phases, duration of flush phases, growth temperature, and flow rates.

The theoretically modeled reflectance profile reproduces the experimental data with no free parameters. The values of  $n, k$  were independently fitted to reflectance from thicker layers of HgTe and CdTe. The

thicknesses of IMP HgTe and CdTe layers were derived from composition and thickness measurements using infrared transmission of the final grown wafer. This makes it possible to use the modeled in situ measured reflectance in a 'predictive mode' to derive the IMP thicknesses of CdTe and HgTe, and hence the composition  $x$  in the interdiffused Hg<sub>1-x</sub>Cd<sub>x</sub>Te alloy.

For structures that required the growth of a larger bandgap HgCdTe capping layer on top of a smaller bandgap active layer, in situ laser monitoring allowed determination of alloy composition in the cap which would be difficult to measure ex situ with the same precision.

Accurate analysis of in situ monitored reflectance during IMP cycles has allowed diagnosis of growth rate instabilities in terms of changes in the HgTe and CdTe parts of the IMP cycle. The identification of the causes enabled subsequent elimination of these instabilities. Such identification would be impossible to obtain ex situ as all the IMP layers interdiffuse to form the HgCdTe alloy. On several occasions, based on reflectance monitoring, growth runs were aborted when growth rates or morphology reached detrimental limits.

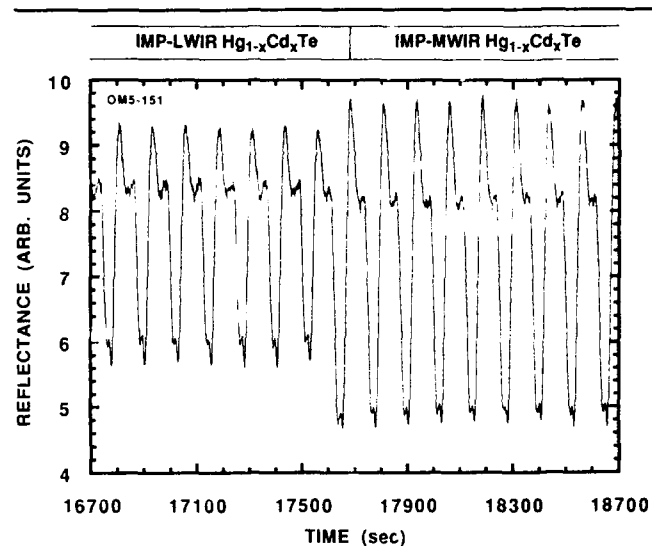


Fig. 9. Details of in situ monitored reflectance profile during transition from IMP LWIR active layer to IMP MWIR HgCdTe cap layer growth.

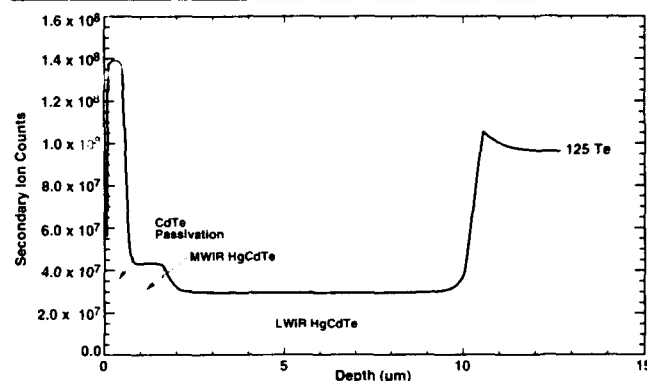


Fig. 10. Ex situ measured SIMS depth profiles clearly showing a change in Cd composition in going from the active layer to the cap layer and a uniform composition within each layer.

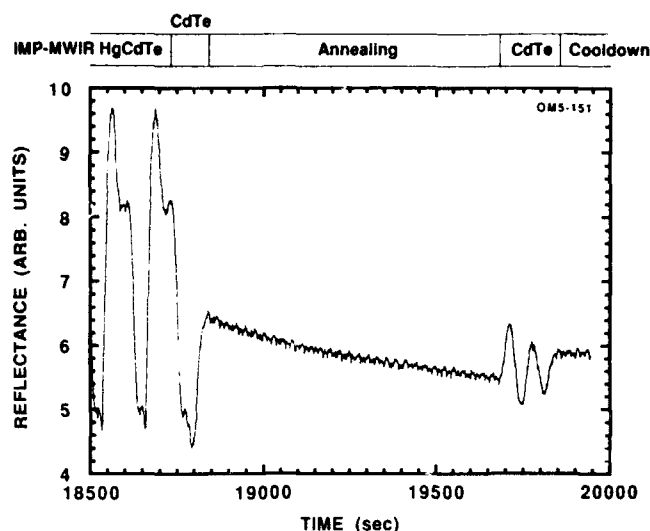


Fig. 11. In situ monitored reflectance profile during CdTe passivation growth.

The uniqueness of in situ laser reflectance monitoring is the opportunity to perform "interactive" crystal growth, i.e., analyzing the reflectance data to derive physical parameters and making appropriate changes, if necessary. This development is a key to an on-line process control of MOCVD crystal growth.

#### ACKNOWLEDGMENT

The authors gratefully acknowledge many stimulating discussions during the course of this work with Bill Tennant and Bill Southwell. Spyros Svoronos is grateful to the Control and Signal Processing Depart-

ment, Rockwell International Science Center, for sabbatical support. This work was carried out under the IR Materials Program funded by DARPA Microelectronics Technology Office; Contract Number MDA972-91-C-0047, Monitored by L. Brown, Wright Laboratories/MLPO.

#### REFERENCES

1. J.P. Faurie, A. Million and J. Piagnet, *J. Cryst. Growth* 59, 10 (1982).
2. D.W. Kisker, P.H. Fouss, S. Brennen, G. Renaud, K.L. Tokoda and J.L. Kahn, *J. Cryst. Growth* 101, 42 (1990).
3. J.B. Theeten, F. Hottier and J. Hallais, *J. Cryst. Growth* 46, 245 (1990).
4. D.E. Aspnes, W.E. Quinn and S. Gregory, *Appl. Phys. Lett.* 56, 2569 (1990).
5. S.J.C. Irvine, J. Bajaj, H.O. Sankur, *J. Cryst. Growth* (in press).
6. S.J.C. Irvine, H. Hill, G.T. Brown, S.J. Barnett, J.E. Hails, O.D. Dosser and J.B. Mullin, *J. Vac. Sci. Technol.* B7, 1191 (1989).
7. H. Sankur, W. Southwell and R. Hall, *J. Electron. Mater.* 20, 1099 (1991).
8. S.J.C. Irvine, D.D. Edwall, L.O. Bubulac, R.V. Gil and E.R. Gertner, *J. Vac. Sci. Technol.* B10, 1392 (1992).
9. J. Turncliffe, S.J.C. Irvine, O.D. Dosser and J.B. Mullin, *J. Cryst. Growth* 68, 245 (1984).
10. J.B. Mullin, J. Geiss, S.J.C. Irvine, J.S. Gough and A. Doyle, *Mat. Res. Soc. Symp. Proc.* 90, 367 (1987).
11. H.A. Macleod *Thin-Film Optical Filters*, Second Ed., Macmillan Publishing Company, New York (1986).
12. D. Rhiger, private communication.
13. M.F.S. Tang and D.A. Stevenson, *Appl. Phys. Lett.* 50, 1272 (1987).
14. M.F.S. Tang and D.A. Stevenson, *J. Vac. Sci. Technol.* A5, 3124 (1987).
15. S.A. Svoronos, J. Bajaj and S.J.C. Irvine (to be published).
16. L.O. Bubulac and C.R. Viswanathan, *Appl. Phys. Lett.* 60 (1992).

# Hall Effect Characterization of LPE HgCdTe P/n Heterojunctions

S.P. TOBIN, G.N. PULTZ, E.E. KRUEGER, M. KESTIGIAN, K.-K. WONG,  
and P.W. NORTON

Loral Infrared & Imaging Systems, Lexington, MA

The field and temperature dependence of the Hall coefficient has been used to simultaneously extract information about the p and n layers in very long wave length infrared P/n HgCdTe heterojunctions. The field dependence allows the effects of high mobility electrons to be separated from those of low mobility holes. The higher the magnetic field, the higher the sensitivity to the parameters of the P layer. For a maximum magnetic field of 8000 gauss, the hole sheet concentration must be at least five times the electron sheet concentration to obtain accurate results for the P layer. This criterion is satisfied for typical liquid phase epitaxy (LPE) heterostructures. The analysis determines the hole sheet resistance (concentration times mobility), rather than the hole concentration or mobility separately. Independent knowledge of the P layer thickness and the relationship between hole concentration and resistivity are needed to convert the Hall measurement results to hole concentrations. Analysis of the field-dependent Hall data is complicated by the finding that at least three electrons of different mobilities are needed to fit the field dependence of the Hall coefficient in n-type LPE HgCdTe layers. These results are consistent with previous conclusions that electrons with different mobilities are needed to model bulk n-HgCdTe, and with a range of mobilities in the graded composition interface between the LPE layer and CdTe substrate. Consistent results are obtained for the concentrations and mobilities of the three types of electrons in the n-HgCdTe layer with and without the P layer present. N and P type carrier concentrations are also consistent with dopant concentrations measured by secondary ion mass spectroscopy.

**Key words:** Hall effect, HgCdTe, LPE, p/n heterojunctions, SIMS analysis

## INTRODUCTION

Much has been written about the Hall effect in HgCdTe, especially about p-type material. The high electron to hole mobility ratio gives rise to "anomalous" negative Hall coefficients when relatively small numbers of electrons are present as intrinsic carriers or unintentional surface inversion layers, or when epitaxial layers of opposite type are intentionally produced. For example, the temperature dependence of the Hall coefficient was used by Lou and Frye<sup>1</sup> to extract information about n-on-p epitaxial layers. The effects are more subtle for the opposite case of p-on-n layers, where the p layer conductivity is small compared to the n layer. In this case, the field dependence of the Hall coefficient is more useful than its temperature dependence because carriers of different mobility can be separated. In this work, we have used

both the field and temperature dependences of the Hall coefficient to simultaneously study the n and p layers of P-on-n heterojunction structures. The emphasis has been on characterizing the p-type layer. The mobility and carrier concentration of the n-type layer can be easily determined by etching off the p layer. A similar operation cannot be performed to isolate the thin (1  $\mu\text{m}$ ) p layer. Junction isolation is ineffective for Hall measurements of the p layer in the very long wave length infrared (VLWIR) ( $x = 0.20$ ) films we studied, since the junction resistance is less than or comparable to the sheet resistance of the layers. The question we sought to answer was whether the p layer would have enough effect on the Hall measurement to extract useful information.

## THEORY

The following multiple-carrier Hall coefficient model was used to calculate theoretical curves and to fit the data:<sup>2,3,4</sup>

(Received October 12, 1992; revised January 13, 1993)

$$eR_H(B) = \frac{\sum_{i=1}^n a_i \mu_i c_i(B)}{\left[ \sum_{i=1}^n c_i(B) \right]^2 + B^2 \left[ \sum_{i=1}^n a_i \mu_i c_i(B) \right]^2} \quad (1)$$

where

$$c_i = \frac{n_i \mu_i}{(1 + \mu_i^2 B^2)} \quad (2)$$

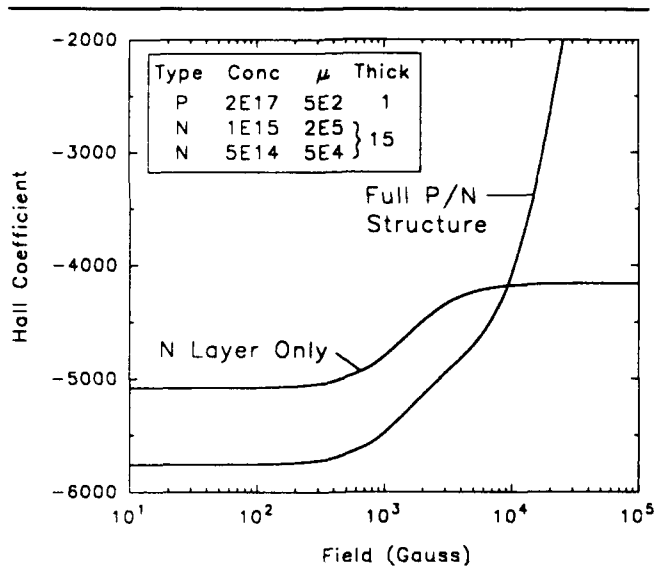
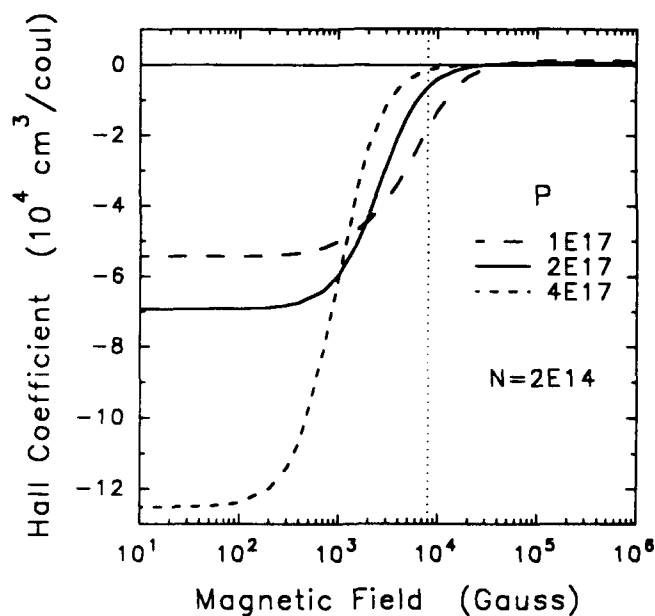
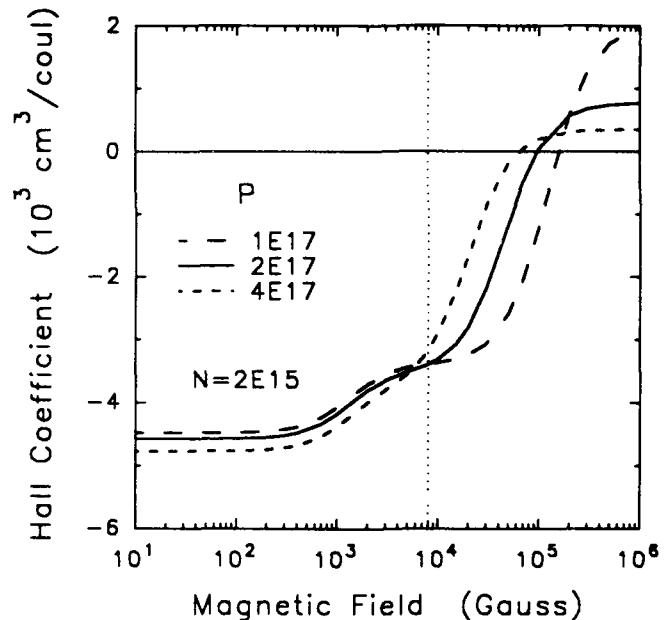


Fig. 1. Calculated Hall coefficient as a function of magnetic field for a typical double layer heterojunction structure, with and without the P layer. For the structure shown in the inset, concentrations are in  $\text{cm}^{-3}$ , mobilities are in  $\text{cm}^2/\text{Vs}$ , and thicknesses are in microns. The presence of the p-type layer causes the Hall coefficient to bend up at high fields, eventually becoming positive.



a



b

Fig. 2. Calculated Hall coefficient vs field for different carrier concentrations in the n and p layers. The assumed structure is as follows: P layer -  $1 \mu\text{m}$ ,  $\mu = 500 \text{ cm}^2/\text{Vs}$ ; constant composition n layer -  $10 \mu\text{m}$ ,  $\mu = 2 \times 10^5 \text{ cm}^2/\text{Vs}$ ; graded composition n layer -  $9 \mu\text{m}$ ,  $\mu = 5 \times 10^4 \text{ cm}^2/\text{Vs}$ . Concentrations in the two n layers are the same; concentration units are  $\text{cm}^{-3}$ . The vertical dotted line shows the maximum magnetic field available in our laboratory. (a)  $n = 2 \times 10^{14} \text{ cm}^{-3}$ , (b)  $n = 2 \times 10^{15} \text{ cm}^{-3}$ .

and  $e$  is the electron charge,  $n_i$  is the concentration per unit volume of the  $i$ th type of carrier,  $\mu_i$  is mobility of the  $i$ th type of carrier,  $a_i$  is the sign of the carrier ( $-1$  for electrons,  $+1$  for holes),  $B$  is the magnetic field, and  $R_H$  is the Hall coefficient. Equation 1 assumes that current flows in parallel for all layers in the structure. In addition to the Hall coefficient, the zero-field resistivity is given by

$$\rho(0) = \left[ e \sum_{i=1}^n c_i(0) \right]^{-1} \quad (3)$$

A nonlinear least-squares fitting routine was used to fit Eq. 1 to the measured field-dependent Hall coefficient data while satisfying Eq. 3 for the measured resistivity. Models with different numbers and types of carriers were used to fit the experimental data, as described below.

Equation 1 is generally valid for parabolic bands and elastic scattering processes, in which case the Hall scattering factor  $r_H$  equals one, independent of field ( $r_H \equiv \langle \tau^2 \rangle / \langle \tau \rangle^2$ , where  $\tau$  is the mean time between collisions of the carriers). It is not generally valid for inelastic scattering processes, nonparabolic bands, or energy-dependent relaxation times. The use of Eq. 1 should, therefore, be questioned for  $\text{HgCdTe}$ . Parat<sup>4</sup> argued that these factors are small compared to the observed field dependence of  $r_H$ . He cited theoretical calculations of the field dependence of  $r_H$  which were less than 10% for  $\text{HgTe}$  and less than 3% for  $\text{CdTe}$ . Gold and Nelson<sup>3</sup> argued that the results of an analysis based on Eq. 1 were both self-consistent and consistent with independently measured material properties of  $\text{HgCdTe}$  such as effective masses and intrinsic carrier concentration. While acknowledging

that some of the experimental field dependence of  $R_H$  may be caused by  $r_L$  variations, we do not believe it to be the dominant effect. It should be kept in mind, however, when interpreting the results.

To evaluate the feasibility of determining heterojunction layer properties from field-dependent  $R_H$  measurements, the Hall coefficient was calculated as a function of field for typical epitaxial structures with and without the p layer. Figure 1 shows an example. The n-type epitaxial layer has been modeled with two electrons of different mobilities.<sup>2</sup> It will be shown later that this structure is roughly consistent with the experimental field-dependent  $R_H$  of n-type epitaxial layers. In the structure of Fig. 1, the composite sheet resistance of the n layers is 18.5  $\Omega/\text{sq}$ , while that of the p layer is 624  $\Omega/\text{sq}$ . The sheet carrier concentrations of the two types are  $2.25 \times 10^{12} \text{cm}^{-2}(\text{n})$  and  $2.0 \times 10^{13} \text{cm}^{-2}(\text{p})$ . Thus, although the number of holes in the structure is considerably larger than the number of electrons, most of the current flows in the n layer. It can be seen that the field dependence of  $R_H$  is similar for the two structures (P/n and n alone) when B is less than 3000 gauss. At higher fields, however,  $R_H$  of the n-type sample reaches an asymptote while the heterojunction  $R_H$  bends sharply toward zero and eventually becomes positive at very high fields. This is a consequence of the larger number of holes than electrons, since in the high-field limit,  $R_H = 1/e(p-n)$ . One would, therefore, prefer to use very high magnetic fields, in the  $10^4$  to  $10^5$  gauss range, to characterize the p-type layer. Unfortunately, magnets of this strength were not available in our laboratory. Even with a maximum field strength of 8000 gauss, however, we can extract some information about the p layer if it is not too thin or too lightly doped.

To quantify this, Fig. 2 shows a series of calculated Hall coefficient curves for heterojunction structures with different n and p carrier concentrations.\* It can be seen that as the ratio of p to n increases, the transition from n-type to p-type behavior shifts to lower fields, and the low-field  $R_H$  becomes more sensitive to the value of p. Not surprisingly, with more holes present, it is easier to measure their concentration. Below some value of the p to n ratio, the curves become insensitive to the p concentration in the accessible field range. For the structure of Fig. 2, the volume concentration threshold ratio  $p(\text{cm}^{-3})/n(\text{cm}^{-3})$  is about 100. However, this value depends on the relative thicknesses of the two layers. More generally, the threshold sheet concentration ratio  $P(\text{cm}^{-2})/N(\text{cm}^{-2})$  is about 5. For lower values of the p/n ratio, we cannot accurately measure effects of the p layer below 8000 gauss; the sample essentially looks n-type. Fortunately, this criterion permits most structures of interest to be analyzed.

\*The assumed structure is somewhat different than in Fig. 1; here we have two separate n layers with different mobilities rather than two electrons in the same layer. However, the two are functionally equivalent. The important feature is two electrons of different mobilities.

## EXPERIMENTAL

The HgCdTe samples were grown by liquid phase epitaxy on CdTe substrates. An n-type In-doped layer was first grown in a Te-rich horizontal slider system, followed by a p-type As-doped layer grown in a Hg-rich vertical dipper system. Typical values for the samples discussed here were thickness = 15  $\mu\text{m}$ , electron concentration =  $1 \times 10^{15} \text{cm}^{-3}$ , and  $x = 0.20$  for the n-layer, and thickness = 1  $\mu\text{m}$ , hole concentration =  $2 \times 10^{17} \text{cm}^{-3}$ , and  $x = 0.24$  for the p-layer. A cloverleaf Hall pattern was defined by photolithography and wet chemical etching down to the CdTe substrate. The central circular area of the pattern was 2 mm in diam. The epitaxial layer thickness was determined from Fourier transform infrared spectroscopy (FTIR) interference fringes at the center of the Hall sample.

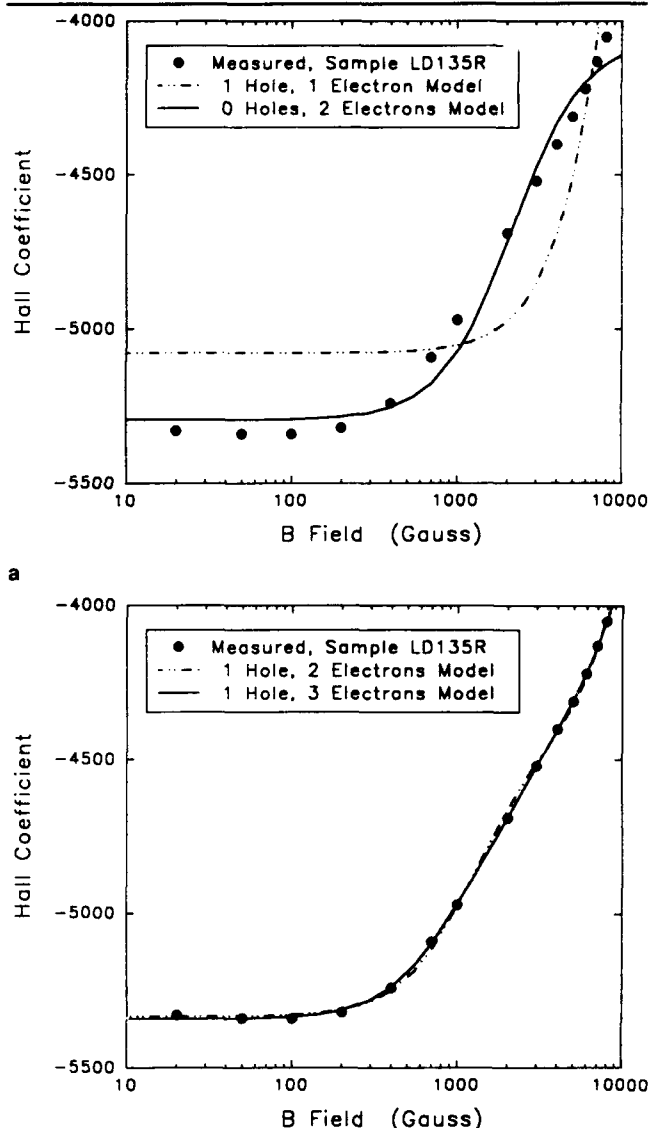


Fig. 3. Best fits of different multiple-carrier models to typical measured data at 77K. At least one hole and two electrons are required for a satisfactory fit. (a) two-carrier models, (b) three- and four-carrier models.

Table I. Fitting Parameters for the Hall Coefficients Fits in Fig. 3

| Model | Fit Error | N1<br>$10^{14}$ | N2<br>$10^{14}$ | N3<br>$10^{14}$ | $\mu 1$<br>$10^4$ | $\mu 2$<br>$10^4$ | $\mu 3$<br>$10^4$ | Total N<br>$10^{15}$ | P<br>$10^{17}$ |
|-------|-----------|-----------------|-----------------|-----------------|-------------------|-------------------|-------------------|----------------------|----------------|
| 1P,1N | 3.02E-2   | 14.4            | —               | —               | 14.3              | —                 | —                 | 1.44                 | 5.50           |
| 0P,2N | 2.12E-3   | 9.98            | 5.41            | —               | 18.7              | 3.31              | —                 | 1.54                 | —              |
| 1P,2N | 1.07E-4   | 9.31            | 6.96            | —               | 18.3              | 5.82              | —                 | 1.63                 | 3.67           |
| 1P,3N | 1.25E-5   | 8.06            | 5.06            | 3.73            | 19.1              | 8.97              | 3.15              | 1.69                 | 3.30           |

Note: Carrier concentrations are in  $\text{cm}^{-3}$  and mobilities are in  $\text{cm}^2/\text{Vs}$ . Carrier concentrations assume a P layer thickness of  $1 \mu\text{m}$  and a hole mobility of  $300 \text{ cm}^2/\text{Vs}$ . The fit error is proportional to the sum of the squares of the differences between measured and calculated points.

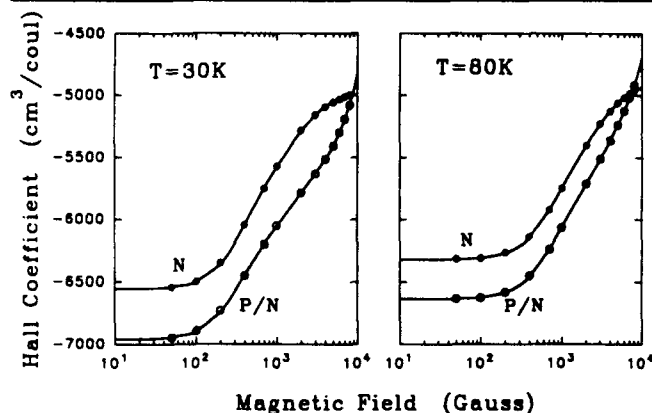


Fig. 4. Measured and calculated Hall coefficients as a function of field, at 30 and 80K. Symbols show measured data and lines are calculated curves. The composition of the n-layer was  $x = 0.203$ . The total thickness of the P-on-n heterojunction sample was  $13.8 \mu\text{m}$ . After etching the same sample to remove the P layer, the thickness was  $9.0 \mu\text{m}$ . Fitting parameters are listed in Table II.

The samples were etched in dilute bromine-methanol just prior to ohmic contact formation with In. Nonalloyed contacts were formed by pressing small, high-purity In spheres onto the surface of the sample with a warm sapphire soldering iron tip without melting. Samples were then immediately measured. We have found that this procedure avoids surface effects and makes special surface passivation coatings unnecessary. In some experiments, the contacts were removed in HCl, the p-layer was removed by etching in 2% bromine in methanol, and contacts were reapplied.

Van der Pauw-Hall coefficient and resistivity measurements were made according to the ASTM standard method,<sup>5</sup> with field reversal,  $f$  factor corrections, and permutation of contacts to reduce measurement errors. It was also verified that the contacts were ohmic. Computer-controlled measurements were made at 14 fields from 20 to 8000 gauss, either in liquid nitrogen (single temperature) or at 21 temperatures from 10 to 300K in a closed-cycle helium cryostat (variable temperature). In the latter case, temperatures were constant to within 0.5K and usually within 0.1K for each set of measurements. The  $\mu$ s were monitored by a GaAs diode sensor mounted on the cold finger. There was good agreement between liquid nitrogen and variable temperature measurements of the same sample, sometimes done several days apart.

Secondary ion mass spectroscopy (SIMS) was used to measure the dopant concentration profiles in some of the samples.<sup>6</sup> Quoted accuracy of the analysis was a factor of two in dopant concentration and 10% in depth, based on ion implanted concentration standards and profilometer measurements of sputter crater depths. The SIMS Te yield technique<sup>7</sup> was also used to measure the composition profile of the heterojunction.

## RESULTS

Figure 3 shows experimental data of Hall coefficient vs field for a heterojunction sample at 77K. The curves show best fits of two-, three-, and four-carrier models to the data. The fitting parameters are summarized in Table I. To quantify the hole concentration, we used a hole mobility of  $300 \text{ cm}^2/\text{Vs}$  for the P layer, appropriate for a hole concentration of about  $2 \times 10^{17} \text{ cm}^{-3}$ .<sup>8</sup> At least one hole and two electrons are required for a satisfactory fit. A significantly better fit is obtained for one hole and three electrons. Although it may not be apparent from the figure, the sum of the squares error of the fit is one order of magnitude lower in the latter case (Table I). Note that although the total change in Hall coefficient with field is only about 33%, the precision of the measurements is much better, on the order of 0.1%. The low noise of the measurement allows very precise fits to be made to the data.

Figure 4 compares field-dependent data at 30 and 80K for a different sample. Data are shown both before and after removal of the P layer by etching. The solid lines are four-carrier (with P layer) and three-carrier (without P layer) fits, with parameters summarized in Table II. Several points are worth noting. First, the shapes of the curves closely follow the theoretical results of Fig. 1. The high-field Hall coefficient approaches a plateau for the n layer alone, but curves upward for the heterojunction. Also, the low-field Hall coefficient is lower for the heterojunction sample. Second, the low to high field transition occurs over a wider range of fields at lower temperatures. This corresponds to a wider range of electron mobilities. The need for a third electron to fit the field dependence is increasingly important at low temperatures.

Figure 5 shows the Hall coefficient and mobility as functions of temperature for the heterojunction sample

Table II. Results of Fitting the Hall Coefficient Data in Fig. 4

| Temp.<br>(K) | Layers | N1<br>$10^{14}$ | N2<br>$10^{14}$ | N3<br>$10^{14}$ | $\mu_1$<br>$10^5$ | $\mu_2$<br>$10^5$ | $\mu_3$<br>$10^4$ | Total N<br>$10^{14}$ | P<br>$10^{17}$ |
|--------------|--------|-----------------|-----------------|-----------------|-------------------|-------------------|-------------------|----------------------|----------------|
| 30           | P/n    | 7.63            | 3.21            | 1.78            | 6.69              | 2.35              | 4.91              | 1.26                 | 2.20           |
|              | n      | 7.20            | 3.50            | 1.85            | 5.78              | 1.90              | 4.70              | 1.26                 | —              |
| 80           | P/n    | 6.90            | 4.25            | 2.92            | 2.37              | 1.00              | 2.90              | 1.44                 | 2.15           |
|              | n      | 6.42            | 4.19            | 2.17            | 2.28              | 0.93              | 2.88              | 1.28                 | —              |

Note: Carrier concentrations are in  $\text{cm}^{-3}$  and mobilities are in  $\text{cm}^2/\text{Vs}$ . The concentrations for the P/n sample assume a F layer thickness of  $1\text{ }\mu\text{m}$  and hole mobility of  $300\text{ cm}^2/\text{Vs}$ .

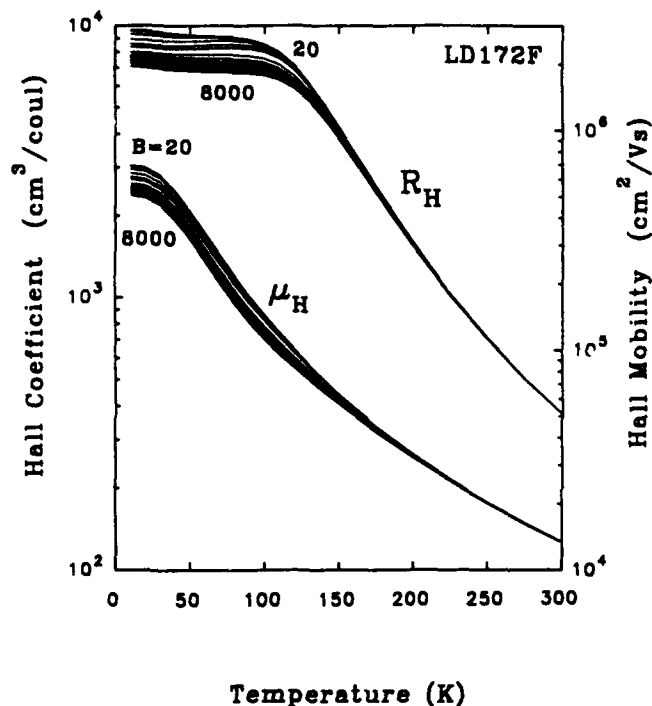


Fig. 5. Hall coefficient and mobility vs temperature for a P/n heterojunction sample. Curves are shown for 14 different fields from 20 to 8000 gauss.

of Fig. 4. The mobility was obtained from the Hall coefficient and zero-field resistivity for comparison to fixed-field data in the literature. Figure 6 shows the results after the P layer was removed. The multiple curves in each figure are for different fields. Figures 5 and 6 are very similar, showing the small influence of the P layer on Hall measurements and illustrating the difficulty of determining any information about the P layer from temperature-dependent measurements alone. However, as shown in Fig. 4, the field dependence clearly distinguishes between the two types of samples.

The four-carrier model (three electrons and one hole) was used to fit the field-dependent data for the P-n heterojunction of Fig. 5 at each temperature. Resulting values of electron concentration and mobility as functions of temperature are shown in Fig. 7. Error bars indicate the support plane 95% confidence ranges of the fits. For holes, we have found that the fitting is sensitive only to the product of hole concen-

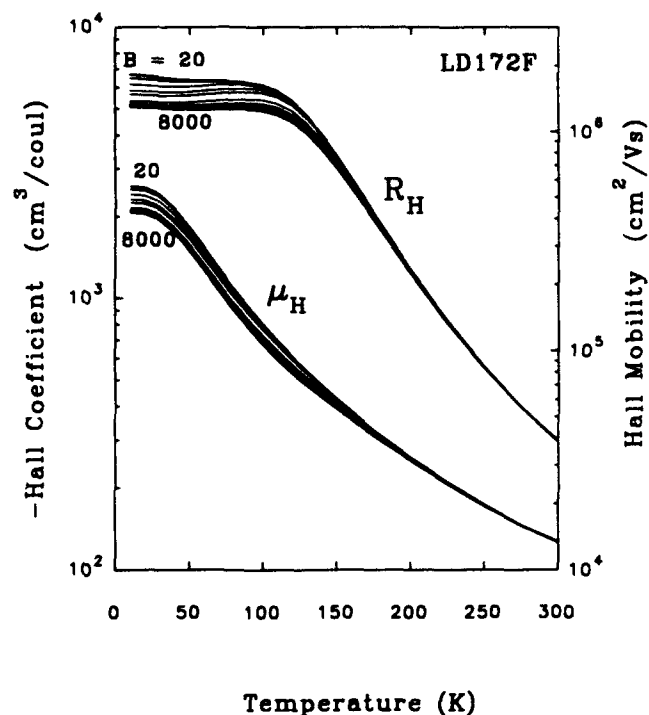


Fig. 6. Hall coefficient and mobility vs temperature for an n-HgCdTe layer. This is the same sample as in Fig. 5, but with the P layer etched off. Curves are shown for 14 different fields from 20 to 8000 gauss.

tration and mobility, and not to the individual parameters. We have, therefore, plotted the hole sheet resistance in Fig. 7, rather than the hole concentration. (Sheet resistance  $= (e P_{sh} \mu_h)^{-1}$ , where  $P_{sh}$  is the hole sheet concentration ( $\text{cm}^{-2}$ ) and  $\mu_h$  is the hole mobility). Error bars are not plotted for the sheet resistance at temperatures above 100K because a statistical analysis showed the value of  $R_{sh}$  had no detectable influence on the results (the variance-covariance matrix was singular). In this case,  $R_{sh}$  was deleted from the statistical analysis. With one fewer parameter, the 95% confidence range decreased; this is especially noticeable in the mobility results. The same result was found for N3 at temperatures above 120K. A physical interpretation of these effects is that the intrinsic electrons in the low-bandgap n-HgCdTe (N1 and N2) increase in number with increasing temperature, while the numbers of holes and N3 electrons remain relatively constant. The fits then become insensitive to the values of P and N3.

Similarly, the three-electron model was used to fit the field-dependent data for the N layer of Fig. 6 at each temperature. The concentrations and mobilities of the three electrons are plotted vs temperature in Fig. 8. The results for each of the three electrons are similar in both Figs. 7 and 8. In these figures, the results are shown only for the extrinsic temperature range below 150K, where the field dependence is large enough to give accurate fitting results. As seen in Figs. 5 and 6, the field dependence of the Hall coefficient is very small, although nonzero, in the intrinsic range. This produces large uncertainties in the fitted parameters.

As an independent check of the results, SIMS was used to measure the dopant concentrations in the n and p layers. Depth profiles of As, In, and composition (x) are shown in Fig. 9. Because the P layer of the Hall sample had been removed by etching, the profiles were measured on another sample from the same LPE run. The average In concentration in the n layer is  $1.24 \times 10^{15} \text{ cm}^{-3}$ , with a standard deviation of  $0.06 \times 10^{15} \text{ cm}^{-3}$ , in good agreement with the electron concentration in Table II. Although not shown in the figure, SIMS measurements of In concentration were also made at the center of the Hall sample used for Figs. 4

to 8. The average concentration was  $1.27 \times 10^{15} \text{ cm}^{-3}$  with a standard deviation of  $0.07 \times 10^{15} \text{ cm}^{-3}$ , again in excellent agreement. The P/n junction depth is  $1 \mu\text{m}$  and the average As concentration over this thickness is  $2.54 \times 10^{17} \text{ cm}^{-3}$ . The composition profile shows a maximum x of 0.223, decreasing to approximately 0.21 at the surface.

## DISCUSSION

One result of this study is that multiple electrons of different mobilities are required to explain the field dependence of the Hall coefficient for n-type epitaxial layers. This is not the first time this has been reported for n-HgCdTe. In fact, we are aware of no published data for n-HgCdTe that shows the Hall coefficient to be independent of field in the extrinsic range, as would be expected for conduction by a single electron. The presence of two electrons in bulk-grown n-type HgCdTe was reported by Finkman and Nemirovsky<sup>2</sup> based on field-dependent Hall measurements. They found two electrons of different mobility but similar concentration, consistent with our results. The origin of the second electron was not determined. Nishizawa et al.<sup>9</sup> reported the presence of two electrons and one hole in bulk p-type HgCdTe. They assigned the lower

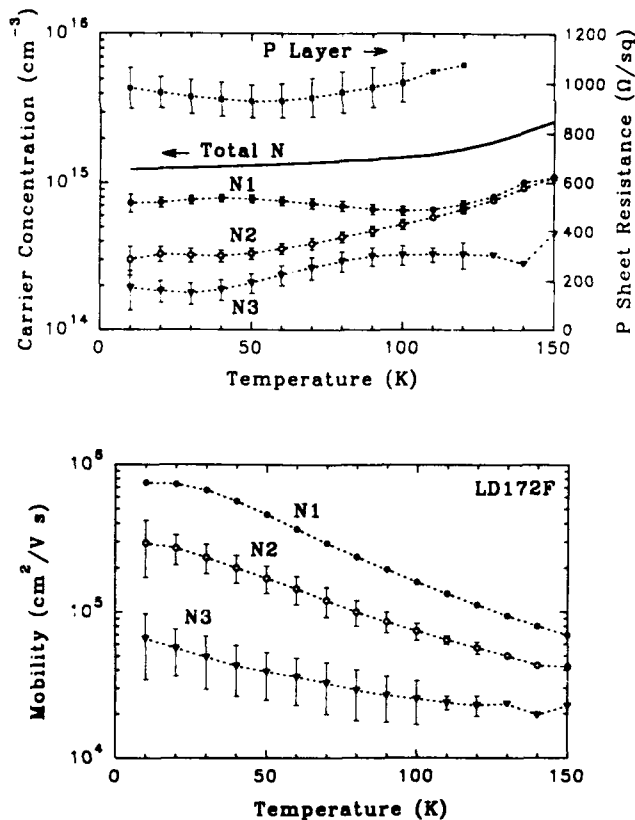


Fig. 7. Results of multiple-carrier Hall analysis for the P/n heterojunction sample of Fig. 5. The three electrons are denoted N1, N2, and N3. Error bars show the support plane 95% confidence ranges for each parameter. Lines connecting data points are intended only to guide the eye. Carrier concentration values were based on an n-layer thickness of  $12.8 \mu\text{m}$  (assumed  $1 \mu\text{m}$  p-layer thickness).

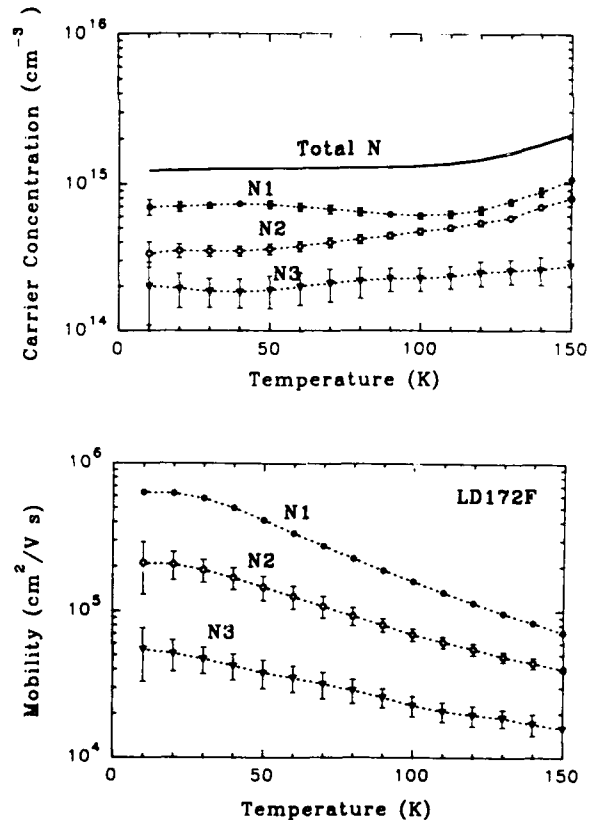


Fig. 8. Results of multiple-carrier Hall analysis for the n-type layer of Fig. 6. The three electrons are denoted N1, N2, and N3. Error bars show the support plane 95% confidence ranges for each parameter. Lines connecting data points are intended only to guide the eye. Carrier concentration values were based on a total epitaxial layer thickness of  $9.0 \mu\text{m}$ .



mobility electron to the conduction band but did not have an explanation for the higher mobility electron. Parat et al.<sup>4</sup> reported two electrons of different mobilities in MOCVD-grown n-type HgCdTe. They showed that the concentration of low-mobility electrons was reduced by surface passivation, due to elimination of an electron accumulation layer. However, even after the surface was passivated, there was still an 18% change in  $R_H$  from 500 to 6000 gauss, which is evidence of electrons with more than one mobility somewhere in the structure. Parat assumed this was residual surface accumulation, but it could also be interpreted as a bulk effect. Multiple electron effects are complicated in our case by the substantial compositional grading which occurs at the interface between the HgCdTe layer and CdTe substrate in the LPE growth process. This grading occurs over a width of 3 to 5  $\mu\text{m}$ , which is a substantial fraction of the total epitaxial layer thickness of 12 to 20  $\mu\text{m}$ . Electrons in this graded region would be expected to have lower mobilities due to a higher CdTe mole fraction and the presence of misfit dislocations near the interface. Since this region is graded, we would expect to see a continuum of electron mobilities. Our fitting procedure can only approximate this continuum as a small number of different electrons with different mobilities. Similarly, a range of mobilities in the bulk, which might arise from inhomogeneity in the material, could only be approximated by a finite number of different electrons. We, therefore, interpret the three electrons in our fits as a superposition of bulk electrons in the constant-composition region and electrons with a range of mobilities in the graded composition region. The fact that N1 and N2 increase with temperature in the intrinsic range while N3 remains relatively constant suggests that the N1 and N2 electrons are present primarily in the uniform composition n layer, while the N3 electrons are mostly localized in the graded composition region. The higher average band gap in the graded region would shift the transition from extrinsic to intrinsic conduction to higher temperatures. The alloy composition of the N3 electrons could in principle be determined by observing the temperature at which their intrinsic concentration begins to rise. However, the field dependence above a temperature of 150K was too small to allow reliable fitting. One interpretation is that the concentration of N3 was just too small compared to the N1 + N2 intrinsic carriers to affect the Hall coefficient.

The presence of multiple electrons makes it more difficult to determine the parameter of interest, namely, the bulk electron concentration. The fundamental parameter measured by the Hall effect is the sheet concentration  $N_{sh}$  ( $\text{cm}^{-2}$ ), not the bulk concentration  $N$  ( $\text{cm}^{-3}$ ), of each carrier. In terms of measured parameters,  $N_{sh} = I B / e V_H$ , where  $I$  is the current,  $B$  is the magnetic field,  $e$  is the electron charge, and  $V_H$  is the Hall voltage. To determine bulk concentrations, a thickness must be assumed. If, as was done by Parat, the low mobility electron is assumed to be in a

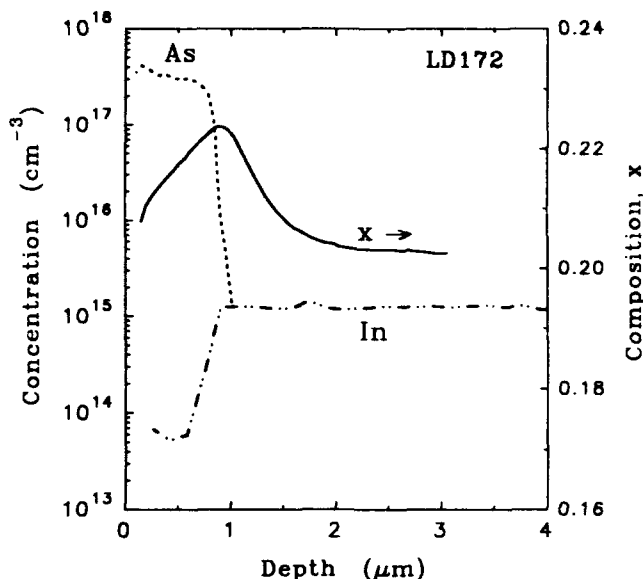


Fig. 9. Secondary ion mass spectroscopy doping and composition profiles for a companion piece to the sample of Figs. 4 to 8. The composition profile is based on the Te yield profile, with the n layer composition set equal to the value of 0.203 measured by FTIR transmission.

surface layer of essentially zero thickness, then the bulk concentration is given by the sheet concentration of the high mobility electron alone divided by the layer thickness. Finkman, on the other hand, found that both electrons were in the bulk, so that the bulk concentration was given by the sum of high and low mobility electron densities. In our case, we believe that surface effects are negligible, and that the total electron density in the extrinsic range should equal the In dopant concentration, which is constant throughout the structure, including most of the graded region (SIMS results). (Indium is known to give essentially 100% electrical activation in Te-rich LPE HgCdTe). In this case, the bulk electron concentration should be the sum of the electron sheet concentrations divided by the total thickness.

This value, shown as Total N in Figs. 7 and 8, is in excellent agreement with SIMS measurements of the In concentration measured at the center of the same Hall pattern. In the extrinsic range, Hall measurements gave  $1.3 \times 10^{15} \text{cm}^{-3}$  for the carrier concentration, while SIMS gave  $1.27 \times 10^{15} \text{cm}^{-3}$  for the In concentration. This agreement supports our interpretation of the measured electron densities as bulk and not surface values. Good agreement for Total N, as well as similar concentrations and mobilities of the three types of individual electrons, is also found before and after removing the P layer. There should be no electron surface effects in the heterojunction sample because there is no free n-type surface; it is replaced by the P layer. Similar analysis results after the P layer is removed argue that in this case, too, we are measuring bulk effects.

The agreement between hole concentration ( $2.2 \times 10^{17} \text{cm}^{-3}$ ) and As concentration ( $2.5 \times 10^{17} \text{cm}^{-3}$ ) is also good. The comparison is not direct, because a value of

hole mobility must be assumed in order to convert measured sheet resistance to hole concentration. The discrepancy is well within the uncertainty in the assumed mobility. The discrepancy is also well within the accuracy of the SIMS As concentration measurement. It has been found that As is 100% electrically active in Hg-rich LPE HgCdTe,<sup>10</sup> so lack of electrical activation is probably not a factor.

The results in Fig. 7 show the hole sheet resistance to be nearly independent of temperature in the range of 10 to 100K. This implies limited hole freezeout over this temperature range, limited at most to the change in hole mobility with temperature. Capper<sup>11</sup> reported acceptor activation energies of 1–5 meV for arsenic at concentrations of  $(1-1.5) \times 10^{17} \text{ cm}^{-3}$  in VLWIR HgCdTe, with lower activation energy for higher concentrations. The lack of freezeout in our P layers doped  $(2-3) \times 10^{17} \text{ cm}^{-3}$  is consistent with an activation energy considerably less than 1 meV.

The heterojunction analysis depends on parallel current flow through the P and n layers. No special methods have been used to insure that the In ohmic contacts penetrate both layers, although the junction is only 1  $\mu\text{m}$  deep and this is certainly possible. However, in the VLWIR samples we have used ( $x = 0.20$ ), the junction impedance is generally smaller than or comparable to the sheet resistance of the P layer. For example, at 77K with a 14  $\mu\text{m}$  cutoff,  $R_0 A$  is 3  $\Omega\text{-cm}^2$ . With a mesa area of 0.12  $\text{cm}^2$ , the junction impedance is 25  $\Omega$ . P layer sheet resistance values are typically 500 to 1000  $\Omega/\text{sq}$ . Current, therefore, tends to travel through the P/n junction to the lower resistance n layer rather than be restricted to the P layer. The relatively large area Hall samples also tend to have enough random defects to shunt the intrinsic junction impedance, even for shorter cutoff material. We have seen no evidence that current blocking by the p-n junction is a significant effect. It is interesting to note that the low junction impedance in VLWIR heterojunctions, which prevents standard transmission line measurements of the P layer sheet resistance, can be used to advantage in the Hall measurement. It is also worth noting that this technique is applicable to heterojunctions of any composition, so long as ohmic contact is made to both layers.

No attempt was made in this work to fit the field-dependent resistivity. Additional information is available from this measurement that may improve the accuracy of the fitting results, especially for holes. This is a good area for future work.

## CONCLUSIONS

The field and temperature dependence of the Hall coefficient has been used to simultaneously extract information about the p and n layers in P/n HgCdTe

heterojunctions. The maximum magnetic field available in the laboratory determines the sensitivity to the parameters of the P layer; more information is available for higher fields. For a field of 8000 gauss, the hole sheet concentration must be at least five times the electron sheet concentration to obtain accurate results for the P layer. This criterion is satisfied for typical LPE heterostructures. The analysis determines the hole sheet resistance (concentration times mobility), rather than the hole concentration or mobility separately. Independent knowledge of the P layer thickness and the relationship between hole concentration and resistivity are needed to convert the Hall measurement results to hole concentrations. Analysis of the field-dependent Hall data is complicated by the finding that at least three electrons of different mobilities are needed to explain the field dependence of the Hall coefficient in our n-type LPE HgCdTe layers. These results are consistent with previous conclusions that electrons of different mobilities are needed to model bulk n-HgCdTe, and with a lower mobility graded region in the graded composition interface between the LPE layer and CdTe substrate. Consistent results are obtained for the concentrations and mobilities of the three types of electrons in the n-HgCdTe layer with and without the P layer present. N and P type carrier concentrations are also consistent with dopant concentrations measured by SIMS.

## ACKNOWLEDGMENT

Part of this work was performed for the Jet Propulsion Laboratory, California Institute of Technology Contract 958970, as sponsored by the National Aeronautics and Space Administration Contract NAS7-918.

## REFERENCES

1. L.F. Lou and W.H. Frye, *J. Appl. Phys.* 56, 2253 (1984).
2. E. Finkman and Y. Nemirovsky, *J. Appl. Phys.* 53, 1052 (1982).
3. M.C. Gold and D.A. Nelson, *J. Vac. Sci. Technol. A* 4, 2040 (1986).
4. K.K. Parat, N.R. Taskar, I.B. Bhat and S.K. Ghandhi, *J. Cryst. Growth* 102, 413 (1990).
5. *Standard Method for Measuring Hall Mobility and Hall Coefficient in Extrinsic Semiconductor Single Crystals*, ANSI/ASTM Method F 76-73.
6. SIMS analysis performed at Charles Evans and Associates, Redwood City, CA.
7. L.O. Bubulac and C.R. Viswanathan, *Appl. Phys. Lett.* 60, 222 (1992).
8. A. Zemel, A. Sher and D. Eger, *J. Appl. Phys.* 62, 1861 (1987).
9. J. Nishizawa, K. Suto, M. Kitamura, M. Sato, Y. Takase and A. Ito, *J. Phys. Chem. Solids* 37, 33 (1976).
10. T. Tung, M.H. Kalisher, A.P. Stevens, and P.E. Herning, *Mat. Res. Soc. Symp. Proc.* 90, 321 (1987).
11. P. Capper, J.J.G. Gosney, C.L. Jones, I. Kenworthy and J.A. Roberts, *J. Cryst. Growth* 71, 57 (1985).

# Assessment of Electrical Inhomogeneity of Undoped and Doped $\text{Hg}_{1-x}\text{Cd}_x\text{Te}$ MOVPE (IMP) Layers by Variable Magnetic Field Hall Profile Measurements

M.L. YOUNG, J. GIESS, and J.S. GOUGH

Defence Research Agency (Malvern), St. Andrews Road, Malvern, Worcs  
WR14 3PS, UK

A Hall profiling technique in which measurements are made at 77K as a function of magnetic field (0.01–1 T) and layer thickness (by chemical thinning) has been developed for the characterization of  $\text{Hg}_{1-x}\text{Cd}_x\text{Te}$  epitaxial layers. The technique has been applied to undoped and lightly In doped MOVPE interdiffusion multilayer process (IMP) layers grown on (100) GaAs and CdTe with  $x$  values between 0.19 and 0.30 in order to investigate the parameters controlling the electrical homogeneity. Results show unpassivated layers with  $x > 0.25$  are uniformly p-type with 77K hole concentrations consistent with Hg vacancy concentrations for the growth conditions while layers with  $x < 0.25$  are anomalous, being either inhomogeneous or uniformly n-type depending on  $x$ . The inhomogeneous layers are mainly n on p layer structures, in which the junction depth,  $X_j$ , but not the carrier concentration is found to be a function of  $x$  and can be comparable to layer thickness at  $x = 0.20$ . Carrier levels in the n and p-type regions are consistent with the net background impurity donor and Hg vacancy concentrations respectively, suggesting that the n-type properties occur through post growth Hg in-diffusion filling in the vacancies. This model was partly confirmed by capping layers with CdTe, which significantly reduced the extent of the n-type region, and by ex-situ annealing experiments to simulate the inhomogeneity. Results show the low temperature process responsible for the type conversion in MOVPE CMT is highly  $x$  dependent, suggesting a variation in the electrical "Hg diffusion coefficient" of over an order of magnitude between 0.20 and 0.30 at 200°C. Carrier and mobility profiles of both as-grown and annealed n-p structures are abrupt and consistent with an interstitial Hg diffusion mechanism.

**Key words:** Electrical inhomogeneity, Hall effect,  $\text{HgCdTe}$ , Hg diffusion in  $\text{HgCdTe}$ , IMP process

## INTRODUCTION

It is important to be able to assess and control the electrical inhomogeneity of  $\text{Hg}_{1-x}\text{Cd}_x\text{Te}$  epitaxial layers used in the fabrication of photovoltaic infrared detectors. This requirement exists for both undoped p-type layers having high concentrations of Hg acceptor vacancies and fully or partly doped n/p layer structures prepared prior to device fabrication. Common to all growth technologies involving  $\text{Hg}_{1-x}\text{Cd}_x\text{Te}$  is the need to be able to control the Hg vacancy acceptor concentration and gradients by growth and annealing as this governs the homogeneity in undoped

layers directly via the vacancy profiles and in doped layers indirectly through the activation and compensation of the dopant impurities. Of importance in this context is the effect of composition and structural properties in addition to stoichiometry on the Hg vacancy diffusion rates as these will influence the growth and annealing procedures required for different device structures. As part of a wider program into the assessment and growth of doped structure, we have developed variable magnetic field Hall and strip measurements as a routine profiling tool for epilayers and applied the technique here to a study of the anomalous electrical properties of undoped and lightly In doped MOVPE interdiffusion multilayer process (IMP) layers.

(Received October 12, 1992; revised March 1, 1993)

The electrical properties of undoped MOVPE  $\text{Hg}_{1-x}\text{Cd}_x\text{Te}$ , particularly when grown on a foreign substrate like GaAs, can be somewhat variable, with both p and n-type layers being reported.<sup>1,2</sup> For thermal growth at temperatures above 300°C, undoped layers are expected to be p-type because of the high concentrations,  $10^{16}$ – $10^{17} \text{ cm}^{-3}$ , of Hg acceptor vacancies incorporated during growth.<sup>3</sup> Despite this, layers are often n-type, particularly at the important composition of  $x = 0.20$ , with carrier concentrations,  $\sim 10^{15} \text{ cm}^{-3}$ , which are generally considered to be typical of the background impurity levels. A major problem with MOVPE appears to be the large diffusion coefficient of the Hg vacancies, with several studies suggesting post growth Hg interdiffusion into the layers as the cause of the anomalous n-type properties.<sup>1,5</sup> Experimental evidence for this model is provided by the work of Ghandi et al.,<sup>6</sup> who showed the carrier type of undoped layers to depend on cool-down procedure and to be p-type if quenched from the growth temperature or grown with a thin CdTe capping layer. In the present work, we have investigated these anomalous properties in detail and present new results on the composition dependence of the conversion process.

### EXPERIMENTAL

Layers were grown in a horizontal atmospheric pressure reactor using the interdiffusion multilayer process, in which alternate layers of CdTe and HgTe are grown and then diffused at the growth temperature to form homogeneous MCT. Growth of the layers was carried out at 370°C using di-isopropyltelluride (DIPT), dimethylcadmium (DMC), and elemental Hg. The IMP period was 0.2  $\mu\text{m}$  and the layers were interdiffused annealed for 10 to 30 minutes in a Hg pressure of  $1 \times 10^{-2} \text{ atm}$ . Substrates were 2° off orientation (100) GaAs and CdTe obtained from commercial suppliers. For growth on GaAs, a 3–4  $\mu\text{m}$  thick CdTe buffer layer was grown prior to the MCT to prevent Ga diffusion and reduce the misfit dislocation density. The MCT layers had  $x$  values between 0.2 and 0.3 and were 10–15  $\mu\text{m}$  thick. The Hg source, which was contained in a boat within the reactor chamber and maintained at 180°C during growth and

interdiffusion anneal, was cooled quickly to minimize post growth annealing. Typically, the time taken for the layer and Hg source to cool to 50°C was 20 and 15 min, respectively, which results in the layers being significantly below the Hg saturated phase boundary throughout cool down.<sup>3</sup> Other details of the growth process, including the In doping, were reported previously.<sup>7</sup> Selected layers were ex-situ isothermally annealed in closed ampoules at 200°C for 1 to 5 h in a Hg-rich atmosphere.

Thickness,  $d$ , and composition,  $x$ , of the layers were determined by IR transmission, the data of Finkman and Schacham<sup>8</sup> at an absorption coefficient of  $600 \text{ cm}^{-1}$  being used to determine  $x$ . These measurements were made on 4 mm square van der Pauw samples used for the Hall effect in order to eliminate errors arising from uniformity variations across wafers and allow a precise correlation of electrical properties with  $x$  and  $d$ . Variable magnetic field Hall measurements over the  $B$  range 0.01 to 1 T were used to assess the electrical properties. Such measurements have already been demonstrated to be effective for assessing inhomogeneity in MCT,<sup>9</sup> but are made here at 77 K as layers are chemically thinned to allow the accurate determination of carrier profiles and junction depth. Layers were etched in 5% bromine: ethylene glycol solution at 25°C in 1 to 2  $\mu\text{m}$  steps. This etch was selected on the basis of etch rate and reproducibility,  $1.0 \pm 0.2 \mu\text{m}$  per min, and Te rich surface condition, which gives low electron surface state densities  $\leq 3 \times 10^{10} \text{ cm}^{-2}$  even at  $x = 0.20$ . The data was analyzed using the expressions for the sheet Hall coefficient,  $R_s$ , and conductivity,  $\sigma_s$ , of a two carrier system given by

$$R_s = \frac{R_n \sigma_n^2 + R_p \sigma_p^2 + B^2 R_n R_p \sigma_n^2 \sigma_p^2 (R_n + R_p)}{(\sigma_n + \sigma_p)^2 + B^2 \sigma_n^2 \sigma_p^2 (R_n + R_p)^2} \quad (1)$$

$$\sigma_s = \frac{(\sigma_n + \sigma_p)^2 + B^2 \sigma_n^2 \sigma_p^2 (R_n + R_p)^2}{\sigma_n (1 + B^2 R_n^2 \sigma_p^2) + \sigma_p (1 + B^2 R_p^2 \sigma_n^2)} \quad (2)$$

where  $\sigma_n = e \mu_n p_n$ ,  $\sigma_p = e \mu_p n_p$ , and  $R_n = -1/en_n$ ,  $R_p = +1/ep_p$ , which assumes a Hall scattering factor of unity. By fitting to the sheet Hall coefficient and Hall mobility variation with  $B$  the sheet parameter  $n_s$ ,  $p_s$ ,  $\mu_n$ ,  $\mu_p$  are obtained for each etched thickness. The criteria

$$n_s = \sum n_s \quad \sigma_s = \sum \sigma_s$$

is applied at each thickness to limit the range of the fitting parameters and allow rapid convergence to the data. The carrier profiles are determined from

$$n\left(d - \frac{\delta d}{2}\right) = \frac{n_s(d) - n_s(d - \delta d)}{\delta d}$$

on the assumption of constant  $\mu_n$  and  $\mu_p$ , which is confirmed in this work by calculating the differential mobility using

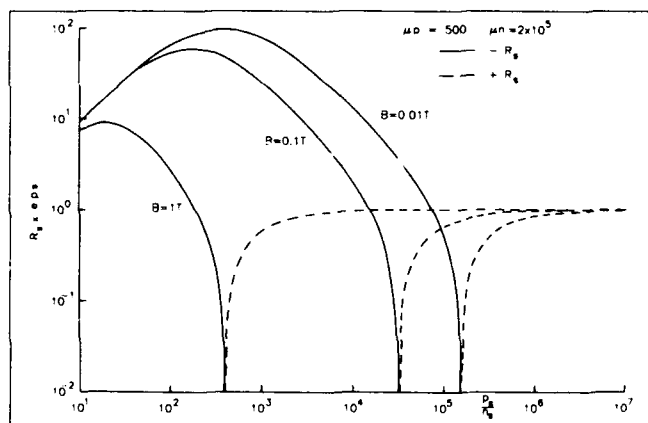


Fig. 1. Theoretical dependence of normalized sheet Hall coefficient on  $\frac{p_n}{n_s}$  ratio.

$$\mu\left(d - \frac{\delta d}{2}\right) = \frac{\sigma_s(d) - \sigma_s(d - \delta d)}{n\left(d - \frac{\delta d}{2}\right)}$$

As an alternative to the fitting procedure, we use a simple graphical analysis for screening samples, which permits an approximate value of  $p_s/n_s$  to be obtained simply from the relative change in the sign and magnitude of  $R_s$  with  $B$  and also allows the  $R_s(B)$  dependence to be predicted for a known structure. Such a plot is shown in Fig. 1, normalized to  $p_s$ , for the range of  $p_s/n_s$  values over which  $R_s$  will be magnetic field dependent at 77K in the present work. Considering the plot as three  $p_s/n_s$  regions, we see that  $R_s$  will be  $B$  dependent and (1) negative when  $10 < p_s/n_s < 3 \times 10^2$ , (2) change sign when  $3 \times 10^2 < p_s/n_s < 1.5 \times 10^5$ , and (3) positive when  $1.5 \times 10^5 < p_s/n_s < 1 \times 10^6$ .

Figure 1 was calculated assuming electron and hole mobilities of  $2 \times 10^5$  and  $500 \text{ cm}^2\text{V}^{-1}\text{s}^{-1}$ , respectively, which are typical of the 77K mobility values measured in undoped MOVPE MCT at  $x = 0.20$  with electron and hole concentrations, of  $1 \times 10^{15}$  and  $1 \times 10^{16} \text{ cm}^{-3}$ , respectively. At higher  $x$  values and carrier concentrations, the electron mobility is lower and this reduces the range of  $p_s/n_s$  values over which  $R_s$  is  $B$  dependent and also the magnitude of the change in  $R_s$  with magnetic field. Use of Fig. 1 for all  $x$  values between 0.20 and 0.30, therefore, results in some over estimate of  $p_s/n_s$  at higher  $x$ , although this is not significant in the present work.

## RESULTS AND DISCUSSION

The electrical properties of layers without CdTe capping layers show a dependence on composition. This dependence is evident from data on a large number of layers grown on both CdTe and GaAs substrates, despite some run to run variability in the properties of layers grown under nominally identical conditions. It is most pronounced in thin layers,  $\sim 10 \mu\text{m}$  thick, on GaAs grown to produce a large variation in  $x$  in a single growth run, effectively by depleting the gas stream through placing substrates along the length of the susceptor, and thereby eliminating run to run variability. The resulting variation of  $R$ -vs- $B$  with  $x$  was then as shown in Fig. 2, with both the sign and magnitude of  $R$  being  $B$  dependent at  $x < 0.25$ . This behavior is consistent with an increase in  $p_s/n_s$  with  $x$  from  $2.5 \times 10^2$  at  $x = 0.218$  to  $> 10^6$  at  $x = 0.25$ . (Precise values of  $p_s/n_s$  determined by fitting to these curves are 370,  $8.0 \times 10^3$  and  $1.7 \times 10^5$ , but to allow comparison we use  $p_s/n_s$  values derived from Fig. 1 here). For the wider range of undoped layers on GaAs, the  $p_s/n_s$  variation with  $x$  is as shown in Fig. 3. For  $x > 0.25$   $R$  is positive and independent of  $B$  and hence  $p_s/n_s$  has the value typical of uniform  $p$  type material, i.e.  $> 1 \times 10^6$ , while for  $x < 0.25$   $p_s/n_s$  is strongly  $x$  dependent.

The results of Fig. 3 are not caused by surface or mixed conduction effects but predominantly arise

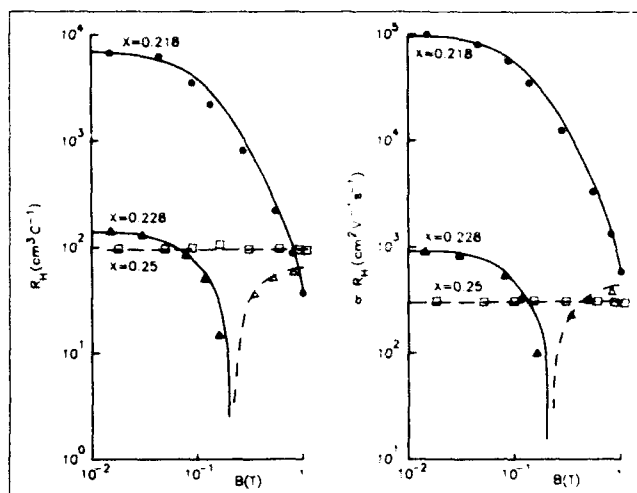


Fig. 2. Variation of  $R(B)$  and  $\sigma R(B)$  with  $x$ . Curves fit to data for  $\frac{p_s}{n_s}$  of  $3.7 \times 10^2$ ,  $7.9 \times 10^3$ ,  $> 2 \times 10^5$ .

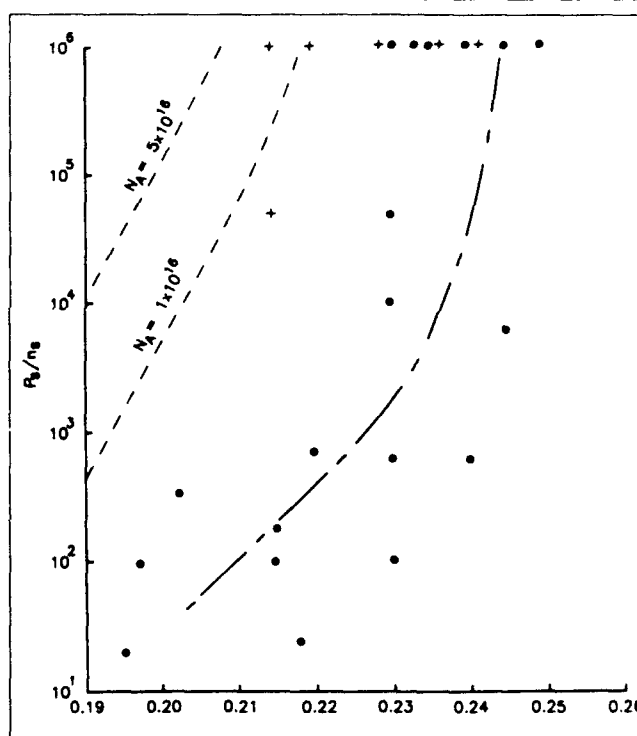


Fig. 3. Dependence of  $\frac{p_s}{n_s}$  on  $x$  of undoped layer on GaAs.  $\cdot$  uncapped,  $+$   $0.2 \mu\text{m}$  CdTe cap; dot-dashed curve  $\frac{p_s}{n_s} = 10^2 \left( \frac{x}{0.2} - 1 \right)$ .

from inhomogeneity. This was proved by thinning layers and establishing that  $R$ -vs- $B$  exhibited a dependence on thickness. Figure 4 shows the  $R$ -vs- $B$  variation with layer thickness on thinning an  $x = 0.218$  sample from 13 to  $10 \mu\text{m}$ . Referring to Fig. 1 we see that this  $R$ -vs- $B$  dependence is consistent with a decrease in  $p_s/n_s$  ratio from  $10^5$  at  $10 \mu\text{m}$  (where  $R$  is positive and  $B$  dependent) to 370 at  $13 \mu\text{m}$  (where  $R$  is negative at all  $B$ ). On further thinning, this sample to  $d < 9 \mu\text{m}$ ,  $R$  was found to be positive and independent of  $B$  thereby showing the underlying bulk to be uniformly  $p$ -type. The carrier profile for this layer, derived from the  $R$ -vs- $B$  data, is shown in Fig. 5. From this it can be seen that the layer consists of an  $n$  on  $p$

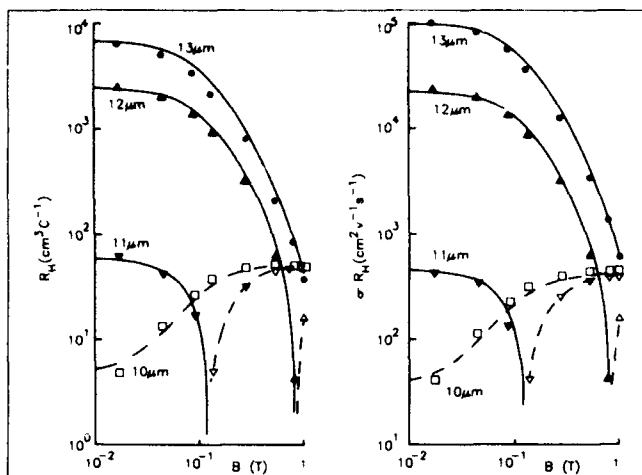


Fig. 4. Variation of  $R(B)$  and  $\sigma R(B)$  with etched thickness of  $x = 0.22$  undoped layer. Curve, fit to data for  $p_n/n_s$  of  $3.7 \times 10^2$ ,  $8.7 \times 10^2$ ,  $1.3 \times 10^4$ ,  $6.1 \times 10^4$ .

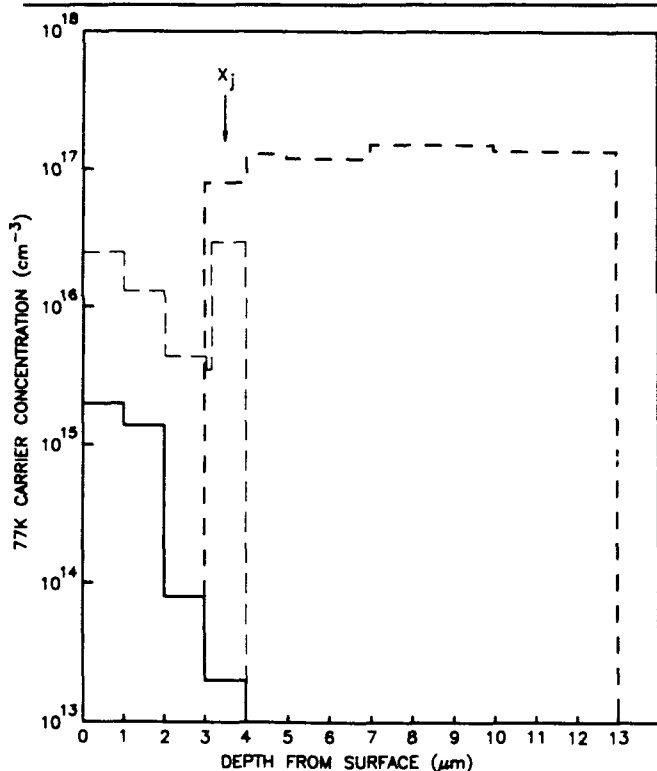


Fig. 5. Differential carrier profile of  $x = 0.22$  undoped layer. Solid line  $n(d)$ , dashed line  $p(d)$ .

structure, with an abrupt junction at a depth  $X_j$  of  $3.5 \pm 0.5 \mu\text{m}$  and almost constant carrier concentrations in the  $n$  and  $p$  regions. We note that the profile calculated from equations which neglect the  $B$  dependence of  $R$ , lightly dashed line, is significantly different from the real profile. The latter simpler analysis, which is often employed in commercial Hall profilers, also introduces errors in mobility profile and junction depth determination. For example, the differential electron mobility profile is flat at  $1 \times 10^5 \text{ cm}^2 \text{ V}^{-1} \text{ s}^{-1}$  for this sample, whereas the simpler analysis shows a gradient in  $\mu_n$ .

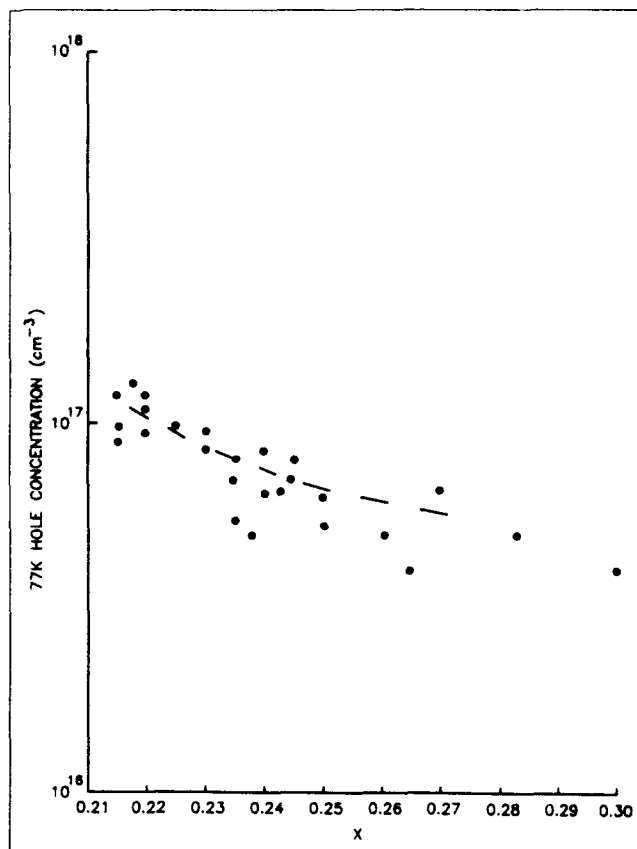


Fig. 6. Variation of 77K hole concentration with  $x$  of undoped layers on GaAs.

On profiling layers across the range of compositions we find all layers with  $x$  between 0.21 and 0.24 to be  $n$  on  $p$ -type structures and those with  $x < 0.21$  and  $x > 0.25$  to be uniform  $n$  and  $p$ -type layers, respectively. Significantly the differential carrier concentrations in the  $n$  on  $p$  structures are similar to those in the uniform  $n$  and  $p$ -type layers, where  $n = 5 \times 10^{14} - 2 \times 10^{15} \text{ cm}^{-3}$  and  $p = 4 - 8 \times 10^{16} \text{ cm}^{-3}$ , respectively. Across the range of  $x$ , there is a slight dependence of  $p$  on  $x$ , see Fig. 6, but to a first approximation  $p$  can be considered constant at  $1 \times 10^{17} \text{ cm}^{-3}$ . However in the  $n$  on  $p$  structures a large variation with  $x$  in the depth of the junction from the surface,  $X_j$ , is found. This dependence, shown in Fig. 7, appears to indicate that  $X_j$  is comparable to the thickness of the layers,  $10 - 15 \mu\text{m}$ , at  $x < 0.21$ . Using the data of Fig. 7, we calculate the  $p_n/n_s$  variation with  $x$  expected for an abrupt junction with constant  $n$  and  $p$  carrier concentrations of  $1 \times 10^{15}$  and  $1 \times 10^{17} \text{ cm}^{-3}$ , respectively. This simple model gives  $p_n/n_s = 10^2 \times (d/X_j - 1)$ , which can be seen from the dashed line in Fig. 3 to give a good fit to the data for uncapped layers, considering the variations in carrier concentrations and layer thickness between samples.

The  $p$  and  $n$ -type carrier concentrations and profiles of the layers are consistent with the inadvertent post-growth Hg indiffusion model normally used to explain the anomalous  $n$  type properties.<sup>4,5,6</sup> The  $p$ -type carrier level will be determined by the concentra-

tion of Hg vacancies.  $N_v$ , which we assume are singly ionized acceptors at 77K, while the n-type will be determined by the concentration of residual impurities. For the present growth conditions,  $N_v$  has been established to be  $\sim 1 \times 10^{17} \text{ cm}^{-3}$  at  $x = 0.20$  and to be lower at higher  $x$  while the background carrier concentration in fully annealed MOVPE layers is typically found to be in the range  $3 \times 10^{14} - 2 \times 10^{15} \text{ cm}^{-3}$ , depending on substrate with layers on GaAs generally having higher backgrounds due to Ga contamination.<sup>10</sup> Also the carrier profiles in these as-grown layers are abrupt and appear to be similar to those reported for Hg diffusion into bulk crystals.<sup>11</sup> Such abrupt profiles, which cannot be fitted by a simple error function, are known to be associated with a diffusion process involving Hg interstitials.<sup>11,12</sup> Furthermore, in agreement with the earlier work, we find the inhomogeneity significantly reduced, although not totally eliminated at low  $x$  by capping layers with  $0.2 \mu\text{m}$  of CdTe. Such  $0.2 \mu\text{m}$  CdTe capped layers have significantly higher  $p/n_s$  values than the equivalent uncapped layer, see Fig. 3, thereby confirming the essential features of the Hg indiffusion model.

The effectiveness of a thin CdTe cap in preventing Hg indiffusion during cooling is attributed to the significantly lower Hg diffusion coefficient,  $D_{\text{Hg}}$  in CdTe than  $\text{HgCdTe}$ . Recent work<sup>13</sup> has shown that  $D_{\text{Hg}}$  varies by nearly six orders across the composition range at  $300^\circ\text{C}$ . By analogy, the Hg diffusion coefficient responsible for the type conversion, defined as  $D_c$ , might also be expected to be a strong function of  $x$ , even though it is recognized that different defects and diffusion mechanisms may be involved. However, despite the implications for device processing, there appear to be few reports of an  $x$  dependence of the conversion process either for bulk or epitaxial material. If the conversion process involves interstitial Hg as proposed by Jones et al.,<sup>12</sup> then  $X_j$  should be proportional to  $\sqrt{D_c t / N_v}$  where  $t$  is the anneal time. In our work, the annealing schedule should be constant even though the Hg pressure and temperature vary during cool down and hence to a first approximation we would expect  $D_c \propto X_j^2$ . From Fig. 7, it can be seen this implies a variation in  $D_c$  of some two orders of magnitude over the  $x$  range 0.20 to 0.30, which seems excessive and may indicate that there are additional mechanisms converting the layers to n-type at low  $x$ . The magnitude of the conversion depth at  $x = 0.20$  seems particularly large given the short cool down

time, 20 min, and relatively low Hg temperatures,  $< 180^\circ\text{C}$ . In this context, we note that to convert  $10 \mu\text{m}$  of bulk crystal in 20 min would require a Hg rich anneal at the higher temperature of  $280^\circ\text{C}$ ,<sup>11</sup> which suggests a faster conversion process for the MOVPE layers.

To establish that the  $p/n_s$  and  $X_j$  dependence on  $x$  was a fundamental effect and not influenced by other factors in the growth process, uniform p type MCT capped layers were Hg rich annealed at  $200^\circ\text{C}$  to form n on p structures. For these experiments, an anneal time was selected which gave values for  $X_j$  at  $x = 0.24$  similar to that for as-grown uncapped layers. Also, some doped layers with [In] concentration  $\sim 1 - 6 \times 10^{15} \text{ cm}^{-3}$  were used in order to eliminate the uncertainty introduced by unknown level of background impurities. The results of these experiments, in which each anneal consisted of samples with a range of  $x$  values,

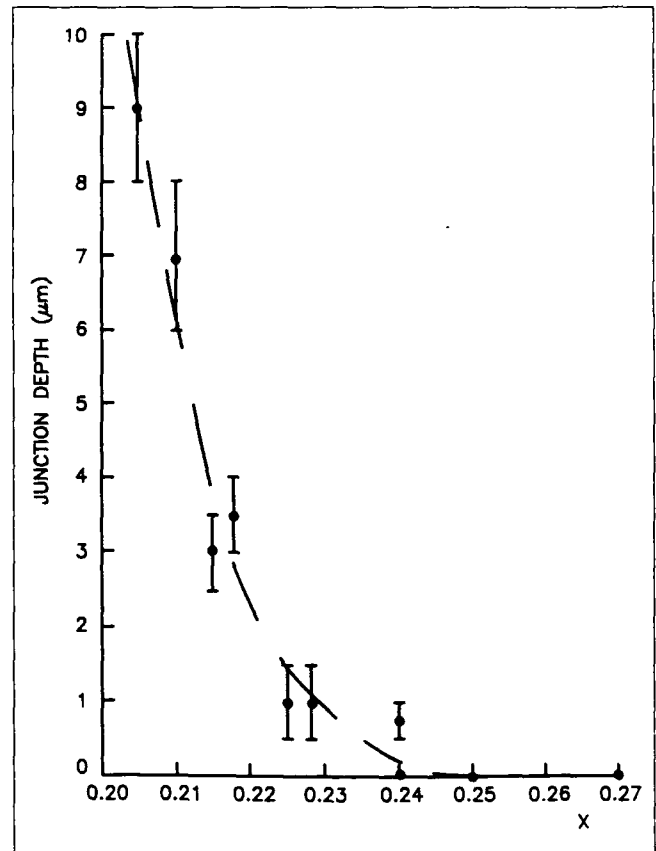


Fig. 7. Variation of n-p junction depth with  $x$  of undoped layer on GaAs.

Table I.  $p/n_s$  and  $X_j$  Dependence on  $x$  of MOVPE Layers Annealed at  $200^\circ\text{C}$  for 75 min in Hg

| Substrate | Doped | In<br>(atom $\text{cm}^{-3}$ ) | $x$  | $p/n_s$     | $X_j$<br>( $\mu\text{m}$ ) | $n_{77\text{K}}$<br>( $\text{cm}^{-3}$ ) | $p_{77\text{K}}$<br>( $\text{cm}^{-3}$ ) |
|-----------|-------|--------------------------------|------|-------------|----------------------------|--|--|
| CdTe      | Yes   | $\sim 2.10^{15}$               | 0.30 | $\geq 10^6$ | 0                          | —  | $2.5.10^{16}$                            |
| GaAs      | No    | —                              | 0.26 | $3.10^2$    | 0.5                        | $1.5.10^{15}$                            | $5.10^{16}$                              |
| GaAs      | No    | —                              | 0.24 | $3.10^1$    | 2.5                        | $3.10^{15}$                              | $6.5.10^{16}$                            |
| CdTe      | Yes   | $3.5.10^{15}$                  | 0.24 | $3.10^1$    | 2.5                        | $2.10^{15}$                              | $4.10^{16}$                              |
| CdTe      | Yes   | $\sim 1.10^{16}$               | 0.22 | $2.10^1$    | 3.5                        | $1.10^{16}$                              | $7.10^{16}$                              |
| CdTe      | Yes   | $\sim 5.10^{15}$               | 0.20 | $\leq 10^1$ | 6                          | $4.10^{15}$                              | $8.10^{16}$                              |

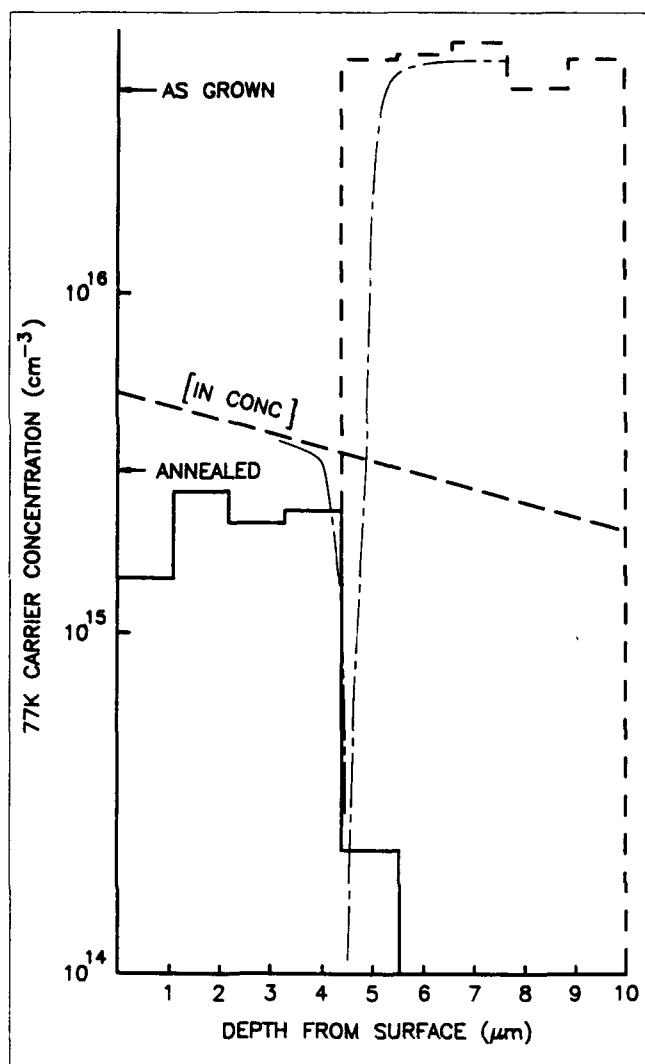


Fig. 8. Differential carrier profile of annealed In doped layer. Solid line  $n(d)$ , dashed line  $p(d)$ . Lightly dashed line error function profile (see text).

are given in Table I. The  $p/n_s$  and  $X_j$  variation with  $x$  in these samples is essentially the same as that shown in Figs. 4 and 7, thereby confirming the detailed behavior of the in-diffusion process and the inferred  $x$  dependence of  $D_c$ , which appears to be a significant effect in short duration low temperature anneals. Despite the good overall agreement, however, these preliminary experiments show the detailed behavior of annealed and as-grown uncapped layers to be different. Firstly, low  $x$  layers on GaAs are found difficult to convert and to exhibit a large decrease in p-type carrier levels on annealing. The reason for this is not fully understood but is thought to be due to a high concentration of background acceptor impurities in low  $x$  layers on GaAs.<sup>14</sup> Secondly, the conversion depth at  $x = 0.20$  is smaller in ex-situ annealed layers on CdTe substrates, particularly when compared to as-grown layers on GaAs. This occurs even though  $N_A$  is 50% greater for layers on GaAs, which should reduce the junction depth.<sup>12</sup> This is also not understood but may be due to  $X_j$  and  $D_c$ , being depen-

dent on the dislocation density, which is some order of magnitude greater for layers on GaAs than CdTe.

An important result in Table I is the good agreement at  $x = 0.20$  with the  $X_j$  values observed in bulk<sup>12</sup> and LPE<sup>15,16</sup> annealed material,  $x^2/t = 11.5$  at 200°C when normalized to  $N_A = 2 \times 10^{17} \text{ cm}^{-3}$ . This suggests the annealing behavior of MOVPE (IMP) material is not significantly different to bulk material with a similar dislocation density,  $< 1 \times 10^6 \text{ cm}^{-2}$ , and donor concentration,  $< 1 \times 10^{16} \text{ cm}^{-3}$ . The latter parameter, donor concentration, seems unlikely to influence  $x$  given the abruptness of the carrier concentration profiles. Figure 8 shows the profile of an annealed In doped sample, from which it is evident that, despite the limited resolution of the measurement, there is a near step like transition in n and p-type carrier concentration in these low temperature annealed structures. To account for such a profile,  $N_A$  must vary by more than an order of magnitude from  $1 \times 10^{15}$  to  $4 \times 10^{16} \text{ cm}^{-3}$  over a distance of half a micron which is not compatible with an error function diffusion profile. To demonstrate this, the carrier profile, neglecting depletion effects, for an error function assuming a surface concentration of  $1 \times 10^{20} \text{ cm}^{-3}$  and an interstitial/vacancy diffusion mechanism has been calculated—dashed line in Fig. 8. Although this agrees reasonably with the data, it still does not give a precise fit and suggests the more comprehensive analysis used by Bogoboyashchii et al.<sup>11</sup> is required. We note that to account for  $X_j$ ,  $D_c$  must have a value greater than the fast component of the Hg self diffusion coefficient and is not compatible with the slow component despite suggestions to the contrary.<sup>16</sup>

## CONCLUSIONS

Variable magnetic field Hall measurements at 77K provide a fast and simple method for screening MCT for inhomogeneity and allowing the sheet hole to electron concentration to be determined in p-n junction structures. When made as a function of layer thickness by chemical stripping the technique can be used to determine accurately the carrier and mobility profiles of epitaxial layers, albeit with a depth resolution of 1  $\mu\text{m}$  at present. Applying the technique to undoped and lightly In doped MOVPE (IMP) layers has allowed the confirmation of the post growth Hg in-diffusion model for the anomalous electrical properties of as-grown layers. These anomalous properties are found to result from an n on p structure and to be  $x$  dependent due to a variation in n to p conversion depth with  $x$  over the range 0.20 to 0.25. Ex-situ annealing experiments, performed to reproduce the inhomogeneity via a low temperature Hg rich anneal, confirm the  $x$  dependence of conversion depth but show it is a weaker function of  $x$  in annealed samples than in as-grown layers. This may be due to the difference in anneal conditions or other factors, such as a type conversion depth dependence on the dislocation density or initial stoichiometry. The conversion depth data suggests there is greater than an order of magnitude variation in the Hg diffusion coefficient



responsible for type conversion over the  $x$  range 0.20 to 0.30 at low temperatures in MOVPE layers. This effect may also occur in MCT grown by other methods as the conversion depth in MOVPE (IMP) annealed layers on CdTe at  $x=0.20$  is similar to that of bulk and LPE. Carrier and mobility profiles of both as-grown and annealed n on p structures are abrupt and consistent with an interstitial Hg model for the conversion process.

### ACKNOWLEDGMENTS

The authors are grateful to Mr. N. Shaw for annealing samples, Mr. M. Houlton for SIMS and Mrs. A. Horsfall for Hall measurements.

### REFERENCES

1. I.B. Bhat, N.R. Taskar and S.K. Ghandi, *J. Vac. Sci. Technol.* A4, 2230 (1986).
2. D.D. Edwall, J. Bajaj and E.R. Gertner, *J. Vac. Sci. Technol.* A8, 1045 (1990).
3. H.R. Vidyantath and C.H. Hiner, *J. Appl. Phys.* 65, 3080 (1989).
4. I.B. Bhat and S.K. Ghandi, *Mater. Res. Soc. Symp. Proc.* 56, 392 (1986).
5. S.J.C. Irvine, J.S. Gough, J. Giess, M.J. Gibbs, A. Royle, C.A. Taylor, G.T. Brown, A.M. Keir and J.B. Mullin, *J. Vac. Sci. Technol.* A7, 285 (1989).
6. S.K. Ghandi, I.B. Bhat and H. Fardi, *Appl. Phys. Lett.* 52, 392 (1988).
7. M.L. Young, M.G. Astles, J.S. Gough, M.R. Houlton and N. Shaw, *Semicond. Sci. Technol.* 6, C31-35 (1991).
8. E. Finkman and S.E. Schiacham, *J. Appl. Phys.* 56, 2896 (1984).
9. A. Zemel, A. Sher and D. Eger, *J. Appl. Phys.* 62, 1861 (1987).
10. R. Korenstein, P. Hallock, B. Macleod, W. Hoke and S. Oguz, *J. Vac. Sci. Technol.* A8, 1039 (1990).
11. V.V. Bogoboyashchii, A.I. Elizarov, V.I. Ivanov-Omskii, V.R. Petrenko and V.A. Petryakov, *Sov. Phys. Semicond.* 19, 505 (1985).
12. C.L. Jones, M.J.T. Quelch, P. Capper and J.J. Gosney, *J. Appl. Phys.* 53, 9080 (1982).
13. N.A. Archer, H.D. Palfrey, A.F.W. Willoughby, this proceeding.
14. G.W. Blackmore, J. Giess, M.G. Astles, N. Shaw, J.S. Gough and M.L. Young, *SIMS VIII*, ed. A. Benninghoven, A.M. Huber and H.W. Werner, (Wiley, Chichester, UK, 1992) p. 467.
15. D.T. Dutton, E. O'Keefe, P. Capper, C.L. Jones, S. Mugford and C. Ard, *Semicond. Sci. Technol.* in press.
16. P. Koppel and K. Owens, *J. Appl. Phys.* 67, 6886 (1990).

# Characterization of $\text{Hg}_{1-x}\text{Cd}_x\text{Te}$ Heterostructures by Thermoelectric Measurements

J. BAARS and D. BRINK

Fraunhofer-Institut für Angewandte Festkörperphysik, Tullastr. 72, D-7800 Freiburg, Germany

D.D. EDWALL and L.O. BUBULAC

Rockwell International Science Center, Thousand Oaks, CA 91360, U.S.A.

P-on-n mercury cadmium telluride (MCT) heterostructures grown by MOCVD with As and In as n- and p-type dopants, respectively, are examined by measuring the Seebeck and Hall coefficients between 20 and 320K. The results are analyzed regarding doping and composition of the layers by least squares fitting the experimental profiles with the calculated temperature dependencies. The electron and hole densities of the layers are calculated taking into account Fermi-Dirac statistics, a nonparabolic conduction band, a parabolic valence band, a discrete acceptor level, and fully ionized donors. For the Seebeck coefficient, the relation we previously showed to be valid for p-type MCT<sup>1</sup> is used. This relation relies on the thermoelectric effect in a temperature gradient resulting from the diffusion of nondegenerate carriers scattered by LO-phonons. It also fits the observed thermoelectric properties of n-type MCT in a wide temperature range. The doping and structural parameters determined from the thermoelectric measurements agreed very well with As and In profiles obtained from secondary ion mass spectroscopy measurements and the data obtained from analyses of infrared transmission measurements.

**Key words:** As doping, HgCdTe, In doping, MOCVD, SIMS, thermoelectric effects

## INTRODUCTION

$\text{Hg}_{1-x}\text{Cd}_x\text{Te}$  (MCT) heterostructures consisting of a thin p-type wide gap ( $x = 0.3$ ) layer deposited on an n-type narrow gap ( $x = 0.22$ ) layer offer considerable advantages for 8–12  $\mu\text{m}$  infrared focal plane arrays. Reliable nondestructive characterization methods to determine doping and compositional profiles of the p-type layer in particular are highly desirable. The examination by Hall effect is difficult because the contribution of an individual layer to the Hall coefficient is proportional to the square of its conductance; and, due to the large electron-to-hole mobility ratio, the conductance of the p-type layer is small compared to that of the n-type layer. The thermoelectric effect, however, is a linear function of the layer conductance and offers greater characterization potential for heterostructures.

In this study, p-on-n heterostructures grown by

metalorganic chemical vapor deposition (MOCVD) with As and In as p- and n-type dopants, respectively, were examined by measuring the Seebeck and Hall coefficients between 20 and 320K. The results were analyzed regarding doping and composition of the layers by least squares fitting the experimental profiles with calculated temperature dependencies. We calculated the electron and hole densities of the layers taking into account Fermi-Dirac statistics, a nonparabolic conduction band, a parabolic valence band, a discrete acceptor level, and fully ionized donors. For the Seebeck coefficient, the relation we previously showed to be valid for p-type MCT is used.<sup>1</sup> This relation relies on the thermoelectric effect in a temperature gradient resulting from the diffusion of nondegenerate carriers scattered by LO-phonons. It also fits the observed thermoelectric properties of n-type MCT in a wide temperature range, even though the electron density is slightly degenerate. The doping and structural parameters determined from the thermoelectric measurements agreed very well with

(Received October 14, 1992; revised January 21, 1993)

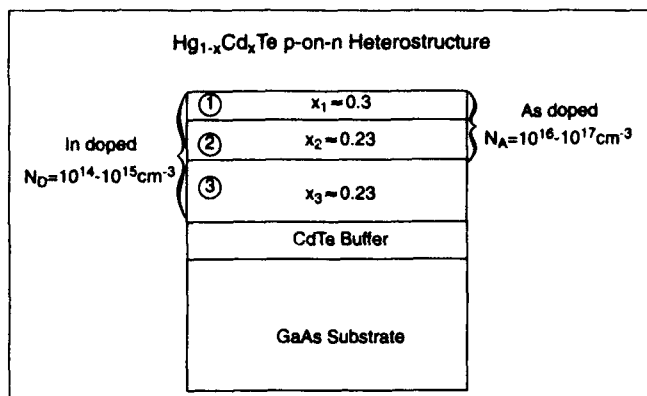


Fig. 1. Schematic cross-sectional view of the MCT p-on-n heterostructures consisting of a p-type wide gap cap (1), a p-type narrow gap absorber (2), and an n-type narrow gap absorber (3). The entire structure is In-doped, and the p-type layers are additionally doped with As.

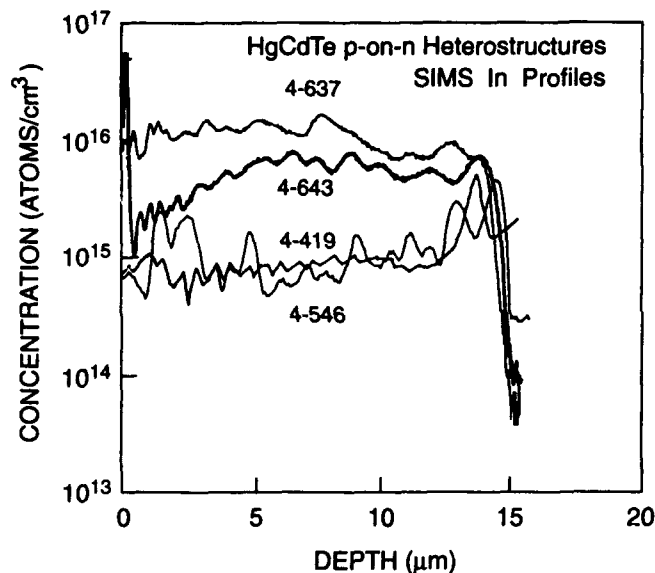


Fig. 2. Indium concentration profiles of the p-on-n heterostructures used in this study as determined by SIMS.

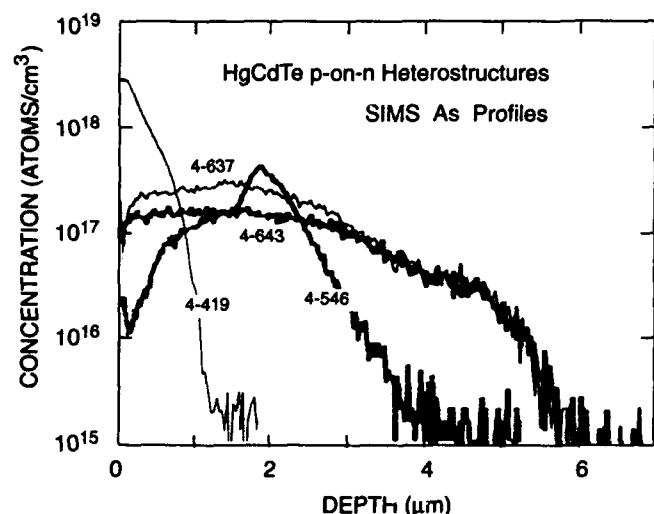


Fig. 3. Arsenic concentration profiles of the p-on-n heterostructures used in this study as determined by SIMS.

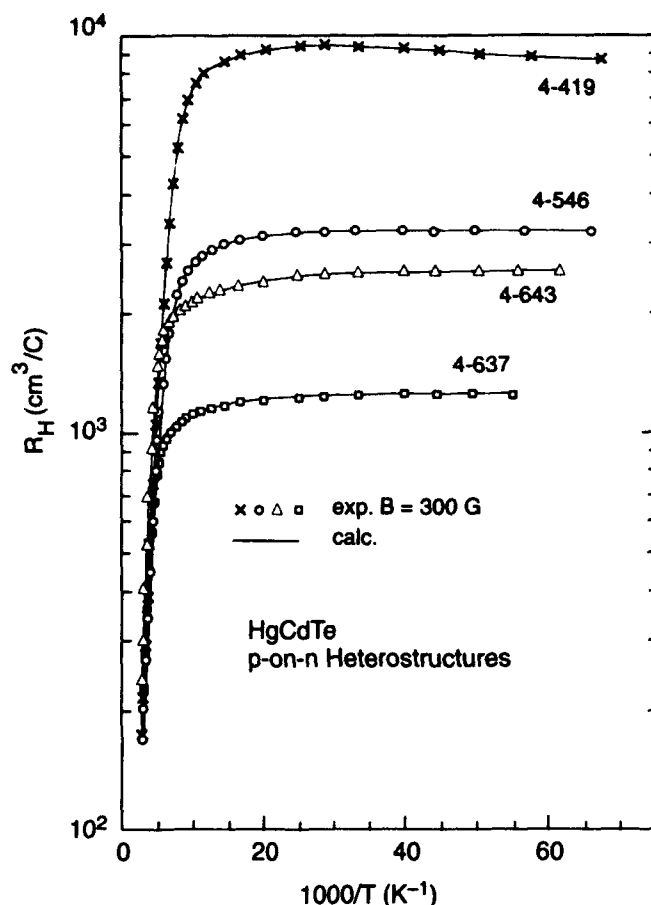


Fig. 4. Hall coefficients,  $R_H$ , of the specimens used in this study for a magnetic field of 300G vs reciprocal temperature between 15 and 320K. The solid curves represent the least squares fits to the experimental data.

the data obtained from infrared transmission analyses and As and In profiles obtained from SIMS measurements.

## EXPERIMENT

The p-on-n MCT heterostructures used for this study were epitaxially grown on  $\langle 100 \rangle$  GaAs substrates by metalorganic chemical vapor deposition using the interdiffused growth method.<sup>2-4</sup> Figure 1 schematically illustrates their layer structure. The heterostructures consist of three layers: a p-type wide-gap cap on top, a p-type narrow-gap absorber, and an n-type narrow-gap absorber on the bottom. The entire structures are In-doped, and the p-type layers are additionally doped with As. The In and As concentration profiles of the specimens shown in Figs. 2 and 3 were determined by SIMS performed at Charles Evans Associates. The SIMS Te profiles were used to analyze the heterostructures regarding layer composition<sup>5</sup> and thickness. The compositions of the narrow gap layers were obtained also from infrared transmission measurements of the fundamental absorption edge at temperatures of 77 and 300K.<sup>6</sup> The results of the analyses are listed in Table I.

In addition to the thermoelectric investigations, the heterostructures were examined by variable tem-

**Table I. CdTe Mole Fractions  $x$ , Acceptor and Donor Densities  $N_A$ ,  $N_D$ , and Thicknesses  $d$  of the Layers for the P-on-N Heterostructures**

| Layer Sample | Method  | $x$  |      |       | $N_A (10^{16} \text{cm}^{-3})$ |             | $N_D (10^{16} \text{cm}^{-3})$ |               |           | $d (\mu\text{m})$ |              |               |
|--------------|---------|------|------|-------|--------------------------------|-------------|--------------------------------|---------------|-----------|-------------------|--------------|---------------|
|              |         | 1    | 2    | 3     | 1                              | 2           | 1                              | 2             | 3         | 1                 | 2            | 3             |
| 4-419        | Seebeck | 0.29 | 0.23 | 0.222 | 2.0                            | 2.0         | 0.7                            | 0.8           | 0.6       | 1.2               | 0.4          | 12.4          |
|              | Hall    | 0.2  | 0.22 | 0.21  | 5.8                            | 1.6         | 1.0                            | 1.4           | 0.8       | 1.1               | 0.6          | 12.3          |
|              | SIMS    | 0.30 | 0.22 | 0.22  | $100 \pm 50$                   | $2 \pm 1$   |                                | $0.8 \pm 0.2$ |           | $1 \pm 0.3$       | $13 \pm 0.3$ |               |
|              | IR      | —    | —    | 0.222 | —                              | —           | —                              | —             | —         | —                 | —            | —             |
| 4-546        | Seebeck | 0.28 | 0.20 | 0.220 | 4.4                            | 0.17        | 2.8                            | 1.2           | 2.0       | 1.9               | 2.1          | 10            |
|              | Hall    | 0.24 | 0.21 | 0.20  | 12                             | 4.5         | 0.3                            | 0.1           | 2.9       | 1.9               | 2.7          | 9.4           |
|              | SIMS    | 0.28 | 0.20 | 0.22  | $10 \pm 5$                     | $1 \pm 0.5$ | $1 \pm 0.5$                    | $1 \pm 0.5$   | $2 \pm 1$ | $2 \pm 0.3$       | $2 \pm 0.3$  | $10 \pm 0.3$  |
|              | IR      | —    | —    | 0.215 | —                              | —           | —                              | —             | —         | —                 | —            | —             |
| 4-637        | Seebeck | 0.30 | 0.21 | 0.234 | 9                              | 1.2         | 6.6                            | 11            | 4.2       | 4.7               | 1.2          | 9.1           |
|              | Hall    | 0.28 | 0.21 | 0.21  | 11                             | 5.8         | 2.8                            | 8.4           | 9.2       | 4.3               | 2.1          | 8.6           |
|              | SIMS    | —    | —    | —     | $20 \pm 5$                     | $3 \pm 1$   | $9 \pm 3$                      | $12 \pm 2$    | $8 \pm 2$ | $4 \pm 0.3$       | $1 \pm 0.3$  | $10 \pm 0.3$  |
|              | IR      | —    | —    | 0.231 | —                              | —           | —                              | —             | —         | —                 | —            | —             |
| 4-463        | Seebeck | 0.30 | 0.29 | 0.220 | 6.6                            | 2.0         | 5.2                            | 4.6           | 4.0       | 4.8               | 0.7          | 9.5           |
|              | Hall    | 0.25 | 0.20 | 0.212 | 15                             | 4           | 10.6                           | 2.3           | 5.0       | 4.2               | 3.5          | 7.3           |
|              | SIMS    | —    | —    | —     | $12 \pm 2$                     | $3 \pm 1$   | $4 \pm 2$                      | $5 \pm 1$     | $5 \pm 1$ | $4.5 \pm 0.3$     | $1 \pm 0.3$  | $9.5 \pm 0.3$ |
|              | IR      | —    | —    | 0.228 | —                              | —           | —                              | —             | —         | —                 | —            | —             |

Note: As determined from variable temperature Seebeck and Hall measurements, from SIMS As and In profiles, and from IR transmission at the fundamental absorption edge. The SIMS values are concentrations of As and In atoms. Accuracy estimates for the parameter values obtained from the Seebeck data analyses are:  $x_1 \pm 5\%$ ,  $x_2 \pm 10\%$ ,  $x_3 \pm 1\%$ ,  $N_{A1} \pm 10\%$ ,  $N_{A2} \pm 20\%$ ,  $N_{D1} \pm 30\%$ ,  $N_{D2} \pm 50\%$ ,  $N_{D3} \pm 10\%$ ,  $d_2/d_1 \pm 10\%$ ,  $d_3/d_1 \pm 20\%$ .

perature Hall-effect and conductivity measurements. Figure 4 presents the Hall coefficients of the specimens for a magnetic field of 300 G plotted vs the reciprocal temperature between 15 and 320K. For the conductivity and Hall effect measurements, we employed the van der Pauw method using Au leads bonded to Au/In contact pads evaporated at the edges of rectangular-shaped specimens measuring  $9 \times 12 \text{ mm}^2$ .

These contacts were also used for the thermoelectric measurements, which were performed by applying a temperature gradient parallel to the p and n layers of the heterostructure. The arrangement for measuring the thermoelectric power of the samples at temperatures between 15 and 320K by this lateral gradient technique is sketched in Fig. 5. Two sapphire plates are attached to the specimen, each covering about one quarter of the sample; a gap is left in the middle. The specimen and the sapphire plates are joined with a low temperature glue (GE 7031) to provide a good thermal contact. The sample is placed in a Sterling type cooling engine, one sapphire plate providing the thermal contact to the cold end, and the other to an electric heating foil. A copper cap at sample temperature served as a radiation shield. AuFe-NiCr thermocouples and Si diodes (Lakeshore DT-470), electrically insulated from the specimen by thin ceramic plates, are used to control the temperatures on both sides of the gap. To provide good thermal contact, the temperature sensors are glued to the

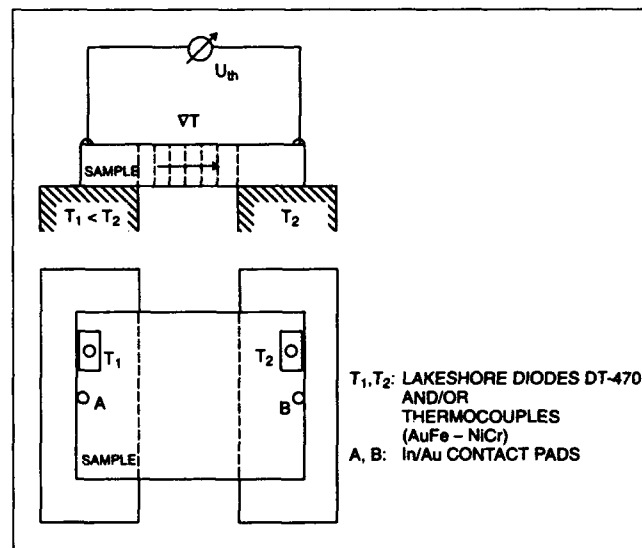


Fig. 5. Schematic arrangement for measuring the thermoelectric power of the heterostructures at temperatures between 20 and 300K.

specimen. A temperature difference of 2K across the gap is chosen for determining the Seebeck coefficient between 20 and 50K, and a difference of 5K at higher temperatures. The Seebeck coefficient  $\alpha$  is determined by the ratio of the measured thermoelectric voltage  $U_{th}$  to the temperature difference  $T_2 - T_1$  applied to the sample (Fig. 5)  $\alpha = U_{th}/(T_2 - T_1)$ .

The thermoelectric data obtained from the specimens using this experimental arrangement is repro-

ducible. The Seebeck coefficient vs temperature measured before and after removing the temperature sensors and gold wires completely, cleaning the sample, and replacing the sensors and wires again, exhibits variances smaller than 2%. Since the accuracy attained in determining the temperature difference across the gap establishes the degree of accuracy obtainable for the Seebeck coefficient, the temperature difference is measured independently by thermocouples and by calibrated diodes. The diodes proved to be reliable temperature sensors for the entire range between 10 and 300K, permitting the temperature to be controlled within one tenth of a degree K. The temperature difference measured by the thermocouples deviated by less than 5% from that obtained from calibrated diodes. Test measurements with zero temperature difference across the gap were also performed to ensure absence of spurious thermoelectric signals.

Prior to the thermoelectric and Hall-effect measurements, the samples were subjected to a special electrochemical etch<sup>7</sup> to provide clean surfaces of stoichiometric composition and thus to avoid surface inversion.

### THERMOELECTRIC MODEL

The differential thermoelectric voltage (DTV) or Seebeck coefficient of isotropic, cubic semiconductors is determined by the thermoelectric contributions due to electrons in the conduction band and holes in the valence band<sup>8</sup>

$$\alpha = (\alpha_e n \mu_e + \alpha_h p \mu_h) / (n \mu_e + p \mu_h) \quad (1)$$

Here,  $n$  and  $p$  are the densities,  $\mu_e$  and  $\mu_h$  are the mobilities, and  $\alpha_e$  and  $\alpha_h$  are the Seebeck coefficients of the electrons and holes, respectively.

The Seebeck coefficient is derived from the linearized Boltzmann equation. The phonon distribution is assumed to be in thermal equilibrium.<sup>9</sup> This assumption is justified for MCT at temperatures  $T > 30$ K, but it may fail at low temperatures when the interaction between the scattering phonons becomes weaker owing to their longer wavelength at lower temperatures. In fact, phonon drag of holes was effective in HgTe at temperatures below 30K.<sup>10,11</sup>

Therefore, the model used is limited to temperatures above 30K, and only the thermoelectric coefficients  $\alpha_{e,h}$  owing to the diffusion of electrons (e) and holes (h) in a temperature gradient are considered:

$$\alpha_{e,h} = k/q (\langle \epsilon \tau_{e,h} \rangle / \langle \tau_{e,h} \rangle - \eta_{e,h}), \quad (2)$$

where  $\epsilon = E/(kT)$ ,  $\eta_e = E_F/(kT)$ , and  $\eta_h = -(E_F + E_g)/(kT)$ .  $E$  is the energy measured from the edge of the conduction band,  $E_g$  the band gap energy,  $E_F$  the Fermi energy,  $T$  the temperature,  $k$  the Boltzmann constant,  $q$  the elementary charge ( $-e$  for electrons and  $+e$  for holes), and  $\tau$  the relaxation time. The kinetic term  $\langle \epsilon \tau_{e,h} \rangle / \langle \tau_{e,h} \rangle$  depends on the charge carrier scattering mechanisms involved. Optical phonons are by far the most effective scatterers for charge carriers in MCT, owing to its high ionicity, except at low tem-

peratures ( $T < 40$ K) where scattering by ionized defects prevails.<sup>11</sup> Excluding temperatures below 40K, this model uses the kinetic term derived by Devlin<sup>9</sup> for pure optical mode scattering of electrons and holes assuming nondegenerate charge carrier densities:

$$\langle \epsilon \tau_{e,h} \rangle / \langle \tau_{e,h} \rangle = 2.5 + 0.5/\exp[0.95(\Theta/T)^2] - 0.86 (\Theta/T)^{2.5}/\exp(\Theta/T) \quad (3)$$

The Debye temperature  $\Theta$  is assumed to be equal to the sum of the CdTe-like and HgTe-like LO phonon frequencies of MCT,  $\omega_{LO1}$  and  $\omega_{LO2}$ , weighed by the mole fractions  $x$  of CdTe and  $1-x$  of HgTe, respectively

$$\Theta = [x \omega_{LO1} + (1-x) \omega_{LO2}] hc/k, \quad (4)$$

where  $hc/k = 1.44$  cmK is the conversion factor to degree K. The LO phonon frequencies ( $\text{cm}^{-1}$ ) are linear functions of  $x$ <sup>12</sup>

$$\omega_{LO1} = (13 + 0.02T)x - 0.02T + 155, \quad (5)$$

$$\omega_{LO2} = -(10 - 0.01T)x - 0.01T + 140. \quad (6)$$

This thermoelectric model was adequate to p-type MCT.<sup>1</sup> It is confined to nondegenerate electron and hole densities, since Eq. 3 is based on the condition of nondegeneracy. In principle, however, the kinetic term may be calculated for the case of arbitrary degeneracy, and full Fermi-Dirac statistics may be used to evaluate the Seebeck coefficient for MCT. To limit the computational effort the model used here is restricted to nondegenerate statistics. P-type MCT with CdTe mole fractions larger than  $x = 0.18$  satisfies the condition of nondegeneracy since the Fermi energy in p-type MCT at temperatures between 10 and 300K is several  $kT$  below the conduction band edge. For n-type MCT, however, nondegeneracy presents a severe restriction with respect to temperature and donor densities. Therefore, the model is not expected to be valid for high donor densities or at low temperatures. For  $x = 0.22$  and donor densities on the order of  $10^{15} \text{ cm}^{-3}$ , for example, the Fermi energy ranges from 1 to 2  $kT$  below the conduction band edge at temperatures above 70K, and it enters the conduction band at about 50K.

Assuming the heavy-hole valence band of MCT to be parabolic and the effect of light holes to be negligible, the Fermi energy for nondegenerate p-type MCT is given by

$$E_F = kT \ln(N_v/p) - E_g, \quad (7)$$

$N_v = 2(2\pi m_{hh}^* kT/h^2)^{3/2}$  being the valence band effective density-of-states and  $m_{hh}^* = 0.5m_0$  the effective mass of the heavy holes. The Fermi energy for n-type MCT is calculated using Altschul and Finkman's<sup>13</sup> polynomial method based on Kane's<sup>14</sup>  $k_p$  model for the conduction band density-of-states

$$E_F = kT \ln[n(B_c N_c)] + \sum_j (B_j/B_c)^{1/2} (n/N_c)^{1/2}, \quad (8)$$

$N_c = 2(2\pi m_{co}^* kT/h^2)^{3/2}$  here being the conduction band effective density-of-states and  $m_{co}^*$  the effective electron mass at the conduction band minimum

$$m_{co}^* = 3m_0 (E_g/E_p)(\Delta + E_g)/(2\Delta + 3E_g). \quad (9)$$

$B_j$  and  $B_j$  for  $j = 1$  to 4 are functions of the band-gap energy and they are given for  $j = 1$  to 4 in Ref. 13.  $m_0$  is the electron rest mass,  $\Delta$ , the spin orbit energy, is approximately 1 eV for MCT with  $x \approx 0.2$ ; and  $E_p = 18 + 3x$  eV.<sup>15</sup>

The model includes a single acceptor level of density  $N_A$  at an energy  $E_A$  above the valence band edge, with a degeneracy factor of 4, and fully ionized donors of density  $N_D$ . This is in agreement with variable-temperature Hall effect measurements performed on the samples used in this study.  $E_A$  varied with the acceptor density. For  $2 \times 10^{16} \leq N_A \leq 6 \times 10^{16} \text{ cm}^{-3}$   $E_A$  ranges from 6 to 8 meV, and it is zero for acceptor densities above  $10^{17} \text{ cm}^{-3}$ .

The electron and hole densities,  $n$  and  $p$ , are determined from the charge neutrality equation and their common relation to the intrinsic carrier density  $n_i$

$$p + N_D^+ = n + N_A^-, np = n_i^2, \quad (10)$$

together with the following empirical relations for  $n_i$ ,<sup>16</sup>  $E_g$ ,<sup>17</sup> and the electron-to-hole mobility ratio:

$$n_i = (5.585 - 3.82x + 1.753 \cdot 10^{-3}T - 1.364 \cdot 10^{-3}xT)10^{14} E_g^{3/4} T^{3/2} e^{-E_g/(2kT)}, \quad (11)$$

$$E_g = -0.302 + 1.93x + 5.35 \cdot 10^{-4}(T^3 - 1822)(1 - 2x)/(T^2 + 255.2) - 0.81x^2 + 0.832x^3, \quad (12)$$

$$\mu_e/\mu_h = b = 610/(E_g T)^{1/2} [1 - (1/15) \log_{10} N_D \tanh(20/T)]. \quad (13)$$

The intrinsic carrier density given by combining Eq. 11 and Eq. 12 was found to compare well with calculations published recently.<sup>18,19</sup> Equation 13 was obtained from fits to the Hall coefficient and conductivity data of the samples used in this study (Fig. 4).

Combining Eqs. 1 to 13 yields the DTV of a single p- or n-type MCT layer caused by a lateral temperature gradient. The thermoelectric voltage  $U_{th}$  of a stack of  $n$  layers ( $j$ ) is equivalent to the voltage produced by  $n$  generators in parallel, the admittances of which are the conductances  $G_j$  of the individual layers, hence  $U_{th} G = \sum_j U_{th} G_j$ ,  $G$  being the total conductance of the layer structure. Since the temperature difference is the same for all layers the total DTV is given by

$$\alpha_t = \sum_j \alpha_j G_j / G = \sum_j \alpha_j \sigma_j d_j / (\sigma d) \quad (14)$$

where  $\sigma = \sum_j \sigma_j d_j / d$  and  $d = \sum_j d_j$  are the conductivity and thickness of the total sample, respectively.

## RESULTS AND DISCUSSION

The thermoelectric model that was adequate for p-type MCT<sup>1</sup> is extended to meet n-type MCT as well. Its validity for n-type MCT was experimentally verified by using an n-type  $x = 0.22$  layer epitaxially grown from the Te-rich solution on a (111)B face of a lattice matched CdZnTe substrate. The CdTe mole fraction was determined from the infrared spectral transmission of the sample at 300 and 77K. The conductivity and Hall coefficient were measured for temperatures between 15 and 320K by using the van der Pauw method and a magnetic field of 300 G. A least squares

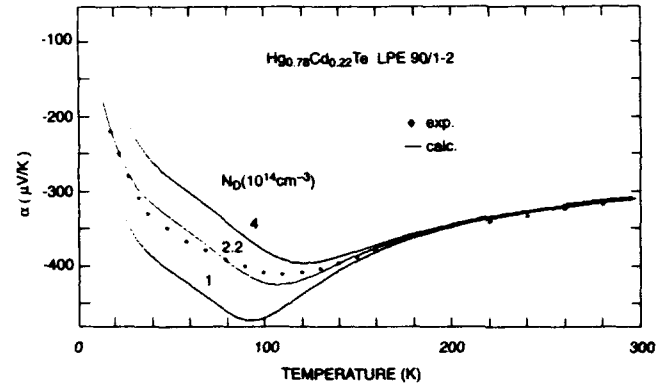


Fig. 6. Seebeck coefficient vs temperature determined from measurements of the thermoelectric power of an n-type MCT epitaxial layer (\*). The least squares fit yields  $x = 0.22$  and  $N_D = 2.2 \times 10^{14} \text{ cm}^{-3}$  in agreement with the Hall-effect analysis. The solid curves are calculated for  $x = 0.22$  and  $N_D = (1, 2.2, \text{ and } 4) \times 10^{14} \text{ cm}^{-3}$ .

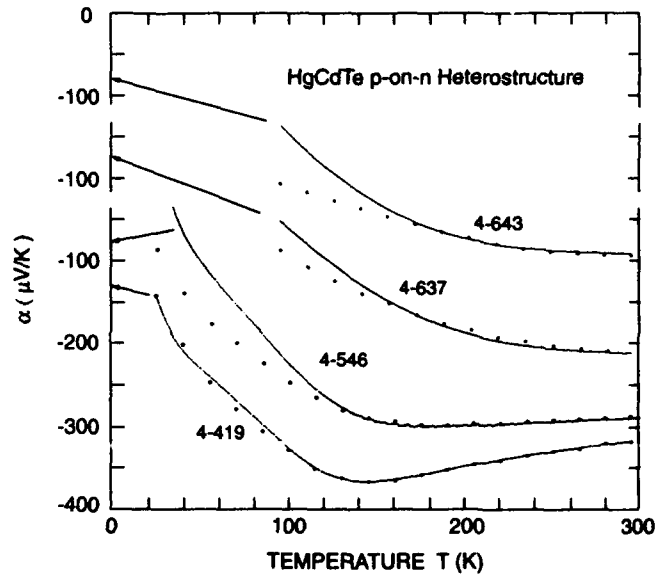


Fig. 7. Seebeck coefficient vs temperature determined from measurements (\*) of the thermoelectric voltage of four p-on-n heterostructures. The solid curves represent least-squares fits to the experimental data of those temperature ranges where the Fermi energy is more than  $1.5kT$  below the conduction band edge of the n-type layer. The fits yielded the data listed in Table I. The temperature ranges of the least-squares fits are 100–300K for sample 4-419, 130–300K for sample 4-546, 160–300K for sample 4-637, and 180–300K for sample 4-643.

fit to the experimental data by  $R_H = -1/(qn)$  with  $n$  determined by Eqs. 10, 11, and 12, yields  $x \approx 0.22$  and  $N_D = 2.2 \times 10^{14} \text{ cm}^{-3}$ .

Figure 6 presents the Seebeck coefficient vs temperature determined from the measurements of the thermoelectric voltage using the lateral gradient method. The experimental data for temperatures between 30 and 300K was fitted by a least-squares method based on Eqs. 1–6 and 8–12.  $N_D$  and  $x$  were considered adjustable parameters. The least squares fit yields  $x = 0.22$  and  $N_D = 2.2 \times 10^{14} \text{ cm}^{-3}$  in agreement with the Hall effect analysis. For comparison the Seebeck coefficients vs temperature calculated for  $N_D = 1 \times 10^{14}$  and  $4 \times 10^{14} \text{ cm}^{-3}$  are shown as well in Fig. 6.

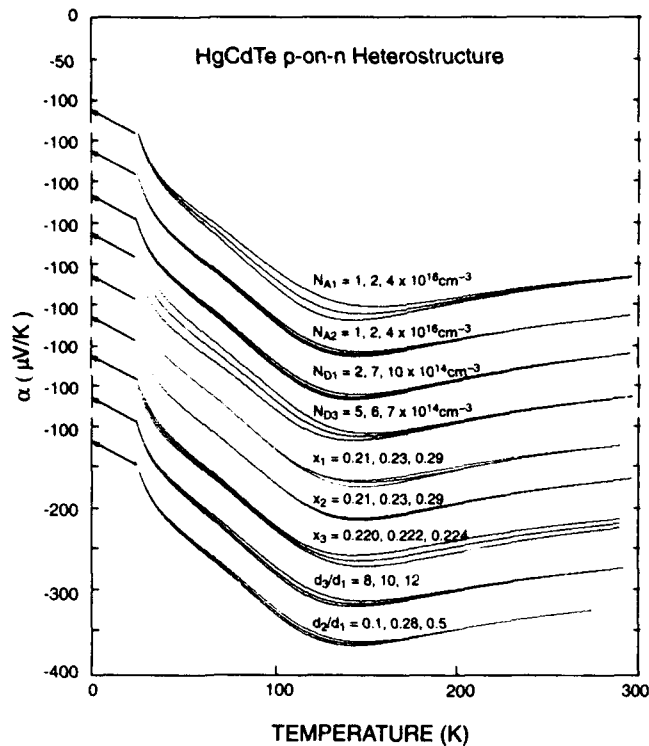


Fig. 8. Effect of parameter variations on the Seebeck coefficient vs temperature. The center curve of each triplet corresponds to the least squares fit to the DTV data obtained from thermoelectric measurements on specimen 4-419 except that of the  $x_1$  triplet where the upper curve represents the fit.

The calculated DTV fits well the experimental data of the n-type sample, even that at low temperatures, though the Fermi energy is only 1kT below the conduction band edge at 30K. Usually nondegenerate statistics are applicable on condition the Fermi energy is at least 2kT below the conduction band edge. The reason that in MCT the condition is eased to 1kT may be due to the very nonparabolic conduction band of much greater density of states higher up in the band.

These results support the validity of the thermoelectric model which has been used to analyze the DTV data obtained from measurements of the thermoelectric voltage performed on p-on-n heterostructures. Figure 7 presents the Seebeck coefficient vs temperature of four p-on-n heterostructures. The Hall coefficients vs reciprocal temperature of these samples are shown in Fig. 4.

Both the experimental Seebeck and Hall coefficient data vs temperature were fitted by a least squares method. The results are listed in Table I. The p-on-n heterostructures are assumed to be composed of three distinct layers with abrupt transitions: a p-type wide gap cap (1) on top, a p-type narrow gap absorber (2), and an n-type narrow gap absorber (3) on the bottom. The mole fractions,  $x$ ; the acceptor and donor densities,  $N_A$  and  $N_D$ , of each layer; and the thickness ratios of the n-type and p-type absorbers to the cap,  $d_3/d_1$  and  $d_2/d_1$ , are considered adjustable parameters. The Seebeck coefficient is calculated by using Eqs. 1 to 14.

To evaluate the Hall coefficient the two-carrier formula for low magnetic fields ( $\mu B \ll 1$ )

$$-qR_H = (nb^2 - p)(nb + p)^{-2} \quad (15)$$

and Petritz's model for a stack of layers<sup>20</sup>

$$R_{Ht} = \sum_j R_{Hj} (\sigma_j / \sigma)^2 d_j / d \quad (16)$$

is used in addition to Eqs. 7 to 13.

Equations 14 and 16 reveal the advantage of the Seebeck coefficient over the Hall coefficient when used for characterizing individual layers of p-on-n heterostructures. The Seebeck coefficient is linearly dependent on the layer conductivity, while the Hall coefficient is proportional to the squared conductivity. Thus, the effect of a thin p-type layer on the total Seebeck coefficient can be accurately determined, whereas there is typically only a very small effect on the Hall coefficient. In fact, the fits to the Hall coefficient data were almost insensitive to variations of the p-type layer parameters; and vice versa, small changes of the measured data yielded large variations of the p-type layer parameters, though the fits to the data of all four heterostructures are excellent, as shown in Fig. 4. Therefore, the values of the p-type parameters listed in Table I, which are obtained from fits to the Hall coefficient, are of considerable uncertainty.

The fits to the thermoelectric data of the heterostructures, on the contrary, are considerably affected by variations of the p-type layer parameters. Figure 8 illustrates the effect of parameter variations on the fit to the Seebeck coefficient data of specimen 4-419. There are pronounced changes of the Seebeck coefficient vs temperature for most of the parameters. Composition changes of the very thin second p-type layer only may be too small to be detected unambiguously.

Analysis of the thermoelectric data of p-on-n heterostructures, however, must be confined to temperatures for which the electron densities in the n-type layers are nondegenerate, because the kinetic term (Eq. 3) is valid for nondegenerate charge carrier densities only. Therefore, the least-squares fits are restricted to the experimental data of those temperatures where the Fermi energy is more than 1kT below the conduction band edge of the n-type layer. Hence, the experimental data of sample 4-419 at temperatures above 100K were used for the least-squares fit only. Interestingly, the fit meets the experimental data at temperatures as low as 25K as well, though the Fermi energy has already entered the conduction band. The DTV data analyses for the other samples with n-type layers of higher donor concentrations is confined to temperatures above 130K (4-546), 160K (4-637) and 180K (4-643).

The accuracy obtainable for the structural and doping parameters of MCT heterostructures from variable temperature thermoelectric measurements can be estimated by considering the effect of parameter variations on the Seebeck coefficient and the reproducibility of the lateral gradient measurements. Accuracy estimates for the parameter values obtained

from the Seebeck data analyses of the specimens examined in this study are given in Table I.

The parameter values obtained from the least-squares fits to the experimental DTV data compare well with those determined by SIMS (Table I). The apparent differences between the SIMS As concentrations and the acceptor densities obtained from the analyses of the Seebeck coefficient are due to the As acceptor activation efficiency.<sup>4</sup> An efficiency of about 50% was found in MOCVD-grown MCT for arsenic concentration in the range of  $10^{16}$  and  $10^{17} \text{ cm}^{-3}$ . The efficiency decreases for As concentrations approaching  $10^{18} \text{ cm}^{-3}$ . The  $x$  values of the n-type layers obtained from the least squares fits are also in agreement with those determined from the infrared spectral transmission of the samples at 300 and 77K.

### CONCLUSIONS

A simple thermoelectric model based on the diffusion of electrons and holes in a temperature gradient, which we have previously shown to be valid for p-type MCT, was extended to meet the thermoelectric properties of n-type MCT as well. The validity of the model for n-type MCT was verified by fitting the Seebeck coefficient data obtained from measurements on an n-type sample ( $x = 0.22$ ,  $N_D = 2.2 \times 10^{14} \text{ cm}^{-3}$ ) at temperatures between 30 and 300K.

The extended thermoelectric model was used to analyze MCT p-on-n heterostructures with respect to doping and composition of the constituent p and n-type layers. The results compare well with SIMS As and In profiles and infrared transmission measurements.

### ACKNOWLEDGMENT

We thank Dr. M. Bruder, AEG Aktiengesellschaft, for supplying the n-type MCT samples, and Dr. J. Ralston for comments and corrections during manuscript preparation.

### REFERENCES

1. J. Baars, D. Brink and J. Ziegler, *J. Vac. Sci. Technol.* B9, 1709 (1991).
2. D.D. Edwall, J.-S. Chen, J. Bajaj and E.R. Gertner, *Semicond. Sci. Technol.* 5, S221 (1990).
3. D.D. Edwall, J.-S. Chen and L.O. Bubulac, *J. Vac. Sci. Technol.* B9, 1691 (1991).
4. D.D. Edwall, L.O. Bubulac and E.R. Gertner, *J. Vac. Sci. Technol.* B10, 1423 (1992).
5. L.O. Bubulac, D.D. Edwall, J. Chung and C.R. Viswanathan, *J. Vac. Sci. Technol.* B10, 1633 (1992).
6. E. Finkman and S.E. Schacham, *J. Appl. Phys.* 56, 2896 (1984).
7. M. Seemann-Eggebert, D. Brink, German Patent DE 40 12 453 A 1.
8. R.A. Smith, *Semiconductors* (Cambridge University Press, Cambridge, 1964), p. 173.
9. S.S. Devlin, *Physics and Chemistry of II-VI Compounds*, ed. by M. Aven and J. Prener (North-Holland, Amsterdam 1967), p. 562.
10. V.V. Sologub, V.I. Ivanov-Omskii, V.M. Muzhdaba and S.S. Shalyt, *Sov. Phys. Solid State* 13, 1452 (1971).
11. J.J. Dubowski, T. Dietl, W. Szymanska and R.R. Galazka, *J. Phys. Chem. Solids* 42, 351 (1981).
12. J. Baars and F. Sorger, *Solid State Commun.* 10, 875 (1972).
13. V. Altschul and E. Finkman, *Appl. Phys. Lett.* 58, 942 (1991).
14. E.O. Kane, *J. Phys. Chem. Solids* 1, 249 (1957).
15. R. Dornhaus and G. Nimtz, *Springer Tracts in Modern Physics*, (Springer, Berlin, 1983), Vol. 98, p. 166.
16. G.L. Hansen and J.L. Schmit, *J. Appl. Phys.* 54, 1639 (1983).
17. D.G. Seiler, J.R. Lowney, C.L. Littler and M.R. Loloee, *J. Vac. Sci. Technol.* A8, 1237 (1990).
18. D.G. Seiler, J.R. Lowney, C.L. Littler and I.T. Yoon, *Mat. Res. Soc. Symp. Proc.* Vol. 216, p. 59, 1991.
19. J.R. Lowney, D.G. Seiler, C.L. Littler and I.T. Yoon, *J. Appl. Phys.* 71, 1253 (1992).
20. R.L. Petritz, *Phys. Rev.* 110, 1254 (1958).



# Photo-Induced Excess Low Frequency Noise in HgCdTe Photodiodes

G.M. WILLIAMS, R.E. De WAMES, J. BAJAJ, and E.R. BLAZEJEWSKI

Rockwell International Science Center, Thousand Oaks, CA 91358

We have investigated the properties of excess low frequency noise in illuminated mid wavelength infrared and long wavelength infrared HgCdTe photodiodes at zero bias. The current power spectrum ( $S_i$ ) dependence is usually close to inverse frequency ( $f$ ), but substantial variations have been observed. The magnitude of  $1/f$  spectra is voltage independent for small bias voltages, but is proportional to the square of the photocurrent ( $I$ ). Consequently, the  $1/f$  knee increases with photocurrent. Variable area device studies indicate that the noise sources are more closely associated with the device area ( $A_i$ ) than perimeter, indicating bulk limitations. The power spectrum can be represented by an empirical relationship of the form  $S_i = \alpha_{ph}^2 / f A_i$ . This defines a figure of merit,  $\alpha_{ph}$ , which takes into the account the relationship between current dependence and device geometry.  $\alpha_{ph}$  is device dependent, suggesting that randomly distributed defects play a role in the difference. This is also supported by noting that devices fabricated in material grown on lattice matched substrates have lower  $\alpha_{ph}$  ( $10^{-16} \text{ cm}^2$ ) than those fabricated in material grown on nonlattice matched substrates ( $10^{-14} \text{ cm}^2$ ), which usually have two orders of magnitude larger dislocation density. We conclude that photo-induced  $1/f$  noise can be reduced via defect reduction and is not fundamental. Data on our best devices indicates that  $\alpha_{ph}$  is somewhat lower for smaller band gap material. The temperature dependence of photo-induced excess low frequency noise is much weaker than that of bias induced excess low frequency noise, indicating unrelated generation mechanisms. In addition, photo-induced  $1/f$  adds in quadrature with bias induced  $1/f$  noise and is not well correlated in magnitude with either bias induced  $1/f$  noise or detector dark currents.

**Key words:** Defects, HgCdTe, low frequency noise, photodiodes

## INTRODUCTION

Excess low frequency ( $1/f$ ) noise in the detector elements of infrared focal plane arrays (IRFPAs) can limit sensor system performance and, therefore, is often a critical detector performance parameter. This is particularly true of detectors used in staring IRFPAs, which employ mosaic arrays and offer maximum signal integration times. HgCdTe detectors are an attractive choice for such systems because intrinsic material properties, like high optical absorption coefficient and long minority carriers lifetimes, allow background limited detector performance at the highest operating temperature. An understanding of the factors responsible for the magnitude of  $1/f$  noise in

HgCdTe photodiodes is desirable for optimized integration into IRFPAs. Photo-induced  $1/f$  noise cannot be reduced by near zero bias input circuits.

Excess low frequency noise in electronic devices is a frequently observed but poorly understood phenomenon. The published literature suggests that this is also the case for HgCdTe photodiodes. We determine that defects of yet unknown origin limit photo-induced  $1/f$  noise, and show that devices fabricated in material grown on lattice matched substrates are less susceptible to this effect. Research is required to identify the responsible defects, so that they may be further reduced.

In the section on experimental details, we describe the device architectures evaluated and measurement techniques. In the section on results, we present our experimental results. In the section entitled Excess

(Received October 12, 1992; revised January 22, 1993)

Low Frequency Noise in HgCdTe Photodiodes, we discuss previous work on  $1/f$  noise in HgCdTe photodiodes. The final section is a summary statement of our conclusions.

### EXPERIMENTAL DETAILS

The detectors investigated are  $\text{Hg}_{1-x}\text{Cd}_x\text{Te}$  photodiodes representative of several technologies. We have investigated devices in material grown by liquid phase epitaxy (LPE), molecular beam epitaxy (MBE), and metalorganic chemical vapor deposition (MOCVD). Substrates for the epitaxial growths include CdZnTe (approximately lattice matched), CdTe (almost lattice matched), PACE-1 (MOCVD CdTe on sapphire), and Pace-2 (MOCVD CdTe on GaAs). Junctions are formed either during the growth process or by ion-implantation followed by a diffusion/activation anneal. Both p/n and n/p architectures have been investigated; p/n devices are doped on both sides of the junction, while n/p devices usually employ Hg vacancies to provide p-type conductivity in lightly n-type compensated material. Device architectures include planar, mesa, and selectively implanted mesas (a planar/mesa combination) of various square junction areas. Material compositions are typically near  $x = 0.3$  for mid wavelength infrared (MWIR) detectors

(cut-off wavelengths in the 4 to 5  $\mu\text{m}$  range) or  $x = 0.2$  for long wavelength infrared (LWIR) detectors (cut-off wavelengths in the 9 to 12  $\mu\text{m}$  range). Passivation is composed of ZnS, or CdTe, or wider bandgap HgCdTe; CdTe and HgCdTe passivation layers are usually overcoated with another material like ZnS,  $\text{SiO}_2$ , or  $\text{Si}_3\text{N}_4$ . Contacts may be gold to p-type material and indium to n-type material, but in most cases adequately low contact resistance is obtained by using the same metal (gold) for both contacts. Obviously, we have investigated only a few combinations of the above processes. As we will show, choice of substrate (lattice matched vs nonlattice matched) will override all other factors. All of the devices investigated were state of the art (i.e. the best available) for their respective technologies.

Measurements are performed with the devices in cryogenic dewars with windows to provide illumination. In most cases, illumination is provided by an object at room temperature; however, in one case a blackbody source was used. In some cases, a cold shutter was employed to vary the background induced photocurrent. Particular care was taken to insure that the source of illumination did not provide significant  $1/f$  noise. Data was taken at temperatures ranging from 65 to 110K, although most of the data

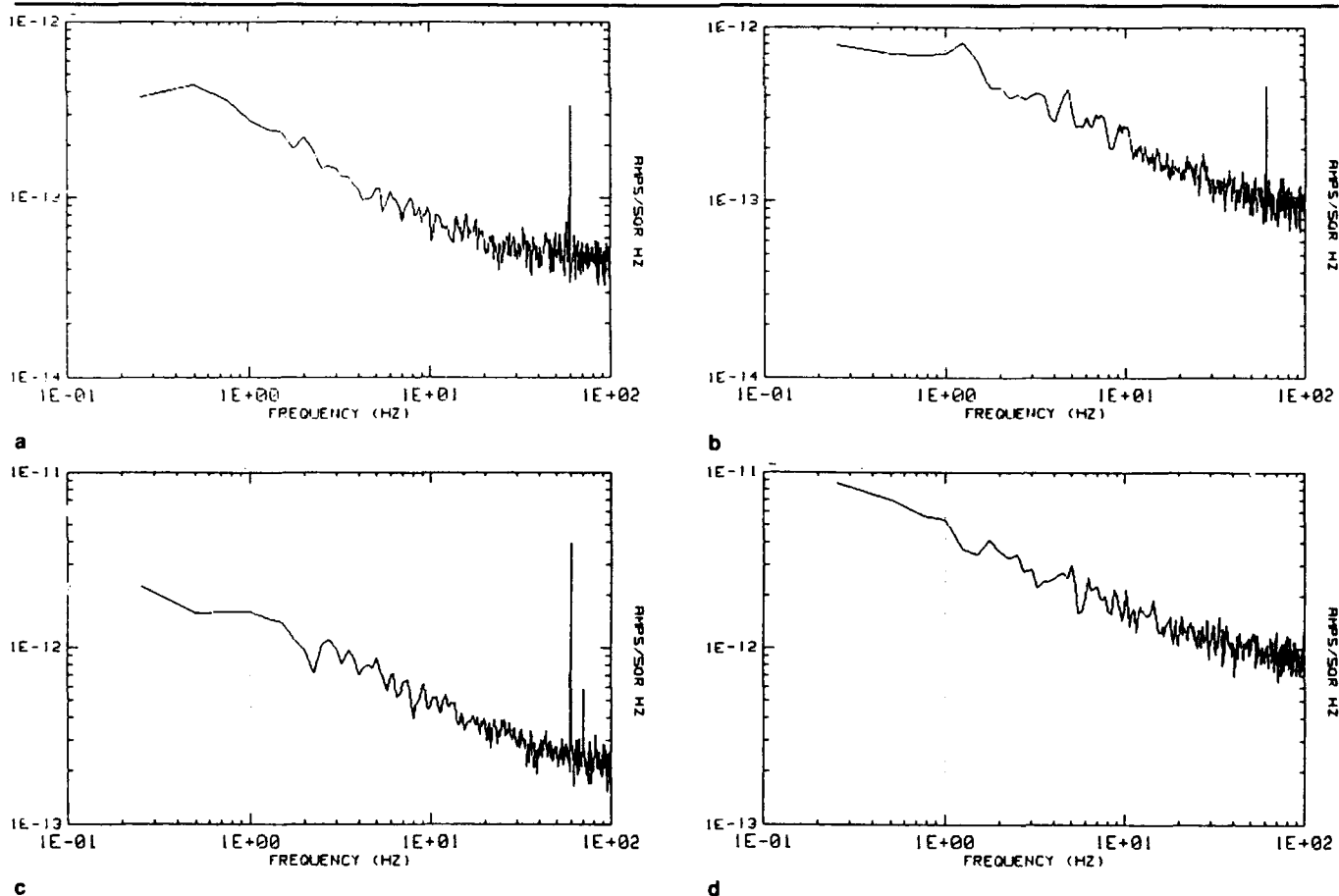


Fig. 1. Noise spectra of variable area ZnS/PACE-1 MWIR HgCdTe diodes at zero bias with photocurrent at 110K. 1a-Aj =  $6.8 \times 10^{-6} \text{ cm}^2$ ,  $I_{ph} = 6.46 \times 10^{-9} \text{ amps}$ ,  $1/f = 2.9 \times 10^{-13} \text{ amps/Hz}^{0.5}$  @ 1 Hz,  $1/f$  knee = 42 Hz; 1b-Aj =  $2.1 \times 10^{-5} \text{ cm}^2$ ,  $I_{ph} = 2.07 \times 10^{-8} \text{ amps}$ ,  $1/f = 7.6 \times 10^{-13} \text{ amps/Hz}^{0.5}$  @ 1 Hz,  $1/f$  knee = 87 Hz; 1c-Aj =  $1.5 \times 10^{-4} \text{ cm}^2$ ,  $I_{ph} = 1.12 \times 10^{-7} \text{ amps}$ ,  $1/f = 1.6 \times 10^{-12} \text{ amps/Hz}^{0.5}$  @ 1 Hz,  $1/f$  knee = 74 Hz; 1d-Aj =  $2.5 \times 10^{-3} \text{ cm}^2$ ,  $I_{ph} = 1.52 \times 10^{-6} \text{ amps}$ ,  $1/f = 5.2 \times 10^{-12} \text{ amps/Hz}^{0.5}$  @ 1 Hz,  $1/f$  knee = 56 Hz.

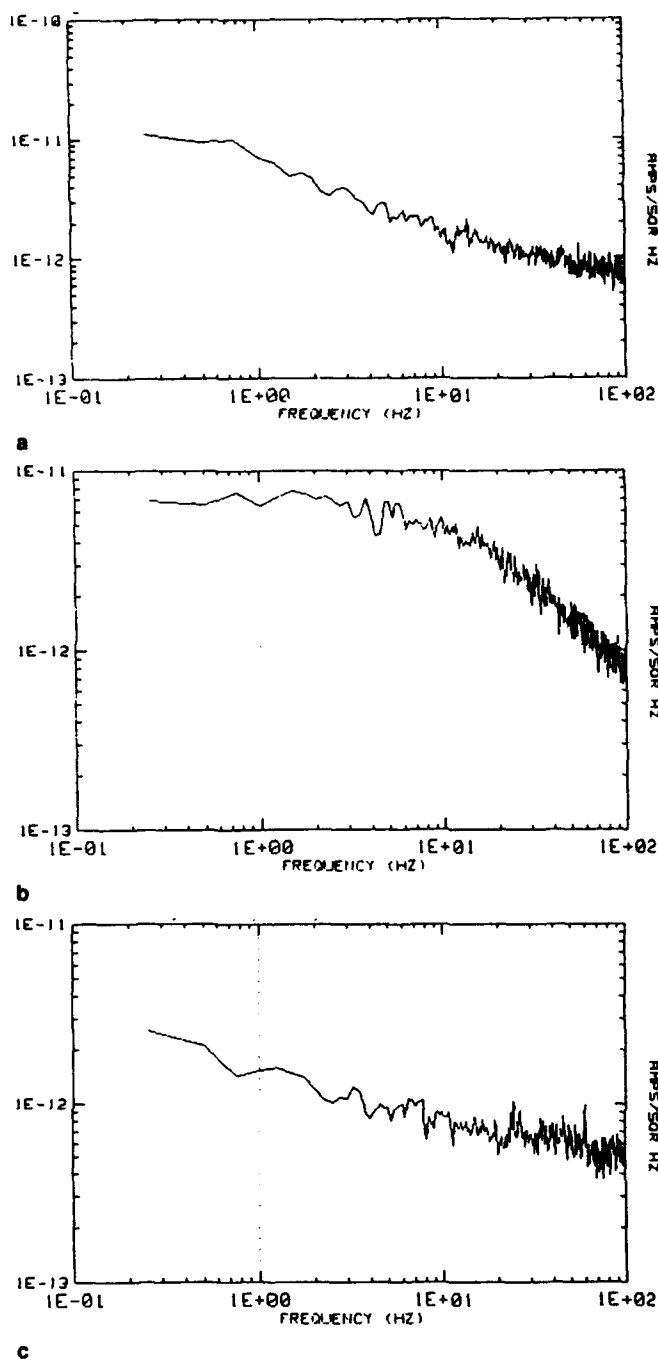


Fig. 2. Noise spectra of LWIR HgCdTe diodes at zero bias with photocurrent at 78K. 2a- $A_j = 2.1 \times 10^{-5} \text{ cm}^2$ ,  $I_{ph} = 1.82 \times 10^{-7} \text{ amps}$ ,  $1/f = 6.95 \times 10^{-12} \text{ amps/Hz}^{0.5}$  @ 1 Hz,  $1/f \text{ knee} = 828 \text{ Hz}$ ; 2b- $A_j = 2.1 \times 10^{-5} \text{ cm}^2$ ,  $I_{ph} = 1.21 \times 10^{-7} \text{ amps}$ ,  $1/f = 9.5 \times 10^{-12} \text{ amps/Hz}^{0.5}$  @ 1 Hz; 2c- $A_j = 2.5 \times 10^{-5} \text{ cm}^2$ ,  $I_{ph} = 4.94 \times 10^{-7} \text{ amps}$ ,  $1/f = 1.8 \times 10^{-12} \text{ amps/Hz}^{0.5}$  @ 1 Hz,  $1/f \text{ knee} = 20 \text{ Hz}$ .

was taken at 78K. Characterization for the purposes of this paper consisted of current-voltage (I-V) curves and noise current spectra collected very near zero bias.

The detectors were connected directly to a room temperature transimpedance amplifier (TIA) for noise measurements. The output of the TIA is coupled to a buffer amplifier (usually a gain of 10) which provides appropriate signal levels to a spectrum analyzer. The

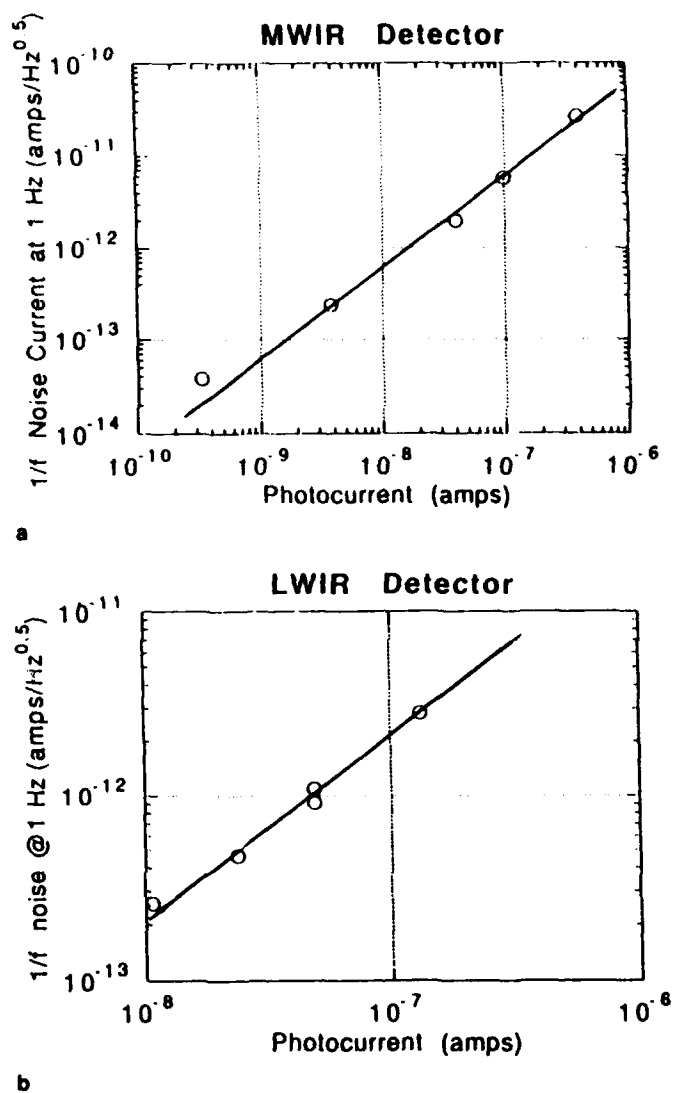


Fig. 3. Plot of photo-induced  $1/f$  noise current at 1 Hz and zero bias vs photocurrent at 78K. (a) MWIR ZnS/PACE-1 detector,  $A_j = 1.6 \times 10^{-4} \text{ cm}^2$ ; (b) LWIR MOCVD/PACE-2 detector,  $A_j = 2.5 \times 10^{-5} \text{ cm}^2$ . The lines represent linear relationships.

usual frequency range measured is 0.25–100 Hz: the noise at 1 Hz is obtained by integrating the noise from 1–2.75 Hz, which is appropriate for a  $1/f$  spectrum since the ratio is the base of the natural logarithms. At the highest gain setting of the TIA, the input referred noise is about  $2 \times 10^{-15} \text{ amps/Hz}^{0.5}$  over this range of frequencies, neglecting peaks due to 60 Hz line or dewar microphonic resonance frequency interference. Detector impedances were high enough under all measurement conditions to insure that the  $1/f$  noise voltage from the TIA ( $80 \text{ nV/Hz}^{0.5}$  at 1 Hz) did not influence measurement results, and  $1/f$  noise current from the TIA was undetectable. The small bias which is a result of the finite input impedance of the TIA and the photocurrent did not influence results as demonstrated by the lack of effect of small applied canceling bias voltage. Bias voltages near zero bias had no effect on measured noise power spectral density (NPSD). Photocurrents are obtained from the I-V

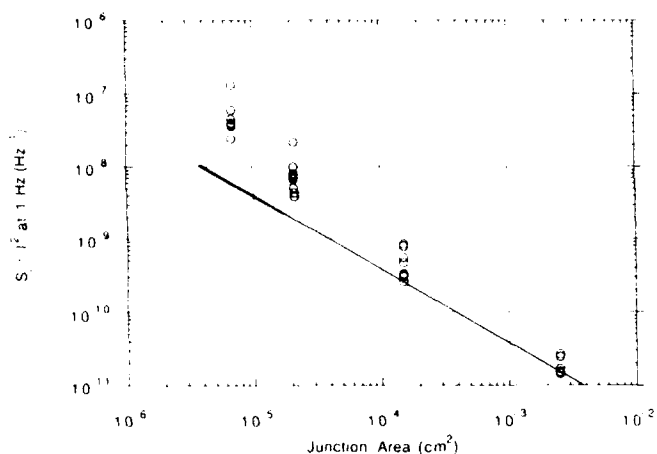


Fig. 4. Plot of the ratio of photo-induced  $1/f$  NPSD at 1 Hz, 78K, and zero bias to the square of the photocurrent vs detector area for an LWIR MOCVD/PACE-2 diode array. The line indicates a  $1/A$  scaling. Data is close to an inverse area dependence, indicating bulk limitations.

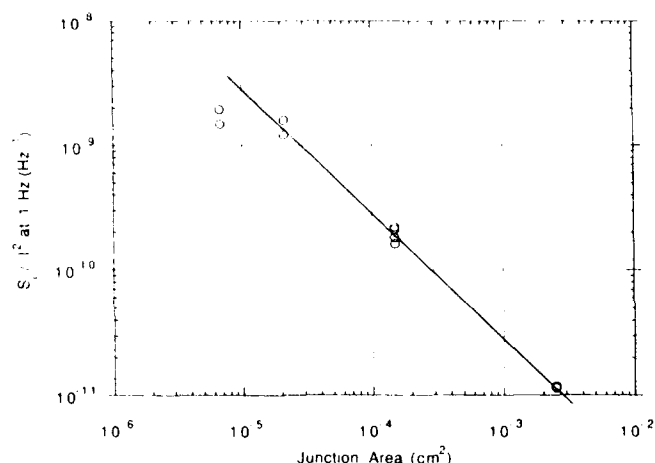


Fig. 5. Plot of the ratio of photo-induced  $1/f$  NPSD at 1 Hz, 78K, and zero bias to the square of the photocurrent vs detector area for an MWIR ZnS/PACE-1 diode array. The line indicates a  $1/A$  scaling. Data is close to an inverse area dependence, indicating bulk limitations.

curves, and junction areas from photomask dimensions corrected for process parameters (principally mesa undercutting during etching).

## RESULTS

### Noise Power Spectral Density and $1/f$ Knee

We show that the photo-induced current NPSD is usually approximately proportional to inverse frequency, although large deviations have been observed. We also note that the  $1/f$  knee frequency (the frequency at which  $1/f$  noise and white noise are equal) is not strongly area dependent for devices exposed to uniform photon flux density.

Examples of photo-induced noise current spectra measured at 110K and zero bias are shown in Figs. 1a–d for four variable area MWIR detectors. These devices are ion-implanted  $n/p$  junctions passivated with ZnS fabricated in LPE grown HgCdTe on Pace-1 substrates. For reference, we denote samples of this type as ZnS/Pace-1. The cutoff wavelength for these particular devices is  $5.1 \mu\text{m}$  at 78K. The photocurrent

comes from viewing a block maintained at room temperature. The data is taken over a frequency range of 0.25–100 Hz with a resolution of 0.25 Hz. The magnitude of the  $1/f$  noise spectra are characterized by the value at 1 Hz. The data show that the current power spectrum is nearly proportional to inverse frequency at low frequency. At higher frequencies (not shown), white noise spectra agreed with calculated full shot noise values based on the measured photocurrent ( $\sqrt{2qI_{ph}}$ ).  $1/f$  noise increases as the devices increase in size, although the  $1/f$  knee frequency is not consistently area dependent. Some of the variation in  $1/f$  knee frequency is due to nonuniform photon flux related to the field of view of different detectors, since the knee frequency (as will be shown) depends on photocurrent in a given device, and some of the variation is due to nonuniformity of photo-induced  $1/f$  noise magnitudes in different devices (which we ascribe to the influence of randomly distributed defects). For uniform illumination conditions and equivalent device quality, we expect the  $1/f$  knee will be area independent for either bulk (area) or surface (lateral) limited devices.

Examples of photo-induced  $1/f$  noise current spectra measured at 78K for LWIR detectors are shown in Figs. 2a–c. Figure 2a shows a spectrum which is typical, exhibiting a  $1/f$  spectrum. The magnitude of the photo-induced  $1/f$  noise is larger in equivalent quality LWIR (such as those in Fig. 1 and Fig. 2a) detectors than MWIR detectors exposed to the same ambient background because of the larger photocurrent in the LWIR detectors. This also results in a larger  $1/f$  noise knee, since the  $1/f$  knee increases with photocurrent. We note that the photocurrent induced spectrum is not always  $1/f$ ; an example is shown in Fig. 2b for a detector from the same array as that shown in Fig. 2a. In this case, the power spectrum shows a flattening at low frequencies and a  $1/f^2$  decrease at higher frequencies which is characteristic of a Lorentzian spectrum obtained when a single time constant process dominates. In spite of the differences in noise behavior, the I-V characteristics of the two devices shown in Figs. 2a and 2b are quite similar. The devices in Figs. 2a and 2b are grown  $p(\text{As})/n(\text{In})$  junctions passivated with CdTe fabricated in MOCVD grown material on PACE-2 substrates. For reference, we denote samples of this type as MOCVD/PACE-2. The cutoff wavelength measured at 78K is  $10.2 \mu\text{m}$  for this array. In Fig. 2c, we show an example noise spectrum from an ion-implanted junction  $p(\text{As})/n(\text{In})$  diode passivated with wide gap HgCdTe fabricated in MBE grown material on a CdZnTe substrate. For reference, we denote samples of this type as MBE/CdZnTe. The cutoff wavelength measured at 78K is  $10.0 \mu\text{m}$  for these devices. The magnitude of photo-induced  $1/f$  noise is smaller than that observed in the other devices shown in this figure in spite of the larger photocurrent, and the  $1/f$  knee is much lower. This is a device of higher quality than those shown so far, in terms of photo-induced  $1/f$  noise. We attribute this difference to a choice of substrate.

### Photocurrent Dependence

In this section, we show that the photo-induced  $1/f$  NPSD is proportional to the square of the photocurrent. This causes the  $1/f$  knee to increase with the photocurrent.

Experimental determination of the photocurrent dependence of  $1/f$  noise at zero bias is shown in Figs. 3a and 3b for an MWIR ZnS/PACE-1 and an LWIR MOCVD/PACE-2 diode, respectively. The data is taken at 78K. These experiments were performed by varying the photocurrent through single diodes, which mitigates the effect of scatter in the performance of different diodes with identical geometry. In the case of the LWIR detector, a sufficient range of photocurrents was obtained by limiting the field of view of a room temperature object; for the MWIR detector, a blackbody with variable aperture was used to provide additional photocurrent range. A dual channel spectrum analyzer which was coupled to separate detectors was used to determine that the observed  $1/f$  noise was not a result of fluctuations in the blackbody source. Photo-induced  $1/f$  noise current is linearly proportional to the photocurrent; therefore, the current NPSD is proportional to the square of the photocurrent. Since the  $1/f$  noise increases as the square of the photocurrent, while shot noise increases directly with the photocurrent, the  $1/f$  knee will increase with the photocurrent.

Based on this relationship between photo-induced  $1/f$  noise and photocurrent, we scale NPSD to the square of the photocurrent to develop a figure of merit. For electronic devices in which the NPSD is related to some power of the current, the current dependence and geometry dependence are uniquely related for homogeneously distributed uncorrelated noise sources (see appendix). We explore this relationship in the following section.

### Area Dependence

We show that the  $1/f$  current NPSD normalized to the square of the photocurrent is approximately inversely proportional to junction area and is not inversely proportional to the perimeter. This result implies bulk limited performance.

Since the proportionality between current NPSD and the square of the photocurrent has been established, plots of NPSD normalized to current vs device area can isolate bulk vs surface limitations, if the devices are reasonably uniform in quality. As shown in the appendix, bulk (area) limited diodes with different areas will have NPSD divided by the square of the current proportional to the inverse of the detector area, while surface (lateral current) limited diodes will have NPSD divided by the square of the current proportional to the inverse of the square root of detector area (for square or circular elements). Because of the normalization to current, the NPSD of small devices will scale with the inverse of detector area and large enough ones with the square root of detector area, reasonably assuming that both area

and lateral contributions are non-zero.

Figure 4 shows a plot of current NPSD divided by the square of the current vs diode junction area for an array of LWIR MOCVD/PACE-2 detectors. These devices have a cutoff wavelength of  $11.6 \mu\text{m}$  at 78K. There is scatter evident in the data for devices of fixed area; normalizing for current differences shows that as yet undetermined factors also play a role. The scatter can be larger than that shown for this particular sample. The scatter must be attributed to inhomogeneous properties of the material and/or device process, since all the properties we can control are the same. Nevertheless, the uniformity is good enough to suggest that  $S_i/I^2$  scales inversely with detector area, especially for the lower noise devices of large area. Even the best small area devices are slightly above a linear trend line (for this sampling). We cannot explain this aspect of the result, but suspect that it may be due to statistical variations

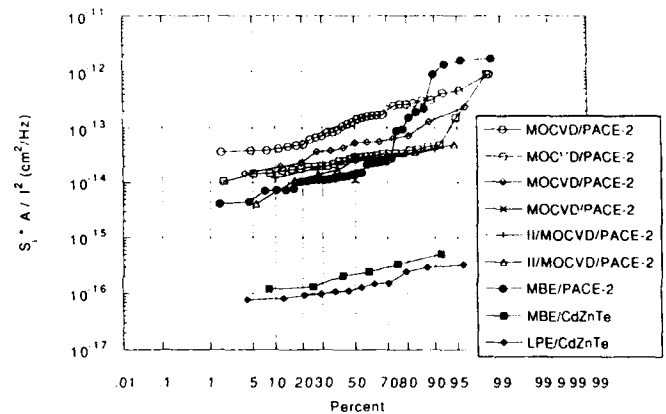


Fig. 6.  $S_i A / I^2$  cumulative distribution function for LWIR arrays at 78K. Devices in material grown on CdZnTe substrates are superior to those in material grown on CdTe/GaAs. The open circles represent an array of detectors with a cutoff wavelength of  $11.6 \mu\text{m}$  at 78K; the open squares and crosses,  $10.2 \mu\text{m}$ ; the open diamonds,  $10.3 \mu\text{m}$ ; the pluses, open triangles, and closed squares  $10.0 \mu\text{m}$ ; the closed circles,  $10.9 \mu\text{m}$ ; and the closed diamonds,  $10.4 \mu\text{m}$ .

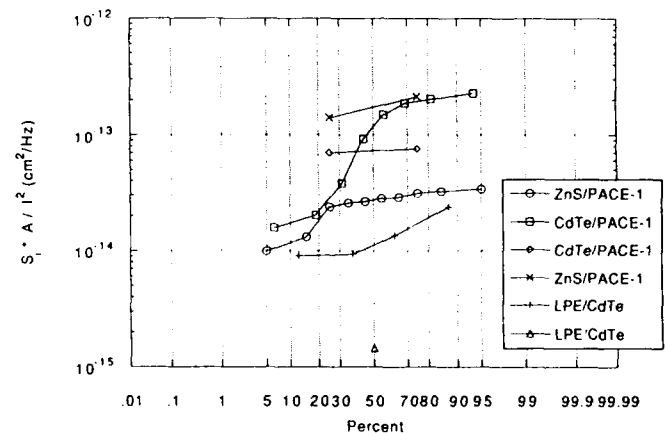


Fig. 7.  $S_i A / I^2$  cumulative distribution function for MWIR arrays. Devices in material grown on CdTe substrates are better than those in material grown on CdTe/sapphire. The open circles represent an array of detectors with a cutoff wavelength of  $5.1 \mu\text{m}$  at 78K; the open squares,  $4.8 \mu\text{m}$ ; the open diamonds and crosses,  $5.0 \mu\text{m}$ ; the pluses,  $5.3 \mu\text{m}$ ; and the triangle,  $5.2 \mu\text{m}$ .

which will be relatively larger on smaller diodes, assuming the inhomogeneous behavior is attributed to randomly distributed defects. Clearly, an inverse square root area dependence is not supported by this data.

Figure 5 shows a plot of current NPSD divided by the square of the current vs diode junction area for an array of ZnS/PACE-1 MWIR detectors. The cutoff wavelength is 5.1  $\mu\text{m}$  at 78K. Again, we see scatter in the data for devices of the same area. The data indicate that  $S_i/I^2$  scales inversely with detector area. In this case, the smallest devices fall below the trend line.

### Technology Comparison

We show that devices grown on lattice matched substrates are superior to those grown on nonlattice matched substrates. For devices on nonlattice matched substrates, the photo-induced 1/f noise figure of merit does not appear to be wavelength dependent.

Based on the experimental results presented in Figs. 1-5, we can describe photo-induced 1/f noise in HgCdTe photodiodes by the following empirical relation:

$$S_i = \frac{\alpha_{ph} I^2}{f A_j} \quad (1)$$

where  $S_i$  is the photo-induced 1/f NPSD (amps<sup>2</sup>/Hz),  $I$  is the photocurrent (amps),  $f$  is the frequency (Hz), and  $A_j$  is the diode junction area (cm<sup>2</sup>). The parameter  $\alpha_{ph}$  defines the quality of diodes relative to photo-induced 1/f noise, and allows comparison of devices fabricated using a variety of technologies measured under different conditions.

In Fig. 6, we show cumulative distribution functions of  $S_i \cdot A_j / I^2$  for LWIR HgCdTe detectors fabricated by a variety of technologies. The MOCVD/PACE-2 technology has been described. The II/MOCVD/PACE-

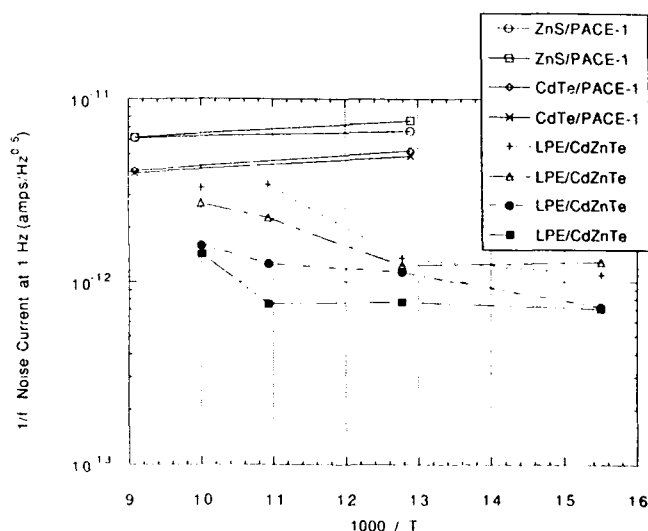


Fig. 8. Temperature dependence of photo-induced 1/f noise for MWIR and LWIR detectors. The dependence is much weaker than that observed for bias induced 1/f noise.

2 technology is similar, except that the junctions are formed by an As implantation followed by an activation anneal. MBE/PACE-2 technology is like the MOCVD/PACE-2 technology, except that the active layer is grown by MBE. LPE/CdZnTe technology is similar to the MBE/CdZnTe technology, except that the growth technique is LPE. The figure shows clearly that devices grown on lattice matched technologies are two orders of magnitude better than those grown on nonlattice matched substrates in terms of  $\alpha_{ph}$ . The two groups of distributions are well separated.

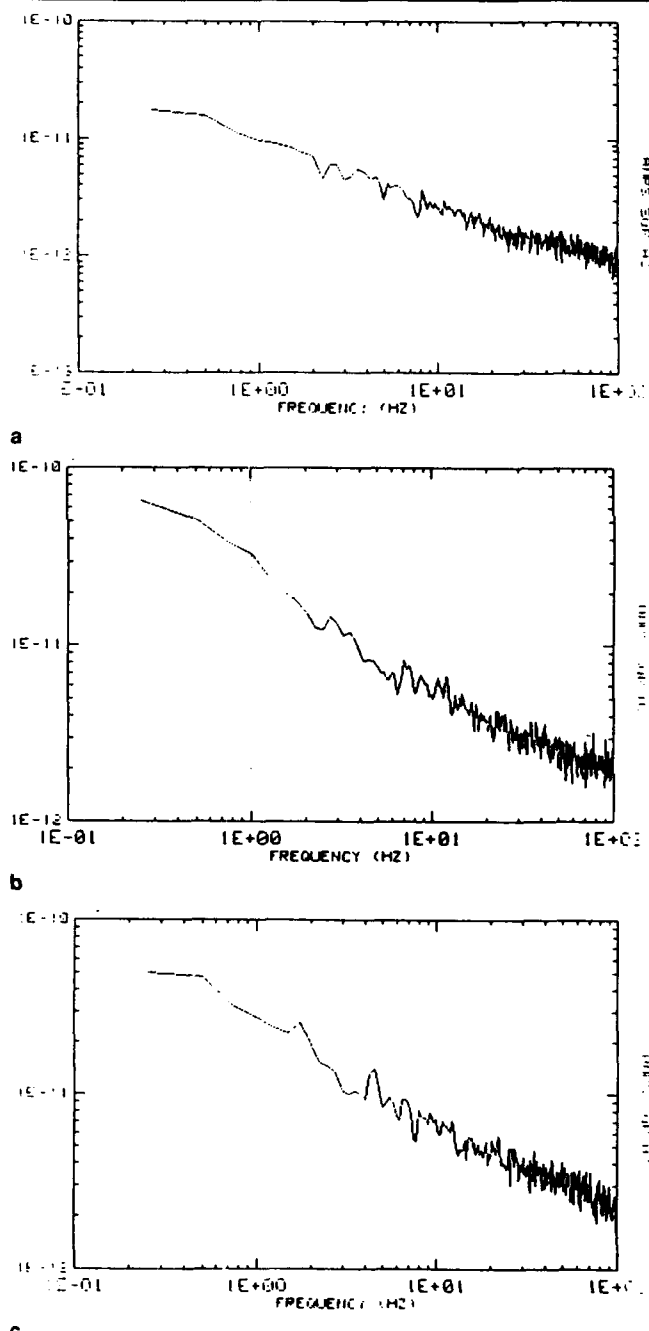


Fig. 9. LWIR MOCVD/PACE-2 diode 1/f noise current measured at 78K under three conditions. 9a -17mV reverse bias (22 nA), no photocurrent; 9b - 0 bias, with 328 nA photocurrent; 9c -17 mV reverse bias, and 328 nA photocurrent. 9c is quadrature sum of 9a and 9b.

In Fig. 7, we show cumulative distribution functions of  $S_i A / I^2$  for MWIR HgCdTe detectors fabricated by a variety of technologies. The ZnS/PACE-1 technology has been described. The CdTe/PACE-1 is similar, except that the surface passivation employs CdTe instead of ZnS. The LPE/CdTe technology represents devices in material grown by LPE on CdTe substrates, and is similar to the LWIR LPE/CdZnTe technology. Devices grown on lattice matched substrates are better than those grown on nonlattice matched substrates, although the difference is not as large as noted for the LWIR detectors and the statistical base is small.

We see that  $\alpha_{ph}$  is not strongly wavelength dependent between LWIR and MWIR detectors on nonlattice matched substrates, considering Figs. 6 and 7 together. The lowest values of  $\alpha_{ph}$  are obtained in LWIR detectors on lattice matched substrates.

### Temperature Dependence

We show that the temperature dependence of photo-induced  $1/f$  noise is weak and is much smaller than the temperature dependence of bias induced  $1/f$  noise.

The temperature dependence of the photo-induced  $1/f$  noise is shown in Fig. 8 for both LWIR and MWIR detectors. The MWIR detectors are ZnS/PACE-1 and CdTe/PACE-1 (cutoff wavelength  $5.0 \mu\text{m}$  at 78K) and the LWIR detectors are LPE/CdZnTe (cutoff wavelength  $10.4 \mu\text{m}$  at 78K). The temperature dependence is clearly quite weak. This stands in distinct contrast to the temperature dependence of dark current induced  $1/f$  noise, which often has a thermal activation energy near  $3/4$  of the band gap. Measurements of the dark current induced  $1/f$  noise at 50 mV reverse bias on the LPE/CdZnTe detectors at 77K and 100K resulted in an activation energy of 64 meV, which is 0.67 of the diffusion current activation energy (95 meV). The diffusion current activation energy is close to the zero temperature band gap of 99 meV. The activation energy for noise corresponds to an order of magnitude change in dark current induced  $1/f$  noise over this temperature range, while the photocurrent induced  $1/f$  noise changes by a factor of two at most.

### Relationship of Other Device Properties

We show that photo-induced  $1/f$  noise is not strongly correlated with other noise and dark current sources.

We have investigated the relationship between photo-induced  $1/f$  noise and other diode figures of merit. In Fig. 9, we show  $1/f$  noise measurements performed on a MOCVD/PACE-2 LWIR detector of area  $2.5 \times 10^{-5} \text{ cm}^2$  at 78K under three conditions. In Fig. 9a, we show a  $1/f$  noise current spectrum taken at 17 mV reverse bias without illumination. The bias induced current is 22 nA and the  $1/f$  noise is  $1.03 \times 10^{-11} \text{ amps/Hz}^{0.5}$  at 1 Hz. In Fig. 9b, we show the  $1/f$  noise current spectrum on the same device taken at zero bias with illumination. The photocurrent is 328 nA and the  $1/f$  noise is  $2.76 \times 10^{-11} \text{ amps/Hz}^{0.5}$  at 1 Hz. The dark current, therefore, generates  $1/f$  noise far more efficiently than the photocurrent. In Fig. 9c, we

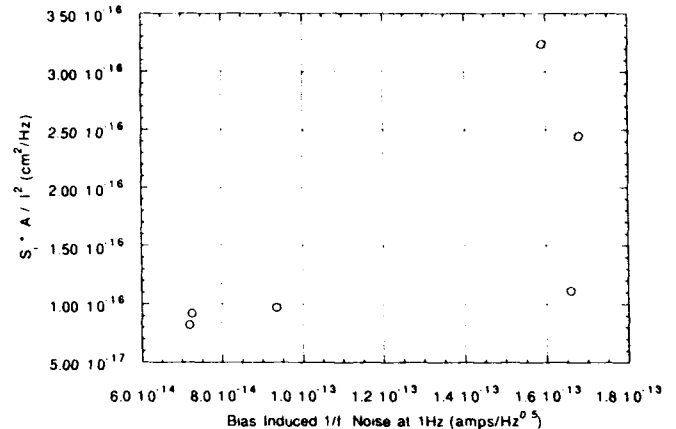


Fig. 10. Photocurrent induced  $1/f$  noise figure of merit ( $S_i A / I^2$ ) vs dark current induced  $1/f$  noise at 50 mV reverse bias. The correlation is weak.

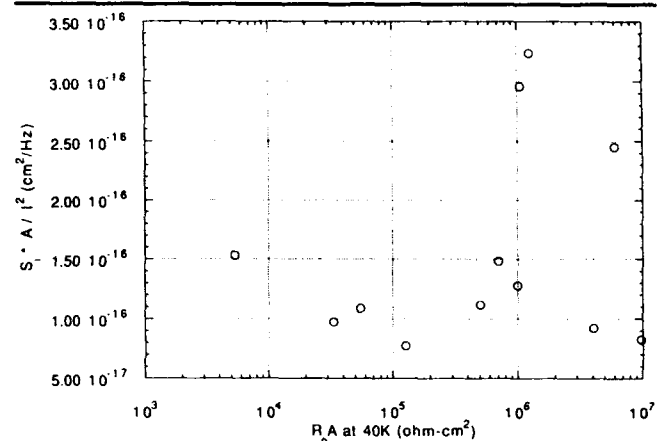


Fig. 11. Photocurrent induced  $1/f$  noise figure of merit ( $S_i A / I^2$ ) vs  $R_0 A$  products measured at 40K. No correlation is observed.

show a  $1/f$  noise current spectrum of this device taken at 17 mV reverse bias combined with same illumination conditions of Fig. 9b. The noise magnitude at 1 Hz in Fig. 9c is  $2.93 \times 10^{-11} \text{ amps/Hz}^{0.5}$  at 1 Hz, and is remarkably close to the quadrature sum ( $2.95 \times 10^{-11} \text{ amps/Hz}^{0.5}$  at 1 Hz) of the noise currents measured in Figs. 9a and 9b. This demonstrates that photo-induced  $1/f$  noise and dark current induced  $1/f$  noise are statistically independent.

In Fig. 10, we show photo-induced  $1/f$  noise figure of merit ( $S_i A / I^2$ ) vs bias induced  $1/f$  noise measured at 50 mV reverse bias in the same LWIR LPE/CdZnTe diodes. Some correlation is indicated, but devices with large dark current induced  $1/f$  noise and low photocurrent induced  $1/f$  noise are found even though only a few devices were evaluated.

In Fig. 11, we show photo-induced  $1/f$  noise figure of merit ( $S_i A / I^2$ ) vs 40K  $R_0 A$  products measured in the same LWIR LPE/CdZnTe diodes. No correlation is seen, although this figure of merit generally correlates with dark current induced  $1/f$  noise.

### EXCESS LOW FREQUENCY NOISE IN HgCdTe PHOTODIODES

Several papers on  $1/f$  noise in HgCdTe photodiodes have been published over the last dozen years. The

literature does not present a clear picture on the nature of this noise, which is ascribed to a variety of phenomena. Researchers have associated  $1/f$  noise with surface generation-recombination (g-r) currents,<sup>2-4</sup> bulk current associated with the depletion region,<sup>5,6</sup> surface related tunneling current,<sup>4-9</sup> band to band tunneling current,<sup>10</sup> bulk band to band tunneling current,<sup>11</sup> band to band and trap assisted tunneling from bulk and surface,<sup>12,13</sup> bulk currents which are not specifically identified,<sup>14</sup> surface and/or bulk material imperfections,<sup>1,9,14</sup> dislocation density,<sup>15</sup> mobility fluctuations in the dominant current component,<sup>8,16</sup> mobility fluctuations in the dominant current component related to quantum  $1/f$  noise and first principle calculations,<sup>7-19</sup> and fluctuations in diffusion current resulting from surface recombination velocity modulation.<sup>20,21</sup> A consistent theme emerging from this work is that  $1/f$  noise is associated with particular current components. A second theme is that current components generate  $1/f$  noise with unequal efficiency ( $1/f$  noise per unit current). The association with nonequilibrium current components naturally accounts for  $1/f$  noise observed in illuminated diodes operated at the open circuit voltage, where the total diode current is zero; behavior which has been previously noted,<sup>25</sup> and is observed in our measurements as well. We logically deduce that for  $1/f$  noise generated by current components other than that which is the least efficient, the excess noise must be associated with the current generation process itself and is not a simple current probing of some quantity which modulates the current.

Mechanisms related to contacts and series resistance have not yet been invoked to account for  $1/f$  noise in diodes, even though such effects are known to be important in HgCdTe photoconductive detectors.<sup>22</sup> In fact, the lack of relationship between total diode current and  $1/f$  noise has been used to show that contacts and series resistance effects are not a dominant factor in bias induced  $1/f$  noise.<sup>2,5,6</sup>

Given the apparent relationship between  $1/f$  noise and components of the current in HgCdTe photodiodes, mathematical expression of the relationship takes a form similar to the one proposed by Hooge.<sup>23</sup> Hooge proposed an empirical expression derived from observation of resistors relating the total current, normalized to the number of carriers in the sample ( $N$ ), to the  $1/f$  noise power spectral density.

$$S_i = \frac{\alpha_H I^2}{fN} \quad (2)$$

$\alpha_H$  is Hooge's constant. In general, the proportionality may involve the current raised to a power other than 2.

Power law relationships between noise power spectral density and current components are often reported. For example, exponent values of  $2^{2-5}$  (i.e. NPSD is proportional to the current squared) have been reported for g-r currents, exponents of 2,<sup>4,8-10</sup> 1,<sup>11-13</sup> 1.5,<sup>12</sup> and 1.8 (with a range from 1-2)<sup>13</sup> for tunneling cur-

rents, and exponent of 1.52<sup>15</sup> for leakage current, and an exponent of 2<sup>1,21</sup> and 1<sup>17-19</sup> for diffusion current. Note that different exponents have been associated with the same current component.

In practice, these relationships are difficult to establish, since the application of bias voltage simultaneously excites all diode current components. Analysis requires separation of active current components unless both the noise and current are dominated by a single component. As an example of the difficulties which may be encountered, the  $1/f$  noise produced by diffusion current is much smaller per unit of current than  $1/f$  noise produced by g-r current.<sup>2,4-6</sup> The difference is large enough that diffusion current induced  $1/f$  noise was not observed in those reports. These publications demonstrated that at elevated temperatures, where the dominant leakage current is diffusion current, the  $1/f$  noise is dominated by a smaller g-r current component. Thus, situations can arise where the dominant leakage current has nothing to do with measured  $1/f$  noise, particularly for MWIR HgCdTe detectors operated near 195K. For this reason, we believe the agreement between theory and experiment in Refs. 17-19 is accidental, since it is unlikely that the diffusion current measured was related to the measured  $1/f$  noise. This problem is also likely to apply to LWIR detectors operated at diffusion limited temperatures.

Given the low efficiency of  $1/f$  noise generation by diffusion currents compared to other current components, attempting to study the properties of diffusion current induced  $1/f$  noise under applied bias is problematic. However, the problems may be circumvented by illuminating the diode at zero applied bias voltage. Only a single component, namely diffusion, of the diode current flows in this case; g-r currents, tunneling currents, and shunt currents are not disturbed from equilibrium values. Diode measurement at zero bias in the dark shows the absence of  $1/f$  noise (any  $1/f$  noise which may be present is much less than observed photo-induced  $1/f$  noise), so the  $1/f$  noise observed under illumination is a result of the diffusion current only. This is strictly true if all of the light is absorbed in the diode neutral region, which suggests that further experiments where the wavelength of the light is varied may be useful in determining the effect of light absorbed in the depletion region. The ability to excite only a single current component is unique to diffusion current. Diffusion current is also a well understood current component in diodes. This combination makes photo-induced  $1/f$  noise an excellent tool for the investigation of excess low frequency noise in diodes.

Photo-induced  $1/f$  noise in HgCdTe has been previously reported.<sup>1,21,24</sup> The photo-induced  $1/f$  NPSD has been observed to scale with the square of the photocurrent.<sup>1,21</sup> Lateral currents can dominate photo-induced  $1/f$  noise, which are explained in terms of surface recombination velocity fluctuations.<sup>21</sup> In contrast, the photo-induced  $1/f$  noise studied in this paper is associated with the device area instead of device perimeter.



Diffusion current induced  $1/f$  noise was recently<sup>20</sup> related to fluctuations in back surface recombination velocity and is a surface dependent model which provides the area scaling relationship we observe. The applicability of this model can be tested by varying sample thickness to distinguish the bulk or surface nature of the noise. Photo-induced  $1/f$  noise has also been observed in InSb,<sup>25</sup> Si,<sup>16</sup> and InGaAs/InP<sup>26</sup> diodes. For the InGaAs/InP diodes,  $S^*A/I^2$  values of  $3 \times 10^{-16}$  to  $4 \times 10^{-15}$  cm<sup>2</sup>/Hz were obtained, and fall within the range reported here for HgCdTe diodes. Insufficient data was given in the Si and InSb references to calculate  $\alpha_{ph}$ .

### SUMMARY, CONCLUSIONS, AND DISCUSSION

Our results demonstrate the dependence of  $S$  on  $I^2$ . This demonstrates that  $N$ , in the description offered by Eq. 2, cannot depend on light intensity; consequently,  $N$  cannot be associated with minority carrier density. The models developed by Kleinpenning<sup>27</sup> and van der Ziel<sup>19</sup> both predict a linear relationship between noise power and current, which is not in agreement with our experiments. The reason is easy to understand; even though the models start from Eq. 2, the factor  $N$  was associated with minority carrier density, which is approximately proportional to current in their diode models. The lack of temperature dependence further supports the conclusion that  $N$  is not related to minority carriers. Note that we cannot associate the temperature dependence of photo  $1/f$  noise with tunneling currents (which are also temperature independent), since we find no bias dependence.

We have developed a figure of merit,  $\alpha_{ph}$  in Eq. 1, which normalized homogenous aspects of photo-induced  $1/f$  noise in diodes. We have indicated in the appendix, where we show that the current and geometry dependencies are uniquely related, what changes would be required for surface vs bulk (area) limitations. If lateral (surface) current sources dominate,  $S/I^2$  should be normalized with the device perimeter instead of junction area.

Formal comparison of Eq. 1 and 2 results in

$$\frac{\alpha_{ph}}{A_j} = \frac{\alpha_H}{N} \quad (3)$$

The terms on either side of the equation must be dimensionless, since  $S$  is proportional to  $I^2$ . Because  $N$ , which can be considered the product of a density and volume, is dimensionless  $\alpha_H$  is also dimensionless. Since  $\alpha_{ph}$  has units cm<sup>2</sup>, the relationship between  $\alpha_{ph}$  and  $\alpha_H$  depends on effective sample thickness. Since we can conveniently change only the area of our HgCdTe detectors, we have not experimentally considered the effects of thickness variations; so, we are not sure what the relevant thickness is: depletion region or one or both of the neutral regions. Also, we do not know what  $N$  is, so establishing a relationship

between  $\alpha_H$  and  $\alpha_{ph}$  is not currently possible.

Most of our area dependent measurements have been performed on devices fabricated on nonlattice matched substrates, which we have shown are noisier than those we have tested which are fabricated on lattice matched substrates. We have also shown that devices fabricated on nonlattice matched substrates are limited by area dependent sources. Nevertheless, lateral components of photo-induced  $1/f$  noise have been demonstrated in devices fabricated on lattice matched substrate material, when the surface is not ideal.<sup>21</sup> There is no conflict here, since it is reasonable that both lateral and area effects contribute to photo-induced  $1/f$  noise in the same way they contribute to  $R_A$  products. The dominant term depends on relative surface and bulk quality, for the size device in question.

Although the figure of merit proposed in Eq. 1 accounts for homogenous dependencies of photo-induced  $1/f$  noise, we have noted that considerable variation is left. The spectrum is not necessarily  $1/f$ , which violates our empirical relationship, Eq. 1, immediately. Investigation of devices of the type shown in Fig. 2b, which exhibit Lorentzian spectra, could be useful in identifying the specific traps whose aggregate behavior is associated with a " $1/f$ " spectrum. This data supports the contention that " $1/f$ " noise is not a universal phenomenon, but is a sum of relaxation processes.<sup>28</sup> Variation in the spectral content of bias induced excess low frequency noise in HgCdTe diodes has also been observed<sup>1</sup>, and is attributed to diverse causes of  $1/f$  noise associated with defects. We have established that devices grown on nonlattice matched substrates have relatively high photo-induced  $1/f$  noise. The dislocation density of material grown on lattice matched substrates is near  $10^5$  cm<sup>-2</sup>, while it is near  $10^7$  cm<sup>-2</sup> on nonlattice matched substrates. This further supports association of photo-induced  $1/f$  noise and defects.

The lack of correlation between photo-induced  $1/f$  noise and other detector figures of merit, like bias induced  $1/f$  noise and low temperature dark currents, suggests that flaws do not affect these phenomena in any specifically consistent way. For example, substantial differences in  $1/f$  noise spectra, as shown by the devices in Figs. 2a and 2b, are not always accompanied by differences in I-V characteristics. Nevertheless, we generally observe that devices which show poor I-V characteristics have large dark current induced  $1/f$  noise and have large photo-induced  $1/f$  noise.

All of these results support a picture of  $1/f$  noise which is induced by defects. These defects, which are randomly distributed and have a multiplicity of types, interact with various current components in different manners. The relationship between defects (traps) and  $1/f$  noise in semiconductors is well established.<sup>29</sup> Furthermore, evidence exists that  $1/f$  noise producing defects may be found in the bulk of the material, at least for GaAs and Si,<sup>30</sup> and does not have to be associated with surfaces.

## ACKNOWLEDGMENT

We would like to acknowledge the efforts of the material growth and device processing teams at Rockwell Science Center in Thousand Oaks, CA; Rockwell Electro-Optical Center in Anaheim, CA; and Aerojet Electronic Systems Division in Azusa, CA; for providing the HgCdTe detector arrays. We thank H. Vydyanath of Aerojet for the devices fabricated in material grown on lattice matched substrates and W.E. Tennant for his support and encouragement.

## APPENDIX: Area Dependence of 1/f Noise

In this appendix we develop expected geometrical dependencies of the noise generated by objects comprised of elements which obey a power law relation between noise and current. Suppose that the current noise power spectral density ( $S_i$ ) of some electronic element has been determined to be proportional to the current ( $I$ ) raised to some power as in

$$S_i = k_e I^\beta \quad (A1)$$

$k_e$  is the proportionality constant for this element, which includes the frequency dependence (if required). We will consider the noise properties of a parallel combination a number ( $n$ ) of such elements. The parallel combination is specifically considered here because we can conveniently change the area of our diodes. For simplicity, we represent diodes by a collection of such elements all of which are assumed to be identical. This does not correspond to reality, as we see from experiment, but is not a bad approximation if there are enough of each of the perhaps diverse types element in a given collection. If the sample is sufficiently inhomogeneous, the reasoning we develop here is useless in the interpretation of experimental results.

We assume that the noise from each element is independent of the presence of the other elements. We may then immediately write, since noise powers add,

$$S_{iT} = \sum_{i=1}^n k_e I^\beta = n k_e I^\beta \quad (A2)$$

where  $S_{iT}$  is the total current NPSD of the network. We emphasize that in this equation  $I$  is the (equal) current flowing in each element, and  $k_e$  is the proportionality constant for an individual element.

If we now view the parallel combination as a single object, we would expect it to follow the form of Eq. A1, such as

$$S_i = k_T I_T^\beta \quad (A3)$$

where  $k_T$  is the proportionality constant for the network and  $I_T$  is the total current. We know from circuit theory that  $I_T = nI$ , so it follows by equating A2 and A3 that

$$k_T = \frac{k_e}{n^{\beta-1}} \quad (A4)$$

This equation clearly indicates that the proportionality constant relating noise power and current

depends on the device geometry, unless  $\beta = 1$  (shot noise). In the case  $\beta = 2$  (which applies to photo-induced 1/f noise in HgCdTe diodes considered here), the proportionality constant is inversely proportional to the number of elements. If these elements are limited by bulk (area) effects, then both  $n$  and  $I$  are proportional to area, so the ratio of the current NPSD to the current squared will be inversely proportional to area; but if the elements are limited by surface effects, the ratio will be proportional to the square root of the area. In arriving at this conclusion, remember that the only elements that count are the ones whose currents generate the noise. Actually, Eq. A4 results from the fact that area (bulk) noise sources (which add in quadrature) must result in NPSDs which increase linearly with area; while lateral (surface) sources must result in NPSDs which increase as root area for square elements, regardless of the noise dependence on current. Failure to appreciate this aspect of 1/f noise behavior can lead to the incorrect assignment of bulk limited performance to surface effects.<sup>4</sup>

This line of reasoning may be extended to include series addition of identical elements. In the more general case of series and parallel combinations of elements,  $n$  becomes proportional to the volume of the sample for bulk limited sources. This is in agreement with the form of Hooge's equation (Eq. 2). It also follows that an  $N \times N$  series/parallel combination of identical elements has the same I-V characteristic as a single element, but only  $1/N$  times as much 1/f noise current. So in general, we expect larger relative 1/f noise in smaller devices, since 1/f noise is usually proportional to the current raised to a power larger than one. This formalism also works, of course, for powers less than one, like Johnson noise ( $\beta = 0$ ).

## REFERENCES

1. R.E. DeWames, M. Hinnrichs, G.M. Williams and J. Bajaj, IRIS Detector Specialty Conference, Aug. 1985
2. S.P. Tobin, S. Iwasa and T.J. Tredwell, *IEEE Trans. Electron Devices* ED-27, 43 (1980).
3. H.K. Chung, M.A. Rossberg and P.H. Zimmermann, *J. Vac. Sci. Technol.* A 3, 189 (1985).
4. W.A. Radford and C.E. Jones, *J. Vac. Sci. Technol.* A 3, 183 (1985).
5. G.M. Williams, J. Bajaj, M. Hinnrichs, J.P. Rode and W.E. Tennant, IRIS Detector Specialty Conference, 1984.
6. J. Bajaj, G.M. Williams, N.H. Sheng, M. Hinnrichs, D.T. Cheung, J.P. Rode and W.E. Tennant, *J. Vac. Sci. Technol.* A 3, 192 (1985).
7. W.W. Anderson and H.J. Hoffman, *J. Vac. Sci. Technol.* A 1, 1730 (1983), *Vac. Sci. Technol.* A 3, 192 (1985).
8. C.E. Jones and W.A. Radford, *Ninth Int. Conf. on Noise in Physical Systems*, Montreal, Canada, May 1987, ed. by C.M. VanVliet (World Scientific, Singapore, 1987), p. 393.
9. Y. Nemirovsky, R. Adar, A. Kornfeld and I. Kidron, *J. Vac. Sci. Technol.* A 4, 1986 (1986).
10. R.E. DeWames, J.G. Pasko, E.S. Yao, A.H.B. Vanderwyck and G.M. Williams, *J. Vac. Sci. Technol.* A 6, 2655 (1988).
11. Y. Nemirovsky, D. Rosenfeld, R. Adar and A. Kornfeld, *J. Vac. Sci. Technol.* A 7, 528 (1989).
12. Y. Nemirovsky and D. Rosenfeld, *J. Vac. Sci. Technol.* A 8, 1159 (1990).
13. Y. Nemirovsky and A. Unikovsky, *J. Vac. Sci. Technol.* B 10, 1602 (1992).

14. J. Bajaj, E.R. Blazejewski, G.M. Williams and R.E. DeWames, *J. Vac. Sci. Technol.* B 10, 1617 (1992).
15. S.M. Johnson, D.R. Rhiger, J.P. Rosbeck, J.M. Peterson, S.M. Taylor and M.E. Boyd, *J. Vac. Sci. Technol.* B 10, 1499 (1992).
16. T.G.M. Kleinpenning, *J. Vac. Sci. Technol.* A 3, 176 (1985).
17. A. van der Ziel, P.H. Handel, X.L. Wu and J.B. Anderson, *J. Vac. Sci. Technol.* A 4, 2205 (1986).
18. X. Wu, J.B. Anderson and A. van der Ziel, *IEEE Trans. Elec. Dev.* ED-34, 1971 (1987).
19. A. van der Ziel, P. Fang, L. He, X.L. Wu and A.D. van Rheezen, *J. Vac. Sci. Technol.* A 7, 550 (1989).
20. R.A. Schiebel, D. Blanks, D. Bartholomew and M. Kinch, IRIS Detector Specialty Conf., Aug. 1992.
21. D.L. Lee, S. Liberman and A. Mestechkin, IRIS Detector Specialty Conference, Aug. 1992.
22. W.A. Beck, G.D. Davis and A.C. Goldberg, *J. Appl. Phys.* 67, 6340 (1990).
23. F.N. Hooge, *Phys. Lett.* 29A, 139 (1969).
24. R.E. DeWames, M. Hinnrichs, J. Bajaj and G.M. Williams, *Bull. of the Amer. Phys. Soc.* 30, 1155 (1985).
25. N.B. Lukyanchikova, B.D. Solganik and O.V. Kosogov, *Solid State Electron.* 16, 1473 (1973).
26. L. He, Y. Lin, A.D. van Rheezen, A. van der Ziel, A. Young and J.P. van der Ziel, *J. Appl. Phys.* 68, 5200 (1990).
27. T.G.M. Kleinpenning, *Ninth Int. Conf. on Noise in Physical Systems*, Montreal, May 1987 ed. C.M. VanVliet (World Scientific, Singapore, 1987), p. 441.
28. P. Dutta and P.M. Horn, *Rev. of Modern Phys.* 53, 497 (1981).
29. C.T. Rodgers, K.R. Farmer and R.A. Buhrman, *Ninth Int. Conf. on Noise in Physical Systems*, Montreal, May 1987, ed. C.M. VanVliet (World Scientific, Singapore, 1987), p. 293.
30. N.V. D'yakonova, M.E. Leninshtein and S.L. Rumyantsev, *Sov. Phys. Semicond.* 25, 1241 (1991).

# Synchrotron White Beam X-Ray Topography Analysis of MBE Grown CdTe/CdTe (111)B

T. FANNING,\* M.B. LEE,\*\* L.G. CASAGRANDE,\*\* D. DI MARZIO,\*\* and M. DUDLEY\*

\*Department of Materials Science & Engineering, SUNY at Stony Brook, Stony Brook, NY 11794; \*\*Grumman Corporate Research Center, Bethpage, NY 11714

The structural quality of CdTe(111)B substrates and MBE grown CdTe epilayers is examined with synchrotron white beam x-ray topography (SWBXT). Reflection SWBXT indicates that CdTe substrates with comparable x-ray double crystal rocking curve full width at half maximum values can have radically different defect microstructures, i.e. dislocation densities and the presence of inclusions. Dislocation mosaic structures delineated by SWBXT are consistent with the distribution of etch pits revealed by destructive chemical etch pit analysis. Direct one-to-one correspondence between distinct features of the topographic image and individual etch pits is demonstrated. Clearly resolved images of individual dislocations are obtained by carrying out transmission SWBXT. Our investigation demonstrates how the extent of twinning in a CdTe epilayer is strongly influenced by the quality of the defect microstructure, and how dislocations propagate from an inclusion.

**Key words:** Defect microstructures, dislocations, MBE-grown CdTe, synchrotron x-ray effects, twinning

## INTRODUCTION

CdTe is a technologically important material, in part, because it is used as a buffer layer for vapor phase growth of HgCdTe. In this work, we have investigated one of the major factors that can limit the crystal quality of CdTe buffer layers, namely, the defect microstructures of the substrates. Specifically, we have carried out a systematic characterization of the structural quality of CdTe substrates and epilayers to better understand how different types of defects determine epilayer quality. The motivation for this study was generated, in part, by our previously published work<sup>1</sup> in which we observed a wide variation in rocking curve full width at half maximum (FWHM) values among CdTe epilayers that were grown with the same molecular beam epitaxy (MBE) growth parameters on substrates with comparable FWHM rocking curve values. The goals of the present study are twofold:

1. To understand the reasons for this nonuniformity of structural quality of the CdTe epilayers as determined by double crystal rocking curve (DCRC), and
2. To establish an alternative criteria of structural quality that, when compared to FWHM values of rocking curves, are more representative of the crystal quality of the epilayer that can be grown on a given CdTe substrate.

CdTe (111)B substrates were chosen for study mainly because CdTe/CdTe is a homoepitaxial system, so that the exact lattice match between the substrate and buffer layer effectively eliminates interfacial strain as a factor in influencing the crystal quality of the buffer layer. Thus, we can make a direct correlation between the structural quality of the CdTe buffer to the defect microstructure of the substrate. Any correlation observed in this system should be highly relevant to factors that determine crystal quality of HgCdTe grown on CdZnTe since HgCdTe/CdZnTe is another lattice-matched system and the crystal structure of HgCdTe is similar to CdTe.

(Received October 13, 1992; revised January 13, 1993)

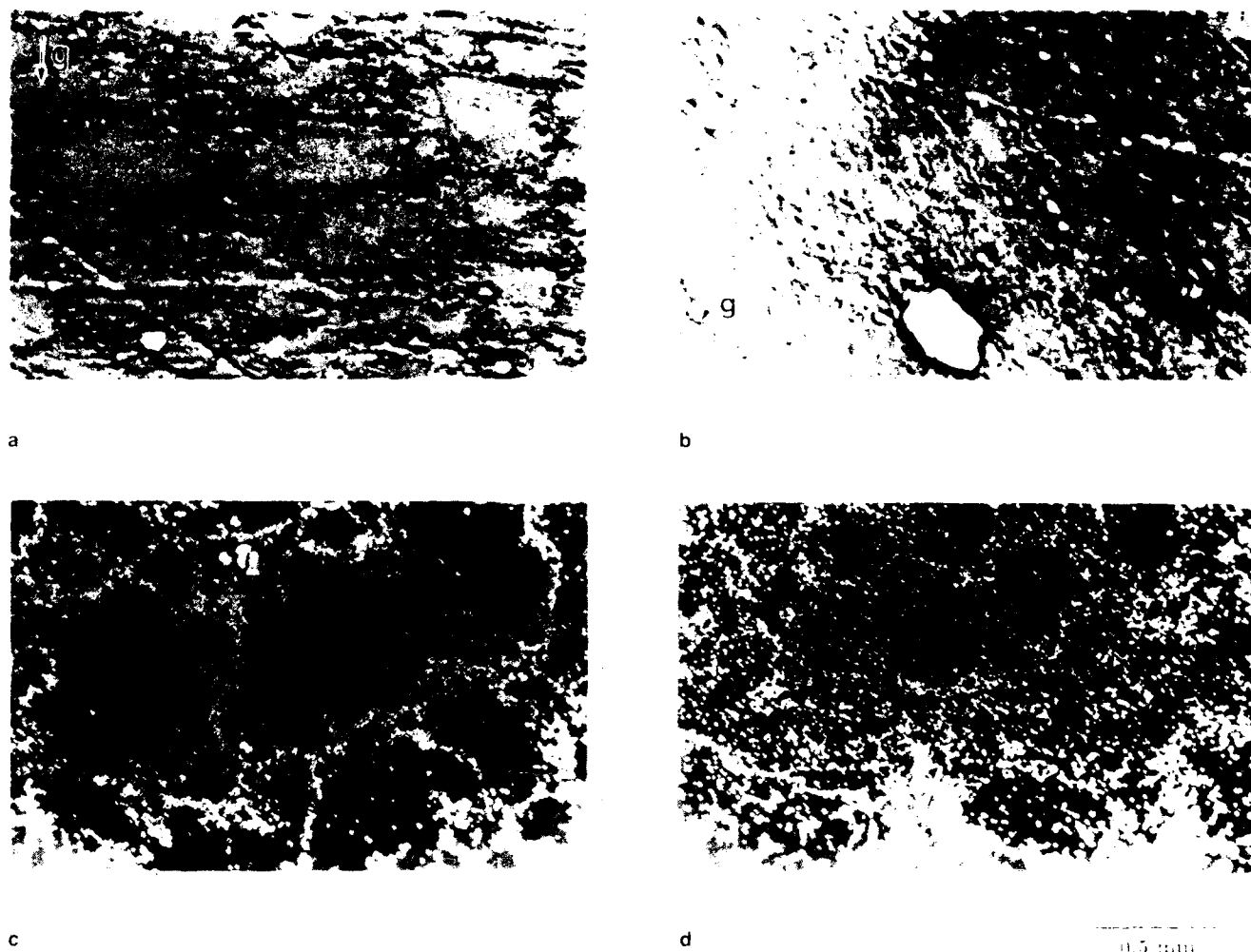


Fig. 1. Reflection SWBXT images of CdTe(111)B substrates ( $g = 333$ ,  $\lambda = 0.89\text{\AA}$ ) with (a) a well defined cellular structure, and (b) a random distribution of dislocations. (c) and (d) are optical micrographs of (a) and (b), respectively, after etching.

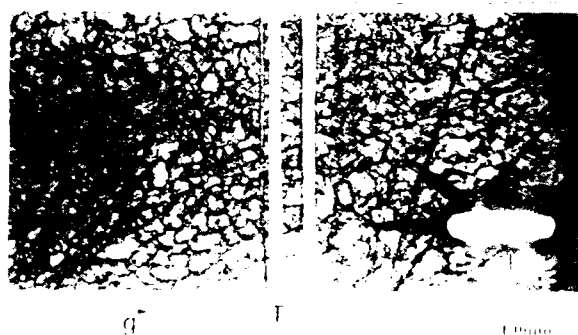


Fig. 2. (a) Transmission SWBXT image of a CdTe substrate ( $g = 333$ ,  $\lambda = 0.55\text{\AA}$ ) note the large inclusion (I) and twin lamella (T) exhibiting orientation contrast.

(111)B was chosen as the growth plane since the formation of microtwins in CdTe and HgCdTe occurs most readily in this growth orientation; the role of substrate defect microstructures in the generation of microtwins in CdTe epilayers, if any, should be most obvious in (111)B growth.

A better understanding of factors that contribute to

formation of twins in (111)B may provide a way of eliminating twin related defects such as hillocks, and may lead to an improvement in the growth of CdTe and HgCdTe in other crystal orientations that are also afflicted by the formation of twins.

To accomplish the goals of this investigation, we utilize synchrotron white beam x-ray topography (SWBXT) extensively. Detailed topographic images of the substrates and epilayers are compared. As will be shown below, the high sensitivity of SWBXT and its ability to nondestructively image structural defects in both CdTe substrates and epilayers allows direct and clear observations of the roles that substrate defect microstructures play in the formation of twins and dislocations in CdTe buffer layers. The wealth of microstructural information obtained from SWBXT will also be used as a basis from which to evaluate relative sensitivity of double crystal rocking curve (DCRC) and etch pit analysis (EPA). Finally, detailed microstructural information obtained from synchrotron white beam x-ray topography will be used to refine the standard with which to judge the structural quality of CdTe substrates.

## EXPERIMENTAL TECHNIQUES

CdTe(111)B substrates used in this study were obtained from the Grumman crystal growth program and three commercial vendors. The quality of Grumman substrates has been reported in detail previously.<sup>1</sup> Prior to MBE growth, all CdTe substrates were chemically polished in accordance with in-house polishing procedures. The epilayer growth was carried out in a Riber 2300 MBE system with one CdTe effusion cell. Details of MBE growth have been described previously.<sup>1</sup>

All rocking curve measurements reported in this paper were carried out at room temperature and utilized Cu K $\alpha_1$  radiation. The size of the x-ray beam used was 1 x 0.4 mm<sup>2</sup>. 1HF:4HNO<sub>3</sub>:25 lactic acid solution was used in EPA. White beam x-ray topographic imaging was carried out on the white beam camera on the Stony Brook Synchrotron Topography Beamline (X-19C) at the National Synchrotron Light Source (NSLS) at Brookhaven National Laboratory. Detailed description highlighting the unique sensitivity of the white beam technique can be found elsewhere.<sup>1,4,5</sup>

## RESULTS

### Substrate Characterization

As pointed out in our earlier work,<sup>1</sup> we have found that SWBXT can detect significant differences in the density and distribution of dislocations and inclusions present among CdTe substrates that have comparable rocking curve mapping profiles. This significant finding is demonstrated in Figs. 1a and 1b which show SWBXT images of two substrates with comparable rocking curves. As can be seen from the figure, the defect microstructure of substrate A (Fig. 1a) is significantly different from that of substrate B (Fig. 1b): substrate A displays well defined cell structures in which low defect density areas are separated by groups of dislocations, while substrate B exhibits a uniformly higher density of dislocations with large inclusions. Figures 1c and 1d show etch pit patterns obtained from the crystals shown in Figs. 1a and 1b, respectively. These micrographs clearly reproduce the patterns shown in the topographs. Similar comparisons between EPA and topography have been made previously for CdTe substrates of different orientation.<sup>6,7</sup> While the overall shapes of the subgrains are clearly comparable on the images presented here, the density of dislocations within the boundaries is too high to establish a one-to-one correlation. However, such a one-to-one correlation is established for isolated dislocations within the subgrain.

Significantly, of the two techniques, only SWBXT is sensitive to strain and capable of providing both qualitative and quantitative information on the nature of the strain fields of individual defects.<sup>5</sup> This high sensitivity to strain allows SWBXT to easily detect the presence of inclusions, which are often difficult to clearly distinguish on optical micrographs

since they are often located in subgrain boundaries and are obscured by other etch pits. The effect of strain generated by inclusions on the crystal quality of CdTe buffer layers will be discussed in the next section.

As a variation in topographic image analysis of CdTe substrates, we have carried out SWBXT in transmission mode. For the transmission work, the thinning of CdTe substrates to a thickness of less than 100  $\mu$ m was necessitated by the high x-ray absorption coefficient of CdTe. Acquisition of the transmission images is made more difficult by extreme brittleness of the thin substrates. However, the transmission images, when compared to the images acquired in reflection geometry, offer better resolution due to the elimination of the overlap of defect images.

A typical example of the transmission SWBXT image is shown in Fig. 2. This image of 30  $\mu$ m thick CdTe reveals the familiar dislocation mosaic structure with an ensemble of low defect density cells separated by groups of dislocations. In addition, large

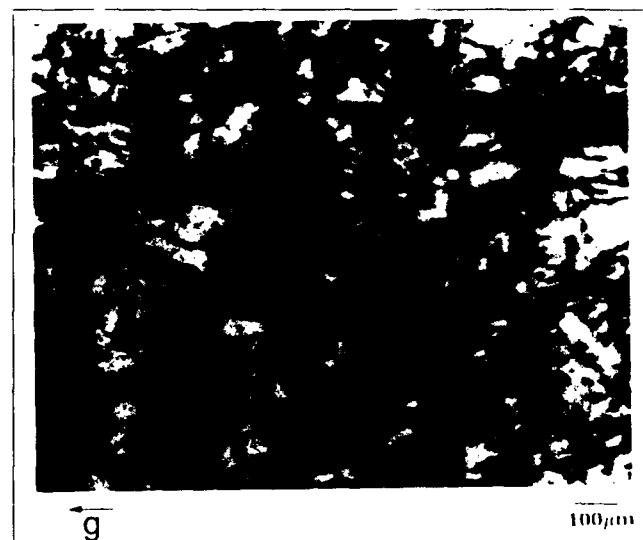


Fig. 3. Transmission SWBXT images of a CdTe substrate ( $g = \bar{1}11$ ,  $\lambda = 0.48\text{\AA}$ ). Note the individual dislocations inside the cell walls and inside the subgrain boundaries.



Fig. 4. (a) Enlargement from Fig. 2 showing details of the local lattice rotation associated with the plastic deformation surrounding the inclusion.

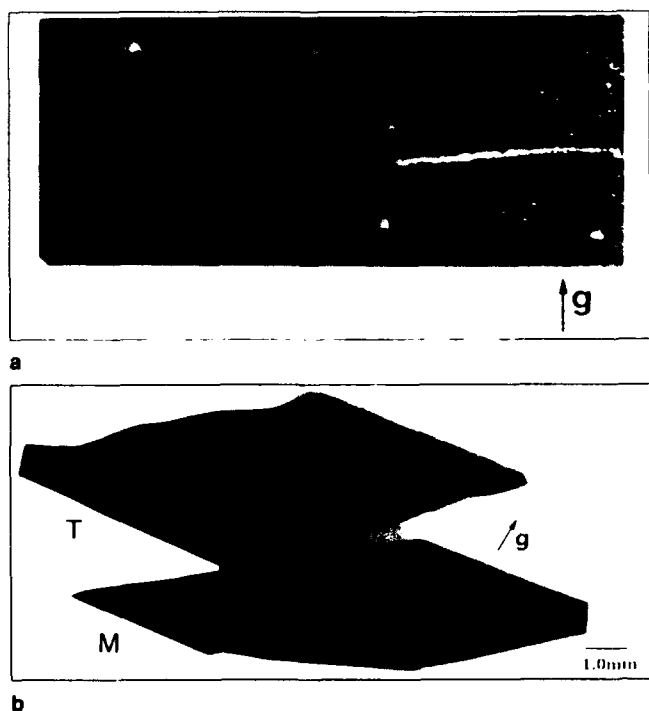


Fig. 5. Reflection SWBXT images of CdTe(111)B epilayers showing: (a) a twin free, 5.2  $\mu\text{m}$  CdTe epilayer ( $g = 333$ ,  $\lambda = 0.89\text{\AA}$ ) of high structural quality, and (b) an epilayer of poor structural quality showing the twin domains (T), ( $g = 422$ ,  $\lambda = 0.86\text{\AA}$ ) and the untwinned matrix (M), ( $g = 133$ ,  $\lambda = 0.94\text{\AA}$ ).

inclusions (I) and a twin lamella (T) exhibiting orientation contrast are observed. Higher magnification images of specific features shown in Fig. 2 dramatically illustrate the increased resolution of transmission SWBXT. For example, a high magnification image of one of the low defect density cells (Fig. 3) reveals the existence of a network of individual dislocations inside the cell wall. Such networks of individual dislocations were not observed this clearly in any of the topographic images taken in reflection geometry. A high magnification image of an inclusion is shown in Fig. 4. Note the broad image of the inclusion. Interchanging the exit and entrance surfaces has the effect of changing the contrast from a diffracted beam divergence effect to a convergence effect. This, in addition to the optical microscopic observation that extensive plastic deformation is evident around the inclusions, leads to the conclusion that the mechanism of contrast formation involves significant local lattice rotation associated with the plastic deformation surrounding the inclusion, leading either to beam divergence or convergence, depending on the diffraction geometry. This information can be used to demonstrate consistency with contrast that is observed on reflection topographs, and enables ready interpretation of reflection images.

#### Epilayer Characterization.

The structural quality of MBE grown CdTe epilayers was also characterized with DCRC and SWBXT. Unless otherwise stated, all DCRC and SWBXT results shown below were generated from the epilayers

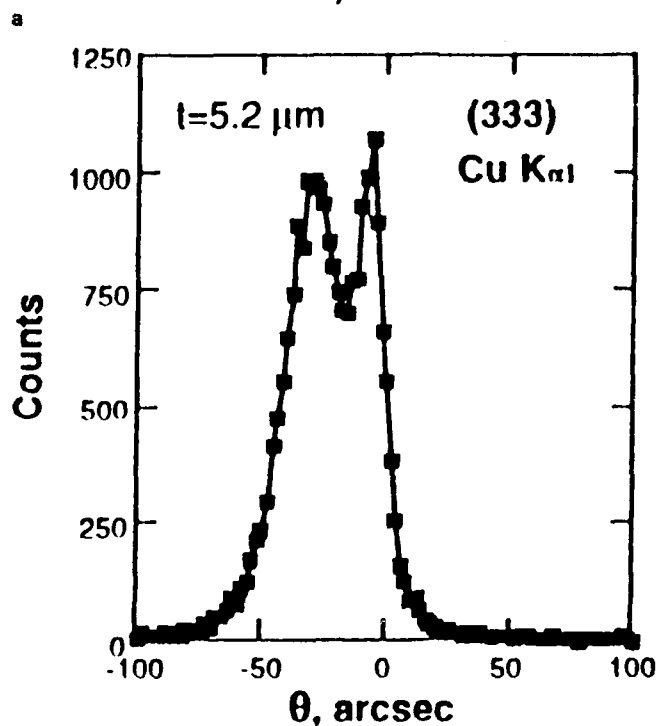
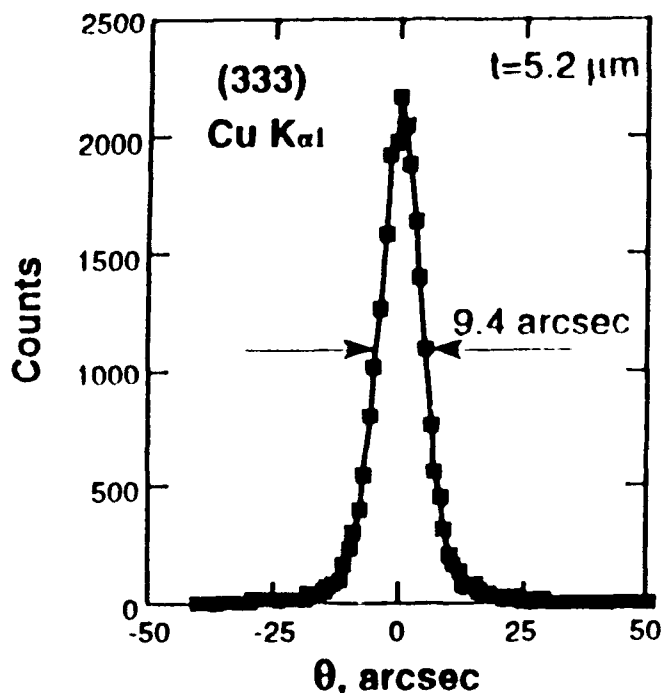


Fig. 6. (a) Rocking curve taken from the epilayer of high structural quality in Figs. 5a and 5b, a rocking curve taken from epilayer in Fig. 5b showing a double peak.

with thickness greater than the absorption depth of the x-ray beam used. These results can, therefore, be interpreted exclusively in terms of the crystal quality of the CdTe epilayer. All epilayers examined here were grown using optimized MBE growth parameters<sup>1</sup> with CdTe(111)B substrates having comparable DCRC FWHM values. Prior to MBE growth, defect microstructures of CdTe substrates were im-

aged with SWBXT. Because of the identical growth parameters used, it is reasonable to hypothesize that any observed differences in crystal quality of the CdTe epilayers shown below are likely due to the differences in defect microstructure of substrates which were not clearly distinguished by DCRC.

To evaluate the above hypothesis, we have compared the structural quality of two epilayers that were grown simultaneously. Synchrotron white beam x-ray topography images of the two substrates used (not shown here) reveal a difference in defect microstructures which is very similar to that already observed in Fig. 1: one substrate displays an ensemble of large, low defect density areas separated by subgrains while the other substrate shows a random distribution of dislocations. Synchrotron white beam x-ray topography images of the epilayers grown on these substrates are shown in Fig. 5a (for the well defined cellular microstructure substrate) and 5b (for the random dislocation microstructure). There is an obvious absence of twinning in Fig. 5a. On the other hand, significant twinning is evident in Fig. 5b, where intense twin and matrix reflections cover the entire area of the epilayer, indicating the presence of small domains of rotational twins (twinning is occurring by a  $180^\circ$  rotation about the  $[111]$  axis) interspersed with the matrix throughout the epilayer. Preliminary studies using the depth profiling technique developed by Dudley and coworkers<sup>8</sup> suggest that twinning is occurring throughout the entire depth of the epilayer. Rocking curve analysis carried out on these epilayers reveals significant differences despite the absence of any differences in the rocking curves of the corresponding substrates. The rocking curve of the crystals shown in Figs. 5a and 5b are presented in Figs. 6a and 6b, respectively. The former rocking curve exhibits a narrow line profile, while the latter exhibits a double peak structure. A double peak was observed at all spots sampled (63 in total) on the crystal. It appears the presence of this double peak is related to the detailed distribution of the twin domains and matrix in the film. Further analysis of the fundamental causes of this double peak are underway.

Crystal quality of another CdTe epilayer grown on a CdTe substrate with a random dislocation distribution is shown in Fig. 7. The topographic image of the epilayer reveals the presence of two distinct regions, one which consists of a composite of twin and matrix domains where the twins dominate and another which is relatively twin free. The locations of twin dominated regions on the topographic image directly coincide with the locations of regions that exhibited severe rocking curve broadening (80–105 arc-s). Since a wide range of misorientation was observed in the predominantly twinned regions, any double peaks, as observed in the prior case, may not be delineated. This correlation clearly establishes the rotational twinning as the cause of the rocking curve broadening. More significantly, the topographic images dramatically illustrate the significance of the dislocation mosaic structure in controlling the degree of twinning

in an epilayer.

In addition to establishing a direct correlation between formation of rotational twin in CdTe epilayers and the quality of substrate defect microstructures, the topographic images also reveal the effect of presence of inclusions on the crystal quality of CdTe epilayers. Structural damage induced by inclusions is clearly shown in the topographic image of a twin free epilayer. As can be seen from Fig. 8, the low defect density of the epilayer allows clear resolution of individual dislocations propagating from an inclusion. Similar propagation of dislocations is also detected for other inclusions present in the epilayer. Thus, the deleterious effects of growing CdTe on inclusion induced strained areas of substrate are demonstrated. This direct observation of dislocation propagating from an inclusion in a CdTe epilayer



Fig. 7. Reflection SWBXT images of a CdTe(111)B epilayer of poor structural quality showing the twin domains (T), ( $g = 422$ ,  $\lambda = 0.86\text{\AA}$ ) and the untwinned matrix (M), ( $g = 133$ ,  $\lambda = 0.94\text{\AA}$ ).

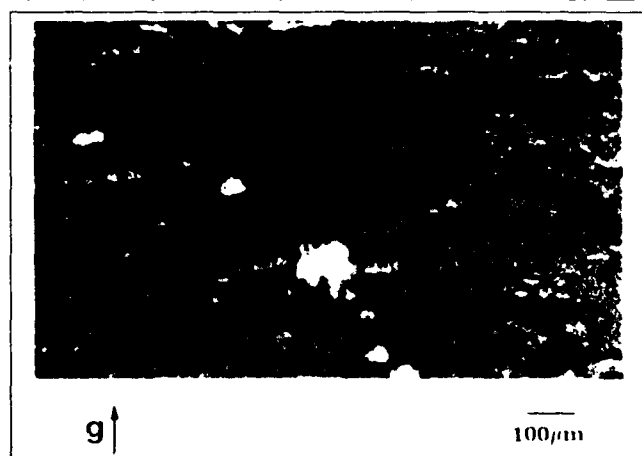


Fig. 8. (a) Enlargement of Fig. 5a showing detail of a large inclusion (I) and the dislocations propagating out from it.

**Table I. CdTe Rocking Curve Values and Thicknesses of Twin Free CdTe Epilayers**

| Crystal | Thickness ( $\mu\text{m}$ ) | Epilayer DCRC FWHM (arc-s) |
|---------|-----------------------------|----------------------------|
| G-01    | 5.4                         | $17.6 \pm 4.6$             |
| G-02    | 3.8                         | $21.4 \pm 4.7$             |
| G-04    | 5.2                         | $11.5 \pm 0.64$            |
| G-05    | 6.5                         | $17.9 \pm 2.65$            |

Note: Error bars are statistical 95% confidence limit of at least nine measurements.



provides the experimental basis from which the dynamics of dislocation generation from such an inclusion can be studied.

## DISCUSSION

Synchrotron white beam x-ray topography results presented here clearly illustrate some important limitations in DCRC and EPA in detecting the presence of specific defects that directly affect the quality of CdTe epilayers. This technology can provide the experimental evidence with which to formulate a more refined set of criteria of structural quality of CdTe substrates.

### Limitations of DCRC

As shown in Fig. 1, detailed dislocation microstructures or the presence of inclusions cannot be unambiguously determined from FWHM values or peak shapes of rocking curves. This insensitivity of DCRC may be related to the fact that the large area incident beam integrates information from several subgrain regions, thus providing an average but not detailed measure of local distortion. The large beam size also contributes to the technique's inability to detect inclusions. Unambiguous detection of inclusion is made more difficult by the fact that broadening of rocking curves due to lattice strain caused by an inclusion cannot be separated from other factors.<sup>9,10</sup> The inability to reveal detailed defect microstructures severely limits the usage of DCRC as a nondestructive screening technique for CdTe substrates.

### Limitations of EPA

Chemical etch pit analysis, unlike DCRC, can accurately determine dislocation microstructures in CdTe. Comparability of the shape of a dislocation mosaic structure delineated by EPA and SWBXT has already been established. However, EPA is a destructive technique, and therefore has obvious limitations. Significantly, the details of dislocation line shapes and propagation cannot be obtained from EPA since dislocations of different type and shape all generate an etch pit of similar morphology, nor can EPA detect defects in regions below the surface of the crystal without repeated etching. In addition, EPA cannot clearly distinguish inclusions located in subgrains. The crucial need to detect inclusions during CdTe substrate screening has already been discussed in detail. These limitations of EPA can be compensated by a judicious usage of SWBXT during the structural evaluation of CdTe.

### Utility of SWBXT

Synchrotron white beam x-ray topography has been used successfully to correlate the presence of specific defect features in CdTe(111)B substrates with the formation of rotational twins and dislocations in CdTe epilayers. Specifically, SWBXT results have demonstrated that (1) randomly distributed dislocation mosaic structures in CdTe substrates, facilitate the formation of rotational twins in the epilayer, and (2)

inclusions induce dislocation propagation in the epilayer. In general, a twin-free CdTe epilayer with excellent dislocation microstructure can be reproducibly grown with MBE if a CdTe substrate with the desirable defect microstructures is used. Table I summarizes rocking curve values of some of the twin free epilayers grown in this work. These findings are powerful demonstrations of the high sensitivity and versatility of nondestructive SWBXT to examine critical microscopic structural details of CdTe substrates that cannot be examined with DCRC and EPA.

The unique sensitivity of SWBXT is also demonstrated by consideration of other aspects of epilayer characterization. As shown earlier, the orientation contrast associated with twin domains allows SWBXT to unambiguously detect the presence of rotational twins. In addition, the utilization of the large beam size associated with a synchrotron source (0.6 cm x 5.0 cm) allows examination of twin distributions in sample areas of similar size to the area of the synchrotron beam. Thus, twin distributions throughout a typical CdTe and CdZnTe sample can be examined with a single SWBXT image. This ability to detect a large area with a single topographic image offers SWBXT distinct advantages over other twin sensitive techniques such as electron channeling or asymmetric reflection rocking curve analysis<sup>11</sup> that can examine the presence of twins only within the limited area of the sample that an electron or x-ray beam covers. One disadvantage of SWBXT is the technique requires the use of a synchrotron source which may not be available for routine characterization of materials.

## CONCLUSIONS

We have presented experimental evidence demonstrating significant limitations in the sensitivity of rocking curve analysis to specific defect microstructures of CdTe which exert a strong influence on the crystal quality of CdTe epilayers. We have also demonstrated that SWBXT does not suffer from such limitations, and have provided evidence justifying a wider usage of synchrotron white beam x-ray topography in the structural characterization and screening of CdTe and a wider variety of other substrate/epilayer systems.

## ACKNOWLEDGMENT

Topography carried out at the Stony Brook Synchrotron Topography Facility at the NSLS which is supported by the U.S. Department of Energy under grant number DE-FG02-84ER45098. T. Fanning and M. Dudley acknowledge financial support from Grumman Corporate Research Center for carrying out this work. The able assistance of J. DeCarlo, F. Chin, and A. Berghmans as well as guidance and support from Dr. R. Silberstein and Dr. R. Pirich are gratefully acknowledged.

## REFERENCES

1. M.B. Lee, T. Fanning, D. DiMarzio, L.G. Casagrande and M. Dudley, *Mat. Res. Soc. Symp. Proc.* 262, 169 (1992).

2. K.A. Harris, T.H. Myers, R.W. Yanka, I.M. Mohnkern, R.W. Green and N. Otsuka, *J. Vac. Sci. Technol.* A8, 1013 (1990).
3. L.G. Casagrande, D. DiMarzio, M.B. Lee, D.J. Larson, Jr., M. Dudley and T. Fanning, *J. Cryst. Growth* 128, 576 (1993).
4. T. Tuomi, K. Naukkarinen and P. Rabe, *Phys. Status. Solidi.* (a) 25, 93 (1974).
5. J. Miltat, *Characterization of Crystal Growth Defects by X-ray Methods*, NATO ASI B63, eds. B.K. Tanner and D.K. Bowen, Plenum Press, New York, (1980) p. 401.
6. Y.-C. Lu, R.S. Feigelson, R.K. Route and Z.U. Rek, *J. Vac. Sci. Technol.* A4, 2190 (1986).
7. D. DiMarzio, L.G. Casagrande, M.B. Lee, T. Fanning and M. Dudley, *Mat. Res. Soc. Symp. Proc.* 262, 215 (1992).
8. G.-D. Yao, M. Dudley and J. Wu, *J. X-ray Sci. & Tech.* 2, 195 (1990).
9. P. Gay, P.B. Hirsch and A. Kelley, *Acta. Metall.* 1, 315 (1953).
10. S.B. Qadri, B.T. Jonker, G.A. Prinz and J.J. Krebs, *J. Vac. Sci. Technol.* A6, 1527 (1988).
11. M. Oron, A. Raizman, Hadas Shtrikman and G. Cinader, *Appl. Phys. Lett.* 52, 1059 (1988).

# Structure of CdTe(111)B Grown by MBE on Misoriented Si(001)

Y.P. CHEN, S. SIVANANTHAN, and J.P. FAURIE

Microphysics Laboratory, Physics Department, University of Illinois at Chicago, Chicago, IL 60607-7059

Single domain CdTe (111)B has been grown on Si(001) substrates tilted  $1^\circ$ ,  $2^\circ$ , and  $4^\circ$  toward [110]. All the layers started with a double-domain structure, then a transition from a double- to a single-domain was observed by reflection high energy electron diffraction. A microscopic picture of this transition is presented. We also measured the tilt between CdTe (111)B and Si (001). The result does not follow the tilt predicted by the currently existing model. A new model of the microscopic mechanism of CdTe (111)B growth is presented. New evidence indicates that optimizing the tilt of the substrate surface is very crucial in improving the CdTe (111)B crystal quality.

**Key words:** CdTe epitaxial layers, MBE, RHEED analysis, Si substrates

## INTRODUCTION

CdTe has been viewed as an important semiconductor over the decades for both its almost ideal use as a substrate for HgCdTe and its potential applications in  $\gamma$ -ray and x-ray detection. However, it is also well recognized that it is technically difficult and costly to produce bulk CdTe single crystals with both high quality and large area. For this reason, epitaxial growth of CdTe on foreign substrates has received a great deal of attention for many years. The possible choices for substrates are InSb, sapphire, GaAs, and Si. Among them Si is the most promising since high quality and large size Si substrates are commercially available. Furthermore, advantage can be taken of the mature Si integrated circuit technology to fabricate monolithic integrated focal plane arrays, by combining the Si integrated circuit for signal processing with the detector fabricated on it. This promising future makes it very attractive for the direct growth of CdTe (111)B on Si (001), which has been an active research program in the Microphysics Laboratory for the last three years.

However, there are several obstacles which need to be overcome in order to produce high quality CdTe on

Si. One is the very large lattice mismatch (19%) between CdTe and Si, which will introduce large dislocation density along the interface. Second is the large thermal mismatch between the two materials, which will produce additional strain to the already strained CdTe layer. In the worse case, the thermal mismatch might cause some practical problems such as cracking or peeling of the CdTe layer for the system of CdTe/Si or HgCdTe/CdTe/Si when cycled from room temperature to low temperature. For the epitaxial relation of CdTe (111)B on Si(001) there is a third obstacle, which is the formation of double domains and twins. Since Si[110] is equivalent to Si[1 $\bar{1}$ 0], the CdTe[11 $\bar{2}$ ] can align with either the Si[110] or the Si[1 $\bar{1}$ 0]. This leads to the formation of double domains, in which one domain differs from the other by a  $90^\circ$  rotation. Furthermore, CdTe (111)B is known to be plagued by microtwin formation. Double-domain and microtwin in CdTe (111)B/Si(001) are structural defects which can significantly degrade the HgCdTe grown on such CdTe buffer layer. Therefore, ways to avoid the formation of the double domains and twins has always been a major concern to us.

We have previously reported<sup>1</sup> that CdTe (111)B, grown on Si(001) tilted  $6^\circ$  or  $8^\circ$  toward [110], always exhibited single-domain structure, but the full width at half maximum (FWHM) of x-ray double crystal

(Received November 12, 1992; revised January 15, 1993)

rocking curves (DCRC) measured from these samples is always large. In order to develop a technique which consistently produces twin-free and single domain CdTe films, we investigate the microscopic mechanism of the formation of double domains and twins and understand how the substrate tilt can help to suppress such formation. In this paper, we present the experimental results of CdTe (111)B grown on Si(001) tilted  $1^\circ$ ,  $2^\circ$ , or  $4^\circ$  toward [110]. We also discuss the microscopic mechanism of growth of single domain CdTe (111)B on slightly misoriented Si(001),

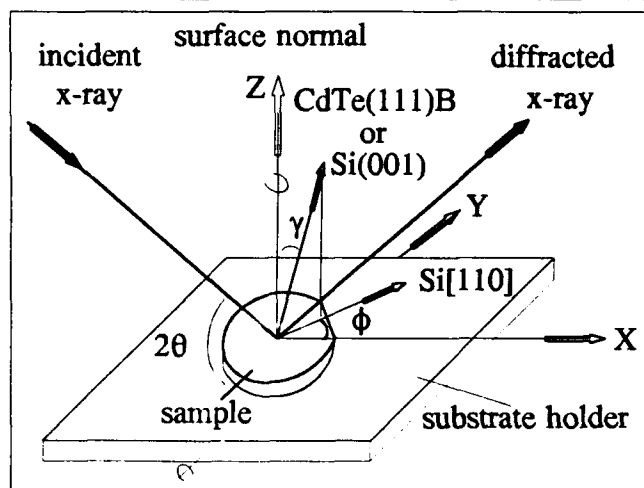


Fig. 1. Double crystal rocking curve measurement for the tilt of the sample with respect to the surface normal. The azimuthal angle is defined as the angle between Si[110] (major flat on the wafer) and the x-ray incident plane.

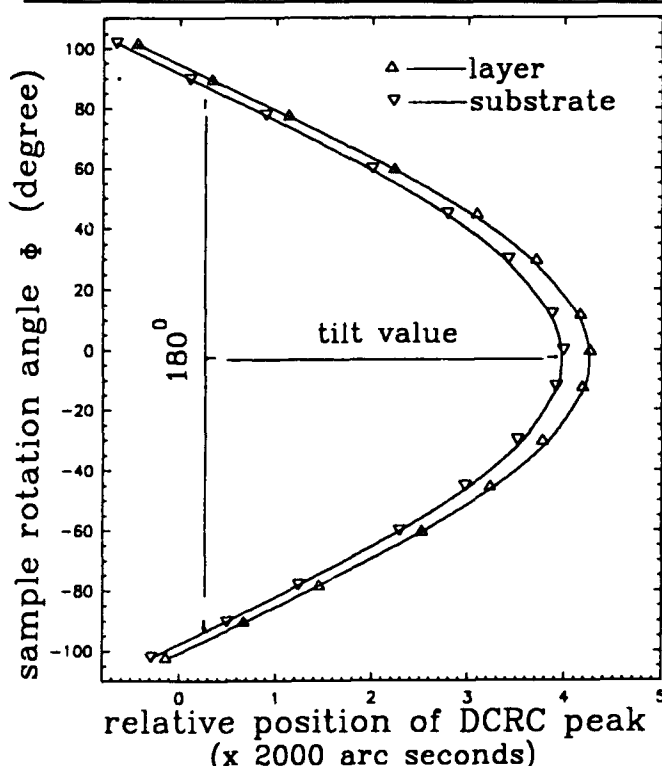


Fig. 2. Double crystal rocking curve measurement result for a sample tilted  $2^\circ$  toward Si[110]. The symbols  $\Delta$  and  $\nabla$  are the experimental data. The solid lines are the fitting curves.

and present a model for this epitaxial growth relationship.

## EXPERIMENTAL

### Growth

All the CdTe layers were grown by molecular beam epitaxy (MBE) in OPUS 45, which is a multiwafer MBE system manufactured by ISA-Riber. This system can handle three 2-in diam substrates per growth run. The details of this system have been described in a previous paper.<sup>2</sup>

The substrates used for the MBE growth of CdTe are 2-in diam Si(001) tilted  $1^\circ$ ,  $2^\circ$ , or  $4^\circ$  toward [110]. Just before they were loaded into the MBE chamber, the Si wafers were cleaned by using a cleaning procedure developed from both the RCA method,<sup>3</sup> and the method described by Ishizaka and Shiraki.<sup>4</sup> The procedure includes a degreasing step, a wet chemical etching and an oxidation step. Between each step, the wafer was thoroughly rinsed with de-ionized water. As a result, at the end of the process the wafer was covered by a protective thin oxide layer. Immediately before deposition of CdTe, the oxide layer was removed in-situ by heating up the wafer over  $850^\circ\text{C}$ .

CdTe (111)B layers were grown on Si(001) by using a two-step method which is similar to the method used routinely for the growth of GaAs on Si. CdTe was first grown at about  $220^\circ\text{C}$  for several min, which was then followed by a growth at about  $260^\circ\text{C}$ . The as-grown layer was then annealed at about  $360^\circ\text{C}$  under Te flux for 10 min. The remainder of the CdTe layer was grown at about  $310^\circ\text{C}$ . At the end of the growth, the layer was annealed in-situ at  $360^\circ\text{C}$  under Te flux for about 30 min. During the annealing no surface re-evaporation was observed by reflection high energy electron diffraction (RHEED). The typical growth rate is about  $2\text{Å/s}$ . In order to investigate the tilt relation between CdTe (111)B and Si(001) with respect to the layer thickness, CdTe (111)B was grown on Si(001) with thicknesses of about 1, 2, 4 and  $8\text{ }\mu\text{m}$ , respectively.

### Characterization

The structure and quality of the CdTe (111)B were monitored in-situ by RHEED through the whole growth stage, then measured ex-situ by DCRC. The tilts of CdTe (111)B with respect to Si(001) were also measured by DCRC. This was carried out in two steps for each layer. First we obtain the tilt of Si(001), denoted by  $\delta_s$ , with respect to surface normal. Then the tilt of CdTe (111)B, denoted by  $\delta_c$ , was measured with respect to the surface normal. Since the normals of the CdTe (111)B, Si(001) and the wafer surface always lie on the same plane, the tilt between Si(001) and CdTe (111)B, denoted by  $\delta$ , is obtained by a simple subtraction,  $\delta = \delta_c - \delta_s$ .

For all the DCRC measurements, a copper anode was used. Si(331) was used as a reference crystal. The x-ray detector is placed at  $2\theta$ , where  $\theta$  is the Bragg refraction angle. The wafer was mounted on a vacuum

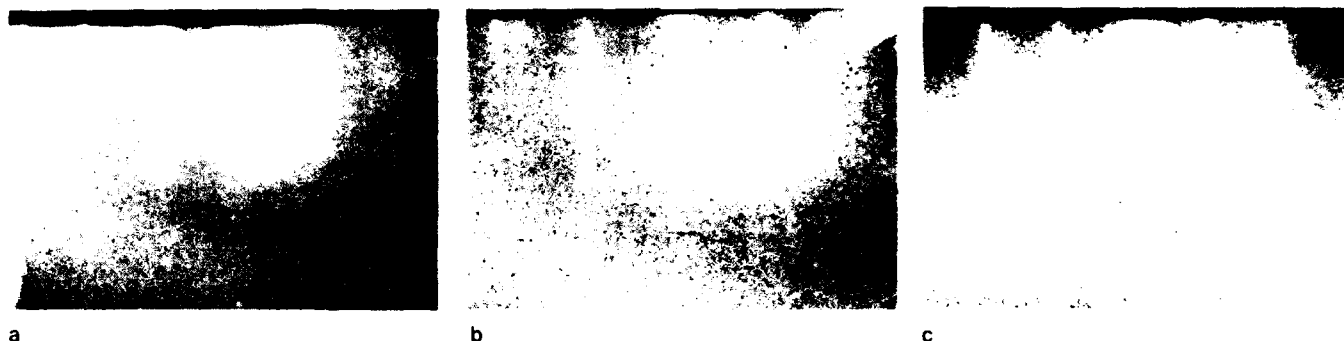


Fig. 3. Reflection high energy electron diffraction patterns of CdTe (111)B, grown on misoriented Si(001), taken at different growth stages while e-beam is along Si[110]: (a) about 360Å CdTe, (b) about 4000Å CdTe, (c) about 7500Å CdTe. The bright spots in (a) and the short light streaks in (b) between the regular streaks demonstrate the weak double-domain structure.

sample holder which allows for translation, tilt, and rotation adjustments. The set-up is illustrated in Fig. 1. The rotation angle of the sample varies from  $-102^\circ$  to  $102^\circ$  in  $12^\circ$  or  $30^\circ$  steps. For a misoriented sample, the position of the peak on the x-ray rocking curve ( $\gamma$ ) is a cosine function of the azimuthal angle ( $\phi$ ). When  $\phi$  is  $0^\circ$ ,  $\gamma$  reaches its minimum for a sample tilted toward [110], or its maximum for a sample tilted toward  $[\bar{1}\bar{1}0]$ . A typical curve of the peak position vs the azimuthal angle is shown in Fig. 2. A routine curve fitting can produce the tilt of a sample with respect to the surface normal.

## RESULTS

We have intensively studied the growth of CdTe (111)B on Si(001) substrates. For this epitaxial relationship, the lattice mismatch between CdTe(111)B and Si(001) can be reduced to 3.4% when CdTe [11 $\bar{2}$ ] is aligned with either one of the Si[110]. Comparing with the overall mismatch of 19%, this epitaxial relation will, to some extent, reduce severeness of the lattice mismatch between the two materials. All our experiments show that CdTe (111)B grown on *exact* nominal Si(001) exhibits double domains. Here we mention the *exact* nominal Si(001), since some of the nominal Si(001) substrates have small accidental tilts. All CdTe (111)B layers grown on misoriented Si(001) are single domain. During the MBE growth, RHEED was performed in-situ on growing CdTe (111)B. From observation of RHEED patterns, we found that CdTe (111)B always started with double-domain structure on the misoriented Si(001), even on substrates with tilts up to four degrees. Then as the growth continues, the one domain gradually overwhelms the other until a single domain covers the whole layer. The size of the transition region from double domains to single domain depends on many parameters, such as substrate tilt, growth condition, the completeness of deoxidation of the substrate and vacuum condition of the growth chamber. Among them, the substrate tilt certainly plays the key role in suppressing double domain formation. A typical domain transition process can be revealed by the RHEED pattern sequence shown in Fig. 3. For a layer with double-domain structure, the RHEED pattern is the superposition of two sets of streaks corresponding to

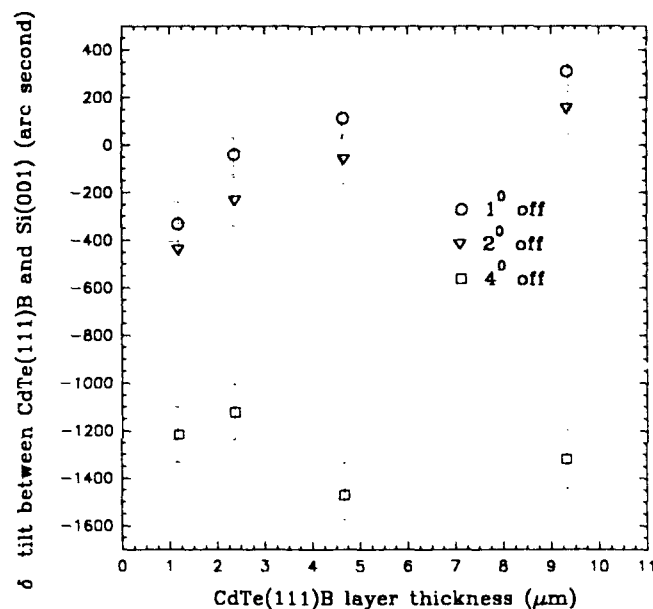


Fig. 4. The tilts between CdTe (111)B and Si(001) vs the layer thickness, obtained by the DCRC measurements. 1, 2, and 4 tilted Si(001) substrates were used in the experiment.

e-beam along both CdTe[11 $\bar{2}$ ] and CdTe[1 $\bar{1}0$ ] which is shown in Figs. 3a and 3b. For a layer with single-domain structure, however, RHEED only shows one set of the streaks as shown in Fig. 3c.

For a heteroepitaxial system where a tilted substrate is used, it has been proposed by Nagai<sup>1</sup> that a tilt between the epilayer and the substrate must be introduced in order to eliminate an incoherent growth, caused by the vertical lattice mismatch between the two materials. The tilt relationship is described by

$$\tan \delta = \frac{\Delta d}{d} \tan \theta$$

where  $\delta$  is the tilt between the epilayer and substrate lattice,  $\Delta d$  is the vertical lattice difference between the two materials,  $d$  is the atomic step height of the substrate and  $\theta$  is the tilt angle of the substrate.

A similar tilt relationship has been observed by E. Ligeon and coworkers<sup>2</sup> for the heterostructure of CdTe(111) on GaAs(001), except that the tilts they observed are always larger than or equal to the values

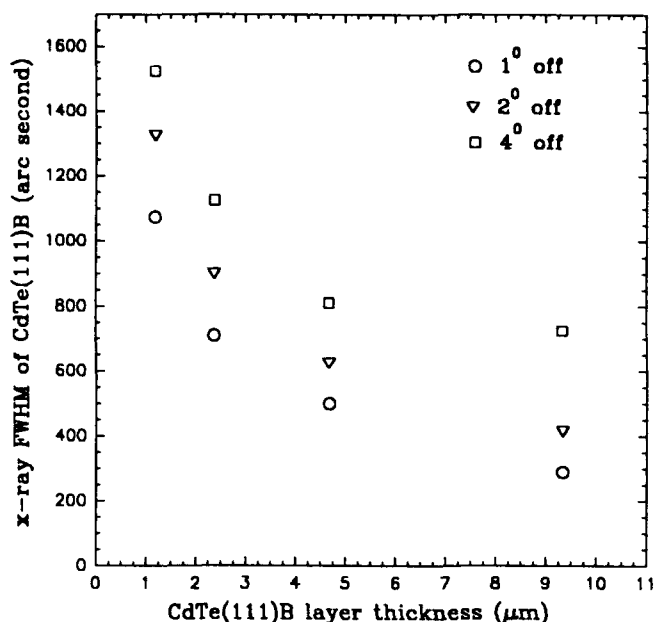


Fig. 5. The x-ray DCRC FWHM of CdTe (111)B vs the layer thickness, the layers were grown on substrates with three different tilt angles.

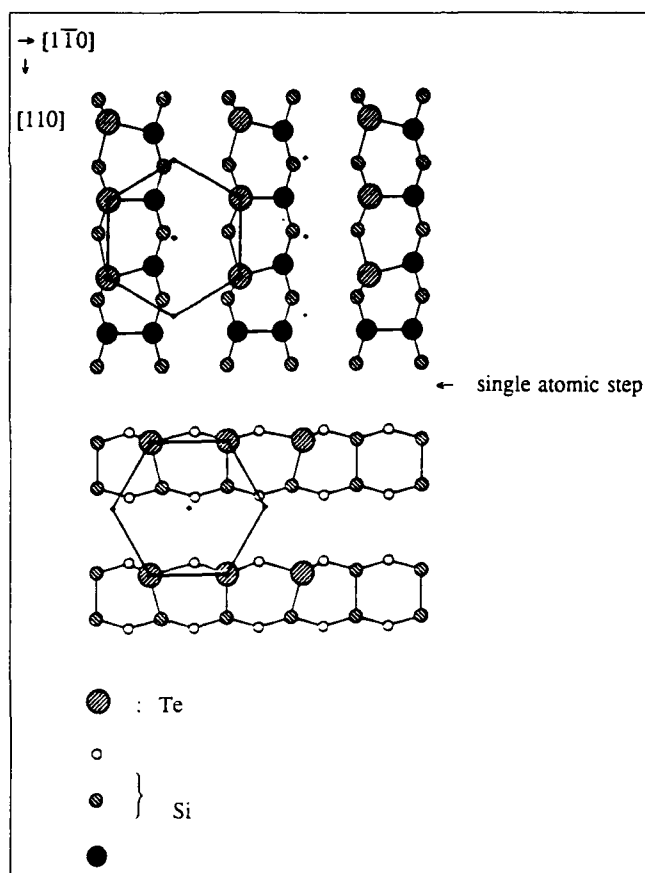


Fig. 6. Microscopic model for the interface between CdTe (111)B and Si(001). The upper and lower terraces on either side of a single-atomic-height step are shown. Silicon atoms from the same sublattice are shown with the same size; decreasing size of the circles corresponds to increasing distance of the atoms below the surface of the upper terrace. Small crosses indicate the position of Cd atoms in the next plane.

calculated from the above formula.

For the epitaxial system of CdTe (111)B on Si(001),  $\Delta d = 3.74\text{\AA}$  (for CdTe)  $- 1.36\text{\AA}$  (for Si)  $= 2.38\text{\AA}$ , and  $\Delta d/d = 1.75$ , if we assume that single-atomic-height steps predominate on the Si(001) surface, or  $\Delta d = 1.02\text{\AA}$  and  $\Delta d/d = 0.38$  for a double-atomic-height step surface. The tilt between CdTe(111)B and Si(001) is expected to be larger than or comparable to the substrate tilt.

The tilts between CdTe (111)B and Si(001), as well as the x-ray FWHM of the CdTe (111)B layer, have been measured by DCRC for the layers grown on the substrates tilted  $1^\circ$ ,  $2^\circ$ , and  $4^\circ$  toward [110]. The results have been shown in Fig. 4. and Fig. 5. Surprisingly, the tilts are very small and fall far short of the values given by above formula. It is also very interesting to note that the tilts between CdTe (111)B and Si(001) are negative in all cases when the layer thickness is less than  $2\text{ }\mu\text{m}$ . Since the tilt  $\delta$  is defined as  $\delta_c - \delta_s$ , the negative value of  $\delta$  means that the tilt of CdTe (111)B with respect to the surface is smaller than the tilt of Si(001) with respect to the surface normal. Even though we are unable to determine the tilt between CdTe (111)B and Si(001) at the beginning of CdTe (111)B growth, it seems from our experimental results that the tilts are the same or more negative than the values observed at a layer thickness of  $1\text{ }\mu\text{m}$ . Here we also observe a transition of the tilt between CdTe (111)B and Si(001) from negative to positive, except in the case where four-degree tilted substrate was used. In that case, the tilt remains negative through the whole layer. In the next section, we discuss the reason for this initial tilt, and the difference between the experimental results and the tilt values predicted by the currently existing model.

## DISCUSSION

Since all the CdTe (111)B layers were grown on Si(001) substrates, let us first briefly review the Si(001) surface structure. It is well established that exact nominal Si(001) is covered with evenly distributed single-atomic-height steps (S-steps) running up and down across the surface. However, a misoriented Si(001) surface is covered with unevenly distributed single-atomic-height steps, or double-atomic-height steps (D-steps), or a mixture of both, depending on the tilt angle of the Si(001). There is a transition from S-steps to D-steps as the tilt angle increases. E. Schröder-Bergen et al.<sup>7</sup> have observed the transition by high-resolution LEED. Pure S-steps are found with a tendency for step pairing with narrower A- and wider B-terraces for a Si(001) surface tilted with  $1.5^\circ$  or less toward [110]. Here an A-terrace, also known as an  $S_A$  step, and a B-terrace, known as an  $S_B$  step, refer to the terrace with its dimer row perpendicular to and parallel with its step edge, respectively. The paired S-steps and pure  $D_B$ -type steps coexist on the Si(001) surface tilted between  $1.5^\circ$  and  $8^\circ$  toward [110]. The pure  $D_B$  steps alone were found only on the Si(001) surface with a tilt larger than eight degrees. Based on their experimental results, it seems reasonable to argue that the paired S-

steps will completely cover, or at least dominate, the Si(001) surface with a tilt less than four degrees toward  $[110]$ . Indeed a  $(2 \times 2)$  surface reconstruction was observed by RHEED on such Si(001) substrates after an oxide layer was removed in vacuum. That means a double-domain structure does exist on a Si(001) surface with a tilt as large as four degrees.

In a previous paper<sup>1</sup>, we presented a microscopic model for the interface formation between CdTe(111)B and Si(001). In this model, a Te atom forms tetrahedral bonds with three Si atoms by kicking out one of the two Si atoms which form the dimer on the surface, leaving single dangling bond upward, as shown in Fig. 6. Then an arriving Cd atom can attach to the dangling bond and initialize the CdTe(111)B growth. In such a CdTe(111)B layer, CdTe $[11\bar{2}]$  always aligns with either Si $[110]$  or Si $[1\bar{1}0]$ . This has been confirmed by our experiments. We have performed DCRC measurements on many CdTe(111)B/Si(001) samples and have found without exception that CdTe $[11\bar{2}]$  always aligns with both the Si $[110]$  and the Si $[1\bar{1}0]$  for double-domain samples, and the CdTe $[11\bar{2}]$  aligns with one of the Si $[110]$  for single domain samples.

With all this concept and fact in mind, it is easy to understand why on exact nominal Si(001) a double-domain and twined layer of CdTe(111)B was always obtained, since the same number of  $S_A$  and  $S_B$  steps with same terrace widths coexist on the Si(001) surface. As for the Si(001) surface, Te atoms have an equal opportunity to form tetrahedral unit cells on both terraces, which leads to the formation of double domains. Even on the same domain, the Te atom can replace either one of the two Si atoms which form the dimer. Therefore, some of the Te atoms form the tetrahedral unit cells with  $[11\bar{2}]$  aligned with Si $[110]$ , and the others form the tetrahedral unit cells with  $[11\bar{2}]$  aligned with Si $[1\bar{1}0]$ , which can lead to the formation of laminar twin.

Now when a Si(001) substrate is slightly tilted toward  $[110]$ , the surface structure changes drastically. First, the steps run down steadily from one side to the other, instead of running up and down as on the nominal Si(001). Second, the size of  $S_B$  and  $S_A$  terraces are no longer equal. Actually, the S-steps on the surface become paired, with a wider  $S_B$  terrace and narrower  $S_A$  terrace. For example, on Si(001) tilted toward  $[110]$  by one degree, the average terrace width is about 80Å. Because of the pairing, the average width of an  $S_A$  terrace might shrink down to 50Å or below. Furthermore, the high-temperature annealing of the substrate at over 850°, and the interaction of Si atoms with Te atoms, will enhance the pairing, as we discussed in previous paper<sup>1</sup>.

When CdTe(111)B is deposited on Si(001) with paired S-steps, we believe the initiation of CdTe(111)B happens on both terraces, which produces an initial layer with double-domain structure. This agrees with our experimental observations by RHEED, as shown in Fig. 3. However, since the  $S_B$  terrace is much wider than the  $S_A$  terrace, the consequences of the initiation of the tetrahedral unit cells on the two

terraces are not equivalent. The tetrahedral unit cells formed on  $S_B$  terraces have their  $[11\bar{2}]$  axes parallel with the step edge, or Si $[1\bar{1}0]$ . Along this direction, the lattice mismatch between the two materials is 3.4%. The small mismatch makes it easy to form long chains of the tetrahedral unit cells. However, the tetrahedral unit cells formed on  $S_A$  terraces have their  $[11\bar{2}]$  axes perpendicular to the step edge. Since the width of an  $S_A$  terrace is very narrow (about tens of angstroms), and along the step edge the relationship of CdTe  $[110]$ /Si $[1\bar{1}0]$  leads to a 19% lattice mismatch, it is very difficult to form long chains of the tetrahedral unit cells on  $S_A$  terraces. The difference will make the coverage of the tetrahedral unit cells on  $S_B$  terraces much faster than that on  $S_A$  terraces. As a consequence, the CdTe(111)B unit cells on  $S_B$  terraces will grow faster than those on  $S_A$  terraces, which will enhance the spread of the domain on an  $S_B$  terrace over that on a nearby  $S_A$  terrace. This was also observed in our experiments by RHEED, where the RHEED streaks are much brighter and smoother when the e-beam is along Si $[110]$  than the same set of the streaks when e-beam is along Si $[1\bar{1}0]$ .

Our experimental results show that the tilt between CdTe(111)B and Si(001) is negative at the early growth stage of CdTe(111)B. One possible explanation is that the tetrahedral unit cells were initiated both on the terrace and at the step edge. The tetrahedral unit cells started at the edge will lead to CdTe(111)B tilted away from Si(001) toward the surface normal. This tilt tends to direct the growth of CdTe(111)B toward nearby  $S_A$  terraces until it meets the domain on the next  $S_B$  terrace. This process completes the conversion of the initial double domain to single domain, and produces a negative tilt between CdTe(111)B and Si(001) at the early stage of CdTe(111)B growth. Such a tilt was indeed observed on all the samples in our experiment, as shown in Fig. 4. In this process, we also expect large distortions along the step edges where two domains meet, which will in turn result in a large dislocation density. The dislocation density seems to be proportional to the step density. The DCRC performed on the samples with 1 μm thickness indicated that the x-ray FWHM does increase as substrate tilt increases, as shown in Fig. 5.

In our experiments, we did not observe the tilt suggested in Nagai's model at the beginning of CdTe(111)B growth. For the epitaxial relationship of CdTe(111)B/Si(001), the atomic-step-height difference between the two materials is as large as 2.38Å, which is almost twice of the Si atomic step height. It seems, therefore, that incoherent growth is inevitable at the beginning of CdTe growth in order to reduce the vertical lattice distortion to a minimum. We have already mentioned that the initiation of CdTe tetrahedral unit cells at the step edge will produce a negative tilt between CdTe(111)B and Si(001), after which the double domains merges into single domain. We call this process the first reorientation of the CdTe(111)B. The tilt ( $\delta'$ ) introduced in this process is

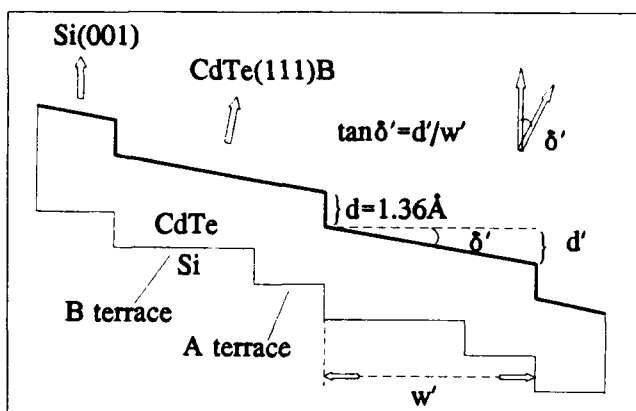


Fig. 7. The first reorientation of CdTe (111)B grown on misoriented Si(001) at the early growth stage. Here we only demonstrate a case in which two terraces merge into one. A negative tilt ( $\delta'$ ) is introduced in the process.

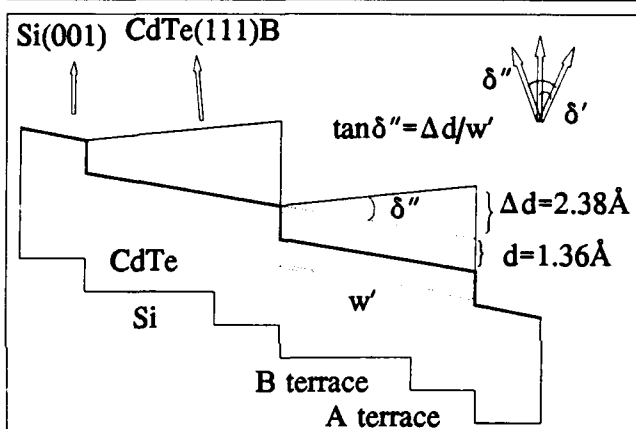


Fig. 8. The second reorientation of CdTe (111)B grown on misoriented Si(001). A positive tilt ( $\delta''$ ) is introduced in order to establish the coherent growth of CdTe(111)B. The final tilt ( $\delta$ ) between CdTe(111)B and Si(001) is expressed as  $\delta = \delta'' - \delta'$ .

illustrated in Fig. 7. For simplicity, we only demonstrate a case in which two terraces merge into one. Actually, it is very difficult to know exactly how many terraces merge into one. At the end of the first reorientation of CdTe (111)B, the step height between two terraces is about 1.36 Å, which indicates an incoherent growth of CdTe (111)B which has a step height of 3.74 Å. In order to establish the coherent growth, the CdTe lattice experiences another reorientation by compressing the lattice near the up step edge and stretching the lattice near the down step edge. This process continues until the step height between the terrace is about 3.74 Å. Such a process gradually turns the CdTe (111)B toward the Si(001), and creates a tilt ( $\delta''$ ) as illustrated in Fig. 8. We call this process second reorientation of CdTe (111)B which is an application of Nagai's model. The final tilt between CdTe (111)B and Si(001) is the combination effect of the first and second reorientation process, and can be expressed as  $\delta = \delta'' - \delta'$ . A quantitative estimate of the tilts is very difficult since the number of the terraces which merge into one is unknown. Such a simple model, however, describes a meaningful microscopic picture of the

growth of CdTe (111)B on misoriented Si(001). First, CdTe (111)B always starts with double-domain structure on a misoriented Si(001) substrate where single-atomic-height steps dominate. Then the domains of the B terraces gradually overwhelm those on A terraces and a single-domain CdTe (111)B is obtained. These are confirmed by the RHEED observation, as shown in Fig. 3. Second, a negative tilt between CdTe (111)B and Si(001) is introduced at the early growth stage of CdTe where the first reorientation process dominates, and the tilt becomes less negative due to the contribution from the second reorientation. We did observe the negative tilt between CdTe (111)B and Si(001) and the transition, as shown in Fig. 4. Although for the four-degree tilted substrate the tilt between CdTe (111)B and Si(001) remains negative, such a discrepancy might be related to the very large step density and the mixture of the double-atomic-height step on the Si surface. More work on substrate tilt needs to be done in order to fully understand the interface structure between CdTe (111)B and Si(001). Third, the large distortion is encountered at the step edges, as a consequence of incoherent growth. Such a distortion is most likely accommodated by introducing dislocation at the step edges. Therefore, the dislocation density is proportional to the step density, or the substrate tilt angle. This agrees very well with the experimental result, as shown in Fig. 5. The x-ray DCRC FWHM of CdTe (111)B does increase as the substrate tilt angle increases. This also indicates that, although the substrate tilt does play an important role in suppressing the formation of double domain, it also bring more misfit dislocations into the CdTe (111)B layer and might degrade the crystal quality.

Based on the above discussion, it is clear that single domain CdTe (111)B can be grown on slightly misoriented Si(001) with a dominant single-step-height surface. The substrate tilt does play an important role in suppressing the formation of double domain, but the tilt of the substrate should be as small as possible in order to avoid the large strain and dislocation caused by the lattice distortion at the step edges. Actually our best CdTe (111)B layers were indeed grown on such a slightly misoriented Si(001) substrate. One of them exhibits single domain and twin free (at least in top portion of the layer). The x-ray DCRC FWHM is as low as 140 arc-s. The photoluminescence performed on this layer exhibits that the FWHM of bound exciton peak at 12K is as low as 1.4 meV. After the layer was ex-situ annealed under Te over pressure, the x-ray DCRC FWHM can be further reduced to 100 arc-s. The mechanism of the dislocation reduction through the ex-situ annealing is currently under investigation. The detail results will be published later.

## CONCLUSION

Growth of CdTe (111)B has been conducted on the Si(001) tilted 1°, 2°, and 4° toward [110]. All layers exhibit double-domain structure at the very begin-



ning of the growth. A transition of domain structure from double to single domain is observed for all layers. The tilt between CdTe (111)B and Si(001) was measured for these layers. The results are completely different from what we expected by applying Nagai's model. We present a new model for the growth of single-domain CdTe (111)B on misoriented Si(001), and the microscopic mechanism for domain transition from double to single, in which the tilt of the substrate toward [110] plays the key role.

#### ACKNOWLEDGMENT

This work was supported by DARPA and monitored by U.S. Air Force Office for Scientific Research through contract no. F49620-90-C-009 DEF. We would like to thank Dr. R. Sporken at Laboratoire Interdisciplinaire de Spectroscopie Electronique (LISE) in Namur, Belgium, and Professor N. Otsuka at Purdue University

for their helpful discussion. The authors would also like to thank Dr. P.S. Wijewarnasuriya and M.D. Lange for their helpful discussion throughout this work, and Z. Ali and N. Ricciardi for technical assistance.

#### REFERENCES

1. R. Sporken, Y.P. Chen, S. Sivananthan, M.D. Lange and J.P. Faurie, *J. Vac. Sci. Technol.* B10, 1405 (1992).
2. R. Sporken, M.D. Lange, J.P. Faurie and J. Petruzzello, *J. Vac. Sci. Technol.* B9, 1651 (1991).
3. W. Kern and D.A. Puotinen, *RCA Rev.* 31, 187 (1970).
4. A. Ishizaka and Y. Shiraki, *J. Electrochem. Soc.* 133, 666 (1986).
5. H. Nagai, *J. Appl. Phys.* 45, 3789 (1974).
6. E. Ligeon, C. Chami, R. Danielou, G. Feuillet, J. Fontenille, K. Saminadayar, A. Ponchet, J. Cibert, Y. Gobil and S. Tatarenko, *J. Appl. Phys.* 67, 2428 (1990).
7. E. Schröder-Bergen and W. Ranke, *Surf. Sci.* 259, 323 (1991).

# X-Ray Diffraction Characterization of LPE HgCdTe Heterojunction Photodiode Material

S.P. TOBIN, E.E. KRUEGER, G.N. PULTZ, M. KESTIGIAN, K.-K. WONG,  
and P.W. NORTON

Loral Infrared & Imaging Systems, Lexington, MA

High-resolution x-ray diffraction has been used to measure the composition difference between P and N layers in HgCdTe heterojunction photodiode material grown by liquid phase epitaxy. The composition (band gap) difference is a critical parameter in long wavelength photodiodes because it affects dark current and the formation of photocurrent collection barriers. We find that symmetric 333 reflections cannot resolve the small composition differences of interest. However, by making use of the asymmetric 246 reflection, small composition differences (0.03) can be resolved. There is good agreement between rocking curves and secondary ion mass spectroscopy composition depth profiles, both in the value of the composition difference and in the extent of compositional grading in the top layer. High-resolution x-ray diffraction shows promise as a nondestructive, relatively rapid technique for screening as-grown heterojunction material for carrier collection barriers.

**Key words:** HgCdTe, LPE, nondestructive screening techniques, XRD, SIMS

## INTRODUCTION

This work addresses the nondestructive evaluation of multiple epitaxial layers of HgCdTe in liquid phase epitaxy (LPE) heterojunction photodiode structures. Such structures typically consist of a thick (15–20  $\mu\text{m}$ ) n-type HgCdTe epitaxial absorbing layer grown on a (111) oriented transparent substrate with a thin (1–2  $\mu\text{m}$ ) p-type higher band gap epitaxial layer forming the heterojunction. The higher band gap layer suppresses dark current, but if the difference in band gaps between the two layers is too large, valence band barriers to photocurrent collection can result.<sup>1</sup> Standard profiling methods used to measure the composition difference ( $\Delta x$ ) between the two layers are destructive, requiring cleaving or etching [secondary ion mass spectroscopy (SIMS), energy dispersive spectroscopy (EDS), ellipsometry, etc.], and not suited to rapid screening. High resolution x-ray diffraction, however, which measures the small difference in lattice spacing for alloys with different  $x$ , is both nondestructive and capable of high throughput.

## EXPERIMENTAL

The HgCdTe samples were epitaxially grown by LPE on (111)CdTe substrates. Base layers were relatively thick (15  $\mu\text{m}$ ), doped with In to  $1 \times 10^{15} \text{ cm}^{-3}$ , and grown by the Te-rich slider technique. Cap layers were thin (1  $\mu\text{m}$ ), doped with As to  $2 \times 10^{17} \text{ cm}^{-3}$ , and grown by a Hg-rich dipping technique.

We used two commercially available, fully automated, multiple crystal diffractometers for this work. The first, made by Blake Industries, used a four-crystal Bartels-type monochromator. The standard beam size was relatively large,  $12 \times 1 \text{ mm}$ , with a scan time of less than 10 min for a high resolution rocking curve. The second was a Bede Scientific Instruments Model 200, with a two-bounce channel cut monochromator and a 111 Si first crystal. The beam size was  $10 \times 1 \text{ mm}$  or  $5 \times 1 \text{ mm}$ . Typical full width at half maximum (FWHM) values for thick LPE layer peaks were 40–50 arc-s for 246 reflections on either machine.

Composition depth profiles were measured by SIMS using the Te yield technique.<sup>2</sup> The alloy composition of the base layer, as measured by room-temperature

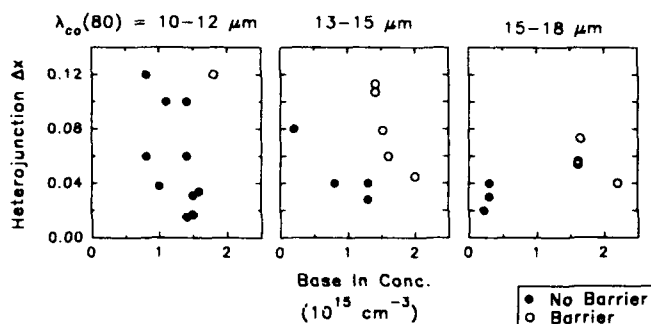


Fig. 1. Relationship between occurrence of heterojunction barriers in photodiodes and the heterojunction structure (composition difference at the heterojunction  $\Delta x$ ), base dopant concentration, and cut-off wavelength). Cut-off wavelengths are at 80K.  $\Delta x$  and In concentrations were measured by secondary ion mass spectroscopy.

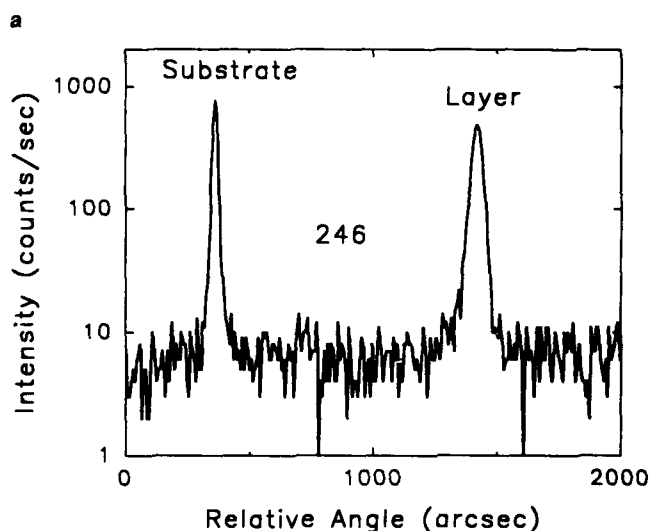
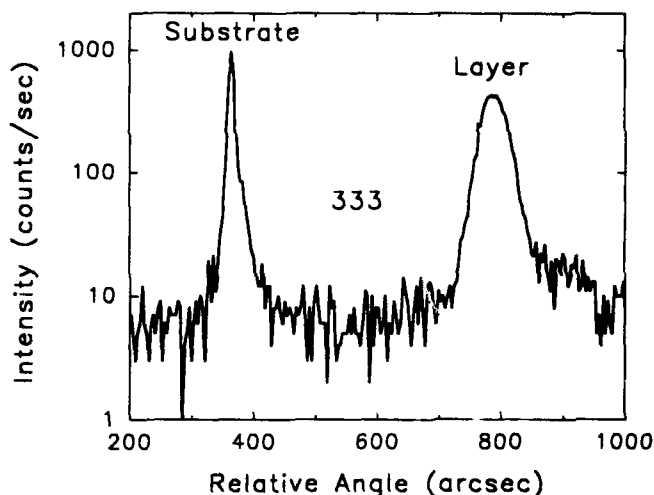


Fig. 2. Rocking curves for a 19  $\mu\text{m}$  thick  $\text{Hg}_{0.80}\text{Cd}_{0.20}\text{Te}$  epitaxial layer on a CdTe substrate. Part of the layer has been removed by etching to expose the substrate. (a) 333 reflection. CdTe substrate FWHM = 9.6 arc-s;  $\text{HgCdTe}$  layer FWHM = 50.8 arc-s. (b) 246 reflection. Substrate FWHM = 21.9 arc-s and layer FWHM = 44.8 arc-s.

Fourier transform infrared spectroscopy (FTIR) transmission, was used to convert Te yield to absolute composition. Indium and arsenic doping profiles were also measured by SIMS.

## HETEROJUNCTION BARRIERS

Barriers to photocurrent collection can be formed in  $\text{HgCdTe}$  heterojunction photodiodes under certain conditions. Symptoms of barriers include low quantum efficiencies which increase with reverse bias and decrease at lower temperatures. Barrier formation is the result of compositional grading at the heterojunction. If the p-n junction is positioned such that compositional grading extends into the neutral n-region, then a valence band barrier results.<sup>1</sup> The height and width of the barrier depend on the compositional grading width, the difference in composition across the heterojunction ( $\Delta x$ ), the p-n junction location relative to the heterojunction, and the n-side depletion width, which is related to the carrier concentration on the n-side and the junction voltage.

We have experimentally correlated the formation of barriers in LPE-grown long wavelength infrared and very long wavelength infrared heterojunction diodes with the heterojunction structure. Figure 1 relates barriers to the n-side doping,  $\Delta x$  at the heterojunction, and the cut-off wavelength (band gap). The doping and  $\Delta x$  were determined by SIMS. The cut-off wavelength was determined from spectral response of photodiodes fabricated by a simple two-mask process (mesa etch, ZnS passivation, and contact metallization). Diodes exhibiting low quantum efficiencies with significant bias and temperature dependences were deemed to have barriers. Figure 1 shows that, for a given LPE growth process, higher base doping (smaller depletion layer width) and higher  $\Delta x$  lead to barrier formation. The same trend was found in Ref. 1. We also find that the sensitivity to barriers increases with reduced band gap; the process window for barrier-free diodes moves to lower doping and  $\Delta x$ . This may be at least partially explained by the reduction in depletion layer width for lower band gaps, due to a lower built-in voltage.

For the purposes of this paper, one of the most important results of Fig. 1 is that compositional differences ( $\Delta x$ ) as low as 0.04 can cause barriers in VLWIR  $\text{HgCdTe}$ . In order for x-ray diffraction to be useful as a nondestructive screening technique for barriers, the detection limit for  $\Delta x$  must be at least 0.04.

## CHOICE OF X-RAY DIFFRACTION CONDITIONS

The x-ray rocking curve method is based on Bragg's law of diffraction,

$$\lambda = 2d \sin \theta \quad (1)$$

where  $\lambda$  is the x-ray wavelength (1.541  $\text{\AA}$  for  $\text{CuK}\alpha$ ),  $d$  is the spacing between the lattice planes of interest, and  $\theta$  is the angle between the incident x-ray and the lattice planes. Layers of  $\text{Hg}_{1-x}\text{Cd}_x\text{Te}$  with different

values of  $x$  will have slightly different lattice plane spacings  $d$ , which will give diffracted Bragg peaks at slightly different angles  $\theta$ . Rotating the sample through a range of angles  $\theta$  while recording the diffracted x-ray intensity gives a rocking curve. The angular separation between intensity peaks can be converted to differences in lattice plane spacing, and then to differences in  $x$ . Because x-rays are diffracted from a region of the sample up to several microns in depth, the compositional difference between surface and buried layers can be measured nondestructively.

As an example, Fig. 2a shows a rocking curve of an LPE-grown epitaxial layer on a CdTe substrate. Conditions were chosen for diffraction from the 333 planes. Diffraction peaks are evident for the epitaxial layer and the substrate. The epitaxial layer has a smaller lattice constant (smaller  $x$ ) than the substrate and, therefore, its peak occurs at a larger Bragg angle. This particular sample was a photolithographically patterned van der Pauw Hall sample, in which part of the film was etched away to reveal the substrate. The x-ray beam overlapped the epitaxial layer and exposed substrate. A rocking curve of the unetched epitaxial layer would have shown only one peak, because the epitaxial layer thickness of 15  $\mu\text{m}$  was too large to allow x-rays to reach the substrate.

The sample of Fig. 2 had a large value of  $\Delta x$ , the difference in composition between the two materials ( $\Delta x = 0.8$ ). As  $\Delta x$  becomes smaller, the two peaks move closer until eventually they cannot be resolved. The minimum resolvable  $\Delta x$  is determined by the width of the individual peaks and the angular separation between the end members of the alloy, CdTe and HgTe. Unfortunately, the lattice constant difference between the end members is rather small for HgCdTe (0.3%) and the diffraction peaks are broadened by crystallographic imperfections (dislocations, compositional nonuniformities). The minimum resolvable  $\Delta x$  is a critical issue, because, as shown in the previous section, relatively small values of  $\Delta x$  at the junction (0.04) have been found to cause collection barriers in VLWIR heterojunction diodes.

The minimum resolvable  $\Delta x$  can be improved by careful selection of the diffraction conditions to minimize the effects of in-plane crystallographic defects and maximize the separation between peaks. The reason for this can be seen with the aid of Ewald sphere diagrams, shown in Figs. 3 and 4. The Ewald sphere is a graphical construction showing the experimental setup in reciprocal lattice space. Points on the surface of the sphere (shown two-dimensionally in the figures) satisfy the Bragg condition. Figure 3 shows the standard symmetric 333 reflection most often used for (111) oriented wafers. The origin in reciprocal space is shown as O. The 333 diffraction spots for a double layer epitaxial structure are shown at the terminus of the vector Q. There are two spots because the base and cap layers are assumed to have different values of  $x$  (larger for the cap). The diffraction spots are shown as elongated parallel to the sample surface because of threading dislocations, which are prima-

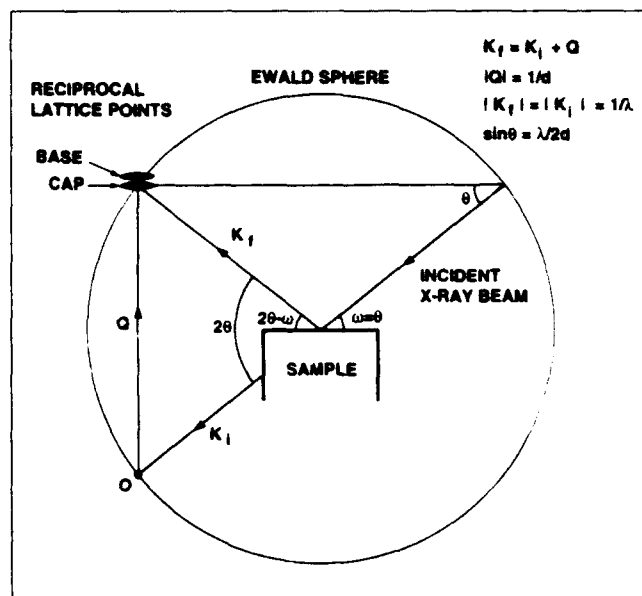


Fig. 3. Ewald sphere diagram for a 333 reflection from a heterojunction structure on a (111) oriented wafer.  $k_i$  is the incident beam,  $k_f$  is the diffracted beam, Q is the diffraction vector, and O is the origin in reciprocal space.

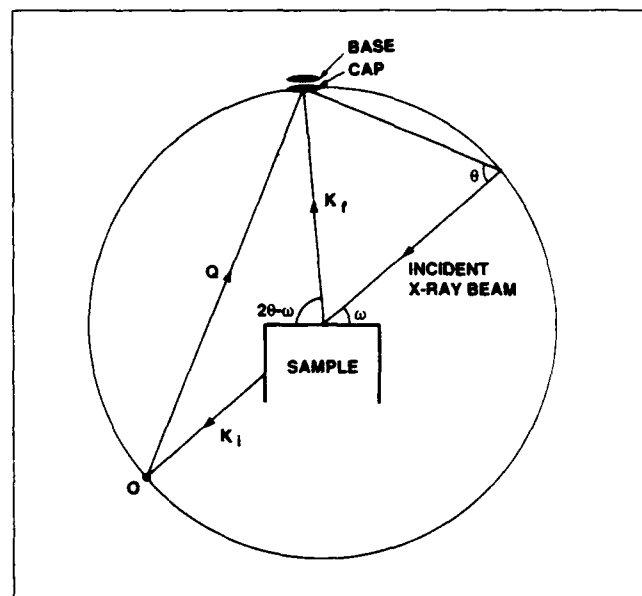


Fig. 4. Ewald sphere diagram for a 246 reflection from a heterojunction structure on a (111) oriented wafer.

rily oriented perpendicular to the surface. The interruption of the lattice in the plane of the film by dislocations leads to broadening of the reciprocal lattice in that direction. (The elongation is grossly exaggerated in the diagram). It can be seen that the surface of the Ewald sphere passes through the diffracted spots of both layers simultaneously. In two-axis diffractometers such as the ones we have used, the x-ray detector subtends a relatively large angle of the Ewald sphere. Therefore, both diffracted spots are detected at the same time and cannot be separated with a 333 reflection. As the angle  $\theta$  is scanned in a rocking curve, the motion of the Ewald sphere will

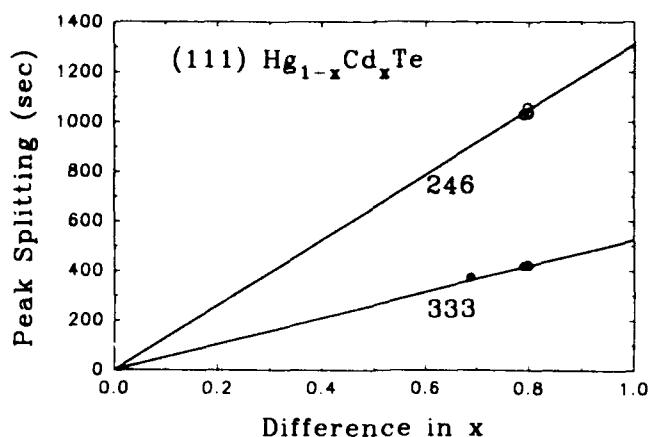


Fig. 5. Calculated rocking curve peak splitting as a function of composition difference for two HgCdTe layers, for 333 and 246 x-ray reflections. Calculations assume complete relaxation of the two layers. Points are measured data of thick single epitaxial layers on CdTe substrates.

Table I. Comparison of 333 and 246 Reflections for  $\text{Hg}_{0.8}\text{Cd}_{0.2}\text{Te}$  ( $a = 6.4642\text{\AA}$ )

| hkl | $\theta$<br>(deg) | $2\theta - \omega$<br>(deg) | $\Delta\theta/\Delta x$<br>(s) | Typ.<br>Base<br>FWHM (s) | Minimum<br>Measur-<br>able $\Delta x$ |
|-----|-------------------|-----------------------------|--------------------------------|--------------------------|---------------------------------------|
| 333 | 38.26             | 38.26                       | 527                            | 50                       | 0.09                                  |
| 246 | 63.09             | 85.30                       | 1313                           | 42                       | 0.03                                  |

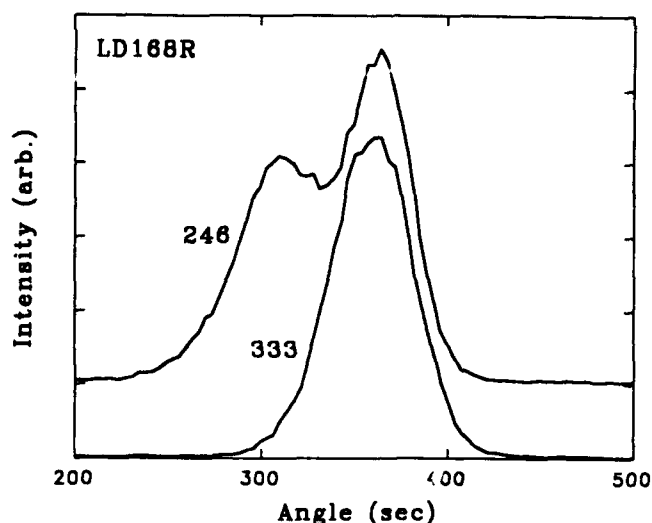


Fig. 6. Comparison of rocking curves from symmetric and asymmetric reflections on the same sample with  $\Delta x = 0.04$ . Base and cap layer peaks can be resolved with a 246 reflection, but not with a 333 reflection.

result in only one broad peak rather than individual peaks for the two layers.

In contrast, Fig. 4 shows the Ewald sphere for an asymmetric 246 reflection. In this case, the Ewald sphere is nearly tangential to the elongated diffraction spots. As  $\theta$  is scanned in a rocking curve, the sphere will pass through one and then the other of the diffraction spots, giving clearly resolved diffraction peaks. The result of choosing the 246 reflection is to narrow the individual peaks by reducing dislocation

broadening effects. In addition, the use of the higher order 246 reflection gives a larger separation between the reciprocal lattice points of the cap and base. This is not shown explicitly in the figure.

In Fig. 2b, we show a 246 rocking curve for the same sample as in Fig. 2a. Note that the angle scale is different, because the smaller d-spacing of the higher order reflection gives a larger peak separation. However, the peak width has not increased proportionately, reflecting the reduced influence of dislocations in this reflection. The ratio of peak widths to peak separation is clearly smaller than in Fig. 2a, giving better resolution in  $\Delta x$ . From Fig. 4, it can be seen that the condition for minimum sensitivity to dislocation broadening is obtained when the diffracted beam is perpendicular to the sample surface. An equivalent condition is that the angle  $(2\theta - \omega)$  equals 90 degrees, where  $\omega$  is the angle between the incident beam and sample surface. For the 246 reflection of (111)-oriented  $\text{Hg}_{0.8}\text{Cd}_{0.2}\text{Te}$  (lattice constant =  $6.4642\text{\AA}$ ), the relevant angles are  $\theta = 63.1$  deg,  $\omega = 40.9$  deg, and  $2\theta - \omega = 85.3$  deg. We have calculated these angles for all of the allowed reflections of (111) HgCdTe, and find the 246 reflection to be the best suited for minimization of dislocation effects.

Figure 5 shows the calculated values of rocking curve peak splitting as a function of  $\Delta x$  for the 333 and 246 reflections. The calculations are for completely relaxed layers, using lattice constants of  $6.481\text{\AA}$  for CdTe and  $6.460\text{\AA}$  for HgTe. In addition to the theoretical lines, experimental points are shown for several thick epitaxial layers like that of Fig. 2, where the assumption of complete relaxation of the layer should be justified. It can be seen that the 246 reflection not only minimizes dislocation effects, but also gives a larger peak splitting for a given  $\Delta x$ . (This is because the Bragg angle is larger for the more closely spaced 246 planes). We have found experimentally that the FWHM values of uniform composition HgCdTe layers are about 50 s for 333 reflections and 42 s for 246 reflections. These values give minimum resolvable  $\Delta x$  values of 0.09 for the 333 reflection and 0.03 for the 246 reflection (Table I). Use of the asymmetric 246 reflection, therefore, allows critical values of  $\Delta x$  to be measured, whereas the symmetric 333 reflection does not.

## RESULTS

Figure 6 shows 333 and 246 rocking curves of a single heterojunction sample. The  $\Delta x$  of the heterojunction was 0.04 by SIMS. The Bragg peaks of the two layers are resolved in the 246 reflection, but not in the 333 reflection.

Figures 7–9 show examples of 246 rocking curves for samples with different values of  $\Delta x$  at the heterojunction. In each case, a composition depth profile measured by SIMS is shown for comparison to the x-ray rocking curve and SIMS measurements were made on different areas of the same wafer.

Figure 7 shows a sample with a relatively large

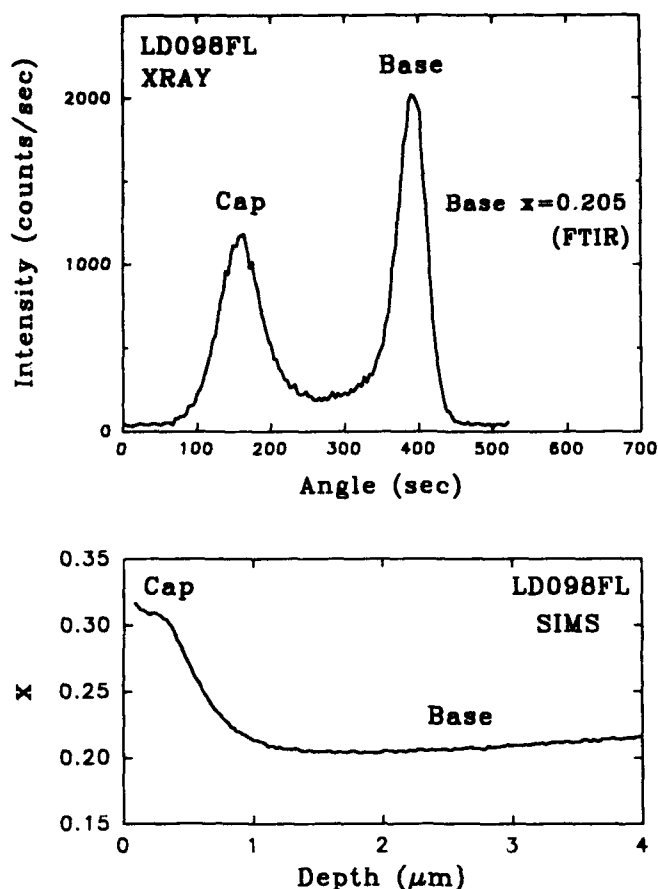


Fig. 7. Comparison of x-ray rocking curve and SIMS composition depth profile for a sample with a large composition difference at the heterojunction.

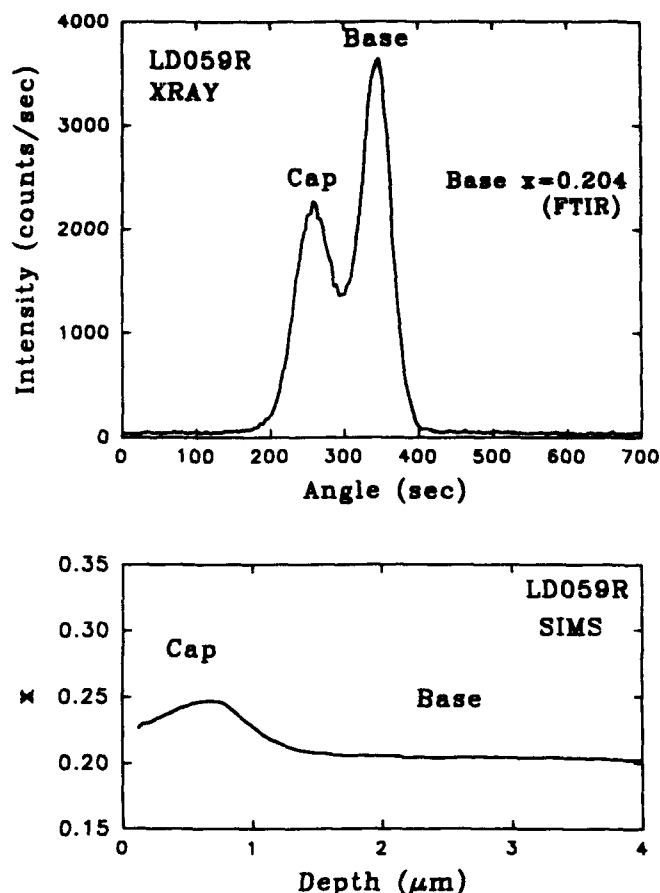


Fig. 8. Comparison of x-ray rocking curve and secondary ion mass spectroscopy composition depth profile for a sample with a small composition difference at the heterojunction.

value of  $\Delta x$ , measured to be 0.11 by SIMS. There are well-defined diffraction peaks for the cap and base, with FWHM values of 69 and 50 arc-s, respectively. The depth profile shows compositional grading between the two layers over a distance of about 0.5  $\mu\text{m}$ . The graded region accounts for the nonzero intensity between the two Bragg peaks. Photodiodes processed from this material had carrier collection barriers, as evidenced by low quantum efficiencies which degraded as the temperature was reduced and improved as reverse bias was applied.

Figure 8 shows a sample with a relatively small value of  $\Delta x$  (0.04 by SIMS). The FWHM for the base is 51 arc-s. In addition to compositional grading between the cap and base layers, there is a noticeable gradient in  $x$  within the cap layer. However, the cap  $x$  is always larger than the base  $x$ . Photodiodes processed from this material had no collection barriers.

Figure 9 shows a sample in which the cap layer composition is strongly graded. The cap layer composition is larger than that of the base near the junction and smaller than that of the base near the surface. In the rocking curve, a very broad peak for the cap layer, therefore, extends on both sides of the relatively narrow base peak (FWHM = 66 arc-s). (Higher  $x$  is to the left in the rocking curve). Although the details of the compositional profile are not readily deconvolved

from rocking curves like Fig. 9, it is apparent that the cap is compositionally graded. In addition, the maximum and minimum  $x$  values of the cap can be estimated. If we know from prior knowledge of the growth process that the maximum value of  $x$  is near the junction, then the critical value of  $\Delta x$  relevant to barrier formation can be determined. To our knowledge, this information is not available by any other nondestructive technique.

The data of Figs. 7–9 have shown that compositional information from rocking curves is in qualitative agreement with composition profiles from SIMS. We have also made a quantitative comparison between the rocking curve peak separation and the SIMS composition difference at the junction ( $\Delta x$ ), as shown in Fig. 10. There is a strong trend of increasing peak splitting with increasing  $\Delta x$ , as expected. The solid line shows a least-squares fit to the data. Samples with  $\Delta x$  values down to 0.03 have measurable peak splittings. Rocking curves have also been measured for many samples with  $\Delta x$  less than 0.03. In this case, the cap layer peak appears as a shoulder on the base layer peak, or is superimposed on it.

The scatter in Fig. 10 is believed to arise from several causes. First, the SIMS and x-ray measurements were not made at the same locations on the samples. More recent work has shown that both the

rocking curve shapes and SIMS composition profiles can vary across the wafers. Spatial variation in  $\Delta x$  of 0.025 have been observed, similar to the scatter in Fig. 10. For example, the dashed line in the figure connects two different SIMS measurements of the same wafer. Second, it is difficult to determine the relationship between  $\Delta x$  and  $\Delta\theta$  for layers of nonuniform composition. In Figs. 8 and 9, for example, the cap peak in the rocking curve corresponds to some composition value, but it will not in general be the peak composition of the SIMS profile. It will generally be smaller, reflecting some average of composition near the peak. Different composition profiles will give different correlations of  $\Delta x$  and  $\Delta\theta$ . Third, there are experimental uncertainties in both the x-ray and SIMS measurements. The diffraction peaks are relatively broad, leading to some uncertainty in determining peak positions and splitting. This uncertainty is estimated to be 4 arc-s. Instrumental accuracy is about 2 arc-s. The  $\Delta x$  uncertainty of the SIMS measurements is estimated to be on the order of 0.01.<sup>2</sup>

In addition to the empirical correlation of Fig. 10, we can also compare the peak splittings to theoretical values for uniform composition layers (Fig. 11). Theoretical curves are shown for the fully relaxed case, in which the lattice constants of both layers assume their bulk values, and for the strained case, where the in-plane lattice constant of the cap is constrained to be

the same as the base. The cap layer unit cell is then tetragonally distorted (the lattice constant perpendicular to the film is larger than that parallel to the film). The latter case assumes that misfit dislocations are not generated to relieve the stress between the cap and base. For the strained case, three lines are shown. The center line, marked  $\Delta\theta$ , is the difference in Bragg angles between the two layers. This is given by:<sup>3</sup>

$$\Delta\theta = -\left(\frac{\Delta a}{a}\right) \cos^2 \phi \tan \theta \quad (2)$$

$$\left(\frac{\Delta a}{a}\right) = \frac{\left(\frac{\Delta a}{a}\right)_{\text{relax}}}{CF} \quad (3)$$

where  $a$  is the lattice constant, the subscripts refer to lattice constants in the relaxed state and perpendicular to the interface,  $\phi$  is the angle between the 246 plane and the 111 surface (22.2 deg),  $\theta$  is the Bragg angle, and CF is a correction factor related to the elastic constants of the material.<sup>4</sup> For (111) CdTe<sup>5</sup> and HgTe,<sup>6</sup> the correction factors are 0.543 and 0.542; we used 0.542 for HgCdTe.

The value of  $\Delta\theta$  is larger than in the relaxed case because the strained lattice constant is larger perpendicular to the film. However, because the unit cell is elastically distorted, the rocking curve splitting no longer measures just  $\Delta\theta$ . An additional term  $\Delta\phi$  describes the difference in inclination between equivalent planes in the base and cap.  $\Delta\phi$  is given by:<sup>3</sup>

$$\Delta\phi = \left(\frac{\Delta a}{a}\right) \cos \phi \sin \phi \quad (4)$$

The rocking curve splitting is then given by  $\Delta\theta + \Delta\phi$  for the 246 reflection in which the x-rays enter at 40.9 deg and leave at 85.3 deg, and by  $\Delta\theta - \Delta\phi$  for the opposite path in which the x-rays enter at 85.3 deg. These lines are shown as 246L and 246H in Fig. 11, for low and high entrance angle. It is worth noting that our measurements were all made in the 246L geometry, which gives the highest peak splitting for a given  $\Delta x$ . The measured points would then be expected to fall between the uppermost line if strained, and the lower line if totally relaxed. This is the case for most points.

Measurements of 246L and 246H reflections for one of the samples (LD060R) were made to see if the cap layer was strained or relaxed. The peak splitting should be different only if the layer is strained. The wafer was rotated by 180 degrees between measurements to reverse the path of the x-rays, and care was taken to measure the same position on the sample. The measured peak splittings were significantly different, 139 and 85 arc-s, showing that the cap layer was not relaxed. Values of 112 arc-s for  $\Delta\theta$  and 27 arc-s for  $\Delta\phi$  were calculated from the peak splittings. Assuming a fully strained layer,  $\Delta\theta$  was used to calculate a value of 0.054 for  $\Delta x$ . For comparison, the value of  $\Delta x$  measured at the junction by SIMS for this wafer was 0.08. The calculated value of  $\Delta\phi$  was 23 arc-s, in good agreement with the measured value. The

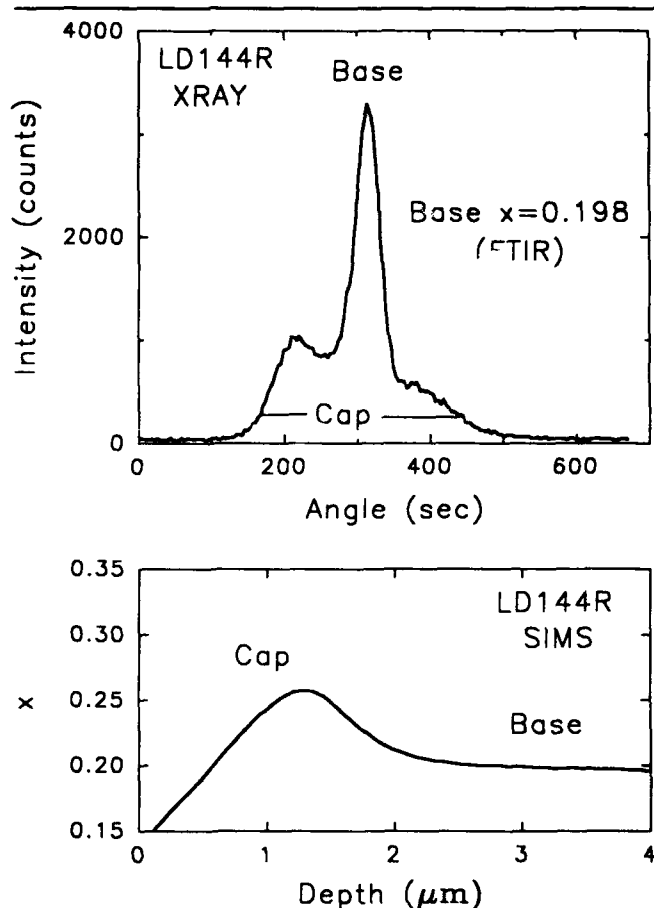


Fig. 9. Comparison of x-ray rocking curve and SIMS composition depth profile for a sample with a large composition gradient in the cap layer.

small discrepancy was probably due to a small tilt between the layers, as discussed below.

As a crosscheck, we also made measurements using the symmetric 444 reflection before and after 180 degree rotation of the sample. We chose the 444 over the 333 reflection because it gives larger peak separations and also a value of  $2\theta - \omega$  closer to 90 degrees. The sample was first tilt-optimized by the method of Tanner<sup>7</sup> to maximize the tilt of the base layer. Peak splittings of 94 and 100 arc-s were measured, yielding a value of 97 arc-s for  $\Delta\theta$ . This gave a value of 0.054 for  $\Delta x$ , identical to the 246 result. This agreement is additional evidence that the layer is strained. Note that if we had assumed a relaxed layer, values of  $\Delta x$  would have been 0.085 for the 246 reflection and 0.100 for the 444 reflection.

As a further check on the finding that the cap layer is elastically strained, we calculated the critical thickness for dislocation formation for cap layers with different values of  $\Delta x$ . Simple theory predicts that below the critical thickness the film will be strained, while above the critical thickness the strain should be partially or completely relaxed by misfit dislocation generation. We found that depending on which critical thickness model was used<sup>8,9</sup> and the value of  $\Delta x$ , a 1  $\mu\text{m}$  cap layer could be either above or below the critical thickness. For a  $\Delta x$  value of 0.05, the critical thickness is at or above 1  $\mu\text{m}$ . The result that sample LD060R was strained is, therefore, reasonable.

It is possible that tilts between the two layers could also affect the peak splittings. For this reason, the tilt of sample LD060R was measured in two ways. First, the 444 measurements above gave a very small tilt of 3 arc-s. This is near our detection limit. Second, six 246L measurements were made at 60 degree wafer rotation intervals. The peak splittings were fit to a sine wave, giving 4 arc-s for the tilt. (Wafer misorientation measured by the same method was 0.37 deg). The two tilt measurements are in good agreement. It, therefore, appears that, at least for this sample, tilts between the cap and base layer are minor. This is not unexpected because the substrate wafers are nominally exactly (111) oriented and the lattice mismatch is small between the two layers.

## DISCUSSION

The empirical correlation of Fig. 10 between peak splitting and  $\Delta x$  at the junction can be used to screen wafers for barriers. Samples with overlapping peaks or splitting less than 50 arc-s should be barrier-free. Those with splittings over 100 arc-s are likely to have barriers for some combinations of base doping and composition. To be more precise, we need to reduce the scatter in the correlation of  $\Delta\theta$  to  $\Delta x$  for heterojunction samples. Based on our present understanding of sample inhomogeneity, we plan to repeat the measurements of Fig. 10, making sure that the x-ray and SIMS measurements are in the same locations. The state of strain will also be evaluated using the high and low 246 reflections; differences in the degree of relaxation could lead to large differences in peak

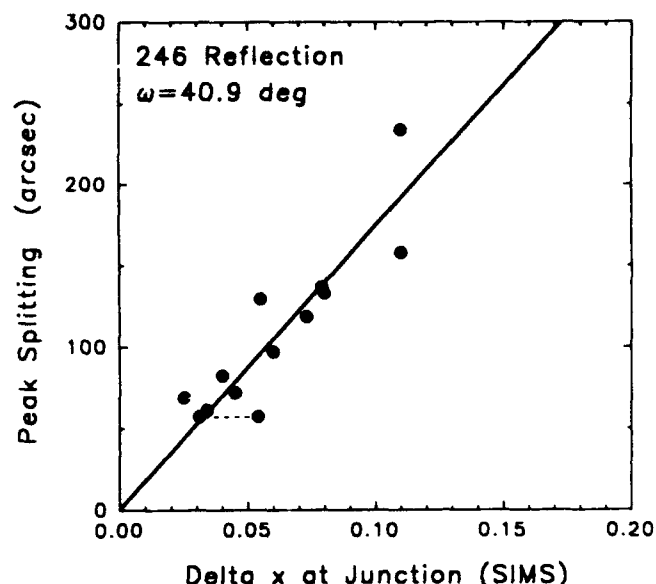


Fig. 10. Correlation between rocking curve peak splitting and SIMS composition difference at the heterojunction for double layer heterojunction samples. The line is a least-squares fit passing through the origin.

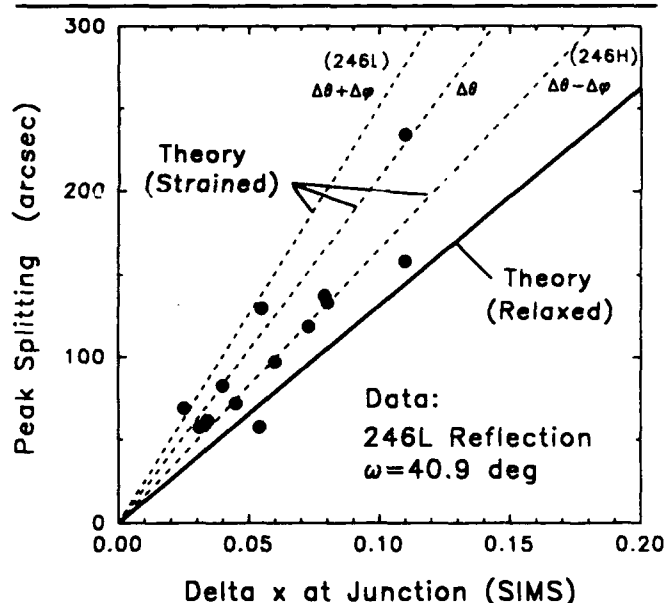


Fig. 11. Comparison of measured and calculated peak splitting as a function of composition difference. The theoretical lines are for uniform composition layers, while the experimental points are for the peak composition in a layer with nonuniform composition. See text for an explanation of the different theoretical lines.

splitting, as shown in Fig. 11. Also, to determine the proper interpretation of  $\Delta x$  for a nonuniform composition structure, it would be useful to be able to simulate rocking curves for different graded structures. Unfortunately, present commercially available simulation software is limited to only symmetric reflections when (111) wafers are used.<sup>10</sup> This limitation is expected to be removed in the near future.

For sample LD060R, the value of  $\Delta x$  measured by x-ray diffraction was lower than the SIMS junction  $\Delta x$  by 0.026. The discrepancy is within the range of  $\Delta x$  differences, we have seen across wafers, so it could be



a sampling problem. We would expect the diffraction  $\Delta x$  to be somewhat smaller because the composition profile is peaked, and the diffraction peak will not be exactly at the peak composition. It seems unlikely that this is the full explanation, but modeling is required to provide quantitative estimates. The discrepancy is larger than the SIMS experimental error.

One drawback of using the 246 reflection is extra setup time involved with initially finding and optimizing the diffracted peak. For the symmetric 333 reflection, the sample and detector are simply aligned to the Bragg angle to detect the diffracted beam. The in-plane rotation of the sample is unimportant. For the asymmetric 246 reflection, however, the in-plane rotation must also be adjusted to align the beam to one of the six equivalent  $\langle 110 \rangle$  directions. Because current CdTe substrates are not supplied with orientation flats, one must scan through a wide range of rotation angles (up to 60 degrees) to find a 246 peak. Our peak-finding procedure has been to first find the 333 peak for a sample. This establishes the absolute Bragg angle. The Bragg angle for a 246 reflection can then be set accurately. Rotation of the sample then locates the Bragg peak. For subsequent samples, only a sample rotation is usually necessary to find the peak. An alternate procedure would be to first make a Laue measurement to determine the in-plane orientation of each sample. The symmetric 444 reflection is also an option when the highest  $\Delta x$  resolution is not required. Its resolution limit should be about 0.05 for relaxed films, compared to 0.03 for the 246 and 0.09 for the 333.

## CONCLUSIONS

We conclude that high-resolution x-ray diffraction is an effective nondestructive material screening technique for measuring critical composition differences in the heterojunction photodiode structure.

## ACKNOWLEDGMENT

Part of this work was performed for the Jet Propulsion Laboratory, California Institute of Technology, Contract 958970, as sponsored by the National Aeronautics and Space Administration, Contract NAS7-918. M. Sanfacon, I. Kofman, and M. Boone are acknowledged for making the measurements. The first author wishes to acknowledge Tom Ryan for suggesting the use of 246 reflections in a Materials Research Society short course, and to thank the reviewer for helpful comments.

## REFERENCES

1. K. Kosai and W.A. Radford, *J. Vac. Sci. Technol.* A8, 1254 (1990).
2. L.O. Bubulac and C.R. Viswanathan, *Appl. Phys. Lett.* 60, 222 (1992).
3. W.J. Bartels and W. Nijman, *J. Cryst. Growth* 44, 518 (1978).
4. J. Hornstra and W.J. Bartels, *J. Cryst. Growth* 44, 513 (1978).
5. S.M. Johnson, W.L. Ahlgren, M.T. Smith, B.C. Johnston and S. Sen, *Mat. Res. Soc. Symp. Proc.* 144, 121 (1989).
6. T. Alper and C.A. Saunders, *J. Phys. Chem. Solids* 28, 1637 (1967).
7. B.K. Tanner, X. Chu and D.K. Bowen, *Mat. Res. Soc. Symp. Proc.* 69, 191 (1986).
8. J.W. Matthews and A.E. Blakeslee, *J. Cryst. Growth* 27, 118 (1974).
9. P.M.J. Maree, et al., *J. Appl. Phys.* 62, 4413 (1987).
10. RADS Dynamical Simulation Software, Bede Scientific Instruments Ltd, 1992.

# Growth Method, Composition, and Defect Structure Dependence of Mercury Diffusion in $\text{Cd}_x\text{Hg}_{1-x}\text{Te}$

N.A. ARCHER, H.D. PALFREY, and A.F.W. WILLOUGHBY

Engineering Materials, The University, Southampton SO9 5NH, UK

Mercury radiotracer diffusion results are presented, in the range 254 to 452°C, for bulk and epitaxial  $\text{Cd}_x\text{Hg}_{1-x}\text{Te}$ , and we believe this to be the first report for metalorganic vapor phase epitaxy (MOVPE) grown  $\text{Cd}_x\text{Hg}_{1-x}\text{Te}$ . For all growth types studied, with compositions of  $x_{\text{Cd}} = 0.2 \pm 0.04$ , the variation of the lattice diffusion coefficient,  $D_{\text{Hg}}$ , with temperature, under saturated mercury partial pressure, obeyed the equation:

$$D_{\text{Hg}} = 3 \times 10^{-3} \exp(-1.2 \text{ eV}/kT) \text{ cm}^2 \text{ s}^{-1}.$$

It was found to have a strong composition dependence but was insensitive to changes of substrate material or crystal orientation. Autoradiography was used to show that mercury also exploited defect structure to diffuse rapidly from the surface. Dislocation diffusion analysis is used to model defect tails in MOVPE  $\text{Cd}_x\text{Hg}_{1-x}\text{Te}$  profiles.

**Key words:** Hg diffusion in CdHgTe, influence of defects on Hg diffusion, MOVPE, radiotracer measurements

## INTRODUCTION

The relationship between defect structure and mercury diffusion in  $\text{Cd}_x\text{Hg}_{1-x}\text{Te}$  was first illustrated by Brown and Willoughby<sup>1</sup> and the influence of defects on electrical properties was demonstrated by Moore and Schaake.<sup>2</sup> Recently, Shin and coworkers<sup>3</sup> have shown how decreasing the dislocation density can yield increased minority carrier lifetimes. To achieve the advances demanded in  $\text{Cd}_x\text{Hg}_{1-x}\text{Te}$  infrared device technology, a better understanding of the interaction of diffusion and defect structure is required.

In an earlier publication,<sup>4</sup> we presented diffusion data for liquid phase epitaxy (LPE) and bulk grown  $\text{Cd}_x\text{Hg}_{1-x}\text{Te}$  and showed that their defect structure provided rapid diffusion paths and was responsible for fast diffusion defect tails observed in concentration profiles. These findings brought further into

question a dual error function interpretation of self-diffusion proposed by earlier workers<sup>5,6</sup> who had discounted the significance of diffusion via defect structure. Shaw<sup>7</sup> has recently discussed cation self-diffusion in  $\text{Cd}_x\text{Hg}_{1-x}\text{Te}$  and favored (sub) grain boundary diffusion, as opposed to dislocation diffusion, as the cause of defect tails in bulk material. Mercury self-diffusion data for epitaxial  $\text{Cd}_x\text{Hg}_{1-x}\text{Te}$  have, until now, been sparse and, to our knowledge, there have been no values for metalorganic vapor phase epitaxy (MOVPE). Most of the results and discussion given here are based on our results for MOVPE samples. The LPE and bulk results have been extended with new values and are also included in this study for comparison.

## EXPERIMENTAL PROCEDURE

All MOVPE, LPE, and bulk grown samples of  $\text{Cd}_x\text{Hg}_{1-x}\text{Te}$  were supplied by Philips Infrared Defence Components, Southampton, and were nominally undoped, but p-type as grown. Metalorganic vapor

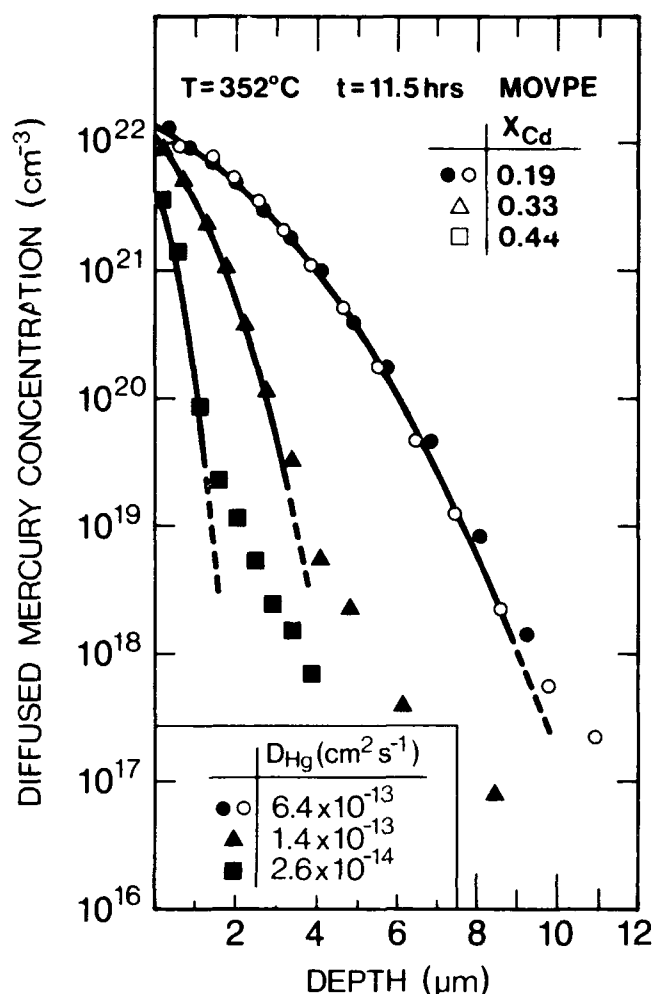
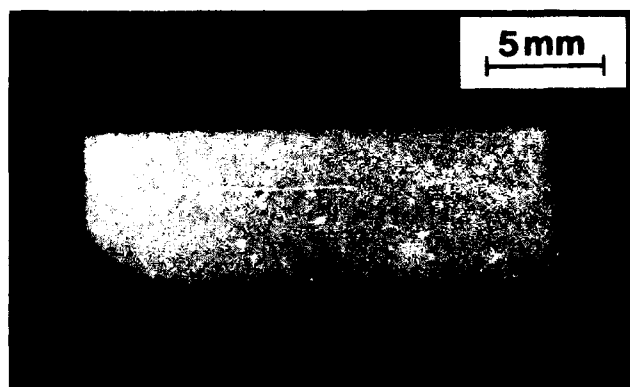


Fig. 1 Diffused mercury concentration profiles in MOVPE  $\text{Cd}_x\text{Hg}_{1-x}\text{Te}$  from three wafers with compositions of 0.19, 0.33, and 0.44, annealed at 352°C for 11.5 h. The agreement in fit for two pieces of the same sample (open and closed circles) is shown for  $x_{\text{Cd}} = 0.19$ .

phase epitaxy samples were grown on GaAs substrates,  $2^\circ$  off (100) toward  $\langle 110 \rangle$ , with 1 to 2  $\mu\text{m}$  thick CdTe buffer layers. Their hillock density was quite low, less than  $10\text{ cm}^{-2}$ , and the etch pit densities were reported, by the suppliers, to be between  $10^7$  and  $10^8\text{ cm}^{-2}$ . Liquid phase epitaxy samples were grown from tellurium-rich melts directly onto CdTe(111)B substrates and had etch pit densities in the range  $10^5$  to  $10^6\text{ cm}^{-2}$ . Bulk grown HgTe,  $2^\circ$  off (111), was obtained from LETI, Grenoble, France.

Mercury enriched with the radiotracer  $\text{Hg}^{203}$  was used to provide a vapor diffusion source and maintain saturated partial pressure within closed-tube anneals. Details of sample preparation and experimental technique have been described in an earlier publication,<sup>8</sup> so only an outline is given here. After annealing, samples were sectioned by etching with 1% bromine methanol solutions. Contact autoradiography was found to be essential to reliably interpret concentration profiles and was used to look for rapid diffusion along defect structure at various depths during sectioning. This was done by placing the sample face down on a photographic film or plate to allow the beta



a



b

Fig. 2. (a) Autoradiograph taken at the diffusion surface of an MOVPE sample,  $x_{\text{Cd}} = 0.19$ , annealed at 307°C for 48 h; (b) autoradiograph taken 3.4  $\mu\text{m}$  from the original surface of the sample shown in Fig. 2a (same scale as 2a).

particles emitted by  $\text{Hg}^{203}$  to produce an image. The penetration of these beta particles in  $\text{Cd}_x\text{Hg}_{1-x}\text{Te}$  could have been several microns, so the image formed was a plan view of the distribution of the remaining radiotracers and not just the immediate surface distribution.

## RESULTS AND DISCUSSION

The diffused mercury concentration profiles of MOVPE samples were found to be very similar to LPE profiles and had at least two components. The diffused mercury concentration,  $C$ , in the near surface component fell with depth,  $x$ , according to a complementary error function (erfc) valid for vapor source diffusion. This component was used to calculate the lattice diffusion coefficient,  $D_{\text{Hg}}$ , of the mercury in  $\text{Cd}_x\text{Hg}_{1-x}\text{Te}$ . Deeper into the sample, a defect tail appeared; the concentration fell less rapidly and was often best described by an  $\ln(C) \propto x$  relationship.

The diffusion length,  $\sqrt{D_{\text{Hg}}t}$ , where  $t$  is the anneal duration, is useful for comparing profile shapes. For both components to be collected, the optimum anneal conditions for an epitaxial layer of thickness,  $L$ , were found to be  $L \approx 16 \sqrt{D_{\text{Hg}}t}$ . This was not always achieved and when  $\sqrt{D_{\text{Hg}}t}$  was too large, the erfc component extended to the substrate, whereas if  $\sqrt{D_{\text{Hg}}t}$  had been too small, only the defect tail would have been mea-

surable. The defect tail intercept with the surface,  $C_{0\text{tail}}$ , and the tail's slope could only be accurately measured when the two components were clearly resolved. Some of the MOVPE samples were cleaved into two after diffusion to compare reproducibility of the profile tail. The  $C_{0\text{tail}}$  values of the two pieces were sometimes found to vary but the defect tail gradients were always the same. The example profiles shown in Fig. 1 are of samples from three MOVPE wafers with compositions of 0.19, 0.33 and 0.44, annealed at  $352^\circ\text{C}$  for 11.5 h. The 0.19 and 0.33 layers were  $12\text{ }\mu\text{m}$  thick and the 0.44 layer was about  $6\text{ }\mu\text{m}$  thick. The value of  $D_{\text{Hg}}$  fell as  $x_{\text{Cd}}$  increased, but the defect tail (clearly resolved here for the  $x_{\text{Cd}} = 0.33$  and 0.44 samples) showed no significant change of slope.

Samples from the same three MOVPE wafers were also annealed at  $307^\circ\text{C}$  for 48 h. When the diffusion length was greater than about  $1\text{ }\mu\text{m}$ , surface autoradiographs showed a fairly uniform distribution of radiotracer. The autoradiograph shown in Fig. 2a was taken at the surface of the  $x_{\text{Cd}} = 0.19$  sample, for which  $\sqrt{D_{\text{Hg}}t} = 1.3\text{ }\mu\text{m}$ . Under these conditions the lattice diffusion component came from a sufficient depth of crystal to dominate the image. However, after sectioning had thinned the lattice diffusion component, deeper autoradiographs revealed clusters of defects that had provided rapid diffusion paths. The autoradiograph shown in Fig. 2b was of the same MOVPE sample as shown in Fig. 2a, but at a depth of about  $3.5\text{ }\mu\text{m}$  from the original surface. The defects were seen as groups of variable size white dots, and occasionally lines, scattered across the sample, with a grey background of diminished lattice diffusion.

When the profile diffusion length was small, far more defect structure could be seen in surface autoradiographs. The autoradiograph shown in Fig. 3a was taken at the surface of the  $x_{\text{Cd}} = 0.44$ , annealed at  $352^\circ\text{C}$  for 11.5 h, where  $\sqrt{D_{\text{Hg}}t} = 0.3\text{ }\mu\text{m}$ . Under these conditions, some defects were seen to have depleted the radiotracer in their surrounding area, producing dark halos around the bright dots. Presumably this was caused by rapid diffusion of mercury into the defects locally exhausting the lattice mercury. Some of the larger dark areas were found to have bright defect lines beneath them in subsequent deeper autoradiographs.

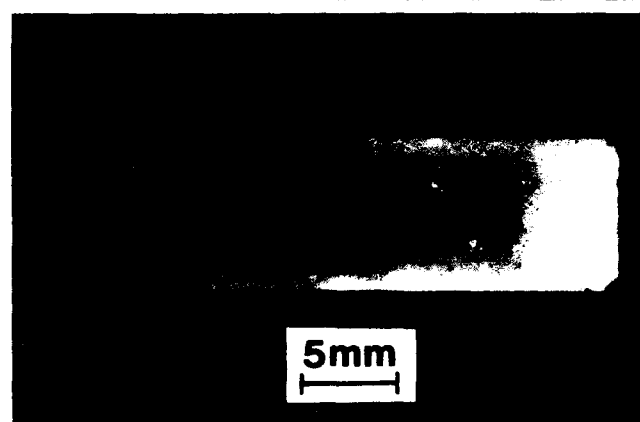
When autoradiographs were taken in the profile tail region, they showed that diffusion was principally via the defect structure. The autoradiograph shown in Fig. 3b was taken of a piece of the same MOVPE sample as Fig. 3a but at a depth of about  $1.8\text{ }\mu\text{m}$  from the original surface. The contribution from lattice diffusion was one tenth of the measured concentration. Many of the defect clusters visible in surface autoradiographs could be identified in deeper autoradiographs, there being no change in their position. This indicated that most of the rapid diffusion paths were normal to the diffusion surface.

The clusters of defects seen in the autoradiographs were too large and too sparse to correspond to individual dislocations as revealed by defect etching.

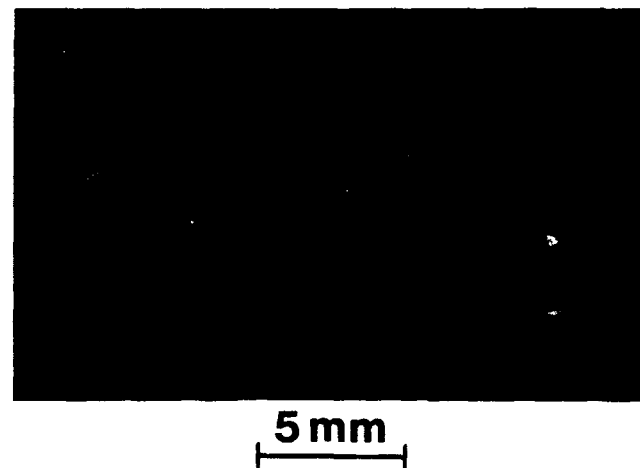
Areas distant from defect clusters on high resolution autoradiographs, taken in the defect tail region, were inspected under high magnification to look for isolated dislocation diffusion. Although the autoradiographs were found to be exposed, the images were relatively featureless, and they could also have been attributed to weak lattice diffusion or background fogging.

The lattice diffusion coefficient was found to be surprisingly similar for all the different growth methods, despite the different substrate materials and crystal orientations of the epitaxial samples (Fig. 4). One LPE sample was pre-annealed with nonradioactive mercury at  $275^\circ\text{C}$  for 43 days prior to a 72 h radiotracer anneal also at  $275^\circ\text{C}$ . This had no measurable effect on the lattice diffusion as  $D_{\text{Hg}}$  had the same value as samples that were not pre-annealed. For  $\text{Cd}_{1-x}\text{Hg}_x\text{Te}$  with  $x_{\text{Cd}} = 0.2 \pm 0.04$  the variation of  $D_{\text{Hg}}$  with temperature, under saturated mercury partial pressure, between 254 and  $452^\circ\text{C}$  obeyed the equation:

$$D_{\text{Hg}} = 3 \times 10^{-3} \exp\left(\frac{-1.2\text{eV}}{kT}\right) \text{cm}^2\text{s}^{-1} \quad (1)$$

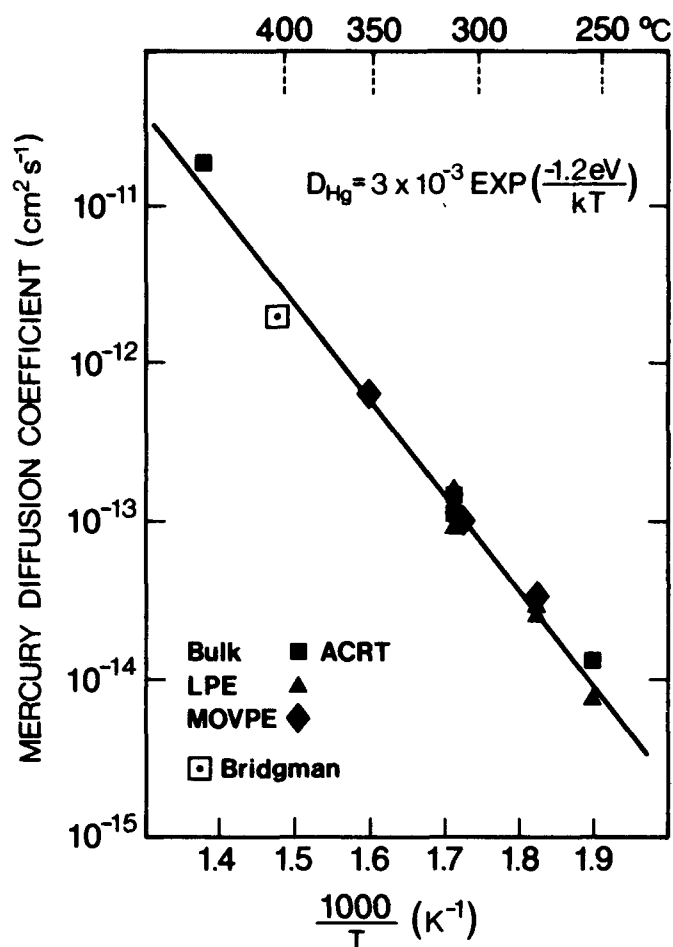


a



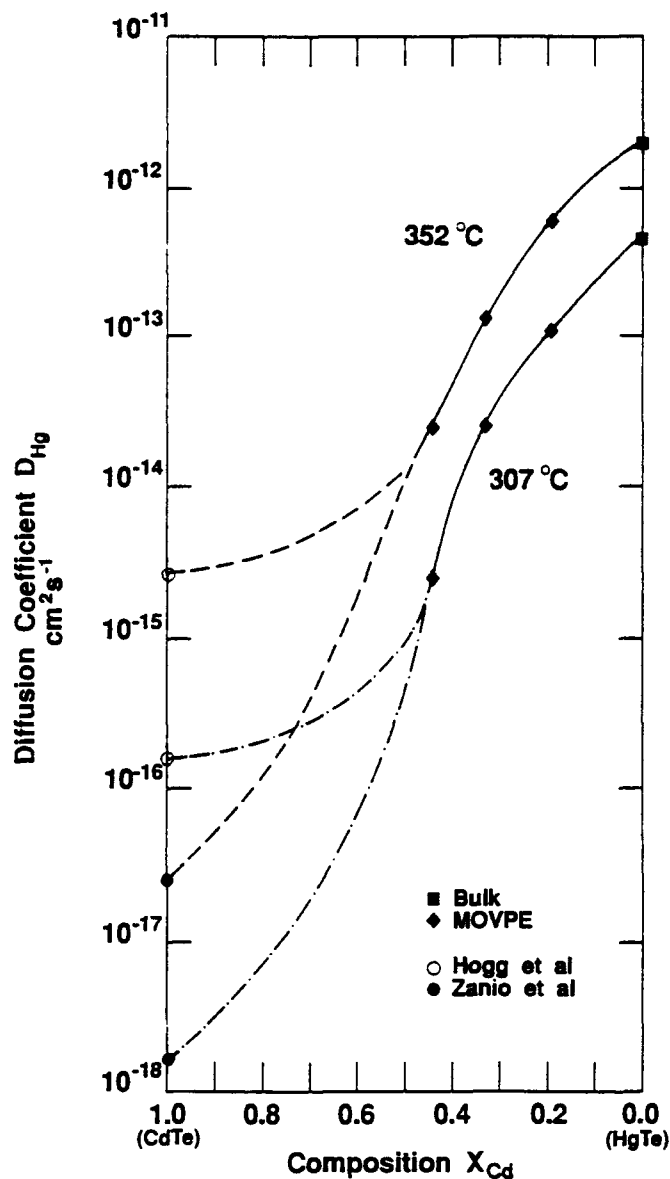
b

Fig.3. (a) Autoradiograph taken at the diffusion surface of an MOVPE sample,  $x_{\text{Cd}} \approx 0.44$ , annealed at  $352^\circ\text{C}$  for 11.5 h; (b) autoradiograph taken  $1.8\text{ }\mu\text{m}$  from the original surface of a piece, from the left hand side, of the sample shown in Fig. 3a.

Fig.4 Variation of  $D_{Hg}$  with temperature.

Lattice diffusion coefficients for bulk grown HgTe and MOVPE grown  $Cd_xHg_{1-x}Te$  measured at 307 and 352°C are plotted against composition in Fig. 4. The solid lines show the general trend between  $x_{Cd} = 0$  to 0.5 and the dashed lines are extrapolations to give the estimated range of  $D_{Hg}$  at higher  $x_{Cd}$  according to literature values for the mercury diffusion coefficient in CdTe,  $D_{Hg}(CdTe)$ . The lower value for  $D_{Hg}(CdTe)$  at each temperature comes from extrapolating the higher temperature interdiffusion results of Zanio and Massopust.<sup>9</sup> These suggest that  $D_{Hg}$  falls by nearly four orders of magnitude at 352°C and more than five orders of magnitude at 307°C, from  $x_{Cd} = 0$  to 1. The higher values for  $D_{Hg}(CdTe)$  shown in Fig. 5 are from Hogg and coworkers;<sup>10</sup> our results indicate that these represent an upper limit on the true values. Still higher values have been published but they would require mercury to diffuse faster in CdTe than it does in  $Cd_xHg_{1-x}Te$ . We suggest that these overestimates of  $D_{Hg}(CdTe)$  may be due to defect tails being measured instead of the erfc component.

The contribution to the profile tail, in MOVPE samples, by the defect clusters may have been indistinguishable from that which would have been produced solely by isolated dislocations. If this were the case then the defect tail could be modeled using the dislocation diffusion analysis developed by Le Claire

Fig.5 Variation of  $D_{Hg}$  with composition.

and Rabinovitch.<sup>11</sup> According to this analysis, for vapor source diffusions, the dislocation density is related to the ratio of  $C_{0\text{ tail}}/C_0$  and, the real surface concentration of diffused mercury,  $C_0$ , by the equation:

$$d = \left( \frac{C_{0\text{ tail}}/C_0}{\pi a^{0.16} (Dt)^{0.92}} \right) \quad (2)$$

where  $a$  is the radius of a dislocation pipe and  $D$  is the lattice diffusion coefficient. The ratio  $C_{0\text{ tail}}/C_0$  took values in the range 0.013 and 0.05 and was found to be fairly insensitive to changes of anneal conditions or material composition. The dislocation densities were calculated to be between  $2 \times 10^6$  and  $4 \times 10^7 \text{ cm}^{-2}$  when a value of  $5 \times 10^{-8} \text{ cm}$  was assigned to  $a$ . This compared well with the etch pit densities and suggested that the dislocation analysis could provide a reasonable model for MOVPE samples. The small variation in  $C_{0\text{ tail}}$

values of the cleaved MOVPE samples corresponded to slight differences in dislocation densities of the two halves.

The defect tail slopes of MOVPE samples were all found to be similar irrespective of quite large changes in the lattice diffusivity. The analysis describes the diffusion coefficient for mercury diffusing within the dislocation cores,  $D_{\text{disloc}}$ , as a function of the defect tail slope such that:

$$\frac{\partial \ln C}{\partial x} = - \frac{A}{\sqrt{(\Delta - 1)a^2}} \quad (3)$$

where  $\Delta$  is the ratio  $D_{\text{disloc}}/D$  and  $A$  is a weak dimensionless function of the dislocation pipe radius and the anneal conditions and is of order unity. Since all the MOVPE defect tail slopes were similar,  $\Delta$  was found to be fairly constant, at about  $10^6$ , indicating  $D_{\text{disloc}}$  had a similar dependence on composition and temperature as  $D_{\text{Hg}}$ . The comparable defect tail gradients found in cleaved samples corresponded to consistent diffusivity within the dislocations.

### CONCLUSIONS

This is the first report of radiotracer mercury self-diffusion in MOVPE material. The diffused mercury concentration profiles in MOVPE  $\text{Cd}_x\text{Hg}_{1-x}\text{Te}$  were found to have a similar form to those of LPE material. Autoradiography was used to show that the concentration profile tails were due to rapid diffusion along defects. This finding was consistent with that for mercury diffusion in bulk grown  $\text{Cd}_x\text{Hg}_{1-x}\text{Te}$  which exhibits a strong contribution from (sub) grain boundary diffusion.

The lattice diffusion coefficient was found not to depend on growth technique or substrate material but was a strong function of temperature and composition. Comparisons of these results with literature values highlight the uncertainty of the value of the mercury diffusion coefficient in CdTe.

### ACKNOWLEDGMENT

Thanks are due to our colleagues at Philips IDC, especially Paul Mackett and Eion O'Keefe, for supplying epitaxial material for this work. The encouragement of Mr. Norman Shaw of the DRA Malvern and valuable discussions with Drs. Derek Shaw and Chris Hogg of the University of Hull were greatly appreciated. This work was carried out with the support of the DRA Malvern.

### REFERENCES

1. M. Brown and A.F.W. Willoughby, *J. Cryst. Growth* 59, 27 (1982).
2. T.M. Moore and H.F. Schaaake, *J. Vac. Sci. Technol. A* 1, 1666 (1983).
3. S.H. Shin, J.M. Arais, M. Zandian, J.G. Pasko and R.E. DeWames, *Appl. Phys. Lett.* 59, 2718 (1991).
4. N.A. Archer, H.D. Palfrey and A.F.W. Willoughby, *J. Cryst. Growth* 117, 177 (1992).
5. J.S. Chen, Ph.D. Thesis, U. of Southern California (1985).
6. M.S. Tang and D.A. Stevenson, *J. Vac. Sci. Technol. A* 6, 2650 (1988).
7. D. Shaw, *Semicond. Sci. Technol.* 7, 1230 (1992).
8. N.A. Archer and H.D. Palfrey, *J. Electron. Mater.* 20, 419 (1991).
9. K. Zanio and T. Massopust, *J. Electron. Mater.* 15, 103 (1986).
10. J.H.C. Hogg, A. Bairstow, G.W. Matthews, D. Shaw and J.D. Stedman. To be published in *Mater. Sci. & Eng. B*.
11. A.D. Le Claire and A. Rabinovitch. *Diffusion in Crystalline Solids*, eds. G.E. Murch and A.S. Nowick (Academic Press, New York, 1984).

# Integrated Heterostructure Devices Based on II-VI Compound Semiconductors

J. REN, Y. LANSARI, Z. YU, J.W. COOK, JR., and J.F. SCHETZINA

Department of Physics, North Carolina State University,  
Raleigh, NC 27695-8202

Integrated heterostructure devices which combine small band gap and large band gap II-VI materials in multilayered structures for light emission and detection applications are described.

**Key words:** Blue-green emission, HgCdTe, HgSe, HgZnSe, integrated heterostructure devices, multilayer structures, ZnSe

## INTRODUCTION

Historically, the study of narrow-gap II-VI compounds such as  $\text{Hg}_{1-x}\text{Cd}_x\text{Te}$  has been driven by the need to develop efficient infrared detectors. Here we describe an exciting new use for narrow-gap II-VI materials, specifically HgSe and HgZnSe, in *integrated heterostructures* involving the wide band gap II-VI material ZnSe and related alloys. ZnSe and related wide band gap II-VI alloys are presently under development worldwide because of the first demonstration of a blue-green laser diode by 3M scientists in June, 1991.<sup>1</sup> Since then, others<sup>2,3</sup> have also published papers on lasers diodes based on wide band gap II-VI heterostructures.

## INTEGRATED HETEROSTRUCTURE DEVICES

The term *integrated heterostructure* or *integrated heterostructure device* (IHD) is here defined as a multilayered structure in which particular layers, or combination of layers, perform distinctly different functions. An example of an IHD is a semiconductor surface emitting laser which contains (a) multilayers for optical mirrors, (b) an active light generation region which might consist of one or more additional layers, (c) p-type and n-type layers which supply the active light generation region with electron and holes

under forward bias, and (d) additional top layers for optically and electrically coupling the laser output to the outside world. These various functions are integrated into a single epitaxial multilayered structure using sophisticated growth techniques such as molecular beam epitaxy (MBE) or metalorganic chemical vapor deposition.

This paper describes new IHDs for the generation of blue/green light (light emitting diodes and lasers) that are composed of both narrow band gap and wide band gap II-VI materials. Several manifestations of this new type of device are shown in Fig. 1. These IHDs combine a light emission multilayered structure (wide band gap II-VI layers) with a graded heterostructure (narrow band gap HgSe-HgZnSe layers) for improved ohmic contact to the upper p-type layer of the light emitting structure. A new IHD for the detection of infrared (IR) radiation is also described.

The problem of obtaining ohmic contact to p-type ZnSe and related alloys is well known.<sup>1-14</sup> This is a fundamental problem related to the deep valence band of ZnSe. As a consequence, all metal contacts, including Au and Pt, are accompanied by appreciable potential barriers ( $\geq 1.5$  V). In contrast, we estimate the valence band offset between HgSe and ZnSe to be about 0.6 eV, based on a "modified" common anion rule which assumes that the band gap difference is split 80%-20% between the conduction and valence bands, respectively. This assumption is consistent

(Received October 12, 1992; revised January 13, 1993)

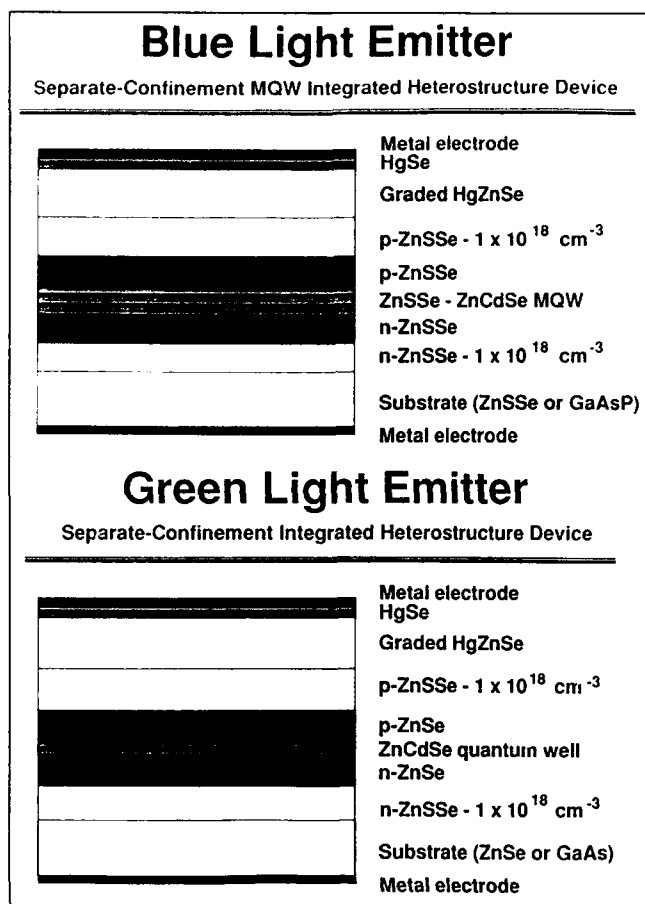


Fig. 1. Integrated heterostructure devices for blue/green light emission applications.

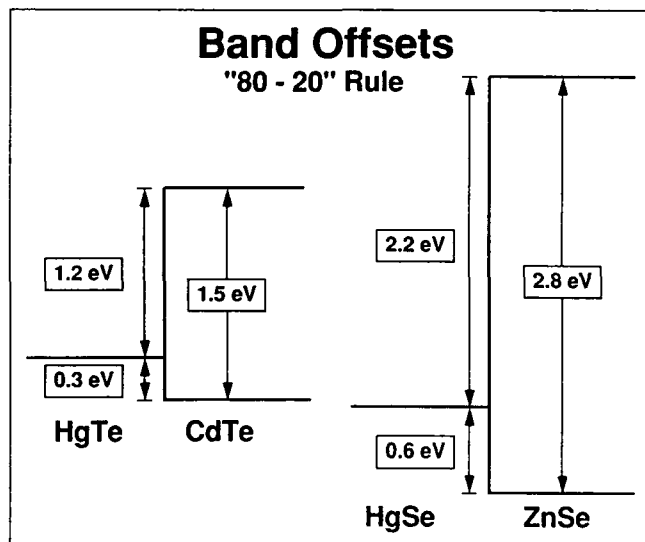


Fig. 2. Estimated valence band offsets between HgTe/CdTe and HgSe/ZnSe based on a modified common anion rule.

with the measured  $\sim 0.3$  eV valence band offset between HgTe and CdTe, as is illustrated in Fig. 2.

Exploiting the smaller valence band offset in the Hg-ZnSe system, step-graded IHD structures of the type shown in Fig. 3 have been successfully grown by MBE. In these experiments, p-type doping of the

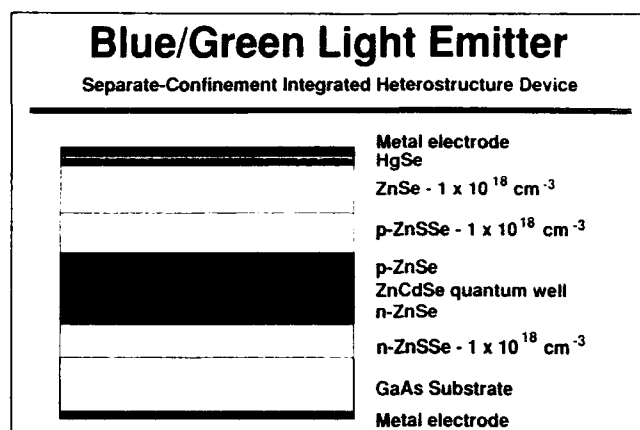


Fig. 3. Step-graded IHD.

ZnSSe and ZnSe layers was achieved by using nitrogen from an Oxford Instruments radical beam source, and the HgSe contact layers were deposited in a separate MBE system. We have developed a portable ultra-high-vacuum (UHV) transfer device, equipped with a small ion pump, that allows us to extract a wafer from one MBE system and transfer it in UHV to a second MBE system (or to an inert gas DRILAB facility). In this way, samples may be protected from oxidation during transfer and/or storage.

Light emitting diodes were fabricated from the MBE-grown samples in the form of  $150 \times 150$   $\mu\text{m}$  square mesas using standard photolithography, etching, and lift off steps. These step-graded IHDs emit blue/green light in the 475–495 nm wavelength region (2.5–2.6 eV) at room temperature, as shown in Fig. 4. A representative current-voltage curve for this type of IHD is shown in Fig. 5. Note that the turn-on voltage is about 2.2 V (1 mA). At 4.4 V, the device produces 50 mA. These new structures display *fundamental improvements* in their electrical properties as compared with similar light emitting structures fabricated using direct metal contacts, which generally exhibit turn-on voltages in excess of 5 V and display soft forward-biased electrical characteristics. These results provide clear experimental evidence that the HgSe layer provides a basis for avoiding non-ohmic effects associated with direct metal-to-semiconductor contacts to p-type ZnSe and ZnSSe through reduction in the energy barrier which impedes the flow of holes at a p-type ZnSe-metal interface.

With appropriate grading of a doped HgZnSe layer, as shown in Fig. 1, it should be possible to reduce the valence band offset between ZnSe and HgSe from  $\sim 0.6$  eV to nearly zero, thus providing a stable low resistance ohmic contact for ZnSe-based light emitting diodes and laser diodes. A similar grading scheme, which employed a graded n-type InGaAs region, was successfully used by Woodall et al.<sup>15</sup> to form an ohmic contact between a metal-InAs junction and n-GaAs. The graded alloy approach works in conjunction with substitutional doping to reduce band offsets between constituent binary materials (ZnSe and HgSe in the present case). P-type doping of a graded HgZnSe



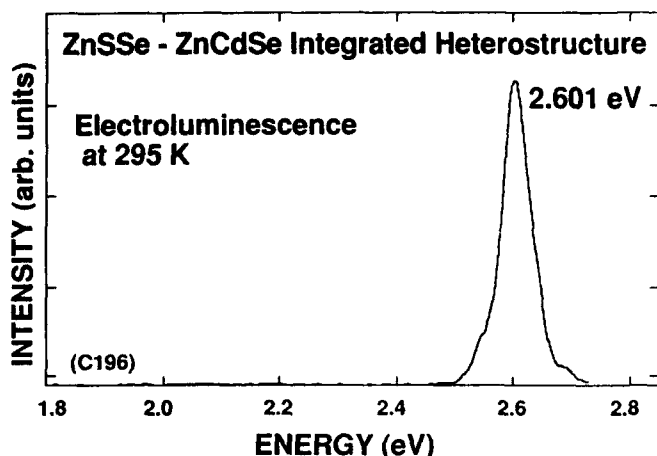


Fig. 4. Integrated heterostructure device emission characteristics.

layer, for example, forces the Fermi energy to lie close to the alloy valence band throughout the graded layer, thus eliminating the *valence band* offset between the binary end points. Correspondingly, reduction in conduction band offsets (such as between InAs and GaAs) requires n-type doping of the graded layer.

#### IHDs FOR INFRARED DETECTOR APPLICATIONS

From the energy band diagrams shown in Fig. 1, together with our current best estimates of the valence band offsets between CdTe, ZnTe, and ZnSe, it is clear that the valence band of HgSe is 0.3–0.6 eV deeper than the valence band of HgTe. If, for the sake of argument, one assumes that the HgSe valence band is *exactly* 0.3 eV deeper than that of HgTe, so that its valence band lines up exactly with that of CdTe (zero valence band offset), then HgSe would serve as an ideal ohmic contact material for p-type CdTe. Of perhaps greater significance, the above arguments imply that the valence band of the ternary alloy  $\text{HgTe}_{1-x}\text{Se}_x$  should line up *exactly* with the valence band of  $\text{Hg}_{1-x}\text{Cd}_x\text{Te}$  for all  $x$ -values. This leads us to suggest a new IHD for the detection of infrared radiation, which includes an epitaxial ohmic contact for p-type  $\text{Hg}_{1-x}\text{Cd}_x\text{Te}$  as shown in Fig. 6, and in which alloy  $x$ -values and  $y$ -values are chosen according to the wavelength band of interest. For example for the detection of long wavelength infrared radiation at 10  $\mu\text{m}$ ,  $x = 0.3$  and  $y = 0.22$  would be appropriate.

#### ACKNOWLEDGMENT

The authors wish to thank K.A. Bowers for help with manuscript preparation. This work was supported by the U.S. Office of Naval Research grant N00014-92-J-1644.

#### REFERENCES

1. M.A. Haase, J. Qiu, J.M. DePuydt and H. Cheng, *Appl. Phys. Lett.* 59, 1272 (1991).
2. H. Jeon, J. Ding, W. Patterson, A.V. Nurmikko, W. Xie, D.C. Grillo, M. Kobayashi and R.L. Gunshor, *Appl. Phys. Lett.* 59, 3619 (1991).

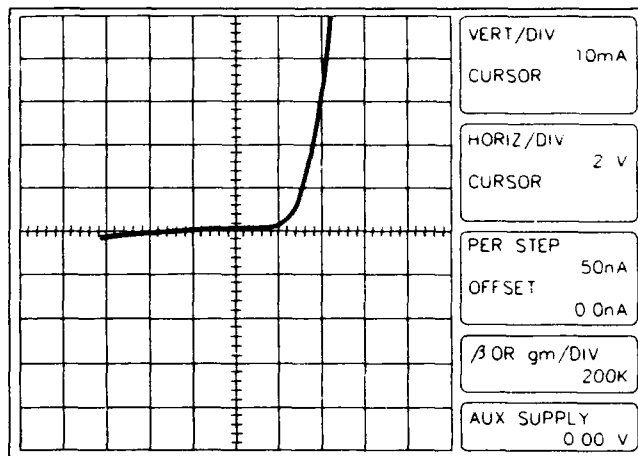


Fig. 5 Current-voltage (I-V) characteristics of blue light emitting IHD.

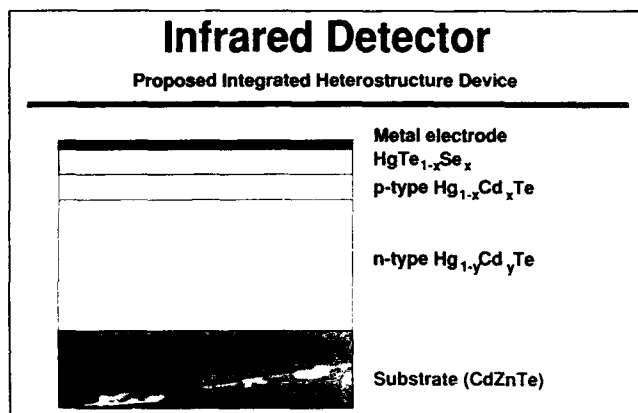


Fig. 6. Proposed IHD for the detection of infrared radiation.

3. Z. Yu, J. Ren, B. Sneed, K.A. Bowers, K.J. Gossett, C. Boney, Y. Lansari, J.W. Cook, Jr. and J.F. Schetzina, *Appl. Phys. Lett.* 61, 1266 (1992).
4. M.A. Haase, H. Cheng, J.M. Depuydt and J.E. Potts, *J. Appl. Phys.* 67, 448 (1990).
5. J. Ren, B. Sneed, K.A. Bowers, D.L. Dreifus, J.W. Cook, Jr. and J.F. Schetzina, *Appl. Phys. Lett.* 57, 1901 (1990).
6. J. Ren, K.A. Bowers, B. Sneed, F.E. Reed, J.W. Cook, Jr. and J.F. Schetzina, *J. Cryst. Growth* 111, 829 (1991).
7. J. Ren, K.A. Bowers, R.P. Vaudo, J.W. Cook, Jr., J.F. Schetzina, J. Ding, H. Jeon and A.V. Nurmikko, *J. Cryst. Growth* 117, 510 (1992).
8. J. Ren, K.A. Bowers, J.W. Cook, Jr. and J.F. Schetzina, *J. Vac. Sci. Technol. B* 10, 909 (1992).
9. R.M. Park, M.B. Troffer, C.M. Rouleau, J.M. DePuydt and M.A. Haase, *Appl. Phys. Lett.* 57, 2127 (1990).
10. R.M. Park, M.B. Troffer, E. Yablonoic and T.J. Gmitter, *Appl. Phys. Lett.* 59, 1896 (1991).
11. W. Xie, D.C. Grillo, R.L. Gunshor, M. Kobayashi, G.C. Hua, N. Otsuka, H. Jeon, J. Ding and A.V. Nurmikko, *Appl. Phys. Lett.* 60, 463 (1992).
12. H. Jeon, J. Ding, A.V. Nurmikko, W. Xie, M. Kobayashi and R.L. Gunshor, *Appl. Phys. Lett.* 60, 892 (1992).
13. W. Xie, D.C. Grillo, R.L. Gunshor, M. Kobayashi, H. Jeon, J. Ding, A.V. Nurmikko, G.C. Hua and N. Otsuka, *Appl. Phys. Lett.* 60, 1999 (1992).
14. H. Jeon, J. Ding, A.V. Nurmikko, W. Xie, D.C. Grillo, M. Kobayashi, R.L. Gunshor, G.C. Hua and N. Otsuka, *Appl. Phys. Lett.* 60, 2045 (1992).
15. J.M. Woodall, J.L. Freeouf, G.D. Pettit, T. Jackson and P. Kirchner, *J. Vac. Sci. Technol.* 19, 626 (1981).

# UV Photon Assisted Control of Interface Charge Between CdTe Substrates and Metalorganic Chemical Vapor Deposition CdTe Epilayers

Y. NEMIROVSKY, A. RUZIN, and A. BEZINGER

Kidron Microelectronics Research Center, Department of Electrical Engineering, Technion—Israel Institute of Technology, Haifa 32000, Israel

The technology to control the interface charge density between CdTe substrates and CdTe epilayers grown by metalorganic chemical vapor deposition is studied. The interface charge is determined by the modified built-in potential derived from capacitance-voltage characteristics of Schottky contacts formed on the epilayers. Novel ultraviolet (UV) photon assisted and photo thermal surface pretreatments that control the interface between p-type CdTe substrates and CdTe epilayers are reported. The substrates are exposed to UV radiation provided by a high pressure Hg lamp operating at 600 W with a wide emission spectrum between 190 and 300 nm. The UV photon assisted surface pretreatment with hydrogen is compared with additional surface pretreatments: thermal pretreatment with hydrogen (without UV photons) and UV photo thermal pretreatment with hydrogen. The UV photon assisted and the UV photo thermal surface pretreatments with hydrogen reduce the interface charge density to a practically negligible value. In addition, the p-type doping level of the substrate is reduced considerably in a layer of few microns adjacent to the interface.

**Key words:** CdTe substrates, epitaxial CdTe, interface charges, MOCVD, UV-assisted surface cleaning

## INTRODUCTION

The interface between CdTe and CdZnTe substrates and CdTe and HgCdTe epilayers often exhibits significant interface charges. These charges are found even in lattice matched structures such as CdTe epilayers on CdTe substrates and HgCdTe epilayers on lattice matched CdZnTe substrates. The problem of interface charge is well known even in technologically more matured heterostructures.<sup>1-6</sup>

The interface between the epilayer and the substrate strongly determines the electrical and electro-optical properties of devices fabricated in the epilayers. The interface is of great significance for the wide range of possible applications, including infrared detectors, solar cells and nuclear radiation detectors. In addition, the interface may affect the growth and the overall properties of the epilayers. Hence, there have been extensive studies to obtain a stoichiometric CdTe surface which is free of impurities, retains its crystalline perfection, and is characterized by a low density of interface states.<sup>7-9</sup>

In the case of CdTe substrates, the origin of the interface charges can be attributed mainly to the usual surface preparation methods: mechano-chemical polishing or mechanical polishing followed by chemical etching to remove the damaged surface layers. In these processes, bromine or inorganic acids as well as organic solvents are usually involved, leaving the surface depleted of Cd or rich in accumulated Te and contaminated by impurities and native oxides.

Hence, in addition to inherent substrate imperfections, the origin of the interface charges can be attributed to either one or more of the following sources: nonstoichiometry, surface oxides, foreign atoms attached to the interface, or mechanical damage at the interface. These probable contributions are all technology related and hence can be reduced with a proper technology.

To understand the nature of the surfaces and interfaces of CdTe substrates, extensive studies have used various analytical tools such as Auger electron spectroscopy, x-ray photoelectron spectroscopy, ellipsometry and additional advanced approaches.<sup>10-17</sup> The electrical properties of the surface of CdTe have been

determined indirectly by characterizing metal-CdTe Schottky junctions.<sup>8,18,19</sup>

In this study, we report 'in situ' UV photon assisted and photo thermal surface pretreatments of CdTe and CdZnTe substrates that yield reproducible interfaces with interface charges whose magnitude is practically negligible.<sup>20</sup> We compare experiments to characterize different technologies of substrate surface preparation (polishing and etching) and various 'in situ' pretreatments prior to deposition [substrate bake up in the presence of hydrogen, without and with ultraviolet (UV) photons].

In addition to the control of the interface charges, the UV photon assisted and photo thermal surface pretreatments with hydrogen exhibit a unique feature: the substrate doping level, in the outer few microns adjacent to the interface, is modified considerably. Substrates with moderate p-type conductivity, with doping levels of the order of  $10^{15}\text{cm}^{-3}$  exhibit a reduction of the doping level to mid  $10^{14}\text{cm}^{-3}$  after the UV photon assisted or photo thermal pretreatment with hydrogen.

The interface analysis is based on the method presented elsewhere in greater detail.<sup>3,4</sup> We study the simplest interface between an epilayer and a substrate of the same material. Specifically, we study the interfaces between metalorganic chemical vapor deposition (MOCVD) grown CdTe epilayers on CdTe substrates. In this manner, we are not concerned with lattice mismatch across the interfaces of heterojunctions or the difference in the chemical nature of the bonds in two different semiconductors. We can focus on the interface charges that are related to the applied technology during substrate preparation, processing steps and various pretreatments in the MOCVD reactor. Indium Schottky contacts are evaporated on the as grown epilayers and the capacitance-voltage characteristics of the structure are measured and analyzed.

## EXPERIMENTAL

The p-type CdTe substrates, with (111) orientation and doping level in the range of  $1\cdot 10^{14}\text{cm}^{-3}$  –  $1\cdot 10^{16}\text{cm}^{-3}$ , were supplied by II-VI Inc. The CdTe epilayers were

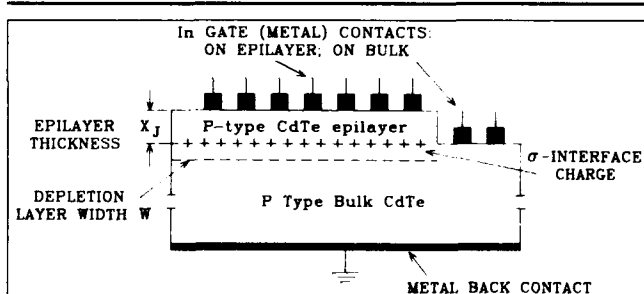


Fig. 1. The measured structure used to determine the interface between MOCVD-grown p-CdTe epilayers and p-type CdTe substrates. Indium contacts (with gate area  $\sim 500\text{ }\mu\text{m} \times 500\text{ }\mu\text{m}$ ) are vacuum evaporated on the epilayer and a large area indium contact is evaporated on the rear side of the bulk substrate.  $X_j$  is the epilayer thickness and  $W$  is the depletion layer width. Interface charge is symbolized by the + signs.

grown on the Te face of the CdTe and CdZnTe substrates by an MOCVD growth process which is described elsewhere.<sup>21,22</sup> The substrates were mechanically polished with  $0.3\text{ }\mu\text{m}$  alumina powder and subsequently chemically etched for 30 s with 10% bromine in methanol solution.

The main features of the MOCVD process are the following: the MOCVD system was manufactured by Thomas Swan Inc., England, and has a horizontal quartz reactor. The graphite susceptor is heated with infrared lamps. The metalorganic sources, DETe and DMCD, supplied by Morton, are kept at  $25^\circ\text{C}$ . Palladium diffused hydrogen serves as the carrier gas. Growth runs, at  $430^\circ\text{C}$ , are performed at a subatmospheric pressure of 300 Torr and the total flow rate is 1.5L/min. The partial pressures of DETe and DMCD in the reactor are 1 Torr and 0.51 Torr, respectively.

Ultraviolet radiation for the surface pretreatment is provided by a high pressure Hg lamp operating at 600 W, with a wide emission spectrum between 190 and 300 nm. The UV radiation is applied as an 'in situ' photon assisted surface pretreatment prior to the MOCVD growth of the epilayers. The UV radiation is used only for the pretreatment of surfaces and interfaces. In contrast, the CdTe epilayers are deposited without UV radiation because of the absence of UV photo enhancement to the growth process in the temperature range reported in the present study. By measuring the growth rate as a function of the reciprocal temperature in the range of  $340\text{--}440^\circ\text{C}$ , we have found that the energy of activation for the epitaxial growth of CdTe on the Te face of (111) oriented CdTe substrates, with and without UV photons, is the same ( $\sim 23 \pm 4\text{ K cal/mol}$ ). However, the quality of the surface morphology is significantly poorer in photon assisted growth due to premature nucleation of CdTe in the vapor phase.<sup>23</sup>

The structure that we use to study the interfaces between CdTe substrates and CdTe epilayers grown by MOCVD, is shown schematically in Fig. 1. A p-CdTe epilayer with doping level  $\sim 10^{13}\text{cm}^{-3}$ , 1–4  $\mu\text{m}$  thick, is grown on the CdTe substrate. A part of the substrate is masked during growth, enabling us to determine with a profilometer the exact thickness of the epilayer. After layer growth, indium gates of known area are evaporated through metal masks to form Schottky contacts on the epilayer and the front bare part of the substrate. A large area indium contact is evaporated on the rear (bottom) side of the substrate. The p-epilayers are fully depleted and the interface charge modifies the depletion layer width, the shape and the magnitude of the measured capacitance-voltage characteristics and the measured built-in potential.

The interface analysis is based on the method presented elsewhere in greater detail.<sup>3,4</sup> The modified built-in potential is calculated by solving the Poisson equation of the structure and by considering the superposition of the interface charge contribution to the built-in potential ( $V_{bi}$ ) to yield the measured apparent built-in potential ( $V_{bi}^{\text{app}}$ ).

The results are summarized by

$$C_m = \frac{\epsilon_s A_g}{\sqrt{2\epsilon_s (V_{bi}'' + V_a) / qN_{a2}}} \quad (1)$$

where  $C_m$  is the measured capacitance,  $V_a$  is the applied voltage and  $N_{a2}$  is the doping level of the substrate. By plotting the measured  $1/C_m^2$  vs  $V_a$ , we can find  $N_{a2}$  from the slope, and the apparent built-in potential,  $V_{bi}''$ , from the voltage axis intersection. From  $V_{bi}''$ , we obtain the magnitude of the interface charge as shown in Ref. 3

$$V_{bi}'' \sim V_{bi} + \frac{qN_{a2}X_j^2}{2\epsilon_s} + \frac{q\sigma X_j}{\epsilon_s} + \frac{q\sigma^2}{2\epsilon_s N_{a2}} \quad (2)$$

where  $X_j$  is the thickness of the epilayer,  $V_{bi}$  is the actual Schottky barrier of the indium gates and  $\sigma$  is the interface charge. The simplified form of  $V_{bi}''$ , given by Eq. 2, is obtained by assuming that the doping level of the epilayer,  $N_{a1}$  is smaller than that of the substrate ( $N_{a1} < N_{a2}$ ).

In order to develop reproducible and controlled interfaces, several substrates were exposed to various surface pretreatments (the same set of substrates was used in all experiments).

The following experiments were performed:

- I. Characterization of bulk substrates. The bulk substrates were polished, etched and characterized by evaporating In Schottky contacts and measuring the  $C_m$ - $V_a$  characteristics (without growth of epilayers). These measurements yield the doping level  $N_{a2}$  of the substrates and the actual Schottky built-in potential of the In contact ( $V_{bi}$ ), without the contribution of the interface charge between the substrate and the epilayer.
- II. Characterization of bulk substrates after exposure to a UV photo thermal pretreatment with hydrogen. The bulk substrates were polished, etched, and exposed to a UV photo thermal surface pretreatment in the growth reactor. In addition to UV radiation, the substrates were baked at 450°C and flushed by hydrogen, flowing at a rate of 100cc/min at a total pressure of 300 Torr. However, the epilayers were not deposited and only the 'in situ' UV photo thermal surface pretreatment with hydrogen was performed for one hour. Subsequently, the bulk substrates were characterized, as described in the previous experiment.
- III. Characterization of the interfaces between MOCVD CdTe epilayers and bulk CdTe substrates, without any pretreatment. The substrates were polished, etched, and loaded into the metalorganic chemical vapor deposition reactor. Subsequently, CdTe epilayers were grown according to the process whose main features are reported above. The interfaces between the

substrates and the epilayers were characterized with capacitance-voltage analysis of indium Schottky contacts evaporated on the epilayers.

- IV. Characterization of the interfaces after a thermal pretreatment with hydrogen. The substrates were polished, etched and exposed for an hour to a thermal surface pretreatment, at 450°C, with palladium diffused hydrogen flowing at 100cc/min at a total pressure of 300 Torr. Subsequently, CdTe epilayers were grown in the MOCVD reactor. The interfaces were characterized as in the previous experiment.

- V. Characterization of the interfaces after exposure to a UV photo thermal surface pretreatment with hydrogen. The substrates were polished, etched, and exposed for an hour, at 450°C, to a UV photo thermal surface pretreatment (as in experiment II). This pretreatment combines the flow of hydrogen with exposure to UV photons provided by the high pressure Hg lamp operating at 600 W. The hydrogen flows at 100cc/min, at a total pressure of 300 Torr. Following the photo thermal surface pretreatment, CdTe epilayers were grown, and the interfaces were once again characterized.

- VI. Characterization of the interfaces after exposure, at 25°C, to a UV photon assisted surface pretreatment with hydrogen. The substrates were polished, etched, and exposed for an hour, at 25°C, to UV photons provided by the high pressure Hg lamp. In addition to the UV photons, the substrates were flushed in hydrogen, flowing at 100cc/min, at a total pressure of 300 Torr. Following the UV photon assisted surface pretreatment, CdTe epilayers were grown, and the interfaces were characterized as in the previous experiments.

The capacitance-voltage characteristics were measured with a Hewlett-Packard impedance analyzer model HP 4192A, in the bias range 0-35V, at 1MHz frequency.

## RESULTS AND DISCUSSION

### Effects of Surface Preparation—Bulk CdTe Substrates

Experiments I and II investigate the effects of surface preparation on the actual built-in potential ( $V_{bi}$ ) of the bulk CdTe/In contact and determine the bulk doping level of the CdTe wafers under study.

In experiment I, the indium contacts are directly evaporated on polished and etched surfaces of bulk substrates, namely untreated surfaces. Relatively large contact capacitances are measured at zero bias and the capacitance dependence on reverse bias, at 300K, follows the depletion approximation. The data can be closely fit by a linear  $1/C_m^2$  dependence on  $V_a$ . The voltage intercept is ~1V and it yields the actual built-in potential in this case ( $V_{bi} = \sim 1V$ ). For sample #149, the zero bias capacitance is 48 pF and the apparent doping level is  $\sim 6.10^{15} \text{cm}^{-3}$ .

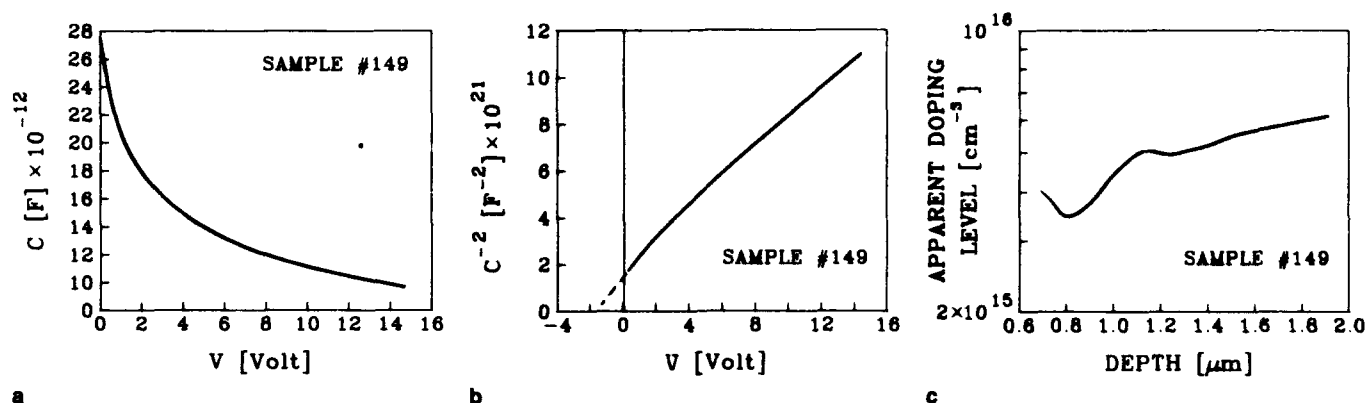


Fig. 2. Capacitance-voltage analysis of a polished and etched p-type CdTe substrate (sample #149) exposed for 1 h to the UV photo thermal surface pretreatment with hydrogen (experiment II, see text). (a) Measured capacitance-voltage characteristic. The capacitance at zero bias is 27.6 pF. (b) Calculated  $1/C^2$  vs voltage curve. The graphically derived actual built-in potential  $V_{bi}$  is 1.5V. (c) Calculated majority carrier concentration as a function of depth.

Figure 2 shows the results of experiment II, where the surfaces of the polished and etched bulk substrates are exposed to the UV photo thermal pretreatment with hydrogen (the details are given in the experimental section). Figure 2a shows that the capacitance at zero bias ( $\sim 27.6$  pF) is considerably lower than that of the untreated surface ( $\sim 48$  pF). The intercept of the  $1/C_m^2$  vs  $V_a$  plot shown in Fig. 2b, yields an actual built-in potential of  $V_{bi} \sim 1.5$  V. The apparent doping level vs depletion width (Fig. 2c) is  $(4-5) \times 10^{15} \text{ cm}^{-3}$ , and it exhibits a gradual decrease with decreasing width of the depletion region. The variation in the measurements of different contacts on the same substrate is very small whereas the measurements of indium contacts on untreated surfaces exhibit variations in capacitance and doping level.

The results of experiments I and II can be compared and interpreted with the previously reported data on the effects of surface preparation on the properties of metal/CdTe junctions by Bube et al.<sup>8,18</sup> and Auger electron spectroscopy studies on etched polar (111) CdTe surfaces of CdTe.<sup>7</sup> These studies indicate the presence of excess Te on the CdTe surface, as a result of the bromine-in-methanol etch.

Hydrogen heat pretreatment of an etched surface removes the etch-induced surface layer and restores it to a stoichiometric cleaved-like surface. Stoichiometric surfaces obtained by hydrogen heat treatment, result in metal/CdTe junctions characterized by large barriers that depend on metal work functions. In contrast, untreated polished and etched surfaces exhibit lower barriers and pinning of the Fermi level. It was also observed that the hydrogen heat treatment decreases the hole density near the substrate surface.<sup>8</sup>

It should be emphasized that the hydrogen heat treatment, previously reported, refers to polished and etched surfaces, exposed to hydrogen for 10 min, at 425°C. In the UV photo thermal surface pretreatment of experiment II, the substrates are exposed at 450°C, for 1 h to flowing hydrogen in the presence of UV photons. This may explain the larger  $V_{bi}$ , observed in Fig. 2.

### Interfaces Between Bulk and EPI, Obtained by Various Technologies

Experiments III-VI study and compare the interfaces between CdTe epilayers and CdTe substrates obtained and controlled by the various surface technologies. Figure 3 exhibits the interface of untreated surface (polished and etched) of experiment III. Figure 4 exhibits the interface obtained with hydrogen thermal pretreatment of experiment IV (at 450°C, for 1 h). Figure 5 exhibits the interface controlled by the UV photo thermal surface pretreatment of experiment V. Finally, Fig. 6 exhibits the interface controlled with the UV photon assisted surface pretreatment of experiment VI. For comparison Figs. 2-6 exhibit the measurements of the same substrate (sample #149), used in all experiments (I-VI).

#### The Interface Without any Pretreatment

Figure 3a shows the measured  $C_m$ - $V_a$  characteristic after the growth of 3.5  $\mu\text{m}$  CdTe epilayer on polished and etched substrate, without any surface pretreatment (experiment III). The zero bias capacitance (3.4 pF) is considerably lower than the value of  $\sim 48$  pF obtained on the bulk substrate in experiment I and the  $\sim 26$  pF obtained in experiment II. The capacitance decreases slowly up to  $\sim 22$  V. Figure 3b shows the  $1/C_m^2$  vs  $V_a$  curve which yields the apparent built-in potential  $V_{bi}'' \approx 256$  V. Using Eq. 2, the interface charge density is evaluated to be a  $\sigma \sim 2.1 \times 10^{12} \text{ cm}^{-2}$ .

In the case of a variable interface charge, the capacitance-voltage characteristic does not behave according to the simple depletion theory, and hence, the usual profiling method obtained by taking the derivative of Fig. 3a, does not yield the correct doping level.<sup>4</sup>

#### The Effect of a Thermal Pretreatment with Hydrogen on the Interface

In this experiment (experiment IV), the substrate was exposed, at 450°C, to the hydrogen thermal surface pretreatment, for one hour prior to the MOCVD

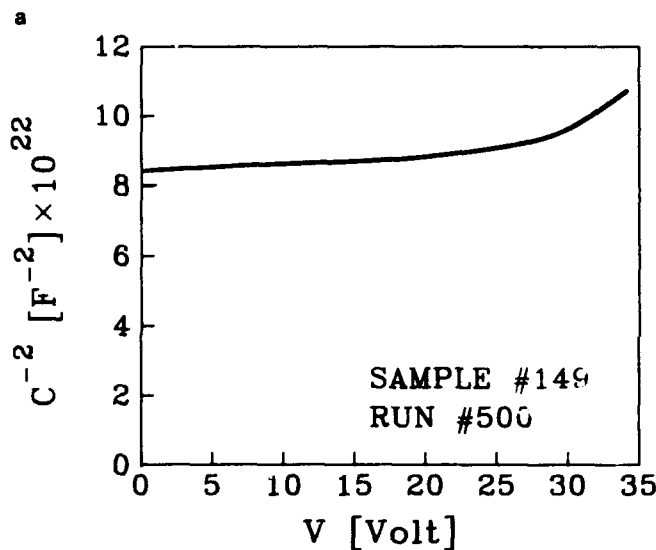
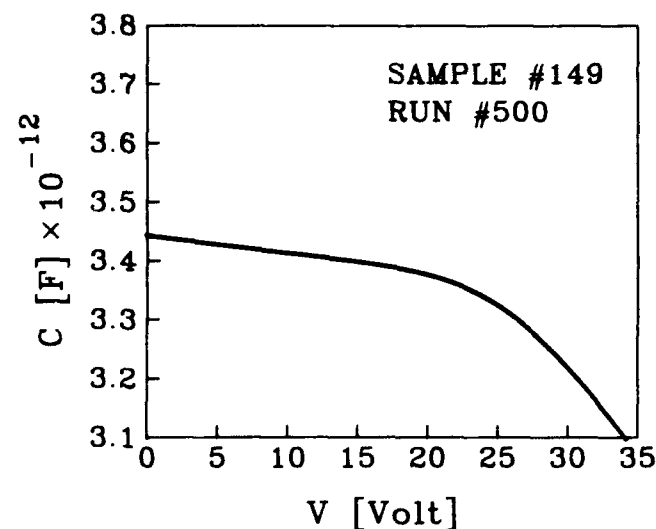


Fig. 3. The analysis of the interface between an MOCVD CdTe epilayer (3.5  $\mu\text{m}$  thick) and a bulk CdTe substrate (sample #149, run #500). The interface was not controlled (without any surface pretreatment, experiment III, see text). Contact area is  $1.96 \cdot 10^{-3} \text{cm}^2$ . (a) Measured capacitance-voltage characteristic. The zero bias capacitance is 3.4 pF. (b) Calculated  $1/C^2$  vs voltage curve. The graphically derived apparent built-in voltage  $V_{bi}$  is 256V.

epilayer growth. Figure 4a shows the measured  $C_m - V_a$  characteristic after the growth of 3.7  $\mu\text{m}$  CdTe epilayer on the same substrate used in the experiment of Fig. 3. The zero bias capacitance ( $\sim 4$  pF) is low and it decreases very slowly up to  $\sim 15$  V. Only above  $\sim 15$  V does the capacitance decrease with applied voltage according to the predictions of the depletion approximation. Figure 4b shows the  $1/C_m^2$  vs  $V_a$  curve which yields a large apparent built-in potential,  $V_{bi} = 167$  V. According to the analysis presented in Ref. 4, the data of Fig. 4 corresponds to the case of a large and variable interface charge. Using Eq. 2, the estimated interface charge is  $\sigma \approx 8 \cdot 10^{11} \text{cm}^{-2}$ .

The origin of the interface charge is not clear since according to the hydrogen heat treatment previously reported,<sup>7,8,18</sup> the predicted surface should have been

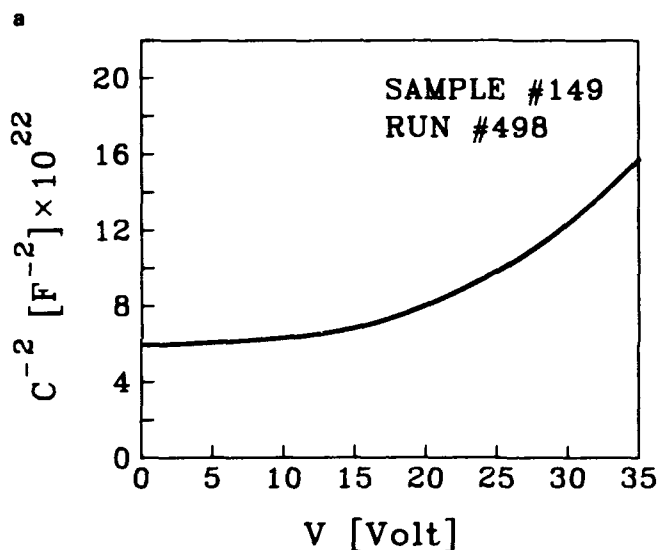
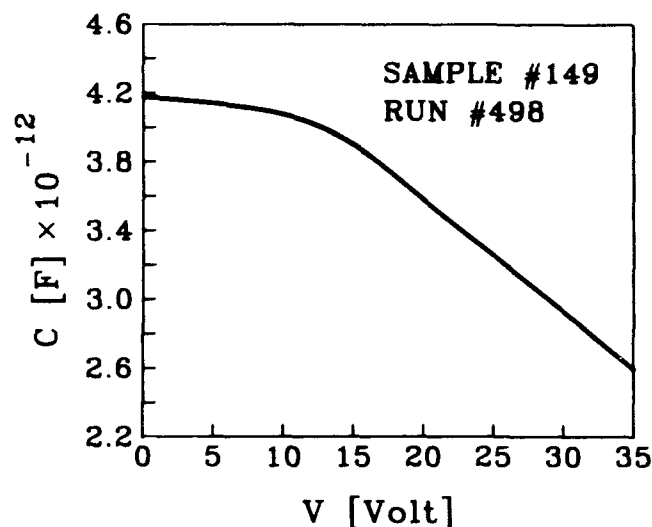


Fig. 4. The analysis of the interface between an MOCVD CdTe epilayer (3.7  $\mu\text{m}$  thick) and a bulk CdTe substrate (sample #149, run #498). The interface was controlled with the hydrogen thermal surface pretreatment (experiment IV, see text). Contact area is  $1.96 \cdot 10^{-3} \text{cm}^2$ . (a) Measured capacitance-voltage characteristic. The zero bias capacitance is 4.12 pF. (b) Calculated  $1/C^2$  vs voltage curve. The graphically derived apparent built-in voltage  $V_{bi}$  is 167V.

free of impurities, stoichiometric and crystalline. One possible explanation is that the higher temperature (450°C) and the longer exposure (one hour), used in the present study, caused, to a certain extent, thermal etching of the surface.

#### The Effect of a UV Photo Thermal Surface Pretreatment with Hydrogen on the Interface

In this experiment (experiment V), the substrate was exposed to the UV photo thermal surface pretreatment for one hour, prior to the growth of the epilayer. Figure 5a shows the measured  $C_m - V_a$  characteristic after the growth of 1.3  $\mu\text{m}$  CdTe epilayer on the same substrate used in the experiments of Figs. 2-4. The measured capacitance-voltage characteristic is well behaved and can be simulated with the

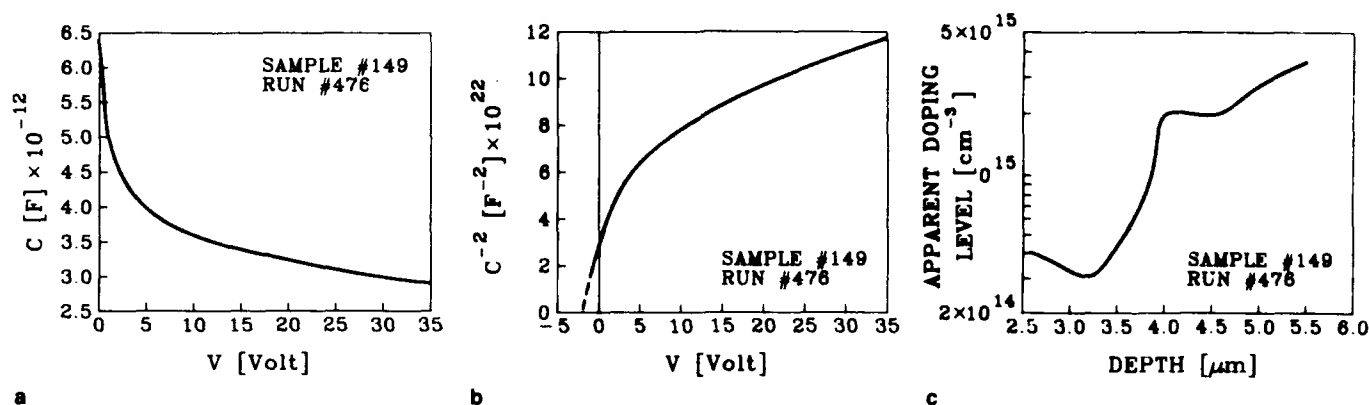


Fig. 5. The analysis of the interface between an MOCVD CdTe epilayer (1.3  $\mu\text{m}$  thick) and a bulk CdTe substrate (sample #149, run #476). The interface was controlled with the UV photo thermal surface pretreatment with hydrogen (experiment V, see text). Contact area is  $1.96 \cdot 10^{-3} \text{cm}^2$ . (a) Measured capacitance-voltage characteristic. The zero bias capacitance is 6.4 pF. (b) Calculated  $1/C^2$  vs voltage curve. The graphically derived apparent built-in potential  $V_{bi}$  is 1.7V. (c) Calculated apparent doping level as a function of depth.

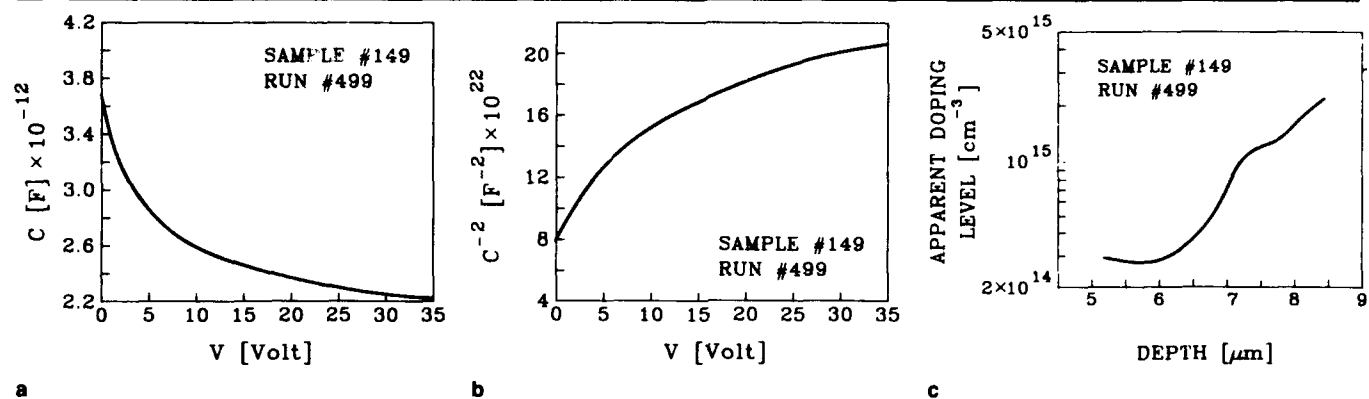


Fig. 6. The analysis of the interface between an MOCVD CdTe epilayer (3.2  $\mu\text{m}$  thick) and a bulk CdTe substrate (sample #149, run #499). The interface was controlled with the UV photon assisted surface pretreatment with hydrogen (experiment VI, see text). Contact area is  $1.96 \cdot 10^{-3} \text{cm}^2$ . (a) Measured capacitance-voltage characteristic. The zero bias capacitance is 3.7 pF. (b) Calculated  $1/C^2$  vs voltage curve. The graphically derived apparent built-in potential  $V_{bi}$  is 2.5V. (c) Calculated apparent doping level as a function of depth.

depletion approximation. The apparent built-in potential derived graphically from the data of Fig. 5b is,  $V_{bi} = 1.7\text{V}$ . Nearly the same value was derived in experiment II for the actual built-in potential of indium contacts on bulk substrates exposed to the same UV photo thermal surface pretreatment. Hence, from Eq. 2, it can be concluded that the interface charge is practically negligible. Figure 5c shows the apparent doping profile obtained from the derivation of Fig. 5a. An apparent reduction in the doping level in a boundary region of several microns inside the substrate, adjacent to the interface is observed. The substrate region with the reduced apparent doping level is referred to as "the surface layer." Interfaces with the same properties were obtained when thicker epilayers, (2–4)  $\mu\text{m}$ , were grown.

#### The Effect of a UV Photon Assisted Surface Pretreatment with Hydrogen on the Interface

In this experiment (experiment VI), the substrate was exposed to the UV photon assisted surface pretreatment for one hour prior to the deposition. Figure 6a shows the measured  $C_{in} - V_s$  characteristic after the growth of 3.2  $\mu\text{m}$  CdTe epilayer on the same substrate used in the previous experiments. The

measured capacitance-voltage characteristic is well behaved and can be simulated with the depletion approximation.

The apparent built-in potential derived graphically from the data of Fig. 6b is  $V_{bi} = 2.5\text{V}$ . Inspection of the right side of Eq. 2 shows that, the contribution of the second term is 0.84V, assuming  $N_{a2} = 1 \cdot 10^{14} \text{cm}^{-3}$  (see Fig. 6c). Hence, it can be concluded that the interface charge is practically negligible. Figure 6c shows the apparent doping profile obtained from the derivation of Fig. 6a. An apparent reduction in the doping level in a boundary region of several microns adjacent to the interface is again observed, as in the UV photo thermal surface pretreatment.

#### CONCLUSIONS

The major results of this study, as exhibited in Figs. 2–6, are summarized in Table I. Controlled interfaces, with lower apparent doping levels at the interface and practically negligible interface charges, are observed after exposure to the UV photo thermal or UV photon assisted surface pretreatments. Similar results are obtained for the interface between CdZnTe (4% Zn) substrates and CdTe epilayers.

An additional experimental observation indicates

Table I. Summary of Major Results of Figures 2-6

| Experiment<br>Pretreatment<br>and Results | Experiment II<br>(Fig. 2)        | Experiment III<br>(Fig. 3)         | Experiment IV<br>(Fig. 4)        | Experiment V<br>(Fig. 5)              | Experiment VI<br>(Fig. 6)        |
|---|----------------------------------|------------------------------------|----------------------------------|---------------------------------------|----------------------------------|
| UV  | +                                | —                                  | —                                | +                                     | +                                |
| Temperature                               | 450°C                            | —                                  | 450°C                            | 450°C                                 | 25°C                             |
| Pretreatment Time                         | 1 h                              | 0                                  | 1 h                              | 1 h                                   | 1 h                              |
| Hydrogen                                  | +                                | +                                  | +                                | +                                     | +                                |
| Epilayer Thickness                        | 0                                | 3.5 $\mu\text{m}$                  | 3.7 $\mu\text{m}$                | 1.3 $\mu\text{m}$                     | 3.2 $\mu\text{m}$                |
| Interface Charge, $\sigma$                | —                                | $2.1 \cdot 10^{12} \text{cm}^{-2}$ | $8 \cdot 10^{11} \text{cm}^{-2}$ | $< \sim 10^{11} \text{cm}^{-2}$       | $< \sim 10^{11} \text{cm}^{-2}$  |
| Bulk Doping Level                         | $6 \cdot 10^{15} \text{cm}^{-3}$ | $6 \cdot 10^{15} \text{cm}^{-3}$   | $6 \cdot 10^{15} \text{cm}^{-3}$ | $6 \cdot 10^{15} \text{cm}^{-3}$      | $6 \cdot 10^{15} \text{cm}^{-3}$ |
| Depth of the<br>Surface Layer             | $\sim 1.2 \mu\text{m}$           | none                               | none                             | $\sim 2.5 \mu\text{m}$                | $\sim 4.2 \mu\text{m}$           |
| Doping of the<br>Surface Layer            | $4 \cdot 10^{15} \text{cm}^{-3}$ | —                                  | —                                | $\sim 5 \cdot 10^{14} \text{cm}^{-3}$ | $3 \cdot 10^{14} \text{cm}^{-3}$ |
| Capacity at $V_a = 0$                     | 27.6 nF                          | 3.4 pF                             | 4.12 pF                          | 6.4 pF                                | 3.7 pF                           |
| $V''_{bi}$                                | 1.5V                             | 2.56V                              | 167V                             | 1.7V                                  | 2.5V                             |

that cleaner surfaces are consistently obtained with the 'in situ' UV photo thermal and photon assisted surface pretreatments. After exposure to the UV pretreatments, the time required to obtain an epilayer of  $\sim 2 \mu\text{m}$  thickness is approximately half the time required to obtain more or less the same thickness, without any pretreatment.

The origin of the observed decrease in the apparent hole concentration inside the substrate near the surface, after the UV photon assisted and photo thermal pretreatments, is not clear. The speculation that hydrogen or hydrogen radicals diffuse into the substrate does not fit the observation that the same effect is obtained in the UV photon assisted pretreatment at 25°C as after the UV photo thermal pretreatment at 450°C. This issue needs further study.

It is believed that UV-induced heterogeneous dissociation of hydrogen on the surface of the substrate produces highly reactive hydrogen radicals. The hydrogen radicals form volatile hydrides with Te atoms<sup>24</sup> as well as possibly additional hydrides with impurity atoms that reside on the surface due to the polishing and rinsing processing steps. In addition, the hydrogen radicals reduce native oxides that are formed on the surface and remove water molecules that are easily adsorbed on  $\text{TeO}_2$  and the polar surface of CdTe. The highly reactive nature of the hydrogen radicals and the photosensitized reactions at the surface, form reproducible and controlled interfaces. These interfaces are characterized by a nonuniform doping profile and exhibit lower apparent doping levels in a surface layer of several microns. Within the sensitivity of the methodology of the present study, the interface charge density of the UV pretreated interfaces, is practically negligible.

## REFERENCES

1. H. Kroemer, *VLSI Electronics: Microstructure Science* (Academic Press, N.Y., 1985), Vol. 10, Ch. 4 and references therein.
2. S.M. Sze, *Physics of Semiconductor Devices*, 2nd. Ed. (Wiley, New York, (1981), Ch. 5
3. D. Goren, N. Amir and Y. Nemirovsky, *J. Appl. Phys.* 71, 318 (1992).
4. Y. Nemirovsky, A. Ruzin and A. Bezinger, to be published in *Trends in Vacuum Science & Technology* (1993).
5. P. Lovecchio, M.B. Reine and M.N. Grimbergen, *J. Vac. Sci. & Technol.* A3, 246 (1985).
6. C.C. Wang, *J. Vac. Sci. Technol.* B9, 1740 (1991).
7. Y.C. Lu, C.M. Stahle, R.S. Feigelson and J. Morimoto, *J. Appl. Phys.* 62, 4453 (1987).
8. J.G. Werthen, J.P. Haering, A.L. Farenbruch and R.H. Bube, *J. Appl. Phys.* 54, 5982 (1983).
9. J.P. Haering, J.G. Werthen and R.H. Bube, *J. Vac. Sci. Technol.* A1, 1469 (1983).
10. R.D. Feldman, R.L. Opila and P.M. Bridenbaugh, *J. Vac. Sci. Technol.* A3, 1988 (1985).
11. V. Solzbach and H.J. Richter, *Surf. Sci.* 97, 191 (1980).
12. A.J. Ricco, H.S. White and M.S. Wrighton, *J. Vac. Sci. Technol.* A2, 910 (1984).
13. M. Hage-Ali, R. Stick, A.N. Saxena and P. Siffert, *Appl. Phys.* 19, 25 (1979).
14. I.M. Dharmadasa, W.G. Herrenden-Harker and R.H. Williams, *Appl. Phys. Lett.* 48, 1802 (1986).
15. A.K. Wahi, G.P. Carey, K. Miyano, T.T. Chiang, I. Lindau and W.E. Spicer, *J. Vac. Sci. Technol.* A8, 1152 (1990).
16. A.K. Wahi, G.P. Carey, K. Miyano, T.T. Chiang, I. Lindau and W.E. Spicer, *J. Vac. Sci. Technol.* A7, 494 (1989).
17. D.J. Friedman, I. Lindau and W.E. Spicer, *Phys. Rev.* B37, 731 (1988).
18. F.F. Wang, A.L. Fahrenbruch and R.H. Bube, *J. Appl. Phys.* 65, 3552 (1989).
19. R.L. Van Meirhaeghe, R. Van de Walle, W.H. Laflere and F. Cardon, *J. Appl. Phys.* 70, 2200 (1991).
20. A. Ruzin, A. Bezinger, and Y. Nemirovsky, to be published, *J. Appl. Phys.* (1993).
21. N. Amir, D. Goren, D. Fekete and Y. Nemirovsky, *J. Electron. Mater.* 20, 227 (1990).
22. Y. Nemirovsky, D. Goren and A. Ruzin, *J. Electron. Mater.* 20, 609 (1991).
23. S.J.C. Irvine, *CRC Critical Reviews in Solid State and Mater. Sci.* 13, 279 (1987).
24. J.T. Cheung, S.H. Shin, J.G. Pasko and R.E. DeWames, *J. Vac. Sci. Technol.* B10, 1538 (1992).



# Heavily Accumulated Surfaces of Mercury Cadmium Telluride Detectors: Theory and Experiment

J.R. LOWNEY, D.G. SEILER, and W.R. THURBER

Semiconductor Electronics Division, National Institute of Standards and Technology, Gaithersburg, MD 20899

Z. YU, X.N. SONG, and C.L. LITTLER

Department of Physics, University of North Texas, Denton, TX 76203

Some processes used to passivate n-type mercury cadmium telluride photoconductive infrared detectors produce electron accumulation layers at the surfaces, which result in 2D electron gases. The dispersion relations for the electric subbands that occur in these layers have been calculated from first principles. Poisson's equation for the built-in potential and Schroedinger's equation for the eigenstates have been solved self-consistently. The cyclotron effective masses and Fermi energies have been computed for each subband density for 12 total densities between  $0.1$  to  $5.0 \times 10^{12} \text{ cm}^{-2}$ . The agreement with Shubnikov-de Haas measurements is very good at lower densities with possible improvement if band-gap narrowing effects were to be included. At higher densities, larger differences occur. The simple 2D description is shown to break down as the density increases because the wave functions of the conduction and valence bands cannot be well separated by the narrow band gap of long-wavelength detectors. These results provide a basis for characterizing the passivation processes, which greatly affect device performance.

**Key words:** HgCdTe photoconductive detectors, Shubnikov-de Haas oscillations, surface passivation, 2D electron gas

## INTRODUCTION

The II-VI compound semiconductor  $\text{Hg}_{1-x}\text{Cd}_x\text{Te}$  is today's most widely used infrared detector material. It provides, for example, high-performance photoconductive (PC) detectors in the 4 to 6 and 8 to 12  $\mu\text{m}$  spectral ranges. The properties of these detectors are very sensitive to their surface passivation, which is often a dominant factor in limiting device performance. The complexity of the surface passivation process arises from the different chemical properties of the constituents and the formation of electrically active defects in the interface region.<sup>1</sup> Often HgCdTe detectors are passivated by processes (e.g. anodic oxidation) that produce accumulated surfaces, which result in 2D electron gases with areal electron densities on the order of  $10^{11}$  to  $10^{12} \text{ cm}^{-2}$ . The resulting surface potential can be greater than the band-gap

energy in long-wavelength detectors, and the surfaces can thus greatly influence the characteristics of the detector. Consequently, the development of theories and models that predict the conduction properties of the electrons in these accumulation layers is very important.

In this paper, first-principles calculations have been used to determine the accumulation-layer potentials, electron densities, cyclotron effective masses, and Fermi energies of the resulting 2D electron gases. Shubnikov-de Haas (SdH) measurements were also carried out on a wide variety of n-type PC detectors to compare them with the calculated results. The electron densities and mobilities of such layers were obtained in the past by Nemirovsky and Kidron<sup>2</sup> by using Hall-effect and capacitance-voltage measurements for a wide range of densities. Nicholas et al.<sup>3</sup> have used SdH measurements to characterize these surface layers, and they have found that the layers can be described by a 2D electron gas with a number

of 2D subbands. SdH oscillations occur in the magnetoresistance at high magnetic field and result from the redistribution of carriers caused by the crossing of the Fermi energy by a Landau level. This technique has the advantage that measurements can be made directly on commercial photoconductive detectors, which have only two terminals. The oscillations are periodic when plotted as a function of the inverse of the magnetic field,  $B$ , and a Fourier transform of the signal as a function of  $1/B$  shows peaks at fundamental frequencies corresponding to the densities of each subband. For parabolic subbands, the electron densities can be obtained directly from these frequencies. However, HgCdTe is very nonparabolic because of its small energy gap, and therefore a model is needed to deduce the densities. The subband Fermi energies can be obtained from the fundamental frequencies once the cyclotron effective masses are determined from the measured temperature dependence of the amplitude of the oscillations. The model then relates these measured quantities to the electron densities.

We have calculated the dispersion relations of the subbands self-consistently from the accumulation-layer potentials to obtain the model needed to relate the electron densities to the measured parameters. There have been various approaches to the solution of the subband dispersion relations, most of which have used a WKB approximation.<sup>4-6</sup> We have followed the work of Nachev,<sup>7</sup> who solved the matrix Hamiltonian for the conduction band and heavy-hole, light-hole, and split-off valence bands. The built-in potential in the electron accumulation layer is included directly in the matrix equation, and a second order differential equation is obtained for a wave function that contains terms that depend both on the potential and the electric field in the accumulation layer. The field terms cause a spin-splitting of the eigenvalues. The actual subband wave functions can then be determined from the solutions of this differential equation.

First we solved Poisson's equation for a continuum model of the electron density to obtain an initial built-in potential. Then we solved Schroedinger's equation for the eigenfunctions and eigenvalues for the electric subbands that are allowed in the 2D electron gas that describes the accumulation layer. From the wave functions obtained, we recomputed the potential and iterated the potential until self-consistency was obtained. We then computed the Fermi energies and cyclotron masses from the calculated subband dispersion relations for twelve electron densities between  $0.1$  to  $5.0 \times 10^{12} \text{ cm}^{-2}$ . Agreement of our theoretical results with our measurements for a detector with an electron density of  $7.9 \times 10^{11} \text{ cm}^{-2}$  is very good. In contrast, the theory predicts values for cyclotron effective masses that are much smaller and Fermi energies that are much larger than the measured values for a detector with  $3.4 \times 10^{12} \text{ cm}^{-2}$ . We expect that if we were to include the effect of band-gap narrowing,<sup>8</sup> which occurs at these fairly large carrier densities, we would obtain better agreement. There is also the possibility that the surface could be under

some strain, which could affect the energy gap.

There is a gradual breakdown in the 2D electron gas model for the accumulation layers as the density increases because the energy gaps are so small in long-wavelength detectors. It becomes difficult for the electrons to remain confined solely to the conduction band because their wave functions can cross the energy gap into the valence band when the potentials become large. For the 2D model to be completely valid, the conduction-band wave functions must decay sufficiently in the energy gap that they can be considered isolated. For the low-order subbands in very heavily accumulated surface layers, this isolation weakens, and a large number of states are then allowed that traverse the entire thickness of the detector. Thus, the model approaches the limiting case of a graded 3D layer with a SdH Fourier transform that has a broad featureless background for the range of 3D electron densities in the accumulation layer.

### THEORY

We have extended the work of Nachev,<sup>7</sup> who has performed the most rigorous analysis of the subband dispersion relations, to the entire set of allowed subbands for a wide range of electron densities. He has derived the  $8 \times 8$  matrix Hamiltonian for the conduction band and the heavy-hole, light-hole, and split-off valence bands for both spin directions ( $\pm$ ). He then reduced the Hamiltonian to a second-order differential equation for the wave function  $\phi_{\pm}$  in the direction  $z$  perpendicular to the accumulated surface:

$$\frac{d^2\phi_{\pm}}{dz^2} = a \frac{d\phi_{\pm}}{dz} + (k^2 - b)\phi_{\pm} \pm \frac{1}{3}ck\phi_{\pm} \quad (1)$$

where

$$a = \frac{2\alpha^2 + \beta^2}{2\alpha + \beta} \frac{dV(z)}{dz} \quad (2)$$

$$b = \frac{3\gamma}{P_0^2(2\alpha + \beta)} \quad (3)$$

$$c = \frac{3(\alpha^2 - \beta^2)}{2\alpha + \beta} \frac{dV(z)}{dz} \quad (4)$$

and

$$\alpha = \frac{1}{E_v(z) - E_c} \quad (5)$$

$$\beta = \frac{1}{E_v(z) - \Delta - E_c} \quad (6)$$

$$\gamma = E_c(z) - E_c \quad (7)$$

In the above equations,  $k$  is the wave number in the plane of the surface and refers to the 2D free electron

gas,  $V(z)$  is the built-in potential in the accumulation layer due to the oxide charge,  $E_c(z)$  and  $E_v(z)$  are the conduction and valence band energies, respectively, including the effect of the potential,  $\Delta$  is the split-off band separation from the valence band edge,  $P_0$  is a number proportional to the momentum matrix element as given in Kane's band model for HgCdTe,<sup>9</sup> and  $E^\pm$  are the eigenvalues for the two spin directions.

The wave functions  $\phi_\pm(k, z)$  are real and the actual subband wave functions,  $\Psi$ , can be computed from them by solving for the eight envelope functions  $f_n$  because

$$\Psi(r) = \sum_{n=1}^8 f_n(z) u_n(r) \quad (8)$$

where  $u_n(r)$  denotes the periodic part of the Bloch function at  $k = 0$ . The envelope wave functions of the conduction band,  $f_1(z)$  and  $f_5(z)$ , are found directly in terms of  $\phi_\pm(k, z)$ :

$$\phi_\pm(k, z) = i(k_x/k)f_1(z) \pm f_5(z), \quad k_x = k_x + ik_y. \quad (9)$$

The other envelope functions are found from the matrix Hamiltonian in terms of these two envelope functions by direct substitution. The equations for them, which are somewhat lengthy, involve the derivatives of  $f_1(z)$  and  $f_5(z)$  as well because of the momentum operator in the Hamiltonian. The volumetric electron density can then be computed directly from  $\Psi$  and the areal density of the 2D electron gas.

The initial potential is found by solving Poisson's equation for a non-quantized 3D free electron gas. The standard Kane  $k$ - $p$  band model,<sup>9</sup> which treats the coupling of the light-hole and split-off valence bands with the conduction band, is used. Poisson's equation is solved by a nonlinear two-point boundary value method based on finite differences with deferred correction and Newton iteration. Equation 1 is then solved by integrating the equation from an initial value and slope at the boundary opposite to the accumulation layer, and eigenvalues are found by selecting those solutions that vanish at the surface.

As in Ref. 7, the interior boundary, where the conduction-band wave functions go to zero, has been chosen to be at the middle of the energy gap for a given eigenvalue or at a maximum distance of 0.5  $\mu\text{m}$  if the eigenvalue always lies above midgap. Thus, we accept only those states that are effectively bound by the conduction band and constitute a 2D electron gas. This approximation is based on the assumption that the wave functions decay sufficiently in the energy gap that those associated with the conduction band can be separated from those associated with the valence band. As the gap becomes very small, this approximation breaks down and a continuum background of states that traverse the entire thickness of the detector becomes allowed. This effect is discussed further below.

Equation 1 is solved for at most 50  $k$  values to construct the dispersion relations for the allowed subbands. A new potential is computed from the calculated wave functions between the surface and

0.1  $\mu\text{m}$ ; beyond this point, the original bulk potential is used. Were we to use the calculated wave functions beyond 0.1  $\mu\text{m}$ , there would be a difficulty because of the artificial boundary condition at 0.5  $\mu\text{m}$  where the wave functions are forced to be zero. The process is iterated until the input and output potentials agree to within 1%. In order to prevent the potentials from gradually diverging from their original values, they are scaled each time by the ratio of the initially computed areal electron density to that just computed.<sup>10</sup> When this factor is between 0.99 and 1.01, convergence is obtained. It was discovered that convergence could be obtained more rapidly, and often only, if the initial potential were modified slightly between the surface and 0.025  $\mu\text{m}$  to take into account the strong differences between the electron density computed initially and quantum-mechanically near the surface in the accumulation layer. The initial potential was thus subsequently scaled by a quadratic function to make it agree better with the shape of the first calculated potential over this range.

Once the self-consistent subband dispersion relations were found, we computed the subband densities, Fermi energies, and cyclotron effective masses at the Fermi energy by performing either a parabolic spline interpolation or linear extrapolation of our computed eigenvalues to the Fermi energy. The spin-averaged cyclotron effective mass,  $m^*$ , is obtained from the expression

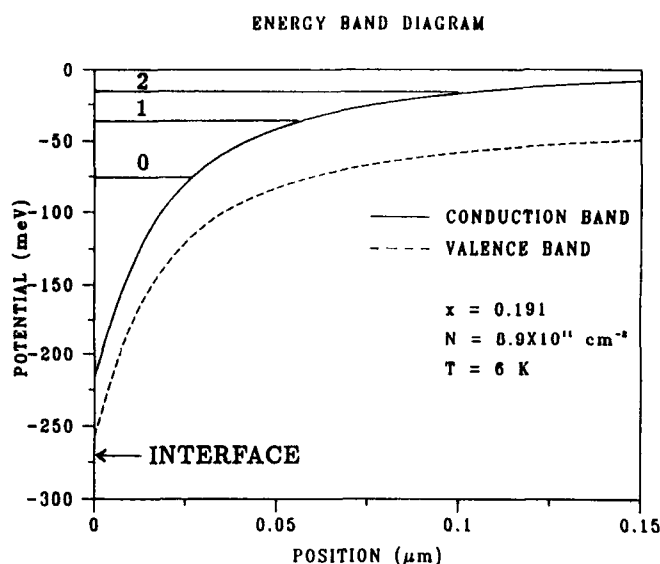
$$(m^*)^{-1} = \frac{\hbar^{-2}}{2} \sum_i \left( \frac{1}{k} \frac{dE_i}{dk} \right) \quad (10)$$

evaluated at the Fermi energy,  $E_F$ . These quantities now allow one to compute the value of the subband densities from the peaks in the Fourier transform of the SdH data. The frequencies corresponding to the peaks equal  $m^*E_F/\hbar e$  for each subband.<sup>11</sup> The value of  $m^*$  is determined from the measured temperature dependence of the amplitude of the SdH oscillations.<sup>12</sup> Thus, one can find the subband density for which the theoretically computed product of  $m^*E_F$  has the measured value for each subband. For the case of parabolic subbands,  $m^*E_F = \hbar^2\pi N$ , where  $N$  is the electron density, and the peak frequencies provide  $N$  directly. We refer to this relation as the parabolic approximation.

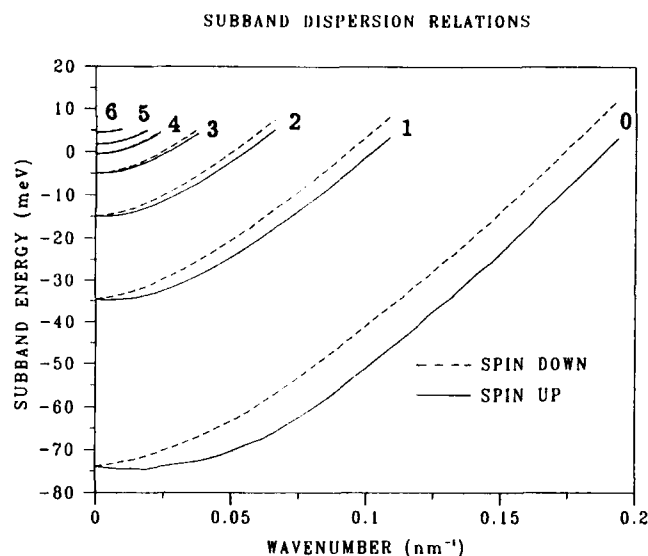
## EXPERIMENT

Shubnikov-de Haas measurements have been made on a series of long-wavelength  $n$ -type HgCdTe PC infrared detectors with accumulation-layer electron densities between mid  $10^{11}$  and mid  $10^{12} \text{ cm}^{-2}$ . They were square with active areas between 2 and  $4 \times 10^{-5} \text{ cm}^2$ . Their top and bottom surfaces were passivated by various methods that produced electron accumulation layers. Indium contacts, sometimes extended, were used to achieve excellent ohmic behavior.

Some of these detectors were measured as a function of temperature between 1.5 and 30K to obtain effective mass data. Here we report on two detectors



a

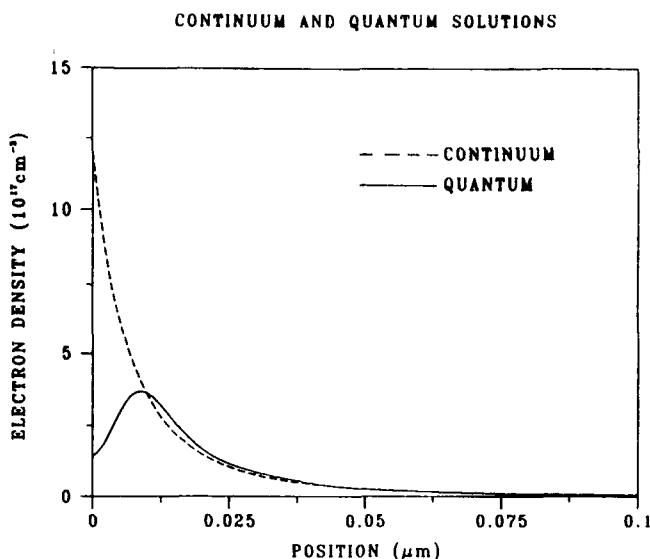


b

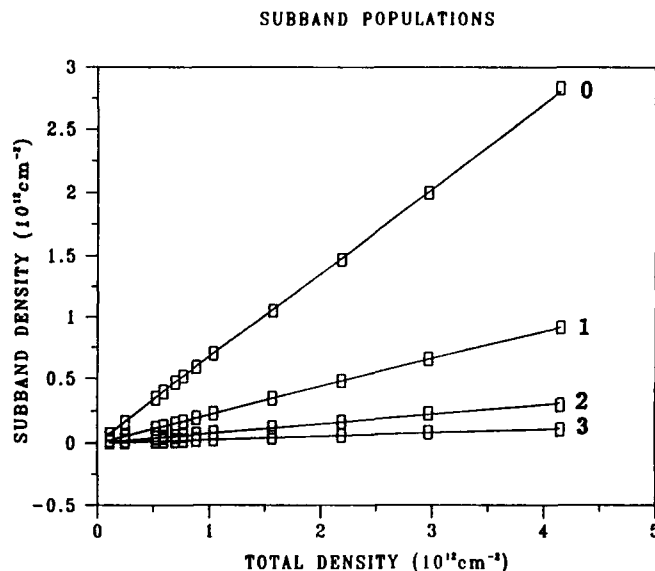
Fig. 1. (a) Built-in potential for accumulation layer with total electron density of  $8.9 \times 10^{11} \text{ cm}^{-2}$  and alloy fraction  $x = 0.191$ . The horizontal lines are the subband-edge energies for the first three subbands ( $n = 0, 1, 2$ ). (b) Dispersion relations for the subbands for this potential, showing spin-splitting. The curves are labeled by subband number from 0 to 6.

that have had extensive measurements made on them. Ac magnetic-field modulation and lock-in amplifier techniques that use the second harmonic detection were used to obtain the signal for magnetic fields up to 12 T.<sup>12</sup> The SdH oscillations are a small percentage of the total magnetoresistance, and ac techniques significantly enhance the measured SdH oscillations in these detectors.

Excellent signal-to-noise ratios were obtained in most detectors even at temperatures as high as 30 K. Measurements made at 30, 60, and 90 degree rotations of the sample about the perpendicular to the surface showed that the peak frequencies varied as  $1/\cos(\theta)$ , where  $\theta$  is the rotation angle, as expected for a 2D electron gas.



a



b

Fig. 2. (a) Electron density computed by solving Poisson's equation for a charge continuum (dashed) and from full quantum-mechanical calculation (solid) for case of Fig. 1. (b) Subband densities as a function of total density. Lines are linear least-squares fit. The curves are labeled by subband number from 0 to 3, and  $x = 0.191$ .

## RESULTS AND DISCUSSION

Calculations of the subband dispersion relations and related quantities have been made for the range of areal electron densities between  $0.1$  and  $5.0 \times 10^{12} \text{ cm}^{-2}$ . The  $x$ -value of the detector was taken to be  $0.191$ , with a corresponding energy gap of  $41.1 \text{ meV}$ ,<sup>13</sup> which is representative of long-wavelength detectors and equal to that of the detectors we report on below. The background electron doping density was assumed to be  $3.9 \times 10^{14} \text{ cm}^{-3}$ , which was reported for these detectors, along with a bulk mobility of  $2.5 \times 10^5 \text{ cm}^2/\text{Vs}$  at  $77 \text{ K}$ . Bulk SdH oscillations were not observed because of their low frequency, which implies that they would have been observed only at low magnetic

fields where broadening effects greatly reduce their signal strength. The temperature is taken to be 6K, at which the material is degenerate. As an example, the built-in field and subband dispersion relations for an areal density of  $8.9 \times 10^{11} \text{ cm}^{-2}$  are shown in Figs. 1a and 1b, respectively. The surface potential in Fig. 1a is about three times greater than the energy of the lowest subband edge and over five times the energy gap. The spin splitting is evident in Fig. 1b, and is greatest for the lowest subband. The density of electrons in the spin-up subband is about 15% greater than in the spin-down subband for the lowest four subbands. At the lower densities, this percentage decreases somewhat, especially for the higher subbands, while at higher densities it remains nearly the same for all subbands. Note also that the deviation from a parabolic to a nearly linear dependence of  $E$  on  $k$  is clear for energies only about 10 meV above the subband edges. The small oscillations in these curves are due to 1% numerical uncertainty in the solutions.

The corresponding electron density in the accumulation layer is shown in Fig. 2a for both the semiclassical result from the initial solution of Poisson's equation and the final quantum-mechanical result from the subbands. The width of the accumulation layer is seen to be about 0.1  $\mu\text{m}$ . The latter density is greatly reduced at the surface because of the boundary condition on the wave functions. It goes to zero discontinuously across the boundary because of the dependence of the wave function on the derivatives of  $f_1$  and  $f_5$ , which undergo a discontinuous change from a finite to zero value at the boundary. Therefore the shape of the potential near the interface is different in the two cases, and the value of electron density obtained quantum-mechanically is less than that of the initial semiclassical solution. The electron densities of the first four subbands are plotted as a function of total density in Fig. 2b. We compute the total density from a sum over only the first four subbands, for which we can perform accurate computations. We estimate the error incurred by this approximation to be less than 1%. The relations are nearly linear with average slopes of 0.673, 0.223, 0.077, and 0.027 for the first ( $n = 0$ ) through fourth ( $n = 3$ ) subband, respectively. The deviations from linearity are less than 1%. These values differ somewhat from our corresponding experimental values of 0.609, 0.258, 0.101, and 0.032, which have deviations from linearity of only a few percent, although the experimental values may not be completely accurate because they are based on the parabolic approximation for the density in the SdH analysis. This near linearity shows that the shape of the potential distribution is relatively insensitive to the magnitude of the surface potential. The difference between theoretical and experimental slopes may indicate that the potential distribution is somewhat distorted, which can be caused by strain or band gap narrowing.

The subband Fermi energies and cyclotron effective masses are shown in Figs. 3a and 3b, respectively, as a function of total density. The Fermi energy in the

bulk is computed to be 5.44 meV for an assumed bulk density of  $3.9 \times 10^{14} \text{ cm}^{-3}$ . The scatter in the mass values is due to the derivative in Eq. 10. Although the calculated eigenvalues appear relatively smooth in Fig. 1b they are only accurate to about 1%, and this uncertainty as well as that due to the discreteness of the  $k$ -values causes the theoretical masses to have errors of about 5% occasionally. A more refined calculation would lead to better accuracy. The strong variations of the masses with density attest to the nonparabolicity of the dispersion relations, which have an effect on the optimization of device performance. The serpentine shape of the curves is due to the strong curvature of the built-in potential.

We have made SdH measurements on a number of

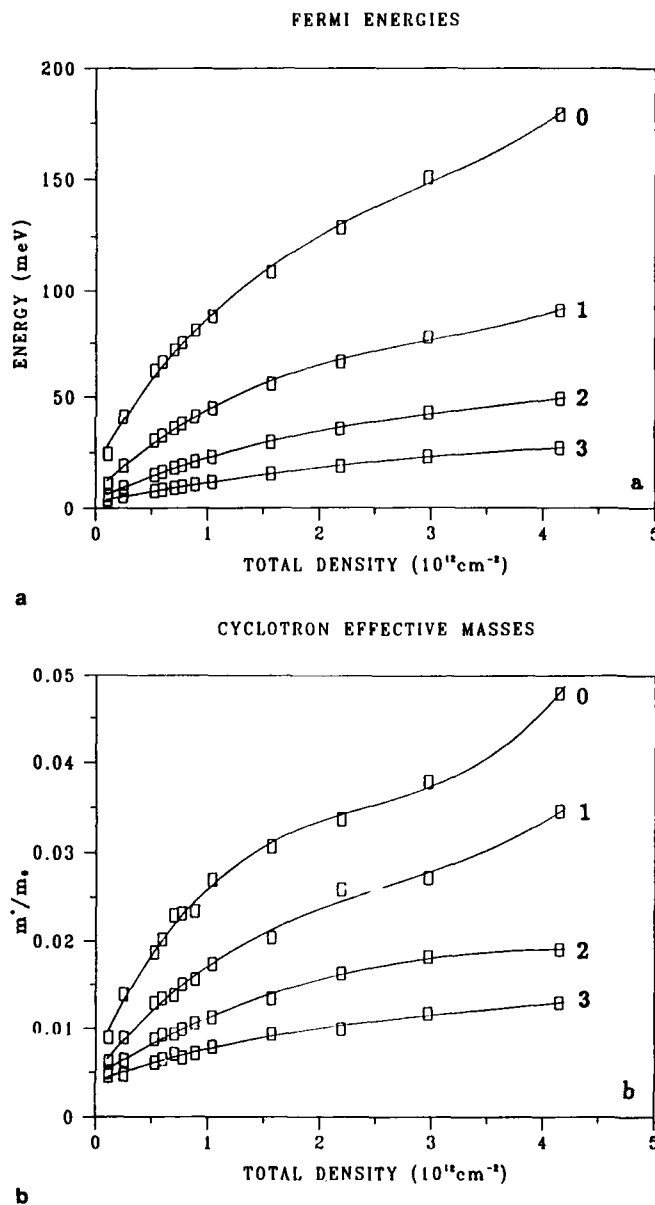


Fig. 3. (a) Subband Fermi energies as a function of total density, measured from the bottom of each subband. (b) Ratio of subband cyclotron effective masses to the electron mass at the Fermi energy as a function of total density. Lines are cubic least-squares fit. The curves are labeled by subband number from 0 to 3, and  $x = 0.191$ .

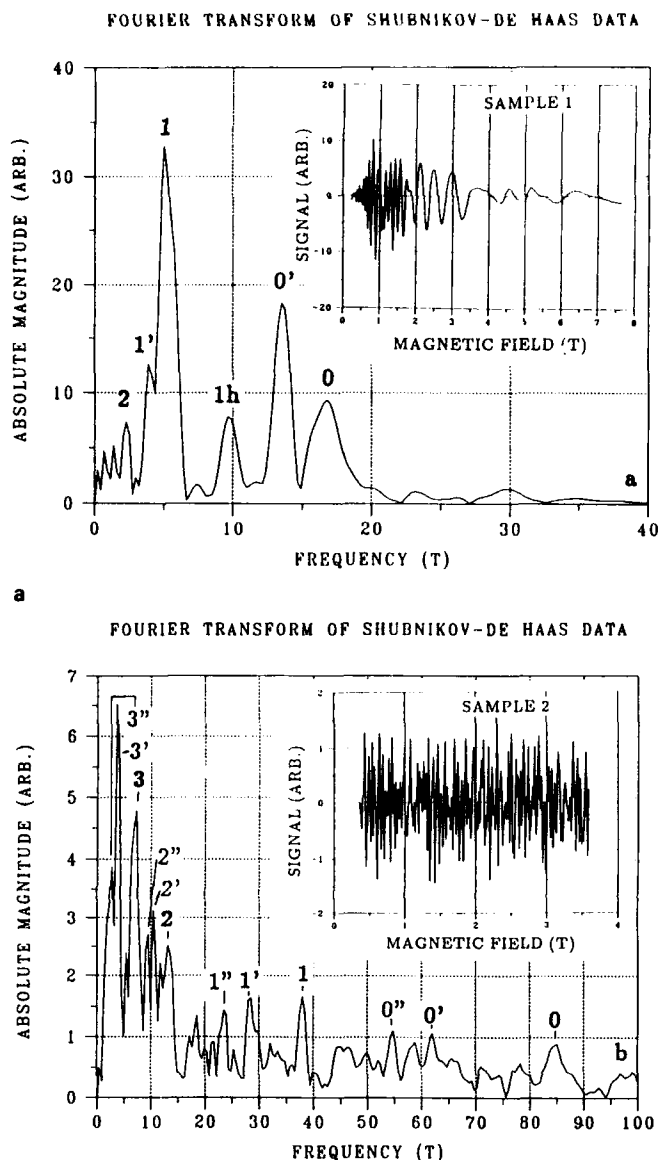


Fig. 4. (a) Fourier transform of SdH data at 5K for Sample 1; the label "h" stands for harmonic; peaks are labeled by subband number. (b) Same for Sample 2, except at 2K. Actual SdH data for the signals as a function of magnetic field are given in insets and  $x = 0.191$ .

long-wavelength, commercial, n-type PC detectors with total densities between  $5 \times 10^{11}$  and  $5 \times 10^{12} \text{ cm}^{-2}$ . The SdH Fourier transforms of two different representative detectors are shown in Figs. 4a and 4b along with the actual SdH data, which show the oscillations vs magnetic field. The notations ' and '' refer to different surfaces or to different regions on the same surface since both surfaces of the detector were passivated. The detector in Fig. 4a was passivated with the usual anodic oxidation process,<sup>1</sup> while that in Fig. 4b was passivated by a different method. The separations of peaks due to spin-splitting are predicted by our theory to be about half of that we observed, and thus we expect that these multiple peaks are due to different surface densities. The splittings vary somewhat from detector to detector as well. Thus, the effect of spin splitting is just to broaden each peak. The

transform corresponding to the detector with lower total density, Sample 1, in Fig. 4a, has clear, strong peaks, while that for the one with higher density, Sample 2, in Fig. 4b, has peaks that rise less above the background. One reason is that the penetration of the energy gap by the wave functions is much greater for the heavily accumulated case, especially for the lowest subband. There is a mixture of subband states bound to the conduction band and continuum states that traverse the entire detector. Thus, the layer of electron accumulation is not well described by a simple 2D electron gas at high densities and small energy gaps. The Fourier transform for a heavily accumulated, narrow gap detector can have a broad background of contributions from the range of 3D states corresponding to the graded 3D electron density in the accumulation layer. The 2D states, which are bound to the conduction band, appear as well in the Fourier transform and rise above the background because they contribute at only one frequency for each subband. The complexity of the background signature in Fig. 4b may indicate that there is nonuniformity in the surface density as well because of the two surfaces and multiple regions within a surface. Even though the relative amplitude of the oscillations of Sample 2 was almost ten times smaller than that of Sample 1, the Fourier transform successfully resolved the signature of the detector.

We have computed the subband electron densities from the measured cyclotron effective masses and Fermi energies for these two detectors. The results from the two surfaces were averaged because we could not resolve the splitting at higher temperatures. For sample 1, the measured data are:  $m_0^* = 0.022 \pm 0.001$ ,  $E_F^0 = 79 \pm 4 \text{ meV}$ ,  $m_1^* = 0.014 \pm 0.001$ , and  $E_F^1 = 42 \pm 3 \text{ meV}$ . The corresponding theoretical values were obtained by finding the total density for which the  $m^*E_F$  values for the subbands best agreed with experiment:  $m_0^* = 0.023 \pm 0.001$ ,  $E_F^0 = 75 \pm 2 \text{ meV}$ ,  $m_1^* = 0.015 \pm 0.001$ , and  $E_F^1 = 38 \pm \text{meV}$ . The predicted total density is found to be  $7.9 \times 10^{11} \text{ cm}^{-2}$ , which is considerably less than the value of  $1.2 \times 10^{12} \text{ cm}^{-2}$  that is obtained from the parabolic approximation for the density. The agreement between theory and experiment is within the assigned uncertainty with the theoretical values for the effective masses slightly larger than measured. Thus, we expect that the energy gap may be smaller than the one we are using. This may occur because of band-gap narrowing, which occurs at high densities because of the many-body interactions between electrons. We estimate the band-gap reduction to be at most 10% at this density.<sup>8</sup> For Sample 2, we report the results for the peaks labeled with '' because the unprimed peaks were above our calculated densities, and some of the single-primed peaks were not as well separated from the background. We do not report the  $n = 2$  and  $n = 3$  peaks because they are also not very well separated. The measured data for the peaks labeled with '' are:  $m_0^* = 0.020$ ,  $E_F^0 = 312 \text{ meV}$ ,  $m_1^* = 0.010$ , and  $E_F^1 = 277 \text{ meV}$ . The uncertainties for these numbers are about 20%.

We obtain from the total density that gives best agreement between our theory and the measured subband  $m^*E_f$  values:  $m_0^* = 0.039 \pm 0.002$ ,  $E_f^0 = 160 \pm 3$  meV,  $m_1^* = 0.029 \pm 0.001$ , and  $E_f^1 = 80 \pm 2$  meV. The predicted total density is then found to be  $5.4 \times 10^{12}$  cm<sup>-2</sup>, which is also considerably less than the value of  $4.3 \times 10^{12}$  cm<sup>-2</sup> from the parabolic approximation. However, Sample 2, which was made by a different process from the traditional anodic oxidation method<sup>2</sup> that was used for Sample 1, disagrees with the predictions, because the measured masses are so much smaller and the Fermi energies so much larger than the predicted values. Band-gap narrowing would be larger for these samples, probably in excess of 10% of the energy gap, and the gap could become very small. However, much more work is needed to understand the cause of this disagreement, which may involve strain as well. The relatively large Fermi energies and small masses could imply that the built-in potential is more like a square well in these detectors with heavy accumulation.

### CONCLUSIONS

The dispersion relations for all the 2D subbands in the accumulation layers of HgCdTe detectors have been computed by solving the  $8 \times 8$  matrix Hamiltonian for a large range of electron densities ( $0.1$  to  $5 \times 10^{12}$  cm<sup>-2</sup>). The subband densities, Fermi energies, and cyclotron effective masses have been computed as a function of the total electron density. The results show strong nonparabolicity and a breakdown in the simple 2D model of the electron gas at high densities and small energy gaps. The near linear dependence of the subband densities on total density, which has been observed experimentally, has been confirmed theoretically. The agreement of our calculations with experiment is good at the lower densities and may possibly be improved by inclusion of the effect of band-gap narrowing. At the higher densities differences are large, and further work including the effects of band-gap narrowing and strain is needed to understand the measurements. Models such as these provide a basis to characterize the electron states in the accumulation layers of these detectors, which have a large effect on device performance.

The direct application of these results to the characterization of detectors is not simple, however. The properties of the accumulation layers constitute only one of the controlling factors in detector performance. Others include the bulk electrical and optical properties, the type and quality of the contacts and packaging, and the effects from the method of delineating the detectors, such as ion milling. The contribution of this work has been to present a direct, two-terminal measurement that can be used to determine the electron density of the accumulation layers of a detector. Failure to have sufficient accumulation can lead to increased surface recombination and degradation of detectivity. Excessive accumulation, on the other hand, can lead to a large shunt conductance, which also can degrade detectivity. Thus, one can use this method to study the dependence of detectivity on the method of passivation and the resulting level of accumulation. The optimum process can be determined, and subsequently this method can be used to monitor the accumulation layers during manufacturing and to monitor their stability as a function of time.

### REFERENCES

1. Y. Nemirovsky and G. Bahir, *J. Vac. Sci. Technol.* A7, 450 (1989).
2. Y. Nemirovsky and I. Kidron, *Solid-State Electron.* 22, 831 (1979).
3. R.J. Nicholas, F. Nasir and J. Singleton, *J. Cryst. Growth* 86, 656 (1988).
4. W. Zawadzki, *J. Phys. C* 16, 229 (1983).
5. Y. Takada, *J. Phys. Soc. Jpn.* 50, 1998 (1981).
6. G. Nachtwei, P. Schulze, G. Gobsch, G. Paasch, W. Kraak, H. Kruger, and R. Herrmann, *Phys. Status Solidi b* 148, 349 (1988).
7. I. Nachev, *Semicond. Sci. Technol.* 3, 29 (1988).
8. G. Trankle, E. Lach, A. Forchel, C. Ell, H. Haug, G. Weimann, G. Griffiths, H. Kroemer, and S. Subbanna, *J. de Phys. Coll.* C5, 48, 385 (1987).
9. E. Kane, *J. Phys. Chem. Solids* 1, 249 (1957).
10. J. Sune, P. Olivo and B. Ricco, *J. Appl. Phys.* 70, 337 (1991).
11. S. Yamada, H. Asai and Y. Kawamura, *J. Appl. Phys.* 72, 569 (1992).
12. D.G. Seiler, G.B. Ward, R.J. Justice, R. J. Koestner, M. W. Goodwin, M. A. Kinch and J. R. Meyer, *J. Appl. Phys.* 66, 303 (1989).
13. D.G. Seiler, J.R. Lowney, C.L. Littler and M. R. Loloee, *J. Vac. Sci. Technol.* A8, 1237 (1990).

# The Role of the Insulator in Determining 1/f Noise in $\text{Hg}_{1-x}\text{Cd}_x\text{Te}$ Integrating MIS Devices

JOSÉ L. MELÉNDEZ\* and JEFF BECK

Texas Instruments, Inc., Central Research Laboratories, Dallas, TX 75265

The low frequency 1/f noise charge found in  $\text{Hg}_{1-x}\text{Cd}_x\text{Te}$  integrating metal-insulator-semiconductor (MIS) devices operating at 40K and low bias above threshold is found to be independent of integration time. The signal theory of random processes is utilized to demonstrate that 1/f noise charge resulting from carrier number fluctuations due to insulator traps should not depend on integration time, while 1/f noise charge resulting from 1/f noise in any current filling the MIS well should be proportional to integration time. This distinction allows for the determination of effective insulator trap densities from low temperature 1/f noise data on simple MIS structures. The technique is applied to a number of n-channel and p-channel devices and the effective trap densities in ZnS are determined.

**Key words:** HgCdTe, 1/f noise, integrating MIS devices, ZnS

## INTRODUCTION

The insulator has been shown to be a source of McWhorter low frequency 1/f noise in many types of devices including silicon metal-oxide-semiconductor field effect transistors (MOSFETs),  $\text{Hg}_{1-x}\text{Cd}_x\text{Te}$  metal-insulator-semiconductor FETs (MISFETs), and p-n junction diodes.<sup>1-4</sup> In this paper, we investigate the relationship between insulator trapping and the 1/f noise measured on integrating MIS devices.

Under the typical operating conditions of an integrating  $\text{Hg}_{1-x}\text{Cd}_x\text{Te}$  MIS device (77K), the 1/f noise behavior can be fairly complex.<sup>5</sup> However, low temperature (40K) and low bias conditions exist at which it is believed that only 1/f noise due to carrier interactions between the  $\text{Hg}_{1-x}\text{Cd}_x\text{Te}$  and insulator traps are important. In particular, insulator charge fluctuations due to trapping and detrapping of inversion layer carriers give rise to threshold voltage fluctuations. These threshold voltage fluctuations cause fluctuations in the well capacity of an MIS device periodically pulsed into deep depletion, so that the initial deep depletion surface potential fluctuates in a 1/f manner. The 1/f noise in the initial deep depletion surface potential gives rise to the 1/f noise observed in the output of the device.

Simple physical ideas and the signal theory of random processes will be utilized to derive an expression for the 1/f noise on an integrating MIS device resulting from carrier number fluctuations due to insulator traps. A similar approach can be utilized for 1/f noise processes which are present in any current filling the MIS well. The resulting expressions differ significantly with regard to the predicted integration time dependence of the measured 1/f noise. 1/f noise charge resulting directly from insulator trapping should be independent of integration time while 1/f noise charge associated with the current filling the MIS well would be expected to increase linearly with integration time.<sup>6</sup> This important distinction indicates that experimental studies of the integration time dependence of 1/f noise will allow one to isolate the role of the insulator.

Experimental verification of the existence of both

\*Present address: Department of Electrical Engineering, Stanford University, Stanford, CA 94305.  
(Received October 12, 1992; revised January 12, 1993)



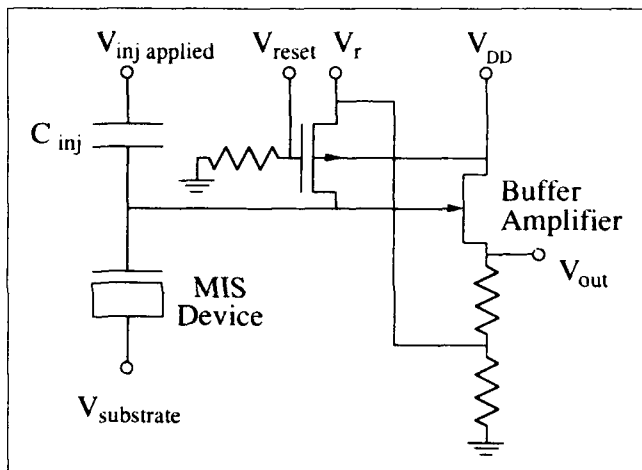


Fig. 1. Floating gate mode readout circuit configuration used for  $1/f$  noise measurements on MIS devices. The buffer amplifier output is the input to the correlated double sampling circuit.

types of  $1/f$  noise dependencies on integration time will be presented. The measurement technique utilized to isolate  $1/f$  noise resulting from insulator trapping/detrapping will be described. Furthermore, since integration time independent  $1/f$  noise can be related to the number of insulator traps by the expressions which we derive, our work has resulted in a technique by which one can extract effective insulator trap densities by performing  $1/f$  noise measurements on simple MIS structures. This technique has been performed on both  $\text{Hg}_{1-x}\text{Cd}_x\text{Te}$  and silicon MIS devices and the results are consistent with trap density extractions performed on MISFET devices.<sup>3,7</sup>

### EXPERIMENTAL

The  $\text{Hg}_{1-x}\text{Cd}_x\text{Te}$  MIS devices were all fabricated on thick substrates with band gaps of about 120 meV at 77K. Both n-type (p-channel) and p-type (n-channel) samples were utilized in the study. All the material was grown by solid-state recrystallization (SSR). On top of the  $\text{Hg}_{1-x}\text{Cd}_x\text{Te}$  substrate is an insulating layer of ZnS. The insulator thicknesses ranged from 0.1 to 0.2  $\mu\text{m}$ . The gates were rectangular with areas on the order of  $10^{-3} \text{ cm}^2$ .

The MIS devices were operated in floating gate mode (FGM).<sup>8</sup> In FGM, the total charge on the node just above the MIS device in Fig. 1, remains fixed while the device integrates charge. The devices are biased into strong inversion by applying the appropriate potential to the substrate,  $V_{\text{substrate}}$ . For p-channel devices, a positive pulse,  $V_{\text{inj}}$ , is then applied to the gate by applying a pulse  $V_{\text{inj applied}}$  through a capacitor (see Fig. 1). The pulse injects the inversion layer holes into the substrate, driving the MIS device into deep depletion when off. The return to equilibrium is limited by the generation rate of the minority carriers, which is largely of a thermal nature in the dark (and partially due to tunneling), but is strongly enhanced in the presence of photon flux. All of the  $1/f$  noise measurements performed on the  $\text{Hg}_{1-x}\text{Cd}_x\text{Te}$  MIS devices were done with the devices under negligible

photon flux. When the well is completely filled with charge, a reset pulse,  $V_{\text{reset}}$ , is applied to ensure that the next cycle begins at the same node potential,  $V_r$ .

A correlated double sampling (CDS) circuit is used to measure the integrating device output voltage for each cycle.<sup>9</sup> After reset and just before inject, the CDS circuit clamps the gate voltage through the unity gain buffer amplifier. At a sample time, chosen to be somewhere within the transition from deep depletion (empty well) to inversion (full well), the voltage on the MIS gate is again sampled. The time that the device is allowed to relax after the inject pulse and before the sample is taken, is the integration time,  $T_{\text{int}}$ . The difference in the two voltages at clamp and sample is the output of the CDS circuit. This voltage is held at the output for a complete cycle.

For  $1/f$  noise measurements it is important to minimize the cycle time in order to reduce aliasing of broadband noise. At 40K, the long storage times limit the minimum cycle time which may be used. This limitation was avoided by applying a "tunnel-to-fill" pulse a few microseconds after each sample is taken. The pulse increases the bandbending producing a large tunnel current in the device which quickly fills the well.

Two measurements are required to determine the  $1/f$  noise originating from the MIS device. The first measures the total noise due to the test system and the device when biased in strong inversion. The second measures the system noise and is performed with the device in accumulation. The system noise does not exhibit a  $1/f$  component and is typically at least an order of magnitude lower at 1 Hz. The system power spectral density in the CDS output is subtracted out and a best line fit is performed in the low frequency region down to 1 Hz. The slope,  $\vartheta$ , and value of the  $1/f$  noise voltage at 1 Hz,  $V_{1f}$ , are recorded and the  $1/f$  noise voltage power spectral density is then given by,

$$S_v = \frac{(V_{1f})^2}{f^\vartheta} \quad (1)$$

where  $f$  is the frequency.  $\vartheta$  was found to be approximately equal to one.

To study  $1/f$  noise in MIS devices, we cannot directly use the most popular  $1/f$  noise quantity,  $V_{1f}$ , because it does not account for the capacitive nature of the integrating structure. In order to quantify the  $1/f$  noise without obscuring the fundamental physics, we define the  $1/f$  noise charge quantity at 1 Hz,  $Q_{1f}$ , which effectively removes capacitance from the problem. That is, we apply the voltage-to-charge transfer function, or effective capacitance,  $C_{\text{eff}}$ , to determine the amount of  $1/f$  noise charge fluctuation represented by the  $V_{1f}$  measured on the gate.  $Q_{1f}$  is given by,

$$Q_{1f} = V_{1f} C_{\text{eff}} \quad (2)$$

An expression for  $C_{\text{eff}}$  is readily obtained by analyzing the small signal circuit model shown in Fig. 2. In Fig. 2,  $C_i$  is the insulator capacitance,  $C_D$  is the depletion capacitance at  $T_{\text{int}}$ ,  $C_s$  is the circuit stray capacitance (which includes the inject and tunnel-to-fill capaci-

tors),  $V_{n1f}$  is the voltage fluctuation at the node which gives rise to the voltage fluctuation,  $V_{1f}$ , measured at the gate, and  $Q_{1f}$  represents the charge fluctuation which gives rise to the measured  $V_{1f}$ . The effective capacitance is given by,

$$C_{eff} = C_s + C_D \left( 1 + \frac{C_s}{C_i} \right) \quad (3)$$

All of the capacitances in Eq. 3 can readily be determined so that  $Q_{1f}$  is evaluated by the use of Eq. 2.

### MIS 1/f NOISE MODEL

The result of the number fluctuation model is an expression for the noise power of the number of fluctuating inversion layer carriers due to insulator traps. The derivation has been reviewed in detail by many authors and so only the key result is presented here.<sup>2,4,7,10,11</sup> The number power spectral density,  $S_{N_e}$ , resulting from inversion layer carriers tunneling into slow insulator traps and the reverse process of trapped carriers tunneling out of insulator traps to add to the inversion layer charge, is given by,

$$S_{N_e} = \frac{AkTN_i(E_f)}{2Kf} \quad (4)$$

where  $A$  is the device area,  $k$  is Boltzmann's constant,  $T$  is the device temperature,  $N_i(E_f)$  is the insulator trap density at the energy corresponding to the inversion state Fermi energy, and  $K$  is the tunneling transmission coefficient. The transmission coefficient is given by,

$$K = \sqrt{\frac{2m^* \Phi_B}{\hbar^2} \left( 1 - \frac{\Phi_B}{E_g} \right)} \quad (5)$$

where  $m^*$  is the effective mass of the tunneling charge carrier,  $\Phi_B$  is the insulator-semiconductor band offset (valence band for tunneling holes and conduction band for electrons),  $E_g$  is the insulator band gap, and  $\hbar$  is Planck's constant.<sup>4,12-14</sup> To allow for an actual distribution of traps in the insulator energy and depth window accessible in a given 1/f noise measurement, we rewrite Eq. 4 as,

$$S_{N_e} = \frac{AkT}{2K} \left( \frac{N_{teff}}{f^n} \right) \quad (6)$$

where  $N_{teff}$  is the insulator effective trap density for the given Fermi level position of the measurement.<sup>11</sup>

The number fluctuations are directly related to trapped charge fluctuations. The charge spectral density fluctuation of trapped charge,  $S_{Q_e}$ , is given by,

$$S_{Q_e} = q^2 S_{N_e} \quad (7)$$

A change in the number of trapped carriers in the insulator gives rise to a change in the flatband voltage of the MIS device. The flatband voltage fluctuation results in a fluctuating threshold voltage. The end result is a 1/f-like fluctuation of the initial deep

depletion voltage on the gate. It can be shown that a fluctuation in the insulator trapped charge will induce a fluctuation in the initial voltage on the gate in deep depletion related by the effective capacitance. This is analogous to the interpretation of  $C_{eff}$  when it was defined in the previous section.

In general, the total charge spectral density of an MIS device,  $S_Q$ , may be expressed as,

$$S_Q = S_{Q_e} + S_{Q_{int}} \quad (8)$$

where  $S_{Q_{int}}$  represents all other 1/f noise sources and is dependent upon the integration time of the measurement.  $S_{Q_e}$  does not depend on integration time and exists at  $T_{int} = 0$ . It is thus assumed that  $S_{Q_e}$  is the only integration time independent 1/f noise quantity and that it is due only to insulator trapping. Taking the square root of Eq. 8, we arrive at the expression for  $Q_{1f}$  valid at 1 Hz,

$$Q_{1f} = \sqrt{S_{Q_e} + S_{Q_{int}}} \quad (9)$$

For the case where integration time dependent 1/f noise is negligible, we use Eqs. 6, 7, and 9 to write,

$$Q_{1f0} = \sqrt{\frac{q^2 AkTN_{teff}}{2K(1Hz)}} \quad (10)$$

where  $Q_{1f0}$  is the integration time independent 1/f noise charge at 1 Hz. Equation 10 relates the measured 1/f noise to the effective insulator trap density provided the measured 1/f noise charge is independent of integration time.

### TRAP DENSITY EXTRACTION

All of the parameters in Eq. 10 are known or can be measured, except the effective insulator trap density. We can thus utilize the expression to obtain information concerning insulator quality with regards to trap density magnitudes. We first make some assumptions:

1. Though the operating MIS device continually cycles through the states of depletion, deep depletion, and inversion, the steady state for 1/f noise modeling is assumed to be the inversion state. The MIS device is inverted for most of the cycle time.
2. The traps giving rise to the observed 1/f noise are located within a few  $kT$  of the Fermi level in

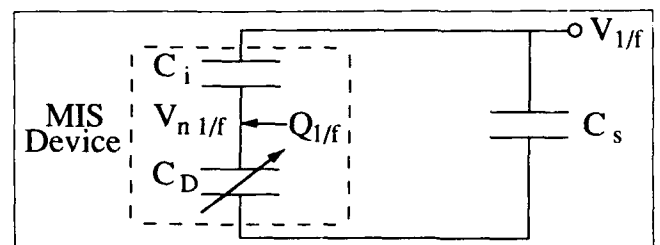


Fig. 2. Small signal circuit model which relates the measured 1/f noise voltage,  $V_{1f}$ , to the 1/f charge fluctuations,  $Q_{1f}$ , in the MIS device.

inversion. The state of occupation of insulator traps more than a few  $kT$  from the Fermi level in inversion, does not change significantly over many cycles.

3. There is an actual distribution of insulator traps with energy as well as position from the interface. Each bias condition accesses a different subset of the total insulator trap population.

Solving Eq. 10 for the effective insulator trap density,

$$N_{\text{eff}} = \left( \frac{Q_{1/f}}{q} \right)^2 \frac{2K}{AkT} (1\text{Hz}) \quad (11)$$

We now have the relationship necessary to extract insulator effective trap densities. However, before we may do so, we must first explain how to measure  $Q_{1/f}$ . In the section entitled Experimental, we described how to obtain  $Q_{1/f}$  at a given device bias and integration time. Therefore, to obtain  $Q_{1/f}$ , we need only to operate the device such that the integration time dependent  $1/f$  noise is negligible.

Integrating  $\text{Hg}_{0.8}\text{Cd}_{0.2}\text{Te}$  MIS devices are normally operated at 77K. For substrate biases on the order of

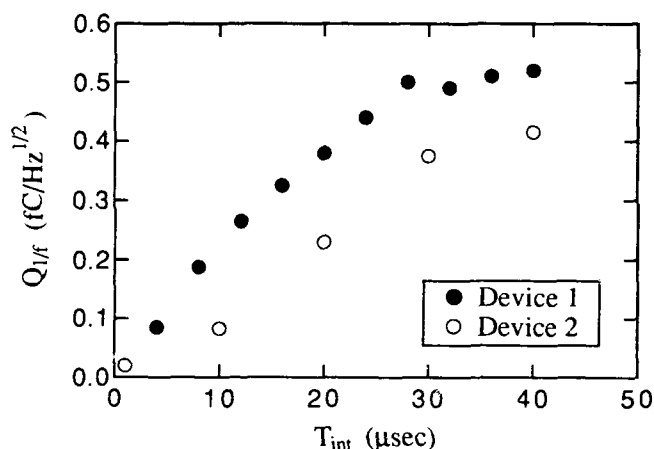


Fig. 3.  $1/f$  noise charge integration time dependence for two typical p-channel  $\text{ZnS}/\text{Hg}_{0.8}\text{Cd}_{0.2}\text{Te}$  MIS devices operated at 77K.

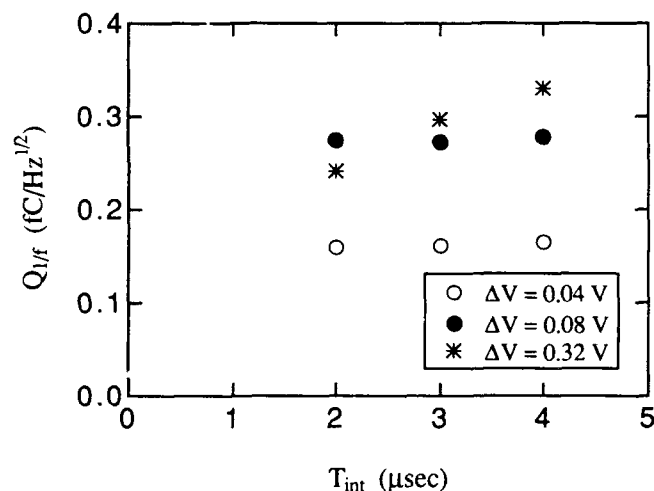


Fig. 4.  $1/f$  noise charge as a function of integration time for three different biases at 40K. At  $\Delta V = 0.32$  V, large field dependent dark currents begin to quench the integration time independent  $1/f$  noise charge.

a few tenths of a volt above threshold, the behavior of  $Q_{1/f}$  with integration time resembles that shown in Fig. 3 for two typical p-channel devices. This behavior is not yet fully understood. However, the integration time dependence of  $Q_{1/f}$  at 77K is believed to be due partially to a field dependent dark current modulated by insulator trapping and partially to any current, filling the well, which has  $1/f$  noise in it.<sup>4,5</sup> A current filling the well which has  $1/f$  noise in it, will give rise to an integration time dependence of  $Q_{1/f}$ , which is linear. A linear region is typically observed in the first portion of the integration time dependence (see Fig. 3). Using the signal theory of random processes, it can be shown that,

$$S_{Q_{1/f}} = T_{\text{int}}^{-2} S_i \quad (12)$$

where  $S_i$  is the input  $1/f$  noise current power spectral density. Equation 12 is valid for frequencies far below the cycle frequency.<sup>5</sup>

An important feature of the  $Q_{1/f}$  behavior depicted in Fig. 3 is the apparent absence of  $1/f$  noise charge at zero integration time when the linear region is extrapolated down to  $T_{\text{int}} = 0$ . Such "zero-time"  $1/f$  noise might be expected to result from insulator trapping and detrapping. It is believed that its absence is due to strong field dependent dark currents which respond to quench the electric field fluctuations resulting from insulator trapping and detrapping. The quenching of integration time independent  $1/f$  noise occurs within the first microsecond and cannot be detected by measurement. The smallest integration time which may be used in a measurement is about 1  $\mu\text{sec}$ .

At low temperatures, it is possible to operate the MIS device with a considerable reduction in the  $1/f$  modulated tunnel current, so that  $Q_{1/f}$  may be measured at integration times larger than a microsecond. Integration time dependent  $1/f$  noise can be made insignificant at 40K for biases below breakdown by the diminished dark currents at the lower temperature and the large storage times available at low biases where tunnel currents are reduced. The quenching effect observed at 77K can be reproduced at 40K by biasing the device past breakdown. Such biasing results in large negatively correlated tunnel currents that quench the  $1/f$  noise resulting from insulator trap interactions (see Fig. 4). In Fig. 4, the largest bias past threshold shown,  $\Delta V = 0.32$  V, is above breakdown, and quenching of the integration time independent component is observed. For the smaller biases, the  $1/f$  noise is independent of integration time since the tunnel currents at these biases are negligible. Continued overbiasing results in complete quenching of the integration time independent  $1/f$  noise component.

### ZnS EFFECTIVE TRAP DENSITIES

Using the methods presented and the relationships developed in the previous sections, effective trap density extractions were performed on a number of p-channel and n-channel  $\text{ZnS}/\text{Hg}_{1-x}\text{Cd}_x\text{Te}$  MIS devices, providing ZnS trap density information around both

the  $\text{Hg}_{1-x}\text{Cd}_x\text{Te}$  valence and conduction band energy levels, respectively.

To calculate  $N_{\text{eff}}$  from measured  $Q_{1/f_0}$  in p-channel  $\text{ZnS}/\text{Hg}_{1-x}\text{Cd}_x\text{Te}$  MIS devices, we must first use Eq. 5 to calculate the transmission coefficient. The effective mass of a hole in ZnS,  $m_h^*$ , is about  $0.58m_0$ , where  $m_0$  is the free electron mass, the valence band offset,  $\Phi_{\text{Bh}}$ , is approximately 2.73 eV and the ZnS band gap is 3.6 eV.<sup>4,15</sup> Substituting into Eq. 5, we find that  $K_h = 3.2 \times 10^7 \text{ cm}^{-1}$ .

Trap density extractions were performed on several p-channel  $\text{ZnS}/\text{Hg}_{1-x}\text{Cd}_x\text{Te}$  devices. The extracted trap densities for three such devices are shown in Fig. 5 as a function of substrate bias above threshold,  $\Delta V$ . Devices #6 and #7 were on the same slice of material. Devices #7 and #8 both had insulator thicknesses of 0.11  $\mu\text{m}$ . Device #6 had an insulator thickness of 0.17  $\mu\text{m}$ . All devices had gate areas of  $1.3 \times 10^{-3} \text{ cm}^2$ . Note the spread of about an order of magnitude in the effective ZnS trap densities shown in Fig. 5 over a given device bias range. The data point at the highest bias shown for a given device, represents the maximum bias at which integration time dependent 1/f noise is insignificant. At higher biases, quenching of integration time independent 1/f noise is observed. The maximum effective trap densities measured for a given device ranged from  $1.8 \times 10^{19} \text{ cm}^{-3} \text{ eV}^{-1}$  for Device #8 to  $1.1 \times 10^{20} \text{ cm}^{-3} \text{ eV}^{-1}$  for Device #7. The highest bias above threshold at which  $N_{\text{eff}}$  could be extracted was 0.16 V for Device #6.

ZnS trap density extraction measurements were also performed on three devices built on a different lot of n-type material. All of the devices had 10  $\mu\text{m}$  cutoffs, gate areas of  $9.7 \times 10^{-4} \text{ cm}^2$ , and ZnS thicknesses of 0.13  $\mu\text{m}$ . The extracted trap densities were found to be significantly lower than those for the three devices previously mentioned, with a narrow range of values from  $5.9 \times 10^{17} \text{ cm}^{-3} \text{ eV}^{-1}$  to  $8.8 \times 10^{17} \text{ cm}^{-3} \text{ eV}^{-1}$ . The difference in trap densities between the lots may be due to the different reactors used in the ZnS deposition.

The typical integration time dependence of 1/f noise for n-channel  $\text{ZnS}/\text{Hg}_{0.8}\text{Cd}_{0.2}\text{Te}$  MIS devices is similar to that shown in Fig. 3 for two p-channel devices. However, the magnitudes of  $Q_{1/f}$  in the n-channel devices are usually at least a factor of 4 less than the  $Q_{1/f}$  in the p-channel devices. Since  $Q_{1/f}$  generally decreases with temperature in p-channel devices, similar behavior was expected for n-channel devices. Experimentally, we have determined that  $Q_{1/f}$  does indeed decrease in n-channel devices with decreasing temperature. In fact,  $Q_{1/f}$  decreases so much that all measurements performed on n-channel  $\text{ZnS}/\text{Hg}_{1-x}\text{Cd}_x\text{Te}$  MIS devices at 40K, have failed to reveal any measurable 1/f noise. The measurements indicate that the effective insulator trap densities are less than what may be detected using the technique described in this paper.

Quantitatively, the measurements on the n-channel devices could have measured  $Q_{1/f_0}$  for values greater than 0.036 fC/Hz<sup>1/2</sup>. This value for  $Q_{1/f_0}$  im-

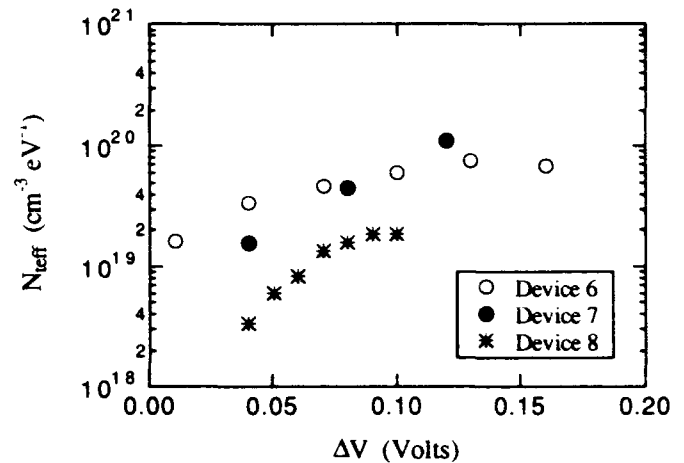


Fig. 5. ZnS effective trap densities measured on three p-channel  $\text{ZnS}/\text{Hg}_{1-x}\text{Cd}_x\text{Te}$  MIS devices as a function of bias above threshold.

plies an upper limit on the  $N_{\text{eff}}$  for the devices. For the n-channel  $\text{ZnS}/\text{Hg}_{1-x}\text{Cd}_x\text{Te}$  system,  $K_e = 2.0 \times 10^7 \text{ cm}^{-1}$  using a ZnS electron effective mass,  $m_e^*$ , of  $0.27m_0$ , and conduction band offset,  $\Phi_{\text{Be}}$ , of  $0.75 \text{ eV}$ .<sup>4</sup> We then find from Eq. 11, that  $N_{\text{eff}}$  for the n-channel devices must be less than  $6.2 \times 10^{17} \text{ cm}^{-3} \text{ eV}^{-1}$ . This result is consistent with studies performed on similar bandgap n-channel  $\text{ZnS}/\text{Hg}_{1-x}\text{Cd}_x\text{Te}$  MISFETs, where an  $N_{\text{eff}}$  greater than  $6.2 \times 10^{17} \text{ cm}^{-3} \text{ eV}^{-1}$  was found only for values of  $\Delta V$  greater than 0.6 V.<sup>3</sup> In our measurements, the largest  $\Delta V$  used was 0.26 V.

## SUMMARY

A model was presented for integration time independent 1/f noise charge in integrating MIS devices based upon the popular number fluctuation model first proposed by McWhorter.<sup>1</sup> We further utilized the relationship developed between 1/f noise and insulator traps, to extract ZnS trap density information from 1/f noise measurements on integrating  $\text{ZnS}/\text{Hg}_{1-x}\text{Cd}_x\text{Te}$  MIS devices. Trap density extractions using p-channel  $\text{ZnS}/\text{Hg}_{1-x}\text{Cd}_x\text{Te}$  MISFETs are not currently available for comparison with our results. The results of the n-channel measurements were consistent with trap density extractions performed using the n-channel  $\text{ZnS}/\text{Hg}_{1-x}\text{Cd}_x\text{Te}$  MISFET structure.<sup>3</sup>

## ACKNOWLEDGMENT

José L. Meléndez acknowledges partial support from the National Science Foundation. The authors wish to thank Rich Schiebel, Mike Goodwin, Mike Kinch, and Dwight Bartholomew for helpful discussions.

## REFERENCES

1. A.L. McWhorter, *Semiconductor Surface Physics* (University of Pennsylvania Press, Philadelphia 1957) 207.
2. Raj Jayaraman and Charles G. Sodini, *IEEE Trans. Electron Devices* 36, 1773 (1989).
3. R. A. Schiebel, *Solid-State Electron.* 32, 1003 (1989).
4. W. W. Anderson and H. J. Hoffman, *J. Vac. Sci. Technol. A* 1, 1730 (1983).
5. José L. Meléndez, S. B. thesis, Massachusetts Institute of

- Technology, 1990.
6. G. Reimbold, *IEEE Trans. Electron Devices* ED-32, 871 (1985).
  7. Raj Jayaraman, Ph. D. thesis, Massachusetts Institute of Technology, 1988.
  8. M. A. Kinch, *Mat. Res. Soc. Symp. Proc.* 90, 15 (1987).
  9. R. A. Schiebel, J. Dodge and R. Gooch, *Electron. Lett.* 26, 702 (1990).
  10. S. T. Hsu, *Solid-State Electron.* 13, 843 (1970).
  11. José L. Meléndez, S. M. thesis, Massachusetts Institute of Technology, 1991.
  12. R. Stratton, G. Lewicki and C. A. Mead, *J. Phys. Chem. Solids* 27, 1599 (1966).
  13. G. Lewicki and C. A. Mead, *Phys. Rev. Lett.* 16, 939 (1966).
  14. W. Franz, in *Handbuch der Physik* ed. by S. Flugge (Verlag Julius Springer, Berlin 1956) 17, 155.
  15. M. J. Yang, private communication (1990).

# Process Modeling of Point Defect Effects in $\text{Hg}_{1-x}\text{Cd}_x\text{Te}$

JOSÉ L. MELÉNDEZ and C.R. HELMS

Department of Electrical Engineering, Stanford University, Stanford, CA 94305

A model is presented which describes the motion of and interactions among some of the native point defects and foreign impurities in  $\text{Hg}_{1-x}\text{Cd}_x\text{Te}$ . Semi-quantitative simulations of typical process problems are performed for cases where only Hg interstitials, Hg vacancies, and cation impurities are important. Results for the formation of n-on-p junctions by the Hg anneal of high vacancy concentration material, indicate that junction depths may be a significant function of the n-type dopant concentration. For the case where low vacancy, n-type material is annealed in a Hg-poor ambient, simulation results confirm the difficulty in forming a high quality, well-defined p-on-n junction. This difficulty arises because of the generation of Hg vacancy/interstitial pairs throughout the bulk during most of the process. It is demonstrated that impurity gettering can be described by our modeling approach. All simulation results attempted to date are consistent with the available experimental data.

**Key words:** Hg annealing,  $\text{HgCdTe}$ , native point defects, process modeling

## INTRODUCTION

In many circumstances, the process physics of  $\text{Hg}_{1-x}\text{Cd}_x\text{Te}$  is dominated by point defects, such as the Hg interstitial and/or Hg vacancy. They may either determine carrier concentrations directly by behaving as active dopants or indirectly through interactions or reactions with the impurities. In either case, it is clear that a thorough understanding of point defects is necessary to optimize fabrication processes and device performance. The ability to simulate and predict defect concentrations and doping profiles through accurate modeling and computer simulation of the process physics will be an important tool for designing advanced process flows and implementing intelligent manufacturing processes.

In this paper, a model will be presented, based upon first order reaction kinetics, which describes the motion of and interactions among some of the native point defects and foreign impurities in  $\text{Hg}_{1-x}\text{Cd}_x\text{Te}$ . We begin by writing a set of chemical equations

representing some of the important quasi-chemical reactions between the various species. From these relationships, reaction rates may be defined indicating the relative strengths of the interactions. A set of continuity equations are then established with generation and recombination terms representing the important interactions.

In some cases, these equations may be simplified so that steady-state analytic approximations can be obtained, but in general numerical techniques are required to obtain the full spatial and temporal defect distributions. In this work, simulations have been run using an iterative Crank-Nicolson approach implemented in the algorithm which we have developed. Values for the various parameters may be obtained from first principle calculations or through quantitative fits to experimental data. At present, the available experimental data are insufficient to permit the unique determination of the parameter values. However, our simulation results have proven useful in understanding the underlying physics of a number of important process steps, in identifying qualitative behavior, and in defining the types of measurements

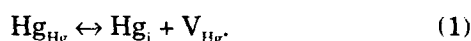
(Received October 12, 1992; revised January 13, 1993)

which are necessary to further define the model. Simulation results for some of the different processing problems will be presented and comparison to experimental observations will be discussed when appropriate.

### Hg<sub>1-x</sub>Cd<sub>x</sub>Te PROCESS MODELS

The modeling approach we have utilized to describe the interactions among point defects and impurities is based upon the solution of a set of coupled continuity equations representing the dominant quasi-chemical kinetics. These equations are established in a straightforward manner once the significant reactions between the various species have been identified. In particular, we begin with the usual Fickian diffusion equations, which are the simplest form of the continuity equations valid only when all reactions between species can be neglected and when there is no recombination or generation of the species in the bulk. Since it is believed that bulk Hg vacancies can be annihilated by recombining with Hg interstitials, it should be clear that the Fickian form is not sufficient. The end result is a set of continuity equations, at least one for each defect or impurity of interest, where each continuity equation describes diffusion with the typical Fickian term, and additional positive reaction rate terms are added if they depict generation or subtracted if they represent recombination. In most cases, two equations are required for impurities, one for the substitutional form, and one for the interstitial form. No distinction is made in our analysis in regard to the various defect ionization states.

The simplest example of the coupled diffusion modeling approach is for the case where only Hg interstitials and Hg vacancies are important. For this example, only the Frenkel defect equation is considered,



In the forward direction, a Hg atom from a lattice site moves into an interstitial position, leaving a vacancy behind, which is equivalent to the thermal generation of both a Hg interstitial and a Hg vacancy. In the reverse direction, a Hg atom moves from an interstitial position into a vacant lattice site. The net effect is recombination, or annihilation, of both a Hg interstitial and a Hg vacancy. The forward rate constant, in this case the generation rate, is labeled  $g$ . The recombination process requires the interaction of both a Hg interstitial and a Hg vacancy and so to first order, the recombination rate is proportional to the product of the concentrations of these defects. The constant of proportionality is the recombination rate constant,  $k_{iv}$ . The resulting continuity equations are,

$$\frac{\partial i}{\partial t} = D_i \frac{\partial^2 i}{\partial x^2} - k_{iv} iv + g \quad (2)$$

$$\frac{\partial v}{\partial t} = D_v \frac{\partial^2 v}{\partial x^2} - k_{iv} iv + g \quad (3)$$

where  $i$  is the concentration of Hg interstitials,  $v$  is the

Hg vacancy concentration, and the  $D$ s are the respective diffusion coefficients, which are assumed independent of the spatial coordinate. Similar relationships have been developed for silicon, where the process physics is largely dominated by Si interstitials and Si vacancies.<sup>1</sup>

Another straightforward example of our modeling approach involves the interaction of cation impurities with the Hg vacancies and Hg interstitials. Two continuity equations are required for a particular cation impurity. One equation models the motion and interactions of the impurity while on substitutional cation sites, while the other equation describes the behavior of the impurity in interstitial sites. The pathway between these two states is given by,



where  $d_i$  is an impurity on a substitutional cation site and  $d_s$  is the interstitial impurity. Equation 4 is analogous to the Frenkel mechanism. The difference here is that the atoms moving between lattice sites and interstitial sites are foreign to the material. As in the previous example, we may define two first order rate constants corresponding to Eq. 4. In the forward direction, the rate is proportional to the concentration of the impurity on substitutional cation sites, where the constant of proportionality is the rate constant  $k_{ds}$ . In the reverse direction, the rate is proportional to the product of the Hg vacancy concentration and the concentration of the impurity on interstitial sites. The constant of proportionality is the rate constant  $k_{div}$ . These rate constants can describe either generation or recombination processes depending on which species is being considered. For example, a reaction in the forward direction results in the recombination of a substitutional cation impurity while an interstitial impurity and Hg vacancy are generated. The resulting continuity equations are,

$$\frac{\partial i}{\partial t} = D_i \frac{\partial^2 i}{\partial x^2} - k_{iv} iv + g \quad (5)$$

$$\frac{\partial v}{\partial t} = D_v \frac{\partial^2 v}{\partial x^2} - k_{iv} iv + g - k_{div} d_i v + k_{ds} d_s \quad (6)$$

$$\frac{\partial d_i}{\partial t} = D_{di} \frac{\partial^2 d_i}{\partial x^2} - k_{div} d_i v + k_{ds} d_s \quad (7)$$

$$\frac{\partial d_s}{\partial t} = D_{ds} \frac{\partial^2 d_s}{\partial x^2} + k_{div} d_i v - k_{ds} d_s \quad (8)$$

Another reaction which we may have considered for the cation impurities is that of the "kickout" mechanism,



However, this is a second order process since it requires that an impurity interstitial kickout a Hg atom from a lattice site, immediately assuming its lattice position. It has thus far not been necessary to invoke the kickout process specifically in modeling the available data, since a two-step mechanism within the first

order framework gives similar results. While equations similar to those shown above have been proposed for silicon, relatively little work has been reported with respect to complete numerical simulations or parameter values.<sup>2</sup>

In a similar fashion to the examples given above, Te vacancies, Te antisites, complexes, and other defects or impurities can also be added to the model. The key to establishing the proper set of continuity equations lies in the accurate identification of the important quasi-chemical reactions. Once the equations have been established, the focus shifts to the difficult problem of determining the parameter values. Even for the simplest example, there are two diffusion coefficients, two rate constants, and a set of unknowns associated with the boundary conditions. In addition, the initial defect profiles must be accurately known in order to solve a particular problem. While the large number of unknowns is discouraging, there is a significant body of experimental results available in the literature to help us focus in on some of the parameters. For example, measurements of the hole concentration for material equilibrated in controlled ambients, give the vacancy concentration as a function of the Hg partial pressure and temperature of equilibration.<sup>3</sup> In addition, theoretical native defect equilibrium calculations may provide the ratios between the various defect species, allowing identification of the most important defects.<sup>4</sup>

## SIMULATION RESULTS AND DISCUSSION

### The "n-on-p process"

In processing  $\text{Hg}_{1-x}\text{Cd}_x\text{Te}$ , it is common to employ a step where Te-rich material is annealed in a Hg-rich ambient. The Te-rich material can contain both excess Te phases as well as Hg vacancies. The excess Te can be a gross defect.<sup>5</sup> A dominant electrical effect is the presence of the Hg vacancies which are at least singly if not doubly ionized acceptors. One of the effects of the Hg anneal is, therefore, to saturate out the Hg vacancies, reducing the acceptor concentration typically to the point where the doping is dominated by a donor, either purposefully introduced or present as a residual impurity. The mechanism thought to be primarily responsible for this effect is the in-diffusion of Hg interstitials which annihilate the Hg vacancies. In this analysis, we will neglect the effect of any Te precipitates (or Te antisites which can be considered the smallest possible Te precipitate).

If the Hg anneal is performed to completion, the Hg vacancy and interstitial concentrations will be uniform and given by defect equilibrium values.<sup>3,6</sup> If the Hg anneal is not performed to completion, the result is a low vacancy concentration n-type skin on a Hg vacancy rich core. The n-on-p junction formed by this process may be utilized in the fabrication of high quality photodiodes.

As an example, we will consider a 200  $\mu\text{m}$  thick slice of  $\text{Hg}_{0.8}\text{Cd}_{0.2}\text{Te}$  which had been Te equilibrated at about 325°C up to time  $t = 0$ . The equilibrium was

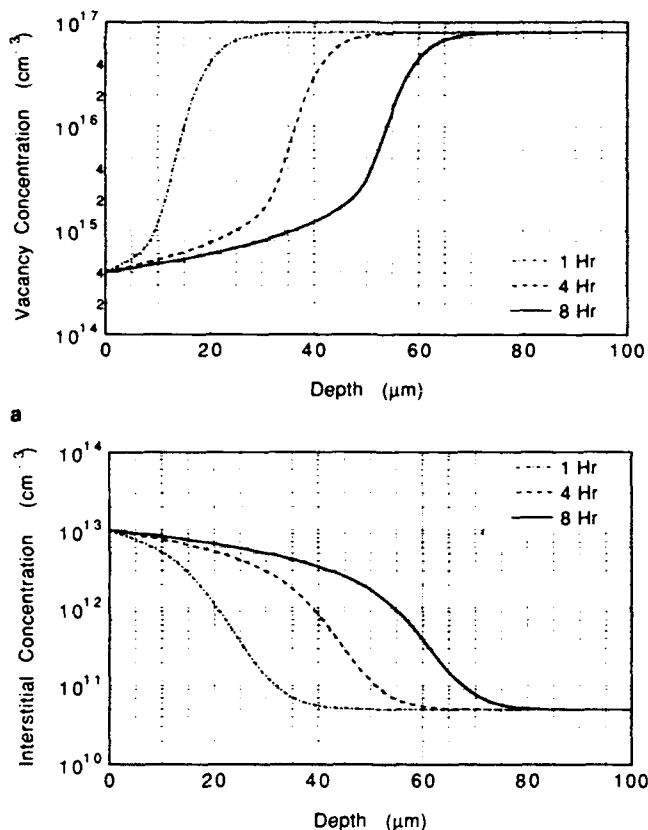


Fig. 1. Simulated defect profiles formed at 325°C by annealing Te equilibrated material in a Hg rich ambient for 1, 4, and 8 h. (a) Hg vacancies (b) Hg interstitials.

assumed to lead to  $8 \times 10^{16} \text{ cm}^{-3}$  Hg vacancies and an arbitrary  $5 \times 10^{10}$  Hg interstitials; the Hg-rich equilibrium values are  $4 \times 10^{14} \text{ cm}^{-3}$  and  $10^{13} \text{ cm}^{-3}$ , respectively. The vacancy equilibrium concentrations were chosen to be consistent with the experimental values determined by Schaake.<sup>6</sup> While the interstitial concentrations are unknown, the product of the Hg vacancy and interstitial concentrations is only a function of the temperature of equilibration and is set by the thermodynamic equilibrium constant ( $g/k_v$ ) of the reaction described by Eq. 1. The thermodynamic equilibrium constant was assumed to be  $4 \times 10^{27} \text{ cm}^{-6}$ . The generation and recombination rates were assumed to be large, but finite, so that assumption of local equilibrium between the interstitials and vacancies is not valid. For simplicity, vacancy diffusion is set to be negligible as defined by the inequality,

$$D_i i_{\text{Hg}} \ll D_v v_{\text{Te}}, \quad (10)$$

where  $i_{\text{Hg}}$  is the Hg interstitial concentration for material equilibrated under Hg-rich conditions and  $v_{\text{Te}}$  is the initial Hg vacancy concentration. The interstitial diffusivity is set so as to obtain a junction depth of about 20  $\mu\text{m}$  when  $g$  and  $k_v$  are "infinite", as defined by the validity range of the steady state analysis.<sup>7</sup> The resulting defect profiles are shown in Fig. 1 for anneals of 1, 4, and 8 h. Since the same surface boundary conditions have been assumed at both 0 and 200  $\mu\text{m}$ ,



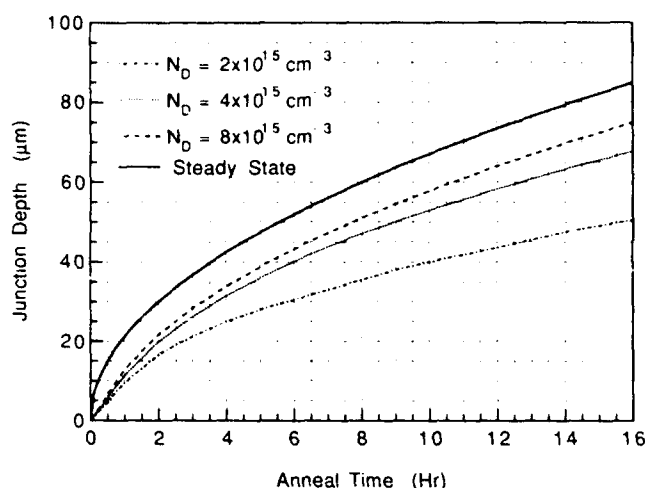


Fig. 2. Simulated n-on-p junction depth at 325°C as a function of anneal time for three different donor concentrations. The solid curve is determined by the steady state approximation.

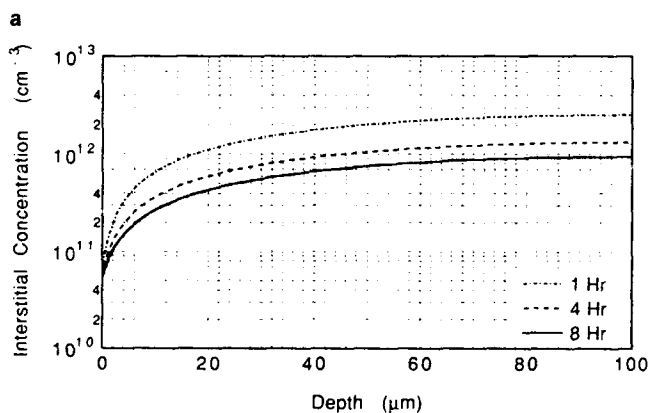
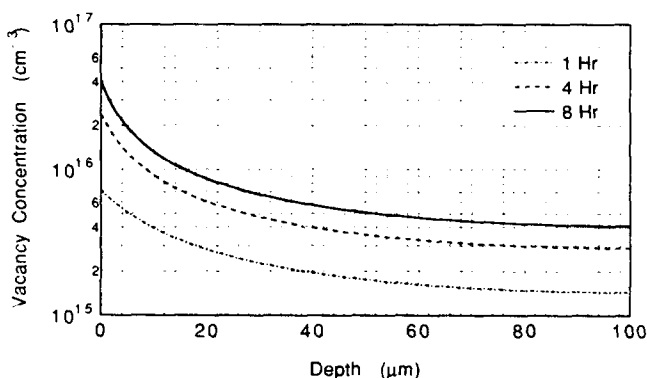


Fig. 3. Simulated defect profiles formed at 325°C by annealing Hg equilibrated material in a Hg poor ambient for 1, 4, and 8 h. (a) Hg vacancies. (b) Hg interstitials.

the resulting profiles are symmetric about 100  $\mu\text{m}$ .

The Hg vacancy profiles are shown in Fig. 1a. In all cases, the width of the transition region from high ( $8 \times 10^{16} \text{ cm}^{-3}$ ) to low ( $\sim 10^{15} \text{ cm}^{-3}$ ) vacancy concentration is a significant fraction of the junction depth. This is qualitatively similar to the vacancy profiles measured by Schwaake et al. at 270°C.<sup>6,7</sup> In this case, the broadness in the transition is a result of "finite" generation and recombination rates, as opposed to

mixed interstitial-vacancy diffusion, since the vacancy diffusion coefficient was set to zero. The Hg interstitial profiles are shown in Fig. 1b. The boundary conditions are such that the surface interstitial concentration reaches  $i_{\text{Hr}}$  within a few seconds. Although the Hg interstitials are always at least one order of magnitude lower in concentration than the Hg vacancies, their large diffusion coefficient allows them to dominate the problem.

For the vacancy profiles shown in Fig. 1a, the n-on-p junction depth will be a function of the donor impurity concentration. Assuming that the vacancies are doubly ionized acceptors, the junction depth dependence for three different uniform donor impurity concentrations is shown in Fig. 2 as a function of the anneal time. The interactions of the dopant with the defects are neglected. For the case where  $g$  and  $k_{\text{iv}}$  are sufficiently large, the steady state analysis is accurate and the junction depth is proportional to the square root of the anneal time. While the finite  $g$  and  $k_{\text{iv}}$  lead to much broader vacancy profiles, the junction depth time dependence continues to vary approximately with the square root of time. The significant dependence of the junction depth on the donor concentration may explain the large discrepancies in junction depths reported in the literature.<sup>7,8</sup>

### The p-on-n problem

The inverse process of annealing low vacancy concentration, Hg equilibrated  $\text{Hg}_{0.8}\text{Cd}_{0.2}\text{Te}$  in a Hg-poor ambient does not generally lead to well-behaved p-on-n junctions.<sup>8</sup> To investigate this problem further, we have performed simulations using the same bulk parameters used to model the n-on-p process. The starting material has been equilibrated under Hg-rich conditions such that the initial vacancy concentration is  $4 \times 10^{14} \text{ cm}^{-3}$ . The surface boundary condition has been changed to allow for the out-diffusion of Hg as an interstitial and for the surface interstitial concentration to reach its Te-equilibrated value within the first few seconds. The defect profiles are shown in Fig. 3 for anneals of 1, 4, and 8 h. Unlike the previous example, the defect concentrations throughout the material have changed significantly even after just 1 h.

The Hg vacancy profiles are shown in Fig. 3a. In all cases, the vacancy distribution is gradual and for a given anneal time, the vacancy concentration throughout the material is within an order of magnitude of the surface concentration. To understand how the vacancy profiles came about, it helps to look at the interstitial profiles shown in Fig. 3b. The slope of the interstitial curve at the surface is an indication of the net flux of Hg out of the material (recall that vacancy motion has been neglected). The Hg interstitials are coming from the bulk, which reduces the bulk interstitial concentration. This out-diffusion disturbs the local equilibrium which results in a net generation of interstitials and vacancies. The generated interstitials continue to out-diffuse. Since the interstitials diffuse quickly, the net generation of vacancies is somewhat uniform throughout the bulk. The final result is a

gradual vacancy profile which does not allow for the formation of an abrupt, well-behaved p-on-n junction diode.

The dependence of the junction depth on the time of anneal is shown in Fig. 4 for three different donor concentrations. As in the previous example, the interaction of the donor impurity with the point defects has been neglected and the vacancies have been assumed to be doubly ionized. The simulated junction depth time dependence is not proportional to the square root of the anneal time and is a strong function of the donor concentration. For the smallest donor concentration shown,  $2 \times 10^{15} \text{ cm}^{-3}$ , the material has been completely converted p-type after just 30 min. For a donor concentration of  $8 \times 10^{15} \text{ cm}^{-3}$ , the material remains n-type for the first half hour. Once a p-region forms, the junction moves quickly converting the entire slice to p-type after just 8 h. This peculiar behavior agrees qualitatively with the experimental results reported in the literature.<sup>8</sup>

### Defect Redistribution

Following the formation of an n-on-p junction by annealing high vacancy concentration material in a Hg-rich ambient, it is likely that the material will be subjected to subsequent capped anneal(s). These anneals can be expected to cause changes in the defect profiles. We have investigated these stability issues in the context of our process models by choosing parameter values and defect concentrations consistent with processing at about 200°C.

The starting material has been Te equilibrated up to time  $t = 0$ . The equilibrium was assumed to lead to  $10^{16} \text{ cm}^{-3}$  Hg vacancies. The Hg-rich equilibrium vacancy concentration is assumed to be  $10^{13} \text{ cm}^{-3}$ . The resulting vacancy profile following a 1 h Hg rich anneal is shown in Fig. 5a for "infinite" generation and recombination rates consistent with the steady state analysis. Figure 5b shows the vacancy profile for the case where  $g$  and  $k_{iv}$  are finite. We continue to assume that vacancy diffusion is negligible.

To accelerate the "aging" process and keep the analysis simple, we simulate a capped anneal of the n-on-p junction performed at 200°C. Hence, the bulk parameters remain unchanged. The surface boundary condition is changed to reflect a perfect barrier to Hg loss. The resulting vacancy profiles are shown in Fig. 5 following a 5, 10, and 20 min simulated capped anneal at 200°C. In both cases, the resulting junction depth and n-on-p diode stability is a function of the donor concentration. In both cases, the junction can be expected to move toward the surface for low donor concentrations. If the impurity concentration is too low, the junction may be annihilated and the material will be converted completely p-type. For large donor concentrations, the junction remains stable for the case of Fig. 5b, but actually moves in deeper for the case of Fig. 5a. These effects can be explained as a vacancy redistribution. During the capped anneal, the interstitials in the n-type skin continue to diffuse to the junction where they annihilate the large num-

ber of vacancies. This motion of interstitials out of the skin region disturbs the local equilibrium, resulting in net generation of interstitials and vacancies in the skin. The generated interstitials continue to diffuse to

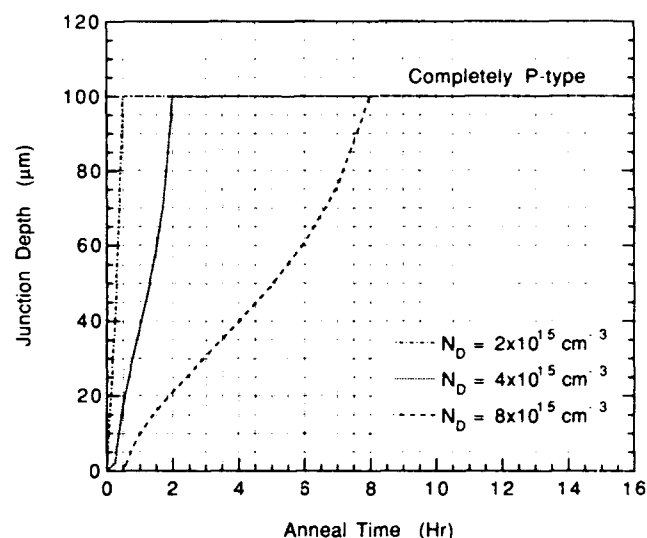


Fig. 4. Simulated p-on-n junction depth at 325°C as a function of anneal time for three different donor concentrations. A junction depth of 100  $\mu\text{m}$  indicates the material has been converted completely p-type.

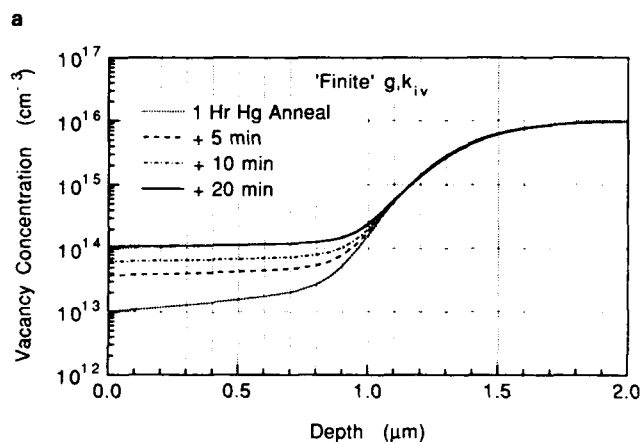
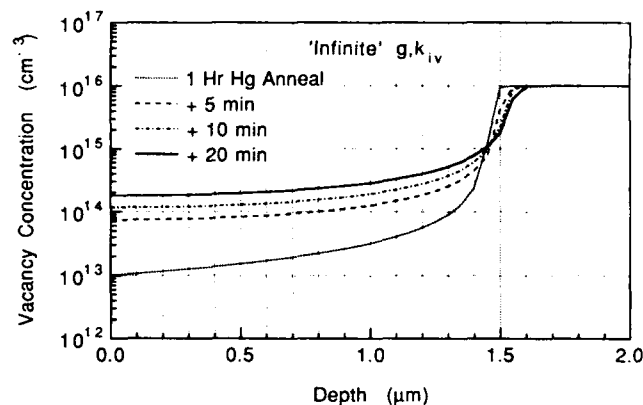


Fig. 5. Simulated Hg vacancy profiles following capped anneals of an n-on-p junction formed by a 1 h 200°C Hg anneal of Te equilibrated material. (a) "infinite"  $g$  and  $k_{iv}$ , (b) "finite"  $g$  and  $k_{iv}$ .

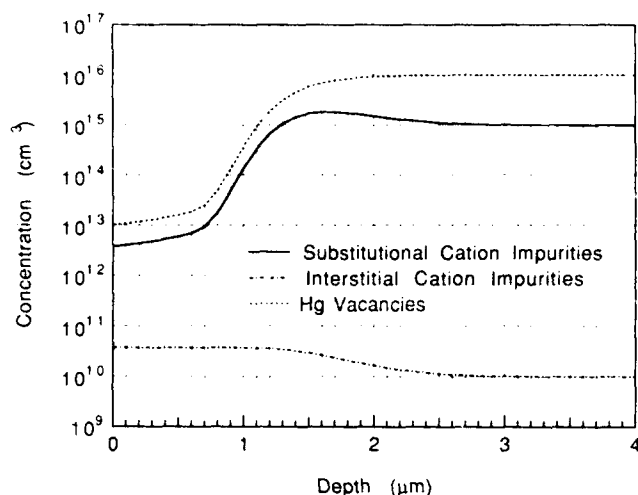


Fig. 6 Mercury vacancy and cation impurity profiles following a 1 h 200 °C Hg anneal of initially Te-equilibrated material.

the junction. For the case of Fig. 5a, the recombination rate is large, so that the annihilated vacancies are limited to a region of about 0.1  $\mu\text{m}$  beyond the initial junction. In Fig. 5b, the initial vacancy profile is broad due to the finite generation and recombination rate. For this latter case, the annihilated vacancies resulting from redistribution are spread out over a micron, thus increasing the junction stability.

### Cation Impurity Gettering

Until now, we have been concerned only with the Hg interstitials, Hg vacancies, and the interactions between them described by Eq. 1. In fact, our modeling approach may be expanded to include other types of defects as well as impurities. As an example, we will look at the effect of the Hg in-diffusion n-on-p process for the case of an initially uniform  $10^{15} \text{ cm}^{-3}$  substitutional cation impurity concentration, where the interaction between the Hg vacancies and impurity cannot be neglected (e.g. Cu, Ag, or Au). The important quasi-chemical reactions are given by Eqs. 1 and 4 and the continuity relationships to be solved are given by Eqs. 5–8. It is assumed that the impurity diffuses rapidly as an interstitial, but that the substitutional impurity is immobile. The choice for the forward and reverse reaction rates of Eq. 4 are arbitrary as well as the resulting interstitial cation impurity concentration. The Hg interstitial and vacancy parameters and equilibrium concentrations are the same as those used in the previous section at 200°C. The Hg vacancy, substitutional impurity, and interstitial impurity profiles are shown in Fig. 6 following a 1 h Hg anneal. The results indicate the redistribution, or gettering, of the cation impurity. The in-diffusing Hg interstitials annihilate Hg vacancies, which drives the reaction described by Eq. 4 to generate more impurity interstitials. These impurity interstitials diffuse ahead of the skin where the Hg vacancy concentration is higher and are converted back to substitutional impurities to maintain local equilibrium. The net result is the movement of the cation impurity out of the n-type skin into the

p-type core.<sup>7</sup> If the Hg anneal is continued to completion, such that the core is annihilated, the simulation results indicate that the substitutional cation impurity is redistributed uniformly throughout the bulk at its original concentration. This result is consistent with the redistribution of residual acceptor impurities reported in the literature.<sup>9</sup>

### SUMMARY AND CONCLUSIONS

A modeling methodology has been developed by which the point defect as well as impurity profiles are described by a set of continuity equations. These relationships account for the diffusivity of the species, as well as the interactions with other point defects and impurities. Numerical solutions for several common process problems have been presented, yielding results consistent with the available experimental data. Unfortunately, the current data base is insufficient to uniquely define the model parameter values.

The simulations of the n-on-p junction formation indicate that the junction depth may be a significant function of the n-type dopant level. The p-on-n process gives junctions which are a strong function of the donor concentration. Future junction depth measurements must carefully account for the donor concentration in order to resolve the actual time dependencies.

The examples in this paper have been limited to Hg interstitials, Hg vacancies, and cation impurities without regard to specific ionization states. In fact, the modeling framework may be further developed to include second phase Te, Te vacancies, Te interstitials, variations due to Cd, anion sublattice impurities and electric field effects involving ionized species. Additional experimental and theoretical work will be necessary to establish the important quasi-chemical reactions and model parameters for the various process problems.

### ACKNOWLEDGMENT

This work has been supported by gift funds from Texas Instruments Inc. José L. Meléndez acknowledges partial support from the National Science Foundation. The authors wish to thank Jazib Hasan for assistance in the software development and Herb Schaake, Jerry Elkind, Arthur Turner, John Tregilgas, and Robert Keller for useful discussions.

### REFERENCES

1. Hal R. Yeager and Robert W. Dutton, *IEEE Trans. Electron Devices* ED-32, 1964 (1985).
2. S.M. Hu, P. Fahey and R.W. Dutton, *J. Appl. Phys.* 54, 6912 (1983).
3. H.R. Vidyantath, *J. Electrochem. Soc.* 128, 2609 (1981).
4. M. Berding and A. Sher, *J. Electron. Mater.* 22, 1005 (1993).
5. H.F. Schaake, J.H. Tregilgas, A.J. Lewis and P.M. Everett, *J. Vac. Sci. Technol. A* 1, 1625 (1983).
6. H.F. Schaake, *J. Electron. Mater.* 14, 513 (1985).
7. H.F. Schaake, J.H. Tregilgas, J.D. Beck, M.A. Kinch and B.E. Gnade, *J. Vac. Sci. Technol. A* 3, 143 (1985).
8. C.L. Jones, M.J.T. Quelch, P. Capper and J.J. Gosney, *J. Appl. Phys.* 53, 9080 (1982).
9. J. Tregilgas, J. Beck and B. Gnade, *J. Vac. Sci. Technol. A* 3, 150 (1985).

# Hg<sub>0.8</sub>Cd<sub>0.2</sub>Te Native Defects: Densities and Dopant Properties

M.A. BERDING, M. VAN SCHILFGAARDE, and A. SHER

SRI International, Menlo Park, CA 94025

We examine the native defect equilibrium in HgCdTe, including cation and anion vacancies, interstitials, and antisites in the analysis. A gradient correction to the local density functional has been added to the defect formation enthalpies calculated within the local density approximation, and preliminary predictions of the dominant ionization states are made. Temperature-dependent defect formation entropies and the temperature dependence of the pre-exponentials are incorporated into the calculation of the defect densities. Degenerate Fermi-Dirac statistics are used for the electronic equilibration, and the intrinsic reaction constant as a function of composition and temperature is calculated. We theoretically substantiate the doubly ionized mercury vacancy as the dominant defect in HgCdTe, and expect the doubly ionized mercury vacancy densities to be comparable in HgZnTe. We predict that tellurium antisites are donors and will be present for some annealing conditions in sufficient quantities to be measured and possibly to affect device performance.

**Key words:** Calculation of defect densities, HgCdTe, HgZnTe, native defects, Te antisites as donors

## INTRODUCTION

The importance of native defects in HgCdTe is undisputed, with the dominant defect believed to be the double acceptor Hg vacancy.<sup>1</sup> The evidence for these defects is largely indirect and depends on their being ionized for observation. Neutral defects and compensating defects are more difficult to measure, and neither their densities nor even their presence is well established.

Our goal is to identify the important native defects in HgCdTe as a function of temperature and mercury pressure. Predictions of the absolute defect concentrations are difficult because of the accuracy required for reaction enthalpies and entropies that enter in exponentials. Our calculations although using a state-of-the-art method, are subject to a number of limitations, such as the supercell approximation that is used to calculate defect formation enthalpies. Despite these limitations, for which error bars can be esti-

mated, we find good agreement with experiment for the defect densities in narrow-gap HgCdTe. While there are some fitted parameters in the theory—for example, the temperature variation of the band gap—none have been chosen to fit the measured defect densities we are predicting. Thus, deviations must be ascribed to deficiencies in our approximations or to physical mechanisms that have not yet been incorporated.

In our previous work, we used the linearized muffin-tin orbital (LMTO) method within the atomic spheres approximation (ASA),<sup>2</sup> and later the full-potential (FP) Harris Foulkes approximation.<sup>3</sup> The ASA substitutes a spheridized density for the true Hohenberg-Kohn density functional in the local density approximation. While the ASA is computationally fast, it cannot reliably predict atomic forces, and therefore lattice relaxations. Because of the elimination of the ASA shape approximation, in the FP calculations, we have predicted the breathing mode relaxations about the defect sites. Using the resulting defect formation enthalpies, in Ref. 3, we predicted

(Received October 12, 1992; revised January 13, 1993)

**Table I. Formation Energies and Ionization States of the Native Point Defects**

| Defect                  | Formation Energy (eV) | Ionization State |
|-------------------------|-----------------------|------------------|
| $V_{\text{Hg}}$         | 1.93                  | shallow acceptor |
| $V_{\text{Te}}$         | 2.39                  | donor            |
| $\text{Te}_{\text{Hg}}$ | 2.68                  | shallow donor    |
| $\text{Hg}_{\text{Te}}$ | 0.75                  | deep acceptor    |
| $\text{Te}_i$           | 4.47                  | shallow donor    |
| $\text{Hg}_i$           | 1.75                  | shallow donor    |
| ZnTe                    | 4.66 (4.8)*           |                  |
| CdTe                    | 4.17 (4.4)*           |                  |
| HgTe                    | 3.37 (3.3)*           |                  |

Note: Formation energies refer to the neutral defect reactions in Eqs. 1–6 in text. See text for discussion of shallow and deep. \*Experimental cohesive energies.

ratios of neutral native defects. In the present paper, we have made several important improvements to this previous work:

- A gradient correction to the local density functional<sup>4</sup> has been included, which we find has a significant impact on the defect formation enthalpies;
- Absolute defect densities are predicted;
- The reaction constant for electron-hole pair production as a function of temperature and cadmium composition for degenerate Fermi-Dirac statistics is predicted; and
- The primary ionization states of the native defects have been tentatively identified and incorporated into the defect equilibrium.

The problem of predicting the defect concentrations is complicated by the fact that we are dealing with an alloy. The defect formation energies were calculated for HgTe, the primary component of the pseudobinary alloys HgCdTe and HgZnTe. Using a tight-binding model we have shown<sup>5</sup> that the vacancy formation energy has a nonlinear dependence on the constituents in the near alloy environment, with the nonlinearity being most dramatic for the removal of the common-lattice atom (i.e. tellurium for HgCdTe and HgZnTe). The variation of the mercury vacancy formation energy, while less dramatic because the first-nearest neighbors are always tellurium, is as much as ~0.1 eV (depending on the constituents in the second-neighbor shell). We have not yet incorporated this level of detail into our first-principles calculations. Additionally, we have not included cadmium- or zinc-based defects (such as the cadmium antisite); because HgTe is the dominant constituent for compositions of technological importance, we believe this exclusion is justified. The alloy effects have been included in the present calculations via the composition dependence of the band gap which, because of its temperature dependence, has been extracted from experiment and the shape of the conduction and valence bands.

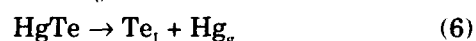
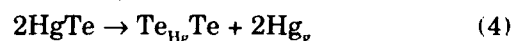
## REACTION ENTHALPIES

We consider the following native defects: mercury vacancy  $V_{\text{Hg}}$ , tellurium vacancy  $V_{\text{Te}}$ , mercury antisite  $\text{Hg}_{\text{Te}}$ , tellurium antisite  $\text{Te}_{\text{Hg}}$ , mercury interstitial  $\text{Hg}_i$ , and tellurium interstitial  $\text{Te}_i$ . A couple of corrections have been added to the reaction enthalpies calculated within the Harris-Foulkes approximation to the FP-LMTO. First, the ASA is used to determine the ionization state of the defect—that is, whether it is a donor or acceptor. We have not yet determined the ionization energies of the defect, but we do indicate whether the state appears to be “deep” or “shallow.” We assume that only the shallow states are electrically active. Because we have not yet determined the ionization energies, we will for the present assume that they are zero for the shallow states—that is, that the donor and acceptor levels lie close to the conduction and valence band edges, respectively. We assume that the deep states are not electrically active. This approximation is likely to be good because, at high temperatures where the defect concentrations are equilibrated, carrier concentrations are high enough so that free carrier screening may effectively reduce the shallow-state activation energies. Details of the calculational method used to determine the ionization states of the various defects will be reported elsewhere.

The second correction to results involves the incorporation of a gradient correction to the local density functional. This correction has not yet been implemented in the FP-LMTO, and thus was done within the ASA. We expect that the FP gradient correction will be nearly equal to that from the ASA, because the density gradient is predominantly radial, the nonspherical components eliminated in the ASA being small. In Table I, we summarize the formation energies including the gradient correction for the neutral defect reactions in Eqs. 1–6 below. Also shown are the cohesive energies of the constituent compounds HgTe, CdTe, and ZnTe from a gradient-corrected self-consistent FP calculation; one can see that the agreement with experiments is quite good. The tentative identification of defect ionization states is also given in Table I.

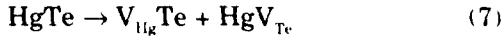
## DEFECT CONCENTRATIONS

Defect concentrations are determined using a quasi-chemical analysis of the defect formation reactions.<sup>6</sup> We consider the following defect reactions



where we have chosen the HgTe unit cell and free

atomic mercury, Hg<sub>g</sub>, as the reference states. Other reactions of interest can be obtained by taking linear combinations of these equations. For example, the neutral Schottky defect reaction is obtained by adding Eqs. 1 and 2 to obtain



or, as it is more commonly written,



The concentrations of the defects in Eqs. 1–6 can be obtained from the evaluation of the corresponding reaction constants:

$$K_{\text{V}_{\text{Hg}}} = [\text{V}_{\text{Hg}}] p_{\text{Hg}} \quad (9)$$

$$K_{\text{V}_{\text{Te}}} = [\text{V}_{\text{Te}}] / p_{\text{Hg}} \quad (10)$$

$$K_{\text{HgTe}} = [\text{HgTe}] / p_{\text{Hg}}^2 \quad (11)$$

$$K_{\text{TeHg}} = [\text{TeHg}] p_{\text{Hg}}^2 \quad (12)$$

$$K_{\text{Hg}_1} = [\text{Hg}_1] / p_{\text{Hg}} \quad (13)$$

$$K_{\text{Te}_1} = [\text{Te}_1] p_{\text{Hg}} \quad (14)$$

In these expressions,  $p_{\text{Hg}}$  is the mercury pressure in atmospheres and square brackets refer to concentrations per cubic centimeter. The evaluation of these reaction constants was discussed in our previous paper<sup>3</sup> as well as in many standard texts.<sup>7</sup>

In the present calculations, we have used the formation energies from Table I and temperature-dependent entropies given in Ref. 3.

Ionized defect concentrations can be determined from the concentration of neutral defects from

$$[D^*] = (g_{D^*} / g_{D^0}) \exp((E_{D^*} - E_F) / k_B T) [D^0] \quad (15)$$

for donors and

$$[A'] = (g_{A'} / g_{A^0}) \exp((E_F - E_{A'}) / k_B T) [A^0] \quad (16)$$

for acceptors. The dot and prime superscripts correspond to a positively and negatively charged species, respectively;  $g_X$  is the degeneracy of the state  $X$ ;  $E_{D^*}$  and  $E_{A'}$  are the positions of the first ionization levels for the donor and acceptor, respectively, in the one-electron picture;  $E_F$  is the Fermi energy;  $k_B$  is Boltzmann's constant; and  $T$  is the temperature in Kelvin. Similar expressions are obtained for the second ionization state.

In addition to the above equations for the determination of the native defect populations, we have the reaction for the generation of electron-hole pairs



The corresponding reaction constant is

$$K_{\text{pn}} = [h^*][e'] = pn \quad (18)$$

where  $p = [h^*]$  and  $n = [e']$ , as in the usual notation.

In general,  $K_{\text{pn}}$  depends on the structure of the conduction and valence bands, the band gap energy, the Fermi energy, and the temperature variation of

these quantities. Several limits are often encountered in the evaluation of  $K_{\text{pn}}$ . First, when the conduction and valence bands are parabolic, although not necessarily isotropic,  $E \sim k^2$ , and the reaction constant can be written in terms of the Fermi-Dirac integrals as

$$K_{\text{pn}} = 4 \left( \frac{2\pi k_B T}{h^2} \right)^3 (m_h m_e)^{3/2} F_{1/2} \left( \frac{E_F - E_c}{k_B T} \right) F_{1/2} \left( \frac{E_v - E_F}{k_B T} \right) \quad (19)$$

where  $F_{1/2}$  is the Fermi-Dirac function;  $E_c$ ,  $E_v$ , and  $E_F$  are the conduction-band, valence-band, and Fermi energy, respectively;  $m_h$  and  $m_e$  are the hole and electron density-of-states effective masses, respectively; and  $h$  is Planck's constant. In the nondegenerate limit, this reduces to the familiar expression

$$K_{\text{pn}} = 4 \left( \frac{2\pi k_B T}{h^2} \right)^3 (m_h m_e)^{3/2} \exp \left( \frac{E_v - E_c}{k_B T} \right) \quad (20)$$

which is independent of the Fermi energy. For the general degenerate case, which will apply even at moderate temperatures for narrow-gap HgCdTe,  $K_{\text{pn}}$  will depend on  $E_F$  and therefore in general will not be independent of the presence of extrinsic carriers. Additionally, the assumption of parabolic bands may be poor for the narrow-gap materials, where the dispersion near the conduction band edge is rather more linear than parabolic,<sup>8</sup> i.e.  $E = \alpha k$ . This case obtains with the Fermi-Dirac integral function of order 2 and

$$K_{\text{pn}} = 2 \left( \frac{2\pi k_B T m_h}{h^2} \right)^{3/2} \frac{2}{\pi^2} \left( \frac{k_B T}{\alpha} \right)^3 F_2 \left( \frac{E_F - E_c}{k_B T} \right) F_{1/2} \left( \frac{E_v - E_F}{k_B T} \right) \quad (21)$$

In the present program, we have used Eq. 21 to evaluate  $K_{\text{pn}}$ , with  $m_h = 0.43$ ,

$$E_g(x, T) = E_c - E_v = -0.313 + 1.787x + 0.444x^2 - 1.237x^3 + 0.932x^4 + (0.667 - 1.714x + 0.760x^2)T / 1000 \quad (22)$$

taken from Ref. 9, and  $\alpha$  chosen to yield good agreement with experimental values of the intrinsic carrier concentrations.<sup>10</sup>

The calculation of the intrinsic reaction constant for narrow-gap HgZnTe is more difficult to evaluate, given the more limited data base for evaluation of the high-temperature band gap, effective masses, and intrinsic carrier concentration.

From the zero-temperature band structures, the valence-band effective masses are found to be comparable for HgCdTe and HgZnTe with equal band gaps, while the conduction-band effective mass for HgZnTe is slightly larger than for HgCdTe.<sup>11</sup> Overall, though, we expect  $K_{\text{pn}}$  for the two materials to be comparable.

To calculate the native defect concentrations at a given temperature and mercury pressure, we have to determine the Fermi energy which satisfies the neutrality condition

$$2\sum[D_i^{\bullet\bullet}] + \sum[D_i^{\bullet}] + [h^{\bullet}] + 2\sum[A_i^{\bullet}] + \sum[A_i^{\bullet\bullet}] + [e^{\bullet}] \quad (23)$$

The concentrations of neutral defects which are independent of the Fermi energy can be solved for directly for a given  $p_{\text{Hg}}$  and  $T$ .

## RESULTS

The low-temperature (77K) hole concentrations as a function of mercury pressure for various equilibration temperatures are shown in Fig. 1 for  $x = 0.2$   $\text{Hg}_x\text{Cd}_{1-x}\text{Te}$ . Shown for comparison are the experimental data from Vydyanath.<sup>1</sup> In the calculations, we allowed both atomic and electronic equilibrations at the high temperature at which the annealing takes place; we then assume the total defect concentrations are frozen-in upon quenching, and that at 77K only the electronic equilibrium is reestablished. In agreement with Vydyanath,<sup>1</sup> we conclude that the mercury vacancy is the dominant defect in  $\text{HgCdTe}$ ; and it behaves as a double acceptor, although we have not yet determined the activation energy. We find the tellurium antisite, which is a donor, is also an important defect.

In Fig. 2, we show a breakdown of the concentrations of various defects as a function of mercury pressure for the lowest and highest annealing temperatures of Fig. 1. The defect densities are those present at the annealing temperature, not at 77K, so as to show the atomic and electronic defects present during equilibration. Although the total number of each class of defects remains unchanged upon quenching, the relative concentrations of the neutral and ionized defects will be affected. From Fig. 2a, one can see that the material is intrinsic at the higher mercury pressures, and becomes extrinsic as the pressure is reduced and then highly compensated at the lowest mercury pressures. If the doubly ionized mercury

vacancy is the dominant defect, the intrinsic regime is characterized by  $[h] \sim p_{\text{Hg}}^{1/2}$ , while the extrinsic, uncompensated, limit is characterized by  $[h] \sim p_{\text{Hg}}^{1/3}$ . It is the conversion to extrinsic behavior and the compensating tellurium antisite donors that are responsible for the roll-off on the low-pressure side of the hole concentration curves in Fig. 1. For the material annealed at 655°C, shown in Fig. 2b, the material is nearly extrinsic (dominated by the doubly ionized mercury vacancy) for mercury pressures throughout the stability region, although compensation by the tellurium antisites becomes more important at the lower mercury pressures. The extrinsic behavior is evident in

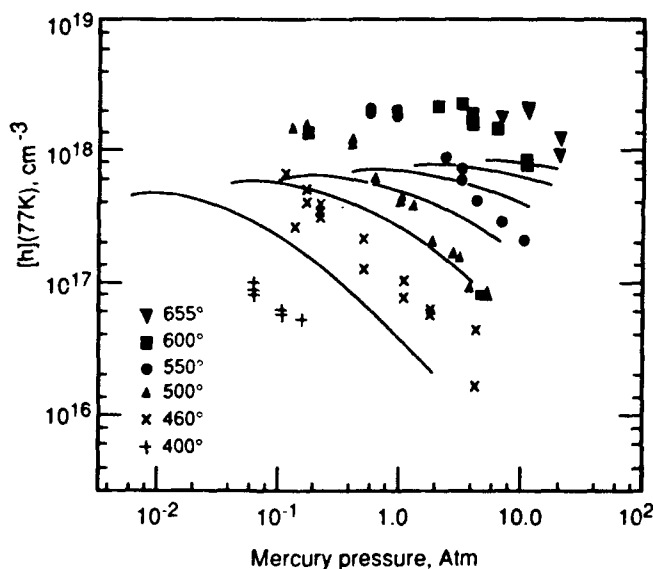


Fig. 1. Hole concentrations at 77K as a function of mercury pressure for material annealed at high temperatures. Experimental data were taken from Vydyanath.<sup>1</sup> Theory is shown as solid lines for pressures within the stability region at a given temperature.

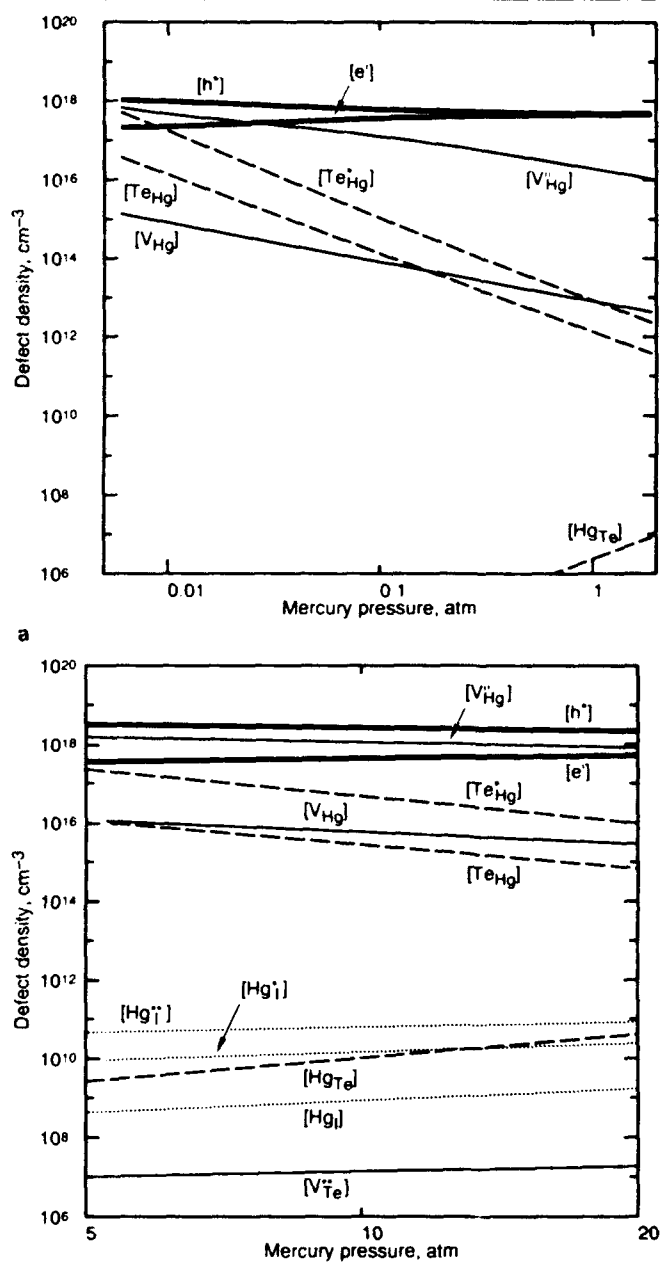


Fig. 2. Predicted defect densities present at the anneal temperature, as a function of mercury pressure for annealing temperatures of (a) 400°C and (b) 655°C.

Fig. 1 by the  $[h] \sim P_{\text{Hg}}^{1/3}$  behavior. As is evident in Fig. 1, the pressure at which the material goes from intrinsic to extrinsic shifts to higher mercury pressure as the annealing temperature is increased.

The discrepancies between our results and experiment can be attributed to a number of factors. First, we have calculated the formation energies for HgTe and applied them directly to HgCdTe, with the alloy taken into account in the calculation of the reaction constant for electron-hole pairs, and in the assumption that the defect ionization levels are at the band edges. Although this should be a reasonable approximation, we have shown that the vacancy formation energies are sensitive to the near-neighbor environment.<sup>5</sup> The removal of this approximation will lead to a raising of the vacancy formation energy by as much as  $\sim 0.1$  eV and, from examination of Fig. 1, will yield better agreement with experiment. Next, we have not taken into account the nonradial relaxation about the vacancy site and its effect on both the formation energy and entropy, nor have we yet included the effect of the entropy of local-mode softening of the ionized vacancy relative to the neutral vacancy. Additionally, the correct ionization energy must be incorporated into the calculation. Finally, we have used a band structure in calculating the reaction constant for electron-hole pairs which yields agreement with the intrinsic carrier concentrations and band gap at  $T < 400\text{K}$ ; the band structure at higher temperatures is speculative, and we need further experiments or theory to confirm its validity.

At the annealing temperature, the material is intrinsic and all of the native defects are nearly completely ionized. While the total numbers of defects are frozen-in upon quenching from high temperature, the ratio of ionized to nonionized defects does change. At 77K, the material is extrinsic and, for material annealed at high temperatures ( $T > 400^\circ\text{C}$ ), is dominated by the acceptor level of the mercury vacancy. Consequently, upon quenching, the ratio of ionized to nonionized defects decreases for acceptor defects and increases for donor defects.

Defect densities present after a low temperature ( $\sim 250^\circ\text{C}$ ) annealing under mercury-saturated conditions are of technological interest. Our predictions for defect concentration as a function of  $1/T$  for mercury pressures corresponding to mercury saturated conditions are shown in Fig. 3. At  $T < 300^\circ\text{C}$ , a mercury-saturated annealing step is effective in reducing the vacancy concentration to less than  $10^{15}\text{ cm}^{-3}$ . Because the density of tellurium antisites varies as  $P_{\text{Hg}}^{-2}$ , compared to  $P_{\text{Hg}}$  for the mercury vacancy, the antisites are most important on the tellurium-rich side of the stability region, and thus are less important for these mercury-saturated annealing.

While the mercury vacancy and tellurium antisite are the primary defects that will affect the electrical activity in Hg<sub>0.8</sub>Cd<sub>0.2</sub>Te, several other defects are of interest because of their role in diffusion, for example the mercury and tellurium interstitials. In Fig. 2, we see that the densities of mercury antisites and mer-

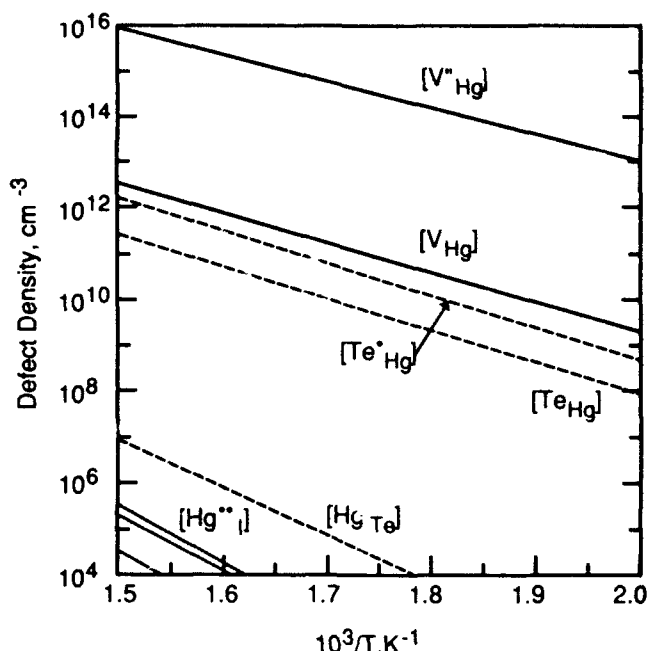


Fig. 3. Defect densities as a function of temperature for mercury-saturated annealing conditions.

cury interstitials are less than  $10^{11}\text{ cm}^{-3}$ , while the densities of tellurium vacancies and interstitials are completely negligible. The defect formation energies used for the calculation of the interstitial densities were from our ASA calculations without lattice relaxations, and therefore carry a larger uncertainty than the antisite and vacancy formation energies. We expect that improvement of the defect total-energy calculations will result in a potentially significant lowering of the formation energy, and consequently an increase in the interstitial defect concentrations. Even so, it is doubtful that we will find tellurium interstitials at densities large enough to account for the tellurium diffusion, which was believed to be via the tellurium interstitials.

While the tellurium antisites are donors and are predicted to be present in significant densities in HgCdTe, we do not predict that equilibrated tellurium antisites are responsible for the experimentally observed p-to-n conversion. Even if such a p-to-n conversion were to occur as a consequence of refinements in our calculations, the conversion would occur on the tellurium-rich side of the stability region. Because antisites are likely to be immobile, relatively high densities of tellurium antisites introduced at high temperatures during growth may persist through low-temperature annealings undertaken to remove mercury vacancies. In this case, the tellurium antisites could be responsible for the p-to-n conversion. A careful correlation of the n-type character with the high-temperature preparation conditions would help to confirm or negate this possibility.

Because of the similar magnitude for the electron and hole effective masses in narrow-gap HgCdTe and HgZnTe, we expect that the intrinsic reaction constants will be similar in the two materials. In addi-



tion, the mercury vacancy formation energy will be similar in the two materials for compositions low in cadmium or zinc, and therefore we expect the defect concentrations to be similar in the low-x materials with comparable band gaps. The tellurium antisite was found to be strained in the HgTe lattice<sup>2,3</sup> and produced a compressive strain in the surrounding lattice. Because of the shorter bond lengths in the HgZnTe alloy, the strain associated with the tellurium antisite is larger than in HgCdTe with a comparable band gap; consequently, the formation energy is expected to be larger in HgZnTe. Thus, we expect the tellurium antisites to be less important in HgZnTe than in HgCdTe. If the tellurium antisite is responsible for the residual n-type character in low-temperature annealed material, lower n-type carrier concentrations will be realizable in HgZnTe.

### CONCLUSIONS

We have calculated the low-temperature hole concentration as a function of annealing temperature and pressure for HgCdTe. We find good agreement with the fit to the experimental data. Remaining discrepancies can be attributed to relaxation and finite ionization energies in the vacancy formation energies, and uncertainties in  $K_{pn}$  at high temperatures. We conclude, in agreement with experiment, that the dominant defect is the doubly ionized mercury vacancy. We do not make any conclusions about the presence of the singly ionized Hg vacancy; we will examine the activation energies for both the singly and doubly ionized states in future work. We find that tellurium antisites are donors and are present in significant densities for low mercury pressures at temperatures above 350K. At lower temperatures

and high mercury pressures, at which annealing typically takes place, tellurium antisite equilibrium densities are negligible. However if their density remains at levels corresponding to high temperature because their low temperature diffusivities are low, then such antisites could affect mobilities and even be the residual donor. None of the other native defects are present in sufficient quantity to influence device characteristics.

### ACKNOWLEDGMENT

This work has been supported by DARPA Contract MDA972-92-C-0053, NASA Contract NAS1-18226, and ONR contract N00014-89-K-132. Computational support provided by the Numerical Aerodynamical Simulation computing facility at NASA Ames Research Center.

### REFERENCES

1. H.R. Vydyanath, *J. Electrochem. Soc.* 128, 2609 (1981).
2. M.A. Berding, M. van Schilfgaarde, A.T. Paxton and A. Sher, *J. Vac. Sci. Technol. A* 8, 1103 (1990).
3. M.A. Berding, M. van Schilfgaarde and A. Sher, *J. Vac. Sci. Technol. B* 10, 1471 (1992).
4. D. Lengreth and D. Mehl, *Phys. Rev. B* 28, 1809 (1983).
5. M.A. Berding, A. Sher and A.-B. Chen, *J. Appl. Phys.* 68, 5064 (1990); *J. Vac. Sci. Technol. A*, 5, 3009 (1987).
6. F.A. Kroger and H.J. Vink, *Solid State Physics Vol. 3*, eds. F. Seitz and D. Turnbull (Academic Press, New York 1956), p. 307.
7. For example, see F. Reif, *Fundamentals of Statistical and Thermal Physics* (McGraw-Hill, New York, 1965).
8. A.-B. Chen, M. van Schilfgaarde and A. Sher, this conference.
9. *Properties of Mercury Cadmium Telluride*, ed. J. Brice and P. Capper (INSPEC, New York, 1987), p. 105.
10. *ibid.*, p. 110.
11. M.A. Berding, S. Krishnamurthy, A. Sher and A.-B. Chen, *J. Vac. Sci. Technol. A* 5, 3014 (1987).

# Observation of Indium-Vacancy and Indium-Hydrogen Interactions in $\text{Hg}_{1-x}\text{Cd}_x\text{Te}$

WM. C. HUGHES, M.L. SWANSON, and J.C. AUSTIN

Department of Physics and Astronomy, University of North Carolina at Chapel Hill, Chapel Hill, NC 27599-3255

We have used a nuclear hyperfine technique, perturbed  $\gamma\gamma$  angular correlation (PAC), to study the interactions between  $^{111}\text{In}$  and native defects and impurities in  $\text{Hg}_{1-x}\text{Cd}_x\text{Te}$ . The PAC technique uses the quadrupole interaction of  $^{111}\text{In}$  with local electric field gradients to characterize the local environment of this donor dopant. We observed that when In was diffused into a bulk or thin film sample of  $\text{Hg}_{1-x}\text{Cd}_x\text{Te}$  ( $x = 0.21$  and  $x = 0.3$ ) at  $350^\circ\text{C}$  and the sample was slow cooled, the In occupied sites with near-cubic symmetry, presumably the substitutional metal site. However, when the sample was quenched, a fraction of the In was incorporated into defects characterized by quadrupole interaction strengths  $\nu_{Q1} = 83$  MHz and  $\nu_{Q2} = 92$  MHz and asymmetries of  $\eta_1 = \eta_2 = 0.08$ . These defects are attributed to the trapping of a metal vacancy at a next-nearest neighbor site to the In atom. The introduction of hydrogen by boiling the samples in distilled water for >4h eliminated the previously observed PAC signals and created defects characterized by  $\nu_{Q3} = 35$  MHz,  $\eta_3 < 0.1$  and  $\nu_{Q4} = 43$  MHz,  $\eta_4 < 0.1$ . These defects are attributed to the decoration of the In- $\text{V}_{\text{Hg}}$  complex by a hydrogen atom. Hall effect measurements showed that hydrogenation increased the hole concentration in p-type quenched samples and even converted n-type indium-doped samples to p-type. A possible model for hydrogen incorporation which includes self-compensation by vacancy creation is suggested.

**Key words:** HgCdTe, In diffusion in HgCdTe, In dopant, trapping of metal vacancies

## INTRODUCTION

Until recently, the study of defects in the ternary semiconductor  $\text{Hg}_{1-x}\text{Cd}_x\text{Te}$  (MCT) has been concerned primarily with their contribution to the material's electrical properties. These measurements have emphasized the conversion of MCT from the as-grown p-type state to n-type, either by doping or as a result of the damage resulting from ion implantation. These investigations have included the electrical characterization of the donor dopant indium and have considered possible defects which hinder the electrical activation of the indium.<sup>1,2</sup> To date, these studies have almost exclusively utilized bulk electrical and optical measurements, and there has been very little research on the specific atomic structure of lattice defects and the local environment of the donor atoms. A complete understanding of the doping of MCT

cannot be gained without such microscopic investigations.

The dominant native defect in as-grown MCT is the Hg vacancy. These vacancies are believed to result from the instability of the Hg-Te bond, which leads to the liberation of Hg vapor when the material is heated. The vacancy concentration in MCT can reach levels as high as  $10^{17}\text{ cm}^{-3}$  when the material is heated in vacuum above  $350^\circ\text{C}$ .<sup>1</sup> Because most methods of MCT growth require elevated temperatures, as-grown MCT usually contains vacancies. It is well established that these defects are the main cause of the material's p-type conductivity. While usually the  $\text{V}_{\text{Hg}}$  are thought to always act as double acceptors, some published results show them to be double acceptors at room temperature and single acceptors at 77K.<sup>3</sup> Recent positron lifetime measurements in MCT show that the charge state of the vacancy is unchanged between 15K and 300K,<sup>4</sup> so that the question of the metal vacancy charge state is unresolved.<sup>5</sup> Typically,

(Received October 12, 1992; revised January 13, 1993)

a conversion of as-grown p-type material to n-type is accomplished by annealing in a Hg-saturated environment, and various methods for performing this anneal are effective.<sup>6</sup> The cause of the resulting n-type conductivity in "pure" material is not well established, but is believed to result from residual impurities or from Hg interstitials.

MCT is often doped, either during growth or subsequently by ion implantation, with donor impurities such as indium, which normally substitute on the cation lattice. Recent calculations and electrical measurements<sup>7</sup> have indicated that indium is almost fully activated at low concentrations but that compensation increases above indium concentrations of  $5 \times 10^{17} \text{ cm}^{-3}$ . Two separate models have been proposed to account for this. In one model, two indium atoms trap a single mercury vacancy, forming  $\text{In}_2\text{Te}_3$ .<sup>1,8</sup> In the other model, single In atoms may be directly compensated by the trapping of one or more mercury vacancies.

Hydrogen is a common impurity in semiconductors. The ubiquity of hydrogen makes it difficult avoid some amount of hydrogen incorporation during growth and during device processing. This problem grows more important with the use of growth<sup>9</sup> and plasma etching<sup>10</sup> techniques that use gases containing hydrogen. Some work has considered hydrogen's effect on electrical and optical properties in CdTe<sup>11</sup> and in MCT.<sup>12</sup> Hydrogen is known to passivate both donors and acceptors in some semiconductors and might be expected to have similar behavior in MCT. In fact, recent infrared transmission measurements on samples which had been boiled in water or exposed to hydrogen plasma seem to show that hydrogen does indeed passivate native  $V_{\text{Hg}}$  acceptor defects.<sup>13</sup> But, relatively little is known about the effects of hydrogen in MCT and related semiconductors, and once again there has been no microscopic characterization of the behavior of hydrogen in MCT.

We have applied the perturbed  $\gamma\gamma$  angular correlation (PAC) technique to the study of defects in MCT. Perturbed  $\gamma\gamma$  angular correlation has been applied successfully to the study of defects in many systems, including metals,<sup>14</sup> semiconductors,<sup>15</sup> and ionic materials.<sup>16</sup> Some observations have elucidated the effects of hydrogen.<sup>17</sup> Since PAC uses an isotope of indium to probe local defect environments, it is ideal for characterizing the structure and behavior of indium-related defects in MCT.

## EXPERIMENTAL

Perturbed  $\gamma\gamma$  angular correlation is a method of nuclear hyperfine spectroscopy related to nuclear magnetic resonance and Mössbauer spectroscopies. The PAC method exploits the electric quadrupole interaction to obtain information on local electric field gradients (EFGs) at the site of the probe nucleus. This information is extracted by measuring the angular correlation between two successive gamma rays emitted from the decaying probe isotope. The EFGs are used to label specific defects containing the probe

nucleus.

<sup>111</sup>In is the most common PAC probe isotope, because it is easily obtainable and has a suitable half-life and nuclear moment in the relevant intermediate state. <sup>111</sup>In decays by electron capture to an excited 7/2 state of <sup>111</sup>Cd. This state then decays to a 5/2 state by emission of a gamma ray. It is the interaction of this state with the local EFG that PAC measures; however, the very short lifetime of the 7/2 state means that the environment is typically still that of the In probe atom. The 5/2 state decays with a half-life of 82 ns to the stable ground state of <sup>111</sup>Cd by emission of a second gamma. If there is no significant rearrangement of the In-containing defect within several half-lives of the 5/2 state (<500 ns) and if the interaction has a suitable magnitude, a measurable PAC signal is observed.

The correlation of the emissions of the two gammas is measured by taking the coincidence spectra,  $I(\Theta, t)$  between the two gamma rays at 90° and 180°. These spectra are divided in an appropriate ratio  $R(t)$  such that the relative detector efficiencies and exponential decay are removed.  $R(t)$  can be fitted using a least squares routine to determine the following information:

- The fraction  $f_d$  of In probe atoms having an EFG associated with a specific defect complex.
- The quadrupole interaction frequency  $\nu_Q$  associated with the EFG.
- The axial asymmetry parameter  $\eta$  of the EFG.
- The orientation of the EFG with respect to the axes of a single crystal.

In addition, a Fourier transform of  $R(t)$  can be used to identify the frequencies of the defects. In the transform, each EFG is associated with three frequency peaks due to the hyperfine splitting of the 5/2 state. These frequencies are in a 1:2:3 ratio for the axially symmetric case and their respective amplitudes go as 3:2:1. More detailed information about the PAC technique is given elsewhere.<sup>14</sup>

The samples used in these experiments were  $x = 0.21$  bulk SSR samples from H.F. Schaake and thin film Te melt LPE samples from Luigi Columbo both of Texas Instruments. Other samples used were LPE grown from Tse Tung of Santa Barbara Research Center with  $x = 0.3$ , having various levels of stable In doping from  $1 \times 10^{14} \text{ cm}^{-3}$  to  $5 \times 10^{15} \text{ cm}^{-3}$ . Unless otherwise specified, all the following results apply to both bulk and thin film samples and to both  $x = 0.21$  and  $x = 0.3$  alloys. The samples were etched for less than 1 min in 0.5% Br/methanol solution to remove surface contamination and oxide. They were then sealed in an evacuated quartz tube with <sup>111</sup>InCl<sub>3</sub> and annealed at 350°C for 6 h to diffuse in the In. All annealing of samples was done in this sealed quartz tube.

The depth of the indium profile in the MCT after diffusion was determined by measuring the radioactivity as a function of etching time. By using the known dimensions of the sample and the density of  $\text{Hg}_{1-x}\text{Cd}_x\text{Te}$ , the etch depth could be estimated from

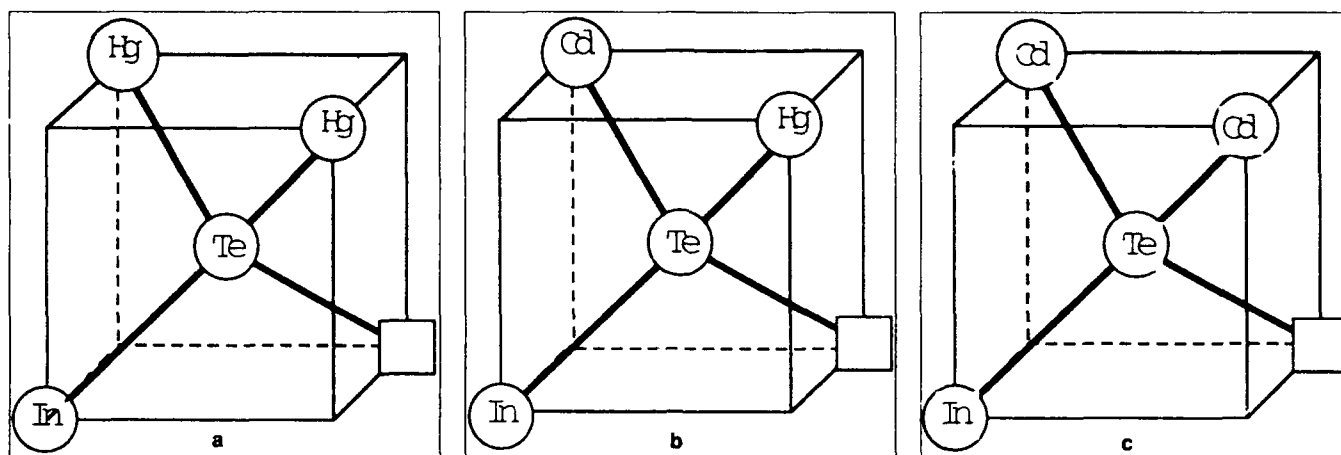


Fig. 1. Possible models for  $\text{In-V}_{\text{Hg}}$  complex. Note the coordination of Hg vs Cd atoms on next-nearest neighbor sites to the In and the V.

the mass loss of the sample. Samples were etched for various times in 0.5% Br/methanol solution and rinsed with methanol. Using this method, it was found that the indium had diffused into the sample on the order of 10  $\mu\text{m}$  after annealing at 350°C for 6 h. This matched closely the profile expected from published values of the diffusivity of indium in vacuum-annealed MCT.<sup>18</sup>

## RESULTS

### Indium-Vacancy Interactions

For samples annealed at 350°C and then allowed to cool slowly in the furnace, no rapid modulation was visible in the PAC spectrum, indicating that the indium atoms were in sites of near-cubic symmetry. This shows that the indium occupied substitutional cation sites with no defects trapped in the vicinity. In particular, it was clear that no Hg vacancies were trapped near the indium atoms after cooling slowly from annealing temperatures up to 400°C. It is believed that this is because during slow cooling a large number of the vacancies are destroyed so that the number of vacancies present reflects the equilibrium at some lower temperature. A distribution of very low quadrupole interaction frequencies was observed ( $\nu_Q < 10$  MHz), consistent with a random distribution of Hg and Cd atoms at the 12 next-nearest lattice sites to an In atom, leading to a slight deviation from cubic symmetry.

When the samples were quenched in vacuum from temperatures of 350°C or above to room temperature, a fraction of In atoms were in defect sites characterized by EFGs of  $\nu_{Q1} = 83$  MHz,  $\eta_1 = 0.08$  and  $\nu_{Q2} = 92$  MHz,  $\eta_2 = 0.08$ . Near-cubic symmetry was restored by annealing in a mercury vapor, providing strong evidence that these EFGs result from the proximity of one or more mercury vacancies. The most likely configuration for these defect pairs involves a single  $\text{V}_{\text{Hg}}$  at a next-nearest site to the indium impurity.<sup>19</sup>

The splitting of the PAC signal into two slightly different frequencies was attributed to the random distribution of mercury and cadmium atoms on the cation lattice. For  $x = 0.21$  alloys, the assumption of

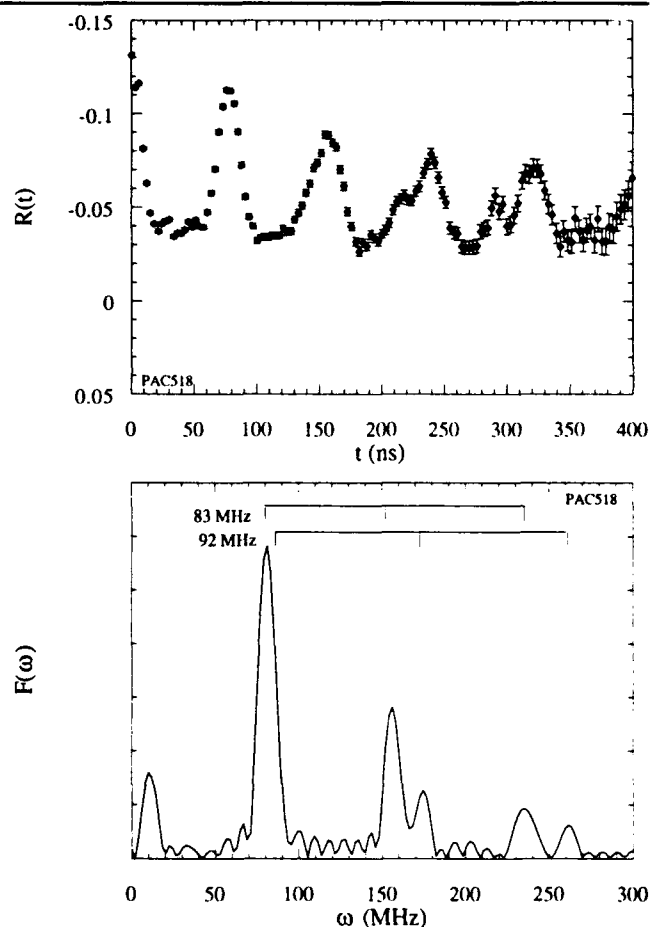


Fig. 2. (top)  $R(t)$  spectrum for a sample of bulk  $\text{Hg}_{0.79}\text{Cd}_{0.21}\text{Te}$  quenched from 350°C and aged at 100°C for approximately 12 h. (bottom) Fourier transform of  $R(t)$  spectrum shown in top panel. Notice the presence of two peaks around 140 MHz.

randomly distributed Cd and Hg atoms leads to a 62% chance that the two next-nearest sites adjacent to the trapped vacancy are both Hg atoms (Fig. 1a), and a 34% chance that one is Hg and one is Cd (Fig. 1b). The ratio of these probabilities corresponds to the observed ratio of the fractions of  $f_1$  and  $f_2$ . Thus, we identify  $\nu_{Q1}$  as the configuration involving two Hg atoms adjacent to the vacancy, and  $\nu_{Q2}$  as the configu-

ration involving one Hg and one Cd atom adjacent to the vacancy. The third possibility, having two Cd ions adjacent to the vacancy, would occur with only a 4% chance (Fig. 1c), giving rise to a fraction that is too small to be observed under these experimental conditions. It is believed that these two adjacent metal sites have a greater influence on the observed field gradient because they are the only ones of the 12 next-nearest neighbor sites which share a Te bond with both the indium probe and the vacancy. Other PAC work on II-VI compounds has shown that the field gradient is oriented in the bond direction,  $\langle 111 \rangle$ ,

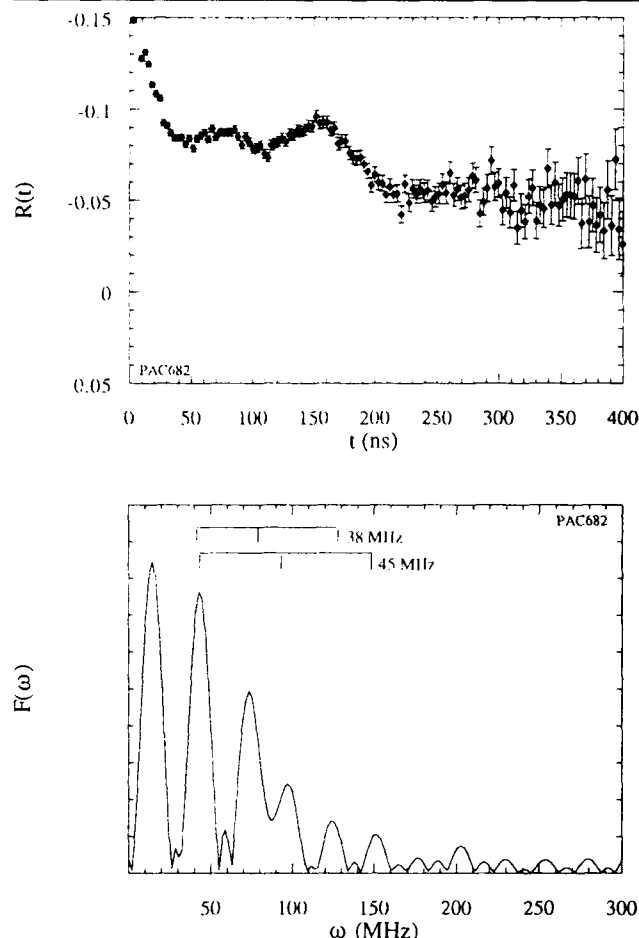


Fig. 3. (top)  $R(t)$  spectrum for a sample of bulk  $\text{Hg}_{0.79}\text{Cd}_{0.21}\text{Te}$  annealed in boiling water for 6 h after the same treatment as in Fig. 2. (bottom) Fourier transform of  $R(t)$  shown in top panel.

rather than the defect direction,  $\langle 110 \rangle$ .<sup>20</sup> Therefore, it would seem the majority of the defect-related field gradient is associated with the electronic distribution about the Te atom shared by the donor and acceptor.

The fraction of In atoms having trapped vacancies increased when the samples were subjected to a secondary anneal near 100°C, presumably because of the migration of isolated vacancies. Following this secondary anneal, the fraction of In atoms which trap vacancies is increased to about 60% (Fig. 2). By measuring the fractions as a function of annealing time at various temperatures, a vacancy migration energy of 0.65 eV was obtained.<sup>21</sup>

The fraction of indium atoms involved in these defects is virtually unchanged when the sample is cooled to 20K. The interaction frequencies  $\nu_{Q1}$  and  $\nu_{Q2}$  shifted continuously and by only a small amount, an effect which is commonly observed by PAC. This indicates that there is no change in the charge state of the indium-vacancy defect complex between 20K and room temperature, since any change in charge state would lead to a large discrete change in the electric field gradient. Although the perturbation of the adjacent donor indium must be considered, this may provide some corroboration for the previously mentioned positron lifetime measurements.<sup>4</sup>

### Hydrogen

The influence of hydrogen on defect complexes in MCT was studied using a combination of PAC and electrical measurements. Hydrogen was introduced to the samples in a way similar to Ref. 14, by annealing in boiling deionized distilled water. Perturbed  $\gamma\gamma$  angular correlation spectra for samples which had been quenched from 350°C and aged around 100°C in vacuum to maximize the concentration of indium-vacancy pairs showed a sharp change after the introduction of hydrogen. The previous defect complexes, signified by  $\nu_{Q1}$  and  $\nu_{Q2}$ , completely vanished, and two new frequencies were observed. These new interaction frequencies were  $\nu_{Q3} = 35$  MHz,  $\eta_3 < 0.1$  and  $\nu_{Q4} = 43$  MHz,  $\eta_4 = 0.1$  (Fig. 3). These frequencies did not appear when unquenched samples having In- $\text{V}_{\text{Hg}}$  complexes were boiled, or in samples which were annealed in a flowing  $\text{O}_2$  atmosphere. Thus, we conclude that the new defects are associated both with the introduction of hydrogen and the prior presence of vacancies.

Table I. Results of Hall Effect Measurements for Te-Melt LPE Grown Thin Film Samples of  $\text{Hg}_{0.7}\text{Cd}_{0.3}\text{Te}$

| Sample Treatment  | Type | Carrier Conc. ( $\text{cm}^{-3}$ ) | Mobility ( $\text{cm}^2/\text{Vs}$ ) | Resistivity ( $\Omega\text{-cm}$ ) |
|---|------|------------------------------------|--------------------------------------|------------------------------------|
| LPE Te-rich grown   | n    | $1.5 \times 10^{15}$               | 16300                                | 0.26                               |
| Quenched from 350°C and aged at 100°C                             | p    | $4.3 \times 10^{16}$               | 300                                  | 0.49                               |
| Annealed in boiling water   | p    | $2.5 \times 10^{17}$               | 120                                  | 0.21                               |
| Quenched from 350°C, aged at 100°C, and annealed in boiling water | p    | $5.6 \times 10^{17}$               | 150                                  | 0.07                               |

Note: Samples were doped in growth with  $3 \times 10^{15} \text{ cm}^{-3}$  stable In atoms. Measurements done at 77K with 5kG field.

Hall effect measurements performed at 77K using the van der Pauw method show that the introduction of hydrogen causes the conversion of n-type samples to p-type (Table I). In  $3 \times 10^{15} \text{ cm}^{-3}$  indium doped thin films, an electron carrier concentration of the order of  $10^{15} \text{ cm}^{-3}$ , was observed. After hydrogenation, a p-type carrier concentration of  $2.5 \times 10^{17} \text{ cm}^{-3}$  was observed. This exceeded the carrier concentration in samples annealed at 350°C and vacuum quenched to create large numbers of vacancies. Thus, it seems that hydrogen introduced in this manner is an acceptor. The H-related defect complex is also found to be stable after annealing below 150°C, at which point all the defects break up and the In atoms are returned to nearly cubic sites (Fig. 4).

Secondary ion mass spectroscopy (SIMS) and ion beam nuclear reaction analysis (NRA) were used to determine the amount of hydrogen incorporated during the boiling. Secondary ion mass spectroscopy measurements showed that deuterium was present throughout a sample boiled in  $\text{D}_2\text{O}$ , while in an unboiled sample the hydrogen concentration was too small to measure. These measurements also showed some incorporation of oxygen into the MCT, but at levels 2–3 orders of magnitude smaller.

The NRA experiment used a 700 keV beam of  $^3\text{He}$  ions to give a resonant  $^3\text{He}(^2\text{H}, ^1\text{H})^4\text{He}$  reaction. Measurement of the emitted  $^4\text{He}$  allows determination of the absolute concentration of  $^2\text{H}$ . This method is described elsewhere in more detail.<sup>22</sup> Samples prepared using conditions similar to those in the SIMS experiments were found to have deuterium concentrations on the order of  $10^{17} \text{ cm}^{-3}$ . Thus, the hydrogen incorporation seems to be responsible for the large p-type conductivity observed. This level of hydrogen incorporation is much larger than would be expected considering recently published measurements of deuterium diffusion in MCT in which deuterium was introduced from  $\text{D}_2$  gas.<sup>23</sup> From the gas phase, a dissociation of the  $\text{D}_2$  molecule is first necessary, but a portion of deuterium in  $\text{D}_2\text{O}$  is already ionized, making it more reactive with the MCT. Therefore, boiling is apparently the more effective means of hydrogen incorporation.

## DISCUSSION AND CONCLUSIONS

We have used the PAC technique to study the interactions among In donors, Hg vacancies, and H impurities in MCT. Other standard experimental techniques such as SIMS, Hall effect, ion beam nuclear reaction analysis, and radiotracer diffusion measurements have been used to support conclusions made from the PAC data. These measurements have allowed us to correlate electronic effects with the microscopic defects which PAC best observes.

The trapping of mercury vacancies by In atoms was observed by PAC only in samples quenched from temperatures above 300°C, where the concentration of mercury vacancies is large. This trapping could be enhanced or reduced by adjusting the annealing conditions. The lack of any significant change in either

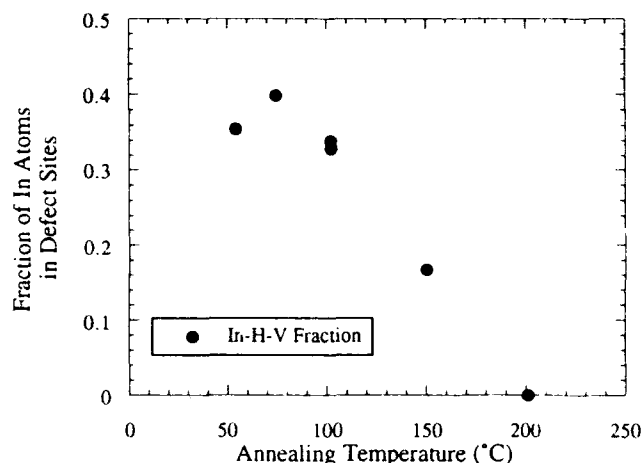


Fig. 4. Stability of  $\text{In-V}_{\text{Hg}}$ -H complexes (circle) as a function of annealing temperature.

$\text{In-V}_{\text{Hg}}$  concentration or the associated PAC frequencies with temperature from 20–300K indicates that the defect was stable over this temperature range and did not change its charge state, in agreement with positron lifetime data.<sup>4</sup>

Hydrogen was found to act mainly as an acceptor when introduced from boiling water, yet it was also found to interact strongly with the acceptor  $\text{In-V}_{\text{Hg}}$  complex, but not with the bare In donor. The exact mechanism of the interaction, including the position of the hydrogen with respect to the In atom and the  $\text{V}_{\text{Hg}}$ , is not yet fully known.

A possible explanation for the p-type activity of hydrogen in MCT is that a H interstitial donor pairs with a double acceptor vacancy. If we assume that the binding energy of a hydrogen interstitial to a metal vacancy is larger than that of a substitutional In to a vacancy, we can see that the introduction of hydrogen will serve to draw vacancies away from the In atoms. This would account for the destruction of In-V complexes after hydrogenation. Since the H-V pair acts as a net acceptor, this model also accounts for the large p-type conductivity of hydrogenated samples. However, it is not yet possible to determine the atomic structure of this H-V pair, that is, the exact position of the H atom with respect to the vacant metal site.

More work will be done with higher indium concentrations to test for the existence of different phases or means of compensation of the In donors at higher concentrations (i.e. formation of  $\text{In}_2\text{Te}_3$  or In clustering). Also, different stoichiometries of MCT will be used to determine the exact effect of varying combinations of metal atoms about the In probe atoms. Finally, work will be performed comparing the behavior of hydrogen to that of other impurities, particularly acceptors such as Cu, As, and Li.

## ACKNOWLEDGMENT

The work was supported by a grant from the U.S. Army Research Office. The authors would like to acknowledge Tse Tung of Santa Barbara Research Center and Herb Schaake and Luigi Columbo of

Texas Instruments for supplying samples. Thanks also go to Gari Harris of the Microelectronics Center of North Carolina for the SIMS measurements, Gil Fountain of Research Triangle Institute for part of the Hall effect measurement, and to Ray Zuhr of Oak Ridge National Lab for Nuclear Reaction Analysis. Finally, thanks to John Gardner of Oregon State for helpful discussions of the defect model for the In-V pair.

## REFERENCES

1. H.R. Vydyanath, *J. Electr. chem. Soc.* 128, 2619 (1981).
2. V.I. Ivanov-Omskii, K.E. Mironov, K.D. Mynbaev and V.V. Bogoboyaschii, *Sov. Phys. Semicond.* 25, 857 (1991).
3. A.I. Elizarov, V.V. Bogoboyaschi and N.N. Berchenko, *Sov. Phys. Semicond.* 24, 278 (1990).
4. C. Gely, C. Corbel and R. Triboulet, *J. Phys. Condens. Matter* 2, 4763 (1990).
5. Y. Marfaing, *J. Vac. Sci. Technol. B* 10, 1444 (1992).
6. C. Uzan-Saguy, D. Lazer and R. Kalish, *J. Cryst. Growth* 101, 864 (1990).
7. V.I. Ivanov-Omskii, K.E. Mironov, K.D. Mynbaev and V.V. Bogoboyaschii, *Sov. Phys. Semicond.* 25, 857 (1991).
8. M. Boukerche, J. Reno, I.K. Sou, C. Hsu and J.P. Faurie, *Appl. Phys. Lett.* 48, 1733 (1986).
9. L. Svob, Y. Marfaing, F. Dejonqueres and R. Druilhe, *Physica B* 170, 550 (1991).
10. M.A. Foad, A.P. Smart, M. Watt, C.M. Sotomayor Torres and C.D.W. Wilkinson, *Electron. Lett.* 27, 73 (1991).
11. L. Svob, A. Heurtel and Y. Marfaing, *J. Cryst. Growth* 86, 815 (1988).
12. A.I. Evstigneev, V.F. Kuleshov, G.A. Lubochkova, M.V. Pashkovskii, E.B. Yakimov and N.A. Yarykin, *Sov. Phys. Semicond.* 19, 562 (1985).
13. Y.F. Chen and W.S. Chen, *Appl. Phys. Lett.* 59, 703 (1991).
14. Th. Wichert and E. Recknagel, *Microscopic Methods in Metals*, Vol. 40 of *Topics in Current Physics*, ed. U. Gonser (Springer, Berlin, 1986), p. 317.
15. R. Kalish, M. Deicher and G. Schatz, *J. Appl. Phys.* 53, 4793 (1982).
16. J.C. Austin, M.L. Swanson, W.C. Hughes, C.T. Kao, L.M. Slifkin, H.C. Hofsass and E.C. Frey, *Phys. Rev. B* 42, 7699 (1990).
17. Th. Wichert, H. Skudlik, M. Deicher, G. Grubel, R. Keller, E. Recknagel and L. Song, *Phys. Rev. Lett.* 59, 2087 (1987).
18. D. Shaw, *Phys. Status Solidi (a)* 89, 173 (1985).
19. W.C. Hughes, M.L. Swanson and J.C. Austin, *Appl. Phys. Lett.* 59, 938 (1991).
20. Thomas Wichert, Thomas Krings and Herbet Wolf, to be published in *Physica B* (1993).
21. W.C. Hughes, M.L. Swanson and J.C. Austin, *Nucl. Instr. and Meth. B* 63, 244 (1992).
22. S.M. Myers, S.T. Picraux and R.E. Stoltz, *J. Appl. Phys.* 50, 5710 (1979).
23. L. Svob and Y. Marfaing, *Mat. Sci. Forum* 65-66, 181 (1990).

# Electrical Effects of Dislocations and Other Crystallographic Defects in $\text{Hg}_{0.78}\text{Cd}_{0.22}\text{Te}$ n-on-p Photodiodes

R.S. LIST

Texas Instruments Incorporated, Central Research Laboratories,  
Dallas, TX 75265

An understanding of the effects of dislocations in HgCdTe diodes is complicated by several issues such as the diode architecture, diode formation process, and the thermal history and location of the dislocations. To help decouple the effects of these factors, high stress films were used to lithographically introduce dislocations<sup>1</sup> with different densities and locations during the fabrication process of ion implanted, n-on-p diodes. Both array and diode test structures were studied. After fabrication, the diodes were characterized with variable temperature I-V measurements and noise measurements. The diodes were then stripped and defect etched to quantify the density and distribution of the dislocations. The effects of these process-induced dislocations were analyzed and compared to the effects of as grown dislocations, subgrain boundaries and dislocations in other device architectures reported in the literature.<sup>1,2</sup> In general, high densities of either as grown or process-induced dislocations in n-on-p, ion implanted diodes severely degrade device performance by producing field dependent dark current. At 77K, dislocation densities greater than the mid  $10^6 \text{ cm}^{-2}$  can produce dark current densities in excess of the diode diffusion current. Dislocations located near the outer periphery of the diode produce approximately ten times the dark current of interior dislocations. Grain boundaries, sub-grain boundaries, and twins also produce sufficient field dependent dark current to limit diode performance at 77K. The dark current produced by dislocations is nearly temperature independent, suggesting rather severe limitations on dislocation densities for low temperature diode operation.

**Key words:** Dislocations, HgCdTe, ion-implanted n-on-p photodiodes, stress effects

## INTRODUCTION

An understanding of the effects of defects in  $\text{Hg}_{0.78}\text{Cd}_{0.22}\text{Te}$  is important not only because of their relatively high density compared to other more mature semiconductor materials, but also because the narrow band gap of  $\text{Hg}_{0.78}\text{Cd}_{0.22}\text{Te}$  cannot mask even minor perturbations associated with defects. There is a large body of literature on the effects of dislocations in conventional wider band gap materials.<sup>3-8</sup> Only a few papers have previously been written on the effects of microstructure and dislocations on electrical device performance, most frequently directed toward metal insulator semiconductor (MIS) structures.<sup>1,9-15</sup> Last year's conference proceedings included an excellent study of the effects of dislocations on p-on-n double

layer heterojunction diodes<sup>2</sup> which is referred to frequently throughout the text of this paper. It is the intent of this investigation to establish a more general perspective of the electrical effects of dislocations in  $\text{Hg}_{0.78}\text{Cd}_{0.22}\text{Te}$  diode devices. Specifically, issues concerning the distinction between dislocations with different thermal histories, different spatial locations within the diode, and different architectural environments are explored.

To address these diverse issues, several different experimental test vehicles were employed. All the experimental structures were grown on nominally 10 micron cut-off wavelength long wave infrared (LWIR) material employing a planar, boron ion implanted n-on-p diode formation process. Test structures on liquid phase epitaxy (LPE) material with variable densities of lithographically defined dislocations<sup>1</sup> were employed for detailed temperature dependent mea-

(Received November 3, 1992; revised January 21, 1993)



surements. Array structures on LPE material with specially chosen high as-grown dislocation densities as well as precisely located lithographically defined dislocations provided a statistical base for quantifying the effects of dislocations. Finally, solid state recrystallized material with exceptionally high densities of grain and sub-grain boundaries was used to

fabricate test structures to examine the effect of these defects. In total, temperature dependent current-voltage, capacitance-voltage, noise, quantum efficiency, and laser beam induced current measurements were performed.

### TEST STRUCTURES

The test structures employed in this study used high stress tantalum films to lithographically define regions of high dislocation density. Details of the technique used to fabricate such structures can be found in the literature.<sup>1</sup> The variably dislocated structures along with undislocated controls were located adjacent to each other on the same film of  $\text{Hg}_{0.78}\text{Cd}_{0.22}\text{Te}$  to remove any systematic material or processing variations. The data presented in Figs. 1, 2, 3, and 4 are from a single slice of  $\text{Hg}_{0.78}\text{Cd}_{0.22}\text{Te}$  with a cutoff wavelength of 9.8  $\mu\text{m}$ . These test structure diodes were  $125 \times 150 \mu\text{m}$ . Six other slices exhibited similar data. Figure 1 exhibits typical results of the defect etches of the  $\text{Hg}_{0.78}\text{Cd}_{0.22}\text{Te}$  beneath each of three distinct diode types with variable densities of lithographically induced dislocations. The most severely dislocated diodes, hereby referred to as severe, were formed by lithographically defining high stress tantalum films coincident with the ion implanted regions. The moderately heavily dislocated diodes, hereby referred to as heavy, used high stress tantalum films covering all regions not receiving the ion implant. The control diodes were not exposed to any high stress tantalum films during processing. There is a large gradient in the dislocation density in the diodes with lithographically defined dislocations. The highest stresses of the tantalum film occur at the outer edge of the diode for both the heavy and severe structures, and this not surprisingly corresponds to the highest dislocation density, at least  $1 \times 10^8 \text{ cm}^{-2}$ . The severe structures have a wider band of high dislocation density, averaging approximately  $2.5 \times 10^7 \text{ cm}^{-2}$  over the entire area of the diode, while the heavy structure averages only about  $1 \times 10^7 \text{ cm}^{-2}$ . The control structures have a uniform dislocation density of approximately  $5 \times 10^5 \text{ cm}^{-2}$ . Approximately 100 diodes of each of the three types were fabricated and measured before being defect etched.

The most obvious effect of dislocations is to increase the diode dark current. A plot of the dark current density vs inverse temperature can potentially yield insight into the dislocation dark current mechanism. Figure 2 exhibits the dark current density vs inverse temperature at two different biases for all three diode types. The low bias curves are more sensitive to diffusion currents while the high bias curves accentuate the tunneling currents. Several conclusions can be drawn from these plots. At high temperatures (above 100K) and low bias (10 mV), the three curves nearly converge to the same dark current densities. It is clear from the near  $\text{Hg}_{0.78}\text{Cd}_{0.22}\text{Te}$  band gap slope of the control curve that its dominant dark current is diffusion current. This implies that dislocations do not significantly increase the diode diffusion current.

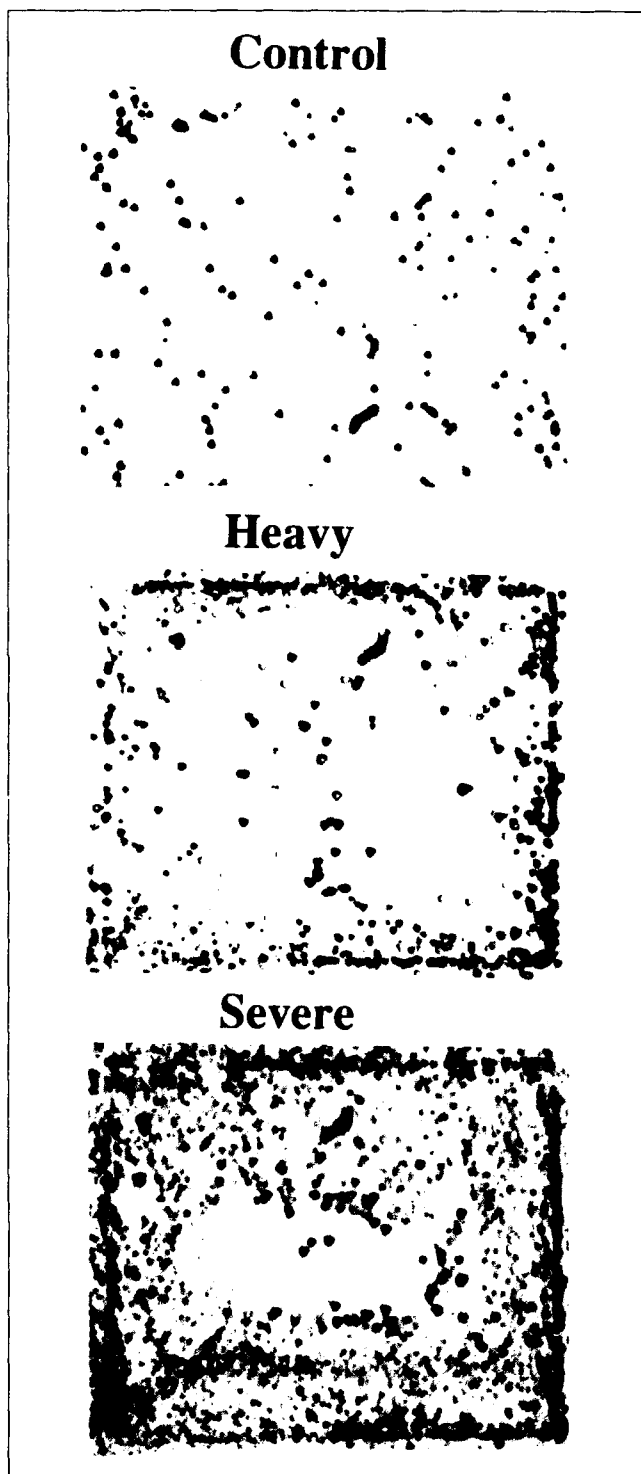


Fig. 1. Defect etches of  $\text{Hg}_{0.78}\text{Cd}_{0.22}\text{Te}$  beneath the three types of test structures: control, heavy, and severe structures. Diode dimensions are  $125 \times 150 \mu\text{m}$ .

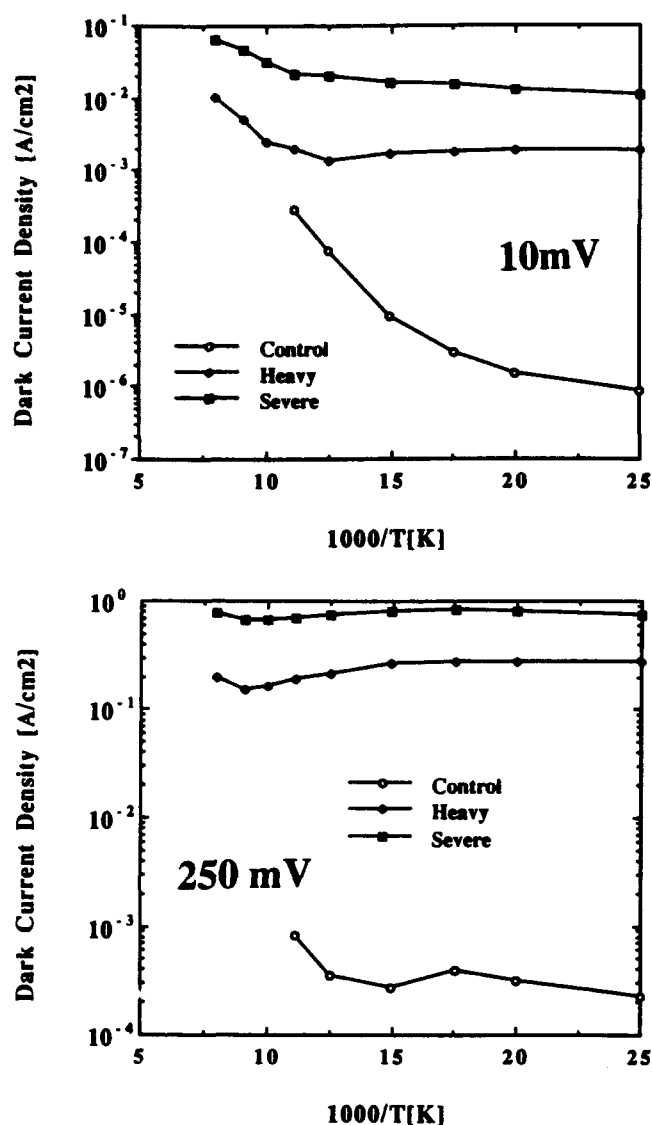


Fig. 2. Dark current density vs  $1000/T$  for the three test structure types at biases of both 10 mV and 250 mV.

On the other hand, at low temperatures (below 50K) and low bias (10 mV), there is a three to four order of magnitude decrease in the dark current associated with the control diodes while that associated with the dislocated diodes is nearly constant. The consistency of the dislocation induced dark current throughout the entire temperature range suggests that the dark current has no appreciable activation energy. The lack of a significant activation energy would exclude both diffusion and G-R currents as possible dominant dislocation induced dark current sources. However, it should be noted that it is difficult to completely exclude G-R current as a major dislocation induced dark current in the 100 to 120K transition region between diffusion and tunneling current. Higher quality data and rigorous fitting would be required to definitively resolve this issue.

The dark currents for all three diode types at a 250 mV bias are nearly temperature independent, implying a tunneling dominated dark current interpreta-

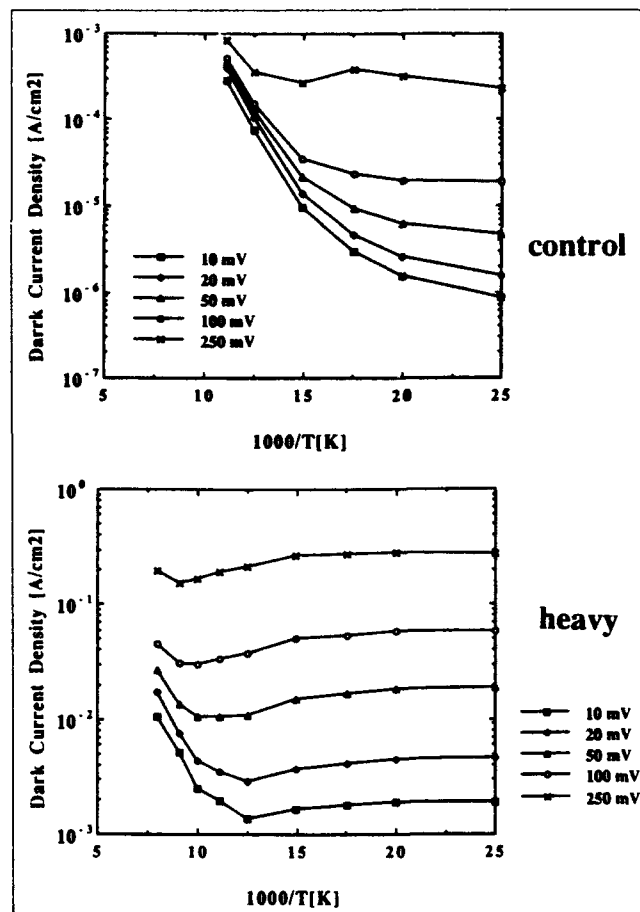


Fig. 3. Dark current densities vs  $1000/T$  and bias for both control and heavy structures.

tion. The three to four order of magnitude offset between the control and dislocated diodes for all temperatures at a 250 mV bias is equal to the offset at 10 mV bias and 40K. This supports the interpretation that all three diode types are tunnel limited at 40K with a 10 mV bias.

In addition to focusing on the temperature dependence of the dark current, it is useful to consider the bias dependence of the dark current in more detail. With the simplest possible assumptions, diffusion current should be independent of diode bias, G-R current should increase as the square root of the bias and tunneling current should increase exponentially with the applied bias. Figure 3 shows the temperature and bias dependence of the dark current of the control and heavy structures. The dark current of the control structure at 80K has very little bias dependence verifying that it is diffusion limited. At 40K, the control exhibits extremely strong nearly exponential bias dependence, verifying a tunneling mechanism. The bias dependence of the heavy structure is less easily interpreted. Between temperatures of 80 and 125K for a 10 mV bias and between temperatures of 100 and 125K for a 50 mV bias, the dark current has a weak, nearly square root bias dependence suggestive of G-R limited dark current. The G-R like dark current appears to become masked by a

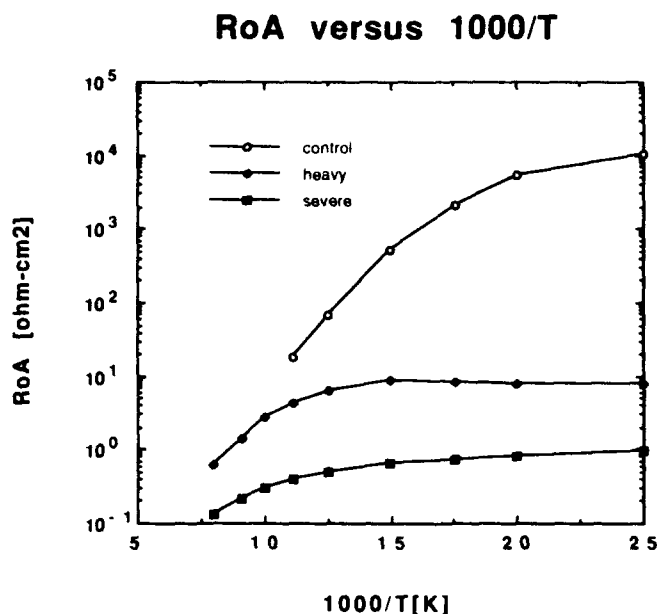


Fig. 4. Dynamic impedance at zero bias,  $R_0A$ , vs  $1000/T$  for control, heavy, and severe structures.

more bias dependent, less temperature sensitive dark current as either the temperature is decreased or the bias is increased. This behavior is consistent with the dominance of tunneling current at high bias and low temperature; however, the observed bias dependence is only slightly superlinear and weaker than the low temperature bias dependence of the control. The dark current of the heavy structures at low temperatures have between a linear and quadratic bias dependence while the severe structures have very nearly a linear bias dependence. This nonexponential, nearly linear bias dependence of the tunneling current from dislocations suggests some type of saturation mechanism. The clear increase in dark current with decreasing temperature below the G-R like region is a manifestation of the decrease in the  $\text{Hg}_{0.78}\text{Cd}_{0.22}\text{Te}$  band gap with decreasing temperature. This increase in dark current with decreasing temperature for all biases clearly removes any thermally assisted mechanisms from consideration.

To quantitatively compare the above effects of dislocations in planar, ion implanted n-on-p diodes with those in the literature<sup>2</sup> for p-on-n double layer heterojunction devices, it is useful to present the dynamic impedance at zero bias,  $R_0A$ . Figure 4 presents the  $R_0A$  of typical severe, heavy and control structures as a function of inverse temperature. These plots are very nearly the inverse of the dark currents at 10 mV bias and can be interpreted in an identical manner. Specifically, at temperatures above about 100K, all diode types have comparable  $R_0A$ s which appear to be limited by diffusion current. At lower temperatures, the control diode  $R_0A$  increases by nearly four orders of magnitude due to a drop in diffusion limited dark current. An additional two order of magnitude increase in low dislocation density  $R_0A$  can be obtained with the use of more advanced passivation processes. On the other hand, the  $R_0A$ s

associated with the dislocated diodes is nearly independent of temperature due to the temperature independence of the tunneling dark current. This imposes severe constraints on the dislocation density for low temperature operation.

If a comparison is made between the above  $R_0A$ s and those for p-on-n diodes in the literature,<sup>2</sup> one finds nearly identical temperature and dislocation density dependence. For both architectures, the diodes with low dislocation densities have  $R_0A$ s which increase rapidly with decreasing temperature. In both cases, diodes with dislocation densities in the mid  $10^3 \text{ cm}^{-2}$  range have  $R_0A$ s of approximately 3 to 10 and 3000 to 10000 ohm-cm<sup>2</sup> at 100K and 40K, respectively. Similarly, diodes of both architectures with dislocation densities in excess of  $1 \times 10^7 \text{ cm}^{-2}$  have nearly temperature independent  $R_0A$ s of less than 10 ohm-cm<sup>2</sup>. The similarity in the effects of dislocations in such vastly different architectures suggests a common origin for the dark current mechanisms. This mechanism is probably trap assisted tunnel-tunnel processes which depend only upon dislocation induced trap states in the n-p junction region. Such a mechanism should be active only if a dislocation actually intersects the p-n junction. It should also be more sensitive to dislocations which intersect the junction and are nearly parallel to it compared to dislocations which intersect the junction perpendicularly. This is based simply on a consideration of maximizing the geometrical overlap between the dislocation and junction. To investigate these properties, it is necessary to consider diodes with much more precisely introduced dislocations.

### ARRAY STRUCTURES

As a result of the local variations in the  $\text{Hg}_{0.78}\text{Cd}_{0.22}\text{Te}$  yield strength and the stress levels of the high stress films employed for forming dislocations, it is difficult to exactly and reproducibly control the distribution of dislocations produced by high stress films, especially in the limit of low dislocation densities. To effect the ability to lithographically introduce dislocations with exacting positions and densities, one can use the material variations to his advantage by employing the combination of slightly sub-yielding stress levels and a large number of potentially yielding diodes. With this approach, most of the diodes will not exhibit process induced dislocations, but a few will manifest a range of dislocation densities including exceedingly low densities located precisely at the discontinuity of the high stress film.

The above approach was employed using a  $64 \times 64$  array with discontinuous high stress film edges coincident with the implanted diode region. In addition, the starting material exhibited a very wide range of dislocation densities to facilitate comparisons between the effects of as grown and process-induced dislocations on diode performance. Of the 4096 diodes, only approximately 300 exhibited dislocations induced by the high stress films, and of those, only about 50 had sufficiently localized distributions of

dislocations to permit quantitative evaluations. This array had a 77K cutoff wavelength of  $9.7\text{ }\mu\text{m}$  and a pixel diode area of  $1800\text{ }\mu\text{m}^2$ .

Any attempt to quantify the effects of dislocations intrinsic to the high temperature material growth process by studying dislocations introduced during low temperature device fabrication must first establish their electrical equivalence. As-grown dislocations may have very different densities of defects, traps, and impurities compared to process induced dislocations due to their much higher annealing temperatures. To establish the effects of randomly distributed as-grown dislocations, etch pit counts were performed on 400 diodes which did not exhibit any process induced dislocations. These diodes were especially chosen from the area of the array with the highest as-grown dislocation density. Figure 5 presents plots of the dark current density of each diode vs their etch pit count for three different biases. Most of the diodes had fewer than 10 dislocations, corresponding to dislocation densities less than  $6 \times 10^5\text{ cm}^{-2}$ . However, many diodes had between 50 and 150 dislocations. There is a very large amount of scatter in the dark current in Fig. 5. Some of the reasons for the scatter will be discussed later. However, the minimum dark current associated with any given number of dislocations appears to increase linearly with the number of dislocations. The slope of this lower threshold line is similar to that obtained from a least squares fit to all the data. In addition, the amount of dark current per dislocation also appears to be linearly related to the diode bias as manifested by the linear increase in slope of the lower threshold line with increasing bias. From these plots, one would conclude that each as-grown dislocation produces a minimum dark current of 8 pA per mV of bias at 77K. If a diffusion limited dark current of approximately  $200\text{ }\mu\text{A}/\text{cm}^2$  is assumed, or inferred from the graph, this implies that the dislocation dark current will be equivalent to the diffusion current at a dislocation density of  $3 \times 10^6\text{ cm}^{-2}$  for a diode operated at a bias of 10 mV. For cutoff wavelengths below  $9.7\text{ }\mu\text{m}$ , biases greater than 10 mV or lower temperature operation, the limiting dislocation density would be less than  $3 \times 10^6\text{ cm}^{-2}$ .

The high stress discontinuous films in the array produced a variety of dislocation distributions, several of which are presented in Fig. 6. It should be noted that several comparable examples of each of these distributions were apparent on the array. Figure 6a shows a control diode which had no process induced dislocations and seven as-grown dislocations. This was the most commonly occurring dislocation distribution. It had a dark current at 10 mV bias of 3.97 nA. The next most common dislocation distribution is shown in Fig. 6b. The edges of the high stress film created several clusters of extremely dense dislocations. The dark current from this diode exceeded the measurement capability of the test set, i.e. it was greater than 60 nA. Even much smaller clusters of process induced dislocations at the edge of the diode

such as those shown in Fig. 6c could produce dark currents exceeding 60 nA. This diode had approximately 30 perimeter process-induced dislocations, 20 interior process-induced dislocations, and 25 interior as-grown dislocations. Figure 6d demonstrates that

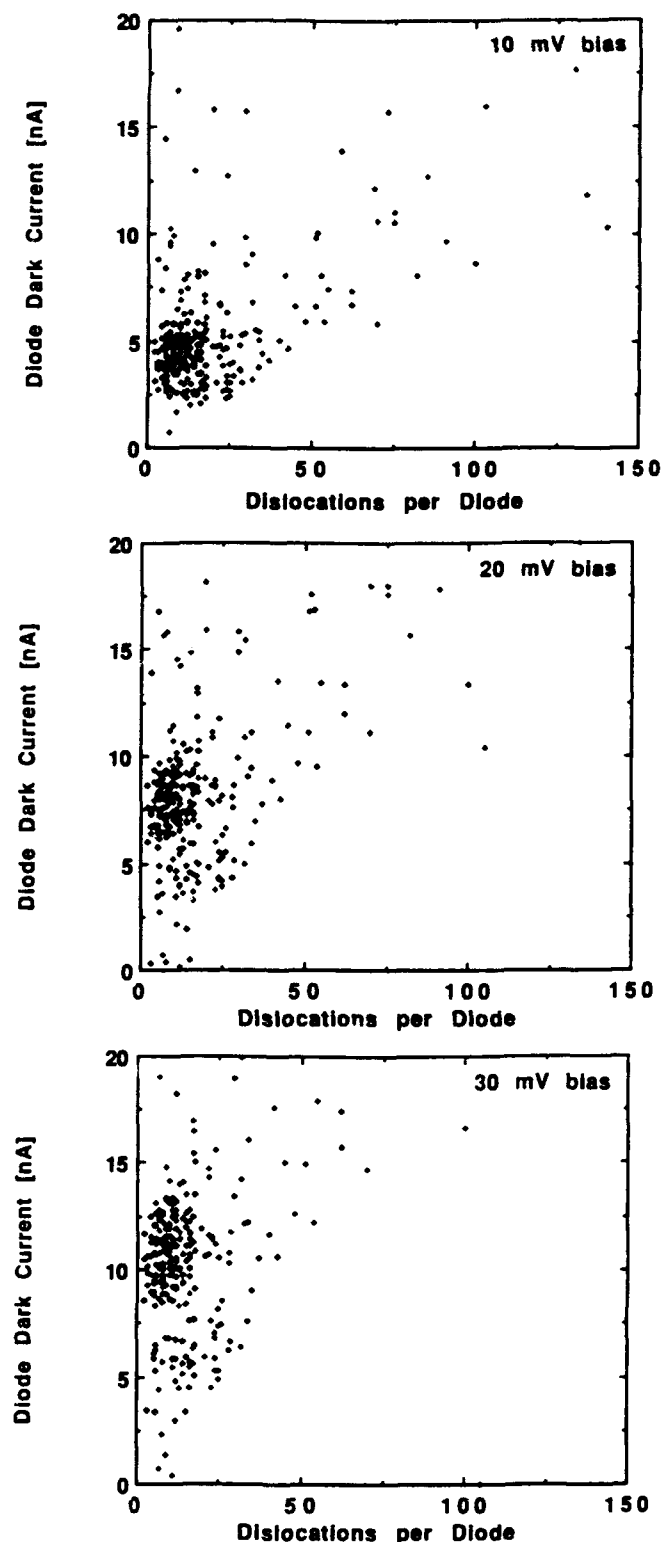


Fig. 5. Dark current vs number of dislocations for isolated as-grown dislocations in array structures at biases of 10, 20, and 30 mV at 77K.

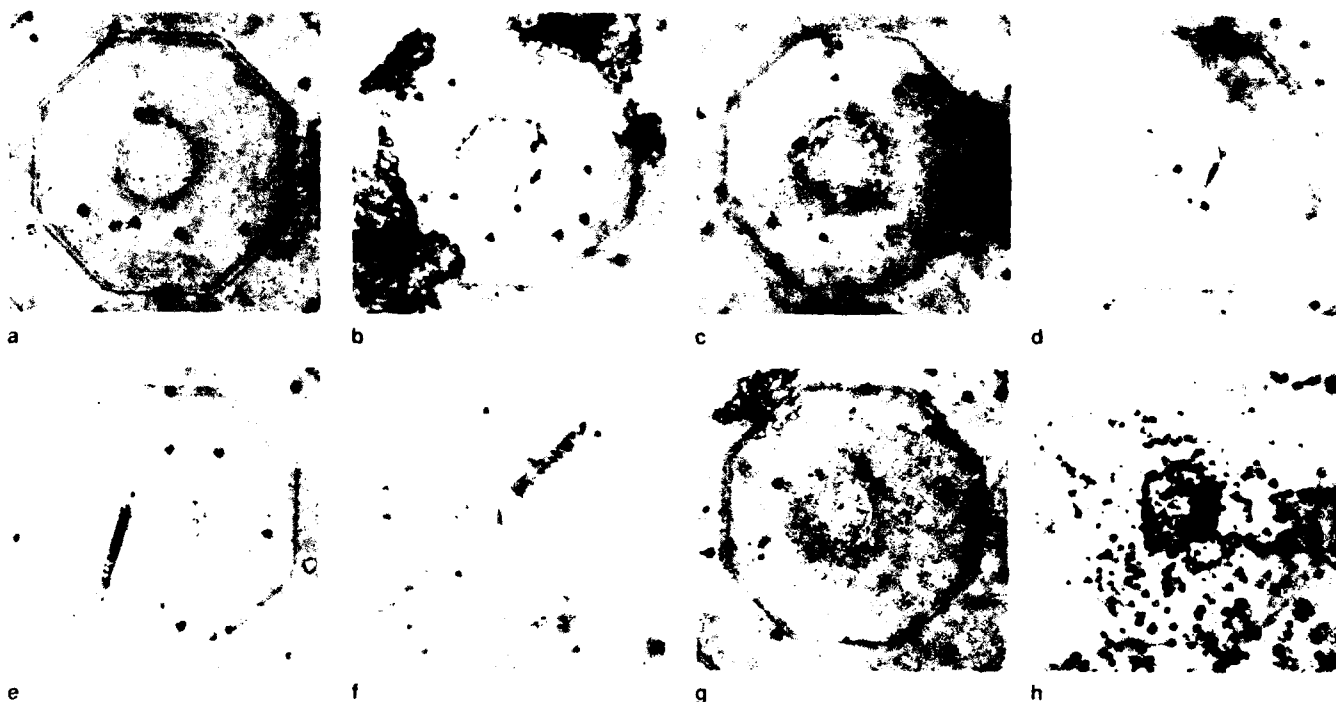


Fig. 6. Defect etches of the  $\text{Hg}_{0.75}\text{Cd}_{0.25}\text{Te}$  beneath array diodes with a variety of dislocation distributions including: (a) control, (b) extremely dense process-induced dislocation clusters, (c) small cluster of process-induced dislocations located at the perimeter of the diode, (d) 15 perimeter process-induced dislocations, (e) process-induced single slip line, (f) two process-induced slip lines, (g) dense exterior cluster of process-induced dislocations, and (h) high density of isolated as-grown dislocations

as few as 15 dislocations can produce excessive dark current if they happen to be concentrated near the diode perimeter. It had 15 perimeter process-induced dislocations, and five interior as-grown dislocations and a dark current of 26.5 nA.

From the above examples, one could attribute the high dark current of the process-induced dislocations either to their intrinsic unannealed nature or to their preferential location near the outer perimeter of the diode. This perimeter location would enable the dislocation to intersect the p-n junction at an angle nearly parallel to it, thereby fulfilling the condition described at the end of the test structure section. To differentiate between these two possibilities, it is useful to examine other process-induced dislocation distributions. In particular, the high stress film can initiate the formation of slip lines which are not confined to the high stress perimeter of the diode but instead propagate along the natural slip directions of the  $\text{Hg}_{0.75}\text{Cd}_{0.25}\text{Te}$  into the interior of the diode. Figures 6e and 6f show such distributions of dislocations. Figure 6e has a single slip line segment in its interior consisting of approximately 25 dislocations in addition to the seven interior as-grown dislocations. This diode has a dark current of only 4.54 nA, significantly less than the 6 nA which would be predicted. This prediction is based on a minimum dark current of 80 pA/dislocation at 10 mV bias in addition to the background diffusion current of 3.5 nA. Similarly, Fig. 6f exhibits a diode with two closely spaced parallel slip line segments which jointly contain 45 dislocations in addition to 18 interior as-grown dislocations. Again

the measured diode dark current of 4.73 nA is much less than the 8.5 nA which would be predicted. These results imply that process-induced dislocations do not intrinsically produce more dark current than as-grown dislocations. In fact, these results suggest that the dark current per dislocation for process-induced, interior dislocations at extremely high local densities such as encountered in slip lines tends to decrease as the density is increased. This can possibly be explained by a reduction in the G-R depletion volume per dislocation as the dislocation density becomes very large. This result is also opposite to that reported in the literature.<sup>4</sup> The reason for this discrepancy is unclear but may be related to the difference between perimeter and interior dislocations.

Two additional dislocation distributions are presented in Figs. 6g and 6h. Figure 6g shows a diode with 13 interior as-grown dislocations, four process-induced perimeter dislocations, and approximately 100 process-induced dislocations just outside the diode region. It has a dark current at 10 mV bias of 7.30 nA, which is what would be expected from the interior dislocations alone, which suggests that external dislocations have almost no effect on the diode dark current. Similar independence of the diode dark current on exterior dislocations was found in test structures. Figure 6h portrays a diode with 203 as-grown interior dislocations. It has 21.67 nA of dark current, which is very close to the value of 20 nA predicted from the trend line for isolated as-grown dislocations.

The observations from the array structures have shed light on several fundamental characteristics of

dislocations. First, they show that the dark current attributable to a dislocation is an extremely strong function of the location of the dislocation within the diode. Dislocations within a few microns of, but not intersecting, the p-n junction have negligible effect on the diode dark current. Isolated interior dislocations which intersect the p-n junction along a line segment not too different in length from the depletion width produce approximately 8 pA/mV of bias. Interior dislocations with local densities exceeding mid  $10^7 \text{ cm}^{-2}$  produce less dark current per dislocation, possibly a result of the decreased effective depletion volume per dislocation for the G-R current at 77K. This saturation density also corresponds to that for which the piezoelectrically generated fields surrounding individual dislocations would start to overlap.<sup>16</sup> Perimeter dislocations appear to produce significantly more dark current than interior dislocations. This increased dark current could be attributable either to the increased geometric overlap with the p-n junction or the increased coupling with potential sources of surface charge. In an attempt to roughly quantify this effect, a perimeter dislocation was for convenience defined to be one with any portion of its etch pit intersecting the p-n junction. Since the etch pit diameters were roughly  $2 \mu\text{m}$  while the junction depletion widths were only a few tenths of a micron, this counting procedure would overestimate the number of perimeter dislocations and thereby underestimate their dark current. Figure 7 shows a plot of the dark current vs number of perimeter dislocations. This plot has a slope of approximately ten times that for isolated as-grown dislocations presented in Fig. 5. The dark current of the perimeter dislocations also appears to be approximately linear with bias implying a lower bound of dark current per perimeter dislocation of 80 pA/mV at 77K.

The dark current of process-induced dislocations was found to either greatly exceed in the case of perimeter dislocations or fall short in the case of interior clusters that of isolated, interior as-grown dislocations. For comparable densities and locations, as-grown and process-induced dislocations appear to have comparable levels of dark current.

In addition to dark current measurements, noise and quantum efficiency measurements were performed. In general, the rms noise of a diode appeared to be proportional to its dark current, hence dislocations indirectly increase the noise level. This behavior is similar to that reported in the literature for p-on-n DLHJ diodes.<sup>2</sup> Perimeter dislocations appear to be particularly noisy since they increase the noise level with dark current at a slope approximately 2.5 times that of other sources of dark current, including interior dislocations. This is possibly due to the stronger coupling of the near surface perimeter dislocations with the noise sources in the surface passivation layer. The quantum efficiency of the diodes appear to be independent of their dislocation density up to the maximum dark current levels measurable on the test set, 60 nA. This would correspond to isolated interior

dislocation densities up to the mid  $10^7 \text{ cm}^{-2}$  range. This was also observed for p-on-n DLHJ diodes.<sup>2</sup>

### EFFECTS OF MICROSTRUCTURE

In addition to dislocations, other crystallographic defects such as sub-grain boundaries, grain boundaries and twin boundaries can have major detrimental effects on diode performance. Figure 8 shows three test diodes with variable amounts of sub-grain microstructure. The three diodes have dimensions of  $50 \times 50 \mu\text{m}$ ,  $75 \times 75 \mu\text{m}$  and  $125 \times 150 \mu\text{m}$ , and a cutoff wavelength of  $9.5 \mu\text{m}$ . The  $50 \times 50 \mu\text{m}$  diode has no microstructure and serves as a convenient control. At 77K, it has a  $R_{\text{sh}}$  of  $114 \text{ ohm-cm}^2$  and dark current densities at 10 and 100 mV biases of 60 and  $79 \mu\text{A/cm}^2$ , respectively, which is nearly diffusion limited. The  $125 \times 150 \mu\text{m}$  diode has two fairly low angle grain boundaries and  $R_{\text{sh}}$ ,  $J(10\text{mV})$  and  $J(100\text{mV})$  values of  $122 \text{ ohm-cm}^2$ ,  $44 \mu\text{A/cm}^2$  and  $123 \mu\text{A/cm}^2$ , respectively. The  $R_{\text{sh}}$  and  $J(10\text{mV})$  values are similar to the control, while the  $J(100\text{mV})$  value is almost twice the control value, suggesting more bias dependent dark current. The  $75 \times 75 \mu\text{m}$  diode has a larger angle sub-

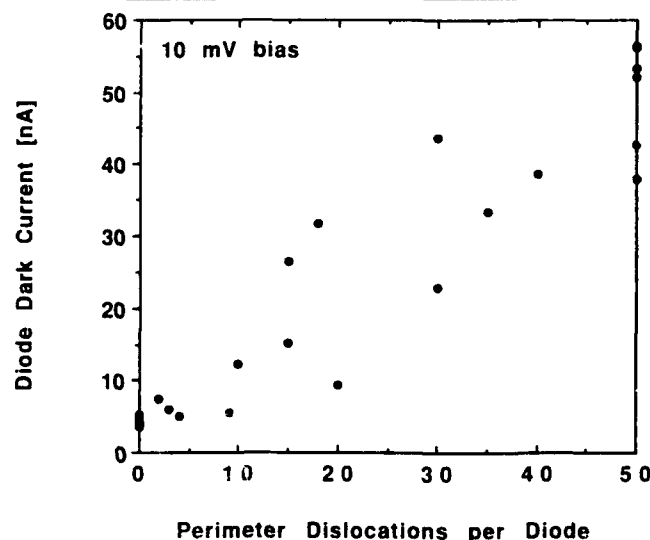


Fig. 7. Dark current vs number of dislocations for process-induced perimeter dislocations.

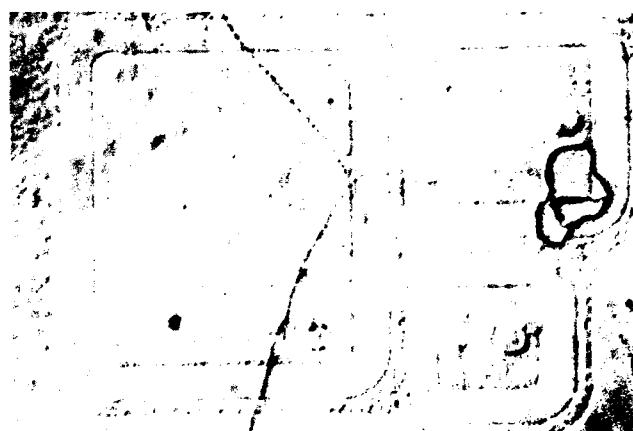


Fig. 8. Defect etch of SSR  $\text{Hg}_{0.78}\text{Cd}_{0.22}\text{Te}$  showing sub-grain boundaries passing through diode regions.

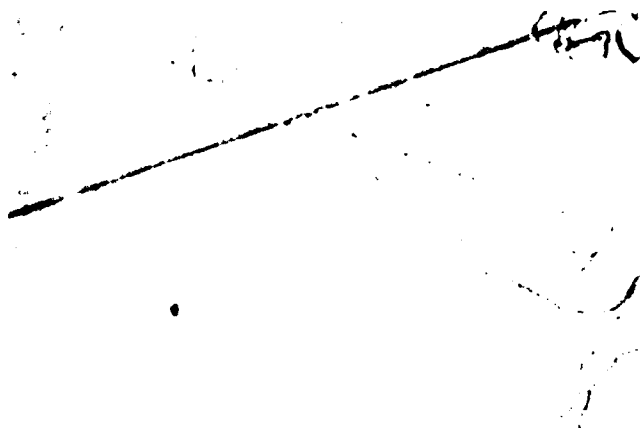


Fig. 9. Defect etch of SSR Hg-Cd-Te showing a grain boundary passing through diode regions.

grain boundary, based on its relatively greater etch pit density, in its interior which results in  $R_A$ ,  $J$  (10mV) and  $J$  (100mV) values of 28  $\text{ohm-cm}^2$ , 313  $\mu\text{A/cm}^2$ , and 1093  $\mu\text{A/cm}^2$ , respectively. This demonstrates that larger angle sub-grain boundaries can strongly affect the dark current both at high and low biases. Figure 9 shows a grain boundary intersecting both the  $75 \times 75 \mu\text{m}$  and  $125 \times 150 \mu\text{m}$  diodes and only a small angle sub-grain boundary intersecting the  $50 \times 50 \mu\text{m}$  diode. Both diodes with the grain boundary have  $R_A$ s of less than 1  $\text{ohm-cm}^2$  while the  $50 \times 50 \mu\text{m}$  diode has a  $R_A$  of 45  $\text{ohm-cm}^2$ . Hence, the amount of dark current associated with a grain or sub-grain boundary appears to be strongly dependent upon the angle of misorientation between the grains or sub-grains. The dependence of the sub-grain boundary dark current on both the angle of misorientation and bias are consistent with interpreting sub-grain and grain boundaries as simply an array of dislocations with a density proportional to the misorientation angle. It should be noted that the dark current per sub-grain boundary dislocation is severely depressed compared to that of isolated dislocations, just as it was for dislocations in process-induced slip lines.

Another interesting crystallographic defect is the twin boundary. Depending upon the perfection of the twinning, twin boundaries can have either few or many dislocations associated with them. Figure 10 displays examples of both these types of twin boundaries in diodes of the array geometry. Surprisingly, twin boundaries both with and without dislocations give rise to comparable amounts of dark current, approximately 20 nA per diode. This implies that the crystallographic defect of the twin itself is sufficient to greatly increase the diode dark current.

### DISCUSSION AND CONCLUSIONS

From the preceeding results, it is apparent that dislocations, sub-grain, grain, and twin boundaries all produce substantial amounts of dark current which can impact n-on-p diode device performance at 77K. Bias dependent studies show that isolated dislocations interior to the diode appear to produce approxi-



Fig. 10. Defect etch Hg-Cd-Te beneath array diodes showing double twin boundaries both decorated and undecorated with dislocations.

mately 8 pA/mV bias/dislocation at 77K. This would lead to dislocation limited dark current at 77K for dislocation densities greater than  $3 \times 10^7 \text{cm}^{-2}$ . Dislocations located along the perimeter of the diode produce at least ten times as much dark current per dislocation as those located in the diode interior, while dislocations which do not intersect the diode appear to have no effect on the diode dark current, even if they are located only a few microns from the p-n junction. Interior dislocations in clusters with densities exceeding the mid  $10^7 \text{cm}^{-2}$  appear to produce substantially less dark current per dislocation than isolated dislocations. Temperature dependent dark

current measurements reveal that at temperatures above 77K, the dislocation induced dark current has a moderate temperature dependence suggestive of G-R current. At temperatures below 77K, the dark current associated with dislocations appears to be nearly temperature independent, with only a slight increase in dark current at reduced temperatures. Dislocations appear to have no measurable effect on the diode diffusion current. This implies that dislocation-induced dark current will start to limit diode performance at low temperatures for dislocation densities substantially less than  $3 \times 10^6 \text{ cm}^{-2}$ . Dislocations appear to increase noise levels only indirectly through their increase in dark current, especially for perimeter dislocations. The quantum efficiency of photodiodes appears to be largely unaffected for dislocation densities less than the mid  $10^7 \text{ cm}^{-2}$  range. Nearly all the above results are consistent with measurements of the effects of dislocation in p-on-n diodes, with the exception of the dependence of dark current on the dislocation density.<sup>2</sup>

Nearly all of these results can be explained by a simple model. This model assumes that dislocations produce trap states which contribute the major tunnel-tunnel dark current at temperatures below 77K. Since no thermally activated processes are involved, the dark current is nearly temperature independent except for the slight decrease in  $\text{Hg}_{0.78}\text{Cd}_{0.22}\text{Te}$  band gap with decreasing temperature. Furthermore, only dislocations which intersect the p-n junction would produce traps effective for tunneling, and those which intersect the p-n junction at an angle nearly parallel to it (perimeter dislocations) would produce a greater number of effective trap states per dislocation than dislocations intersecting the junction at a nearly perpendicular angle (interior dislocations). Perimeter dislocations also intersect the junction in close proximity to a surface which could act as a source of dark current and noise. The presence of dislocation induced trap states in the p-n junction as well as the additional dark current associated with surfaces are common to both n-on-p and p-on-n architectures and can explain their similarities. At temperatures between 77K and 120K, one has the option of invoking G-R current as the dominant dark current mechanism. This explains the moderate bias and temperature dependence of the dark current in this temperature range, as well as the apparent decrease in dark

current per dislocation at extremely high dislocation densities. It is possible but more restrictive to propose that the apparent dislocation induced G-R current is simply a transition between the dislocation induced tunneling current and dislocation independent diffusion current. At higher temperatures, the dark current is masked by diffusion current which appears to be independent of the dislocation density. The transition temperatures of the above model are based on dislocation densities of  $1 \times 10^7 \text{ cm}^{-2}$  and diode biases of 10 mV. Higher dislocation densities or diode biases would increase the transition temperatures.

## ACKNOWLEDGMENT

The author would like to acknowledge several individuals for essential contributions, most notably Dave Fleming, Jenny Moore, Cora Fletcher, and Patty Benken for device fabrication and Rich Schiebel, Roger Strong, Joyce Wright, Doug Mercer, Dwight Bartholomew, Bryan Seymour, and Henry Bradford for electrical characterizations.

## REFERENCES

1. R.S. List, *J. Vac. Sci. Technol. B* 10, 1651 (1992).
2. S.M. Johnson, D.R. Rhiger, J.P. Rosbeck, J.M. Peterson, S.M. Taylor and M.E. Boyd, *J. Vac. Sci. Technol. B* 10, 1499 (1992).
3. H.J. Queisser, *Defects in Semiconductors*, Proc. Mater. Res. Soc. Symp., eds. S. Mahajan and J.W. Corbett (Elsevier, New York, 1983), vol. 14, p.323.
4. P.R. Wilshaw and T.S. Fell, *Inst. Phys. Conf. Ser.* 104, 85 (1989).
5. *Defect Electronics in Semiconductors*, ed. H.F. Matare, (Wiley-Interscience, New York 1971), p. 442.
6. Henry Kressel, *Semiconductors and Semimetals*, (Academic Press, New York, 1981) vol.16, p.1.
7. R.G. Rhodes, *Imperfections and Active Centres in Semiconductors* (Pergamon, New York, 1964).
8. S.R. Morrison, *Grain Boundaries in Semiconductors*, eds. Pike, Seager and Leamy (Elsevier, New York, 1982), p. 193.
9. J.H. Tregilgas, T.L. Polgreen and M.C. Chen, *J. Cryst. Growth* 86, 460 (1988).
10. P.W. Norton and A.P. Erwin, *J. Vac. Sci. Technol. A* 7, 503 (1989).
11. H.F. Schaake and A.J. Lewis, *Mater. Res. Soc. Symp. Proc.* 14, 301 (1983).
12. A.J. Syllais and L. Columbo, *Proc. IEDM Conf. 1982*, (IEEE, New York, 1982), p. 137.
13. L. Columbo and A.J. Syllais, *Proc. IEDM Conf. 1983*, (IEEE, New York, 1983), p. 718.
14. D. Chandra, J.H. Tregilgas and M.W. Goodwin, *J. Vac. Sci. Technol. B* 9, 1352 (1991).
15. H. Takigawa, T. Akamatsu, T. Kanno and R. Tsunoda, *Proc. IEDM Conf. 1981* (IEEE, New York, 1981), p. 172.
16. H. Booyens and J.H. Basson, *Phys. Status Solidi A* 85, 243 (1984).



# Large Improvement in HgCdTe Photovoltaic Detector Performances at LETI

G. DESTEFANIS and J.P. CHAMONAL

LETI (CEA-Technologies Avancées), DOPT-CEN/G-85 X,F38041 Grenoble Cedex, France

The standard infrared photovoltaic technology developed for HgCdTe by LETI and industrialized by SOFRADIR is based on the very simple approach of planar ion-implanted n-on-p homojunctions. Both the growth by liquid-phase epitaxy of excellent-quality epitaxial layers and the simplicity of the planar ion-implanted process enables state-of-the-art detectors to be achieved with a high technological yield. These detectors present high shunt impedance, good quantum efficiency, and a low  $1/f$  noise level. The diodes are diffusion-limited down to temperatures much lower than 77K. Their saturation current is limited by the minority-carrier lifetime in the p-side material.  $R_0A$  values around 30 ohm-cm<sup>2</sup> are routinely obtained for 10.0  $\mu$ m cutoff wavelength detectors at 77K. In this paper, we show that with a new process we can increase the diode  $R_0A$  by more than one order of magnitude. This effect is obtained as a result of an increase of minority-carrier lifetime in the n-on-p homojunction configuration. The maximum  $R_0A$  value obtained was 655 ohm-cm<sup>2</sup> on a 10.0  $\mu$ m cutoff wavelength detector at 77K. Furthermore, other figures of merit such as quantum efficiency or shunt impedance are slightly improved, and  $1/f$  noise is not affected. The data presented in the 40–200K temperature range and 9–13  $\mu$ m cutoff wavelength range show that this decrease of dark current is kept throughout these temperature wavelength ranges. Therefore, we show that a simple planar ion-implanted homojunction can lead to very large  $R_0A$ , close to theoretical limits and comparable to data published for p-on-n heterojunctions.

**Key words:** HgCdTe, ion implantation,  $1/f$  noise, liquid-phase epitaxy, minority-carrier lifetime, photovoltaic detectors, planar homojunctions

## INTRODUCTION

The most commonly used technique for fabricating infrared photovoltaic detectors in mercury cadmium telluride is to make simple n-p homojunctions by ion implantation in undoped crystals. Many bibliographical references can be found.<sup>1,2,9,11</sup> The emergence in the last ten years of high-quality thin epitaxial layers grown by liquid-phase epitaxy (LPE) on the Te-rich side<sup>3</sup> enabled backside-illuminated focal-plane arrays with increasing complexities<sup>4</sup> to be achieved. Proper control of surface passivation, stoichiometric equilibrium, ion implantation, and annealing stages in low-defect high-purity epitaxial layers led to control of a high-quality diode technology. As a result, diodes could exhibit very high shunt impedance, low  $1/f$  noise level, and the good quantum efficiency re-

quired to develop high-performance complex devices with a sufficient technological yield. This last point is seen as a direct consequence of the fully compatible planar structure used in the ion implantation process. At the same time, progress in crystal growth by molecular beam epitaxy (MBE), LPE, and metal-organic chemical vapor deposition (MOCVD) resulted in the development in some laboratories<sup>5,6,7</sup> of heterojunctions with doped structures. Because of minority-carrier lifetime and mobility considerations<sup>8</sup> and technological problems related to surface passivation control, p-on-n heterostructures were preferred to n-on-p. All the data published by several laboratories converge to demonstrate that such a structure, when optimized, can now lead to diodes with both high quantum efficiency and high  $R_0A$  product. The latter parameter approaches the theoretical limit of Auger 1 lifetime in the n-type layer.<sup>10</sup> A noteworthy point concerning the  $R_0A$  parameter is that a p-on-n

(Received October 12, 1992; revised January 21, 1993)

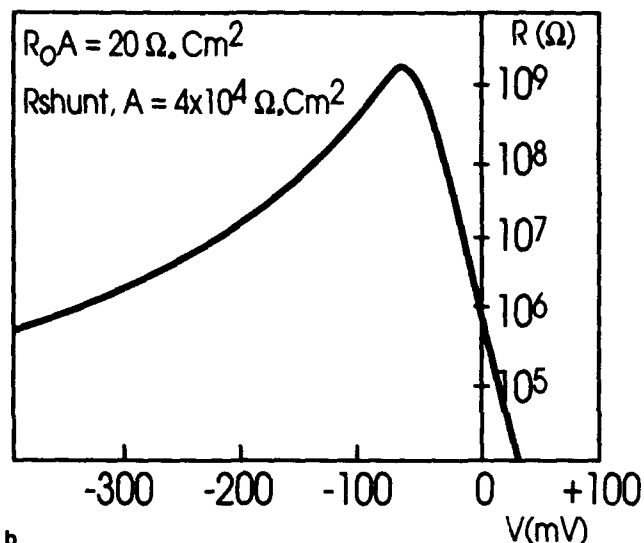
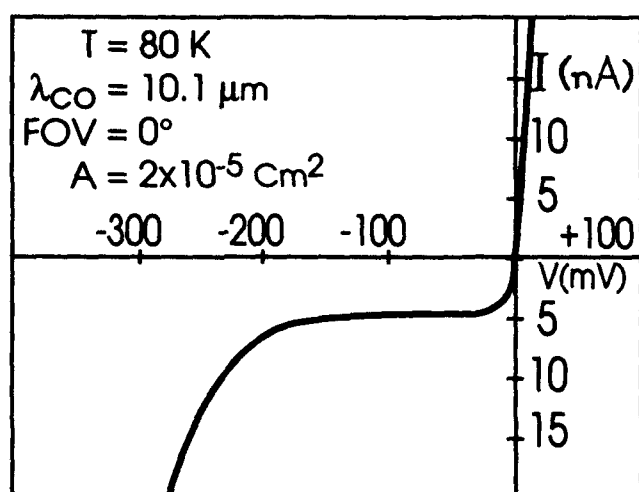


Fig. 1. Typical characteristics of standard diodes: (a) I-V characteristic, and (b) R-V characteristic.

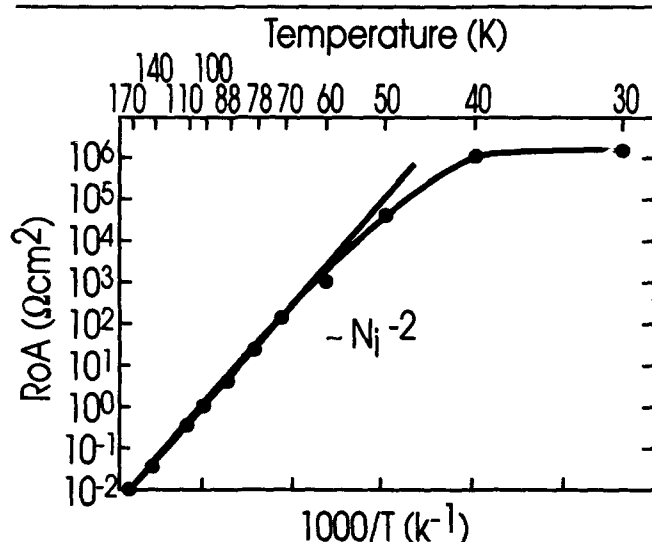


Fig. 2.  $R_0A$  product vs reciprocal temperature of a standard diode with 10.1  $\mu\text{m}$  cutoff wavelength at 80 K under 0° field of view.

heterostructure leads experimentally to  $R_0A$  values one order of magnitude higher than those for standard n-on-p homojunctions in the 9–13  $\mu\text{m}$  range. Without considering technological difficulties related to the fabrication of p-on-n heterojunctions (crystal growth and mesa process), this dark current reduction can make these devices attractive compared with simple n-on-p homojunctions. In this paper, we show that such a high  $R_0A$  product can be achieved with simple n-on-p ion-implanted planar homojunctions.

#### STANDARD PROCESS AND NEW PROCESS

The standard technology developed at LETI has been described elsewhere.<sup>1,2,4</sup> Its main characteristics are as follows. The material used is a  $\text{Hg}_{1-x}\text{Cd}_x\text{Te}$  epitaxial layer grown by LPE on the Te-rich side by the slider technique; the substrate is a  $\text{Cd}_{1-y}\text{Zn}_y\text{Te}$  (111)B lattice-matched crystal. The undoped layer is as-grown p-type and presents, after n-type annealing, a residual donor concentration in the low  $10^{14} \text{ cm}^{-3}$

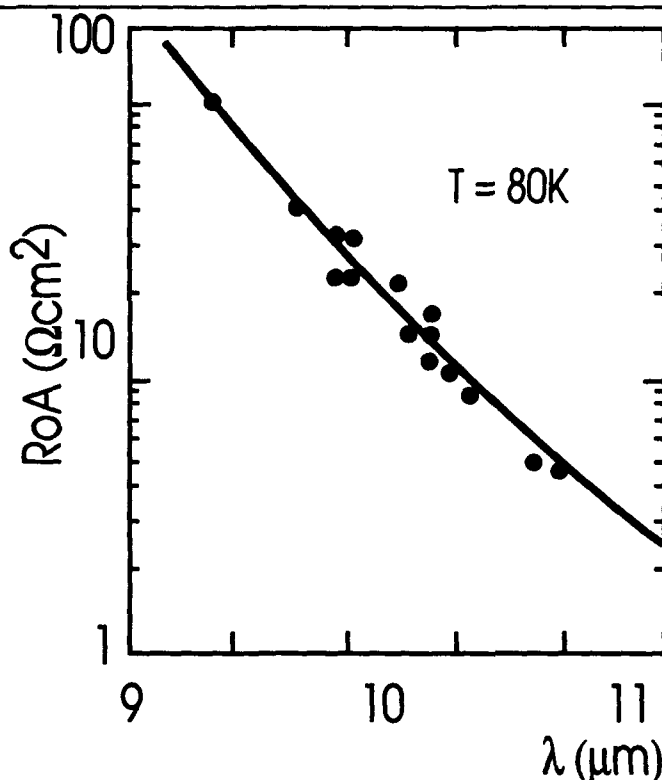


Fig. 3.  $R_0A$  product vs cutoff wavelength of standard diodes at 80 K.

range, with large electron mobilities and large minority-carrier lifetimes.<sup>3</sup> Photovoltaic detectors fabricated in this material are simple n-on-p homojunctions made by ion implantation. The device structure is planar, and high-quality complex arrays interconnected by indium bumps on Si readout circuits have been achieved with this technology.<sup>4</sup> Diodes made in such a way exhibit excellent performance as far as criteria such as quantum efficiency, shunt impedance, and 1/f noise level are concerned, along with high technological yield. As can be seen in Fig. 1, diodes obtained with this process are strongly diffusion-limited at 80 K and even down to much lower tempera-

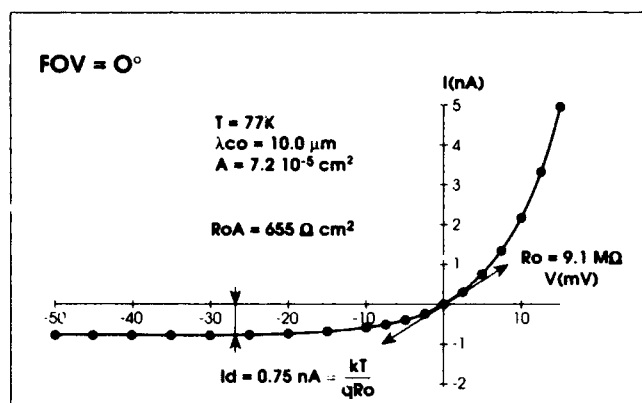


Fig. 4 Current-voltage characteristic of an n-on-p ion-implanted homo-junction made with the modified process.

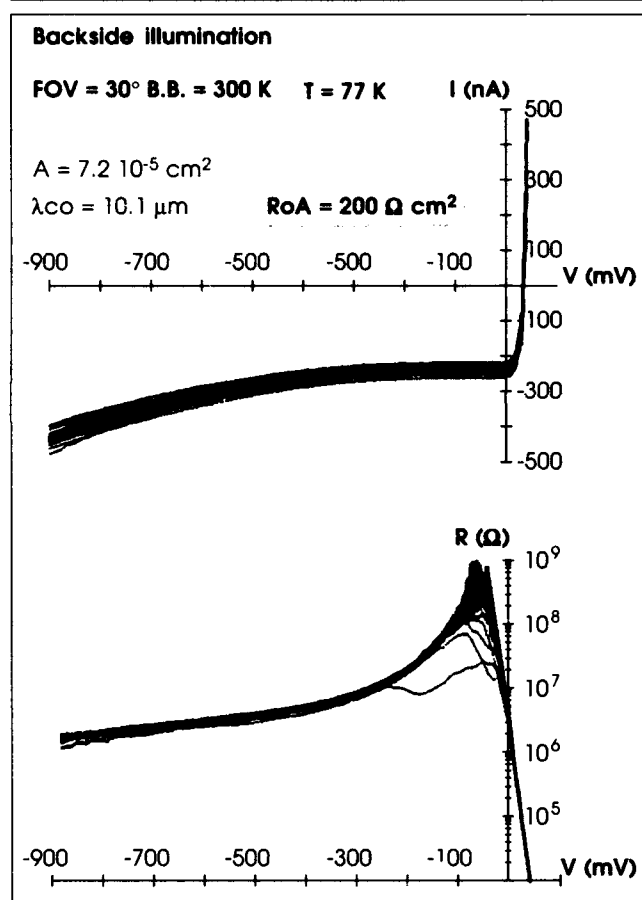


Fig. 5. Current-voltage and R-V characteristics of a 32-element diode array made with the new process.

tures (60K), as can be deduced in Fig. 2 from the  $n_i^2$  dependence of  $R_oA$  vs temperature. We note that the  $R_oA$  product is a constant when the diode area ( $A$ ) is made to vary over more than two orders of magnitude. Moreover, the  $R_oA$  product in our standard diodes is fully consistent with the minority-carrier lifetimes and diffusion lengths. These observations together with others led us to think that our diodes have a dark-current limitation arising mainly from the bulk lifetime of minority carriers in the Hg-vacancy-doped p-type crystal. Typical values of  $R_oA$  at 80K are shown

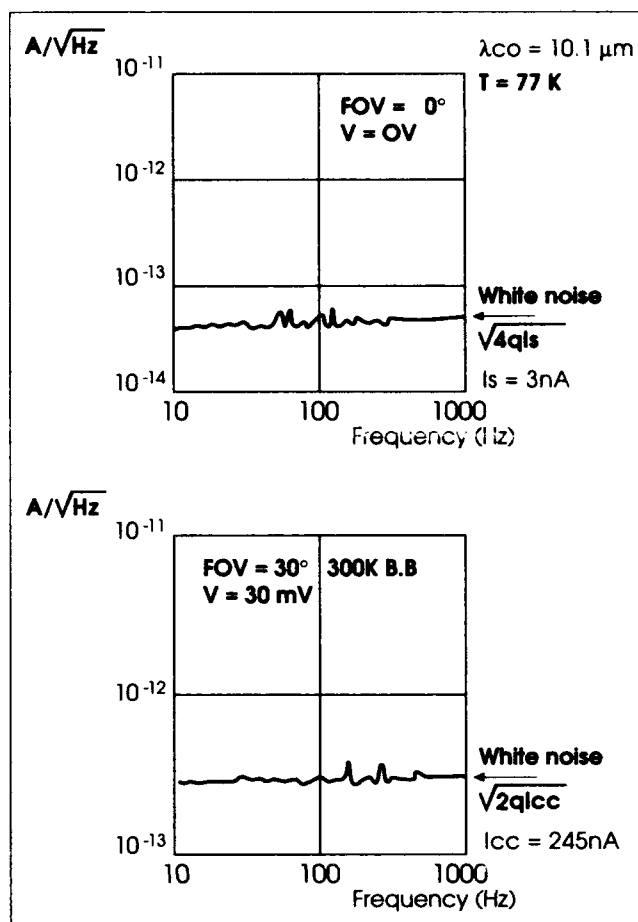


Fig. 6. Noise spectral density measured on a typical diode of the device presented in Fig. 5 for two illumination and polarization conditions.

in Fig. 3. These  $R_oA$  values are high enough to provide BLIP operation of most devices under usual illumination conditions. They are, however far below the theoretical figures obtained for an Auger 7 limited lifetime. This model predicts that  $R_oA$  values in the 200–300 ohm-cm<sup>2</sup> range are achievable for n-on-p diodes ( $N_a = 10^{16}$  cm<sup>-3</sup>) with a 10 μm cutoff wavelength and 77K operating temperature,<sup>9</sup> provided these diodes are strictly limited by the bulk minority-carrier lifetime. We have, therefore, developed at LETI/LIR a new n-on-p homojunction diode process that allows a substantial increase in this lifetime. This process results in highly improved  $R_oA$  figures, which are presented here.

## NEW TECHNOLOGY: DEVICE PERFORMANCES

The new technology presents the following similarities with the standard: diodes n-on-p homo-junctions made by ion implantation in planar structures. In both cases, HgCdTe epitaxial layers are 8–12 μm thick and are grown on CdZnTe substrates by LPE. The carrier concentration of the p-type material is similar in the standard and the new process, and the surface passivation is kept the same. Figure 4 presents the current-voltage (I-V) characteristic of an

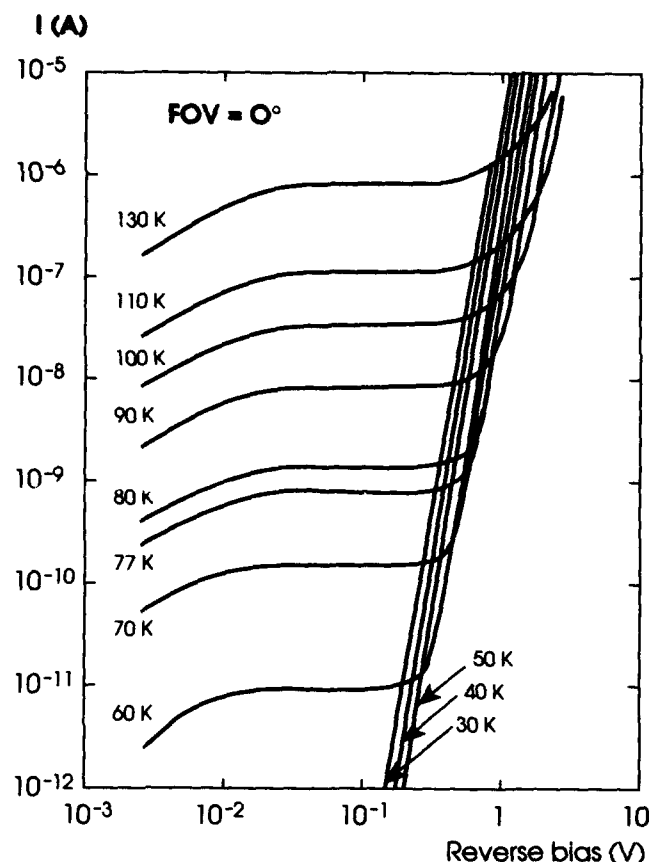


Fig. 7. Current-voltage characteristics vs temperature of the diode presented in Fig. 4. (Area =  $7.2 \times 10^{-5} \text{ cm}^2$ , cutoff wavelength =  $10.0 \text{ } \mu\text{m}$  at 77K).

n-on-p ion-implanted homojunction diode made with the modified process. Under a zero field of view at 77K, the  $R_oA$  of this detector is  $655 \text{ ohm-cm}^2$  for a cutoff wavelength of  $10.0 \text{ } \mu\text{m}$ . The saturation current is clearly visible and well correlated to the diode zero-bias shunt impedance ( $I_s = KT/qR_o$ ). Together with its high  $R_oA$  value, this diode exhibits a very large quantum efficiency of 80% (with anti-reflecting coating and backside illumination) for the peak wavelength of the spectral response ( $\lambda_{\text{peak}} = 8.75 \text{ } \mu\text{m}$ ). The shape of the spectral response is similar to what is obtained with our standard process (for the same operating temperature and cutoff wavelength), and is correlated to an increase of a factor of 3–4 of the minority-carrier diffusion length in the p-type base of the diodes (as measured from diode size). These  $R_oA$  values are within a factor of 2 of those predicted by an Auger 7 limited lifetime.

Figure 5 shows both the current-voltage and the resistance-voltage ( $R$ - $V$ ) characteristics at 77K of a 32-element linear array backside-illumination with a  $30^\circ$  field of view and 300K background. The  $R_oA$  product ( $200 \text{ ohm-cm}^2$ ) of this  $10.1 \text{ } \mu\text{m}$  cutoff wavelength device is obtained together with a quantum efficiency of 85% for the peak response ( $\lambda_{\text{peak}} = 8.9 \text{ } \mu\text{m}$ ). Most diodes exhibit high shunt impedances ( $\approx 10^8$  to  $10^9 \text{ ohm}$ ) and large breakdown voltages ( $\approx 1 \text{ volt}$ ). Figure 6 presents two noise-spectral-density measurements made on a diode typical of the array pre-

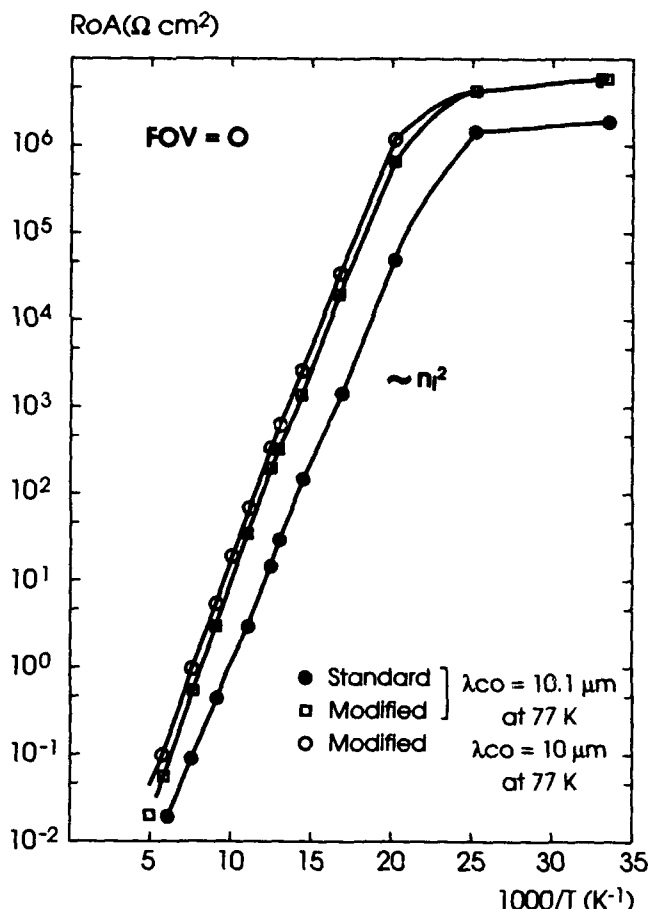


Fig. 8.  $R_oA$  product vs cutoff wavelength at 78K for devices made with the new process and the standard process.

sented in Fig. 5. Under a  $0^\circ$  field of view and 0-Volt-bias operation, no excess of low-frequency noise can be observed down to at least 10 Hz, and the white noise is well correlated to the saturation current. Under  $30^\circ$  field of view, 300K background, backside illumination, and 30 mV reverse bias, the noise measured is the shot noise of the photonic current. Consequently, we show that the improved performance of the diode  $R_oA$  product is obtained while still keeping the other figures of merit, such as shunt impedance and low  $1/f$  noise level.

In Fig. 7, we show the current-voltage characteristic vs temperature of the device presented in Fig. 4. We can observe the diffusion current plateau, which is perfectly visible at least down to 60K, at which point its value is as low as 9 pA (diode area  $7.2 \times 10^{-5} \text{ cm}^2$ ). For lower temperatures ( $T \leq 50 \text{ K}$ ), the current is well below 1 pA up to 200 mV bias. In Fig. 8, the complete  $R_oA$  evolution vs temperature is presented under a  $0^\circ$  field of view for diodes with similar cutoff wavelengths made with either the standard or the modified process. Both devices show the  $n_i^2$  dependence of the diffusion regime in a large range of temperature ( $T > 50 \text{ K}$ ). The  $R_oA$  saturation observed at very low temperature ( $T < 40 \text{ K}$ ) is due to instrumental limitations of impedance measurement ( $R > 5 \times 10^{10} \text{ ohm}$ ). The Arrhenius plot of  $R_oA$  vs reciprocal temperature

shows for standard diodes an activation energy slightly smaller compared with those achieved by the modified process. This subgap dependence could be the effect of a trap that limits the minority-carrier lifetime in the material used in the standard process. A selection of data obtained on devices at 78K with cutoff wavelengths ranging between 9.5 and 12  $\mu\text{m}$  can be seen in Fig. 9. We show that the  $R_0A$  increase of one order of magnitude observed at 10  $\mu\text{m}$  with the modified process is kept for longer cutoff wavelengths up to 11.7  $\mu\text{m}$ . The dashed lines drawn in this figure to fit data correspond to a theoretical diffusion-regime-dependence of  $R_0A$  vs cutoff wavelength. Finally, Fig. 10b presents the  $R_0A$  product of diodes in a wide range of temperatures and wavelengths. The curves are calculated using a diffusion regime ( $n_i^2$ ) that correlates for several temperatures experimental data corresponding to detectors of different cutoff wavelength. These results for diodes made by the new process (Figure 10b) are to be compared with those presented in Fig. 10a corresponding to the standard process. This comparison clearly shows that a gain of approximately 10K is obtained for the operating temperature without performance degradation, over the whole range of both wavelength (9–13  $\mu\text{m}$ ) and temperature (50–100K).

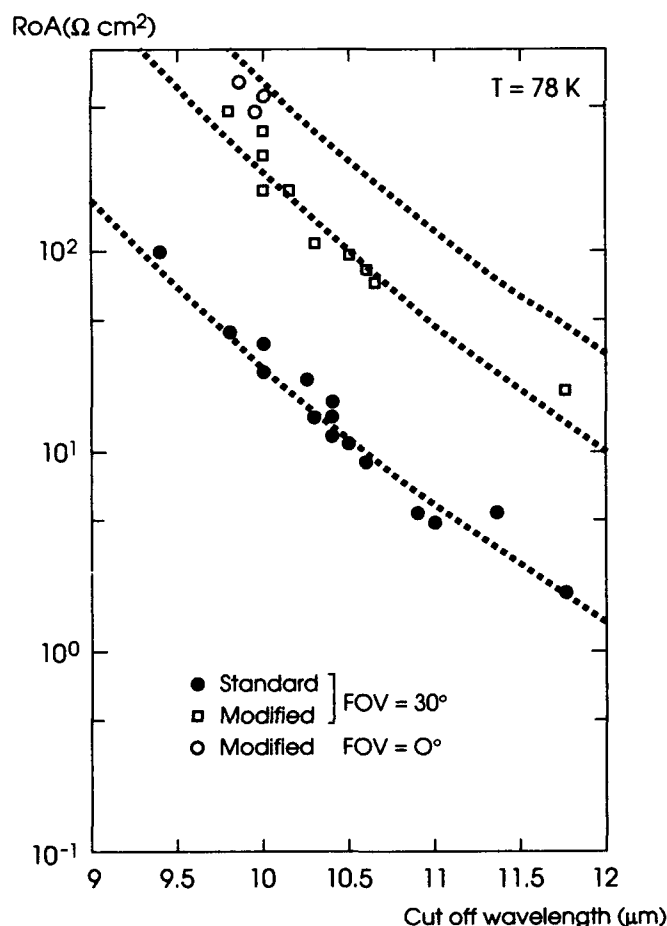


Fig. 9.  $R_0A$  product vs cutoff wavelength at 78K for devices made with the new technology compared to those made with the standard process.

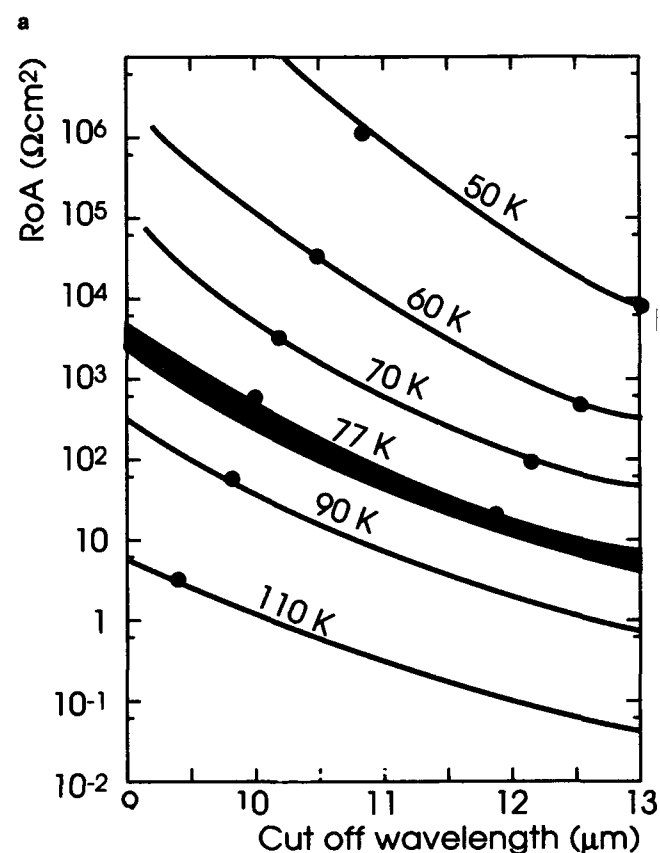
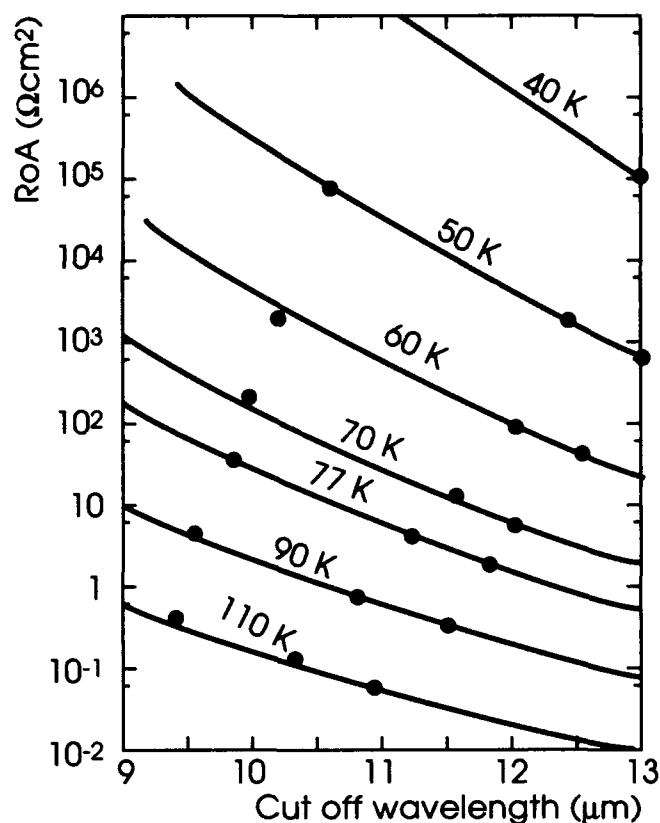


Fig. 10.  $R_0A$  product vs wavelength at several temperatures: (a) standard process, and (b) new process.

## SUMMARY AND CONCLUSION

The data presented in this paper show that the  $R_0A$  product of a simple n-on-p homojunction made in HgCdTe by ion implantation can be drastically improved. For 10  $\mu\text{m}$  cutoff wavelength detectors, values in the range of 200–300  $\text{ohm-cm}^2$  can easily be achieved and correspond approximately to what is predicted for a detector limited by an Auger 7 recombination mechanism. Higher values in the range 400–650  $\text{ohm-cm}^2$  were obtained in slightly thinner epitaxial layers. This  $R_0A$  improvement of one order of magnitude is observed even for detectors up to 12  $\mu\text{m}$  cutoff wavelength and over a large range of temperatures. Moreover, other figures of merit, such as 1/f noise level, shunt impedance, or quantum efficiency are kept unchanged or even improved. The data presented here are close to what is theoretically achievable for a p-on-n heterojunction (800  $\text{ohm-cm}^2$  for a 10.0  $\mu\text{m}$  cutoff-wavelength detector at 77K intrinsically limited by an Auger 1 recombination process). The two structures, the n-on-p planar ion-implanted homojunction and the p-on-n heterojunction, are similar as far as  $R_0A$  product is concerned, but other figures of merit (shunt impedance, low frequency noise, quantum efficiency, technological yields) have to be considered to make an objective comparison. The last remark concerns the real need to obtain very high  $R_0A$  values for devices. For 10.0  $\mu\text{m}$  cutoff wavelength

at 77K with a normal background devices are BLIP for  $R_0A$  as low as 5  $\text{ohm-cm}^2$ . Only if the detectors are to be used in more severe conditions (low flux applications, higher operating temperatures, longer cutoff wavelengths, small bias polarization), can the need for high  $R_0A$  values be justified.

## ACKNOWLEDGMENT

The authors are grateful to all their collaborators at the Infrared Laboratory of LETI who contributed to this study. The authors are also indebted to SOFRADIR for the constant interest shown in the progress of this study. This work is supported by DGA/DRET (French Ministry of Defense).

## REFERENCES

1. G. Destefanis, *Semicond. Sci. Technol.* 6, C88, C92 (1991).
2. G. Destefanis, *J. Cryst. Growth* 86, 700 (1988).
3. B. Pellicciari, *J. Cryst. Growth* 86, 146 (1988).
4. D. Amingual, J.P. Chamonal, J. Cluzel and G. Destefanis, at SPIE Conference, San Diego, July 1992. *Infrared Detectors State of the Art*, to be published in SPIE Proceedings.
5. P.R. Norton, *Opt. Eng.* 30, 1649 (1991).
6. C.C. Wang, *J. Vac. Sci. Technol.* B9, 1740 (1991).
7. G.N. Pultz, P.W. Norton, E.E. Krueger and B. Reine, *J. Vac. Sci. Technol.* B9, 1724 (1991).
8. A. Rogalski and W. Larkowski, *Electron Techn.* 18, 55 (1985).
9. A. Rogalski, *Infrared Phys.* 28, 139 (1988).
10. A. Rogalski, A. Jozwikowska, K. Jozwikowski and J. Rutkowski, *Infrared Phys.* 33, 463 (1992).
11. L.O. Bubulac, *J. Cryst. Growth* 86, 723 (1988).

# Influence of Hg Pressure on Diffusion Coefficient of As in HgCdTe

D. CHANDRA, M.W. GOODWIN, M.C. CHEN, and J.A. DODGE

Central Research Laboratories, Texas Instruments Inc., Dallas, TX 75265

Arsenic diffusion coefficients were measured in HgCdTe at 350°C within the single phase field. The diffusion coefficients displayed a strong dependence on Hg pressure, increasing by more than  $1 \times 10^3$  with decreasing Hg pressure. These measurements were performed by growing As doped HgCdTe films by Hg-rich liquid phase epitaxy on undoped or In-doped base layers, where the growth temperature ranged between 330 and 350°C. Use of these low growth temperatures under Hg-rich conditions permitted attainment of virtual step profiles in As, with negligible diffusion into the base layers. These provided ideal starting points for subsequent diffusion anneals. Diffusion of arsenic under selected low Hg pressures was then employed to tune the positioning of the p/n junction for double layer heterojunction films, by locating it ahead of the heterointerface. Formation of valence band barriers to the photogenerated minority carriers across the junction could thus be avoided. When on the other hand, diffusion experiments were performed under Hg saturated conditions, the heterointerface moved at a faster rate than the p/n junction, leading to the formation of valence band barriers.

**Key words:** As diffusion coefficients, HgCdTe, Hg-rich LPE, influence of Hg pressure on diffusion

## INTRODUCTION

Double layer HgCdTe heterostructures with a mid wavelength infrared top layer offer superior performance parameters when compared with single layer HgCdTe by reducing the diffusion currents from the wider band gap side of the junction. Optimization of the heterojunction performance depends critically on tuning dopant profiles with compositional variations. For p on n heterojunctions in HgCdTe for example, the dopant diffusion coefficients of relevance may involve both the acceptor impurity and the donor impurity. The former is commonly arsenic and is maintained at a level 50 to 100 times the level of the donor impurity, usually indium. As such, the p/n junction position almost exclusively depends on the arsenic diffusion coefficient.

## EXPERIMENTAL PROCEDURES

Arsenic doped HgCdTe films were grown on HgCdTe substrates. These substrates in turn were prepared by growing LPE HgCdTe films on CdZnTe substrates. Growth of the arsenic-doped HgCdTe films was

achieved routinely by dipping liquid phase epitaxy (LPE), primarily employing Hg-rich melts. The film thickness usually varied between 2 and 5  $\mu\text{m}$ . In several cases, thicker films were grown, ranging up to 6–8  $\mu\text{m}$ . The substrate HgCdTe thickness ranged between 10 and 70  $\mu\text{m}$ . Unlike the arsenic-doped cap layers, the base or the substrate layers were either undoped or for double layer heterojunctions, doped with indium. Following growth, the films were annealed at 350°C under selected Hg pressures. Various combinations of anneals were then employed, either to decrease the Hg vacancy concentration in the base layer to levels below  $5 \times 10^{13} \text{ cm}^{-3}$  or to restore the activity of As as an acceptor or both.

Processes developed permitted growth of specular, uniform thickness cap films from the Hg-rich melts on HgCdTe base films. The growth temperature ranged between 330 and 350°C, usually staying between 330 and 340°C for the overwhelming majority of the runs employed. The resulting As profiles were measured by secondary ion mass spectrometry (SIMS), using either  $\text{Cs}^+$  or  $\text{O}_2^+$  primary ions, employing a Cameca 3f ion mass spectrometer (IMS). The compositional profile across the heterostructure was determined either by the  $^{125}\text{Te}$  secondary electronegative ion yield dur-

(Received October 12, 1992; revised January 15, 1993)

ing SIMS where a  $\text{Cs}^+$  primary ion beam was used or by directly determining Cd variation when  $\text{O}_2^+$  primary ions were employed. The former method is based on the observation that a linear relationship exists between the ion yield and the Cd fraction.<sup>1</sup> For determining As profiles, on the other hand, use of  $\text{O}_2^+$  primary ions were observed to be most appropriate. No significant matrix effects were observed, as apparent from the shape of the arsenic profiles obtained. Nevertheless, the data were normalized with respect to  $^{123}\text{Te}$ . Limit of detectability of As when employing  $\text{O}_2^+$  primary ions ranged between  $1$  and  $2 \times 10^{15} \text{ cm}^{-3}$ , though the precise limit depended on the sputtering rate.

Mesa diodes were built on the double layer heterojunctions. The diode performance was correlated with measured As and In profiles and the compositional gradients.

## RESULTS AND DISCUSSIONS

As indicated, for the purposes of this study, all the anneals were performed at  $350^\circ\text{C}$ . For each individual

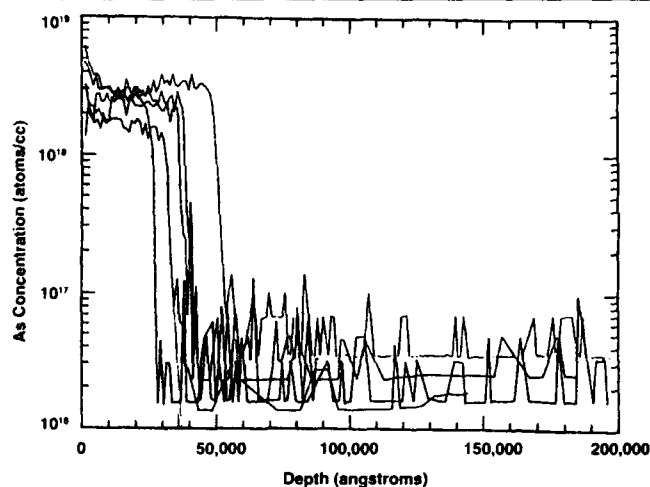


Fig. 1. Arsenic profiles in 'as-grown' double layer structures.

anneal, the Hg overpressure was selected and maintained constant. The matrix of Hg pressures employed ranged between the Hg-saturated limit (0.8 atm) and the Te-saturated limit ( $1.2 \times 10^{-3} \text{ atm}$ ).<sup>2</sup> Each film sample was sectioned into approximately seven individual pieces, where one piece was left unannealed to confirm the initial As profile. For these investigations, the compositional dependence of the As diffusion coefficient was ignored.

Figure 1 displays the As profiles obtained for five representative double layer structures immediately following growth. Note that virtual step profiles in As are observed for all of the samples, even though the individual cap layer thicknesses vary. Diffusion into the base layer is negligible. Figure 2 displays the As profiles for three pieces sectioned from the same double layer film: Fig. 2a showing the as-grown profile, Fig. 2b showing the profile following 1 h at  $350^\circ\text{C}$  at a mercury overpressure of 0.16 atmosphere, Fig. 2c showing the profile following 4 h at  $350^\circ\text{C}$  at the same mercury overpressure. The solid lines in Figs. 2b and 2c indicate the best fit possible assuming just composition independent Fickian diffusion. For both of these fits, only the magnitude of the diffusion coefficient was allowed to be varied. The quality of the agreement between the experimental data and the predicted behavior is excellent almost to the SIMS detectability limit, which in these cases ranged between  $1$  and  $2 \times 10^{15} \text{ cm}^{-3}$ . The magnitude of the diffusion coefficient required to yield best fit with the experimental profile results obtained following 4 h at  $350^\circ\text{C}$  appears slightly higher—at  $4.67 \times 10^{-12} \text{ cm}^2/\text{s}$ —compared to the similar value obtained from the profile data after 1 h at  $350^\circ\text{C}$ —at  $4.07 \times 10^{-12} \text{ cm}^2/\text{s}$ . Additional measurements of diffusion coefficients were performed at this mercury overpressure (0.16 atm). Similar experiments were also performed at mercury overpressures of 0.52 atm, 0.33 atm, 0.22 atm, and 0.11 atm in addition to the mercury-saturated limit of 0.80 atm. For all pressures down to 0.16 atm, it

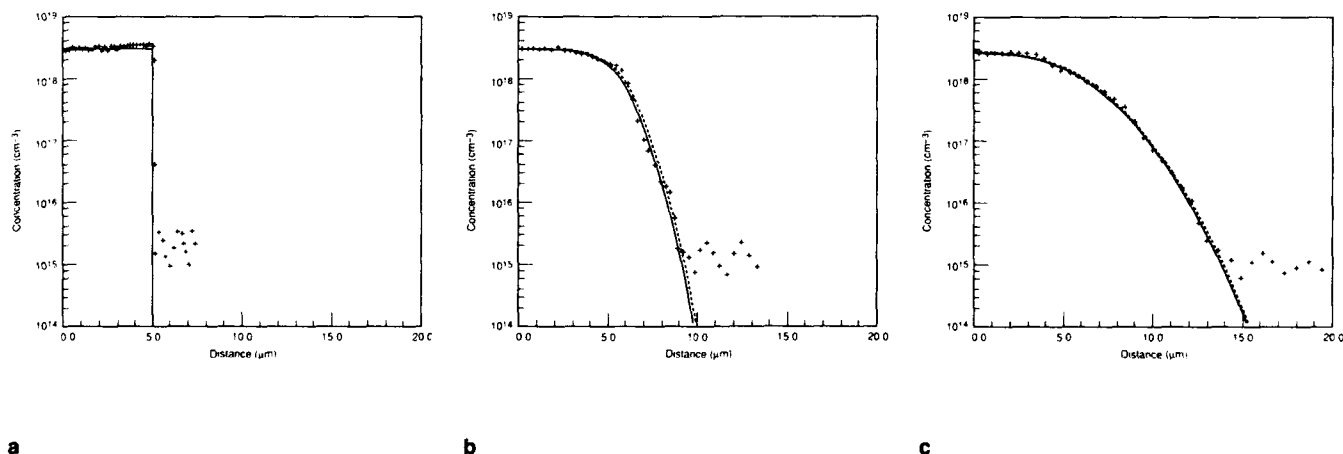


Fig. 2. (a) As-grown profile, as described in the text; (b) distribution of arsenic after 1 h at  $350^\circ\text{C}$ ; Hg overpressure: 0.16 atm; the solid line shows the best fit obtained assuming composition independent Fickian diffusion; and (c) distribution of arsenic after 4 h at  $350^\circ\text{C}$ ; Hg overpressure: 0.16 atm; the solid line shows the best fit obtained assuming composition independent Fickian diffusion.

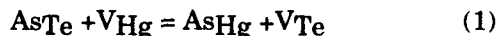


appears to be possible to describe the profiles very well with concentration independent Fickian diffusion. For the cap and base layer thicknesses employed, the diffusion can be very closely approximated by 'diffusion from an infinitely thick layer into an infinite body'.<sup>3-5</sup> For the mercury overpressure of 0.11 atm, however, the profiles observed begin to deviate from the simple case described above. An example is shown in Fig. 3. The arsenic concentration profile was obtained following 1 h at 350°C under a mercury overpressure of 0.11 atm. The solid line is the best fit attainable employing the concentration independent diffusion model used above. It appears that the results may correspond somewhat more appropriately to a multi-component diffusion behavior. With decreasing mercury overpressures, the behavior appears to become relatively complex. These results will be described elsewhere.

Figure 4 displays the measured diffusion coefficients at 350°C for the respective mercury overpressures employed during this investigation. The diffusion coefficient corresponding to the Hg saturated limit agrees very well with results obtained by other workers,<sup>6</sup> where the diffusion measurements were performed under Hg saturated conditions.

The dependence of the diffusion coefficient on Hg partial pressure can be approximated to the first order by invoking several quasi-chemical/defect equilibria. We also make the reasonable simplifying assumptions:

- When grown from the Hg-rich melt, that is under Hg-saturated conditions, the arsenic atoms occupy sites in the chalcogen sublattice ( $As_{Te}$ ). These are the equilibrium locations and the arsenic sites (defects) are then in equilibrium with both the Hg vacancies ( $V_{Hg}$ ) and Te vacancies ( $V_{Te}$ ).
- Assume only vacancy driven substitutional diffusion, since  $V_{Hg} \gg V_{Te}$  As will transport almost exclusively by employing vacancies in the metal sublattice. Hence, As 'dissolved' in the metal sublattice will participate in the transport.
- Then expressing the effective arsenic diffusion coefficient ( $D_{As}^T$ ) as proportional to the product  $[As_{Hg}] * D_{As}^{Hg}$  where  $[As_{Hg}]$  is the concentration of the dominant mobile species—arsenic atoms occupying sites in the metal sublattice—and  $D_{As}^{Hg}$  is the corresponding (vacancy driven) substitutional diffusion coefficient (similar to cases analyzed by Stevenson and Tuck):<sup>7,8</sup>



Adding Eqs. 1 and 2 yields



Therefore,

$$K_1 = \frac{[As_{Hg}]}{[As_{Te}][V_{Hg}]^2}$$

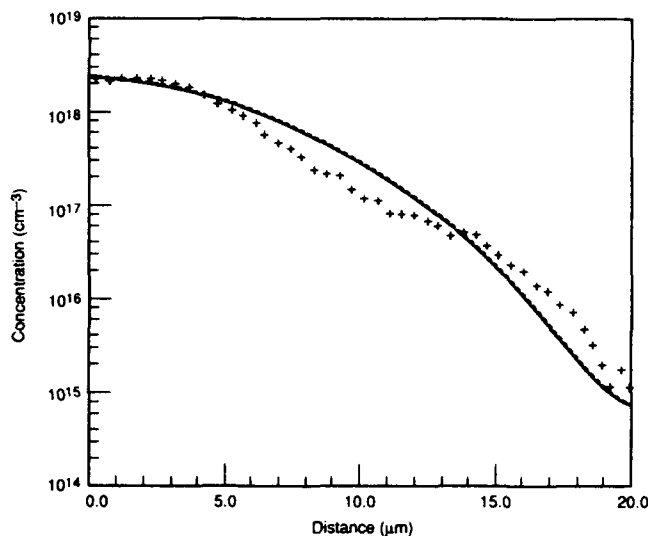


Fig. 3. Distribution of arsenic after 1 h at 350°C; Hg overpressure: 0.11 atm; the solid line shows the best fit obtained assuming composition independent Fickian diffusion.

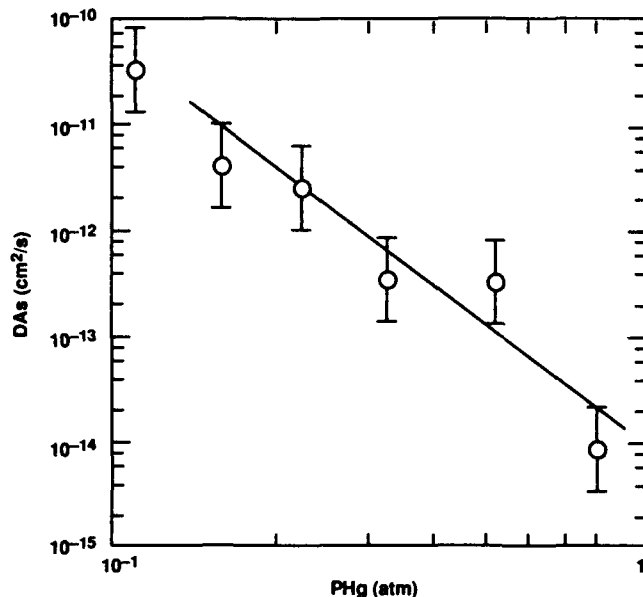


Fig. 4. Dependence of the diffusion coefficient of arsenic at 350°C in mercury cadmium telluride on the Hg overpressure.

If  $[As_{Hg}] \ll [As_{Te}]$ , and since

$$V_{Hg} \propto \frac{1}{P_{Hg}}$$

then

$$[As_{Hg}] \propto \frac{1}{P_{Hg}^2}$$

Now since

$$D_{As}^T \propto [As_{Hg}] * D_{As}^{Hg}$$

where

$$D_{As}^{Hg} \propto \frac{1}{P_{Hg}}$$

Therefore,

$$D_{As}^T \propto \frac{1}{P_{Hg}^3}$$

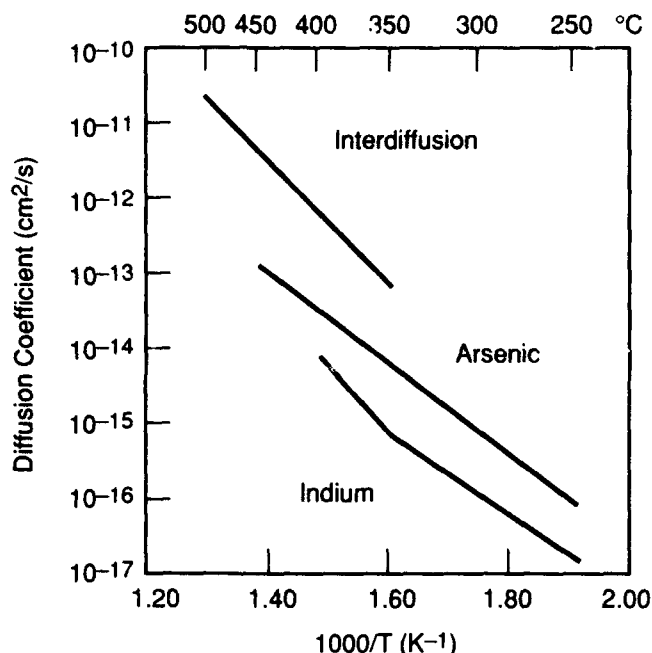


Fig. 5. Relative magnitudes of the interdiffusion coefficient, the arsenic diffusion coefficient, and the indium diffusion coefficient under mercury-saturated condition within the range of relevance to DLHJ growth.

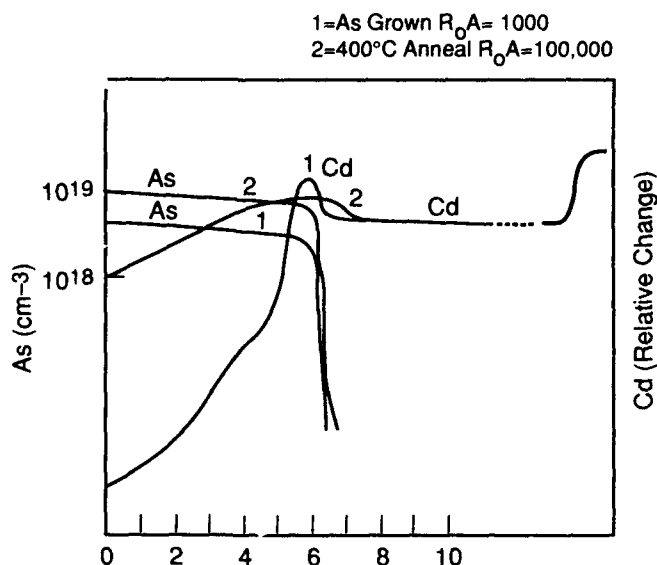


Fig. 6. Arsenic and cadmium profiles, as determined by SIMS for two pieces of DLHJ cut from the same sample, but subjected to different annealing conditions as described in the text.

Similar observations can also be made starting from a slightly different but generally similar site transfer reactions provided by Vydyanath et. al.<sup>9,10</sup>



yielding

$$[\text{As}_{\text{Hg}}] = K_2 [\text{As}_{\text{Te}}'] [h \cdot]^2 \frac{1}{P_{\text{Hg}}^2}$$

Again for

$$\begin{aligned} [\text{As}_{\text{Te}}'] &\gg [\text{As}_{\text{Hg}}] \\ [\text{As}_{\text{Hg}}] &\propto \frac{1}{P_{\text{Hg}}^2} \end{aligned}$$

This leads as before to

$$D_{\text{As}}^{\text{r}} \propto \frac{1}{P_{\text{Hg}}^2}$$

Within the pressure range shown in Fig. 4, this dependence on Hg partial pressure is approximately obeyed. With additional decrease in the Hg partial pressure, arsenic transport assumes more complex characteristics. Note that when grown from the Hg-rich melt, As is already 100% active as an acceptor, occupying sites in the chalcogen (Te) sublattice. No activation or site transfer anneal of any kind is necessary. Progressive deactivation of As may occur when annealed at 350°C under decreasing Hg pressures. It appears to be possible to completely restore this activity by a low temperature mercury-saturated anneal within the sensitivity of the measurements. When Hall measurements were performed following mercury-saturated anneals at temperatures ranging between 230 and 270°C on samples which have been preannealed at 350°C under mercury overpressures falling within the range indicated in Fig. 4 above, arsenic appeared to be totally active. Nevertheless, this method may not be sufficiently sensitive to evaluate the degree of activation of arsenic within the 'tail' region: this issue requires additional study. Note that the low temperature mercury saturated anneal also serves the purpose of stoichiometric adjustment, reducing mercury vacancy concentration below  $5 \times 10^{13} \text{cm}^{-3}$ . Hence, no separate higher temperature mercury saturated 'activation anneal' may be necessary. These results and additional experimental details have been presented elsewhere.<sup>11</sup> Higher temperature mercury-rich activation anneals have been claimed to be necessary by other workers,<sup>12,13</sup> where the mercury overpressures employed were lower than the range employed during the present investigations.

The significant improvement in flexibility available from these results is apparent when only the diffusion coefficients available in the literature<sup>6,14,15</sup> are employed (Fig. 5). All these experiments, with the exception of those to determine the interdiffusion coefficients,<sup>14,15</sup> were performed under Hg-saturated conditions. The interdiffusion coefficients were measured both under Hg-rich and Te-rich conditions.<sup>14</sup> Apparently, the interdiffusion coefficients exceed the respective As diffusion coefficients significantly, which in turn are significantly higher than the corresponding In diffusion coefficients. Note that, unlike the trend observed above for the As diffusion coefficients, the interdiffusion coefficients decrease with decreasing Hg partial pressures, with values obtained under Te-saturated conditions being lower than those under Hg saturated conditions.<sup>14</sup> The separation between these two limits increases with decreasing temperature.<sup>14</sup>

The influence of these parameters was demonstrated during the present investigations. Figure 6 shows the As and Cd profiles, as determined by SIMS for two sample pieces sectioned from a double layer

heterojunction and annealed. The first piece was not subjected to any high temperature anneal. Its stoichiometry was only adjusted by a low temperature Hg-saturated anneal. The second piece was annealed at 400°C under Hg-saturated conditions for 1 h and then stoichiometrically adjusted by the low temperature Hg-saturated anneal. It is apparent that the compositional junction has widened faster after the 400°C anneal than the p/n junction. Hence, a valence band barrier has now formed, with the corresponding  $R_0A$  increasing by 100 x.

For the example cited above, a smaller valence band barrier appears to exist even for the 'as-grown' piece. The Hg-rich anneal, therefore, increases the height of the barrier. With the results obtained during these investigations, it appears possible to 'tune' the position of the p/n junction with respect to the heterostructure interface. Note that as indicated above, with decreasing mercury overpressure, arsenic diffusion coefficients increase strongly, but the interdiffusion coefficients decrease, though not by such large degrees (Fig. 4 above and Tang and Stevenson).<sup>14</sup> The entire range of behavior—ranging from heterojunctions with valence band barriers to heterojunctions with no barriers to complete homojunctions—can be reproducibly obtained. Hence, use of this method can be extended to reproducibly position the p/n junction such that a heterojunction with no valence band barrier is formed, even though a valence band barrier might have existed for the 'as-grown' material. Figure 7a displays a representative set of  $R_0A$  values at 78°K for diodes fabricated on a 10.6  $\mu\text{m}$  cutoff (as measured also at 78°K) HgCdTe DLHJ film. Figure 7b shows the capacitance voltage (I-V) and resistance (R-V) behavior for a representative diode from this film. The leakage currents were lower than 50  $\mu\text{A cm}^{-2}$  at a reverse bias of 50 mV and almost independent of bias up to a reverse bias of 300 mV. Quantum efficiency vs bias measurements were performed at 78.2K on the diodes up to a reverse bias of 0.3 V. The measured quantum efficiency appeared totally unchanged with increasing reverse bias. From specimen to specimen, the quantum efficiency measured varied between 50 and 60%, without use of any anti-reflection coating. But in each instance, the respective magnitudes remained invariant with increasing reverse bias. Hence, no valence band barriers existed.

## CONCLUSION

Strong dependence of arsenic diffusion coefficients on mercury partial pressure appears to be a powerful method in optimizing p on n heterojunction performance.

## REFERENCES

1. L.O. Bubulac and C.R. Viswanathan, *Appl. Phys. Lett.* 60, 222 (1992).
2. H.R. Vidyantath, *J. Electrochem. Soc.* 128, 2609 (1981).
3. W. Jost, *Diffusion in Solids, Liquids and Gases*, Academic, New York, 1962.
4. B.I. Boltaks, *Diffusion in Semiconductors*, Academic, New York, 1963.

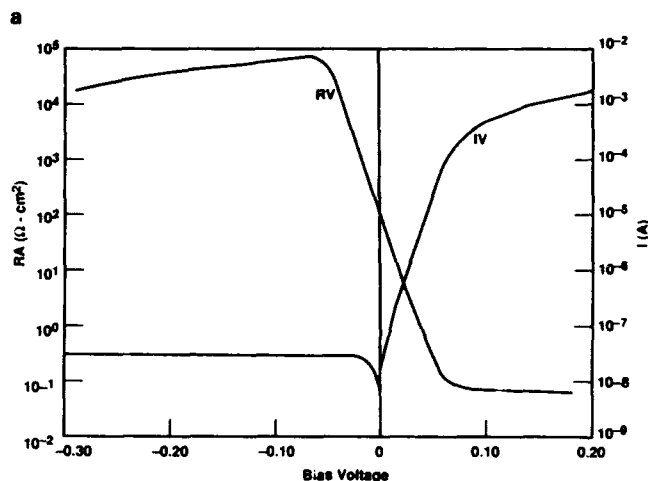
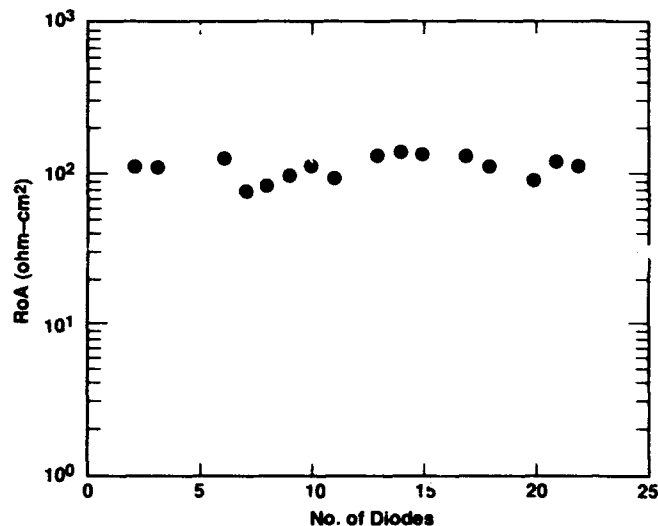


Fig. 7. (a)  $R_0A$  values for test diodes fabricated on a 10.60  $\mu\text{m}$  (at 78K) cutoff mercury cadmium telluride DLHJ film. The p/n junction position was optimally adjusted by using a Hg deficient anneal at 350°C followed by a low temperature Hg saturated anneal, and (b) typical I-V and differential resistance of test diode built on a 10.60  $\mu\text{m}$  (at 78K) cutoff mercury cadmium telluride DLHJ film.

5. S.K. Gandhi, *The Theory and Practice of Microelectronics*, John Wiley and Sons, New York, 1968.
6. T.H. Myers, K.A. Harris, R.W. Yanka, L.M. Mohnkern, R.J. Williams and G.K. Dudoff, *J. Vac. Sci. Technol.* B10, 1438 (1992).
7. D.A. Stevenson, *Diffusion in the Chalcogenides of Zn, Cd and Pb*, *Atomic Diffusion in Semiconductors*, ed., D. Shaw, Plenum Press, New York, 1973.
8. B. Tuck, *Atomic Diffusion in III-V Semiconductors*, Adam Hilger, Bristol, 1988.
9. H.R. Vidyantath, *J. Vac. Sci. Technol.* B9, 1716 (1991).
10. H.R. Vidyantath, J. A. Ellsworth, and C.M. Devaney, *J. Electron Mater.* 16, 13 (1987).
11. D. Chandra, M.W. Goodwin, M.C. Chee and J.A. Dodge, *Proc. IRIS Materials Specialty*, 1992, to be published.
12. L.O. Bubulac, D.D. Edwall, and C.R. Viswanathan, *J. Vac. Sci. Technol.* B9, 1695 (1991).
13. L.O. Bubulac, S.J.C. Irvine, E.R. Gertner, J. Bajaj, W.P. Lin and P. Zucca, *Int. Conf. on Narrow Gap Semiconductors*, 19-23 July, 1992.
14. M.-F.S. Tang and D.A. Stevenson, *J. Vac. Sci. Technol.* A5, 3124 (1987).
15. D.A. Stevenson and M.-F.S. Tang, *J. Vac. Sci. Technol.* B9, 1615 (1991).

# Annealing Effect on the P-Type Carrier Concentration in Low-Temperature Processed Arsenic-Doped HgCdTe

S.H. SHIN, J.M. ARIAS, M. ZANDIAN, J.G. PASKO, L.O. BUBULAC,  
and R.E. DE WAMES

Rockwell International Science Center, Thousand Oaks, CA 91360

We report the results of annealing effects on the As-doped alloy HgCdTe grown by molecular beam epitaxy (MBE), arsenic (As) diffusion in HgCdTe from Hg-rich solutions at low temperatures, and As ion implantation at room temperature. Hall-effect measurements, secondary ion mass spectrometry and p-on-n test photodiodes were used to characterize the As activation. High As-doping levels ( $10^{17}$ – $10^{19}$  cm $^{-3}$ ) could be obtained using either MBE growth, As diffusion or As ion-implantation. Annealed below 400°C, As doping in HgCdTe shows n-type characteristics, but above 410°C demonstrates that all methods of As doping exhibit p-type characteristics independent of As incorporation techniques. For example, for samples annealed at 436°C ( $P_{\text{Hg}} \sim 2$  atm), in addition to p-type activation, we observe a significant improvement of p/n junction characteristics independent of the As source; i.e. As doping either in situ, by diffusion, or ion implantation. A study of this As activation of As-doped MBE HgCdTe as a function of anneal temperature reveals a striking similarity to results observed for As diffusion into HgCdTe and implanted As activation as a function of temperature. The observed dependence of As activation on partial pressure of Hg at various temperatures in the range of 250 to 450°C suggests that As acts as an acceptor at high Hg pressure ( $>1$  atm) and as a donor at low Hg pressure ( $<1$  atm) even under Hg-rich conditions.

**Key words:** As activation, As diffusion, MBE HgCdTe, p-on-n photodiodes

## INTRODUCTION

Arsenic is an extremely useful dopant for HgCdTe due to the very high doping concentrations ( $10^{17}$ – $10^{19}$  cm $^{-3}$ ) possible and to its low diffusivity, both of which are important for electronic and optical device applications such as infrared focal plane arrays (IRFPA) and infrared long wavelength lasers. Many challenging problems remain to be solved to develop a basic understanding of this material and its associated processing parameters.

High performance HgCdTe FPAs require intentionally doped material with controllable and reproducible concentrations of both donor and acceptor elements for the p/n junction formation. However, there still is considerable disagreement with regard to the reported As electrical activity. Group V elements are electrically active p-type in material grown under Hg-saturated conditions (e.g. Bridgman and Hg-rich liquid phase epitaxy [LPE]), but both As and

Sb are incorporated as electrically active n-type dopants in alloy HgCdTe grown by molecular beam epitaxy (MBE)<sup>1</sup> under Hg-rich and Te-rich conditions. Capper<sup>2</sup> recently concluded that in Te-rich LPE and metalorganic chemical vapor deposition (MOCVD) material, group V acceptor elements require a high temperature activation anneal. He also stated that this type of anneal does not activate acceptors in MBE layers because group V elements occupy metal sites as donors.

Only a few studies<sup>3–6</sup> of the As-doping behavior of HgCdTe alloys during MBE growth using As<sub>4</sub> (As<sub>2</sub>) or As atoms from the As cracking cell as the dopant and As diffusion into HgCdTe at low temperature ( $T < 300^\circ\text{C}$ ) have been reported recently. Although it was not the most optimum solution, we have overcome the amphoteric behavior of As in MBE alloy HgCdTe and achieved p-type MBE HgCdTe doping with As using the interdiffused HgTe/CdTe superlattice approach.<sup>4</sup> This process consists of growing a HgTe/CdTe superlattice at  $T_s < 165^\circ\text{C}$  intentionally doped with As in the CdTe cycle, followed by an ex situ high tempera-

(Received October 12, 1992; revised January 13, 1993)

**Table I. Electrical Properties of Open-Tube and Closed-Ampoule Annealed MBE HgCdTe Layer (#440) with Hall-Effect Measurements at 77K**

|                                   | Low T Anneal at 250°C |                      | High T/Low T Anneal at 436/250°C |                      |
|-----------------------------------|-----------------------|----------------------|----------------------------------|----------------------|
|                                   | Closed                | Open                 | Open/Closed                      | Open/Open            |
| Carrier Conc. (cm <sup>-3</sup> ) | $1.4 \times 10^{15}$  | $1.6 \times 10^{15}$ | $2.3 \times 10^{15}$             | $1.5 \times 10^{15}$ |
| Mobility (cm <sup>2</sup> /V.s)   | $8.0 \times 10^4$     | $5.3 \times 10^4$    | $7.1 \times 10^4$                | $7.1 \times 10^4$    |

ture annealing at 436°C/10 min under Hg atmosphere for As activation and interdiffusion of the HgTe/CdTe(As) superlattice. Arsenic ion-implantation<sup>7</sup> has been a widely studied alternative to direct doping during the epitaxial film growth as the p-type dopant, and a recent study<sup>8</sup> indicates that As can be more effectively incorporated in Te lattice sites of HgCdTe to produce p/n junction photodiodes via post-implant thermal annealing at 400–450°C/250°C in a quartz ampoule.

After the discovery of As-doping in HgCdTe by Hg-solution growth,<sup>9</sup> we speculated that the key to understanding As-doping behavior relied on an excess Hg environment and especially in the Hg vacancy reduction to prevent As atoms from substituting on cation sites. Development of As diffusion<sup>10</sup> into HgCdTe from Hg-solution and MBE<sup>11</sup> HgCdTe growth under Hg-rich surface conditions has promoted a reexamination of familiar paradigms in defect chemistry of HgCdTe material. Consider, for example, high temperature annealing of As-doped HgCdTe by Te-rich LPE and vapor phase epitaxy (VPE) (MBE or MOCVD) techniques, sometimes converting to p-type. Vydyanath<sup>12</sup> found that a 500°C Hg-saturated ex situ pre-anneal on epilayers followed by a second post-growth ex situ 200°C Hg-saturated anneal yielded in some cases p-type behavior for the Sb dopant, but for other films the Sb-doped films remained n-type even when subjected to the ex situ pre-anneal. Most recently, Harman<sup>13</sup> also discovered that epilayers as-grown from a Te-rich solution containing As or Sb are p-type if the furnace was cooled from the growth temperature and subjected to an in situ 30 min anneal at 400°C with both the cooling and annealing carried out under nearly one atmosphere of Hg-vapor pressure. He concluded that the problem with group V acceptor doping in Te-rich LPE HgCdTe is not an incorporation of the group V element into the epilayer during the growth, but an activation of the impurity onto Te sites after growth. In that sense, Vydyanath argued that the group V elements are amphoteric and form compensating defects by incorporating group V elements as donors on Hg sites and acceptors on Te lattice sites under Te-rich growth conditions. The primary purpose of this work is to shed more light on the p-type As activation mechanism and to present a diffusion technology for p-on-n photodiode fabrication.

### EXPERIMENTAL DETAILS

Recently, we have demonstrated that post growth annealing can lead to a significant reduction of the dislocation density of MBE HgCdTe/GaAs epilayers.<sup>14</sup>

Moreover, we have also observed that As-diffusion in MBE HgCdTe in Hg-solution can produce high performance p-on-n photodiodes.<sup>15</sup> Using this high temperature annealing process, first MBE grown HgCdTe layers doped with As were studied by annealing as a function of temperature. The temperature dependence of carrier concentrations and mobilities were measured by Hall-effect measurements at 77K. Secondly, LPE Hg<sub>1-x</sub>Cd<sub>x</sub>Te epilayers with  $0.22 < x < 0.3$  were also used to study As diffusion and As ion implantation experiments. Group V elements such as As and Sb atoms can also be introduced into the HgCdTe material by diffusion from an As source dissolved in Hg-rich or Te-rich solution in a high temperature furnace or by ion implantation in which charged As<sup>+</sup> ions are driven into the HgCdTe sample by a particle accelerator. Particularly in ion-implanted HgCdTe material, structural damage results and requires thermal annealing to remove the lattice defects and also to activate As dopants in the material. Additionally, the Hg-vacancies generated either during the growth or material processes have been known to limit the lifetime of HgCdTe devices, and therefore, low temperature Hg-annealing at 250°C is also required.

To carry out the As activation annealing experiments, the As sources were incorporated by As doping in MBE alloy HgCdTe, As diffusion into LPE HgCdTe epilayers, and As ion implantation. In addition, p/n junctions formed by As-doped HgTe/CdTe as an As source were studied to obtain the junction movement due to diffusion and activation. Arsenic diffusion was performed under both Hg-rich and Te-rich conditions using Hg/As and Te/As melt solutions at different diffusion conditions. The third As source used for the experiment was As ion implantation into HgCdTe epilayers. The diffusion and implantation doping was investigated by fabricating p/n junctions.

Since a standard Hg-anneal above 410°C in a closed quartz ampoule can deteriorate the HgCdTe sample surfaces, a high pressure open-tube annealing process has been developed to perform high temperature As activation as well as diffusion. The standard closed tube annealing process also suffers quite often from air leaks, frequent implosions and water or impurity contamination while opening the ampoules; furthermore, this technique is not practical for manufacturing environments. High temperature As activation was carried out using a converted vertical LPE furnace. The details of the high pressure open tube annealing apparatus have been reported elsewhere;<sup>16</sup> the essentials are outlined as follows. The apparatus

Table II. Annealing Effects of As-Doped MBE HgCdTe ( $x = 0.26$ ) with Hall-Effect Measurements at 77K

| Anneal Temp.<br>(°C) | Anneal Time<br>(h) | Carrier Type<br>(n/p) | Carrier Conc.<br>(cm <sup>-3</sup> ) | Mobility<br>(cm <sup>2</sup> /V.s) |
|----------------------|--------------------|-----------------------|--------------------------------------|------------------------------------|
| as grown             | 0/0                | n(?)                  | $1.7 \times 10^{15}$                 | $4.0 \times 10^2$                  |
| 250/200              | 20/20              | n                     | $4.0 \times 10^{15}$                 | $9.0 \times 10^3$                  |
| 350/200              | 4/20               | n                     | $2.4 \times 10^{15}$                 | $1.3 \times 10^4$                  |
| 400/200              | 2/20               | n                     | $2.6 \times 10^{15}$                 | $2.6 \times 10^4$                  |
| 425/200              | 0.5/20             | n                     | $5.7 \times 10^{15}$                 | $2.8 \times 10^3$                  |
| 450/200              | 0.16/20            | p                     | $7.0 \times 10^{16}$                 | $2.8 \times 10^2$                  |

consists of an inner quartz reaction tube and an outer thick quartz tube that is mounted between two stainless steel flanges and maintained at 100-150 psi during annealing. We have not determined the Hg partial pressure during the annealing which is found to be close to the near saturated Hg pressure based on the As diffusion coefficient at a given temperature. The high temperature annealing effects on in situ grown p-on-n MBE HgCdTe photodiodes were investigated by post-growth annealing prior to mesa test diode fabrication.

### Open-Tube Annealing in a Mixture of Hydrogen and Hg Atmosphere

First, we carried out experiments with annealing n-type HgCdTe ( $x = 0.22$ ) in a mixture of hydrogen and Hg atmospheres to examine the effect of hydrogen in electrical properties of HgCdTe epilayers and to compare the results with a standard closed ampoule annealing process. Hall-effect measurements of closed-tube and open-tube Hg-annealing of MBE HgCdTe epilayers are summarized in Table I. After low temperature annealing at 250°C using both annealing methods, we achieved the same electron concentration of  $1.4\text{--}2.3 \times 10^{15} \text{ cm}^{-3}$  and mobility of  $5.3\text{--}8.0 \times 10^4 \text{ cm}^2/\text{V.s}$  within a factor of two. Electrical properties of closed-ampoule and open-tube annealed MBE HgCdTe epilayers are indistinguishable. In the case of high temperature open-tube annealing followed by two different processes, the comparable values of carrier concentration and mobility indicate that high-pressure open-tube annealing is a viable means of controlling carrier concentrations as well as As activation and diffusion processes. These results are critical for high temperature anneals since CdZnTe substrates can contain fast diffusing impurities and compensate the HgCdTe epilayers. Impurity outdiffusion from both CdTe and CdZnTe substrates during the LPE growth and high temperature annealing was observed on both MBE and LPE HgCdTe materials.<sup>17,18</sup>

### Annealing Effects on As-Doped MBE HgCdTe Alloy

Arsenic-doped epitaxial layers of HgCdTe with  $0.22 < x < 0.3$  were grown on (211)B CdZnTe substrates in the Riber 2300 MBE system with a standard As cell, producing As<sub>4</sub> tetramers. Arsenic doping was achieved during the alloy HgCdTe growth. The As source temperature was 160°C. Growth rates were about 5  $\mu\text{m}/$

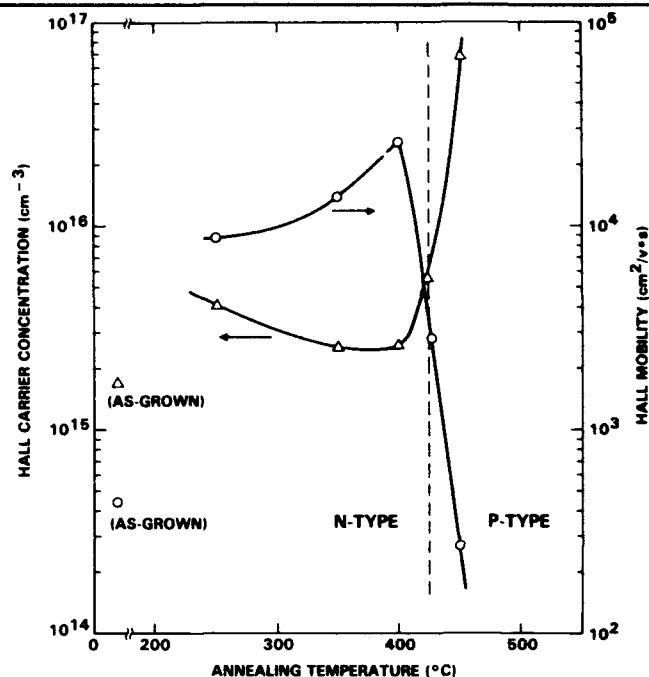


Fig. 1. Temperature dependence of As activation for an As-doped MBE HgCdTe layer with  $x = 0.268$ . Arsenic activation was achieved by post growth annealing temperatures above 425°C followed by low temperature Hg-annealing at 200°C.

h at 195°C and the thickness of the epitaxial layers was typically in the 10–20  $\mu\text{m}$  range. As-grown As doped layers showed a negative Hall coefficient with a 77K carrier concentration of  $2 \times 10^{15} \text{ cm}^{-3}$  and a very low mobility of 420  $\text{cm}^2/\text{V.s}$ . As activation was achieved by post-growth thermal annealing above 425°C followed by 200°C anneals in Hg-rich ambient. The annealing temperature was varied in increments of 30–50°C from 250°C/20 h to 450°C/10 min, and then followed by 200°C low temperature Hg-annealing.

Material characteristics after post-growth annealing are summarized in Table II. The Table II data are plotted in Fig. 1 and show the variation of hole concentration and mobility as a function of annealing temperature in the temperature range 250–450°C. The n-type carrier concentration (as grown MBE HgCdTe  $x = 0.26$ ,  $n = 2 \times 10^{15} \text{ cm}^{-3}$ ,  $\mu = 420 \text{ cm}^2/\text{V.s}$  at 77K) decreases as the temperature increases to 400°C, and then converts to p-type due to As activation. The temperature dependence of carrier concentration indicates that the effect of As compensation is increased as the annealing temperature increases until it con-

verts to p-type. However, a significant increase in mobility values from 420 to  $2.6 \times 10^4 \text{ cm}^2/\text{V.s}$  indicates that defect structures such as neutral pairs associated with interstitial and substitutional As and possibly As precipitates due to As doping anneal out as temperature increases. The p-type carrier concentration of the layer after high temperature annealing was  $7 \times 10^{16} \text{ cm}^{-3}$  which agrees within a factor of two compared with As levels found by secondary ion mass spectroscopy (SIMS) analysis. Surprisingly, although the n-type carrier concentrations between the as-grown and 250°C annealed HgCdTe were similar, the electron mobility was much higher in the annealed sample than in the as-grown sample. This difference in electron mobility is apparently associated with low temperature As doping in alloy HgCdTe because the mobility of n-type HgCdTe should be in the range of high  $10^4$  to low  $10^5 \text{ cm}^2/\text{V.s}$  at 77K. The most likely explanation is that As dopants may be incorporated into dimers rather than As atomic species, giving a heavy compensation because of low surface mobility at low growth temperature. Furthermore, the extremely low n-type mobility of the as-grown sample suggests that the incorporated arsenic can be formed as As precipitates in the alloy HgCdTe layers grown at the low temperature around 190°C. Even this low temperature annealing at 250°C could equilibrate the defect structures related to As doping. As anneal temperature increases, the effect of defect equilibrium was changed slowly by the post growth annealing of the layers, and indicates that as-grown material was compensated up to 400°C annealing.

In general, our experimental results of As-doped MBE alloy HgCdTe are in good agreement with the results of phosphorus doped bulk HgCdTe by Vydyanath et al.<sup>20</sup> According to their findings, the hole concentration increased with increase in partial pressure of Hg, in contrast to the behavior observed in undoped HgCdTe. For example, the 77K hole concentration, when annealed at 450°C and low partial

pressure of Hg ( $P_{\text{Hg}} < 0.4 \text{ atm}$ ), was lower than the total concentration of phosphorus in the samples and lower than the intrinsic carrier concentration of the undoped HgCdTe samples. Further, the hole concentrations of P-doped crystals at high Hg pressure were higher than those of the undoped HgCdTe indicating that phosphorus acts as an acceptor at high  $P_{\text{Hg}}$  and as a donor at low  $P_{\text{Hg}}$ . These annealing results on phosphorus-doped HgCdTe were explained on the basis of a defect model in which phosphorus behaves amphoterically, acting as a single acceptor occupying interstitial sites and Te lattice sites at high pressures, and as a single donor occupying Hg lattice sites at low Hg pressures. The defect model by Vydyanath<sup>20</sup> also predicts a majority of the phosphorus to be present as neutral pairs ( $P_i P_{\text{Te}}$ ) at moderate Hg pressures along with Hg vacancy pairs. Our experimental results on As-doped MBE HgCdTe indicate that the behavior of As in HgCdTe is similar to that observed in phosphorus in bulk HgCdTe, except that low temperature incorporated As in MBE HgCdTe appears to be more heavily compensated with As precipitates since the growth temperature of 190–195°C could be too low for the arsenic to come across the barrier and diffuse into proper lattice sites. This needs to be confirmed by transmission electron microscopy (TEM) or other analysis. Vydyanath also found that the site transfer reactions associated with transfer of the group V elements from metal lattice sites to Te lattice sites are proportional to the square of the Hg over pressure,  $\text{As} \sim P_{\text{Hg}}^2$ . If Vydyanath's model is operative, then the resultant As transfer reactions will strongly depend on the Hg vapor pressure rather than the Hg annealing temperature, itself.

### Annealing Effects on As Diffused HgCdTe

Arsenic diffusion experiments were carried out as a comparison to As doping in MBE alloy HgCdTe. The As diffusion in HgCdTe epilayers was performed in the 250–480°C temperature range after first dissolving As and HgCdTe in a Hg solution. The As dopant was added along with Te to the Hg melt solution similar to the Hg-rich LPE<sup>19</sup> growth procedure. In our typical As/Hg solutions, 3–4% Te, 0.01% CdTe and As-doped Te (for As concentrations in the  $10^{18}$  and  $10^{19} \text{ cm}^{-3}$  range) were placed in a reaction quartz tube before the heat up cycle. The As diffusion was performed by immersing the HgCdTe epilayers in the As/Hg solution, followed by a subsequent n-type anneal at 250°C under a Hg environment. The diffusion times and temperatures were tailored to obtain an As diffusion depth of 2–4  $\mu\text{m}$ .

### As Diffusion from Hg-Rich Solution

#### High Temperature Diffusion

To confirm the p-type characteristics of diffused As, we diffused As at 480°C for 30 min, followed by a low temperature (250°C/20 h) anneal and performed differential Hall measurements, as shown in Fig. 2. The surface concentration of As was  $10^{18} \text{ cm}^{-3}$  and dropped

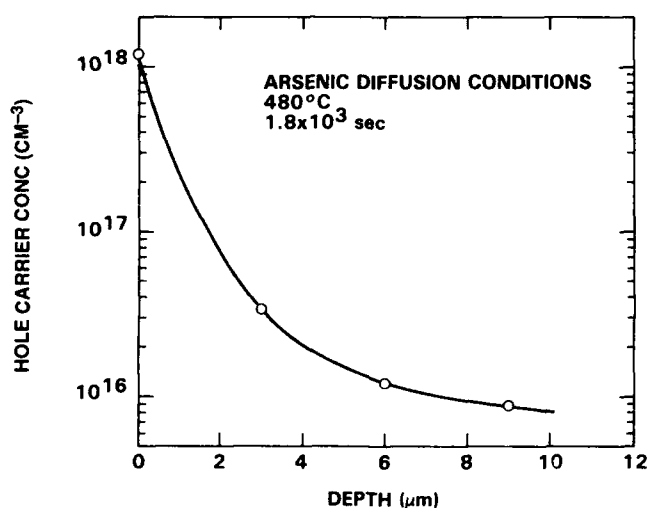


Fig. 2. Differential Hall measurements vs depth profile for 77K hole carrier concentrations after As diffusion in undoped LPE HgCdTe layer.

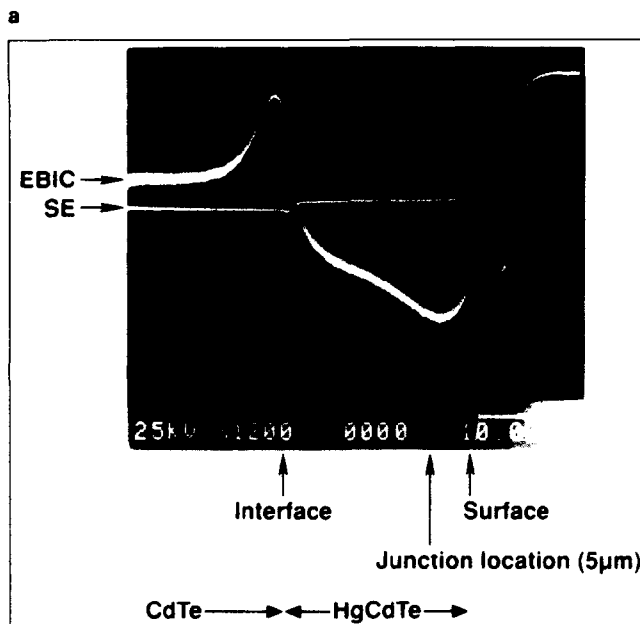
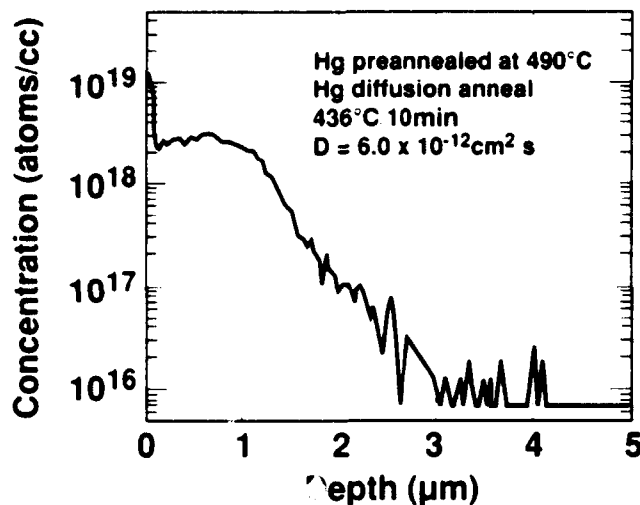


Fig. 3. (a) Secondary ion mass spectroscopy depth profile of As diffusion into LPE HgCdTe at 436°C for 10 min in Hg-rich ambient, and (b) EBIC trace showing the junction depth superimposed on SEM cross-sectional view of cleaved HgCdTe p/n junction device.

to  $10^{16} \text{ cm}^{-3}$  deep inside the HgCdTe layer. Figure 3a shows the SIMS depth profiles of As diffusion into long wavelength infrared (LWIR) HgCdTe at a much lower temperature of 436°C for 10 min in a Hg/As solution, and Fig. 3b shows an electron beam-induced current (EBIC) trace of the junction depth superimposed on a scanning electron microscopy (SEM) cross-sectional view of a cleaved HgCdTe p-on-n diode. The p-n junction depth was determined by EBIC to be approximately 3–5  $\mu\text{m}$  from the surface, which is in accordance with the As profile as determined by SIMS. The As diffusion coefficient estimated from the junction depth was approximately  $6.0 \times 10^{-12} \text{ cm}^2/\text{s}$  at 436°C, which is at least an order of magnitude faster than previous experimental values.

In Fig. 4 is shown a SIMS profile obtained after As

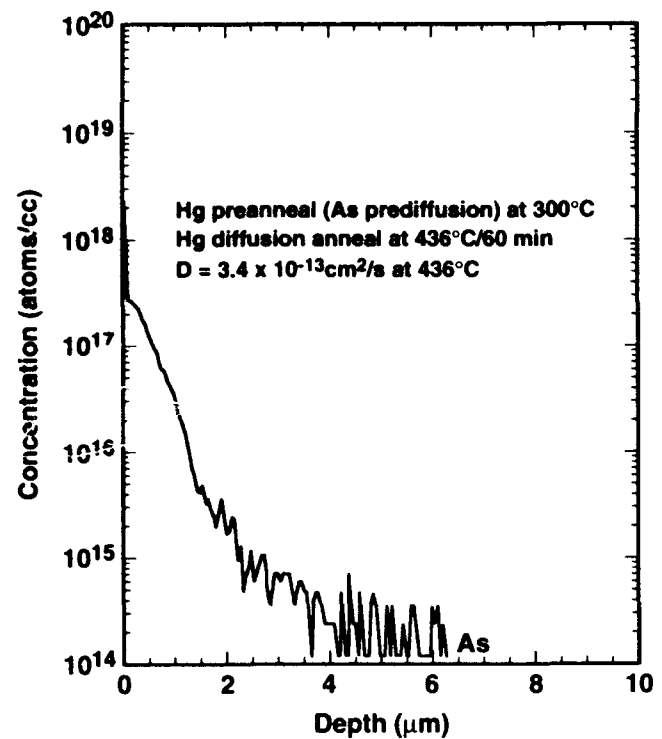


Fig. 4. Arsenic diffusion profiles in Hg saturated, pre-annealed HgCdTe after 436°C/60 min diffusion anneal.

Table III. Low and High Temperature As Diffused HgCdTe ( $x = 0.22$ )

| Dif. & Anneal Temp.(°C) | Dif. & Anneal Time (h) | Carrier Type (n/p) | Carrier Conc. ( $\text{cm}^{-3}$ ) | Mobility ( $\text{cm}^2/\text{V.s}$ ) |
|-------------------------|------------------------|--------------------|------------------------------------|---------------------------------------|
| 277/200                 | 0.5/20                 | n                  | $7.7 \times 10^{14}$               | $7.4 \times 10^4$                     |
| 420/200                 | 0.16/20                | p                  | $1.3 \times 10^{17}$               | $3.1 \times 10^2$                     |

Table IV. Low and High Temperature Sb Diffused HgCdTe ( $x = 0.22$ )

| Dif. & Anneal Temp.(°C) | Dif. & Anneal Time (h) | Carrier Type (n/p) | Carrier Conc. ( $\text{cm}^{-3}$ ) | Mobility ( $\text{cm}^2/\text{V.s}$ ) |
|-------------------------|------------------------|--------------------|------------------------------------|---------------------------------------|
| 240/200                 | 0.5/20                 | n                  | $1.1 \times 10^{15}$               | $1.2 \times 10^5$                     |
| 420/200                 | 0.16/20                | p                  | $1.8 \times 10^{17}$               | $2.1 \times 10^2$                     |

predeposition diffusion/anneal at 300°C, followed by 436°C/60 min annealing in a Hg-saturated ambient. The profiles presented in Figs. 3a and 4 have a similar As diffusion depth profile although the diffusion times are quite different in both cases. The surface component of the profile within about 1.5  $\mu\text{m}$  of the surface has an apparently low diffusion coefficient and the tail component a relatively high diffusion coefficient (Fig. 4). It is possible that the tail regions of the As diffusion profiles in HgCdTe are due to short circuit paths down dislocations or other defects. Attempts were made to evaluate diffusion coefficients for the surface components of the profiles. The apparent diffusion coefficient at 436°C varied from  $3.4 \times 10^{-13} \text{ cm}^2/\text{s}$  to  $6.0 \times 10^{-12} \text{ cm}^2/\text{s}$  for two different pre-annealing temperatures of 300 and 490°C, respectively,



showing over an order of magnitude increase in diffusion coefficients for the different surface conditions but under the same Hg partial pressure. The diffusion coefficient measured at 436°C for the samples pre-annealed at the lower temperature of 300°C agrees with the measurements of As diffusion by Myers et al.<sup>17</sup>

#### Low Temperature As Diffusion

Low temperature As diffusion ( $T < 300^\circ\text{C}$ ) was also carried out for LPE HgCdTe in a Hg-rich solution to see whether p-type activation could be achieved. This particular low temperature process will be very useful to obtain p/n junctions with minimum interdiffusion of two heterojunction layers and impurity control for device processing. Both As and Sb diffused at below 300°C show n-type characteristics, but when

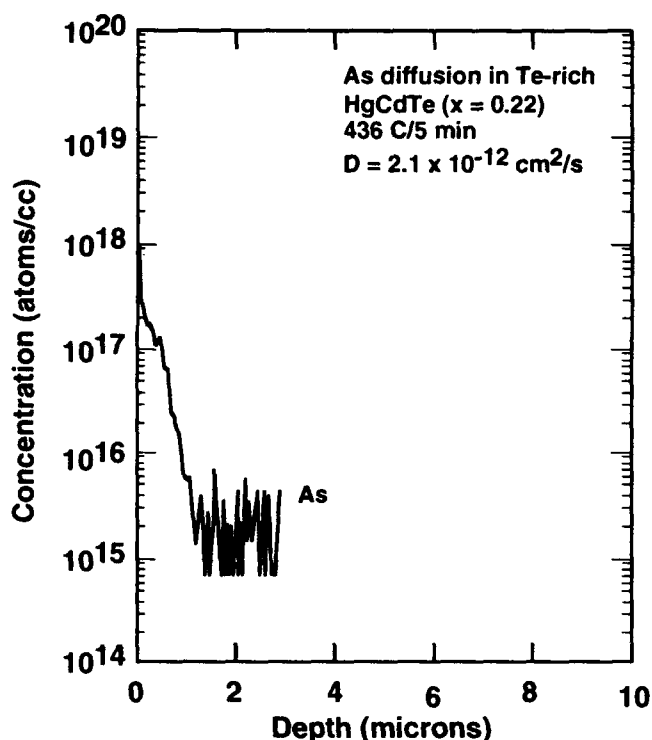


Fig. 5. Secondary ion mass spectroscopy As depth profile of As-diffused HgCdTe from Te-rich solution.

annealed at high temperature (436°C/250°C), p-type behavior was observed in both cases. The observed n-type characteristic of low temperature As diffused samples may not be related to the As although its diffusion was confirmed by SIMS As profiles. Results for samples low temperature diffused without high temperature annealing, and high temperature diffused followed by low temperature n-type annealing are summarized in Tables III and IV. The depth of the As and Sb regions were confirmed by SIMS analysis in the order of 1–2  $\mu\text{m}$  after in situ diffusion anneal at 436/20 min. The As and Sb diffusion layer was also investigated by mesa test p/n junction diodes. The mesa diodes were poorer than typical diodes fabricated by high temperature diffusion. After As and Sb diffused into HgCdTe at 420°C/20 h, the p-type carrier concentration was measured by differential Hall measurements. The 30  $\mu\text{m}$  thick epilayer was completely converted to p-type with carrier concentration of  $6.7 \times 10^{16} \text{ cm}^{-3}$  and mobility of 416  $\text{cm}^2/\text{Vs}$  at 77K. These results appear to be similar to low temperature grown MBE HgCdTe doped with As. Therefore, n-type characteristics observed in MBE As-doped HgCdTe may not be related to Te-rich conditions. They are rather closely related to low partial pressure of Hg in high vacuum and a low temperature growth process.

#### As Diffusion from Te-Rich Solution

The difficulty of achieving acceptor doping with small segregation coefficient of group V elements in Te-rich LPE was reported by Vydyanath et al.<sup>12</sup> In the as-grown material, group V elements were found to be n-type. However, when post growth annealed at 500°C, p-type conduction was sometimes obtained for group V elements (P, As, and Sb), except Bi. To assign doping efficiency in the Te-rich condition (extremely low Hg partial pressure), As diffusion was carried out in a Te-rich LPE solution. This may overcome the serious problem of small segregation coefficient ( $k = 10^{-4}$ ) of group V elements in Te-rich LPE material. A vertical LPE furnace was used to perform As diffusion into a Te-rich LPE HgCdTe layer doped with In at 436°C for 5–10 min without dissolving the HgCdTe layer, and the As distribution was confirmed by SIMS

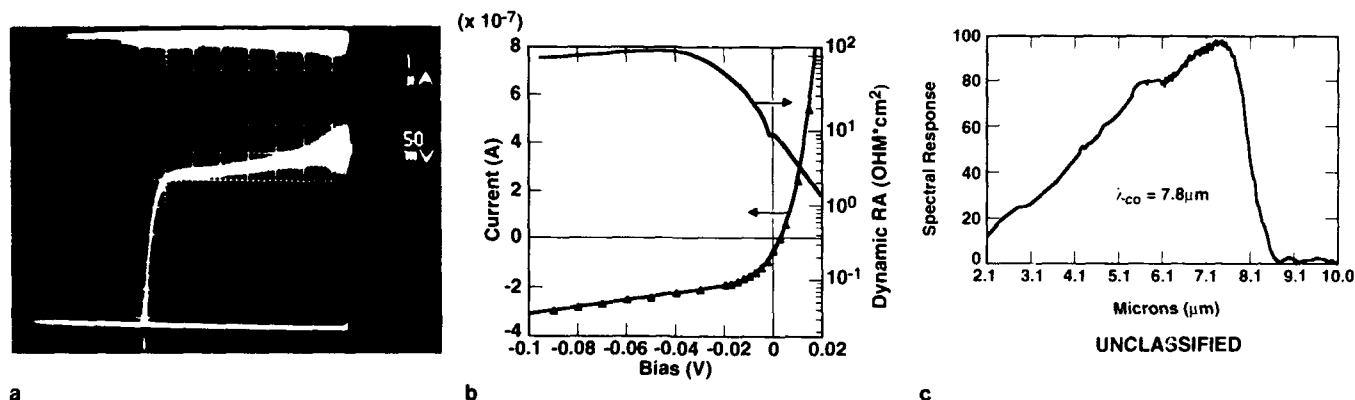


Fig. 6. Current-voltage characteristics of As diffused p/n junction formed from Te-rich solution showing that As is p-type although As was diffused from Te-rich solution; (a) I-V curve tracer, (b) detailed I-V and differential resistance, and (c) spectral response measured at 77K.

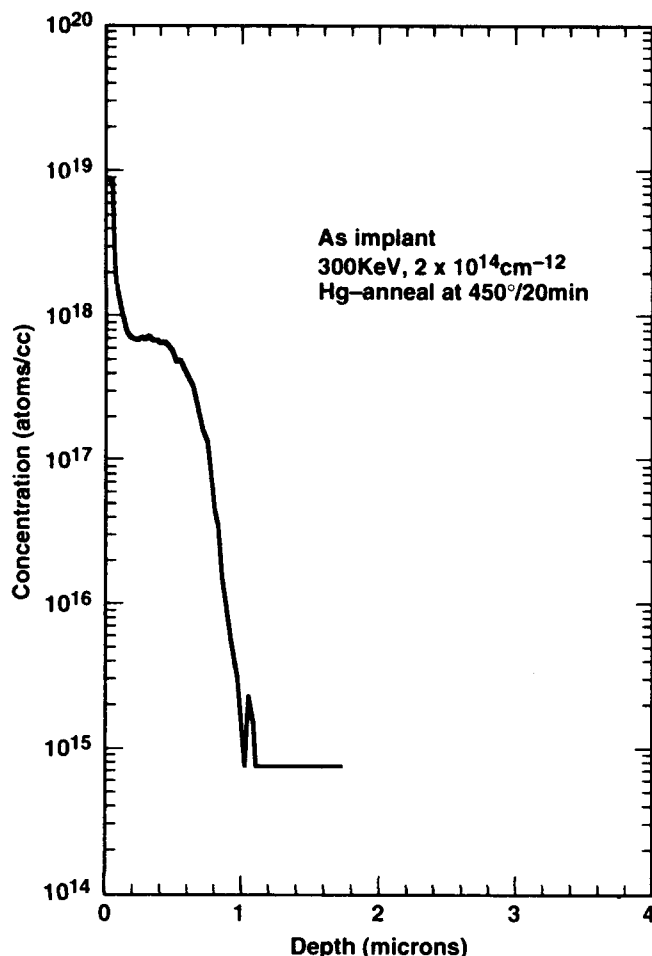
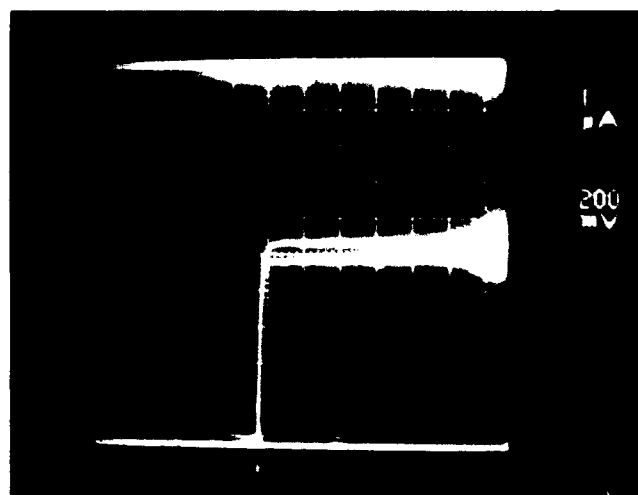


Fig. 7. Secondary ion mass spectroscopy profile of As-implantation in LPE HgCdTe ( $x = 0.3$ ).

analysis. The sample surface after As diffusion from Te-rich solution was not deteriorated. Thermal degradation of the surface at high temperature ( $>400^\circ\text{C}$ ) in quartz ampoule annealing is avoided by high pressure open tube Hg annealing. As shown in Fig. 5, SIMS analysis reveals an As level present at  $1.5 \times 10^{17} \text{ cm}^{-3}$  in the As diffused sample with a depth of about  $1.0 \mu\text{m}$ . This resulted in a value for the As diffusion coefficient of  $2.1 \times 10^{-12} \text{ cm}^2/\text{s}$  at  $436^\circ\text{C}$ . Because As was diffused into an In-doped HgCdTe base layer, after high temperature annealing, it was processed to produce p/n junction mesa test diodes after low temperature n-type anneal at  $250^\circ\text{C}/20 \text{ h}$  (Fig. 6). The purpose of fabricating diodes on the annealed material was to demonstrate As activation. No attempt was made to optimize diode characteristics or to maximize  $R_0A$  products. The low  $R_0A$  product is not typical for this cut-off wavelength. It happens to be the very first diodes we fabricated.

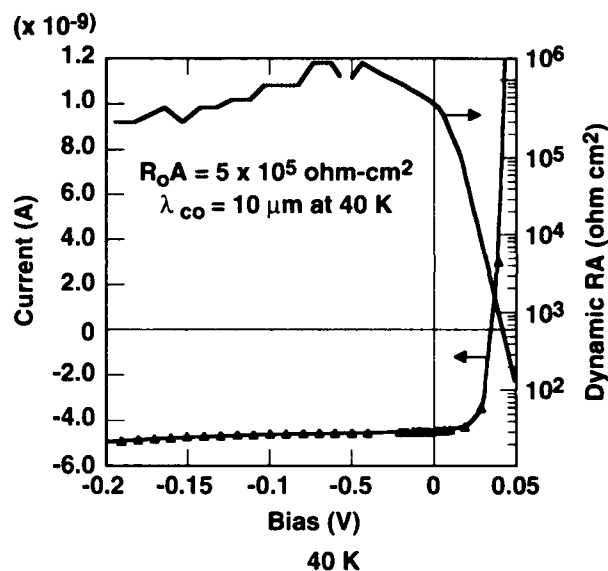
#### Annealing Effects on As Ion-Implanted HgCdTe

While the As diffusion technique has been used to fabricate high performance HgCdTe photovoltaic photodiodes, this method is limited to mesa structures and cannot easily be used to fabricate planar device structures. Although the mesa device struc-



77 K

a



40 K

UNCLASSIFIED

b

Fig. 8. Current-voltage characteristics of As-implanted LWIR HgCdTe diode (a) at 77K and (b) at 40K.

ture does have certain advantages, it is more difficult to deposit passivation layers and to obtain uniform mesa etching characteristics.

As implantation in In-doped HgCdTe was investigated to establish an improved understanding of As activation and annealing effects associated with diffusion and redistribution of As profiles. Ion implantation was performed at 300K using As ions at 50–500 keV and  $2 \times 10^{14} \text{ cm}^{-2}$  dose. This procedure was studied extensively and developed for LPE and MOCVD HgCdTe p-on-n photodiodes by Bubulac et al.<sup>7,8</sup> The annealing study on As-doped MBE HgCdTe indicates that it requires a temperature of at least  $425^\circ\text{C}$  for 30 min to activate the doped As after the

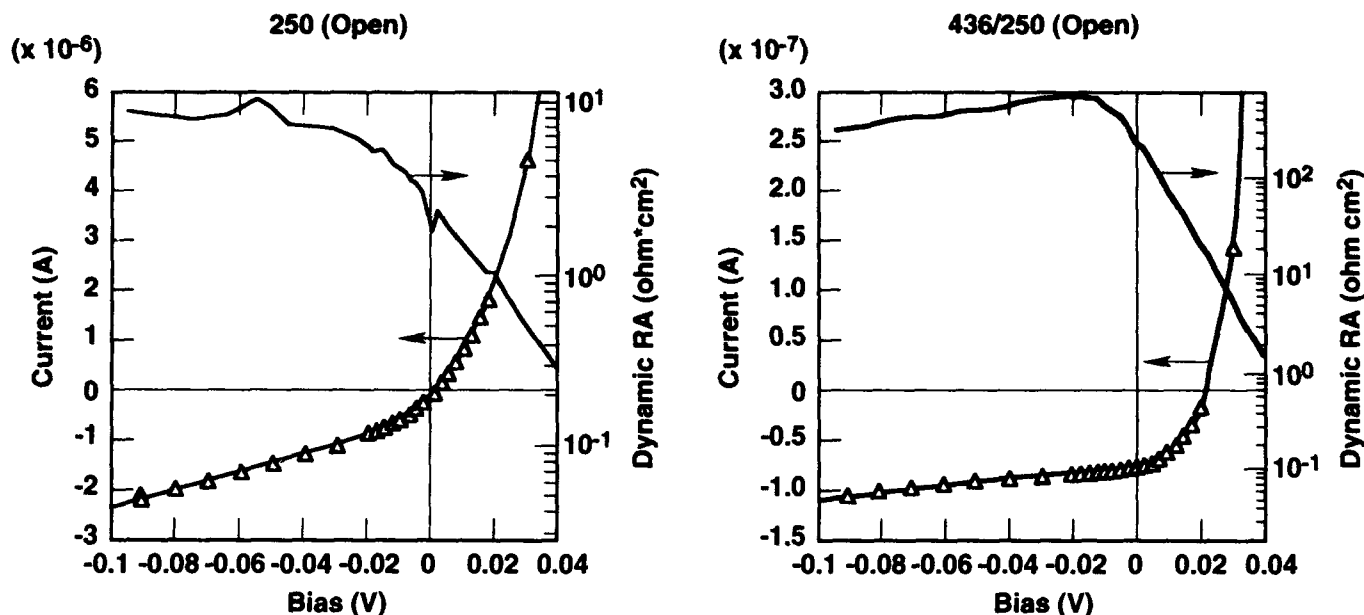


Fig. 9. Current-voltage characteristics of in situ grown p-on-n MBE HgCdTe photodiodes after (a) low temperature (250°C), and (b) high temperature (436/250°C) Hg-annealing.

alloy growth. Therefore, annealing temperatures for As activation were varied from 430 to 460°C in a saturated Hg vapor pressure to activate, diffuse the implanted As, and to form a 2–3  $\mu\text{m}$  deep p-on-n junction. Secondary ion mass spectroscopy was carried out to monitor the depth distribution of the As atoms. A typical As diffusion profile from an ion-implanted source in an LPE HgCdTe layer is shown in Fig. 7. The main As diffusion profile shows a junction depth of about 1  $\mu\text{m}$  based on a background indium concentration of  $3 \times 10^{15} \text{ cm}^{-3}$ . The SIMS instrumental background was mid  $10^{14} \text{ cm}^{-3}$ , and no tail component was observed down to the SIMS detection limit. After low temperature annealing, mesa diodes were fabricated and tested. Figure 8 shows a typical current-voltage (I-V) characteristic of these As-implanted mesa devices measured at 77K and 40K. These homojunction diodes appear to be limited by unpassivated bare surface conditions; CdTe passivated diodes have shown better low temperature performance.

#### Annealing Effects on In Situ Grown p-on-n MBE HgCdTe Photodiodes

To determine the effect of annealing on the in situ grown junction MBE HgCdTe epilayers,<sup>10</sup> the one sample was loaded into the open-tube furnace and annealed at 436°C for 10 min, followed by 250°C low temperature annealing under Hg-ambient. The other portion of the same sample was subjected to anneal only at low temperature at 250°C in Hg ambient to reduce the native vacancy acceptor concentrations. To characterize the grown junction, mesa test diodes were fabricated from both samples and diode characteristics were compared. Figure 9 shows I-V characteristics at 77K for both photodiodes with two different annealing temperatures. The as-grown junction

photodiode after 250°C anneal (Fig. 9a) were leaky, nonuniform, and had low quantum efficiency in addition to low  $R_0A$  of 2.2  $\text{ohm}\cdot\text{cm}^2$  ( $\lambda_c = 9.7 \mu\text{m}$  at 77K). When annealed at 436°C for 10 min, followed by 250°C low temperature anneal, the leakage current was significantly reduced and  $R_0A$  increased to 210  $\text{ohm}\cdot\text{cm}^2$  as shown in Fig. 9b. At the same time, diode yield and uniformity including quantum efficiency (55% without any anti-reflection coating) are improved significantly.

#### DISCUSSION

The electrical activity of As and Sb doping in HgCdTe epitaxial layers has been studied. The transition from n-type to p-type characteristics has been observed in both low temperature grown MBE HgCdTe and As (or Sb)-diffused HgCdTe in Hg-rich solution at temperatures of about 250°C. Under Hg-rich LPE conditions at 200–250°C, As and Sb elements are n-type rather than p-type, which is also observed in As-doped HgCdTe grown by MBE. However, both n-type materials obtained by As-diffusion in a Hg-rich environment and MBE grown at low temperatures were converted to p-type after a high temperature activation anneal, followed by a 250°C Hg-anneal.

In our annealing experiments, we have found that HgCdTe epilayers containing As by the MBE growth technique remained n-type after post-growth annealing up to 400°C under Hg saturated conditions followed by 200°C Hg annealing. However, the As-doped layer converted to p-type after 420°C for 30 min Hg-annealing and the ex situ 200°C Hg-annealing. Furthermore, we also ascertained that the As-diffused films in Hg solution are either n or p-type depending on the diffusion temperatures. At 430°C, As diffused into HgCdTe films followed by an ex-situ 200°C Hg-saturated anneal yielded p-type, but at 260°C, As-

diffused films followed by 200°C ex-situ anneal remained n-type. The latter case is similar to that of low temperature grown MBE HgCdTe epilayers. In addition, the As-diffused epilayer converted to p-type after 436°C Hg-saturated ex situ annealing followed by 200°C Hg-saturated low temperature annealing. In both cases for high and low temperature As-diffusion under excess Hg environment, As should go into Te sites, and As on Te sites should behave as acceptors. Therefore, conceivably the p-type activation of group V elements is not only related to an excess-Hg condition such as Hg-rich LPE growth; rather, it is also strongly related to the annealing temperature which is associated with Hg vapor pressure. Since the HgCdTe sample was heated up to 250°C for over an hour under Hg-rich environments prior to As-diffusion, it is possible that As occupies interstitial sites at 250°C. Thus, the experimental results show that the group V elements appear to occupy inactive or n-active sites when introduced at low temperatures and transfer to available, presumably Te, p-active sites at high temperature. Furthermore, similar activity behavior has been observed in the case of As implantation in HgCdTe.

For the As diffusion studies, two HgCdTe samples were pre-annealed at two different temperatures at 490 and 300°C. A HgCdTe sample was immersed in the As/Hg solution at 300°C for deposition of the As diffusion source at the sample surface and the diffusion anneal was carried out in Hg-ambient. The other sample was pre-annealed at 490°C in the Hg-diffusion furnace. One diffusion temperature, 436°C, was used in these experiments. These high temperature and low temperature pre-anneals were carried out in situ and followed by the As diffusion experiments. Both As profiles are of similar depth as shown in Figs. 3 and 4. The diffusion coefficient values varied from  $3.4 \times 10^{-13}$  cm<sup>2</sup>/s to  $6 \times 10^{-12}$  cm<sup>2</sup>/s for the pre-anneal temperatures of 300 and 490°C, respectively, showing an increase in diffusion coefficient with increasing pre-anneal temperature. The dependence of As diffusion coefficients on pre-annealing parameters was the result of different surface conditions due to Hg partial pressure changes. The reasons for this behavior of the diffusion coefficient with pre-anneal temperature is that the enhanced As diffusion appears to be related to a diffusion mechanism via Hg vacancies. Therefore, overall dependence of As activation and diffusion on Hg-partial pressure can be explained by a defect equilibrium model. This is consistent with changes in the Schottky constant,<sup>13</sup> which relates the concentrations of  $V_{Hg}$  and  $V_{Te}$ , where  $V_{Hg}$  and  $V_{Te}$  denote concentrations of Hg and Te vacancies, respectively. As the partial Hg vapor pressure increases,  $V_{Hg}$  remains almost constant and  $V_{Te}$  increases at least an order of magnitude for HgCdTe by high temperature Hg-annealing.

### SUMMARY

Effects of annealing on As activation were studied on As-doped MBE HgCdTe equilibrated under vari-

ous Hg partial pressures at temperatures varying from 250 to 450°C. The acceptor carrier concentration in the HgCdTe was augmented with increases in the partial pressure of Hg, and then converted to p-type after post growth annealing above 425°C. This behavior of As activation is also observed in As-diffused HgCdTe in Hg-rich conditions, indicating that As-diffused HgCdTe at low temperatures in the range from 240 to 300°C was n-type even though As was diffused under Hg-rich conditions. Either high temperature annealing of the As-diffused HgCdTe layers at 436°C or high temperature As diffusion at 436°C followed by low temperature annealing at 250°C for 15 h always produces p-type As-doped HgCdTe material. Comparable behavior of As activation has been also observed in the case of As ion implantation in HgCdTe. Vydyanath et al.,<sup>20</sup> observed similar behavior of As p-type doping at high temperature at high partial pressure of Hg in P-doped bulk HgCdTe ( $x = 0.2$ ) crystals subsequent to anneals at various temperatures, which indicates that P acts as an acceptor at high  $P_{Hg}$  and as a donor at low  $P_{Hg}$ . Therefore, in the case of As doped MBE HgCdTe heterojunction structures grown at low temperature and under low partial pressure of Hg, As activation at high temperature is necessary to produce high performance photodiodes.

### REFERENCES

1. M. Boukerche, P.S. Wijewanasuriva, S. Sivananthan, I.K. Sou, Y.J. Kim K. Mahavedi and J.P. Faurie, *J. Vac. Sci. Technol. A* 6, 2830 (1988).
2. P. Capper, *J. Vac. Sci. Technol. B* 2, 1667 (1991).
3. J.W. Han, S. Hwang, Y. Lansari, R.L. Harper, Z. Yang, N.C. Giles J.W. Cook, Jr., J.F. Schetzina and S. Sen, *J. Vac. Sci. Technol. A* 7, 305 (1989).
4. J.M. Arias, M. Zandian, J.G. Pasko, S.H. Shin, L.O. Bubulac and R.E. DeWames, *J. Appl. Phys.* 69, 2143 (1991).
5. C.J. Summers, R.G. Benz, B.K. Wagner, J.D. Benson and D. Rajavel, *Proc. SPIE* 1106, 1 (1990).
6. O.K. Wu, G.S. Kamath, W.A. Radford, P.R. Bratt and E.A. Patten, *J. Vac. Sci. Technol. A* 8, 1034 (1990).
7. L.O. Bubulac, W.E. Tennant, D.S. Lo, D.D. Edwall, J.C. Robinson, J.C. Chen and G. Bostrup, *J. Vac. Sci. Technol. A* 5, 3166 (1987).
8. L.O. Bubulac, D.D. Edwall and C.R. Viswanathan, *J. Vac. Sci. Technol. B* 9, 1695 (1991).
9. M.H. Kalisher, *J. Cryst. Growth* 70, 365 (1984).
10. J.M. Arias, S.H. Shin, J.G. Pasko, R.E. DeWames and E.R. Gertner, *J. Appl. Phys.* 65, 1747 (1989).
11. J.P. Faurie, M. Boukerche, J. Reno, S. Sivananthan and C. Hsu, *J. Vac. Sci. Technol. A* 3, 55 (1985).
12. (a) H.R. Vydyanath, J.A. Ellsworth and C.M. Devaney, *J. Electron. Mater.* 16, 13 (1987) and (b) H.R. Vydyanath, *J. Vac. Sci. Technol. B* 9, 1716 (1991).
13. T.C. Harman, (unpublished results).
14. S.H. Shin, J.M. Arias, M. Zandian, J.G. Pasko and R.E. DeWames, *Appl. Phys. Lett.* 59, 2718 (1991).
15. J.M. Arias, S.H. Shin, J.G. Pasko, R.E. DeWames and E.R. Gertner, *J. Appl. Phys.* 65, 1747 (1989).
16. C.C. Wang, S.H. Shin, M. Chu, M. Lanir and A.H.B. Vanderwyck, *J. Electrochem. Soc.* 127, 175 (1980).
17. T.H. Myers, K.A. Harris, R.W. Yanks, C.M. Mohnkan, R.J. Williams and E.K. Dudoff, *J. Vac. Sci. Technol. B* 10, 1438 (1992).
18. P. Rudolph, M. Muhlberg, M. Neubert, T. Boeck, P. Mock, L. Parthier and K. Jacobs, *J. Crystal Growth* 118, 202 (1992).
19. P.E. Herning, *J. Electron. Mater.* 13, 1 (1984).
20. H.R. Vydyanath, R.C. Abbott and D.A. Nelson, *J. Appl. Phys.* 54, 1323 (1983).

# MBE HgCdTe Heterostructure p-on-n Planar Infrared Photodiodes

J.M. ARIAS, J.G. PASKO, M. ZANDIAN, S.H. SHIN, G.M. WILLIAMS,  
L. O. BUBULAC, R.E. DE WAMES, and W.E. TENNANT

Rockwell International Science Center, Thousand Oaks, CA 91360

We recently succeeded in fabricating planar  $\text{Hg}_{1-y}\text{Cd}_y\text{Te}/\text{Hg}_{1-x}\text{Cd}_x\text{Te}$  ( $x < y$ ) heterostructure photodiodes with the p-on-n configuration. Here we discuss early results in detail and present new results on an expanded range of infrared operation. The material used for this demonstration was grown by molecular beam epitaxy on lattice-matched CdZnTe substrates. The p-on-n planar devices consist of an arsenic-doped p-type epilayer ( $y \sim 0.28$ ) atop a long wavelength infrared n-type epilayer ( $x = 0.22-0.23$ ). The planar junctions were formed by selective pocket diffusion of arsenic deposited on the surface by ion implantation. Detailed analysis of the current-voltage characteristics of these diodes as a function of temperature shows that they have high performance and that their dark currents are diffusion-limited down to 52K. Low frequency noise measurements at a reverse bias voltage of 50 mV resulted in noise current values (at 1 Hz) as low as  $1 \times 10^{-14}$  amps/Hz<sup>0.5</sup> at 77K. Average  $R_0A$  values greater than  $10^6 \Omega\text{-cm}^2$  at 40K were obtained for these devices with cut-off wavelength values in the 10.6 to 12  $\mu\text{m}$  range. Seventy percent of these devices have  $R_0A$  values greater than  $10^5 \Omega\text{-cm}^2$  at 40K; further studies are needed to improve device uniformity. These results represent the first demonstration that high performance long wavelength infrared devices operating at 40K can be made using HgCdTe material grown by a vapor phase epitaxy growth technique.

**Key words:** HgCdTe, MBE, planar photodiodes, p-on-n heterostructures

## INTRODUCTION

In the last several years, we have seen significant advances in the performance of long wavelength infrared (LWIR) p-on-n HgCdTe double layer photodiodes.<sup>1-6</sup> These devices have use in infrared focal plane detector arrays for military sensors and have potential commercial applications. P-on-n junctions are highly desirable because they offer significantly better performance (higher  $R_0A$  products) than n-on-p junctions for LWIR detection applications.<sup>1-2</sup> One important advantage of the p-on-n device is that the n-type HgCdTe carrier concentration is easy to control in the  $10^{14}-10^{15} \text{ cm}^{-3}$  range using extrinsic doping; while for the n-on-p device, the control of p-type carrier concentration at these low levels is very difficult. Because of the lower carrier concentrations achieved in the n-type HgCdTe base epilayers, they have longer minority-carrier lifetimes than in p-type base layers.

Current p-on-n HgCdTe LWIR photovoltaic fabrication technology is based on a mesa device configuration, where wet or dry chemical etching is used to delineate the devices. A critical step in the processing of mesa devices is the etching and deposition of CdTe as a passivant to reduce surface currents,<sup>7</sup> which is important, especially for small area devices typically used for imaging applications. In silicon and III-V compounds, this surface problem has been addressed by using a planar structure where the critical surface passivation step is not required since the junction interface is buried.

Because of the attributes of this structure, we have developed a process to make planar p-on-n devices using  $\text{Hg}_{1-y}\text{Cd}_y\text{Te}/\text{Hg}_{1-x}\text{Cd}_x\text{Te}$  ( $x < y$ ) heterostructures. We formed the planar photodiodes by selective pocket diffusion of arsenic deposited on the wide band gap  $\text{Hg}_{1-y}\text{Cd}_y\text{Te}$  surface by ion implantation. While the successful use of ion implantation to fabricate arsenic-doped p-on-n mesa HgCdTe diodes had been reported,<sup>8</sup> an extension of this technique to fabricate planar devices had not been. Recently, we reported

(Received October 14, 1992; revised January 15, 1993)

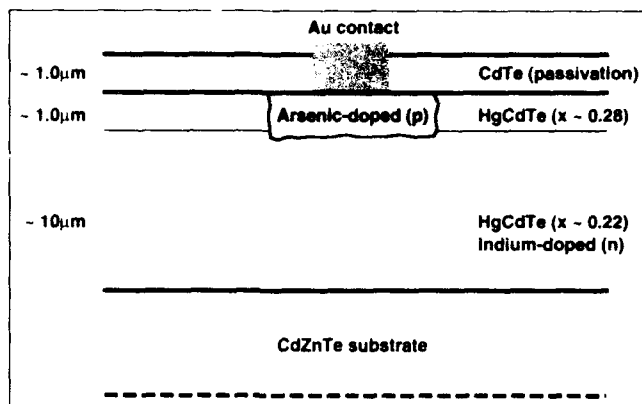


Fig. 1. Schematic cross section of passivated p-on-n planar arsenic-doped HgCdTe heterostructure diode.

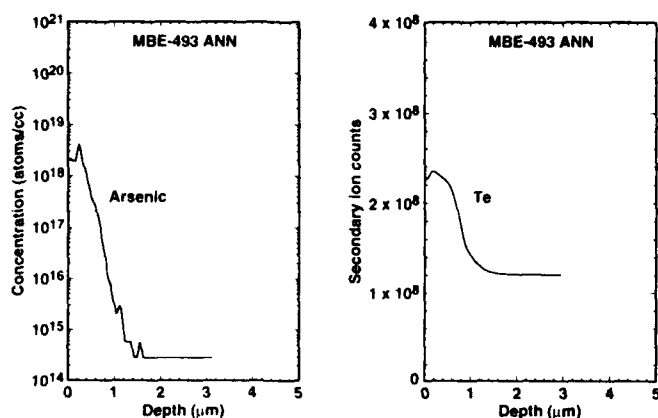


Fig. 2. Typical arsenic and tellurium SIMS profiles for a p-on-n planar  $\text{Hg}_{0.78}\text{Cd}_{0.22}\text{Te}/\text{Hg}_{0.72}\text{Cd}_{0.28}\text{Te}$  heterostructure (No. 493) device.

the fabrication and successful operation of planar p-on-n HgCdTe heterostructure devices.<sup>9</sup> After the initial results, we have carried out further device studies, grown new structures and fabricated more devices with expanded infrared cut-off wavelengths. Here we discuss the early results in detail and present new results.

## EXPERIMENTAL

Figure 1 is a schematic of the planar HgCdTe diode heterostructure. The planar devices were formed using  $\text{Hg}_{1-x}\text{Cd}_x\text{Te}/\text{Hg}_{1-y}\text{Cd}_y\text{Te}$  ( $x < y$ ) heterostructures grown by MBE. A detailed discussion of MBE HgCdTe growth procedures used here can be found in Refs. 10 and 11. The structures were grown on a near lattice-matched (211)  $\text{Cd}_{0.96}\text{Zn}_{0.04}\text{Te}$  substrate to minimize the dislocation density in the HgCdTe epilayers. The HgCdTe epilayers had etch pit density counts in the low  $10^5 \text{ cm}^{-2}$  range. The (211)B surface orientation was chosen because adequate HgCdTe surface morphology and high performance photodiodes were previously obtained on epitaxial layers grown on this orientation.<sup>10,11</sup>

The multi-layers with different gaps were grown at low temperatures ( $T \sim 190^\circ\text{C}$ ) to provide epitaxy-quality interfaces. These in situ grown interfaces are the key to eliminate surface dark currents and variations

caused by hard-to-control surface conditions. The n-type narrow band gap base layer for these structures was about  $8\text{--}10 \mu\text{m}$  thick and doped with indium in the  $2\text{--}3 \times 10^{15} \text{ cm}^{-3}$  level, while the wider band gap capping layer ( $y \sim 0.28$ ) was  $0.5\text{--}1 \mu\text{m}$  thick and not intentionally doped. The structure was terminated with a thin ( $500\text{\AA}$ ) CdTe layer for protection and passivation of the surface.

The formation of planar photodiodes was achieved by first selectively implanting arsenic through windows made on a mask of photoresist/ZnS and then diffusing the arsenic through the cap layer into the narrow gap base layer. The selective implantation of arsenic was carried out at room temperature; the beam energy was  $350 \text{ keV}$  and the ion dose was  $1 \times 10^{14} \text{ cm}^{-2}$ . After the structure was selectively implanted, it was annealed under Hg overpressure in a high pressure system.<sup>12</sup> The sample underwent two consecutive annealings, one at  $435^\circ\text{C}$  for approximately 20 min and the other at  $250^\circ\text{C}$  for 24 h immediately after. The first annealing was carried out to diffuse the arsenic into the base LWIR layer and to make the doped region p-type by substitution of arsenic atoms on the Te sublattice, while the second one was to annihilate Hg vacancies formed in the HgCdTe lattice during growth and diffusion of arsenic. No deleterious junction effects are expected from the implantation step since the residual damage after annealing is confined in the wider gap region near the surface while the p-on-n junction is located  $1 \mu\text{m}$  underneath. Figure 2 shows typical As and Te secondary ion mass spectroscopy (SIMS) profiles that were obtained on a sample (No. 493) that was subjected to this process. The Te yield profile curve reflects the changes of concentrations of the matrix elements Hg and Cd so accurately that the Te yield curve can be interpreted as a scaled plot of the energy gap as a function of depth.<sup>13</sup> As illustrated in these two curves, the arsenic diffused about  $1 \mu\text{m}$  from the surface; and this was sufficient to form the p-on-n junction near the narrow gap layer. This is desired to avoid nonuniformities in quantum efficiency and dark currents.

## DEVICE RESULTS

After diffusing the arsenic into the base layer, we used this material to fabricate planar devices of the following areas:  $30 \times 30$ ,  $50 \times 50$ ,  $125 \times 125$ , and  $500 \times 500 \mu\text{m}^2$ . The planar devices were further protected (as illustrated in Fig. 1) with polycrystalline CdTe (thickness  $\sim 1 \mu\text{m}$ ) deposited at room temperature in an e-beam system. Electrical contacts were made with gold on top of the p-type capping layer and on the n-type layer.

The spectral response was measured with a Nicolet Fourier transform infrared spectrometer; the 50% spectral cut-off wavelength ( $\lambda_{co}$ ) was used to determine the energy gap of HgCdTe. The 77K spectral response for these devices was broadband, a typical spectral response curve for a device (No. 496) with  $\lambda_{co}$  of  $10.0 \mu\text{m}$  is illustrated in Fig. 3. This  $\lambda_{co}$  value is consistent with the composition value of the narrow

gap layer ( $x = 0.225$ ) calculated from the absorption edge of the room-temperature infrared transmission spectrum using the Hansen, Schmit, and Casselman equation.<sup>14</sup>

Backside-illuminated quantum efficiency of these diodes, without anti-reflection coating, was measured at zero bias. For the quantum efficiency measurement, we used a standard blackbody source, a 25  $\mu\text{m}$  focused spot, a narrow bandpass (9  $\mu\text{m}$ ) filter and phase sensitive detection techniques. Quantum efficiency values of 52% were measured at 77K for the 50  $\times$  50  $\mu\text{m}^2$  planar devices. A typical three-dimensional spot scan quantum efficiency measurement for a planar device (No. 508,  $\lambda_{\text{co}} = 10.0 \mu\text{m}$ ) is illustrated in Fig. 4. The measured backside illuminated infrared optical response area ( $A_0$ ) for this device was 68  $\times$  68  $\mu\text{m}$  while the nominal junction area ( $A$ ) of this device was 50  $\times$  50  $\mu\text{m}$ ; from this data, the device lateral optical collection length was estimated to be 9  $\mu\text{m}$  at 77K. This value is consistent with the predicted theoretical minority carrier diffusion length of HgCdTe of similar composition and n-type carrier concentration, assuming an Auger-limited minority carrier lifetime and a hole mobility of 450  $\text{cm}^2/\text{V}\cdot\text{s}$ .<sup>4</sup>

The 77K performance of seven different p-on-n planar MBE HgCdTe diode arrays is summarized in Fig. 5. We have plotted mean and median zero bias impedance area ( $R_0A$ ) products as a function of device cut-off wavelength for the LWIR diode arrays. As illustrated in the figure, mean and median  $R_0A$  values for the seven samples are nearly equal which indicates that the devices are highly uniform at 77K. These devices were measured under zero background. These data were obtained measuring devices with nominal junction areas of 30  $\times$  30 and 50  $\times$  50  $\mu\text{m}$  which are typical device sizes in HgCdTe photovoltaic focal plane arrays. The number of devices measured per test array was usually 60. The data follow the solid curve which is the result of an  $R_0A$  calculation based on the ideal diode equation using  $n_D - n_A = 3 \times 10^{15} \text{ cm}^{-3}$  and Auger-limited minority carrier lifetime.

Figure 6 shows 40K and 77K  $R_0A$  cumulative distribution functions of a typical p-on-n planar LWIR diode array (No. 496), with junction areas of 30  $\times$  30

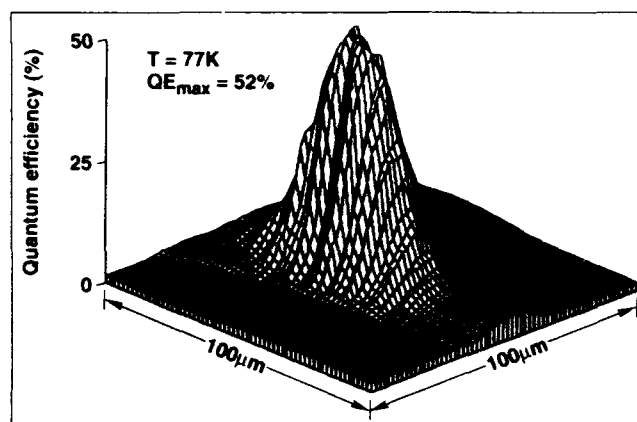


Fig. 4. Long wavelength infrared ( $\lambda_{\text{co}} = 10 \mu\text{m}$ ) three-dimensional quantum efficiency spot scan at 77K of a HgCdTe ( $x = 0.225$ ) heterostructure planar photodiode (No. 508). Device junction area is 50  $\times$  50  $\mu\text{m}^2$ .

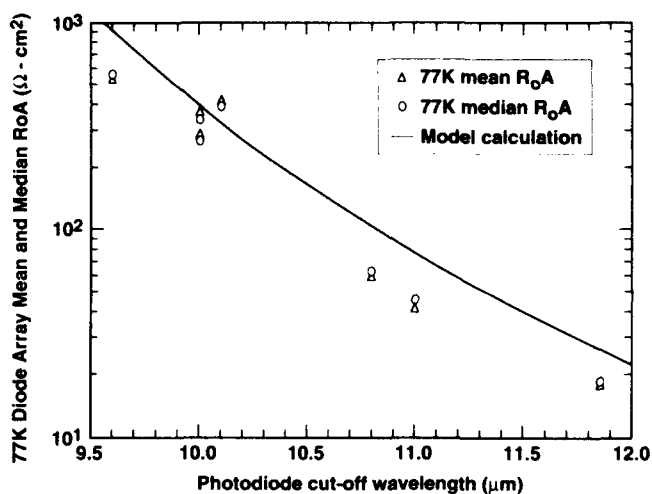


Fig. 5. Mean and median  $R_0A$  products at 77K as a function of wavelength cutoff for seven p-on-n planar MBE HgCdTe diode arrays, each with approximately 60 devices.

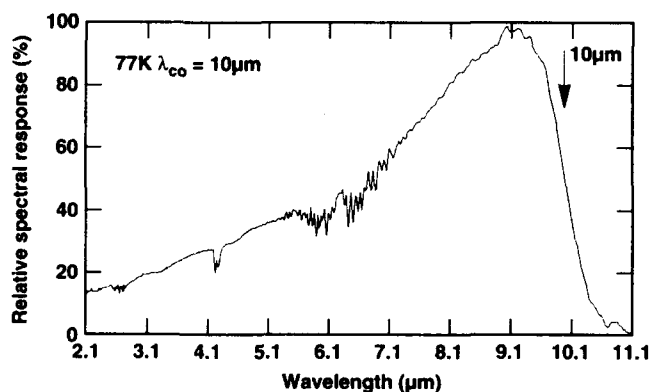


Fig. 3. Long wavelength infrared ( $\lambda_{\text{co}} = 10 \mu\text{m}$ ) relative spectral response (per watt) at 77K of a MBE HgCdTe ( $x = 0.225$ ) heterostructure planar photodiode (No. 496).

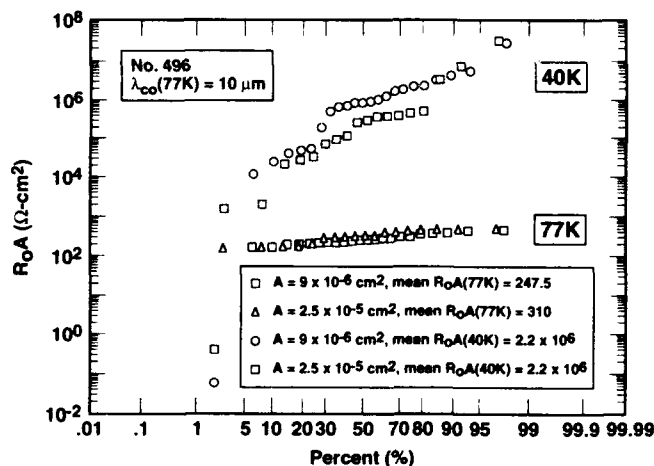


Fig. 6.  $R_0A$  cumulative distribution functions at 77K and 40K of 60 planar p-on-n HgCdTe diodes (No. 496). Device junction areas are 9  $\times 10^{-6}$  and 2.5  $\times 10^{-5} \text{ cm}^2$ .

$\mu\text{m}$  and  $50 \times 50 \mu\text{m}$ . Mean  $R_0A$  values of 247 and  $310 \Omega\text{-cm}^2$  were obtained for the  $30 \times 30$  and  $50 \times 50 \mu\text{m}$  sizes, respectively. The devices exhibit good  $R_0A$  uniformity at 77K with standard deviation to mean ratio values of 37 and 35% for the two different device areas. In general,  $R_0A$  operability at 77K is good; >97% of the diodes have  $R_0A > 100 \Omega\text{-cm}^2$ .

At 40K, device uniformity and operability of these devices need further improvements since large spreads in  $R_0A$  values were obtained. For example, while mean  $R_0A$  values of  $2 \times 10^6 \Omega\text{-cm}^2$  were achieved for these LWIR ( $\lambda_{co} = 11 \mu\text{m}$  at 40K) devices, the median values were only  $7.8 \times 10^5$  and  $2.5 \times 10^5 \Omega\text{-cm}^2$  for the  $30 \times 30$  and  $50 \times 50 \mu\text{m}$  devices, respectively. The figure also shows that the operability at 40K is not satisfactory; 30% of the devices have  $R_0A$  values below  $1 \times 10^5 \Omega\text{-cm}^2$ . Similar results at 40K were obtained with the other samples which have cut-off wavelength values in the 10.6 to 12  $\mu\text{m}$  range. Further

MBE HgCdTe growth and device processing studies are needed to identify the cause for devices that have  $R_0A$  values  $< 10^5 \Omega\text{-cm}^2$ . Another important area to study is the effect that defects in the CdZnTe substrates have on device performance and uniformity at 40K. P-on-n and n-on-p diodes made with HgCdTe material grown by liquid phase epitaxy<sup>15, 17</sup> also suffer in uniformity as temperature decreases from 77 to 40K; therefore, this problem is not unique to MBE.

Figure 7 illustrates detailed current-voltage (I-V) and dynamic impedance area-voltage (RA-V) diode characteristics at 77K for typical  $50 \times 50 \mu\text{m}$  detectors. At 77K, the device dark currents are diffusion limited and dynamic RA products for the diodes reach values of  $10^4$ – $10^5 \Omega\text{-cm}^2$  at an applied reverse bias of 50 mV.

To determine the mechanisms controlling the device leakage currents, the I-V characteristics were measured as a function of temperature. Figure 8 illustrates the temperature dependence of the zero-bias resistance area ( $R_0A$ ) product for a planar device. The solid line is a fit to the experimental data assuming diffusion currents are dominating the observed dark currents. The energy band gap ( $\lambda = 10.4 \mu\text{m}$  at 77K) calculated from this fit is in good agreement with the measured optical band gap ( $\lambda_{co} = 10.0 \mu\text{m}$  at 77K) for the device. As illustrated in the figure, at temperatures above 52K, the  $R_0A$  products are limited by diffusion processes. For temperatures below 52K, the  $R_0A$  products still increase but more gradually, and the observed temperature dependence is less sensitive than that expected for generation-recombination currents. At 40K, the detailed analysis of the I-V characteristics (Fig. 9) over a broad range of voltages suggests that the dark currents consist of a mixture of diffusion, generation-recombination, and tunneling currents.

Device low frequency (1/f) noise is an important parameter which can limit the performance of a

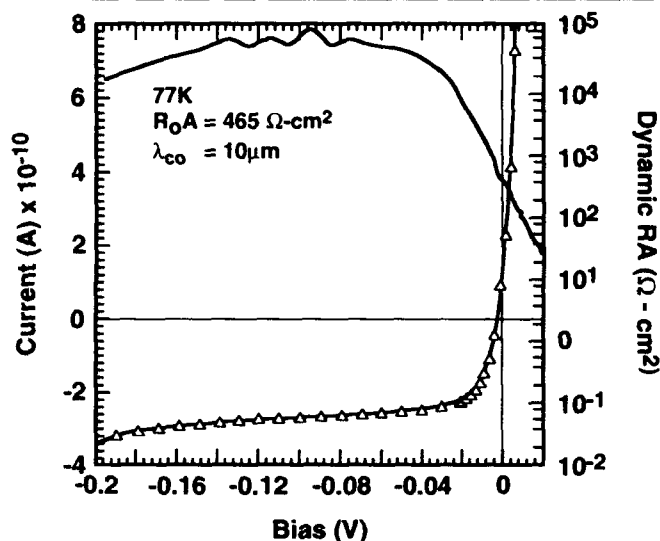


Fig. 7. Detailed I-V and dynamic impedance characteristics at zero background of an MBE HgCdTe planar p-on-n heterostructure (No. 496) diode at 77K ( $\lambda_{co} = 10 \mu\text{m}$ ).

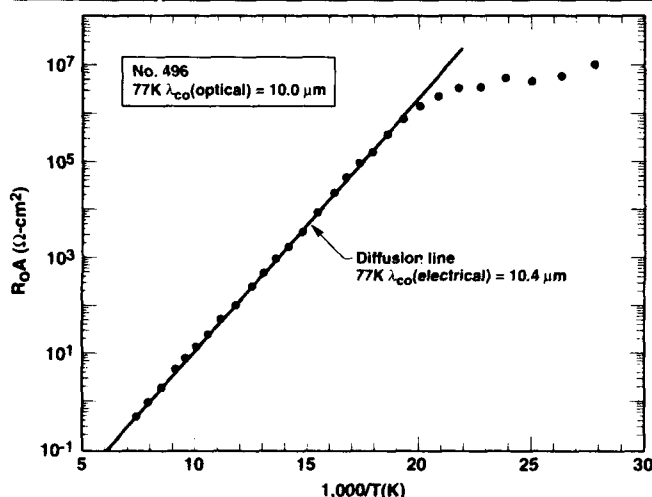


Fig. 8.  $R_0A$  dependence on reciprocal temperature of LWIR p-on-n planar photodiode fabricated with a HgCdTe heterostructure (No. 496).

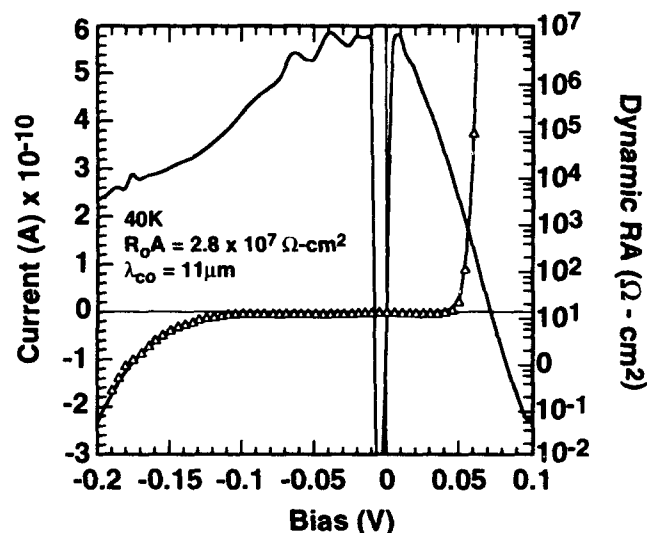


Fig. 9. Detailed I-V and dynamic impedance characteristics at zero background of an MBE HgCdTe planar p-on-n heterostructure (No. 496) diode at 40K ( $\lambda_{co} = 11 \mu\text{m}$ ).



staring focal plane array. It becomes more important as the devices are operated at slower readout frequencies and under applied bias. Noise measurements for these planar diodes were made as a function of frequency at zero background, 77K, and at a diode reverse bias of 50 mV. An example of a diode (junction area =  $2.5 \times 10^{-5} \text{ cm}^2$ ) noise spectrum taken at 77K is shown in Fig. 10. The device had a  $1/f$  noise current value (at 1 Hz) as low as  $1 \times 10^{-14} \text{ A/Hz}^{1/2}$ . The noise current for this device was essentially independent of frequency down to 1 Hz. In Fig. 11, we plotted  $1/f$  noise current as a function of device  $R_0A$  product at 77K for 29 diodes made with sample No. 508 ( $\lambda_{co} = 10 \mu\text{m}$ ). As illustrated in the figure, we see again that the  $R_0A$  operability at 77K is good (96% of the diodes have  $R_0A > 100 \Omega\text{-cm}^2$ ). In general, devices with high  $R_0A$  values have low  $1/f$  noise current values.

### SUMMARY

In summary, we have demonstrated the feasibility of fabricating planar HgCdTe heterostructure photodiodes of the p-on-n configuration. The results indicate that the planar LWIR devices are uniform at 77K. Detailed analysis of the current-voltage characteristics of these diodes as a function of temperature shows that they have high performance and that their dark currents are diffusion limited down to 52K. Low frequency noise measurements at a reverse bias voltage of 50 mV resulted in noise current values (at 1 Hz) as low as  $1 \times 10^{-14} \text{ amps/Hz}^{0.5}$  at 77K. High performance LWIR devices operating at 40K have been demonstrated for the first time using HgCdTe material grown by MBE. Average  $R_0A$  values of  $2 \times 10^6 \Omega\text{-cm}^2$  at 40K were obtained for devices with cut-off wavelengths of  $11 \mu\text{m}$ . Further studies are needed to improve device uniformity and operability at 40K. These results are important because they represent the first steps toward the development of a fully planar p-on-n fabrication technology. This planar process has substantial potential for LWIR HgCdTe because it could simplify FPA processing.

### ACKNOWLEDGMENT

This work has been sponsored by Rockwell International IR&D funds. The authors thank D.M. Stephenson for ion implantation of arsenic and A.H. Vanderwyck for e-beam CdTe deposition.

### REFERENCES

1. P.R. Norton, *Opt. Eng.* 30, 1649 (1991).
2. C.C. Wang, *J. Vac. Sci. Technol.* B9, 1740 (1991).
3. W.A. Radford, Abst. Innovative LWIR Detector Workshop, Pasadena, CA, April 7, 1992.
4. G.N. Pultz, P.W. Norton, E.E. Krueger and M.B. Reine, *J. Vac. Sci. Technol.* B 9, 1724 (1991).
5. S.M. Johnson, D.R. Rhiger, J.P. Rosbeck, J.M. Peterson, S.M. Taylor and M.E. Boyd, *J. Vac. Sci. Technol.* B 10, 1499 (1992).
6. R.E. DeWames, J.M. Arias, L.J. Kozlowski and G.M. Williams, SPIE Conf. Proc. 1735, *Infrared Detectors: State of the Art 2* (1992).
7. W.E. Tennant, C.A. Cockrum, J.B. Gilpin, M.A. Kinch, M.B. Reine and R.P. Ruth, *J. Vac. Sci. Technol.* B 10, 1359 (1992).

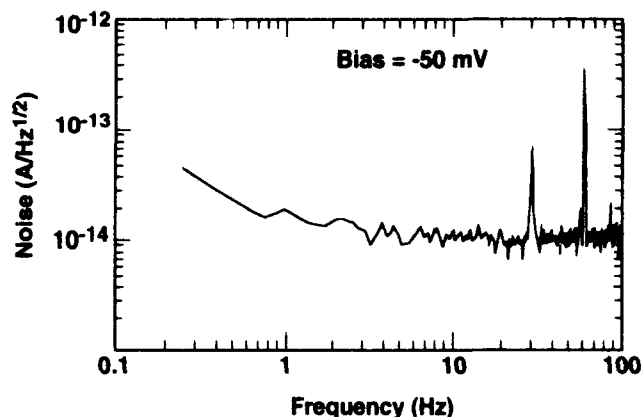


Fig. 10. Noise spectrum at low background and 77K for a HgCdTe planar p-on-n heterostructure diode measured at -50 mV.

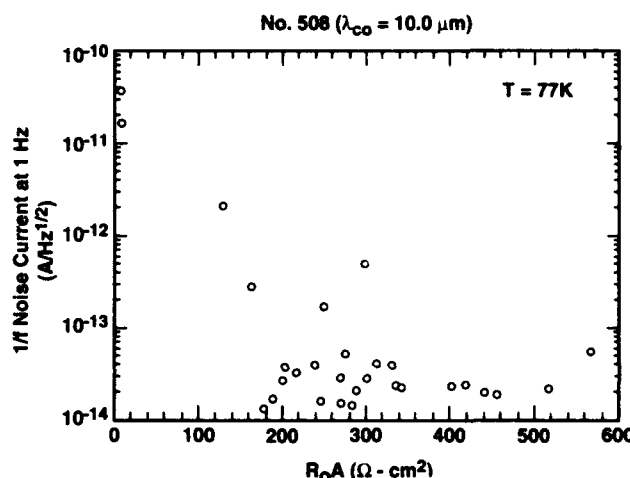


Fig. 11. Low frequency noise current at 1 Hz vs  $R_0A$  product for an array (No. 508) of planar p-on-n LWIR ( $\lambda_{co} = 10 \mu\text{m}$ ) diodes. The measurements for these devices were made at 77K, zero background, and at a diode reverse bias of 50 mV.

8. L.O. Bubulac, D.S. Lo, W.E. Tennant, D.D. Edwall, J.C. Chen, J. Ratusnik, J.C. Robinson and G. Bostrup, *Appl. Phys. Lett.* 50, 1586 (1987).
9. J.M. Arias, J.G. Pasko, M. Zandian, S.H. Shin, G.M. Williams, L.O. Bubulac, R.E. DeWames and W.E. Tennant, *Appl. Phys. Lett.* 62, 976 (1993).
10. J.M. Arias, S.H. Shin, J.G. Pasko, R.E. DeWames and E.R. Gertner, *J. Appl. Phys.* 65, 1747 (1989).
11. J.M. Arias, M. Zandian, J.G. Pasko, S.H. Shin, L.O. Bubulac, R.E. DeWames and W.E. Tennant, *J. Appl. Phys.* 69, 2143 (1991).
12. S.H. Shin, J.M. Arias, M. Zandian, J.G. Pasko and R.E. DeWames, *J. Electron. Mater.* 22, 1039 (1993).
13. L.O. Bubulac and C.R. Viswanathan, *Appl. Phys. Lett.* 60, 222 (1992).
14. G.L. Hansen, J.L. Schmit and T.N. Casselman, *J. Appl. Phys.* 53, 7099 (1982).
15. H.R. Vidyantath, J. Ellsworth, L. Fishman, S.R. Hampton, P.B. Ward, J.J. Kennedy, B. Dean, C.J. Johnson, G.T. Neugebauer, J. Sepich, R. Rai and S. Mahajan, Ext. Abst. of the 1991 U.S. Workshop on the Physics and Chemistry of HgCdTe and Other II-VI Compounds, Oct. 1991, Dallas, TX.
16. R.E. DeWames, J.G. Pasko, E.S. Yao, A.H.B. Vanderwyck and G.M. Williams, *J. Vac. Sci. Technol.* A 6, 2655 (1988).
17. R.E. DeWames, G.M. Williams, J.G. Pasko and H.B. Vanderwyck, *J. Cryst. Growth* 86, 849 (1988).

# Nanometer Fabrication in Mercury Cadmium Telluride by Electron Cyclotron Resonance Microwave Plasma Reactive Ion Etching

C.R. EDDY, JR.,\* C.A. HOFFMAN,<sup>†</sup> J.R. MEYER,<sup>‡</sup> and E.A. DOBISZ<sup>‡</sup>

Naval Research Laboratory, Washington, DC 20375-5000

It has been recently reported (J.R. Meyer, F.J. Bartoli, C.A. Hoffman, and L.R. Ram-Mohan, *Phys. Rev. Lett.* 64, 1963 [1990]) that novel electronic and optical effects are anticipated in nanometer scale features of narrow band gap semiconductors such as mercury cadmium telluride (MCT). These efforts could lead to the creation of non-linear optical switches, high efficiency infrared lasers, and unique nanoelectronic devices. This work reports on the first realization of MCT nanostructures through the application of e-beam lithography and reactive ion etching with an electron cyclotron resonance (ECR) microwave plasma source. It is shown that the low energy ions produced by an ECR system can etch MCT with good selectivity over an e-beam resist mask and with high resolution. Using these fabrication methods, 40–70 nm features with aspect ratios of 3–5:1 and sidewall angles greater than 88° have been demonstrated. Qualitative investigations of some of the etch mechanisms of this technique are made, and results suggest a desorption limited process.

**Key words:** E-beam lithography, HgCdTe, plasma reactive ion etching

## INTRODUCTION

In this paper, we report the first successful application of electron cyclotron resonance microwave plasma reactive ion etching (ECR-RIE) to the processing of mercury cadmium telluride (MCT), and the first fabrication of Hg-based nanostructures. Although this work is focused on the realization of MCT nanostructures, it should be emphasized that ECR-RIE is equally attractive as a means of producing the micrometer-scale mesas associated with long wave infrared detection devices. Furthermore, ECR-RIE would optimize the producibility of such devices through improved uniformity over large areas combined with the promise of reduced damage levels.

Due in part to rapid advances in the submicron patterning technology for wide-gap semiconductors, the last few years have seen the emergence of many new and surprising phenomena related to lateral confinement. These include a quenching of the Hall effect,<sup>1</sup> non-local magnetoresistance,<sup>2</sup> lateral superlattices,<sup>3</sup> "electron optics" (including focusing<sup>4</sup> and refraction<sup>5</sup>), and even experiments which probe the activities of single electrons (e.g. the Coulomb-blockade<sup>6</sup>).

Meyer et al.<sup>7,8</sup> have recently pointed out that quantum wires and quantum dots fabricated from HgTe-CdTe heterostructures should be ideal for probing such phenomena and for discovering new ones. The most obvious advantage is the extremely light effective mass,  $m^*$ , which accompanies the narrow energy gap. In fact, in HgTe-CdTe superlattices both electrons and holes often display  $m^*$  as small as  $0.001 m_0$ , where  $m_0$  is the rest mass of an electron.<sup>9</sup> This leads to giant subband splittings compared to those obtained in wide-gap systems with the same confinement dimensions. A clear illustration is shown in Fig. 1, which plots theoretical electron dispersion relations for GaAs-AlGa<sub>1-x</sub>As ( $E_g = 1500$  meV) and HgTe-CdTe ( $E_g = 10$  meV) quantum wires of the same width (2000 Å). Subband separations for the narrow-gap wire are seen to exceed 10 meV, which means that  $\Delta E > k_B T$  for temperatures up to 110K, even with this relatively modest degree of confinement. In addition, the small effective mass along the wire direction in the HgTe-CdTe would give larger mobilities than GaAs at high temperatures.

Furthermore, new phenomena should occur as a consequence of the unique narrow-gap band structure. The lateral confinement of a semimetallic HgTe-CdTe superlattice leads to the introduction of a sizeable energy gap, which should be tunable with the application of a magnetic field. The anti-crossing of

(Received October 12, 1992; revised January 15, 1993)

(\*Code 6675, <sup>†</sup>Code 5613, <sup>‡</sup>Code 6864)

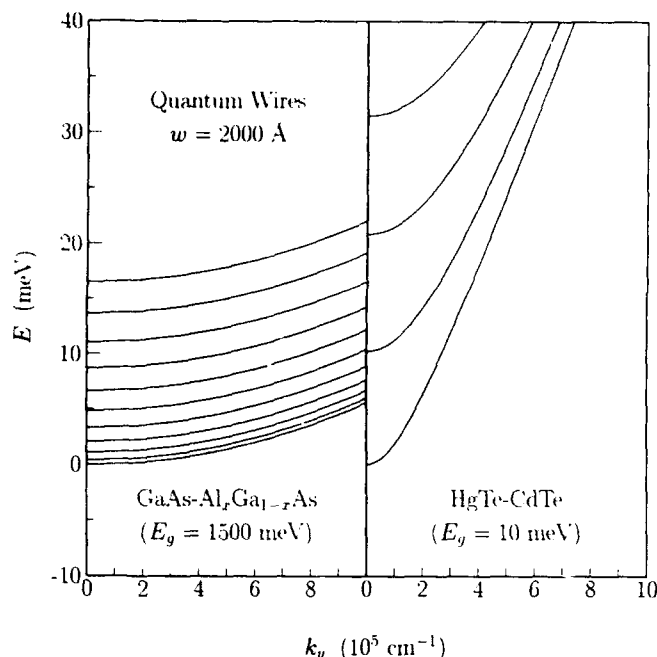


Fig. 1. Calculated dispersion relations along the wire, for GaAs-Al<sub>x</sub>Ga<sub>1-x</sub>As (left panel) and HgTe-CdTe (right panel) quantum wires of equal width (2000 Å).

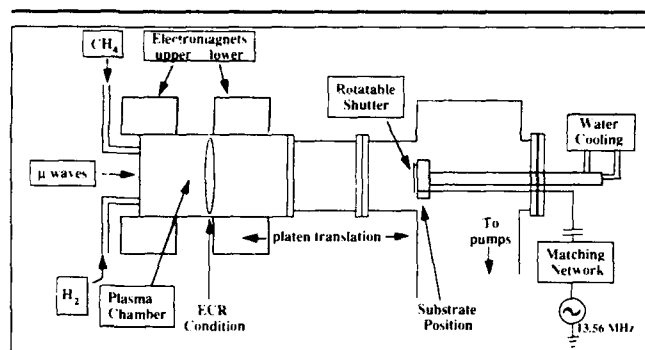


Fig. 2. Schematic diagram of electron cyclotron resonance microwave plasma reactive ion etching apparatus.

the E1 and HH1 bands in semi-metallic superlattices also leads to a variation on the quantized ballistic conductance which has been observed in laterally confined GaAs-based structures.<sup>10</sup> For HgTe-CdTe the interaction of the multiple quantum wells results in a conductance per well that should be quantized in fractional rather than integer units of  $2e^2/h$ .

Besides being ideal for the study of mesoscopic physics, in which the device size is small enough that the conduction electrons sense the entire structure, HgTe-CdTe nanostructures may ultimately find practical importance in such applications as medium wavelength infrared (MWIR) and long wavelength infrared (LWIR) lasers, LWIR nonlinear optical switches, and high-speed electronics. In particular, operation at higher temperatures, enabled by the exceptionally large subband splittings, will make quantum devices much more commercially attractive. In general, confinement effects in narrow-gap HgTe-CdTe nanostructures lead to far greater resolution of the quantum electronic/optical behavior, in-

creased subband densities-of-states, and significant enhancement of Auger recombination lifetimes.<sup>11</sup>

The fabrication of HgTe-CdTe nanostructures will require a dry etch process. Reports on dry etch processing of HgTe-CdTe describe the use of parallel plate radio frequency (rf) reactive ion etching (RIE) with methane/hydrogen ( $\text{CH}_4/\text{H}_2$ ) gas mixtures, an approach which has produced MCT mesas with dimensions in the 2–40  $\mu\text{m}$  range.<sup>12,13</sup> However, further reductions in the size of anisotropically etched features would require reduced process pressures. This is the result of the fact that, on an atomistic scale, anisotropic etching is achieved by unidirectional ions produced, in RIE, when the ion mean free path is longer than the width of the sheath or dark space. Such conditions are achieved in a rf RIE by operating at a low pressure using large sheath electric fields (high electrode voltages) which are required for effective rf coupling to the plasma. This situation, in which energetic conditions at the substrate are tied to the maintenance of the plasma results in the unfortunate characteristic that as pressure is reduced, the ion energy impinging upon the substrate is invariably increased, likely resulting in more damage to the substrate. Thus, it is impractical to employ parallel plate rf RIE to delineate nanometer scale features in MCT with its low threshold for damage.

However, RIE with an electron cyclotron resonance (ECR) microwave plasma source avoids these operational limitations. In an ECR source, the discharge is maintained by microwave (2.45 GHz) energy which is efficiently coupled to the natural resonance frequency of an electron gas in the presence of a static magnetic field (875 gauss). The electrons are accelerated in the resonance region and subsequently ionize and excite the neutral gas resulting in a low pressure, almost collisionless plasma. Because ECR plasmas are electrodeless, operate at low pressures, and consist of high densities of low energy ions,<sup>14</sup> they are particularly well suited for nanofabrication in MCT. The application of a small, negative bias to the substrate platen provides control of ion energies (and, therefore, ion induced damage levels) almost independently of plasma conditions. Furthermore, a recent study comparing several energetic etch processes used in the nanofabrication of GaAs demonstrated that ECR-RIE generated the lowest levels of sidewall damage, on the order of levels associated with wet chemical etching.<sup>15</sup> This result is encouraging to the current application of ECR-RIE, but it remains to be seen if similar environments (<100 eV ion energies) will result in equivalently reduced damage levels in MCT. Prior studies<sup>16</sup> on the argon ion milling of MCT over a similar ion energy range (100–150 eV) have demonstrated significant damage levels to the substrate. However, the ion milling process has also been shown to produce considerably higher damage levels, at comparable ion energies, relative to reactive ion etch processes.<sup>17</sup> Thus, while experimental evidence for low damage levels was not obtained in this study, there remains a high expectation for minimal damage

to MCT as a result of ECR-RIE processing.

### EXPERIMENTAL DETAILS

The samples used in this study were liquid phase epitaxially grown  $\text{Hg}_{1-x}\text{Cd}_x\text{Te}$  thin films ( $x \approx 0.2$ ). The substrates were patterned by two techniques:

- optical lithography in an AZ resist ( $\approx 1 \mu\text{m}$  thick) to produce  $2.5 \mu\text{m}$  lines, and
- e-beam lithography in the negative e-beam resist SAL-601 ( $\approx 60 \text{ nm}$  thick) to produce lines 40–500 nm wide and dots 100–500 nm in diameter.

The e-beam lithography was performed using a JEOL JBX-5DII system at 50 kV with a 15 nm diameter probe. Samples patterned by optical lithography were used to determine etch rate dependencies on the parameters of interest and the high resolution of the process was demonstrated on e-beam patterned samples.

The ECR-RIE system is shown schematically in Fig. 2. Microwave radiation enters the plasma/vacuum chamber through a quartz microwave/vacuum window and is absorbed at the electron cyclotron resonance condition. The two electromagnets provide the required 875 gauss field for resonance. The ECR module (model ECR908 manufactured by Microscience, Inc.) which includes the microwave generation and transmission equipment, electromagnets, and vacuum/plasma chamber, is attached to a high vacuum chamber to allow downstream processing. The entire system is pumped by a 1000 l/s turbomolecular pump and routinely achieves a base pressure of  $< 5 \times 10^{-8}$  Torr. The substrates are mounted onto an electrically isolated, liquid-cooled, translatable platen using a thermally conductive paste (MUNG-I, Commonwealth Scientific, Inc.). Substrate temperature is measured with a thermocouple that contacts the backside of a substrate mounting plate (1.6 mm thick, 316 stainless steel). All interfaces between the substrate back surface and the thermocouple are mechanically held in tight contact and the difference in the temperature between the substrate and the thermocouple has been measured and is less than five degrees. During processing, the substrate platen is negatively biased using capacitively coupled rf (13.56 MHz) energy.

In this study, we focused on the effects of substrate bias and methane concentration on the etch rate, surface morphology, and anisotropy of etch features. The substrate bias provides a measure of the incident ion energy. The actual ion energy is approximately 20 eV higher as a result of the difference between the plasma and floating potentials.<sup>14</sup> This rf induced dc bias was measured using a dc probe and was varied from -25 V to -100 V, corresponding to rf power densities of 0.05 to 0.45 W/cm<sup>2</sup>. Biases in excess of this level were not examined in an effort to minimize the expected damage to the substrate. The methane concentration in hydrogen was varied from 10% to 25%, with total flow rates between 10 and 15 sccm, and was determined by partial pressure measurements using a capacitance manometer.

The time-averaged etch rate was determined by examining the etch depth with cross-sectional scanning electron microscopy (SEM) and dividing by total etch time. Sidewall angles and anisotropy for features were also determined from the cross-sectional SEM micrographs. In this study, anisotropy is defined as the ratio of the etch rates perpendicular and parallel to the substrate surface, and the sidewall angle is related to the anisotropy by the relationship: sidewall angle =  $\arctan(\text{anisotropy})$ . The evaluation of critical dimension control in this etch process would require SEM characterization of patterned samples prior and subsequent to etching. Since high resolution SEM imaging of 60 nm thick resist patterns requires metal coating, it was not possible to image the same sample before and after etching. However, we are reasonably confident that the lithographic dimensions are preserved due to the following observations. First, the etched feature dimensions are comparable to those measured in resist patterns subjected to similar lithographic exposures. Secondly, our previous etching experience has shown that mask sidewall erosion is manifested by trapezoidal shaped features. In this case, the feature dimension was smaller at the top of the feature than at the bottom. Such feature shapes were not observed in the HgCdTe patterns described here.

### RESULTS AND DISCUSSION

In some plasma etching processes, certain products of the surface chemistry can have low volatility. In these cases, the etch mechanism is said to be desorption limited. Thus, bombardment of the reacted surface by ions of an energy greater than some finite threshold is required to promote the etching process.<sup>18</sup> As ion energy increases above that threshold, more material is expected to be ejected from the surface per incident ion, resulting in an increased etch rate if all other parameters are held constant. Our evaluation of the etch rate dependence on substrate bias shows a similar desorption limited behavior in the ECR-RIE of  $\text{Hg}_{1-x}\text{Cd}_x\text{Te}$  with methane/hydrogen gas mixtures. The experiments were performed at a total pressure of 1.0 mTorr, methane concentrations in hydrogen of

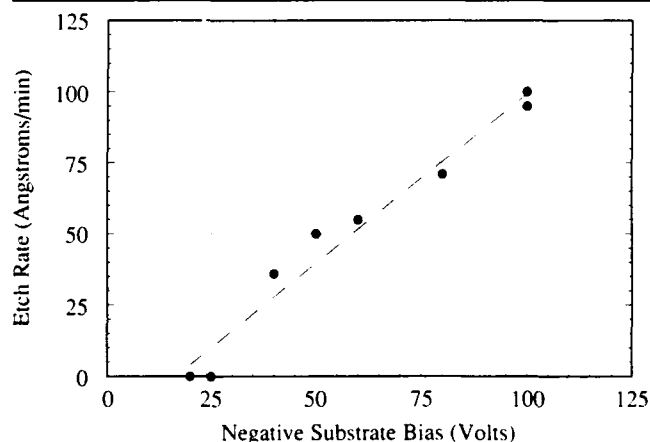


Fig. 3. Etch rate vs substrate bias.

10%, substrate temperatures of 30°C, and an ECR condition—substrate separation distance of 46 cm. The substrate bias was varied from -25 to -100 V. At -25 V substrate bias, there was no etching. However, SEM micrographs showed deposition of what is believed to be a hydrocarbon film. As the substrate bias was increased from -25 V to -100 V, the etch rate demonstrated a monotonic increase, reaching a value of  $\approx 100 \text{ Å/min}$  at -100 V, Fig. 3. This behavior provides clear support for an ion assisted or desorption limited process. The etch products responsible for this limitation are believed to be the group II etch products which have reacted with methyl radicals on the surface.<sup>19-22</sup>

Previous workers have proposed that the methyl radical is a vital etch specie in the  $\text{CH}_4/\text{H}_2$  etching of GaAs,<sup>19</sup> AlGaAs,<sup>20</sup> and InP<sup>21</sup> as well as MCT.<sup>22</sup> They found that an increase in the flux of methyl radicals to the substrate resulted in an increase of the etch rate. We examined the effect of varying the percent-

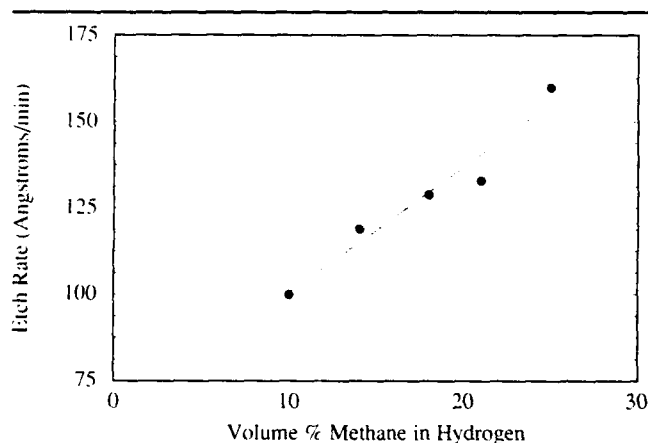


Fig. 4. Etch rate vs percentage of methane in gas mixture.

age of  $\text{CH}_4$  in  $\text{H}_2$  to further evaluate the importance of the methyl radical in the etching of MCT. In this study, the applied bias was -100 V, and the total pressure, substrate-ECR condition separation distance and substrate temperature were held at 1 mTorr, 46.25 cm and 30°C, respectively. We found that as the percentage of methane was increased from 10 vol.% to 25 vol.%, the etch rate monotonically increased from 100 to 165 Å/min, Fig. 4. These observations are in agreement with the previous works,<sup>19-22</sup> and support the proposed etch mechanism involving the reaction of methyl radicals with the group II elements of the film. A further observation with regard to methane concentration, relates to the overall cleanliness and anisotropy of etch features. At 25%  $\text{CH}_4$  in  $\text{H}_2$ , considerable amounts of co-deposition, probably hydrocarbon-like in nature, are observed. At 10% methane concentration, the surface was much cleaner but there was a significant degree of undercut in the etched features. Mogab and Levinstein<sup>23</sup> have proposed that methyl radicals in the plasma form a hydrocarbon-film on the sidewall which serves as an etch block and enhances the anisotropy. A 10% methane concentration may be insufficient to promote this sidewall deposition mechanism resulting in severe degradation of the anisotropy. The best etch profiles, having both good anisotropy and clean surfaces, were observed at the intermediate methane concentration of 18%.

The nanofabrication capabilities of the ECR-RIE process were demonstrated on e-beam patterned samples with SAL-601 resist. SAL-601 demonstrated good adhesion and a high selectivity, as only 60 nm was required to etch 400 nm of MCT. The e-beam patterned samples were inserted into the ECR-RIE system and etched under optimized conditions determined empirically and described here and elsewhere.<sup>24</sup>

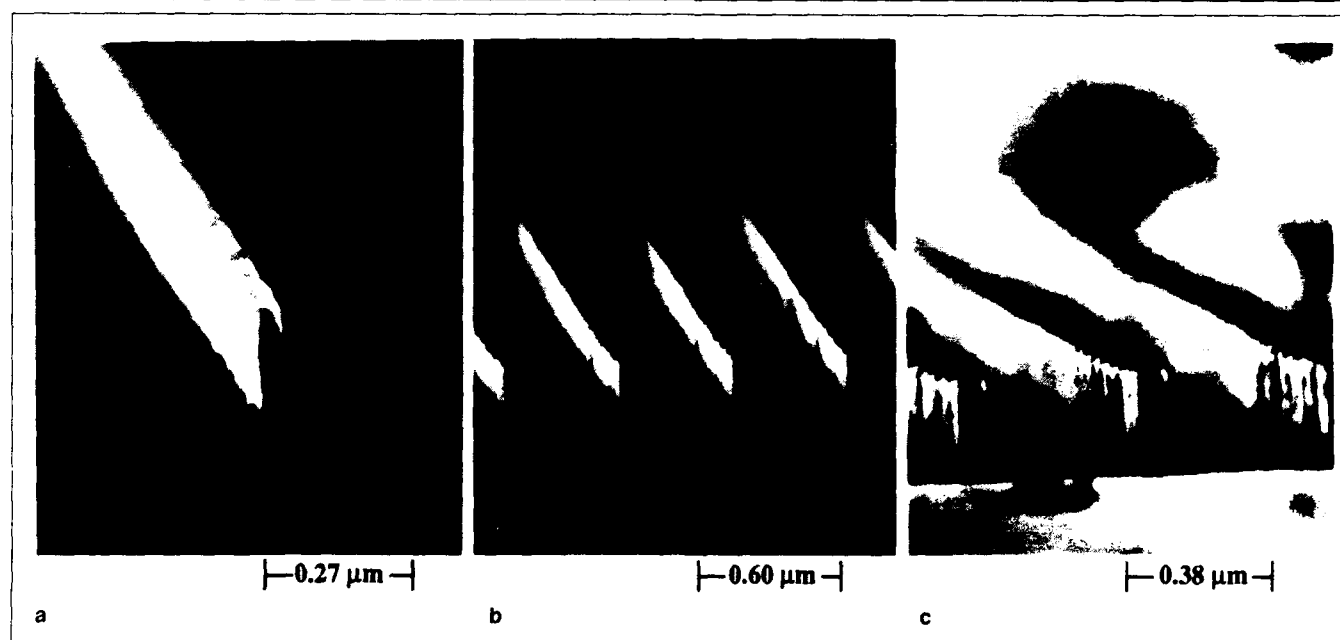


Fig. 5. (a) 40 nm, (b) 60 nm, and (c) 70 nm lines fabricated in mercury cadmium telluride after 12 min of exposure to an optimized ECR-RIE process.



- (1991).
3. L.P. Kouwenhoven, F.W.J. Hekking, B.J. van Wees, C.J.P.M. Harmans, C.E. Timmering and C.T. Foxon, *Phys. Rev. Lett.* 65, 361 (1990).
  4. H. van Houten, B.J. van Wees, J.E. Mooij, C.W.J. Beenakker, J.G. Williamson and C.T. Foxon, *Europhys. Lett.* 5, 721 (1988).
  5. J. Spector, H.J. Stormer, K.W. Baldwin, L.N. Pfeiffer and K.W. West, *Appl. Phys. Lett.* 56, 2433 (1990).
  6. P.L. McEuen, E.B. Foxman, U. Meirav, M.A. Kastner, Y. Meir, N.S. Wingreen and S.J. Wind, *Phys. Rev. Lett.* 66, 1926 (1991).
  7. J.R. Meyer, F.J. Bartoli, C.A. Hoffman and L.R. Ram-Mohan, *Phys. Rev. Lett.* 64, 1963 (1990).
  8. J.R. Meyer, F.J. Bartoli, C.A. Hoffman and L.R. Ram-Mohan, *Superlatt. and Microstruct.* 7, 387 (1990).
  9. J.R. Meyer, C.A. Hoffman and F.J. Bartoli, *II-VI Semiconductor Compounds*, ed. M. Jain, (World Scientific, London, in press).
  10. B.J. van Wees, H. van Houten, C.W.J. Beenakker, J.G. Williamson, L.P. Kouwenhoven, D. van der Marel and C.T. Foxon, *Phys. Rev. Lett.* 60, 848 (1988).
  11. Y. Jaing, M.C. Teich, W.I. Wang and J.R. Meyer, *J. Appl. Phys.* 71, 3394 (1992).
  12. A. Semu, L. Montelius, P. Leech, D. Jamieson and P. Silverberg, *Appl. Phys. Lett.* 59, 1752 (1991).
  13. J.K. Elkind and G.J. Orloff, *J. Vac. Sci. Technol. A* 10, 1106 (1992).
  14. J. Asmussen, *Handbook of Plasma Processing Technology*, eds. S.M. Rossnagel, J.J. Cuomo and W.D. Westwood (Noyes Publications, Park Ridge, NJ, 1990), p. 285.
  15. G.F. Doughty, R. Cheung, M.A. Foad, M. Rahman, N.I. Cameron, N.P. Johnson, P.D. Wang and C.D.W. Wilkinson, *Photons and Low Energy Particles in Surface Processing*, eds. C.J.H. Ashby, J.H. Brannon and S.W. Pang, *MRS Symp. Proc.* 236, 223 (1992).
  16. G. Bahir and E. Finkman, *J. Vac. Sci. Technol. A* 7, 348 (1989).
  17. O.J. Glembocki and E.A. Dobisz, *J. Vac. Sci. Technol. A* 9, 1410 (1991).
  18. G.S. Oehrlein, *Handbook of Plasma Processing Technology*, eds. S.M. Rossnagel, J.J. Cuomo and W.D. Westwood (Noyes Publications, Park Ridge, NJ, 1990), p. 196.
  19. R. Cheung, S. Thoms, S.P. Beamout, G. Doughty, V. Law and C.D.W. Wilkinson, *Electron. Lett.* 23, 857 (1987).
  20. L. Henry, C. Vandry and P. Granjoux, *Electron. Lett.* 23, 1253 (1987).
  21. T.R. Hayes, M.A. Dreisback, P.M. Thomas, W.C. Dautremont-Smith and L.A. Heimbrook, *J. Vac. Sci. and Technol. B* 7, 1130 (1989).
  22. A. Semu and P. Silverberg, *Semicond. Sci. Technol.* 6, 287 (1991).
  23. C.J. Mogab and H.J. Levinstein, *J. Vac. Sci. Technol.* 17, 721 (1980).
  24. C.R. Eddy, Jr., E.A. Dobisz, C.A. Hoffman and J.R. Meyer, *Appl. Phys. Lett.* 62, 2362 (1993).
  25. G. Franz, *J. Electrochem. Soc.* 137, 2896 (1990).
  26. A. Scherer and H.G. Craighead, *Appl. Phys. Lett.* 49, 1284 (1986).

# Low Threshold Injection Laser in HgCdTe

Ph. BOUCHUT, G. DESTEFANIS, A. MILLION, T. COLIN, and J. BABLET  
 LETI (CEA-Technologies Avancées), DOPT-CEN/G-85 X, F38041  
 GRENOBLE CEDEX, France

Narrow-stripe transverse injection lasers in HgCdTe have been successfully fabricated and operated. The double heterostructure of the laser was grown by molecular beam epitaxy on a {111} CdZnTe substrate. The n type base was extrinsically indium doped but other p type layers were only doped by deviation from stoichiometry. Laser emission at 3.4  $\mu\text{m}$  and 3.56  $\mu\text{m}$  was obtained at 78K under pulsed current conditions. Threshold current density as low as 90 A/cm<sup>2</sup> at 40K was achieved. Over 65K, the threshold current variation with temperature showed a sharp increase due to a drift-current leakage in the structure.

**Key words:** CdZnTe substrate, double heterostructures, HgCdTe, In doping, injection laser, MBE

## INTRODUCTION

As the technology and metallurgy of HgCdTe (MCT) become more mature, complex electro-optical components are being produced, and all but a few are for infrared detection applications. Even though the laser effect by optical pumping was demonstrated long ago,<sup>1</sup> an injection laser diode was achieved only recently.<sup>2</sup> This time lag owes much to the fact that the laser diode is more demanding of the complex metallurgical structure in order to obtain low threshold currents. A first step in this direction was accomplished by the Rockwell team using a fully doped double-heterojunction (DHJ) diode.<sup>3</sup> A further step would be the use of quantum wells in the active part of the laser diode. Many quantum-well structures have been grown in which the laser effect was obtained by optical pumping,<sup>4-6</sup> but none was purposely doped and suitable for injection laser application.

At the present time, the real difficulty is to p type dope the capping layer of a p/n DHJ while keeping the quantum well from diffusing into the active layer. The p type doping is obtained either by an interdiffused multilayer process (IMP)<sup>7</sup> or by As implantation.<sup>8</sup> Both techniques suffer from the need of a high temperature anneal ( $T > 350^\circ\text{C}$ ) in order to accomplish diffusion and/or activation of the extrinsic impurity in the entire capping layer. At this temperature, a high

interdiffusion coefficient for CdTe/HgTe of nearly  $10^{-13}$  cm<sup>2</sup>/s will result in mixing of the quantum well with its surrounding matrix.<sup>9</sup> Another means of low-temperature p-type doping should be developed to prevent the quantum well from diffusing in the active layer.

In this paper, we show that low threshold p on n laser diodes are obtained using intrinsic as-grown p-type doping for the active as well as the capping layers. The metallurgical and technological process maintains a temperature of 200°C, consistent with the use of quantum wells in the active layer. The immediate price to pay for this is an increase of leakage current above 65K.

## EXPERIMENTAL PROCEDURE

The laser metallurgical structure is a p/p/n<sup>+</sup> DHJ grown by molecular beam epitaxy on a near-lattice-matched Cd<sub>0.96</sub>Zn<sub>0.04</sub>Te (CZT) substrate. The growth orientation is along a slightly misoriented <111> direction in order to get a good surface morphology without twin lamella defects. The growth temperature is 200°C and the growth rate is 3  $\mu\text{m}/\text{h}$ . Both the n and p-confinement layers have a 42% cadmium content, whereas the p active layer has a 36% cadmium content. The compositions were chosen to achieve a 3.5  $\mu\text{m}$  wavelength emitting laser while keeping a sufficient barrier height at 77K to confine carriers without impeding the series resistance of the diode. The base of the laser is a 5  $\mu\text{m}$  thick extrinsic



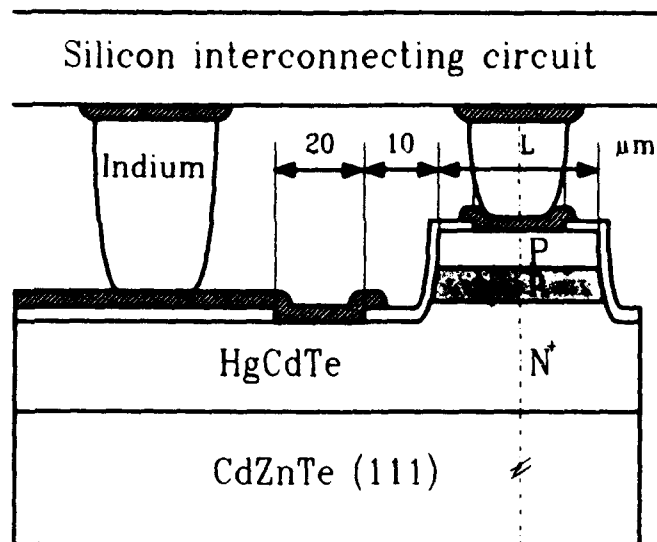


Fig. 1. Schematic diagram of a stripe-geometry, transverse-injection, HgCdTe laser:  $L = 35, 45, \text{ or } 55 \mu\text{m}$ .

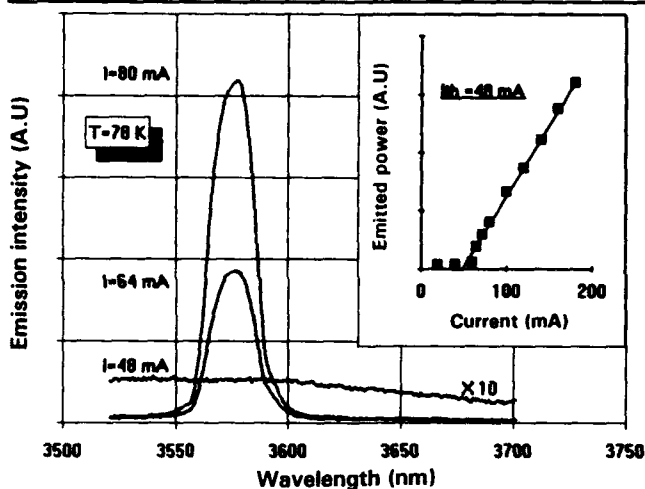


Fig. 2. Comparison of emission below and above threshold for a  $55 \mu\text{m}$  stripe width laser, operated in the pulsed-current mode at 78K. The  $P$  vs  $I$  characteristic showing a 48 mA threshold is displayed in the inset.

cally doped layer. Indium is incorporated during the growth at a  $10^{17} \text{ cm}^{-3}$  level. The other layers are p type doped with mercury vacancies by stoichiometry deviation. The hole concentration in these layers is determined by the  $200^\circ\text{C}$  growth temperature: 2 to  $4 \times 10^{16} \text{ cm}^{-3}$  range for the active layer and  $10^{16} \text{ cm}^{-3}$  for the cladding layer. The thickness of the active and upper confining layers are, respectively, 1 and  $1.5 \mu\text{m}$ . Laser stripes are chemically etched with different widths of 35, 45, and  $55 \mu\text{m}$ . As the substrate is insulating, transverse injection of current must be performed, and n type contacts are made on both sides of the stripe (Fig. 1). The distance from the n type contact to the etched side of the mesa is kept constant and equal to  $10 \mu\text{m}$  for every mesa width. The n as well as p type contacts are made by means of a  $20 \mu\text{m}$  wide evaporated gold metallization.

Laser modules are cleaved along {110} planes at a length of  $340 \mu\text{m}$ . As the metallization does not extend to the cleaving area, it leaves a  $20 \mu\text{m}$  long zone at

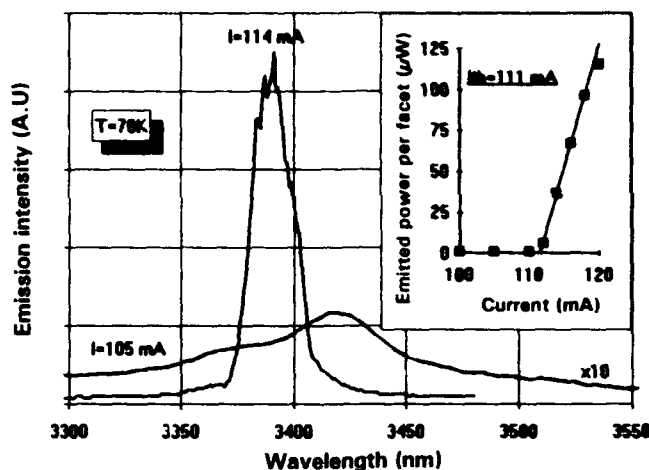


Fig. 3. Comparison of emission below and above threshold for a  $45 \mu\text{m}$  stripe width laser, operated in the pulsed-current mode at 78K. The  $P$  vs  $I$  characteristic shows that threshold is at 111 mA and the slope above threshold is  $7.7 \text{ mW/A}$ .

each end of the laser, where apart from diffusion current, the reabsorption effect will tend to increase threshold current. The full device consists of seven optically uncoupled lasers that are connected to a silicon injection and fanout circuit by means of the indium-bump hybridization technique. At 78K, the laser's series resistance is in the 10–20 ohm range. This value is at least twice as high as the simple series resistance extrapolated from the resistivity and geometric parameters of each sheet of material constituting the DHJ. We thus have to assume that the metal to  $\text{Hg}_{0.58}\text{Cd}_{0.42}\text{Te}$  interfaces are non-ohmic and present a high contact resistance. This point should be worked on further in the future. The hybridized silicon circuit also acts as a thermal sink for these hot areas.

Our final structure is different from that of the Rockwell group<sup>3</sup> in the following aspects:

- No extrinsic p type doping of the cladding layer.
- {111} MBE growth orientation.
- Low-temperature process ( $\leq 200^\circ\text{C}$ ).
- Smaller geometric design.

Devices are mounted in a variable-temperature cryostat, providing a 20 to 300K temperature range with a ZnSe window. The lasers are positioned at the entrance slit of a 320 mm focal length Czerny Turner type monochromator, with a detector at the exit slit of the monochromator. The final spectral resolution of this experimental setup is set by the detector width ( $400 \mu\text{m}$ ), which fixes a value for spectral resolution of 6 nm. A small misalignment may occur that could induce a slight shift ( $\leq 1 \text{ nm}$ ) of the absolute wavelength, but photon flux is always maximum. With this experimental setup, measurement of emitted power is easy. The laser is imaged on a larger detector ( $1.2 \times 1.2 \text{ mm}^2$ ) using the optics of the monochromator in which the grating is replaced by a plane mirror. The detectors are cooled MCT photovoltaic diodes with a cut-off wavelength of  $5.7 \mu\text{m}$ , aligned in the same 77K cryostat. The lasers are operated in the pulsed-current mode, with a duty cycle ratio of 1% and a 100 ns pulse.

## RESULTS

Evidence of laser emission at 3.58  $\mu\text{m}$  and 78K is presented in Fig. 2. The light output intensity vs current displays the characteristic change of slope with an extrapolated threshold current of 48 mA for a 55  $\mu\text{m}$  mesa width. Above the threshold, a single stimulated emission line peaks out of a broad spontaneous-emission continuum. The full width at half maximum of the peak is 23 nm, which is quite large for a laser line, and no longitudinal cavity modes can be resolved in this spectrum.

Better mode spacing is obtained in another sample (Fig. 3) for a 45  $\mu\text{m}$  wide laser. The laser line is at 3.39  $\mu\text{m}$  and the wavelength separation between modes is  $\Delta\lambda \sim 4$  nm. The group index  $n_{\text{eff}}$  deduced from  $n_{\text{eff}} = \frac{\lambda^2}{2L\Delta\lambda}$ , where  $L$  is the length of the laser, gives  $n_{\text{eff}} = 4.23$ . The full width at half maximum of the broad laser line is approximately the same as in the first sample ( $\sim 24$  nm), showing that numerous longitudinal modes ( $\sim 12$ ) exist in the laser line.

On this laser, the measured threshold current has a value of 111 mA, and the slope above threshold is 7.7 mW/A per facet, which means that a differential quantum efficiency of 4.2% is obtained at 78K. This value is two orders of magnitude greater than those obtained by optical pumping in MCT for a comparable laser length.<sup>10</sup> This laser was able to sustain 120  $\mu\text{W}$  peak power without degrading effects on the uncoated emitting facet.

As the temperature changes from 20 to 90K, the threshold current presents a minimum at 40K (Fig. 4). This minimum, as well as the variation of threshold current with temperature, is the same for all mesa stripe widths. At 40K, the threshold is as low as 6 mA for the 55  $\mu\text{m}$  wide laser. Above 65 K, there is a very sharp increase in threshold current. This increase can be fitted by a conventional exponential law  $I_{\text{th}} = I_0 \exp(T/T_0)$ , where  $T_0 \sim 8\text{K}$ . Such a low  $T_0$  parameter is rather unusual. Our data, in Fig. 5 and Ravid's,<sup>10</sup> obtained by optical pumping in different MCT monolayers, agree that a value of 30K for  $T_0$  would be more expected from MCT material in this compositional range. As the equivalent current density in our laser diode (1 kA/cm<sup>2</sup>  $\mu\text{m}$  at 78K) is lower than in optically pumped lasers,<sup>10</sup> less Auger recombination or carrier heating should occur, leading to an even higher  $T_0$  value for the laser diode. The explanation of such behavior is to be found in the non-ideal electrical characteristics of the DHJ diode. The extreme sensitivity of threshold current to temperature has been attributed in InGaAs P lasers<sup>11</sup> to carrier leakage through the higher band gap layers of the DHJ.

In our case, as the doping level in the p-type cladding layer is low ( $10^{16} \text{ cm}^{-3}$ ) a substantial electric field exists across this layer. In such a case, the hole current can be written as

$$J_p = e \mu_p n_A E, \quad (1)$$

with  $e$  the electric charge,  $\mu_p$  the hole mobility,  $n_A$  the doping level in the p-type cladding layer, and  $E$  the

electric field. The ratio of the drift and diffusion leakage across the p-type heterojunction is given approximately by

$$\frac{J_{\text{drift}}}{J_{\text{diff}}} \sim \frac{\mu_n}{\mu_p} \frac{L}{e D_n n_A} J_p, \quad (2)$$

where  $L$  is the thickness of the cladding layer and is assumed to be small compared with the electron diffusion length in the p type cladding layer,  $\mu_n$  is the electron mobility, and  $D_n$  the electron diffusion constant. Taking  $\mu_n = 30000 \text{ cm}^2/\text{V.s}$ ,  $\mu_p = 400 \text{ cm}^2/\text{V.s}$ ,  $L = 1.5 \mu\text{m}$ ,  $D_n = 180 \text{ cm}^2/\text{s}$  at 78K, and  $n_A \sim 10^{16} \text{ cm}^{-3}$ .

We can verify that the drift current is larger than the diffusion current when  $J_p$  exceeds 25 A/cm<sup>2</sup>. This means that even at the lowest threshold current in our laser, drift out balances diffusion current and is the predominant electron leakage mechanism across

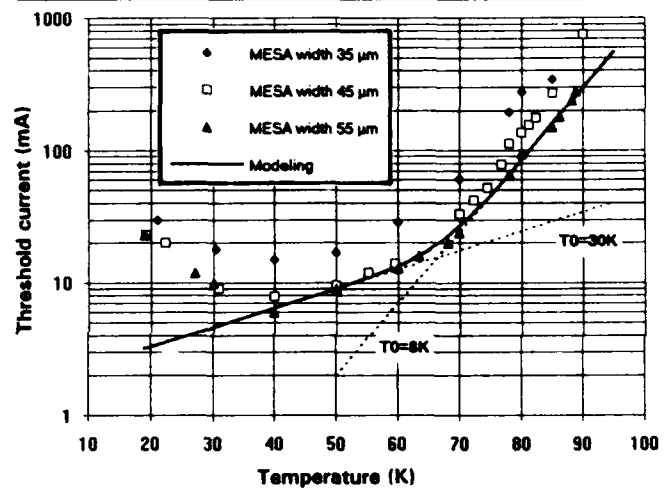


Fig. 4. Variation of threshold current with temperature for three different laser stripe widths. The full line is obtained by using the model with its parameters as in the text. Dotted lines are the fitted exponential variation of threshold current with a  $T_0$  parameter of 8 or 30K, as shown.

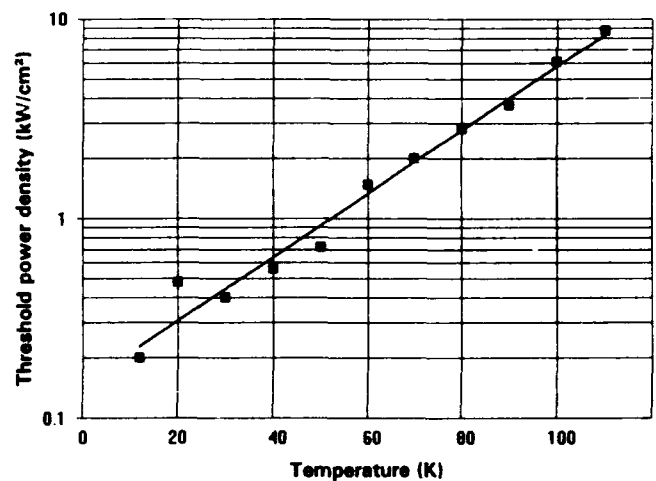


Fig. 5. Variation of threshold power density with temperature obtained in a 1  $\mu\text{m}$  thick liquid phase epitaxy layer. Laser emission is at 3.49  $\mu\text{m}$  at 12K. Optical pumping source is laser diode emitting at 855 nm. The full line is for exponential variation of threshold power density with a  $T_0$  parameter = 28K.

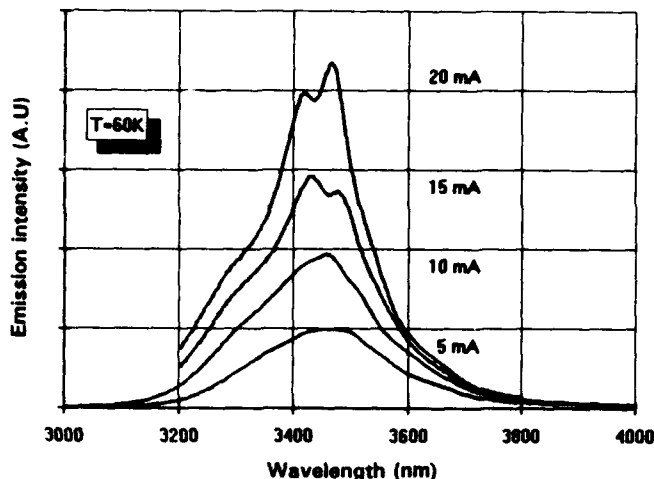


Fig. 6. Emission intensity vs wavelength. Laser is operated in the continuous-current mode at 60K.

the barrier. Since the drift current increases with the field  $E$  and  $E$  increases with  $J_p$ , it follows that the proportion of leakage current to total current continues to grow as the threshold of the laser increases with temperature. Such a variation strongly affects the original dependence of threshold current on temperature.

A simple model of this variation is given by Anthony<sup>12</sup> for drift dominated leakage current. In the case of purely radiative recombination in the active volume, the threshold current is found to be

$$I_{th} = (b + 1) I_0 + [1 - (1 + 4 \gamma \delta R^2 I_0)^{1/2}] b / 2 \gamma \delta R^2 \quad (3)$$

where  $I_0$  is the no carrier loss threshold current;  $b = \mu_n / \mu_p$  is the ratio of electron to hole mobilities;  $\gamma$  is proportional to the fraction of the active-layer carrier concentration injected into the p type confinement layer, with  $\gamma = C \exp(-\Delta E_b / kT)$ , where  $C$  depends on the density of states at the heterobarrier and  $E_b$  is the barrier height;  $R$  is the resistance of the p type confinement layer with no injected charge; and  $\delta = \mu_p^2 e A / G_R d L^2$ , with  $A$  the device area,  $G_R$  the radiative recombination constant, and  $d$  the active-layer thickness. The hypothesis that recombination in the active volume is entirely radiative may not be true but is accounted for, empirically, by the original dependence of  $I_0$  (mA) on temperature:  $I_0 = 1.7 \exp(T/30)$ .

Using all the preceding parameters plus  $R = 10 \Omega$  (including contact resistance on the p side),  $G_R = 10^{-7} \text{ cm}^3/\text{s}$ ,  $C = 11$ , and  $\Delta E_b = 60 \text{ meV}$  (fixed by a valence-band offset equal to 350 meV between CdTe and HgTe), we can see (Fig. 4) that good agreement is obtained between the modeling and our data. The whole temperature variation of our experimental threshold current (over 40K) is unambiguously set by two temperature dependent parameters. One is the no-carrier-loss threshold  $I_0$ , which can be known independently from optical pumping experiments, and the other is  $\gamma$  which is fixed by the barrier height of the heterostructure (known from the metallurgical composition of the DHJ).

From the modeling, we can deduce that 2/3 of the

total current at 78K is of no use for laser action. This shows that an increase in differential quantum efficiency and a decrease in threshold current, by a factor of 3, can still be achieved with this type of laser structure. Enhancing the barrier height on the p type side would slide the leakage current knee to higher temperature. Use of asymmetric DHJ could prove valuable for maintaining low leakage on the p type side while decreasing series resistance of the n type side.

Below 40K, the model does not account for the increase in threshold current. This remains true even if the series resistance of the device is made to vary with the p resistivity of the cladding layer. Another mechanism, either thermal or electrical, must be added to fit the data.

When continuous operation is attempted, as is shown in Fig. 6, a narrowing of the spontaneous emission peak from 282 nm at 5 mA to 201 nm at 20 mA is observed. Localized peaks tend to stand out from the broad continuum at an injection current corresponding to the threshold current in pulse operation at this temperature (60K). We interpret these peaks as evidence of stimulated emission arising in the continuous mode, but spontaneous emission still represents the maximum of emitted energy. As the current is increased, more thermal power is dissipated in the structure, which tends to quench stimulated emission.

## CONCLUSION

We have shown that narrow stripe HgCdTe DHJ injection lasers may have threshold current as low as 48 mA and differential quantum efficiency as high as 4.2% at 78K for 3.4 and 3.56  $\mu\text{m}$  emission wavelengths. These performances were obtained on an n type indium doped {111} MBE heterostructure without extrinsic p type doping for the active and cladding layers.

Use of quantum wells in the active part of the p on n heterostructure could be tried to further reduce the threshold current. This gain would be better seen for temperatures below 65K, where low drift-leakage current occurs.

Even if continuous stimulated emission can be observed at 60K, the resistance of the device is too high to enable continuous operation at 78K. In the mid term, reduction in series resistance of the device must be achieved by correct control of both extrinsic p-type doping and the metal to MCT interface.

## ACKNOWLEDGMENT

The authors are indebted to M. Wolny for valuable discussion on heterojunction modeling. This work was supported by DGA/DRET (French Ministry of Defense).

## REFERENCES

1. I. Melngailis and A. Strauss, *Appl. Phys. Lett.* 8, 179 (1966).
2. M. Zandian, J.M. Arias, R. Zucca, R.V. Gil and S.H. Shin, *Appl.*

- Phys. Lett.* 59, 1022 (1991).
3. R. Zucca, M. Zandian, J.M. Arias and R.V. Gil, *J. Vac. Sci. Technol. B* 10, 1587 (1992).
  4. K.K. Mahavadi, M.D. Lange and J.P. Faurie, *Appl. Phys. Lett.* 54, 2580 (1989).
  5. N.C. Giles, J.W. Han, J.W. Cooks and J.F. Schetzina, *Appl. Phys. Lett.* 55, 2026 (1989).
  6. J. Bleuze, N. Magnea, L. Ulmer, J.L. Pautrat and H. Mariette, *J. Cryst. Growth* 117, 1046 (1992).
  7. P. Capper, P.A.C. Whiffin, B.C. Easton, C.D. Maxey and I. Kenworthy, *Mater. Lett.* 6, 365 (1988).
  8. L.O. Bubulac, W.E. Tennant, D.S. Lo, D.D. Edwall, J.C. Robinson, J.S. Chen and G. Bostrup, *J. Vac. Sci. Technol. A* 5, 3166 (1987).
  9. M.F.S. Tang and D.A. Stevenson, *J. Vac. Sci. Technol. A* 5, 3124 (1987).
  10. A. Ravid, A. Zussman, G. Cinader and A. Oron, *Appl. Phys. Lett.* 55, 2704 (1989).
  11. L.C. Chin, K.L. Yu, S. Margalit, T.R. Chen, U. Noren, A. Masson and A. Yariv, *J. Quantum Electron* 19, 1335 (1983).
  12. P.J. Anthony and N.E. Schumaker, *J. Appl. Phys.* 51, 5038 (1980).

# Vapor Phase Equilibria in the $\text{Cd}_{1-x}\text{Zn}_x\text{Te}$ Alloy System

H.R. VYDYANATH, J.A. ELLSWORTH, and R.F. FISHER

Aerojet Electronic Systems Division, 1100 W. Hollyvale Street, Azusa, CA 91702

J.J. KENNEDY

U. S. Army CECOM Night Vision and ElectroOptics Directorate, Fort Belvoir, VA 22060

C.J. JOHNSON and G.T. NEUGEBAUER

II-VI Inc., 375 Saxonburg Boulevard, Saxonburg, PA 16056

$\text{Cd}_{1-x}\text{Zn}_x\text{Te}$  compounds of different compositions have been prepared at temperatures ranging from 400 to 1000°C by annealing elemental Te in sealed quartz ampoules, in an atmosphere comprising vapors of Cd and Zn whose partial pressures were varied by varying the composition of the binary  $\text{Cd}_{1-y}\text{Zn}_y$  alloys which provided the Cd and Zn vapors in these annealing experiments. The chemical compositions of the resulting  $\text{Cd}_{1-x}\text{Zn}_x\text{Te}$  compounds have been analyzed using electron probe microanalytical techniques. Results indicate that presence of a 0.5% Zn along with Cd in a closed or semi-closed system may prove to be beneficial in preventing decomposition and/or formation of a metal/non metal phase during annealing of  $\text{Cd}_{0.96}\text{Zn}_{0.04}\text{Te}$  substrates. Using the thermodynamic data in the literature for the binary  $\text{Cd}_{1-y}\text{Zn}_y$  alloys and with the assumption that the activities of the Cd and Zn components are weakly dependent on temperature, the partial pressures of Cd and Zn in equilibrium with the  $\text{Cd}_{1-x}\text{Zn}_x\text{Te}$  compounds at various temperatures have been evaluated.

**Key words:** CdZnTe alloys, Te annealing in Cd and Zn vapor, vapor-phase equilibria

## INTRODUCTION

The importance of  $\text{Cd}_{1-x}\text{Zn}_x\text{Te}$  as a substrate material for the growth of epitaxial HgCdTe is well recognized.<sup>1-4</sup> Because of the high vapor pressures of the constituent elements and also the presence of a large deviation from stoichiometry in CdTe and related II-VI compounds, it becomes imperative to maintain precise thermodynamic conditions under which these crystals are stable at high temperatures. II-VI crystals when exposed to any high temperature processing under ill defined thermodynamic conditions will readjust their stoichiometry corresponding to free evaporation conditions; in addition, pseudobinary crystals such as (Cd,Zn)Te may even decompose if the surrounding atmosphere is deficient in the metal or the nonmetal constituents. In the case of (Hg,Cd)Te crystals, since the partial pressure of Hg is over-

whelmingly larger than that of Cd at any temperature,<sup>5,6</sup> one needs only to maintain a Hg vapor around the crystals to keep them within the existence region; the negligible vapor pressure of Cd required for equilibrium is provided by the evaporation of just a fraction of a monolayer of the crystal. (In fact, imposing a Cd pressure in addition to that of Hg will change the composition of (Hg,Cd)Te to much higher Cd compositions.) However, in the case of (Cd,Zn)Te crystals, the partial pressure of Zn may not be negligible in comparison with that of Cd and the crystals could decompose without the presence of zinc also in the vapor in addition to Cd. In a series of annealing experiments, Neugebauer<sup>7</sup> has inferred that annealing  $\text{Cd}_{0.96}\text{Zn}_{0.04}\text{Te}$  crystals in the presence of only Cd vapor, results in a significant increase in the etch pit density pointing to a possible loss of Zn in these anneals; he has also observed that samples which were annealed in the presence of a Cd-Zn vapor corresponding to the composition of a Cd-25% Zn

(Received November 5, 1992; revised January 13, 1993)

**Table I. Summary of Mole Fractions, Activities, and Activity Coefficients for the Zn and Cd Components of Binary  $\text{Cd}_{1-y}\text{Zn}_y$  Alloys at 527°C<sup>a</sup>**

| Zn Component         |                 |                      | Cd Component        |                 |                      |
|----------------------|-----------------|----------------------|---------------------|-----------------|----------------------|
| $\gamma_{\text{Zn}}$ | $a_{\text{Zn}}$ | $\gamma_{\text{Zn}}$ | $(1-y)_{\text{Cd}}$ | $a_{\text{Cd}}$ | $\gamma_{\text{Cd}}$ |
| 0.0                  | 0.0             | 4.12                 | 0.0                 | 0.0             | 4.6                  |
| 0.1                  | 0.29            | 2.9                  | 0.1                 | 0.32            | 3.2                  |
| 0.2                  | 0.45            | 2.25                 | 0.2                 | 0.47            | 2.35                 |
| 0.3                  | 0.56            | 1.87                 | 0.3                 | 0.56            | 1.87                 |
| 0.4                  | 0.65            | 1.63                 | 0.4                 | 0.64            | 1.6                  |
| 0.5                  | 0.71            | 1.42                 | 0.5                 | 0.68            | 1.36                 |
| 0.6                  | 0.77            | 1.28                 | 0.6                 | 0.74            | 1.23                 |
| 0.7                  | 0.81            | 1.16                 | 0.7                 | 0.80            | 1.14                 |
| 0.8                  | 0.86            | 1.08                 | 0.8                 | 0.85            | 1.06                 |
| 0.9                  | 0.92            | 1.02                 | 0.9                 | 0.92            | 1.02                 |
| 1.0                  | 1.0             | 1.0                  | 1.0                 | 1.0             | 1.0                  |

binary alloy, showed similar results pointing to a possible loss of Cd in the latter anneals. Obviously, to prevent decomposition,  $\text{Cd}_{0.96}\text{Zn}_{0.04}\text{Te}$  crystals in these experiments need to be annealed in the presence of a binary  $\text{Cd}_{1-y}\text{Zn}_y$  alloy of a precise composition  $y$  of Zn with  $y$  being between 0 and 0.25.

The present work is aimed at establishing the vapor pressures of Cd and Zn in equilibrium with various  $\text{Cd}_{1-x}\text{Zn}_x\text{Te}$  compounds at different temperatures such that these crystals which serve as substrates can be maintained under well defined physico-chemical conditions which do not cause them to decompose during any high temperature processing such as is encountered in post growth annealing, epitaxial growth and/or device processing.

### BINARY Cd-Zn ALLOY THERMODYNAMICS

Table I summarizes the literature data<sup>a</sup> of the mole fractions, activities, and activity coefficients for the Zn and Cd components of the binary  $\text{Cd}_{1-y}\text{Zn}_y$  alloys at 527°C.

Activities  $a_{\text{Zn}}$  and  $a_{\text{Cd}}$  for the Zn and Cd components are related to the mole fractions of the respective components via the relations.

$$a_{\text{Zn}} = y \gamma_{\text{Zn}} \quad (1)$$

and

$$a_{\text{Cd}} = (1-y) \gamma_{\text{Cd}} \quad (2)$$

where  $y$  and  $(1-y)$  refer to mole fractions and  $\gamma_{\text{Zn}}$  and  $\gamma_{\text{Cd}}$  to activity coefficients of the Zn and Cd components over the binary  $\text{Cd}_{1-y}\text{Zn}_y$  alloys.

Activities  $a_{\text{Zn}}$  and  $a_{\text{Cd}}$  are also related to the partial pressures via the relations

$$a_{\text{Zn}} = p_{\text{Zn}}/p_{\text{Zn}}^{\circ} \quad (3)$$

and

$$a_{\text{Cd}} = p_{\text{Cd}}/p_{\text{Cd}}^{\circ} \quad (4)$$

where  $p_{\text{Zn}}$  and  $p_{\text{Cd}}$  refer to partial pressures of the Zn and Cd components over the binary  $\text{Cd}_{1-y}\text{Zn}_y$  alloys,

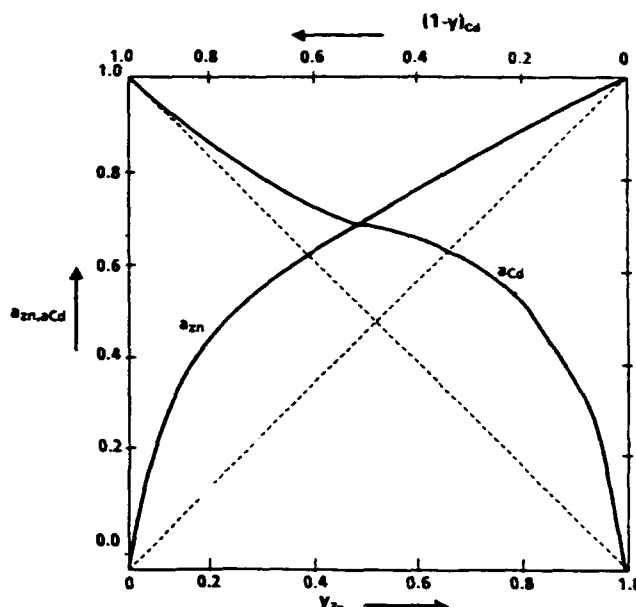


Fig. 1. Plot of activity vs mole fraction for the Cd and Zn components in the binary  $\text{Cd}_{1-y}\text{Zn}_y$  alloys at  $T = 527^\circ\text{C}$  from data in Ref. 8.

and  $p_{\text{Zn}}^{\circ}$  and  $p_{\text{Cd}}^{\circ}$  refer to the vapor pressures of pure Zn and Cd at the same temperature.

Thus, from relations 1 through 4, we can calculate the partial pressures of Zn and Cd over the binary  $\text{Cd}_{1-y}\text{Zn}_y$  alloys via relations

$$p_{\text{Zn}} = y \gamma_{\text{Zn}} p_{\text{Zn}}^{\circ} \quad (5)$$

and

$$p_{\text{Cd}} = (1-y) \gamma_{\text{Cd}} p_{\text{Cd}}^{\circ} \quad (6)$$

the vapor pressures of the pure components are given by

$$p_{\text{Zn}}^{\circ} = 1.36 \times 10^5 \exp(-1.21 \text{ eV/kT}) \text{ atm} \quad (7)$$

and

$$p_{\text{Cd}}^{\circ} = 1.7 \times 10^5 \exp(-1.08 \text{ eV/kT}) \text{ atm} \quad (8)$$

If we assume the activities of the Zn and Cd components over the binary  $\text{Cd}_{1-y}\text{Zn}_y$  alloys to be weakly temperature dependent, we can immediately calculate the partial pressures of Zn and Cd over the binary alloys at different temperatures.

Using the data shown in Table I, we have plotted the activity vs mole fraction for the Zn and Cd components for the binary  $\text{Cd}_{1-y}\text{Zn}_y$  alloy system at 527°C (Fig. 1).

As can be noted from the plot shown in Fig. 1 and the data in Table I, the activities for the two components follow Raoult's Law—where the activity coefficient is closer to unity—at mole fractions approaching unity and follow Henry's Law—where the activity coefficient is a constant—for mole fractions approaching zero. The ideal solution behavior is denoted by dotted lines and the activity coefficients of both the components are in excess of unity for all mole fractions away from unity indicating a repulsive interaction between the two components.

## EXPERIMENTAL

The traditional method of directly measuring the vapor pressures of the constituent elements prevailing over binary and pseudobinary compounds entails preparation of the compounds of precise composition and analyzing spectroscopically the vapor emanating from the crystals at the elevated temperature. This method allows for the measurement of the vapor pressures of all the constituent elements composing the compound and facilitates evaluation of thermodynamic parameters concerning the formation of the compounds. Using this approach, Brebrick and co-workers have established the vapor pressures and relevant thermodynamic parameters for  $\text{HgTe}^9$  and  $(\text{Hg,Cd})\text{Te}$  compounds.<sup>5,6</sup> These thermodynamic data have proven to be invaluable in designing experiments concerned with crystal growth, annealing and high temperature device processing of these materials to prevent decomposition and/or second phase formation. Unfortunately, such measurements have not yet been carried out on  $(\text{Cd,Zn})\text{Te}$  crystals.

The experimental approach we have developed in our work here is simple and novel and although it does

not allow one to evaluate all the thermodynamic quantities relating to the formation of the  $\text{Cd}_{1-x}\text{Zn}_x\text{Te}$  compounds of various compositions—as the direct vapor pressure measurement does—it establishes the compositions of the binary  $\text{Cd}_{1-x}\text{Zn}_x$  alloys whose vapors are in equilibrium with  $\text{Cd}_{1-x}\text{Zn}_x\text{Te}$  crystals of various compositions at different temperatures.

In our work, a thin film of Te is evaporated onto the walls of a sealed quartz ampoule containing a  $\text{Cd}_{1-x}\text{Zn}_x$  alloy of a certain composition. The alloy source is maintained at a slightly lower temperature (Fig. 2) than the Te film so that during the reaction, or during the cool down of the ampoule from the high temperature to room temperature, there is negligible con-

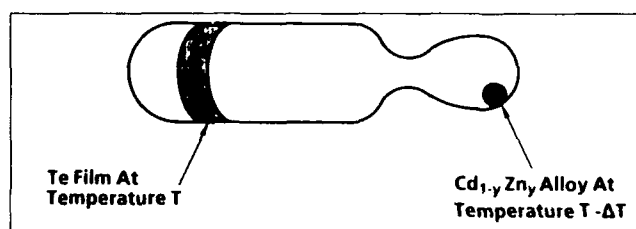


Fig. 2. Annealing setup for  $\text{Cd}_{1-x}\text{Zn}_x\text{Te}$  compound formation.

Table II. Summary of Zn Compositions of  $\text{Cd}_{1-x}\text{Zn}_x\text{Te}$  Compounds in Equilibrium with  $(\text{Cd,Zn})$  Vapors from Binary  $\text{Cd}_{1-y}\text{Zn}_y$  Alloy Sources at Various Temperatures

| Temp °C | $(\text{Cd}_{1-y}\text{Zn}_y)$ | $\text{Cd}_{1-x}\text{Zn}_x\text{Te}$ | Partial Pressure of Zn, $p_{\text{Zn}}$ (atm) | Calculated Partial Pressure of Cd, $p_{\text{Cd}}$ (atm) | $p_{\text{Zn}}/p_{\text{Cd}}$ ratio |
|---------|--------------------------------|---------------------------------------|---|--|-------------------------------------|
| 400     | $6.3 \times 10^{-3}$           | $9 \times 10^{-2}$                    | $3 \times 10^{-6}$                            | $1.4 \times 10^{-3}$                                     | $2.1 \times 10^{-3}$                |
|         | $4 \times 10^{-2}$             | $4 \times 10^{-1}$                    | $1.7 \times 10^{-5}$                          | $1.35 \times 10^{-3}$                                    | $1.3 \times 10^{-2}$                |
|         | $2 \times 10^{-1}$             | $6.5 \times 10^{-1}$                  | $5.4 \times 10^{-5}$                          | $1.2 \times 10^{-3}$                                     | $4.6 \times 10^{-2}$                |
|         | $5 \times 10^{-1}$             | $8 \times 10^{-1}$                    | $8.5 \times 10^{-5}$                          | $9.5 \times 10^{-4}$                                     | $8.9 \times 10^{-2}$                |
| 500     | $5.7 \times 10^{-3}$           | $1.3 \times 10^{-1}$                  | $4.2 \times 10^{-5}$                          | $1.6 \times 10^{-2}$                                     | $2.6 \times 10^{-3}$                |
|         | $4 \times 10^{-2}$             | $4.8 \times 10^{-1}$                  | $2.5 \times 10^{-4}$                          | $1.6 \times 10^{-2}$                                     | $1.6 \times 10^{-2}$                |
|         | $2 \times 10^{-1}$             | $7 \times 10^{-1}$                    | $8 \times 10^{-4}$                            | $1.4 \times 10^{-2}$                                     | $5.7 \times 10^{-2}$                |
| 600     | $5.4 \times 10^{-3}$           | $1.7 \times 10^{-1}$                  | $3.1 \times 10^{-4}$                          | 0.1  | $3.1 \times 10^{-3}$                |
|         | $4 \times 10^{-2}$             | $3.7 \times 10^{-1}$                  | $2 \times 10^{-3}$                            | $9.5 \times 10^{-2}$                                     | $2.1 \times 10^{-2}$                |
|         | $2 \times 10^{-1}$             | $6 \times 10^{-1}$                    | $6.4 \times 10^{-3}$                          | $9 \times 10^{-2}$                                       | $7.1 \times 10^{-2}$                |
|         | $5 \times 10^{-1}$             | $8 \times 10^{-1}$                    | $10^{-2}$                                     | $7 \times 10^{-2}$                                       | 0.14                                |
| 700     | $4.9 \times 10^{-3}$           | $2 \times 10^{-1}$                    | $1.5 \times 10^{-3}$                          | 0.43   | $3.5 \times 10^{-3}$                |
|         | $2 \times 10^{-1}$             | $7.5 \times 10^{-1}$                  | $3.3 \times 10^{-2}$                          | 0.37   | $8.9 \times 10^{-2}$                |
|         | $5 \times 10^{-1}$             | $7.8 \times 10^{-1}$                  | $5.2 \times 10^{-2}$                          | 0.29   | 0.18                                |
| 800     | $6.8 \times 10^{-3}$           | $1.1 \times 10^{-1}$                  | $8.2 \times 10^{-3}$                          | 1.43   | $5.7 \times 10^{-3}$                |
|         | $4.5 \times 10^{-2}$           | $2.6 \times 10^{-1}$                  | $4.5 \times 10^{-2}$                          | 1.38   | $3.2 \times 10^{-2}$                |
|         | $2 \times 10^{-1}$             | $4.7 \times 10^{-1}$                  | 0.126   | 1.23   | 0.10                                |
|         | $5 \times 10^{-1}$             | $6.5 \times 10^{-1}$                  | 0.2   | 0.97   | 0.21                                |
| 900     | $9.5 \times 10^{-3}$           | $3 \times 10^{-2}$                    | $3.4 \times 10^{-2}$                          | 3.9  | $8.8 \times 10^{-3}$                |
|         | $4.5 \times 10^{-2}$           | 0.2                                   | 0.14  | 3.7  | $3.7 \times 10^{-2}$                |
|         | 0.2                            | 0.32                                  | 0.38  | 3.3  | 0.11                                |
|         | 0.49                           | 0.68                                  | 0.60  | 2.7  | 0.22                                |
| 1000    | $9.5 \times 10^{-3}$           | $3 \times 10^{-2}$                    | 0.09  | 8.95   | $10^{-2}$                           |
|         | $4.8 \times 10^{-2}$           | 0.16                                  | 0.37  | 8.69   | $4.3 \times 10^{-2}$                |
|         | 0.19                           | 0.45                                  | 0.94  | 7.83   | 0.12                                |
|         | 0.49                           | 0.75                                  | 1.54  | 6.22   | 0.25                                |

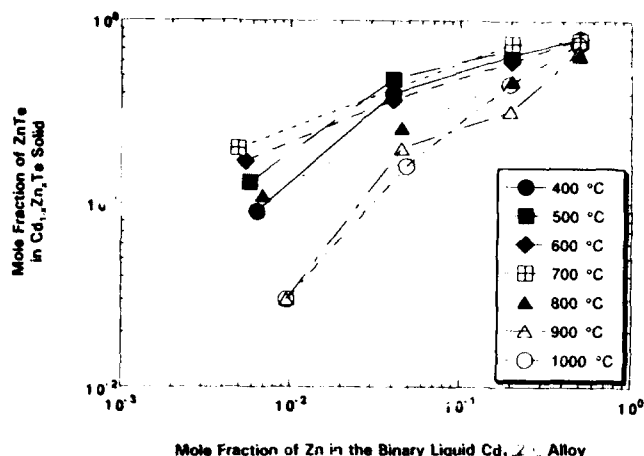


Fig. 3. Mole fraction of ZnTe in the solid  $\text{Cd}_{1-x}\text{Zn}_x\text{Te}$  compound as a function of the mole fraction of Zn in the liquid binary  $\text{Cd}_{1-y}\text{Zn}_y$  alloy in equilibrium with it.

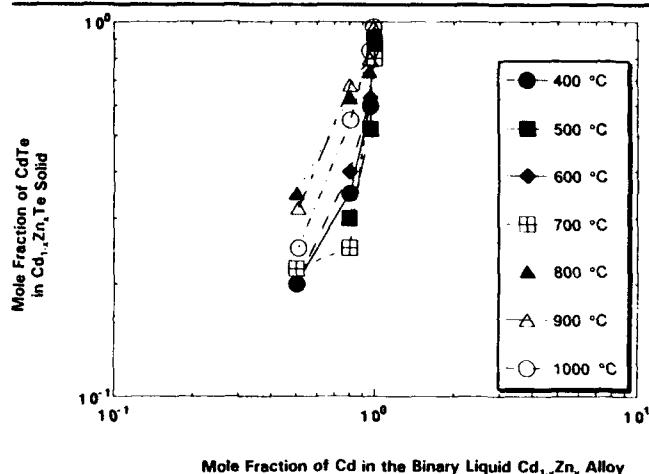


Fig. 4. Mole fraction of CdTe in the solid  $\text{Cd}_{1-x}\text{Zn}_x\text{Te}$  compound as a function of the mole fraction of Cd in the binary liquid  $\text{Cd}_{1-y}\text{Zn}_y$  alloy in equilibrium with it.

densation of the Cd-Zn alloy near the Te end. The ampoules with the Te film at one end and the binary  $\text{Cd}_{1-y}\text{Zn}_y$  alloys at the other (cooler end) are then annealed at temperatures varying from 400 to 1000°C for a period of anneal ranging from several hours at 1000°C to over a week at 400°C.

It is to be noted that the ampoules were held at a temperature (~400°C) slightly below the melting point of Te for four to five days before they were raised to temperatures above the melting point of Te. This procedure ensured conversion of Te to  $(\text{Cd,Zn})\text{Te}$  solid at a temperature below the melting point of Te and prevented the Te film from forming a liquid which would coalesce and form globules, otherwise, at temperatures above the melting point of Te. At the end of the equilibration period, the Te film is converted to  $\text{Cd}_{1-x}\text{Zn}_x\text{Te}$  solid of a certain composition depending on the composition  $y$  of the binary  $\text{Cd}_{1-y}\text{Zn}_y$  alloy, whose vapors it is in equilibrium with.

Since the vapor pressure of Te is much lower than that of Cd and Zn at a given temperature, Te film stays at the high temperature end of the ampoule. As a result, most of the  $\text{Cd}_{1-x}\text{Zn}_x\text{Te}$  compound formation

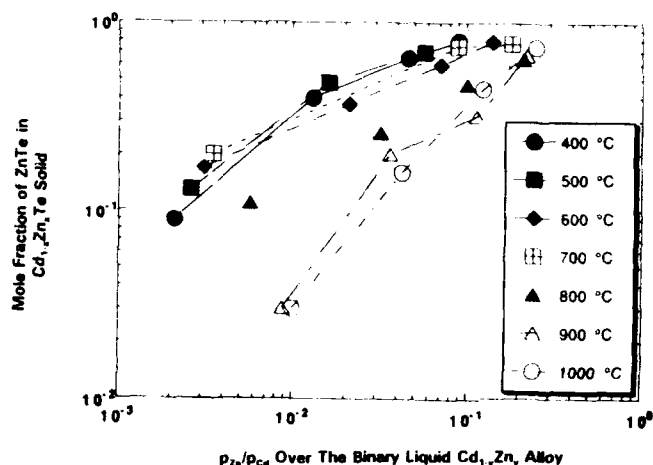


Fig. 5. Mole fraction of ZnTe in the solid compound  $\text{Cd}_{1-x}\text{Zn}_x\text{Te}$  as a function of the ratio  $p_{\text{Zn}}/p_{\text{Cd}}$  in the binary liquid  $\text{Cd}_{1-y}\text{Zn}_y$  alloy in equilibrium with it.

occurs at the Te end and almost none at the  $\text{Cd}_{1-y}\text{Zn}_y$  alloy end. At the end of the anneal, the  $\text{Cd}_{1-x}\text{Zn}_x\text{Te}$  compound films are scraped off the walls of the ampoule and are analyzed for Cd, Zn and Te using electron microprobe analytical techniques.

## RESULTS AND DISCUSSION

The compositions  $x_{\text{ZnTe}}$  of the  $\text{Cd}_{1-x}\text{Zn}_x\text{Te}$  compounds formed from the reaction of Te with the vapor of the binary  $\text{Cd}_{1-y}\text{Zn}_y$  alloys are summarized in Table II for various Zn compositions  $y$  of the binary alloys. These data are also plotted in Fig. 3. Figure 4 shows  $x_{\text{CdTe}}$  as a function of the mole fraction  $(1-y)$  of Cd in the binary  $\text{Cd}_{1-y}\text{Zn}_y$  alloys at various temperatures. Also shown in Table II are the calculated values of the partial pressures of Cd and Zn and the ratio  $p_{\text{Zn}}/p_{\text{Cd}}$  over the  $\text{Cd}_{1-x}\text{Zn}_x\text{Te}$  solids in equilibrium with Cd and Zn vapors of the binary  $\text{Cd}_{1-y}\text{Zn}_y$  alloys. These calculations were carried out using Eqs. 5 through 8 and assuming the activities to be temperature independent. Figures 5 and 6 show  $x_{\text{ZnTe}}$  and  $x_{\text{CdTe}}$  as a function of  $p_{\text{Zn}}/p_{\text{Cd}}$  and  $p_{\text{Cd}}/p_{\text{Zn}}$ —the ratios of the partial pressure of Zn to that of Cd and vice versa—at various temperatures.

As can be noted from the results shown in Figs. 3 and 4, the compositions of ZnTe and CdTe in the  $\text{Cd}_{1-x}\text{Zn}_x\text{Te}$  compounds increase with increase in the Zn and Cd mole fractions, respectively, in the binary  $\text{Cd}_{1-y}\text{Zn}_y$  alloys. The variation of ZnTe and CdTe mole fractions with Zn and Cd mole fractions in the binary alloys appears to be similar at all temperatures below 800°C confirming the validity of our initial assumption that the activities of the Cd and Zn components in the binary alloys are weakly dependent on temperature. Also to be noted from the figures is the fact that the mole fraction of CdTe in the  $\text{Cd}_{1-x}\text{Zn}_x\text{Te}$  compound increases superlinearly with the mole fraction of Cd in the binary alloy (Fig. 4), whereas that of ZnTe increases sublinearly with the mole fraction of Zn in the binary alloy (Fig. 3).

Also to be noted from the results shown in Figs. 3 and 4 is the decrease of the ZnTe mole fraction in the



compound at  $T > 800^\circ\text{C}$  compared with that at lower temperatures for the same mole fraction of the Zn in the binary alloy. This inference suggests that the free energy of formation of the compound  $\text{Cd}_{1-x}\text{Zn}_x\text{Te}$  appears to be somewhat temperature dependent or that the activities of Cd and Zn in the binary  $\text{Cd}_{1-x}\text{Zn}_x$  alloys are not temperature independent at  $T \geq 800^\circ\text{C}$ .

Figure 5 showing the variation of ZnTe mole fraction as a function of  $p_{\text{Zn}}/p_{\text{Cd}}$  indicates that the  $p_{\text{Zn}}/p_{\text{Cd}}$  ratio varies from  $10^{-3}$  to slightly greater than  $10^{-1}$  for  $x_{\text{ZnTe}}$  to vary from 0.1 to near unity in the  $\text{Cd}_{1-x}\text{Zn}_x\text{Te}$  system. In contrast, in the  $\text{Hg}_{1-x}\text{Cd}_x\text{Te}$  system, the  $p_{\text{Cd}}/p_{\text{Hg}}$  ratio is very much lower—on the order of  $10^{-7}$  to  $10^{-8}$ —and  $x_{\text{CdTe}}$  varies from near zero to unity for a  $p_{\text{Cd}}/p_{\text{Hg}}$  variation of merely a factor of 2 to 3.

Finally, results shown in Fig. 3 suggest that a  $\text{Cd}_{1-y}\text{Zn}_y$  binary alloy with  $y = 0.005$  is the one to be used—as a source material during any high temperature processing—to prevent decomposition of the technologically most important composition of  $x_{\text{ZnTe}} = 0.04$  required as substrates in the growth of long wavelength infrared (Hg,Cd)/Te epilayers.

### SUMMARY

Annealing experiments which are simple and yet novel, have been carried out to establish the compositions of the  $\text{Cd}_{1-y}\text{Zn}_y$  alloys in equilibrium with  $\text{Cd}_{1-x}\text{Zn}_x\text{Te}$  compounds of different compositions at various temperatures. Presence of a 0.5% Zn along with Cd in a closed or semi-closed system may prove to be beneficial in preventing decomposition and/or formation of a metal/nonmetal second phase during annealing or any high temperature processing of  $\text{Cd}_{0.96}\text{Zn}_{0.04}\text{Te}$  substrates.

### ACKNOWLEDGMENT

The authors H.R. Vydyanath, J.A. Ellsworth, R.F. Fisher, C.J. Johnson, and G.T. Neugebauer gratefully acknowledge the support of the U.S. Army CECOM Night Vision and ElectroOptics Directorate on SBIR Contract No. DAAB07-91-C-K753.

### NOTE

After submission of this manuscript, we have become aware of the following published work related to discussion in our paper:

- M. Azoulay, S. Rotter and G. Gafni, "Zinc Segregation in  $\text{CdZnTe}$  grown under Cd/Zn Partial Pressure Control," *J. Cryst. Growth* 117, 276 (1992). These authors find that the presence of Zn in the vapor prevents decomposition of  $\text{CdZnTe}$  during crystal growth.
- Iwao Katayama, Takeo Inomoto, Zensaku Kozuka and Takamichi Iida, "Activity Measurement of Zn in  $\text{ZnTe-CdTe}$  Solid Solutions by EMF Method," *Mater. Trans. JIM* 32, 169 (1991). These authors note a weak temperature dependence of activity of Zn for metal rich  $\text{Cd}_{1-x}\text{Zn}_x\text{Te}$  between 550 to  $600^\circ\text{C}$  and measure activities of Zn—for metal rich conditions (Te poor conditions)—

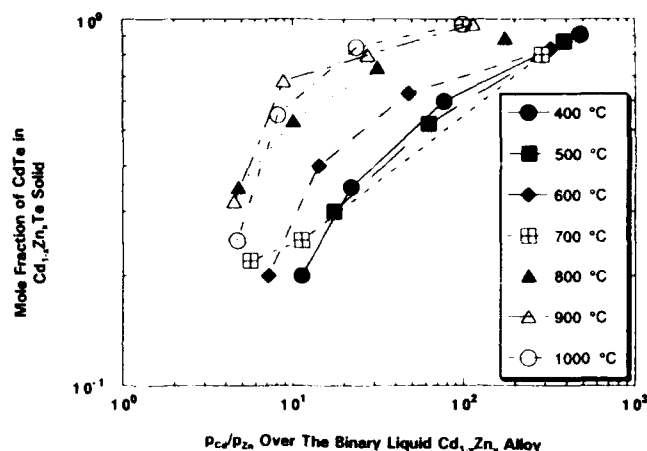


Fig. 6. Mole fraction of CdTe in the solid  $\text{Cd}_{1-x}\text{Zn}_x\text{Te}$  compound as a function of the ratio  $p_{\text{Cd}}/p_{\text{Zn}}$  in the binary liquid  $\text{Cd}_{1-y}\text{Zn}_y$  alloy in equilibrium with it.

$$\alpha_{\text{Zn}}(600^\circ\text{C}) = 0.14 \text{ for } X_{\text{ZnTe}} = 0.6$$

and

$$\alpha_{\text{Zn}}(600^\circ\text{C}) = 0.04 \text{ for } X_{\text{ZnTe}} = 0.19.$$

For comparison, in our work we get

$$X_{\text{ZnTe}}(600^\circ\text{C}) = 0.6 \text{ for } y_{\text{Zn}}(\text{Cd}_{1-y}\text{Zn}_y) = 0.2$$

or

$$\alpha_{\text{Zn}} = 0.45$$

and

$$X_{\text{ZnTe}}(600^\circ\text{C}) = 0.17 \text{ for } y_{\text{Zn}}(\text{Cd}_{1-y}\text{Zn}_y) = 5.4 \times 10^{-3}$$

or

$$\alpha_{\text{Zn}} = 0.035.$$

- T.C. Yu and R.F. Brebrick "The Hg-Cd-Zn-Te Phase Diagram," *J. Phase Equilibria* 13, 476 (1992). These authors have fit their calculations with EMF data of Katayama et al. above and have presented a detailed analysis of the Cd-Zn-Te system.

### REFERENCES

1. J.J. Kennedy, P.M. Amirtharaj, P.R. Boyd, S.B. Qadri, R.C. Dobbyn and G.G. Long, *J. Cryst. Growth* 86, 93 (1988).
2. S. Sen, W.H. Konkel, S.J. Tighe, L.G. Bland, S.R. Sharma and R.E. Taylor, *J. Cryst. Growth* 86, 111 (1988).
3. Al. Sher, A.B. Chen and W.E. Spicer, *J. Vac. Sci. Technol. A* 3, 105 (1985).
4. S.B. Qadri, E.F. Skelton, A.W. Webb and J.J. Kennedy, *Appl. Phys. Lett.* 46, 257 (1985).
5. J.P. Schwartz, T. Tung and R.F. Brebrick, *J. Electrochem. Soc.* 128, 438 (1981).
6. T. Tung, L. Golonka and R.F. Brebrick, *J. Electrochem. Soc.* 128, 451 (1981).
7. G.T. Neugebauer (unpublished).
8. R. Hultgren, R.L. Orr, P.D. Anderson and K.K. Kelley, *Selected Values of Thermodynamic Properties of Metals and Alloys*, John Wiley and Sons, Inc. p.637 (1963).
9. R.F. Brebrick and A.J. Strauss, *J. Phys. Chem. Solids* 26, 989 (1965).

# Thermomigration of Te Precipitates and Improvement of (Cd,Zn)Te Substrate Characteristics for the Fabrication of LWIR (Hg,Cd)Te Photodiodes

H.R. VYDIYANATH, J.A. ELLSWORTH, and J.B. PARKINSON

Aerojet Electronic Systems Division, 1100 W. Hollyvale Street, Azusa, CA 91702

J.J. KENNEDY

U.S. Army CECOM Night Vision and ElectroOptics Directorate, Fort Belvoir, VA 22060

B. DEAN, C.J. JOHNSON, G.T. NEUGEBAUER, and J. SEPICH

II-VI Inc., 375 Saxonburg Boulevard, Saxonburg, PA 16056

POK-KAI LIAO

Texas Instruments, Inc., Dallas, TX 75265

(Cd,Zn)Te wafers containing Te precipitates have been annealed under well defined thermodynamic conditions at temperatures below and above the melting of Te. Results of the examination of the wafers with infrared microscopy before and after the anneals indicate a substantial reduction of the Te precipitates in wafers annealed at temperatures in excess of the melting point of Te compared with those annealed at temperatures below the melting point of Te. These results confirm the thermomigration of liquid Te precipitates to be the principally operative mechanism during annealing in the elimination of these precipitates in (Cd,Zn)Te wafers. The occurrence of Te precipitates in (Hg,Cd)Te epitaxial layers grown on (Cd,Zn)Te substrates containing Te precipitates is also explained on the basis of thermomigration of these precipitates during LPE growth from the substrates to the epilayers. Absence of occurrence of Te precipitates in (Hg,Cd)Te epilayers grown on annealed (Cd,Zn)Te substrates with negligible Te precipitates is also confirmed. Usefulness of annealing (Cd,Zn)Te substrates—to eliminate Te precipitates—prior to epilayer growth is confirmed via demonstration of improved long wavelength infrared (Hg,Cd)Te device array performance uniformity in epitaxial layers grown on (Cd,Zn)Te substrates with negligible Te precipitates after annealing.

**Key words:** CdZnTe substrates, LPE, LWIR HgCdTe device arrays, thermomigration of Te, LPE

## INTRODUCTION

In a previous paper,<sup>1</sup> we demonstrated a process of step annealing—under well controlled thermodynamic conditions—which eliminates most of the Te precipitates present in CdTe and (Cd,Zn)Te substrate crystals as well as in the (Hg,Cd)Te epilayers grown on them. We also proposed thermomigration of liquid Te

precipitates as the mechanism responsible for the elimination of Te precipitates during annealing.

In this paper, we present experimental results of anneals—at temperatures below and above the melting point of Te—which confirm the mechanism of the thermomigration of Te precipitates to be principally operative in their elimination during annealing. Actual implementation of the step anneal process to reduce Te precipitates in (Cd,Zn)Te substrates and (Hg,Cd)Te epilayers is demonstrated. The process of

(Received November 5, 1992; revised January 13, 1993)

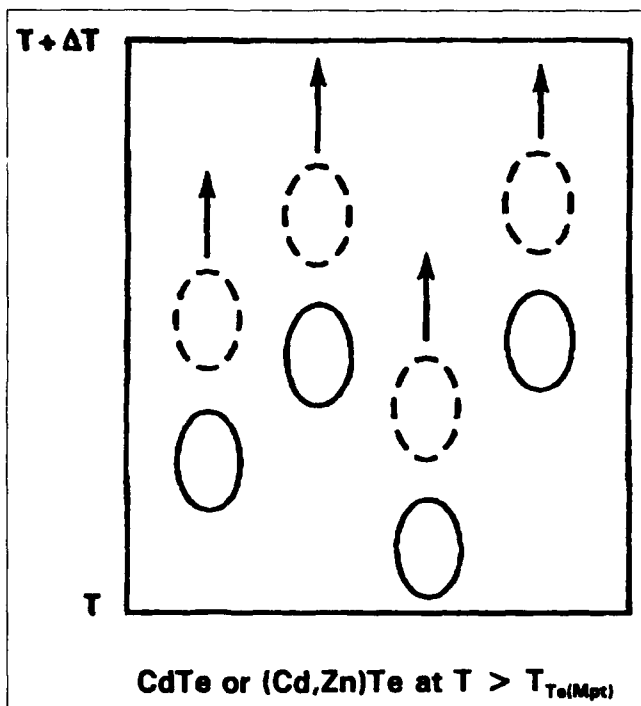


Fig. 1. Schematic of the process of thermal migration of liquid Te precipitates toward the higher temperature region of the wafer, under the influence of a temperature gradient.

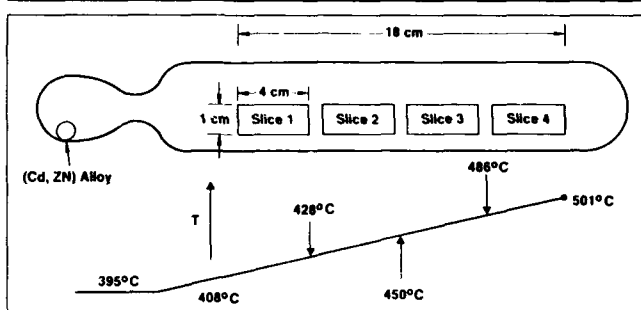


Fig. 2. Experimental setup to demonstrate thermomigration of Te precipitates via annealing experiments at below and above melting point of Te.

thermomigration of Te precipitates occurring during the LPE growth process is examined.

Finally, we have fabricated several long wavelength infrared (LWIR) (Hg,Cd)Te device arrays in epitaxial layers grown on annealed and unannealed (Cd,Zn)Te substrates and have demonstrated improved device  $R_{\text{A}}$  performance uniformity in epitaxial layers grown on annealed (Cd,Zn)Te substrates with minimum Te precipitates.

### EXPERIMENTAL

CdTe substrates were grown at II-VI Inc. The  $\text{Cd}_{0.96}\text{Zn}_{0.04}\text{Te}$  substrates were obtained from various boules grown at II-VI Inc. as well as at Texas Instruments Inc. The substrates were annealed in sealed quartz ampoules. In the case of  $\text{Cd}_{0.96}\text{Zn}_{0.04}\text{Te}$  crystals, a  $\text{Cd}_{0.96}\text{Zn}_{0.04}$  source was used, instead of pure Cd, to prevent any loss of Zn from these substrates.

(Hg,Cd)Te films were grown at Aerojet on the

unannealed as well as the annealed substrates, by liquid phase epitaxy from the-rich solutions at  $\sim 500^\circ\text{C}$ . Detailed infrared (IR) microscope examination of the substrates and (Hg,Cd)Te films was carried out at the U.S. Army Night Vision Labs. and II-VI Inc.: (Cd,Zn)Te substrates were examined in the transmission mode whereas the (Hg,Cd)Te epitaxial layer cleaved cross sections were examined in the reflection mode. Long wavelength infrared (Hg,Cd)Te photodiodes were fabricated at Aerojet in a p-on-n device configuration in an  $8 \times 8$  mosaic array format. While most of the metallurgical characterization of the substrates and epilayers was carried out at II-VI Inc., all the electrical, optical, and electro-optical characterization of (Hg,Cd)Te material and devices was carried out at Aerojet.

### VALIDATION OF THERMOMIGRATION OF Te PRECIPITATES DURING ANNEALING

As described in our earlier paper,<sup>1</sup> thermomigration of Te precipitates entails the movement of these precipitates in a liquid state under the influence of a temperature gradient in the direction of the higher temperature zone. This process is envisioned to occur as a result of the dissolution of (Cd,Zn)Te in liquid Te (precipitate) at the higher temperature and precipitation at the lower temperature with Cd and Zn diffusing through the liquid Te medium (Fig. 1).

If thermomigration is the principal mechanism responsible for the elimination of Te precipitates during annealing, annealing at temperatures above the melting point of Te should show marked decrease in Te precipitates compared to that at temperatures below the melting point of Te. This is indeed the case in the annealing experiments we have carried out in our work.

In the first set of annealing experiments, a (Cd,Zn)Te wafer supplied by Texas Instruments Inc., which was known to have a uniform density of Te precipitates at  $\sim 3 \times 10^5 \text{ cm}^{-2}$  was cut up into several pieces, approximately 4 cm long and 1 cm wide. Four of these pieces were annealed in the same ampoule for  $\sim 100$  h in a temperature gradient ranging from approximately 400 to  $500^\circ\text{C}$  (Fig. 2). The temperature gradient in the ampoule as shown in Fig. 2 was such that, two of the slices were at a temperature below  $450^\circ\text{C}$ , and two of the remaining ones at a temperature above  $450^\circ\text{C}$ . The eutectic temperature in the Cd-Te system on the Te-rich side of the phase diagram is around  $437^\circ\text{C}$ .<sup>2</sup> Thus, the thermomigration of Te precipitates can be expected to occur at  $T > 437^\circ\text{C}$ . Indeed, as can be inferred from the IR micrograph results shown in Fig. 3, Te precipitates are significantly minimized in two of the slices which were at temperatures above the melting point of Te. Incomplete elimination of Te precipitates in these anneals is ascribed to an insufficient time of anneal. Periods of anneal longer than 100 h at  $500^\circ\text{C}$  or higher temperature step anneal starting from  $900^\circ\text{C}$  and ramping down to  $500^\circ\text{C}$ ,<sup>1</sup> is needed to completely eliminate the Te precipitates.

A second set of anneals was carried out where the

entire ampoule was in one temperature zone at  $T = 400$  and  $T = 500^\circ\text{C}$ . Anneals at  $400^\circ\text{C}$  for 30 days did not result in the reduction of Te precipitates subsequent to anneal whereas samples annealed at  $500^\circ\text{C}$  for seven days showed a significant reduction in the density of Te precipitates. Rocking curve measurements were also made on these samples before and after the anneals. These results which are summarized in Table I indicate that the rocking curve width actually decreases slightly after the anneal at  $400^\circ\text{C}$  and increases slightly after the anneal at  $500^\circ\text{C}$ . Increase in the rocking curve width accompanied by reduction in Te precipitates has also been observed by Kennedy<sup>3</sup> during CdZnTe ingot anneal at tem-

peratures substantially above the melting point of Te. We interpret the degradation in the microstructure of the wafers as evidenced by increase in the rocking curve width after the anneal at  $500^\circ\text{C}$ , to be due to the reduction of Te precipitates via thermomigration, during which process regrowth of (Cd,Zn)Te gives rise to imperfect crystallinity.

Additional evidence for the mechanism of liquid Te precipitate thermomigration during annealing has already been discussed in our earlier paper<sup>1</sup> and will only be briefly described here. First, after an incomplete anneal (deliberate or otherwise) a higher density of Te precipitates is usually observed at the wafer surfaces than in the bulk of the wafers, (Fig. 12 of Ref.

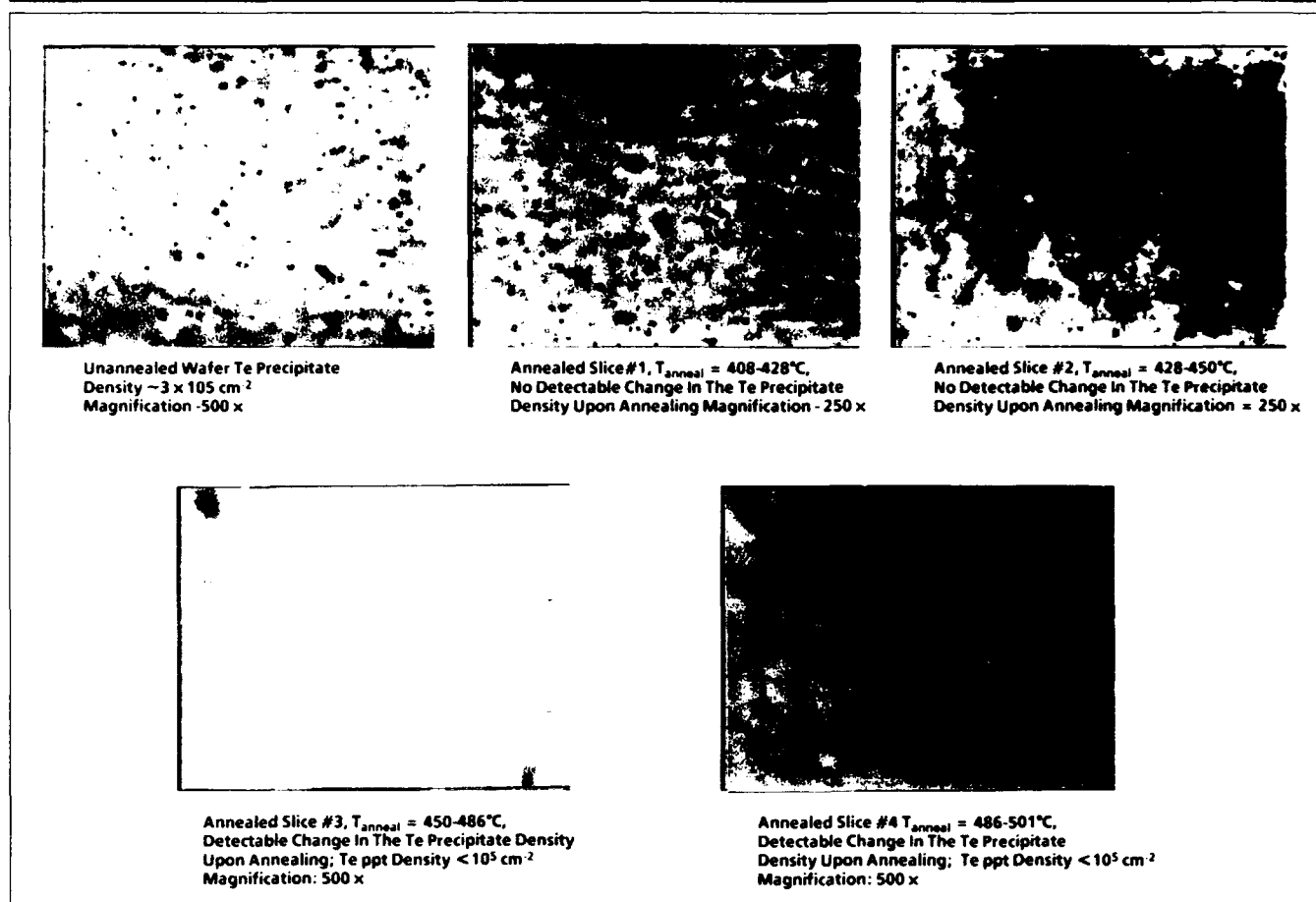


Fig. 3. Infrared transmission micrographs of unannealed and annealed slice of a (Cd,Zn)Te wafer TI 998-1-6 showing reduction in Te precipitate density at  $T_{\text{anneal}} > 450^\circ\text{C}$ .

Table I. X-Ray DCRC (FWHM) and Te Precipitate Density Data on a (Cd,Zn)Te Substrate TI 998-1-1 Before and After Anneals at 400 and  $500^\circ\text{C}$

| Sample ID    | Temp. of Anneal and Period of Anneal | Te Precipitate Density, $\text{cm}^{-2}$ |                      | DCRC Data FWHM (arc-s) |              |
|--------------|--------------------------------------|--|----------------------|------------------------|--------------|
|              |                                      | Before Anneal                            | After Anneal         | Before Anneal          | After Anneal |
| TI 998-1-1-A | $400^\circ\text{C}$ , 4 weeks        | $\sim 3 \times 10^4$                     | $\sim 3 \times 10^4$ | 40.4                   | 26.7         |
| TI 998-1-1-B | $500^\circ\text{C}$ , 7 days         | $\sim 3 \times 10^4$                     | $< 10^4$             | 37.6                   | 57.0         |

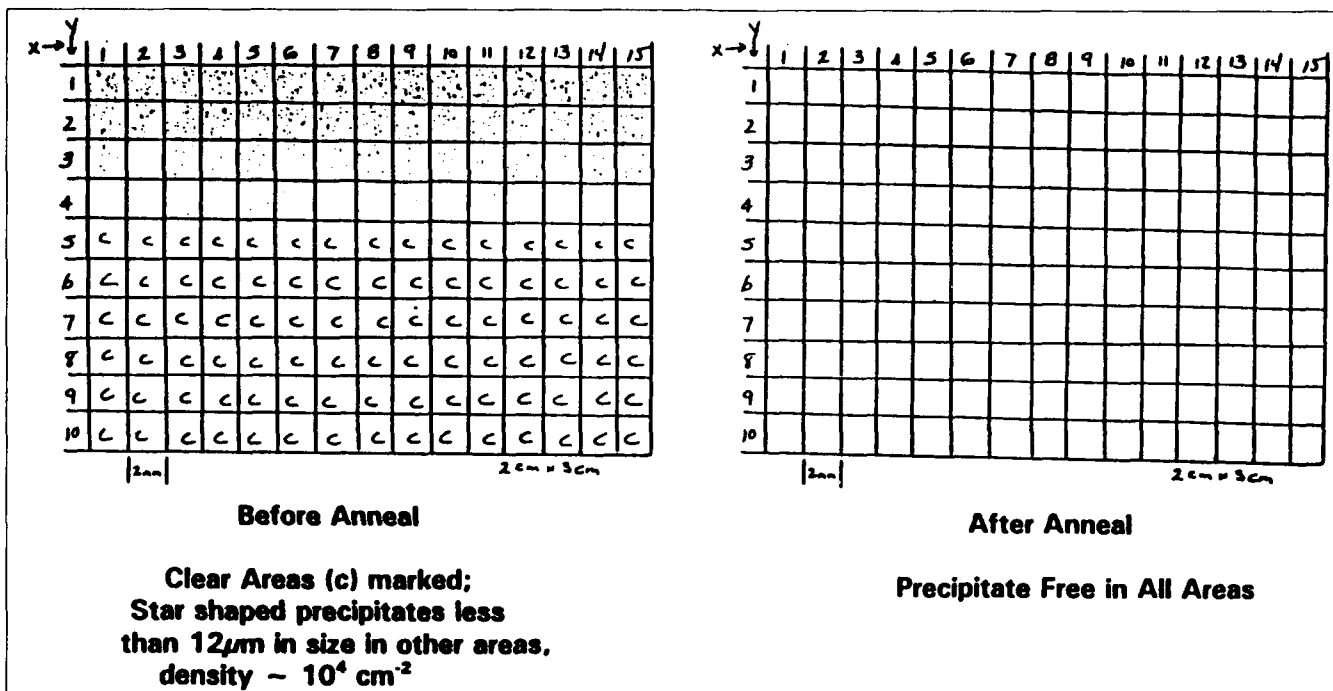


Fig. 4. Tellurium precipitate mapping for (Cd,Zn)Te wafer II-VI 5971-4a, before and after annealing.

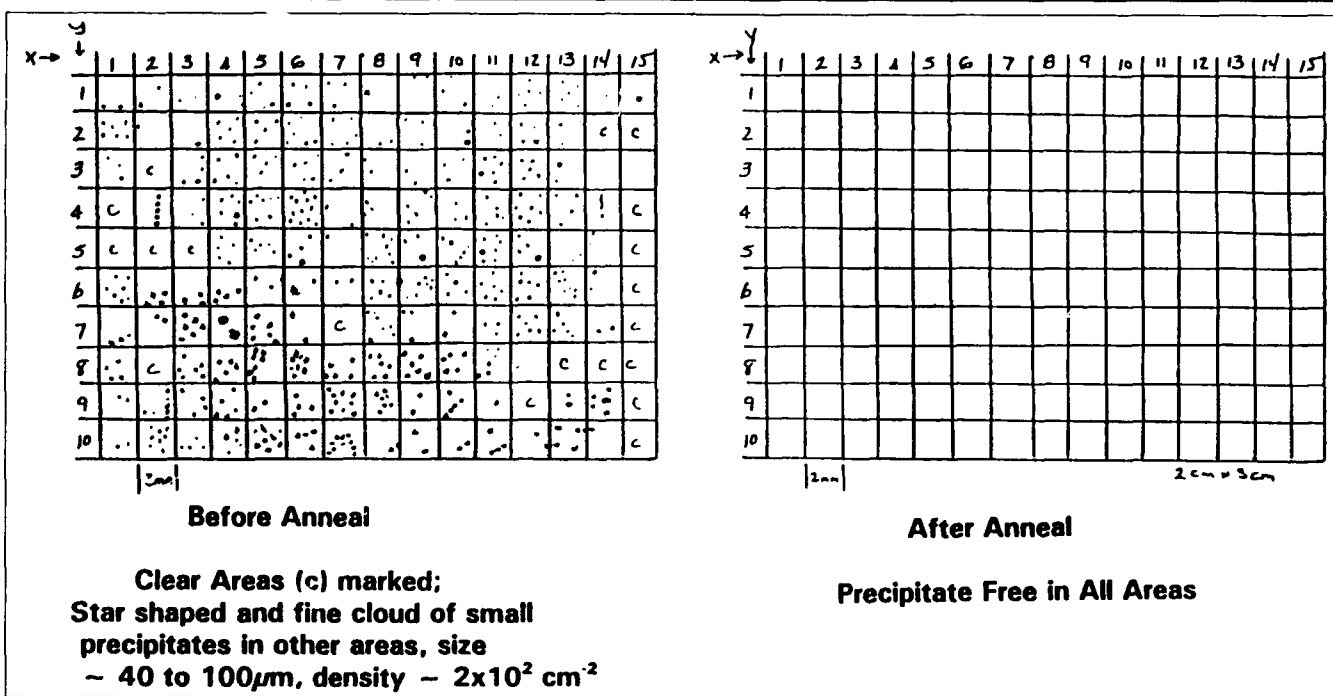


Fig. 5. Tellurium precipitate mapping for (Cd,Zn)Te wafer II-VI 5968-14B, before and after annealing.

1) and this rules out in-diffusion of Cd and Zn from the vapor causing conversion of Te precipitates to (Cd,Zn)Te because in-diffusion of Cd and Zn in solid state would cause the elimination of Te precipitates easier at the surfaces than in the bulk because of larger diffusion distances involved in the bulk conversion process. On the other hand, Te precipitate thermomigration in liquid state (Fig. 1) can explain the clustering of Te precipitates at the surfaces rather than within the bulk because of a higher temperature

prevailing at the surfaces. Second, as discussed in our earlier paper,<sup>1</sup> the fact that it is more difficult to eliminate smaller Te precipitates than the bigger ones during annealing also rules out in-diffusion of Cd and Zn from the vapor causing conversion of Te precipitates to (Cd,Zn)Te; the mechanism of Te precipitate thermomigration can explain the difficulty of elimination of smaller Te precipitates based on the fact that as the Te precipitates become smaller, surface tension effects inhibit the rate of thermomigra-

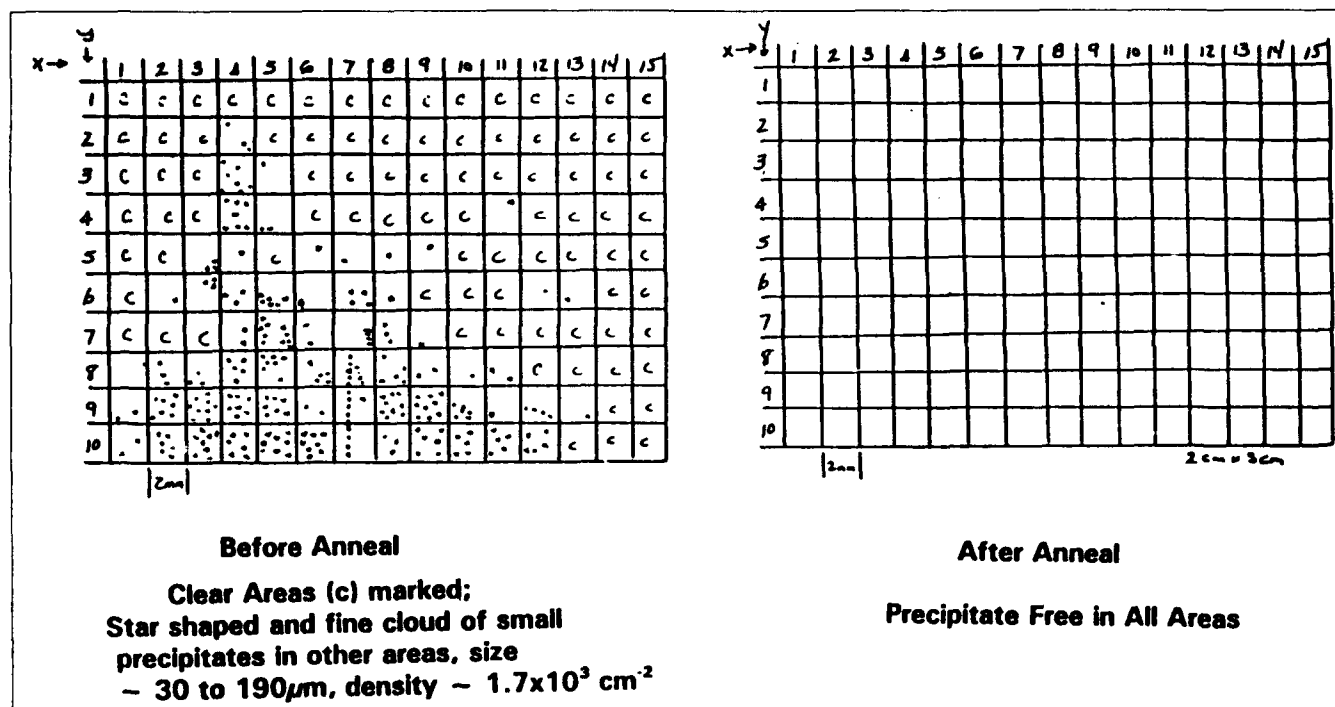


Fig. 6. Tellurium precipitate mapping for (Cd,Zn)Te wafer II-VI 5968-5A, before and after annealing.

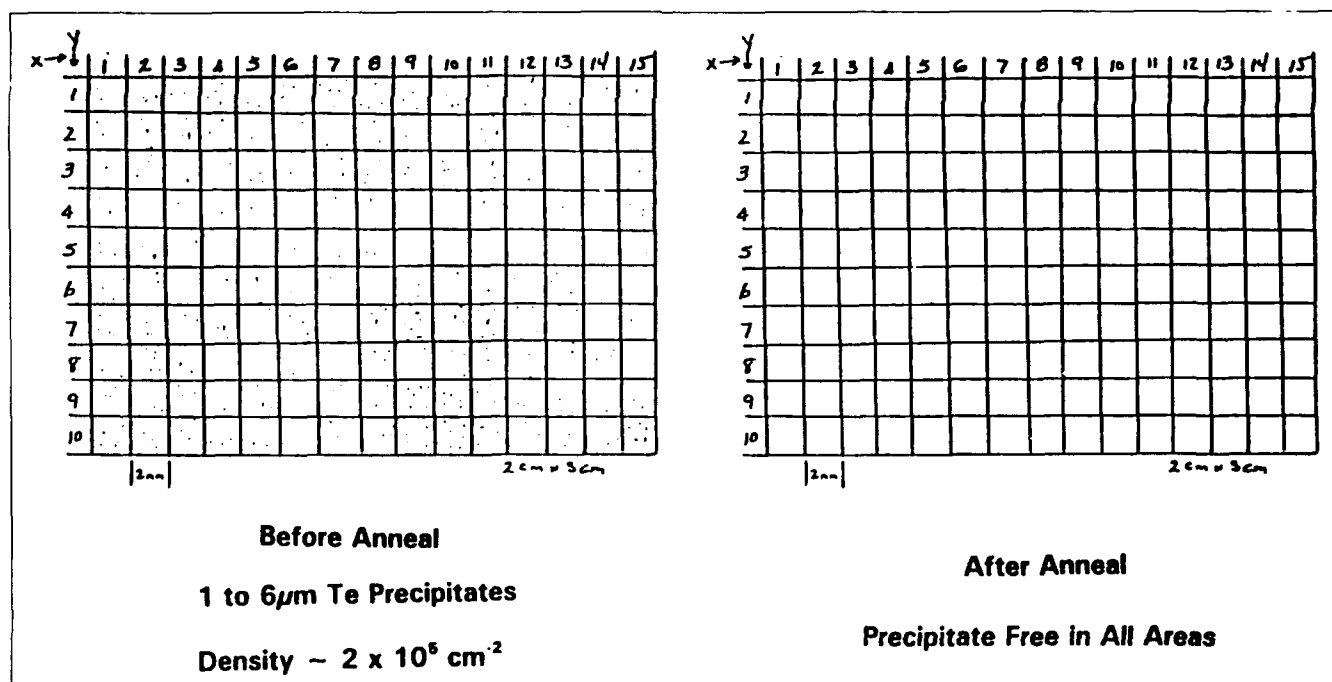


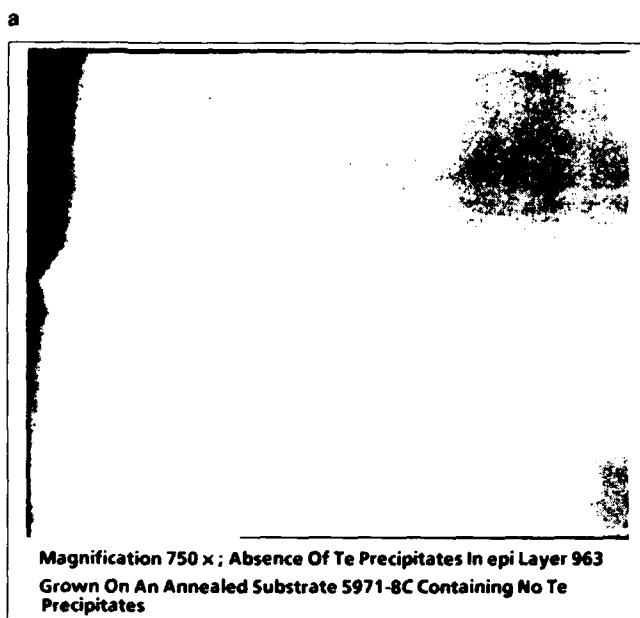
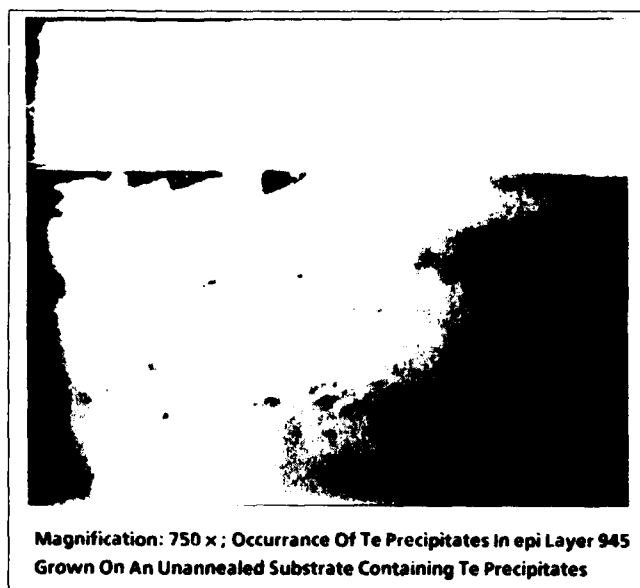
Fig. 7. Tellurium precipitate mapping for (Cd,Zn)Te wafer II-VI 5971-8C, before and after annealing.

tion, as was well demonstrated by Anthony and Cline<sup>4,5</sup> for the thermomigration of liquid droplets in KCl. Third, the traceability of the occurrence of Te precipitates in the (Hg,Cd)Te epilayers to the presence of Te precipitates in the substrates (Fig. 9 of Ref. 1) strongly suggests that the Te precipitates are migrating in a liquid state toward the (Hg,Cd)Te epilayer during the LPE growth where a severe temperature gradient is present in the (Hg,Cd)Te epilayers and CdZnTe sub-

strates once a few monolayers of (Hg,Cd)Te are grown (see Appendix A for details).

#### Te PRECIPITATE THERMOMIGRATION DURING THE LPE GROWTH PROCESS

It is important to note that the existence of a temperature gradient in the CdTe or (Cd,Zn)Te wafers is necessary for the process of Te precipitate thermomigration to occur during annealing. We have



**b**  
Fig. 8. Reflection IR micrographs of cross sections of (Hg,Cd)Te layers grown on unannealed and annealed (Cd,Zn)Te substrates.

previously argued<sup>1</sup> that such a temperature gradient prevails in our annealing experiments because of the low thermal conductivity of CdTe and (Cd,Zn)Te; we also conjectured that such a temperature gradient may prevail during the process of epitaxial growth. This is indeed so once the growth of a few monolayers of (Hg,Cd)Te has occurred. Because of the band gap of LWIR and mid wavelength infrared (MWIR) (Hg,Cd)Te layers being in the IR, absorption of heat from the Te melt is efficient and in conjunction with a thermal conductivity that is low, the temperature gradient of the (Hg,Cd)Te-(Cd,Zn)Te interface could approach hundreds of degrees per centimeter. (See Appendix A for details.) In fact, Te precipitate thermomigration during the epitaxial layer growth

could be orders of magnitude more dominant than during a substrate step anneal process. Thus, in the LPE growth process if the substrate has a large density of Te precipitates, these precipitates will easily migrate to the (Hg,Cd)Te epilayer. Thus, it is important to eliminate them in the substrates via step annealing before initiating the LPE growth.

#### IMPLEMENTATION OF STEP ANNEAL TO REDUCE Te PRECIPITATES IN (Cd,Zn)Te SUBSTRATES AND (Hg,Cd)Te EPILAYERS

In this section, we demonstrate the implementation of the step anneal process to reduce Te precipitates in substrates by presenting results of the IR microscopy examination of Te precipitate density measurements in (Cd,Zn)Te substrates before and after anneal along with results in cross sections of epilayers grown on these substrates. The IR microscopy maps of precipitates on four different (Cd,Zn)Te substrates before and after annealing are displayed in Figs. 4 through 7. As evident from these maps, most of the precipitates with different shapes such as triangles, hexagons, and stars have been eliminated subsequent to step anneals starting at  $T = 900^{\circ}\text{C}$  and ending at  $500^{\circ}\text{C}$ , following the recipe discussed in our earlier paper.<sup>1</sup>

Figure 8 shows the reflection mode IR micrographs of cross sections of epilayers grown on unannealed and annealed substrates. The micrographs indicate the presence of Te precipitates in film 945 grown on an unannealed substrate labeled II-VI 5971-4 and their absence in film 963 grown on an annealed substrate labeled II-VI 5968-5A. This inference reiterates the point made by us earlier<sup>1</sup> that the presence of Te precipitates in epilayers is traceable to that in substrates on which they are grown.

Tables II and III summarize all these data along with x-ray DCRC data on substrates and epilayers. Rocking curve broadening was observed in all the epilayers and in substrates after anneal. Rocking curve broadening in epilayers grown on annealed substrates is readily explained with the fact that annealing causes Te precipitate thermomigration and degradation in the crystallinity of the substrates, which, then, is replicated in the epilayers. For films grown on unannealed substrates containing Te precipitates, we ascribe the rocking curve broadening to Te precipitate thermomigration which occurs during the epilayer growth from the substrates to the epilayers.

#### DEMONSTRATION OF IMPROVED LWIR (Hg,Cd)Te DEVICE ARRAY PERFORMANCE UNIFORMITY VIA REDUCTION OF Te PRECIPITATES IN (Cd,Zn)Te SUBSTRATES AND (Hg,Cd)Te EPILAYERS

In principle, dislocations, Te precipitates, extraneous impurities, and native point defect centers could all affect the (Hg,Cd)Te photodiode device performance by acting as Shockley-Read and tunneling centers. To date, interaction between the various defects and

their impact on the device performance is not well understood. We present in Fig. 9 results of device  $R_0A$  performance on two sets of LWIR (Hg,Cd)Te arrays, one array labeled 949-M1-19 fabricated in a (Hg,Cd)Te epilayer grown on an unannealed (Cd,Zn)Te substrate with  $\sim 3 \times 10^4 \text{ cm}^{-2}$  EPD and  $\sim 2 \times 10^4 \text{ cm}^{-2}$  Te precipitates and the other array labeled 963-M1-23 fabricated in a (Hg,Cd)Te epilayer grown on an annealed (Cd,Zn)Te substrate with  $\sim 1.5 \times 10^5 \text{ cm}^{-2}$  EPD and  $2 \times 10^5 \text{ cm}^{-2}$  Te precipitates before anneal but none after. Additional characteristics of the films and corresponding substrates are summarized in Tables II and III discussed earlier. As can be seen from the device  $R_0A$  performance results shown in Fig. 9, it is clear that for temperatures of operation at  $T \leq 40 \text{ K}$  array 963-M1-23 which has no Te precipitates is superior in its uniformity even at temperatures down to 20K compared with array 949-M1-19 containing  $\sim 10^4$  Te precipitates. From the temperature dependence of  $R_0A$  of these devices, it appears that they are g-r current noise limited at  $T \leq 40 \text{ K}$ , and it is very likely that the Te precipitates act as g-r and tunneling centers in the epilayers affecting the device performance at  $T \leq 40 \text{ K}$  in these devices. Array 949-M1-19 containing Te precipitates shows nonuniformity in  $R_0A$  performance at  $T \leq 40 \text{ K}$  because of the poorer

performance of devices located in regions of Te precipitates.

## CONCLUSION

Thermomigration of Te precipitates in the liquid state has been confirmed to be the principally operative mechanism responsible for the elimination of these precipitates during annealing of (Cd,Zn)Te substrates under well defined thermodynamic conditions. Additionally, thermomigration of Te precipitates from the substrates to the (Hg,Cd)Te epitaxial layers during LPE growth is also documented and explained. Growth of Te precipitate free (Hg,Cd)Te epitaxial layers on annealed (Cd,Zn)Te substrates with no Te precipitates is demonstrated.

Finally, the usefulness of eliminating Te precipitates in (Cd,Zn)Te substrates prior to the growth of epitaxial (Hg,Cd)Te layers is demonstrated via fabrication of LWIR device arrays with improved  $R_0A$  performance uniformity in epitaxial (Hg,Cd)Te grown on annealed (Cd,Zn)Te substrates with no Te precipitates.

## ACKNOWLEDGMENT

The authors (H.R. Vydyanath, J.A. Ellsworth, J.B. Parkinson, B. Dean, C.J. Johnson, G.T. Neugebauer,

**Table II. Summary of the Characteristics of Unannealed (Cd,Zn)Te Substrates and of the Corresponding LPE (Hg,Cd)Te Films Grown on Them**

| (Cd,Zn)Te Substrate Characteristics |               |                        |                      |  |         |                      | (Hg,Cd)Te Film Characteristics              |                   |  |                                  |  |
|-------------------------------------|---------------|------------------------|----------------------|--|---------|----------------------|---|-------------------|--|----------------------------------|--|
| Substr. ID                          | 300K Trans. % | Avg. DCRC FWHM (arc-s) | EPD $\text{cm}^{-2}$ | Te Precipitate, Size ( $\mu\text{m}$ ), Shape & Density ( $\text{cm}^{-2}$ ) | Film ID | Thick. $\mu\text{m}$ | $\lambda_{\text{co}}$ $\mu\text{m}$ (300 K) | DCRC FWHM (arc-s) | Precipitates In Substr./ Film Cross Sec. | 77K Carr. Conc. $\text{cm}^{-3}$ | 77K Carr. Mob. $\text{cm}^2/\text{Vs}$ |
| 5971-4                              | 56-62         | 33-50                  | $10^5$               | <10, Stars, $10^4$   | 945     | 18                   | 7.8   | 107               | Yes                                      | $3 \times 10^{14}$ n-type        | $2 \times 10^5$                        |
| 5891-15                             | 27-60         | 13-17                  | $3 \times 10^4$      | 20-65 Triangles & Hex. $2 \times 10^4$                                       | 949     | 20                   | 7.2   | 80                | Yes                                      | $8 \times 10^{14}$ n-type        | $1.5 \times 10^5$                      |

**Table III. Summary of the Characteristics of Annealed (Cd,Zn)Te Substrates Before and After Annealing and of the Corresponding LPE (Hg,Cd)Te Films Grown on Them**

| (Cd,Zn)Te Substrate Characteristics |               |                        |                      |  |         |                      | (Hg,Cd)Te Film Characteristics              |                   |  |                                  |  |
|-------------------------------------|---------------|------------------------|----------------------|--|---------|----------------------|---|-------------------|--|----------------------------------|--|
| Substr. ID                          | 300K Trans. % | Avg. DCRC FWHM (arc-s) | EPD $\text{cm}^{-2}$ | Te Precipitate, Size ( $\mu\text{m}$ ), Shape & Density ( $\text{cm}^{-2}$ ) | Film ID | Thick. $\mu\text{m}$ | $\lambda_{\text{co}}$ $\mu\text{m}$ (300 K) | DCRC FWHM (arc-s) | Precipitates In Substr./ Film Cross Sec. | 77K Carr. Conc. $\text{cm}^{-3}$ | 77K Carr. Mob. $\text{cm}^2/\text{Vs}$ |
| 5968-5A                             | 58-64         | 21-63                  | $2 \times 10^5$      | 30-190 Stars, Clouds $3 \times 10^4$   | 962     | 24                   | 7.7   | 125               | No                                       | $2 \times 10^{14}$               | $1.4 \times 10^5$                      |
| 5971-8C                             | —             | —                      | $1.5 \times 10^5$    | 1-6 Pep. $2 \times 10^5$   | 963     | 23                   | 7.5   | 115               | No                                       | $6 \times 10^{14}$               | $1.5 \times 10^5$                      |

Note: \*Before anneal; almost none after anneal. †Before anneal; none after anneal.



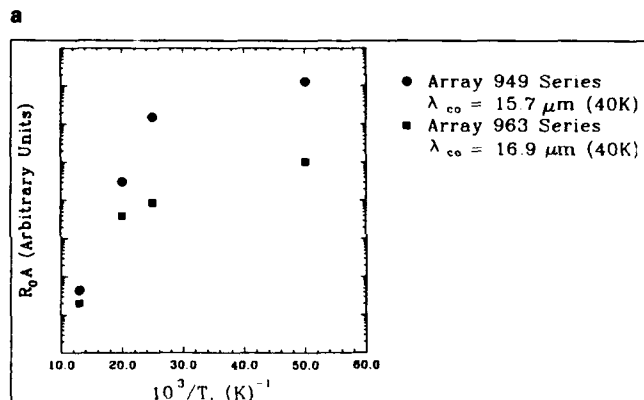
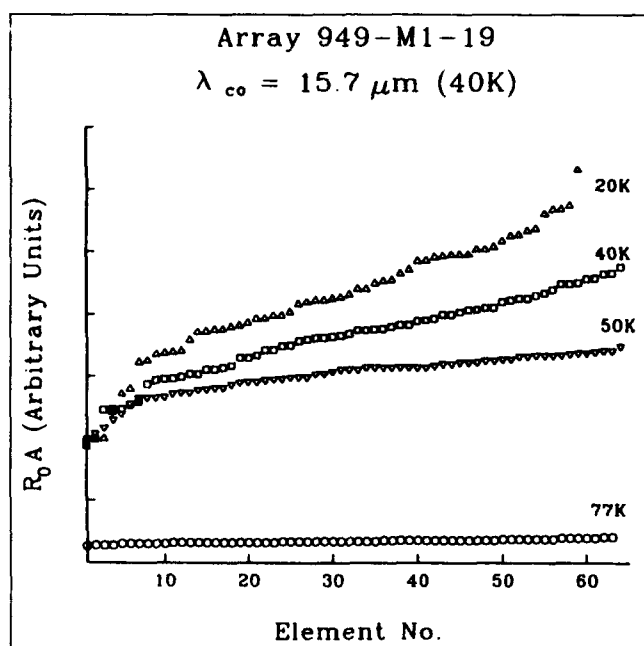


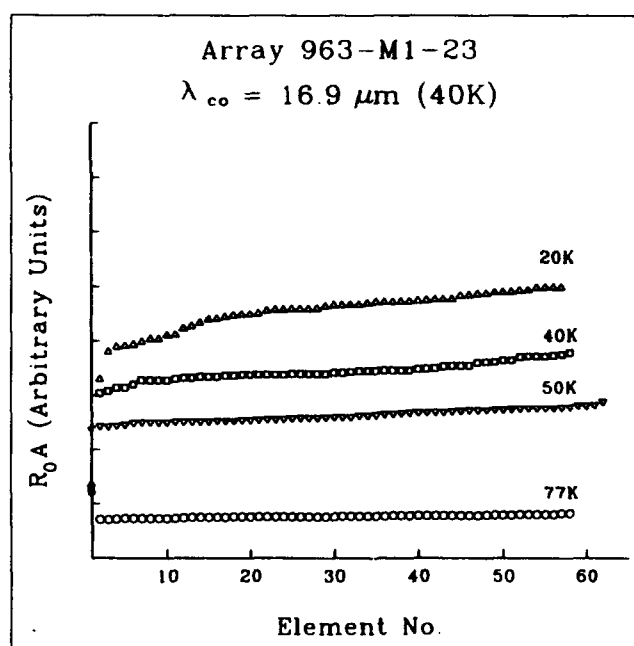
Fig. 9. Demonstration of improved  $R_0A$  performance uniformity in LWIR photodiodes fabricated in Te precipitate free (Hg,Cd)Te epitaxial layers grown on annealed (Cd,Zn)Te substrates (a)  $R_0A$  performance (arbitrary scale) ranking data for array 949-M1-19 fabricated in (Hg,Cd)Te layer grown on an unannealed (Cd,Zn)Te substrate II-VI 5891-15 with  $3 \times 10^4 \text{ cm}^{-2}$  Te precipitates; (b)  $R_0A$  performance (arbitrary scale) ranking data for array 963-M1-23 fabricated in (Hg,Cd)Te layer grown on an annealed (Cd,Zn)Te substrate II-VI 5971-8C containing  $10^5 \text{ cm}^{-2}$  Te precipitates before anneal and none after the anneal. (Fig. 7 and Table II); and (c)  $R_0A$  performance (arbitrary scale) for arrays 949 series and 963 series as a function of temperature.

and J. Sepich) gratefully acknowledge the support of the U. S. Army CECOM Night Vision and ElectroOptics Directorate on SBIR Contract No. DAAB07-91-C-K753.

## APPENDIX A

### Estimates of Temperature-Gradients in (Cd,Zn)Te Substrates and Epitaxial (Hg,Cd)Te During LPE Growth

The band gap of both LWIR and MWIR (Hg,Cd)Te around  $500^\circ\text{C}$ , the temperature of LPE growth, is near 0.3–0.4 eV and, therefore, absorption occurs at



wavelengths out to about 3 to 4  $\mu\text{m}$ , which represents about 15% to 30% of the blackbody-spectrum energy. Also, since the thermal energy at  $500^\circ\text{C}$  (of 0.067 eV) is already around 20% of the band gap energies, strong plasma absorption will occur at all wavelengths in the (Hg,Cd)Te layers while it does not, in the hot (Cd,Zn)Te substrates with a much higher band gap of about 1.3 eV. With the one-dimensional thermal-conduction equation,

$$\frac{dT}{dx} \approx \frac{q}{k} (A-1)$$

the (Cd,Zn)Te LW absorption will be on the order of  $10^{-2} \text{ W/cm}^2$  which with  $K \approx 0.02 \text{ W/cm}^\circ\text{K}$ , implies a temperature gradient only of the order of  $0.5^\circ\text{C/cm}$ .

However, as soon as there is a layer of (Hg,Cd)Te on the surface of (Cd,Zn)Te, a major change takes place. The blackbody power density near the growth temperature of  $500^\circ\text{C}$  is around  $2 \text{ W/cm}^2$ , while the thermal conductivity of hot LWIR (Hg,Cd)Te is closer to  $k \approx 0.01 \text{ W/cm}^\circ\text{K}$ . Allowing for  $\geq 22\%$  surface reflectance, a thermal gradient of the order of  $150^\circ\text{C/cm}$  in the (Hg,Cd)Te epitaxial layer and of the order of  $75^\circ\text{C/cm}$  in (Cd,Zn)Te substrates is implied.

As heating progresses, the gradients will be progressively reduced by thermal diffusion, but equation A-1 will govern the initial stage of heating, which represents the worst-case thermal gradient.

## REFERENCES

1. H.R. Vydyanath, J.A. Ellsworth, J.J. Kennedy, B. Dear, C.J. Johnson, G.T. Neugebauer, J. Sepich and P.K. Liao, *J. Vac. Sci. Tech. B* 10, 1476 (1992).
2. P.M. Hansen, *Constitution of Binary Alloys*, McGraw-Hill, NY (1958) p. 444.
3. J.J. Kennedy (unpublished research).
4. T.R. Anthony and H.E. Cline, *J. Appl. Phys.* 42, 3380 (1971).
5. T.R. Anthony and H.E. Cline, *J. Appl. Phys.* 43, 2473 (1972).

# Evidence for $1/f$ Noise in Diffusion Current Due to Insulator Trapping and Surface Recombination Velocity Fluctuations

R.A. SCHIEBEL, D. BLANKS, D. BARTHOLOMEW, and M.A. KINCH

Central Research Laboratories, Texas Instruments Inc., Dallas TX 75265

In this paper, we present evidence for  $1/f$  noise in diode diffusion current due to fluctuations in surface recombination velocity caused by insulator trapping. Using a unique structure consisting of a thin HgCdTe film with a pn junction on one side and an insulated gate on the other, we demonstrate that the noise measured in the junction is a strong function of the surface potential on the opposite side of the film. We compare the results to model predictions, finding good qualitative agreement.

**Key words:** Device modeling, HgCdTe, insulator trapping,  $1/f$  noise

## INTRODUCTION

Low frequency  $1/f$  noise is often a limiting factor in the performance of long wavelength focal plane arrays. An understanding of its origins is hence essential to intelligent development of low noise processes and device designs. This topic has been addressed several times over the last 15 years.<sup>1-11</sup> The  $1/f$  noise has been attributed to diffusion,<sup>3,7,9</sup> depletion region generation-recombination,<sup>1,3-7</sup> or tunneling<sup>2,4,8,10</sup> currents, and unknown causes.<sup>8,11</sup> Semi-empirical models have been proposed that relate the noise to mobility fluctuations in diffusion or depletion generation-recombination current,<sup>12</sup> and insulator trap occupancy fluctuations in surface tunneling current.<sup>2</sup>

To date, no work has examined the possibility of  $1/f$  noise in diffusion current arising from fluctuations in surface recombination velocity due to insulator trapping. This is surprising, since insulator trapping is a well-accepted phenomena affecting the surface potential and surface recombination velocity, and the relation between diffusion current and surface recombination velocity is discussed in most basic device physics textbooks.

In this and a companion work,<sup>13</sup> we propose that  $1/f$  noise in diffusion current may be caused by fluctuations in the surface recombination velocity resulting from insulator trapping. This should be a particularly important mechanism for diffusion limited de-

vices, particularly those with long diffusion lengths where noise-producing surfaces are effectively closer to devices. Since this model is based on diffusion current, it offers an alternative explanation to those models based on mobility fluctuations.<sup>12</sup>

In this paper, we present evidence for the existence of this noise mechanism, accompanied by modeling results. To do so, we use results obtained with a unique back gated diode structure, illustrated in Fig. 1 (and discussed at length below). In a companion paper,<sup>13</sup> we develop the theory for this model.

## THEORETICAL BASIS

The basic physical phenomena may be simply described: Virtually all insulators have traps with long time constants. The charging and discharging of these traps produces surface potential fluctuations at that surface. If the insulator traps are distributed uniformly in energy and space, McWhorter<sup>16</sup> showed that the power spectral density of these fluctuations has a  $1/f$  spectrum.

Surface recombination may be due to a variety of physical processes, the most common being fast surface states and mid band gap states in inversion or depletion layers. In either of these cases, the surface recombination rate depends on surface potential. In the case of fast surface states, the surface potential determines the occupancy of these states. In the case of inversion layers, the surface potential determines the occupancy of mid band gap states, as well as which combinations of thermal and tunneling processes are

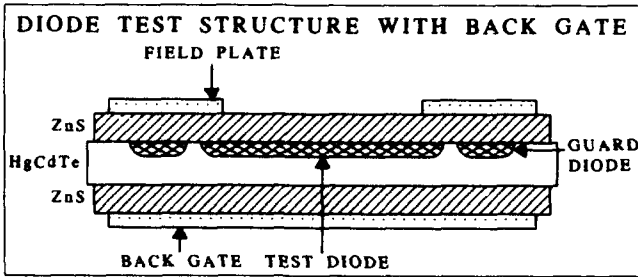


Fig. 1. Cross section of a test diode on thinned HgCdTe with a back gate.

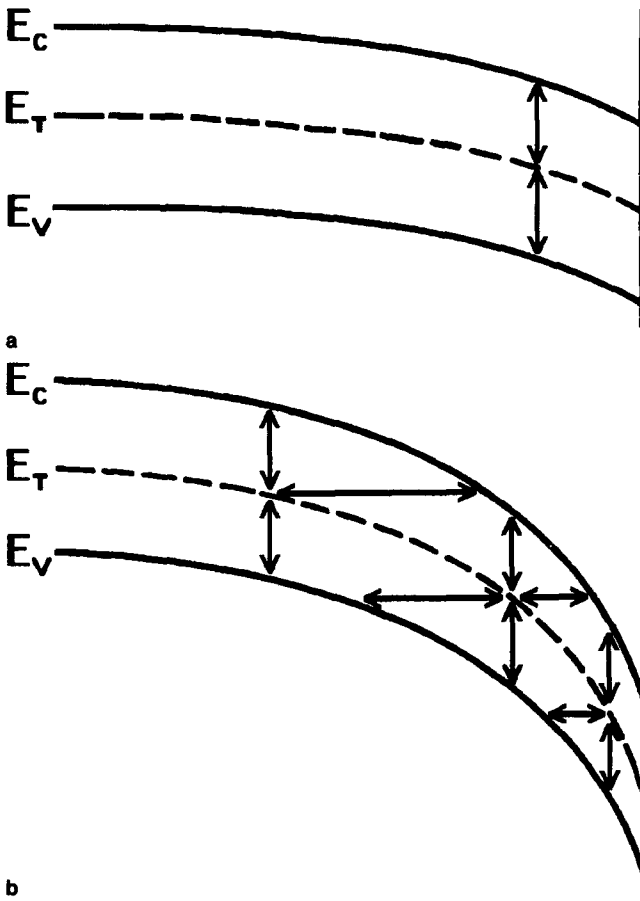


Fig. 2. Surface recombination processes possible via mid band gap states for (a) a weakly inverted surface, and (b) a strongly inverted surface. For the small band bending illustrated in (a), only thermal processes are possible. For the greater band bending illustrated in (b), all combinations of thermal processes with tunneling transitions to the conduction and/or valence band are possible.

possible. This latter case is illustrated in Fig. 2.

Finally, the diffusion current in a pn junction with dimensions less than a diffusion length depends strongly on the surface recombination velocity. Hence, fluctuations in insulator trap occupancy produce surface potential fluctuations, which in turn modulate the surface recombination velocity and ultimately produce noise in the diffusion current.

Expressing mathematically the preceding arguments regarding diode diffusion current  $I$ , surface recombination velocity  $s$ , surface potential  $\psi_s$ , and insulator traps  $N_{IT}$ , we obtain the following for the

diode diffusion current noise spectral density  $S_I$

$$S_I = \left( \frac{\partial I}{\partial s} \right)^2 \left( \frac{\partial s}{\partial \psi_s} \right)^2 \left( \frac{\partial \psi_s}{\partial N_{IT}} \right)^2 S_{N_{IT}} \quad (1)$$

where  $S_{N_{IT}}$  is the insulator trap noise spectral density. The above forms the basis for obtaining a mathematical expression for  $S_I$ .

It is clear that we must first develop a relation for the diode diffusion current as a function of surface recombination velocity, develop a theory for surface recombination velocity as a function of surface potential, and only then proceed to developing the relation for diffusion current noise spectral density. This is done in a companion paper.<sup>13</sup>

Much of the groundwork for developing this expression is well established. Diffusion current for a thin-base diode is described in numerous device physics texts;<sup>14</sup> the relation between diffusion current and surface recombination velocity is analytic.

The calculation of surface recombination velocity for an inversion layer (or fast surface states) has also been derived for the case of trap assisted tunneling through mid band gap states, resulting in an integral expression.<sup>15</sup> The relation between surface potential and fixed charge density is available from simple MOS theory. Finally, the insulator trap noise spectral density,  $S_{N_{IT}}$ , is obtained from McWhorter's original insulator trapping model<sup>16</sup> (subsequently developed by Hsu<sup>17</sup> and Anderson and Hoffman<sup>2</sup>) and is given by

$$S_{N_{IT}} = \frac{N_T A}{f} \quad (2)$$

where  $A$  is the device area,  $f$  is the frequency, and  $N_T$  is the effective density of insulator traps per unit area, defined by

$$N_T = \frac{k T N_T(E)}{\kappa}, \quad (3)$$

where  $k$  is Boltzmann's constant,  $T$  is the device temperature,  $N_T(E)$  is the volume density of insulator traps per energy, and  $\kappa$  is the characteristic decay rate (per unit distance) of the electron or hole wavefunction into the insulator.

Inspection of Eqs. 1 and 2 shows that the diode current noise spectral density  $S_I$  (in units of  $A^2/Hz$ ) is proportional to the device area. Hence, the diode noise current  $i_n$  (the square root of the diode current noise spectral density) should be normalized to the square root of the area. Hereafter, we will refer to the 1 Hz diode noise current value, divided by *root area*, as the *noise figure*, with units  $A/(cm \cdot Hz^{1/2})$ .

The details of these calculations, as well as a discussion of the model's predictions, are discussed elsewhere.<sup>13</sup> We concentrate in this work on the results that are relevant to the back gated structure discussed below.

To obtain a manageable expression for the noise current due to a depletion or inversion layer, we assume a thin p-type base of thickness  $d$  and minority carrier diffusion length  $L$  such that  $d \ll L$  and that thermal transitions dominate in the inversion/deple-

tion layer. This is probably a reasonable assumption, since the variable temperature noise data gives a substantial activation energy for the measured noise, indicating that thermal processes are dominant.

The noise current is then given by<sup>13</sup>

$$i_n = \frac{qn_i^2}{\tau_p(n_s + n_i) + \tau_h(p_s + p_i)} \frac{1}{E(\psi_s)(C_{ins} + C_{sc})} \left[ \frac{N_T A}{f} \right]^{1/2} \quad (4)$$

where  $q$  is the electron charge,  $n_i$  is the intrinsic carrier concentration,  $n_s$  is the surface electron concentration,  $p_s$  is the surface hole concentration,  $E(\psi_s)$  is the surface electric field,  $\psi_s$  is the surface potential,  $C_{ins}$  is the insulator capacitance per unit area, and  $C_{sc}$  is the semiconductor capacitance per unit area.

The remaining symbols are familiar from Shockley-Read-Hall recombination theory:<sup>18</sup>  $n_i$  is the electron concentration with the Fermi level at the trap level, given by  $N_C \exp(-E_{CT}/kT)$ , where  $N_C$  is the conduction band density of states and  $E_{CT}$  is the energy difference between the conduction band edge and trap level.  $p_i$  is the hole concentration with the Fermi level at the trap level, given by  $N_V \exp(-E_{TV}/kT)$ , where  $N_V$  is the valence band density of states and  $E_{TV}$  is the energy difference between the trap level and the valence band edge.  $\tau_n = 1/\gamma_C N_{GT}$  and  $\tau_p = 1/\gamma_V N_{GT}$ , where  $\gamma_C$  is the electron capture coefficient,  $\gamma_V$  is the hole capture coefficient, and  $N_{GT}$  is the mid band gap trap density.

Equation 4 peaks for intermediate values of surface potential (or fixed charge density), and is dominated in this range by either  $n_i$  or  $p_i$ , depending on the relative values of  $\gamma_V$  and  $\gamma_C$ . For  $n_{iV} \ll p_{iV}$

$$i_n = \frac{qN_{GT}n_i}{E(\psi_s)} \frac{q}{(C_{ins} + C_{sc})} \left[ \frac{N_T A}{f} \right]^{1/2} \quad (5)$$

and for  $n_{iV} \gg p_{iV}$

$$i_n = \frac{qN_{GT}p_i}{E(\psi_s)} \frac{q}{(C_{ins} + C_{sc})} \left[ \frac{N_T A}{f} \right]^{1/2} \quad (6)$$

Figure 3 shows the calculated dark current and noise figure vs backside fixed charge density, assuming a trap at exactly half the band gap, with backside fixed charge as a variable. Figure 4 shows, in more detail, the calculated noise figure vs fixed charge density, including the limiting cases discussed above.

The results of Figs. 3 and 4 may be understood in purely qualitative terms without regard to the mathematical details of this model. As the back side fixed charge density (or equivalently the back side surface potential) is increased, the amount of recombination at the back surface also increases until strong inversion is reached. The dark current follows the increase in surface recombination; a step increase in dark current is observed as the backside condition changes from flatband to strong inversion.

At sufficiently high fixed charge densities, tunneling processes via mid band gap states become possible

and add to the surface recombination, giving rise to additional steps in the dark current. The sensitivity of the dark current to back side surface potential is discussed at greater length in Refs. 13 and 15.

The noise, in contrast, is proportional to the *derivative* of the diffusion current with respect to back side surface potential,  $\partial I/\partial \psi_s$  (in accordance with Eq. 1) and peaks where this slope is highest, in some instances picking out the onset of tunneling processes. Referring to Fig. 2, it is clear that several recombination processes are possible; the process responsible for the most generation-recombination (most diffusion current) is not necessarily the process that is most sensitive to surface potential (most 1/f noise). This issue is discussed at greater length in Ref. 13.

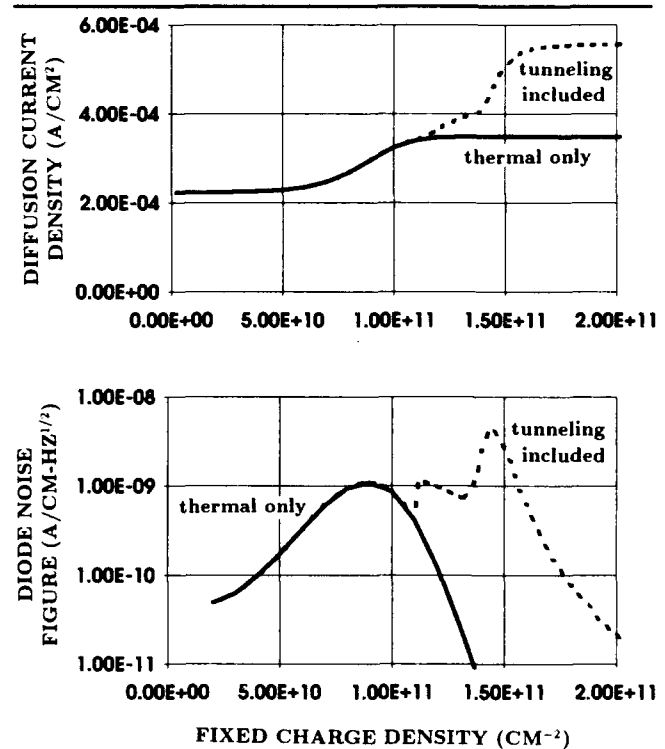


Fig. 3. Calculated diffusion current density and noise figure vs backside fixed charge density.  $E_{CT} = E_{TV} = 62.5$  mV,  $\gamma_C = 10^{-8}$  cm³/s,  $\gamma_V = 10^{-7}$  cm³/s,  $N_T(E)/\kappa = 2 \times 10^9$  cm²/eV,  $N_{GT} = 10^{16}$  cm<sup>-3</sup>,  $N_A = 10^{16}$  cm<sup>-3</sup>,  $\lambda_c = 9.92$   $\mu$ m,  $T = 77$ K, p-side thickness = 5  $\mu$ m.

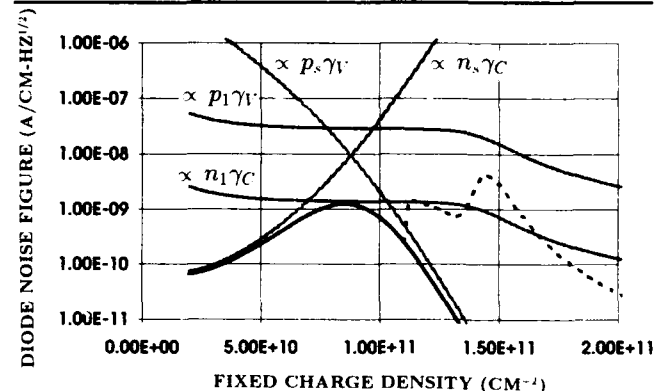


Fig. 4. Calculated noise figure vs backside fixed charge density, showing limiting cases. Same parameters as Fig. 3.

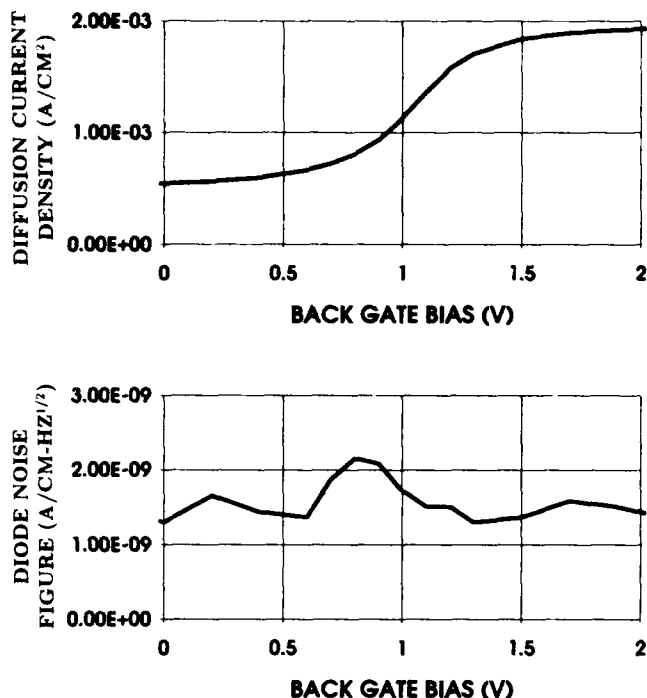


Fig. 5. Diffusion current and noise figure vs back gate bias.  $T = 80\text{K}$ . Dimensions:  $5 \times 6 \text{ mil}^2$ .

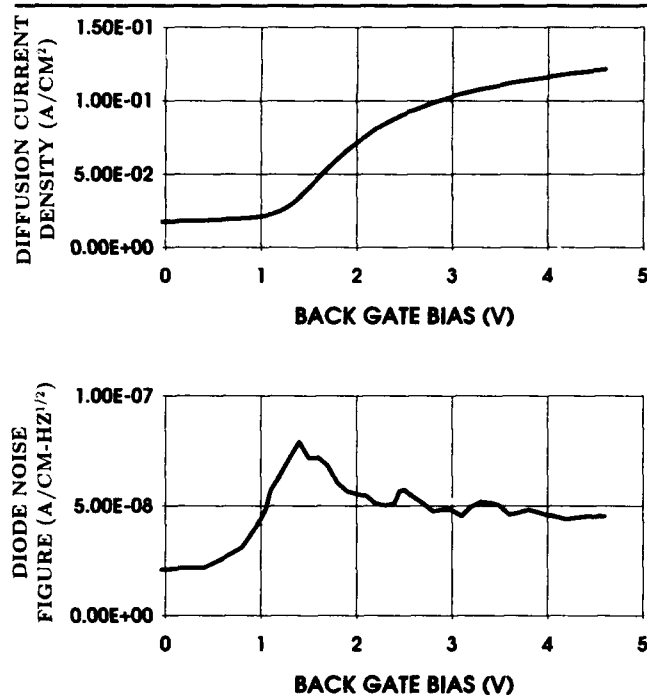


Fig. 6. Diffusion current and noise figure vs back gate bias.  $T = 115\text{K}$ . Dimensions:  $5 \times 6 \text{ mil}^2$ .

## EXPERIMENTAL

To demonstrate the existence of this noise mechanism, we constructed a unique back-gated structure, shown in Fig. 1, on thinned (about  $10 \mu\text{m}$  thick) p-type low phase epitaxy HgCdTe, with a Hg vacancy concentration of approximately  $8 \times 10^{15} \text{ cm}^{-3}$  and a  $9.8 \mu\text{m}$  cutoff wavelength at  $77\text{K}$ , corresponding to a  $77\text{K}$  band gap of  $126 \text{ meV}$ . On the frontside, test diodes

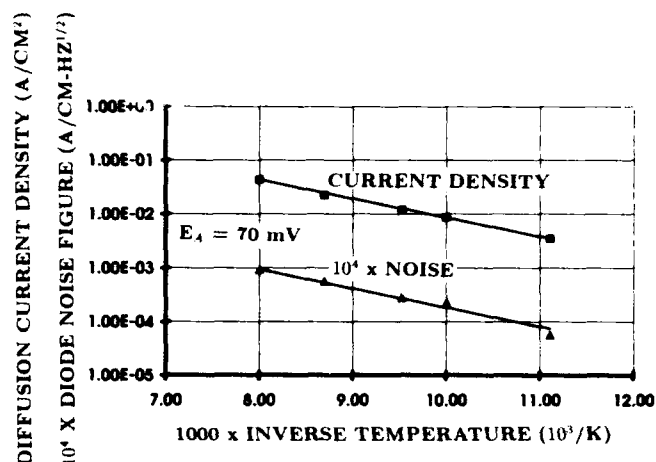


Fig. 7. Temperature dependence of noise figure and diffusion current for the device of Fig. 6.

with guard diodes were formed by ion implantation; on the backside, a MIS gate was fabricated using  $3500\text{\AA}$  ZnS as insulator. By adjusting the potential on this back gate, we are able to adjust the surface potential at the back surface and are thereby able to adjust the surface recombination rate at this back surface as well.

Figure 5 shows the dark current and noise figure vs backgate bias at  $80\text{K}$ . Clearly, a step in the dark current is observed as the backside is inverted, as predicted by the dark current model presented by Omaggio.<sup>15</sup> A less dramatic effect is observed in  $1/f$  noise. Nonetheless, a peak is observed in  $1/f$  noise as the backside surface potential is swept.

Subsequent testing showed that the  $1/f$  noise on either side of the peak had a strong dependence on diode bias, suggesting that noise mechanisms in the pn junction, such as depletion region generation-recombination or surface tunneling, dominate to obscure the effects of the back gate. To more clearly observe diffusion limited  $1/f$  noise, we made measurements at higher temperatures where these mechanisms are less significant.

Figure 6 shows the results of measurements taken at  $115\text{K}$ . The  $1/f$  noise peaks sharply as the surface potential is increased. Additional structure in the noise scan at higher back gate biases suggests the turn-on of tunneling transitions, in qualitative agreement with the calculations of Fig. 3.

Our last consideration is the thermal dependence of the  $1/f$  noise and the diffusion current. The analysis in the previous section indicates that the main temperature dependence is determined by  $n_1$  or  $p_1$ , so that the activation energy of the noise current reflects the energy difference of the trap from the conduction or valence band, respectively. However, without knowledge of the electron or hole capture coefficient values, it is impossible to distinguish between the two.

Figure 7 shows variable temperature data on the same device as shown in Figs. 5 and 6. The activation energy for the  $1/f$  noise is  $70 \text{ meV}$ ; a similar activation energy is noted for the dark current density. The

agreement in activation energies suggests that the diffusion current is likewise dominated by surface recombination (and not by a bulk lifetime-limiting mechanism) through the same trap. A similar activation energy for 1/f noise and diffusion current is consistent with the model discussed in Ref. 13, although not guaranteed.

### CONCLUSIONS

Low frequency 1/f noise in diode diffusion current may be produced by fluctuations in surface recombination velocity due to insulator trapping. Through use of a unique backgated diode structure, we have demonstrated the existence of this noise mechanism and that the surface potential at surfaces within a diffusion length of a junction directly affects both the noise and diffusion current measured in that junction.

### ACKNOWLEDGMENT

The authors gratefully acknowledge the work of Martha Ohlson in the processing of these devices and Jerry Hoy in their testing.

### REFERENCES

1. S.P. Tobin, S. Iwasa and T.J. Tredwell, *IEEE Trans. Elect. Dev.* ED-27, 43 (1980).

2. W.W. Anderson and H.J. Hoffman, *J. Vac. Sci. Technol.* 1730, A1 (1983).
3. T.G.M. Kleinpenning, *J. Vac. Sci. Technol.* 17, A3 (1985).
4. W.A. Radford and C.E. Jones, *J. Vac. Sci. Technol.* 18, A3 (1985).
5. H.K. Chung, M.A. Rosenberg and P.H. Zimmerman, *J. Vac. Sci. Technol.* 189, A3 (1985).
6. J. Bajaj, G.M. Williams, N.H. Sheng, M. Hinnrichs, D.T. Cheung, J.P. Rode and W.E. Tennant, *J. Vac. Sci. Technol.* 192, A3 (1985).
7. A. van der Ziel, P.H. Handel, X.L. Wu and J.B. Anderson, *J. Vac. Sci. Technol.* 2205, A4 (1986).
8. R.E. Dewames, J.G. Pasko, E.S. Yao, A.H.B. Vanderwyck and G.M. Williams, *J. Vac. Sci. Technol.* 2655, A6 (1988).
9. A. van der Ziel, P. Fang, L. He, X.L. Wu, A.D. van Rhee and P.H. Handel, *J. Vac. Sci. Technol.* 550, A7 (1989).
10. Y. Nemirovsky and D. Rosenfeld, *J. Vac. Sci. Technol.* 1159, A8 (1990).
11. J. Bajaj, G.M. Williams, R.E. Dewames and M. Brown, *J. Vac. Sci. Technol.* 1617, B10 (1992).
12. T.G. M. Kleinpenning, *Physica* 289, 98B (1980).
13. R.A. Schiebel, to be published.
14. For example, see M.B. Reine, A.K. Sood and T.J. Tredwell, *Semiconductors and Semimetals* 18, 201, New York: Academic Press (1980).
15. J.P. Omaggio, *IEEE Trans. Elect. Dev.* ED-37, 141 (1990).
16. A.L. McWhorter, *Semicond. Surf. Phys.* p. 207, University of Pennsylvania Press, Philadelphia (1957).
17. S.T. Hsu, *Solid-State Electron.* 1451, 13 (1970).
18. W.T. Shockley and W.T. Read, Jr., *Phys. Rev.* 835, 87 (1952).

# Properties of InAs/(Ga,In)Sb Strained Layer Superlattices Grown on the {111} Orientations

J.A. DURA, J.T. ZBOROWSKI, and T.D. GOLDING

Department of Physics and Space Vacuum Epitaxy Center, University of Houston, Houston, TX 77204

D. DONNELLY and W. COVINGTON

Department of Physics, Sam Houston State University, Huntsville, TX 77341

Following the proposal of the extreme type-II InAs/(Ga,In)Sb strained layer superlattice system by Mailhot and Smith in 1987 for long wavelength infrared detection, a number of groups have experimentally investigated (100) oriented InAs/(Ga,In)Sb strained layer superlattices and demonstrated that these structures can possess energy gaps in the 8–12  $\mu\text{m}$  range with absorption coefficients comparable to HgCdTe. However, a number of advantages are predicted if these structures are grown on the {111} orientations. In this paper, we present details of our investigation of the growth of InAs/GaSb heterostructures and InAs/(Ga,In)Sb strained layer superlattices on the (111)A and (111)B orientations by molecular beam epitaxy, compared to growth on the (100) orientation. Heterojunction growth and incorporation rates of Sb (As) into InAs (GaSb) on (111)A, (111)B, and (100) orientations have been assessed and implications for growth and optical properties of InAs/(Ga,In)Sb strained layer superlattices are discussed. GaSb/InAs and InAs/GaSb interfaces on the (111)B orientation are investigated by x-ray photoelectron spectroscopy, and the structural quality of InAs/(Ga,In)Sb strained layer superlattices are investigated by x-ray diffraction.

**Key words:** InAs/GaInSb strained-layer superlattices, MBE, x-ray photoelectron spectroscopy, x-ray diffraction

## INTRODUCTION

InAs/Ga<sub>1-x</sub>In<sub>x</sub>Sb superlattices have been proposed for infrared detector applications in the 8–14  $\mu\text{m}$  range<sup>1,2</sup> and beyond. The motivation to investigate the system is that it may enjoy a number of advantages over bulk Hg<sub>1-x</sub>Cd<sub>x</sub>Te, that include lower leakage current due to suppression of tunneling (larger effective mass), lower Auger recombination rates,<sup>3</sup> and III-V device fabrication and materials processing techniques.

The band alignment of the InAs/Ga<sub>1-x</sub>In<sub>x</sub>Sb system is type II, similar to the closely lattice matched InAs/GaSb. However, because electrons tend to be localized in the InAs, and holes in the GaSb, there is a rapid decrease in the optical absorption coefficient with increasing layer thickness. For InAs/GaSb super-

lattices with band gaps less than 0.1 eV, the absorption coefficients are too small for infrared (IR) detector applications. Mailhot and Smith<sup>2</sup> proposed using internal strain effects to increase the energy separation between the InAs conduction band and Ga<sub>1-x</sub>In<sub>x</sub>Sb heavy hole valence band by adding In to the antimonide layers, enabling small band gaps to be achieved with sufficiently short periods to provide acceptable absorption coefficients. Following the proposal of InAs/Ga<sub>1-x</sub>In<sub>x</sub>Sb strained layer superlattices (SLS) for IR application, a number of groups have reported IR absorption,<sup>4,5</sup> (Fig. 1) and photoresponse<sup>6</sup> in InAs/Ga<sub>1-x</sub>In<sub>x</sub>Sb SLS structures. All studies to date have been on (100) oriented structures. However, it has been predicted that there are a number of advantages if the structures are grown on the (111) orientation.<sup>7</sup> Because of an increased Ga<sub>1-x</sub>In<sub>x</sub>Sb heavy hole mass along the [111] direction, there is a corresponding reduction in the quantum confinement en-

(Received October 12, 1992; revised January 15, 1993)

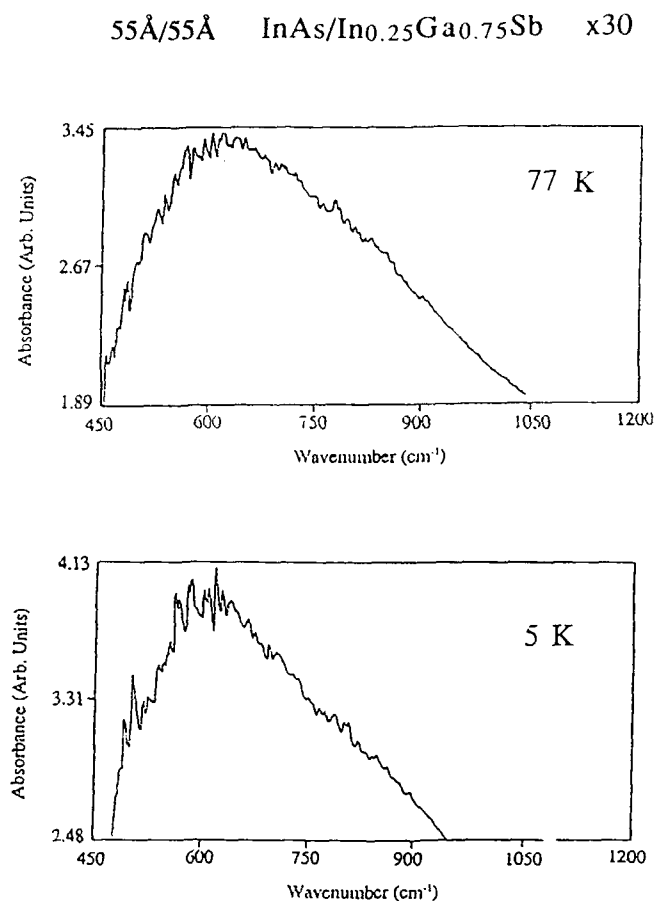


Fig. 1. Fourier transform infrared absorption spectrum for a 30 period nominally grown 55Å/55Å InAs/Ga<sub>0.75</sub>In<sub>0.25</sub>Sb (100) oriented SLS. A shift toward higher wavenumbers with decreasing temperature is observed.

ergy, enabling thinner period structures to be grown with the same cut-off wavelength, resulting in increased absorption coefficients. In addition, strain induced piezoelectric fields can further reduce the superlattice band gap (red shift). This allows additional reductions in the superlattice layer thicknesses for the same band gap adding to the enhanced absorption attainable in the (111) orientations. While this piezoelectric induced red shift is negligible for the shorter period structures corresponding to 8–12  $\mu\text{m}$  operation, it becomes increasingly important as superlattice layer thicknesses increase. An enhancement of the absorption coefficient compared to (100) has been demonstrated in InAs/GaSb superlattices grown by metalorganic chemical vapor deposition.<sup>8</sup> Further, the dependence of the optical properties on interface bonding has been demonstrated in (100) oriented InAs/Ga<sub>1-x</sub>In<sub>x</sub>Sb SLS.<sup>3</sup> Chemical differences in the (111) orientation may enable better control of interface compounds due to the ability to choose a surface which preferentially terminates in group III or group V. The chemical variations are related to the differences in the bond configurations at the respective surfaces. Figure 2 shows that the [111] orientations differ structurally from the (100) in that they are composed of anion and cation layers connected in

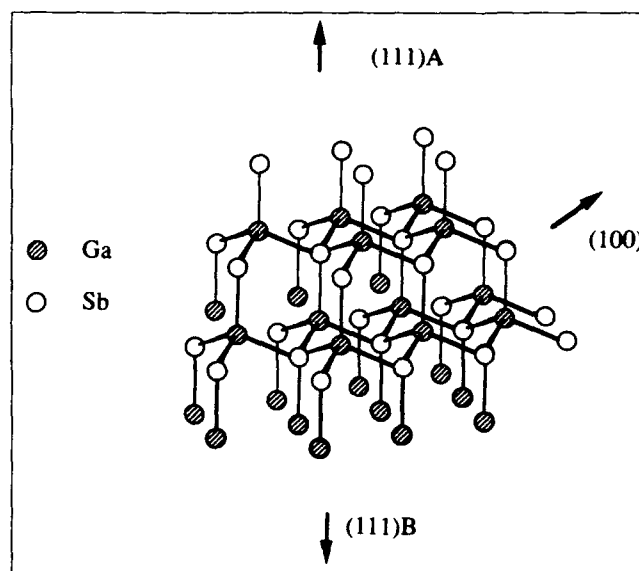


Fig. 2. Zincblende crystal structure of GaSb showing the differences between the structure and bonding of the (111)A, (111)B, and (100) orientations.

close proximity by three bonds per atom, and separated at a larger distance by a single bond per atom perpendicular to the planes. It is energetically favorable for the surface to terminate these structures across the single bond. On the (111)A and (111)B faces, the terminal plane is composed of the group III and group V elements, respectively. This is in contrast to the more symmetric (100) orientation in which the group III and group V planes alternate with equal spacing connected by two bonds per atom. Furthermore, nominally molecular beam epitaxy (MBE) grown (100) oriented GaSb is p-type due to the presence of Ga antisites. Growth on the (111)B orientation may reduce Ga antisite formation by increasing the binding energy of the adsorbed Sb.<sup>9</sup>

In this paper, we report results of our preliminary investigation into the MBE growth and properties of InAs/(Ga,In)Sb SLS grown on [111] oriented GaSb substrates. Additional results are published elsewhere.<sup>10</sup> Our results focus on heterojunction, multilayer, and superlattice growth. Heterojunction growth and incorporation rates of Sb (As) into InAs (GaSb) on (111)A, (111)B, and (100) orientations have been assessed and implications for InAs/Ga<sub>1-x</sub>In<sub>x</sub>Sb SLS are discussed.

## EXPERIMENTAL PROCEDURES

All structures were grown by (MBE) using As<sub>2</sub> (cracker cell), Sb<sub>4</sub>, and liquid-metal Ga and In sources. As<sub>2</sub> was employed due to previous studies of the InAs/(Ga,In)Sb system in the (100) orientation that found that As<sub>4</sub> was incompatible with the growth of high quality epitaxial layers.<sup>11</sup> Growth was monitored in-situ by reflection high energy electron diffraction (RHEED). The substrates were not intentionally doped (p-type) GaSb etched in HCl rinsed in deionized water and indium bonded to molybdenum blocks. Heterostructures for secondary ion mass spectrometry (SIMS)



investigations of cross incorporation rates were grown simultaneously on (100), (111)A, and (111)B substrates. With the cell shutter closed, the As (Sb) background pressure was  $4.0 \times 10^{-7}$  ( $4.5 \times 10^{-9}$ ) Torr and  $1.55 \times 10^{-6}$  ( $1.10 \times 10^{-6}$ ) Torr when open. GaSb and InAs growth rates were 0.6  $\mu\text{m/h}$  and 0.2  $\mu\text{m/h}$ , respectively. Growth temperatures (455°C for the SIMS heterostructures, and 430–470°C for InAs/(Ga,In)Sb superlattices) were measured by an optical pyrometer with an accuracy estimated at  $\pm 10^\circ\text{C}$ . The pyrometer readings were calibrated to the temperature at which the oxide layer is known to desorb from the substrate, 540°C for all orientations. X-ray photoelectron spectroscopy (XPS) and Auger electron spectroscopy (AES) were performed in a chamber vacuum interlocked with the growth chamber. A  $\text{MgK}\alpha$  source and cylindrical mirror analyzer with a resolution of approximately 0.1 eV was employed. Secondary ion mass spectrometry depth profiles were taken using a Cameca ims 5f using a  $\text{Cs}^+$  primary. The In+Cs and As+Cs (Ga+Cs and Sb+Cs) yields were normalized to  $10^5$  counts in the InAs (GaSb) regions of the heterostructure. X-ray diffraction scans were taken with a Siemens D5000 diffractometer using  $\text{CuK}\alpha$  radiation and equipped with a graphite analyzer crystal.

## RESULTS AND DISCUSSION

For MBE growth of mixed group V systems, cross incorporation of the group V elements can be problematic, and is particularly significant to the InAs/(Ga,In)Sb superlattice system. Unintentional As (Sb) incorporation in  $\text{Ga}_{1-x}\text{In}_x\text{Sb}$  (InAs) layers decreases the strain in the superlattice. While this can be compensated by increased In in the (Ga,In)Sb layers, a more critical effect is that cross incorporation also reduces the extreme type-II band alignment, seriously compromising absorption coefficients. Furthermore, superlattice/substrate lattice matching requires careful characterization of cross-incorporation rates to fully account for their effect on the lattice constant of each superlattice layer. Efforts to minimize cross incorporation are, therefore, critical to attaining acceptable optical properties in these structures.

The simultaneous growth of heterostructures on the (100), (111)A, and (111)B orientations permits direct comparison of the relative incorporation rates of the unintended group V element into the epilayers under identical growth conditions. The structures grown were nominally: 0.3  $\mu\text{m}$  GaSb/0.3  $\mu\text{m}$  InAs/0.5  $\mu\text{m}$  GaSb buffer layer on GaSb substrates. Secondary ion mass spectroscopy was used to provide a direct measure of elemental composition. The SIMS depth profile across the upper interface of each heterostructure is shown in Fig. 3, and the results are summarized in Table I.

We find the relative rates of incorporation of As into GaSb in the (111)A, (111)B, and (100) orientations to be 3.0:1.0:2.0. The surface most likely to be Ga terminated incorporates the most As, while the surface with the greatest tendency toward Sb termination

incorporates the least. It is noteworthy, however, that the incorporation of As<sub>2</sub> into the GaSb structures scales with the number of Ga back bonds per atom.

Similarly, we find that the relative rates of incorporation of Sb into InAs in the (111)A, (111)B, and (100) orientations are 3.0:1.0:0.85, or roughly 3:1:1. Thus, for the incorporation of Sb from the tetramer,  $\text{Sb}_4$ , the relative incorporation rates into the (100) surface drops in comparison to dimer,  $\text{As}_2$ , incorporation, by a factor of two. This may be explained by the fact that tetramer incorporation requires the presence of two adjacent pairs of group V sites. The probability of incorporation is proportional to the number of available sites. The (100) surface has a lower coordination number than (111). Given a pair of group V sites, there are only two possible adjacent pairs, compared to four possible pair sites on the (111) surfaces. This would explain the decrease in the tetramer incorporation onto the (100) surface by a factor of two compared to dimer incorporation. Taking into account lower order effects, there are four additional pair sites on the (111) surface which are adjacent to only one of the sites in the original pair. These, however may contribute to the further relative enhancement of dimer incorporation on the [111] surfaces relative to the (100), reflected in the fact that the dimer incorporation ratio is 3:1:0.85 rather than 3:1:1.

Because of the change of both anion and cation across the InAs/(Ga,In)Sb interface, two possible compounds (InSb and GaAs) can be formed. The compound type has been shown to play a critical role in the optical properties of InAs/(Ga,In)Sb SLS.<sup>12</sup> Transport

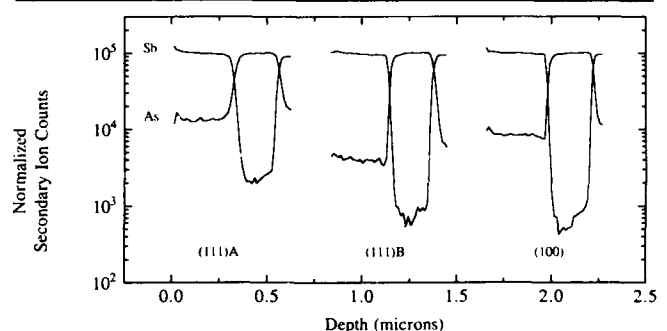
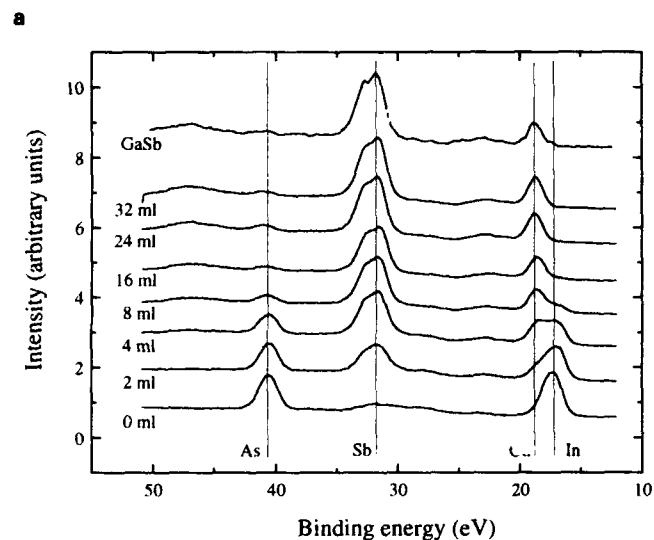
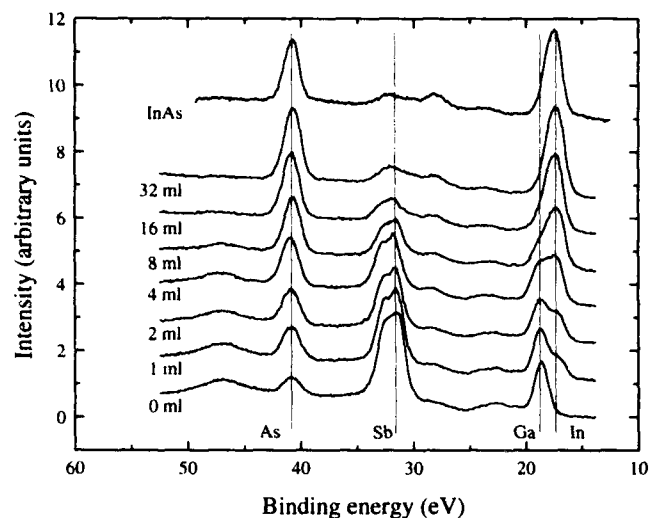


Fig. 3. Secondary ions mass spectroscopy depth profiles of nominal 3000Å/3000Å/buffer GaSb/InAs/GaSb heterostructures. The As and Sb normalized secondary ion counts are shown for GaSb/InAs interfaces. The interfaces shown from left to right are for (111)A, (111)B, and (100) orientations.

Table I. Cross Incorporation Compositions in InAs/GaSb Heterostructures

|                                | x(111)A              | x(111)B              | x(100)               |
|--------------------------------|----------------------|----------------------|----------------------|
| $\text{GaSb}_{1-x}\text{As}_x$ | 0.118<br>$\pm 0.005$ | 0.040<br>$\pm 0.002$ | 0.078<br>$\pm 0.002$ |
| $\text{InAs}_{1-x}\text{Sb}_x$ | 0.024<br>$\pm 0.004$ | 0.008<br>$\pm 0.002$ | 0.007<br>$\pm 0.002$ |

Note: Composition of epitaxial layers grown on the (111)A, (111)B, and (100) orientations as determined by SIMS.



**Fig. 4.** X-ray photoelectron spectroscopy spectra of epilayers of (a) InAs on GaSb and (b) GaSb on InAs, grown in the (111)B orientation with nominal thicknesses in the range of 1 to 32 monolayers. Also shown, to indicate the spectra from pure compounds, are data from thick films of InAs and GaSb in (a) and (b), respectively.

studies on the related AlSb/InAs system also indicate distinct differences in carrier mobility and lifetime broadening between structures grown to induce different interface compounds.<sup>13</sup> It is also desirable that heterostructures be grown without the formation of extended compounds which could act as recombination and scattering sites. To examine the (111) interfaces for extended compound formation, we investigated XPS extinction curves of both InAs on GaSb and GaSb on InAs on the (111)B orientation. This orientation was studied first to further investigate x-ray diffraction results which indicated lower structural quality of superlattices grown on the (111)B orientation compared with (111)A. By inversion symmetry, InAs on GaSb (111)B has the same epitaxial relationship as GaSb on InAs (111)A; therefore, we have probed both *solid state* reaction configurations. However, growth is a nonequilibrium process and for a full

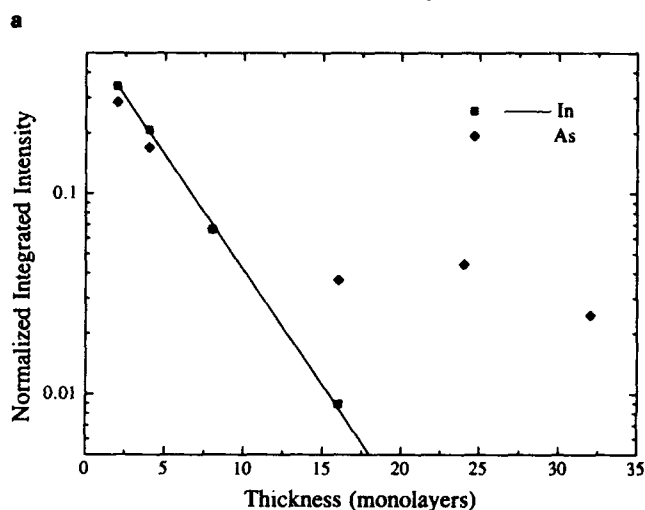
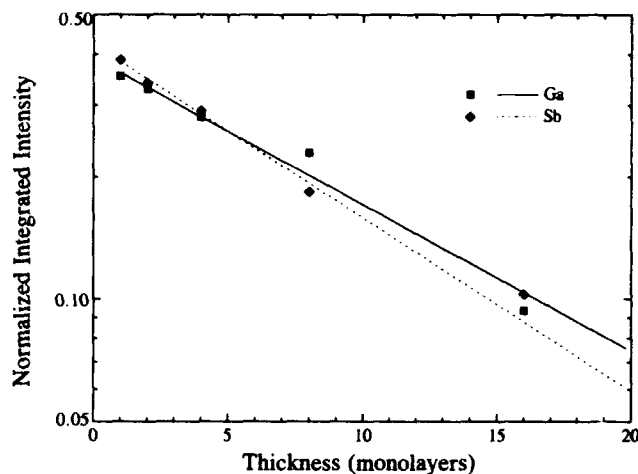


**Fig. 5.** X-ray photoelectron spectroscopy extinction curves of (a) Ga and Sb, and (b) In and As signals from the data shown in Fig. 4.

investigation of compound formation, in MBE grown materials, measurements of both overlayer types on the (111)A surface need to be performed. Work on the (111)A interfaces are in progress.

Details of the technique used in producing XPS extinction curves can be found elsewhere.<sup>14</sup> X-ray photoelectron spectroscopy spectra with binding energy ranging from 10 to 50 eV were taken immediately after growth of overlayers of InAs on GaSb (Fig. 4a) and GaSb on InAs (Fig. 4b). Peaks representing each element are fit to a mixture of Gaussian and Lorentzian peak shapes, taking into account backgrounds due to overlapping features and peaks from other elements. As a baseline, indicative of the spectra of the pure compounds, the spectra from thick films of InAs and GaSb are shown at the tops of Fig. 4a and 4b, respectively. The integrated intensities (II) of the fitted peaks are normalized by the sum of the II for a given scan, yielding the normalized integrated intensities (NII) plotted in Fig. 5a and 5b. Given a sharp interface the NII from the buried layer should decay exponentially with increased thickness of the overlayer. As shown in Fig. 5b, we find this to be the case for GaSb over InAs. The deviation from the linear

relation in the As signal at thicker overlayers of GaSb on InAs was caused by a measurable incorporation of As into the GaSb. When the thickness of the GaSb overlayer was enough to cause the As signal from the underlying InAs to decay to the point at which it equaled the level of As in the GaSb, the As signal leveled off to this constant amount. From the XPS results, we note that the As incorporation was roughly 6% which agrees qualitatively with the SIMS data taken on a sample grown under slightly different conditions. The Sb signal was also seen to deviate from an exponential decay at a 32 monolayer InAs coverage to a value which would correspond to 6% Sb incorporation (see Fig. 5a). This is much larger than measured in the SIMS data and is believed to be due to a monolayer of Sb residing on the surface, as was previously observed in the case of (100) InAs growth.<sup>14</sup> In addition, if compound formation had occurred, the region of mixed composition at the interface would result in a lower slope of the extinction curve in the region of thinner overlayers. This is not seen for either InAs on GaSb (111)B or GaSb on InAs(111)B.

High quality InAs/Ga<sub>1-x</sub>In<sub>x</sub>Sb superlattices on the (111)A orientation have been grown; however, we note that growth on the (111)B orientation has proven more difficult. Figure 6 shows an x-ray diffraction  $\theta$ - $2\theta$  scan near the (111) peak of a 43Å/43Å InAs/Ga<sub>0.9</sub>In<sub>0.1</sub>Sb superlattice grown on the (111)A orientation. The three central peaks, in order of increasing  $2\theta$ , are due to the substrate, the superlattice fundamental, and the buffer layer. The As absorption has shifted the nominally GaSb buffer layer peak to higher  $2\theta$  than that of the pure GaSb substrate. The high number of satellites observed is indicative of a high quality periodic structure further confirming the ability to grow InAs/(In,Ga)Sb mixed interfaces in the (111)A orientation. The suppressed intensity of alternating satellites is indicative of the intended equal thicknesses of the InAs and (Ga,In)Sb layers. Fourier transform infrared spectroscopy absorption and photoconductive studies of several superlattice structures are currently in progress.

## CONCLUSION

InAs/(Ga,In)Sb strained layer superlattices and InAs/GaSb heterojunctions have been grown on the (111)A, (111)B, and (100) orientations, and been characterized by a XPS, SIMS, and x-ray diffraction. The cross incorporation of the group V elements into the heterojunctions has been analyzed by SIMS. The relative rates of incorporation of As into GaSb in the (111)A, (111)B, and (100) orientations was determined to be 3.00:1.01:2.00, and for incorporation of Sb into InAs, 3.00:1.03:0.85. An argument based on the number of adjacent pairs of group V sites has been presented to account for the differences in these ratios. X-ray electron spectroscopy extinction curves

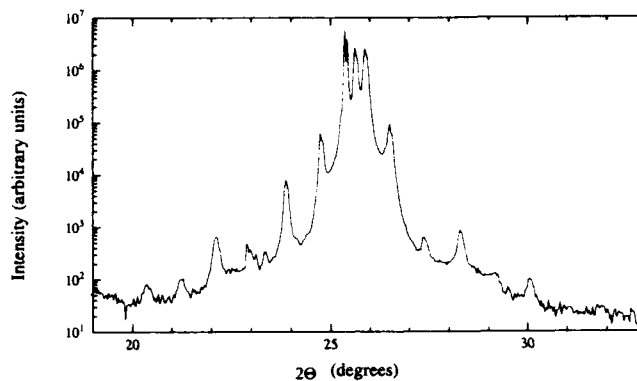


Fig. 6. X-ray diffraction  $\theta$ - $2\theta$  scan in the region of the (111) peak of 50 period (111)A oriented 43Å/43Å InAs/Ga<sub>0.9</sub>In<sub>0.1</sub>Sb SLS.

qualitatively confirm the degree of cross incorporation seen in the SIMS study and show no evidence of extended compound formation at (111)B interfaces of InAs on GaSb or GaSb on InAs. X-ray diffraction Bragg scans of a typical (111)A InAs(Ga,In)Sb SLS are presented demonstrating the high structural quality attained.

## ACKNOWLEDGMENTS

The authors wish to thank Dr. J.E. Baker for the SIMS data. This work was supported by the Texas Advanced Technology Program, NASA, and the R.A. Welch Foundation.

## REFERENCES

1. D.L. Smith and C. Mailhot, *J. Appl. Phys.* 62, 2545 (1987).
2. C. Mailhot and D.L. Smith, *J. Vac. Sci. Technol.* A7, 445 (1989).
3. R.H. Miles, D.H. Chow and T.C. McGill, *Proc. of the 7th Int. Narrow Gap Semicond. Conf.* July 1992, Southampton, U.K.
4. I.H. Campbell, I. Sela, B.K. Laurich, D.L. Smith, C.R. Bolognesi, L.A. Samoska, A.C. Gossard and H. Kroemer, *Appl. Phys. Lett.* 59, 846 (1991).
5. T.D. Golding, H.D. Shih, J.T. Zborowski, W.C. Fan, C.C. Horton, P.C. Chow, A. Vigliante, B.C. Covington, A. Chi, J.M. Anthony and H.F. Schaaake, *J. Vac. Sci. Technol.* B 10, 880 (1992).
6. D.H. Chow, R.H. Miles, J.R. Soderstrom and T.C. McGill, *Appl. Phys. Lett.* 56, 1418 (1990).
7. C. Mailhot and D.L. Smith, *J. Vac. Sci. Technol.* B 5, 1268 (1987).
8. M. Lakrimi, C. Lopez, R.W. Martin, G.M. Summers, G.M. Sundaram, K.S.H. Dalton, N.J. Mason, R.J. Nicholas and P.J. Walker, *Surf. Sci.* 263, 575 (1992).
9. K.F. Longenbach and W.I. Wang, *Appl. Phys. Lett.* 59, 2427 (1991).
10. J.A. Dura, J.T. Zborowski and T.D. Golding, *Mat. Res. Soc. Symp. Proc.* 263, 35 (1992).
11. R. Fashe, J.T. Zborowski, T.D. Golding, H.D. Shih, P.C. Chow, K. Matsuichi, B.C. Covington, A. Chi, J. Zheng and H. F. Schaaake, *J. Cryst. Growth* 111, 667 (1991).
12. R.H. Miles, D.H. Chow and T. C. McGill, *Proc. 7th Int. Narrow Band Gap Semicond. Conf.*, July 1992, Southampton, U.K.
13. G. Tuttle, H. Kroemer and J.H. English, *Mat. Res. Soc. Symp. Proc.* 145, 415 (1989).
14. J.T. Zborowski, W.C. Fan, T.D. Golding, A. Vigliante and P.C. Chow, *J. Appl. Phys.* 71, 5908 (1992).

# Auger Lifetimes in Ideal InGaSb/InAs Superlattices

C.H. GREIN, P.M. YOUNG, and H. EHRENREICH

Division of Applied Sciences, Harvard University, Cambridge, MA 02138

T.C. MCGILL

California Institute of Technology, Pasadena, CA 91125

Quantitative calculations are reported of both band-to-band Auger and radiative recombination lifetimes in thin-layered type II  $\text{In}_x\text{Ga}_{1-x}\text{Sb/InAs}$  superlattices with energy gaps in the 5–17  $\mu\text{m}$  range, using accurate band structure and numerical techniques. Results for an 11  $\mu\text{m}$  superlattice are compared with similar calculations for bulk HgCdTe and a HgTe/CdTe superlattice having the same energy gap. The results show the n-type Auger rates to be comparable and the p-type rates to be suppressed by three orders of magnitude in some experimentally realizable structures. Thus, well fabricated III-V superlattices appear to be excellent candidates as a new class of infrared detectors.

**Key words:** Auger lifetime, InGaSb/InAs superlattices, radiative recombination lifetime

## INTRODUCTION

The thin-layered type II staggered  $\text{In}_x\text{Ga}_{1-x}\text{Sb/InAs}$  superlattice (SL) has been proposed as an infrared (IR) detector candidate.<sup>1</sup> It has been suggested<sup>2</sup> that p-type Auger recombination rates are suppressed in some of these SLs due to a large strain-induced light hole-heavy hole splitting. We perform quantitative calculations of band-to-band Auger and radiative recombination rates, employing realistic nonparabolic band structures.<sup>3</sup> The results verify that p-type Auger recombination rates are suppressed relative to those of bulk HgCdTe and SL HgTe/CdTe with the same energy gap due to the absence of strain splitting in the latter two systems. Auger recombination rates of n-type InGaSb/InAs SLs are comparable to those of n-type bulk HgCdTe and SL HgTe/CdTe with the same energy gap. Radiative recombination rates are almost always smaller than Auger recombination rates for unintentionally doped samples. Superlattice based IR detectors are versatile because of their multispectral response and their ability to suppress both n-

and p-type Auger recombination rates in samples with properly chosen alloy composition ratios, and well and barrier widths.

## DISCUSSION

The minority carrier distribution function in an IR detector relevant to calculations of Auger and radiative recombination rates is an equilibrium Fermi distribution. This is a consequence of energy relaxation times<sup>4</sup> of photoexcited carriers ( $\sim 10^{-12}\text{s}$ ) being several orders of magnitude shorter than Auger and radiative lifetimes ( $\sim 10^{-4}$  to  $10^{-10}\text{s}$ ) for carrier densities of experimental interest. We calculate the lifetimes of a single excess nonequilibrium minority carrier in the region of highest occupation. For an n-type material, the excess carrier is a hole at the top of the heavy hole band (HH1 in Fig. 1), and results are averaged over the flat portions of this band. For a p-type material, the excess carrier is an electron at the bottom of the conduction band (C1 in Fig. 1).

The established methods for calculating band-to-band Auger recombination<sup>5-7</sup> are here extended to superlattices. Since the proposed III-V IR detectors employ thin layered ( $\sim 25\text{\AA}$ ) SLs, electrons in the C1

(Received October 14, 1992)

band have significant dispersion in the  $\perp$  direction requiring a three-dimensional calculation, in contrast with earlier two-dimensional calculations of Auger lifetimes of electrons confined in quantum wells.<sup>8</sup> An envelope function formalism<sup>9</sup> is used to describe the SL states, and SL  $K \cdot p$  theory<sup>10</sup> is used to obtain the energy bands and the wave functions  $\langle r | L, K \rangle$  for band  $L$  and wave vector  $K$ . The overlap integrals required to evaluate the screened Coulomb potential matrix elements were obtained to first order in  $|K_1 - K_1'|^2$  in a manner similar to that described in Refs. 5, 11, and 12. Due to the highly nonparabolic nature of the band structure (see Fig. 1), parabolic approximations are not applicable. The p-type Auger lifetime (i.e. the lifetime of the photoexcited minority electron 1') is given by

$$\frac{1}{\tau_A} = \frac{3e^4 \hbar^3}{2\epsilon^2 \pi^3 m^4} \iint f_p(K_1) f_p(K_2) \times \frac{\beta_{C1,HH1}(K_1, K_1') \beta_{LH1,HH1}(K_2, K_2')}{|\lambda^2 + |K_1 - K_1'|^2|} \times \delta \left( \begin{array}{l} E_{C1}(K_1) + E_{LH1}(K_2) \\ - E_{HH1}(K_1') - E_{HH1}(K_2') \end{array} \right) d^3 K_1 d^3 K_2 \quad (1)$$

in the absence of exchange interactions.<sup>13</sup> The  $K_i$  refer to the superlattice states defined in Fig. 1,  $E_L(K)$  are the band energies, and  $\epsilon$ ,  $m$ ,  $f_p$ , and  $\lambda^{-1}$  are the dc dielectric constant of the barrier layers, the free electron mass, the hole Fermi function, and the Debye screening length respectively. The quantity  $\beta_{L,L'}(K, K') = |\langle L, K' | (K - K') \cdot p | L', K \rangle|^2 / [E_L(K') - E_L(K)]^2$  involves the superlattice momentum matrix elements.  $K_1'$  denotes the minority carrier 1', and crystal momentum conservation determines  $K_2' = K_1 + K_2 - K_1'$ . A similar expression applies to n-type Auger recombination. Following Ref. 14, the p-type radiative lifetime of electron 1' is given by

$$\frac{1}{\tau_R} = \frac{ne^2}{\pi \hbar^2 c^3 m^2 \epsilon} |\langle C1, K_1' | p | HH1, K_1' \rangle|^2 f_p(K_1') \times [E_{C1}(K_1') - E_{HH1}(K_1')] \quad (2)$$

where  $n$  is the index of refraction. A similar expression applies to n-type radiative recombination.

These expressions were evaluated numerically for realistic SL band structures. Equation 1 involves six integrals. One integral, over the energy conserving delta function, was performed analytically. If the minority carrier has no component of its momentum in the  $\parallel$  direction, then rotational symmetry in the plane permits the analytical evaluation of a second integral. Thus, four to five nested integrals were

evaluated numerically. This task is at the limits of what can be performed with distributed desktop computing. The error in the lifetime due to numerical integrations on a finite mesh was no more than 40%.

Figure 1 shows the calculated band structure of 25Å  $\text{In}_{0.25}\text{Ga}_{0.75}\text{Sb}/41\text{Å InAs}$  for the in-plane ( $\parallel$ ) and growth ( $\perp$ ) directions. This superlattice has been studied experimentally at 77K as a candidate material for 11  $\mu\text{m}$  IR detectors.<sup>1</sup> Auger transitions involve limited regions of  $K$  space due both to restrictions imposed by energy and crystal momentum conservation and occupation probabilities. Typical transitions which satisfy the constraints are shown. In the n-type material, transitions dominantly involve crystal momentum changes in the  $\perp$  direction. Here, electrons 1 and 2 are in regions of high occupation, implying a fast recombination rate. In the p-type material, transitions dominantly involve crystal momentum changes in the  $\parallel$  direction. Here, hole 1 is in a region of low occupation, thus suppressing Auger transitions. This suppression, a consequence of the large strain-induced LH1-HH1 splitting, accounts in part for the promise of  $\text{In}_{0.25}\text{Ga}_{0.75}\text{Sb/InAs}$  for IR detectors.<sup>1</sup>

Figure 2 shows the regions of  $K$  space important for p-type Auger recombination in 25Å  $\text{In}_{0.25}\text{Ga}_{0.75}\text{Sb}/41\text{Å InAs}$  for  $p = 10^{16} \text{ cm}^{-3}$  at 77K. The structures marked

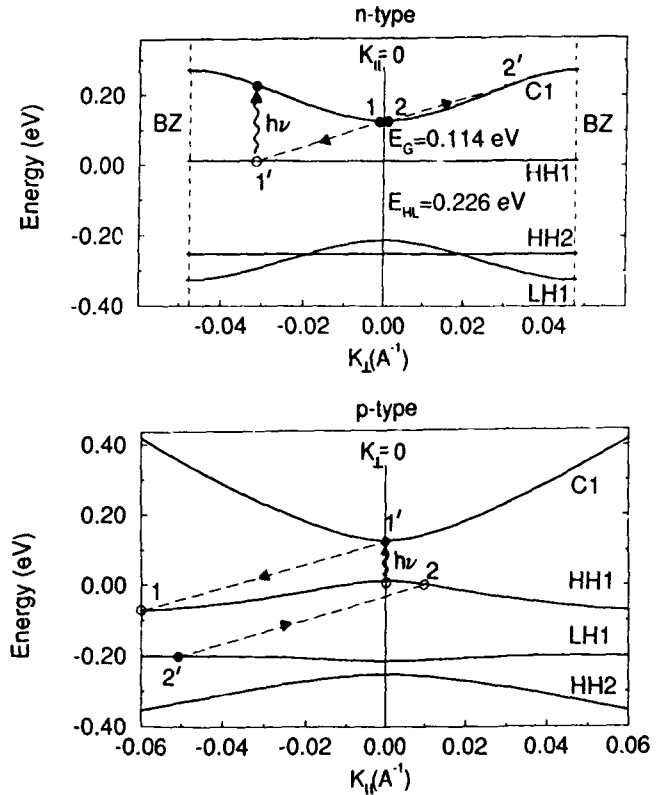


Fig. 1. The calculated band structure of a 25Å  $\text{In}_{0.25}\text{Ga}_{0.75}\text{Sb}/41\text{Å InAs}$  superlattice in the growth ( $\perp$ ) and in-plane ( $\parallel$ ) directions. C1, HH1, HH2, and LH1 refer to conduction, heavy, and light hole bands. BZ indicates the Brillouin zone boundary in the  $\perp$  direction. Wavy lines indicate possible IR photon absorptions; diagonal dashed lines show typical Auger recombination transitions.  $E_g$  is the energy gap, and  $E_{hl}$  is the zone-center light hole-heavy hole splitting. The perpendicular width of the C1 band is 0.149 eV.

"Hole 1" and "Hole 2" indicate the positions in K space of holes 1 and 2 (defined in Fig. 1) taking part in the same transition, which provide the largest contributions to the recombination rate. The Auger rate is approximately independent of  $K_{\perp}$  due to the flatness of the HH1 and LH1 bands in the  $\perp$  direction. The K space volumes associated with "Hole 1" and "Hole 2" are equal, as is required by detailed balance. The "Hole 1" structure is broader because the HH1 band is flatter near hole 1 (see Fig. 1). Transitions for which the positions of holes 1 and 2 are reversed are suppressed by a smaller overlap of the electron and hole wave functions. For n-type recombination, the important region of K space for both electrons 1 and 2 (defined in Fig. 1) is a sharp peak centered at the zone center of width  $0.012 \text{ \AA}^{-1}$  for  $n \approx 10^{16} \text{ cm}^{-3}$ .

Figure 3, exhibiting the Auger lifetimes of five  $\text{In}_{0.25}\text{Ga}_{0.75}\text{Sb/InAs}$  superlattices of different layer thicknesses, illustrates the IR multi-spectral characteristics. The energy gaps of the five superlattices A, B, C, D, and E are 17.0, 13.8, 10.9, 9.0, and 5.2  $\mu\text{m}$ , respectively. The experimentally studied SL<sup>1</sup> C has background doping levels  $n = 5 \times 10^{15} \text{ cm}^{-3}$  and  $p = 3 \times 10^{16} \text{ cm}^{-3}$  and corresponds to the band structure of Fig. 1. The lifetimes are plotted for the fixed carrier concentrations shown to illustrate phase space effects on Auger lifetimes. The dashed line permits comparison of  $\tau_A$  for equal  $n$  and  $p$  doping levels. The n-type lifetimes increase with increasing energy gap because the  $\perp$  bandwidth of the C1 band becomes less than the energy gap  $E_G$ . The n-type transition of Fig. 1 is no longer possible since  $2'$  cannot be accommodated in the C1 band. By contrast, the p-type lifetimes decrease with increasing energy gap because  $E_G$  becomes greater than the zone center HH1-LH1 splitting  $E_{\text{HL}}$ . A greater volume of phase space is thus available for  $2'$  in the LH1 band. The flatness of the HH1 and LH1 bands gives rise to a maximal p-type Auger rate when  $E_G \approx E_{\text{HL}}$  because energy and crystal momentum conservation conditions can be easily satisfied by carriers in regions of high occupation.

The Auger lifetimes of a 37Å HgTe/16Å CdTe SL and bulk  $\text{Hg}_{0.79}\text{Cd}_{0.21}\text{Te}$  having the same energy gap, 0.114 eV, as the 25Å  $\text{In}_{0.25}\text{Ga}_{0.75}\text{Sb/41Å InAs}$  SL have also been calculated. The II-VI SL has the same axial electron effective mass (0.025  $m$ ) as the III-V SL. For  $n = 5 \times 10^{15} \text{ cm}^{-3}$  and  $T = 77 \text{ K}$ , the II-VI SL has an Auger lifetime of  $9 \times 10^{-8} \text{ s}$  and the II-VI bulk has a lifetime of  $1 \times 10^{-7} \text{ s}$ , both somewhat less than the value of  $2 \times 10^{-7} \text{ s}$  of the III-V SL. More significant differences are found in the p-type lifetimes due to the different valence band structures. For  $p = 3 \times 10^{16} \text{ cm}^{-3}$  and  $T = 77 \text{ K}$ , the II-VI SL and bulk II-VI material have Auger lifetimes of  $9 \times 10^{-11} \text{ s}$  and  $5 \times 10^{-9} \text{ s}$ , respectively, compared to  $5 \times 10^{-6} \text{ s}$  for the III-V SL. The extremely short lifetime of the II-VI SL results from the approximate equality of the energy gap and the HH1-LH1 splitting. The II-VI bulk lifetime is shorter compared to the III-V SL because the small effective-mass light hole band provides phase space for recombination transitions that is absent for larger

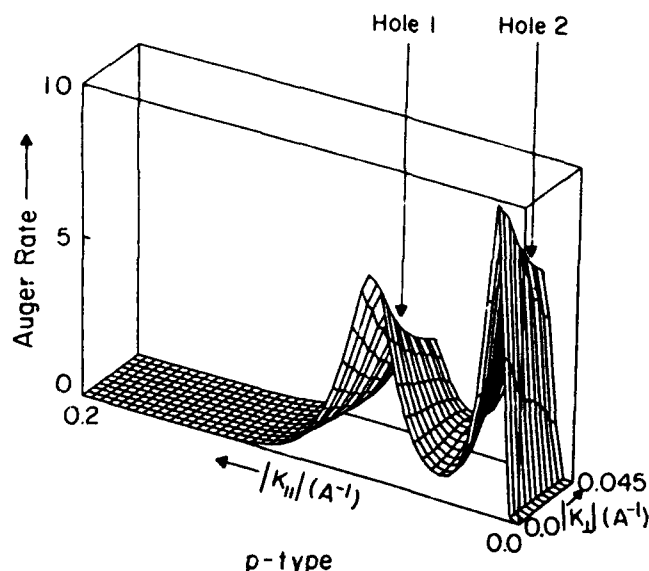


Fig. 2. The p-type Auger rate for holes 1 and 2 (cf Fig. 1) in arbitrary units for 25Å  $\text{In}_{0.25}\text{Ga}_{0.75}\text{Sb/41Å InAs}$  SL with  $p = 10^{16} \text{ cm}^{-3}$  and  $T = 77 \text{ K}$  in K-space.

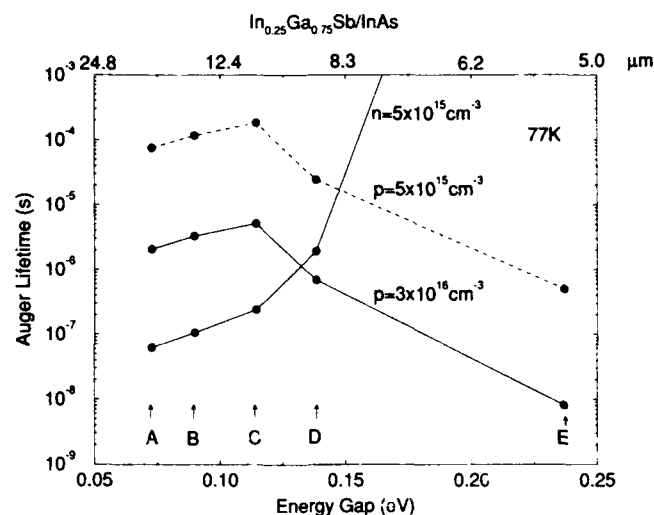


Fig. 3. Calculated Auger recombination lifetimes at 77K of 30Å  $\text{In}_{0.25}\text{Ga}_{0.75}\text{Sb/48Å InAs}$  (A), 28Å  $\text{In}_{0.25}\text{Ga}_{0.75}\text{Sb/45Å InAs}$  (B), 25Å  $\text{In}_{0.25}\text{Ga}_{0.75}\text{Sb/41Å InAs}$  (C), 25Å  $\text{In}_{0.25}\text{Ga}_{0.75}\text{Sb/37Å InAs}$  (D), and 25Å  $\text{In}_{0.25}\text{Ga}_{0.75}\text{Sb/25Å InAs}$  (E) superlattices as a function of energy gap for the indicated doping levels. Solid circles are the calculated points. The band structure for C is given in Fig. 1. The heavy hole-light hole splittings for superlattices A, B, D, and E are 0.201, 0.227, 0.219, and 0.188 eV, respectively.

masses. It should be noted that other choices of II-VI SL barrier and well widths and compositions may result in improved Auger rates.

The calculated Auger and radiative lifetimes of a single band edge minority carrier in the 25Å  $\text{In}_{0.25}\text{Ga}_{0.75}\text{Sb/41Å InAs}$  superlattice are plotted in Fig. 4 as a function of doping levels for  $T = 77 \text{ K}$  and  $T = 90 \text{ K}$ . The decreasing lifetimes with increasing doping levels are due to more probable carrier-carrier collisions. We note that the radiative lifetimes are almost always longer than the Auger lifetimes. The n-type lifetimes are only weakly temperature dependent because the near zone center electrons 1 and 2 of Fig.

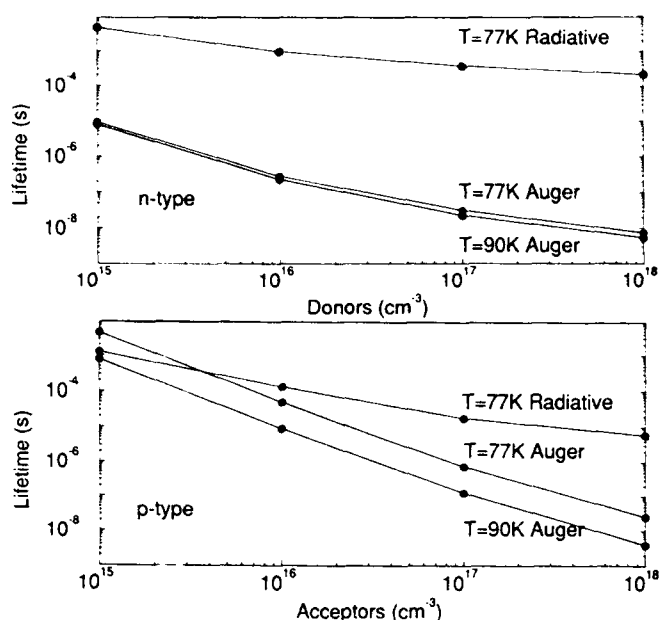


Fig. 4. Calculated n-type and p-type Auger and radiative recombination lifetimes of a 25Å  $\text{In}_{0.25}\text{Ga}_{0.75}\text{Sb}/41\text{Å InAs}$  superlattice as a function of doping at  $T = 77\text{K}$  and  $T = 90\text{K}$ .

1 are almost statistically degenerate for the doping levels considered. The p-type lifetimes decrease by a factor of five to six as  $T$  is changed from 77 to 90K. Hole 1 of Fig. 1 lies in the tail of the hole Fermi distribution. Its occupation probability is, therefore, strongly temperature dependent. The lifetime obeys an approximate power law relationship with the carrier concentration:  $\tau_A \sim n^{-1.7}$  and  $\tau_A \sim p^{-2.1}$  for carrier densities between  $5 \times 10^{15}$  and  $10^{17} \text{ cm}^{-3}$ . In the simplest parabolic band case, in which carriers involved in Auger recombination are located at the band edges,  $\tau_A \sim n^{-2}$  and  $p^{-2}$ . The deviations found here are associated with band structure and occupation number effects.

### CONCLUSION

In summary, we find on the basis of carrier lifetime calculations that  $\text{In}_{1-x}\text{Ga}_x\text{Sb}/\text{InAs}$  is a promising superlattice for IR detector applications in the 5–17  $\mu\text{m}$  range. The 11  $\mu\text{m}$  SL has an n-type Auger lifetime somewhat larger than those of bulk  $\text{HgCdTe}$  and a  $\text{HgTe}/\text{CdTe}$  SL with the same energy gap. In superlattices, the n-type Auger recombination may be sup-

pressed by reducing the  $\perp$  bandwidth of the conduction band (by increasing the barrier thickness) to a value less than the energy gap. The p-type Auger lifetime of the 11  $\mu\text{m}$   $\text{InGaSb}/\text{InAs}$  SL is approximately three orders of magnitude longer than bulk  $\text{HgCdTe}$  and five orders of magnitude longer than the  $\text{HgTe}/\text{CdTe}$  SL with the same energy gap. The suppression of p-type recombination is due to the flatness of the light and heavy hole bands whose splitting exceeds the energy gap, thus limiting phase space for recombination transitions. This splitting can be increased further (without changing the energy gap) through the choice of other alloy compositions and layer thicknesses, which will further suppress p-type recombination in  $\text{In}_x\text{Ga}_{1-x}\text{Sb}/\text{InAs}$  superlattices.

### ACKNOWLEDGMENT

The authors are grateful to R.H. Miles for making data available prior to publication. Helpful discussions with him are also greatly appreciated. This work was supported by DARPA and JSEP through ONR contract Nos. N00014-86-K-0033 and N00014-89-J-1023, respectively.

### REFERENCES

1. D.H. Chow, R.H. Miles, J.N. Schulman, D.A. Collins and T.C. McGill, *Semicond. Sci. Tech.* 6, C47 (1991); R.H. Miles, private communication.
2. The idea for this SL and its properties originated with D. Smith and C. Mailhot in association with T.C. McGill.
3. C.H. Grein, P.M. Young and H. Ehrenreich, *Appl. Phys. Lett.* 61, 2905 (1992) (shorter version).
4. R. Ferreira and G. Bastard, *Phys. Rev. B* 40, 1074 (1989).
5. A.R. Beattie and P.T. Landsberg, *Proc. R. Soc. Lond. Ser. A* 249, 16 (1959).
6. A.R. Beattie and G. Smith, *Phys. Status Solidi* 19, 577 (1967).
7. P.T. Landsberg, *Solid State Electron.* 30, 1107 (1987).
8. Y. Jiang, M.C. Teich and W.I. Wang, *J. Appl. Phys.* 69, 836 (1991).
9. G. Bastard, *Proc. of the NATO Advanced Study Institute on Molecular Beam Epitaxy in Heterostructures*, Erice, Italy, 1983, eds. L.L. Chang and K. Ploog (Martinus-Nijhoff, Dordrecht, 1984), p.381.
10. N.F. Johnson, H. Ehrenreich, P.M. Hui and P.M. Young, *Phys. Rev. B* 41, 3655 (1990).
11. E. Antoncik and P.T. Landsberg, *Proc. Phys. Soc.* 82, 337 (1963).
12. M. Takeshima, *J. App. Phys.* 43, 4114 (1972).
13. The lifetime would differ by less than 33% if exchange interactions were included.
14. G.P. Agrawal and N.K. Dutta, *Long Wavelength Semiconductor Lasers* (Van Nostrand Reinhold Co., New York, 1986).

# In-Situ Ellipsometric Measurements of the MBE Growth of CdTe/HgTe and CdTe/ZnTe Superlattices

M.A. FOLKARD, G. SHEN, V. KUMAR, T.A. STEELE, D. REES,  
I.K. VARGA, D. CARR, K. FUELOEP, B.A. JOHNSON, P.J. ORDERS, and  
R.H. HARTLEY

CMTEK Pty. Ltd., P.O. Box 1500, Salisbury 5108, South Australia

H. BUSKES

BHP Research, Melbourne Laboratories, P.O. Box 264, Clayton 3168,  
Australia

M. GAL

School of Physics, University of New South Wales, Kensington 2033,  
Australia

Phase modulated ellipsometric data recorded during molecular beam epitaxial growth of CdTe/HgTe and CdTe/ZnTe superlattices on (100) and (211)B oriented Cd<sub>0.96</sub>Zn<sub>0.04</sub>Te and GaAs substrates are presented. The measurements provide a continuous monitor of the growth process, thickness, growth rate, compositional data, and evidence of interdiffusion in CdTe/HgTe superlattices at elevated temperatures. The thickness measurements are independent of growth kinetics and surface orientation and agree well with those obtained from x-ray diffraction and reflection high energy electron diffraction. Ellipsometry shows that the incorporation of Hg in CdTe is significantly higher on (100) oriented surfaces than on (211)B oriented surfaces. Fine structure in the data from CdTe/ZnTe superlattices may be associated with a surface reconstruction during deposition of each CdTe layer. The experimental results for CdTe/HgTe superlattices compare well with results of thin film multi-layer calculations. The general applicability of ellipsometry as an in-situ analytical technique for epitaxial growth of a range of semiconductor superlattices is discussed.

**Key words:** CdTe/HgTe superlattice, CdTe/ZnTe superlattice, in-situ ellipsometry, MBE

## INTRODUCTION

Superlattices of II-VI compound semiconductors provide a variety of novel and physically interesting material systems which have application in infrared detection,<sup>1,2</sup> modulation doping,<sup>3</sup> dislocation filtering,<sup>4</sup> and nonlinear optics.<sup>5</sup> They also provide a means of studying interdiffusion of the constituent elements across well defined interfaces that are produced during low temperature growth by molecular beam epitaxy (MBE).

We have investigated the MBE growth of CdTe/HgTe and CdTe/ZnTe superlattices and interdiffusion in CdTe/HgTe superlattices with phase modulated ellipsometry (PME), which is a sensitive ana-

lytical technique capable of providing detailed information on the MBE growth process.<sup>6,7</sup> These measurements provide a continuous monitor of the growth of such structures, accurate values of individual layer thicknesses, information on interface roughening, and compositional data for layers comprised of ternary alloys. We compare PME data from the growth of CdTe/HgTe superlattices on (100) oriented surfaces with data from the growth of CdTe/HgTe superlattices on (211)B oriented surfaces, and we contrast these results with the PME data from CdTe/ZnTe superlattice growths on GaAs(100) substrates. Evidence of interdiffusion across the CdTe-HgTe interfaces during post growth annealing of (211)B superlattice structures is presented.

Growth rates determined by PME are compared with those measured by the frequency of reflection



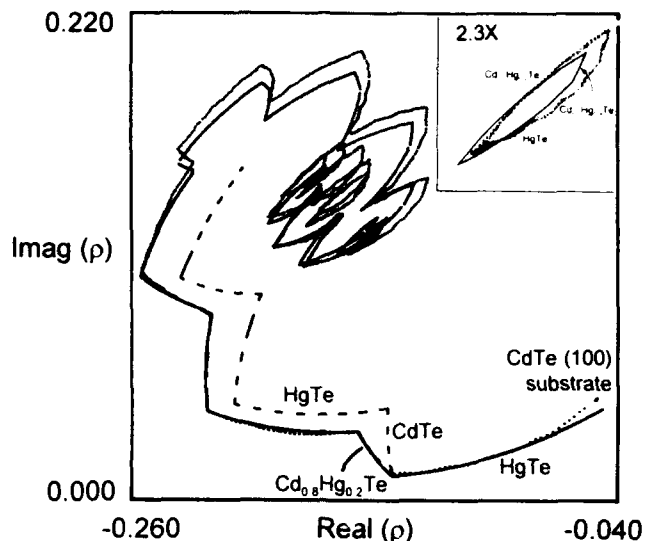


Fig. 1. Comparison of PME measurements from the growth of a 200 period  $\text{Cd}_{0.8}\text{Hg}_{0.2}\text{Te}/\text{HgTe}$  superlattice (dotted curve) on a  $\text{Cd}_{0.96}\text{Zn}_{0.04}\text{Te}(100)$  substrate with the results of thin film multilayer calculations (solid and dashed curves). The solid and dashed curves represent a  $\text{Cd}_{0.8}\text{Hg}_{0.2}\text{Te}(60\text{\AA})/\text{HgTe}(59\text{\AA})$  and a  $\text{CdTe}(60\text{\AA})/\text{HgTe}(59\text{\AA})$  superlattice, respectively. The inset in the upper right hand corner shows more clearly the behavior of both the experimental and model trajectories at the center of the spiral.

high energy electron diffraction (RHEED) intensity oscillations and x-ray diffraction measurements of superlattice periodicity. Results of x-ray diffraction and low temperature photoluminescence (PL) measurements of the  $\text{CdTe}/\text{ZnTe}$  superlattices are also presented. In addition, the results of standard thin film multilayer calculations<sup>4</sup> of superlattice growth are compared with the  $\text{CdTe}/\text{HgTe}$  ellipsometric data. These calculations are furthermore used to predict the general suitability of in-situ PME measurements for real time analysis of  $\text{GaAs}/\text{AlAs}$ ,  $\text{InAs}/\text{InSb}$ , and  $\text{Si}/\text{Ge}$  superlattice growths.

### EXPERIMENTAL

An MBE facility, designed and manufactured in house, was used to grow the  $\text{CdTe}/\text{ZnTe}$  superlattices while the  $\text{CdTe}/\text{HgTe}$  superlattices were grown with a Riber 32 R&D MBE machine. The growth chambers of both machines were equipped with commercial effusion cells, RHEED systems, and phase modulated ellipsometers. The ellipsometer, which is identical for both machines, consists of a 5 mW He-Ne laser, polarizer crystal, and phase modulator operating at 40 kHz to condition the input beam together with an analyzer crystal and Si photodiode detector on the output arm. The angle,  $\theta_i$ , which the incident beam makes with the surface normal of the epilayer is  $60^\circ$  for the in house designed machine and  $70^\circ$  for the Riber machine. The output signal is digitized and processed to obtain the Fourier components which are used to calculate the ratio of complex reflectivities for the epilayer/substrate combination. Phase modulated ellipsometry and RHEED are used to monitor thermal treatment of the as loaded substrates, buffer layer growths, superlattice growths, and annealing

experiments.

The  $\text{CdTe}/\text{ZnTe}$  superlattices were grown on  $\text{GaAs}(100)$  substrates which were buffered by a 0.5  $\mu\text{m}$  thick  $\text{ZnTe}$  layer. The substrates were chemically cleaned using standard procedures and bonded to Mo carriers with In. The oxide layer was thermally removed in-situ under a Zn flux. The  $\text{ZnTe}$  buffer layers were grown with elemental Zn and  $\text{Te}_2$  sources at a substrate temperature of  $330^\circ\text{C}$  and at a rate of 0.4  $\mu\text{m}/\text{h}$ . The superlattices were grown at a substrate temperature of  $280^\circ\text{C}$ . Compositional modulation was controlled by opening and closing shutters to the Cd and Zn cells while the  $\text{Te}_2$  shutter remained open throughout the growth. The elemental flux ratios were maintained metal rich for the  $\text{CdTe}$  growth and marginally  $\text{Te}_2$  rich for the  $\text{ZnTe}$  growth. Essentially equivalent growth rates for  $\text{CdTe}$  and  $\text{ZnTe}$  ranging between 0.4  $\mu\text{m}/\text{h}$  and 0.5  $\mu\text{m}/\text{h}$  were used. Growth rates were measured from phase modulated ellipsometry data and by the frequency of RHEED intensity oscillations. The superlattices were further characterized by low temperature PL and x-ray diffraction measurements.

The  $\text{CdTe}/\text{HgTe}$  superlattices were grown on  $\text{Cd}_{0.96}\text{Zn}_{0.04}\text{Te}$  substrates with either (100) or (211)B orientation. These substrates were chemically cleaned, etched in a  $\text{Br}_2\text{-CH}_3\text{OH}$  solution and bonded to Mo carriers with Ga. They were heated to  $320^\circ\text{C}$  for several minutes prior to growing a thin  $\text{CdTe}$  buffer layer.

The superlattices were grown at substrate temperatures between  $180^\circ\text{C}$  and  $195^\circ\text{C}$ . Compositional modulation was controlled by opening and closing shutters to the  $\text{CdTe}$  and  $\text{Te}_2$  cells while the Hg shutter remained open throughout the growth. The  $\text{CdTe}$  growth rate was typically 0.9  $\mu\text{m}/\text{h}$  for both (100) and (211)B orientations while the  $\text{HgTe}$  growth rate was 0.9  $\mu\text{m}/\text{h}$  on the (100) surface and 3.6  $\mu\text{m}/\text{h}$  on the (211)B surface. Growth rates were measured by PME and, in the case of the (100) orientation, were compared with oscillating RHEED data and x-ray diffraction measurements of periodicity. No oscillations in RHEED intensity were observed for growth on (211)B surfaces.

### RESULTS AND DISCUSSION

We present ellipsometric data plotted in the  $\rho$ -plane and recorded during the MBE growths of  $\text{CdTe}/\text{HgTe}$  and  $\text{CdTe}/\text{ZnTe}$  superlattices. Data relating to substrate preparation processes and buffer layer growths are not included here. The quantity  $\rho$  represents the ratio of complex reflectivities  $R_p$  and  $R_s$  for light with linear polarization states parallel and perpendicular to the plane of incidence, respectively. Displayed in this manner,<sup>6,7</sup> the measurements provide a straightforward means of obtaining a continuous record of the growth as well as periodicity and compositional information throughout the entire superlattice growth. These capabilities are demonstrated in the results presented in this section.

Figure 1 illustrates the ellipsometric data (dotted

curve) recorded and displayed during the growth of a 200 period  $\text{Cd}_{0.8}\text{Hg}_{0.2}\text{Te}/\text{HgTe}$  superlattice on a  $\text{Cd}_{0.96}\text{Zn}_{0.04}\text{Te}(100)$  substrate. It represents the first 16 periods of the superlattice growth which begins in the lower right corner of the figure with a HgTe layer of thickness 60Å followed by a  $\text{Cd}_{0.8}\text{Hg}_{0.2}\text{Te}$  layer of equivalent thickness. These two layers which define the superlattice period ( $P = 120\text{\AA}$ ) are repeated sequentially to produce the 200 period structure. The thickness of each layer is measured directly from the ellipsometric data with better than monolayer resolution. Each segment of the trajectory in the figure corresponds to part of a spiral whose center is known and is characteristic of an infinitely thick layer of  $\text{Cd}_{0.8}\text{Hg}_{0.2}\text{Te}$  or HgTe. As the thickness corresponding to one complete spiral of either  $\text{Cd}_{0.8}\text{Hg}_{0.2}\text{Te}$  or HgTe is known, the growth rate of individual layers is determined by the angle swept by each spiral segment about its center in a given time. The abrupt changes in direction of the dotted trajectory in Fig. 1 are a direct result of the programmed compositional modulation during growth of this structure. After deposition of approximately 30 periods, the trajectory near the center of the spiral (shown more clearly as the dotted curve in the inset to Fig. 1) appears similar in shape to the cross section of a convex lens. The upper arcs are generated by the  $\text{Cd}_{0.8}\text{Hg}_{0.2}\text{Te}$  layers and the lower arcs are generated by the HgTe layers.

The individual layer thicknesses derived from the PME data are in good agreement with those measured by RHEED intensity oscillations during the  $\text{Cd}_{0.8}\text{Hg}_{0.2}\text{Te}$  layer growths ( $\text{Cd}_{0.8}\text{Hg}_{0.2}\text{Te}$  thickness = 60Å from RHEED) and measurement of periodicity by double crystal x-ray diffraction ( $P = 119\text{\AA}$ ). The agreement between the experimental data (dotted curve) and the results of standard thin film multi-layer calculations (solid curve in Fig. 1) where the thicknesses of the individual layers were set to 60Å and 59Å for  $\text{Cd}_{0.8}\text{Hg}_{0.2}\text{Te}$  and HgTe, respectively also confirm the experimentally determined PME layer thicknesses and growth rates.

Two different results from thin film multi-layer calculations are also shown in Fig. 1 for purposes of comparison with the experimental data. The calculation models the experimental geometry and uses our measured values of complex refractive index for He-Ne radiation. The solid curve, already alluded to above, represents the result of a calculation for the growth of the first 11 periods of a  $\text{Cd}_{0.8}\text{Hg}_{0.2}\text{Te}(60\text{\AA})/\text{HgTe}(59\text{\AA})$  superlattice, whereas the dashed curve in the figure is the result of the same calculation for the growth of the first three periods of a  $\text{CdTe}(60\text{\AA})/\text{HgTe}(59\text{\AA})$  superlattice where the Hg content in the CdTe layers is assumed to be zero. The  $\text{Cd}_{0.8}\text{Hg}_{0.2}\text{Te}/\text{HgTe}$  calculation is also compared with the experimental data in the inset to Fig. 1 where we show the detailed structure of both layers near the center of the spiral. Included in the calculation is a transition layer of composition  $x = 0.1$  and thickness 15Å, such that the 59Å HgTe layers consist of 15Å of  $\text{Cd}_{0.1}\text{Hg}_{0.9}\text{Te}$  and 44Å of HgTe. This adjustment to the structure is a

means of incorporating the effects of surface roughening during the CdTe layer growth.<sup>7</sup> It improves the agreement with the experimental data after the third period, while having virtually no impact on the trajectory for the first three periods. Clearly, better agreement is achieved between experiment and theory when the refractive index of the 'CdTe' layers is set to match that of a  $\text{Cd}_{0.8}\text{Hg}_{0.2}\text{Te}$  layer. This incorporation of Hg in CdTe layers on (100) oriented surfaces is a consequence of the growth procedure whereby the Hg shutter is left open throughout the growth. The result agrees well with a direct measure of Hg incorporation in CdTe made previously<sup>6</sup> and with data on similar superlattices.<sup>9-11</sup>

The ellipsometric data (dotted curve) recorded and displayed during the growth and annealing of a seven-period  $\text{CdTe}(25\text{\AA})/\text{HgTe}(25\text{\AA})$  superlattice on a  $\text{Cd}_{0.96}\text{Zn}_{0.04}\text{Te}(211)\text{B}$  substrate are shown in Fig. 2. This superlattice was grown specifically to study the effects of post growth annealing on interdiffusion. The structure was grown at a substrate temperature of 185°C. The growth begins at point A with a HgTe layer of thickness 32Å followed by a CdTe layer of thickness 25Å. The next three HgTe layers decreased in thickness to a stable value of 23Å, presumably due to an initial  $\text{Te}_2$  flux transient. The growth was terminated at point B. The superlattice was then heated in the growth position to 280°C for 40 min during which time the ellipsometry signal moved from point B to point C at an approximately constant rate. Because growth proceeds via step edge propagation on a (211)B surface, no RHEED intensity oscillations were detected, hence layer thicknesses were measured solely by ellipsometry.

The results of thin film multi-layer calculations for

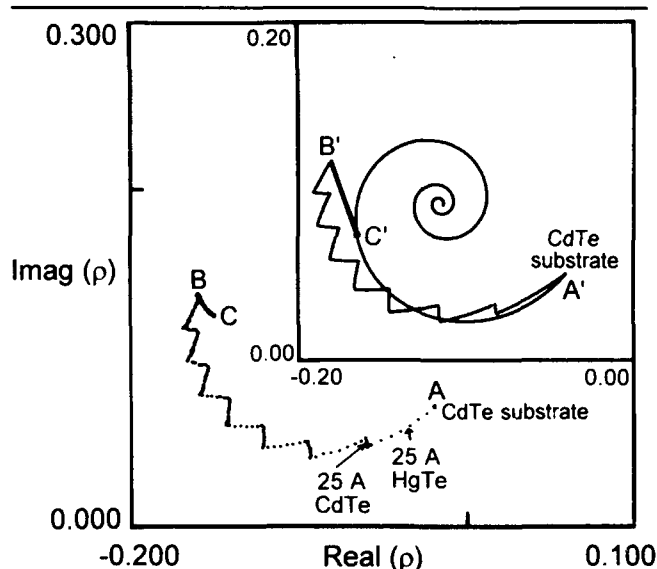


Fig. 2. Phase modulated ellipsometry measurements of the growth (AB) and annealing (BC) of a seven-period  $\text{CdTe}/\text{HgTe}$  superlattice on a  $\text{Cd}_{0.96}\text{Zn}_{0.04}\text{Te}(211)\text{B}$  substrate. The growth temperature was 185°C. The inset in the right hand corner shows the results of model calculations for this superlattice and its equivalent uniform CMT layer. The point C' shows the expected position in the  $p$ -plane for complete interdiffusion of the superlattice.

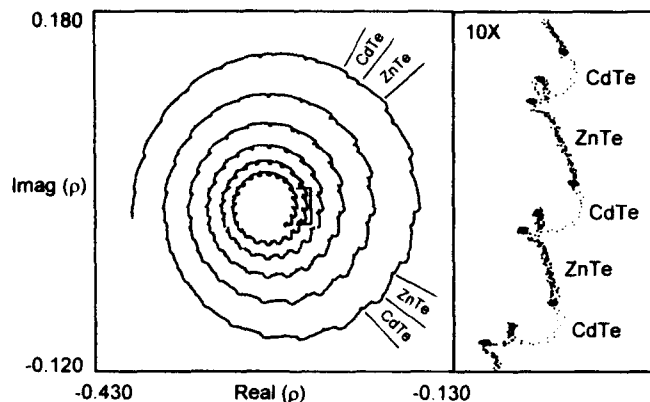


Fig. 3. Phase modulated ellipsometry measurements of the complete growth of a 208-period CdTe/ZnTe superlattice. The superlattice has a periodicity of 50Å and was grown on a GaAs(100) substrate with a 0.5 μm ZnTe buffer layer. Analysis of the data gives individual layer thicknesses of 25Å for both CdTe and ZnTe. An expanded plot of two periods from the fifth loop is shown at the right.

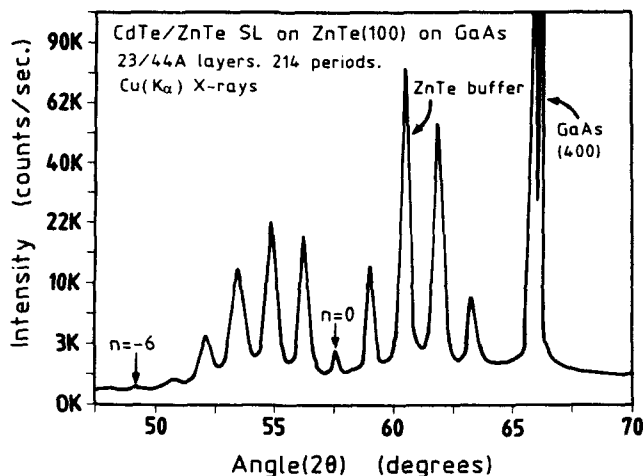


Fig. 4. X-ray diffraction scan ( $\theta$ - $2\theta$ ) using Cu  $K\alpha$  radiation of a 214-period CdTe/ZnTe superlattice. The superlattice has a periodicity of 67Å and was grown on a GaAs(100) substrate with a 0.5 μm ZnTe buffer layer. Satellite peaks of order  $n = 7$  are observable and are indicative of high structural quality material.

the seven-period CdTe/HgTe superlattice growth and the equivalent uniform  $\text{Cd}_{0.5}\text{Hg}_{0.5}\text{Te}$  alloy are plotted on the same scale as the experimental data in the inset to Fig. 2. The point labeled C' represents the thickness of the  $\text{Cd}_{0.5}\text{Hg}_{0.5}\text{Te}$  layer which is equivalent to the total thickness of the superlattice (355Å). The line labeled B'C' in the figure represents the expected annealing behavior of the ellipsometric data if interdiffusion is significant. The model calculation of the superlattice growth, which excludes Hg incorporation in the CdTe layers, agrees well with the experimental data in marked contrast with the corresponding comparison in Fig. 1 on (100) oriented substrates. The results thus indicate that Hg incorporation in CdTe layers differs significantly between (100) and (211)B orientations. Similar differences in Hg incorporation between (100) and (111)B orientations have been reported previously.<sup>9</sup> The shift (BC) in the data, on annealing the superlattice, qualitatively agrees with an interdiffusion process (B'C') in the structure. How-

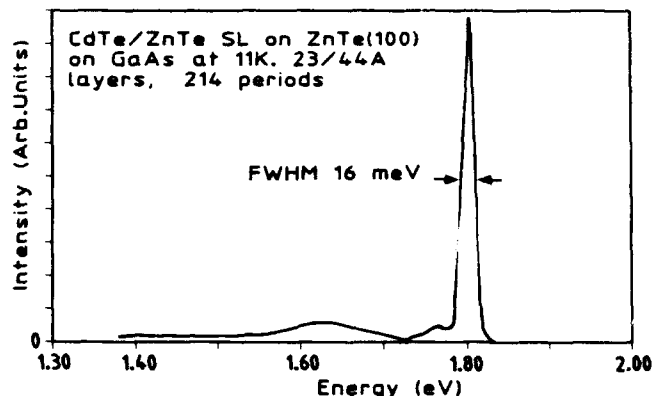


Fig. 5. Photoluminescence measurement of the superlattice shown in Fig. 4. The intense, narrow exciton peak at 1.81 eV is indicative of material with highly uniform layer thicknesses and sharp interfaces.

ever, the magnitude of the shift in the experimental data suggests that this process is incomplete after 40 min at 280°C.

The ellipsometric data recorded during the growth of a 208-period CdTe/ZnTe superlattice on ZnTe/GaAs(100) are shown in Fig. 3. The spiral represents the complete record of the superlattice growth which starts at the left of the figure with a CdTe layer of thickness 25Å followed by a ZnTe layer of equivalent thickness. The data points describe a clockwise spiral towards a center that is characteristic of an infinitely thick structure. The trajectory does not reach its infinitely thick limit after 208 periods due to the low absorption of 633 nm radiation in CdTe ( $k = 0.23$ ) and ZnTe ( $k = 0$ ). It is clearly more difficult to distinguish between spiral segments associated with CdTe and ZnTe layers (two sets of adjoining layers are marked on the spiral) compared with the data in Figs. 1 and 2. However, the sensitivity of the measurement is such that on an expanded scale the 25Å CdTe and ZnTe layers are easily identifiable. A ten times expanded plot of data from two periods of the superlattice measured near the end of the growth (the region marked on the fifth loop of the spiral) is shown on the right side of Fig. 3. The spiral segments from CdTe and ZnTe layers (labeled in the expanded plot) show characteristic differences in form. The ZnTe segments are simple arcs of a circle from which thickness and growth rate can be obtained in a straightforward manner. On the other hand, the CdTe segments, which are responsible for the spiralling characteristic of the trajectory, are more complex in shape showing reproducible fine structure (small loops) in each layer. The origin of this fine structure in the CdTe data, which is not evident in the CdTe/HgTe superlattices, is not clear to us at present. We suspect that it may be associated with a surface reconstruction during the CdTe part of the growth due to the difference in II-VI flux ratio for the CdTe and ZnTe layers. However, we have yet to confirm this.

Reflection high energy electron diffraction intensity oscillations were observed during the growth of the CdTe and ZnTe superlattice layers. These measurements of growth rate give layer thicknesses of

25Å and 24Å for CdTe and ZnTe, respectively. Ellipsometric measurements of ZnTe thickness give a value of 27Å, in good agreement with RHEED data. In addition, x-ray diffraction measurements of superlattice periodicity ( $P = 50\text{\AA}$ ) compare well with the data from the in-situ techniques.

Presented in Figs. 4 and 5 are post growth characterization measurements of a 214-period CdTe(23 Å)/ZnTe(44 Å) superlattice, using x-ray diffraction and low temperature PL. The details of the measurements are summarized in the figures. The satellite peaks in the  $\theta$ -2 $\theta$  x-ray scan of Fig. 4 are grouped in two envelopes with those centered near  $55^\circ$  arising from strained CdTe layers and those centered near  $62^\circ$  arising from strained ZnTe layers. The satellite peak spacing gives a periodicity of 71Å in good agreement with the results of the in situ measurements. The number of satellite peaks present in the spectrum (up to  $n = 7$ ) is indicative of high structural quality material with good layer thickness uniformity and interface sharpness. The PL spectrum in Fig. 5 provides similar evidence of good interface sharpness and well width (CdTe) uniformity from the intense and narrow (FWHM = 16 meV) exciton peak at 1.81 eV. This measurement compares favorably with previously published CdTe/ZnTe PL data.<sup>12</sup>

Finally, we discuss the general applicability of in-situ PME measurements for real time analysis of the growth of quantum well structures. The results of thin film multi-layer calculations are used here as a basis for comparison between the growth of InAs/InSb, Si/Ge, GaAs/Al<sub>0.8</sub>Ga<sub>0.2</sub>As and CdTe/HgTe quantum wells. All individual layer thicknesses are 50Å and the angle of incidence is  $70^\circ$ . Complex refractive indices for these materials at 633 nm were obtained from the literature.<sup>13-15</sup> The results are plotted in the  $p$ -plane and are shown in Figs. 6-9.

Each material system produces a characteristic trajectory determined by unique combinations of refractive indices and layer thicknesses with abrupt changes in direction as a result of compositional modulation. The rate at which the trajectory reaches a stable and reproducible pattern (as seen in the inset of Fig. 1) in the  $p$ -plane is related to the magnitudes of the materials imaginary components of refractive index. The InAs/InSb superlattice requires only 25 periods of 100Å to reach the stable central region of its trajectory, correspondingly, CdTe/HgTe takes approximately 40 periods and Si/Ge takes approximately 50, while the GaAs/Al<sub>0.8</sub>Ga<sub>0.2</sub>As superlattice continues to spiral until approximately 250 periods of 100Å are grown. The abrupt changes in direction with changes in composition suggest that ellipsometric measurements will be sensitive to individual layer composition as well as provide a continuous monitor of layer thicknesses and growth rates for all of these materials.

### CONCLUSION

We have shown that PME measurements of the MBE growth of CdTe/HgTe and CdTe/ZnTe superlattices provide a continuous monitor of the growth

process, compositional information, thickness, and growth rate data. The thickness measurements are dependent on compositional differences in successive layers (e.g. heterostructures and superlattices), but are independent of growth kinetics and surface orientation and so complement RHEED analyses. Phase modulated ellipsometry also provides evidence of interdiffusion during post growth annealing of the CdTe/HgTe structures. The CdTe/HgTe experimental data are well described by thin film multilayer calculations which indicate that Hg incorporation in the CdTe layers is significantly higher on (100) oriented surfaces than on (211)B oriented surfaces. The experimental results from CdTe/ZnTe superlattice growths differ significantly from those for CdTe/HgTe

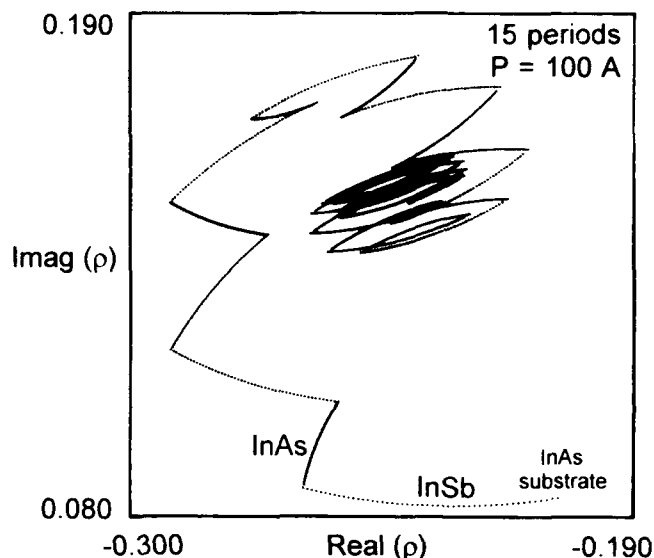


Fig. 6. Result of a thin film multi-layer calculation plotted in the  $p$ -plane for the first 15 periods of an InAs(50Å)/InSb(50Å) superlattice grown on an InAs substrate. Complex refractive indices at 633 nm for InAs and InSb are  $3.962-0.665j$  and  $4.250-1.799j$ , respectively.

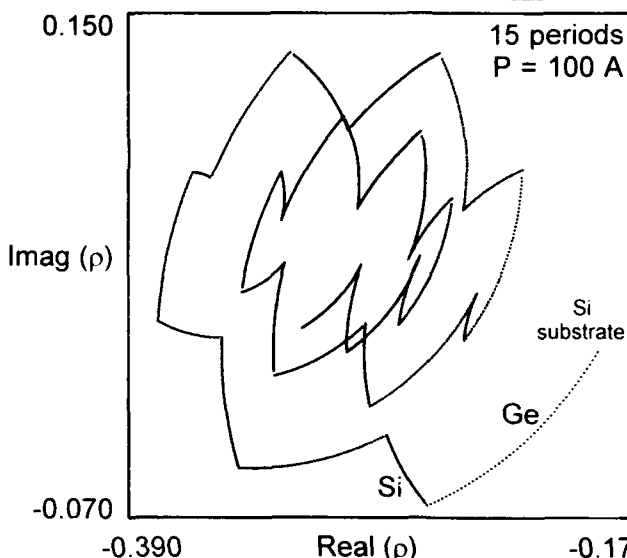


Fig. 7. Result of a thin film multi-layer calculation plotted in the  $p$ -plane for the first 15 periods of a Si(50Å)/Ge(50Å) superlattice grown on a Si substrate. Complex refractive indices at 633 nm for Si and Ge are  $3.87-0.013j$  and  $5.48-0.793j$ , respectively.

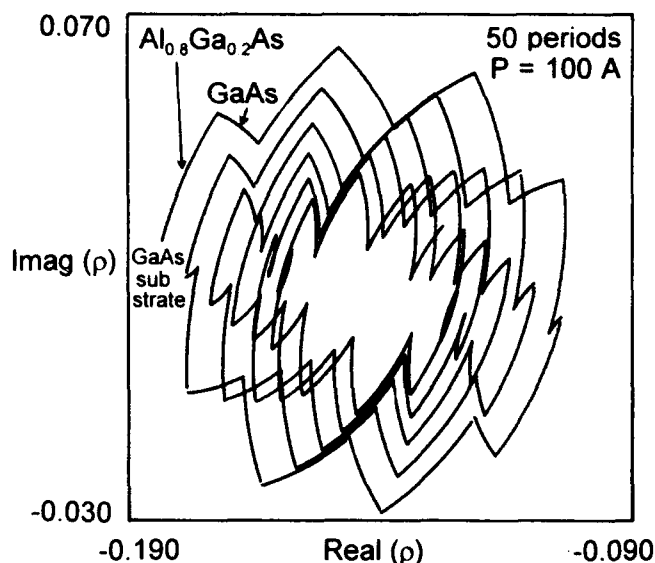


Fig. 8. Result of a thin film multi-layer calculation plotted in the  $\rho$ -plane for the first 50 periods of a GaAs(50Å)/Al<sub>0.8</sub>Ga<sub>0.2</sub>As(50Å) superlattice grown on a GaAs substrate. Complex refractive indices at 633 nm for GaAs and Al<sub>0.8</sub>Ga<sub>0.2</sub>As are 3.85–0.19j and 3.26–0.0j respectively.

superlattices as a result of markedly different refractive indices at 633 nm for ZnTe and HgTe. Reproducible fine structure in those parts of the CdTe/ZnTe trajectory associated with CdTe, is suggestive of a sensitivity of the measurements to surface reconstructions. These superlattices are shown to have high structural quality, good layer thickness uniformity, and sharp interfaces. Model calculations of InAs/InSb, Si/Ge, and GaAs/Al<sub>0.8</sub>Ga<sub>0.2</sub>As superlattice growths indicate that PME will be a sensitive measure of growth and composition for a range of quantum well systems.

#### ACKNOWLEDGMENT

We thank A. Davidson, B. Middlemiss, and C. Noble for technical assistance and J. Bedson for help with x-ray measurements. This work is supported by a grant (#17022) for Generic Industrial Research and Development from the Department of Industry, Technology and Commerce. The authors are grateful for the ongoing funding of this work from the Australian Defence Science and Technology Organisation.

#### REFERENCES

1. J.N. Schulman and T.C. McGill, *Appl. Phys. Lett.* 34, 663 (1979).

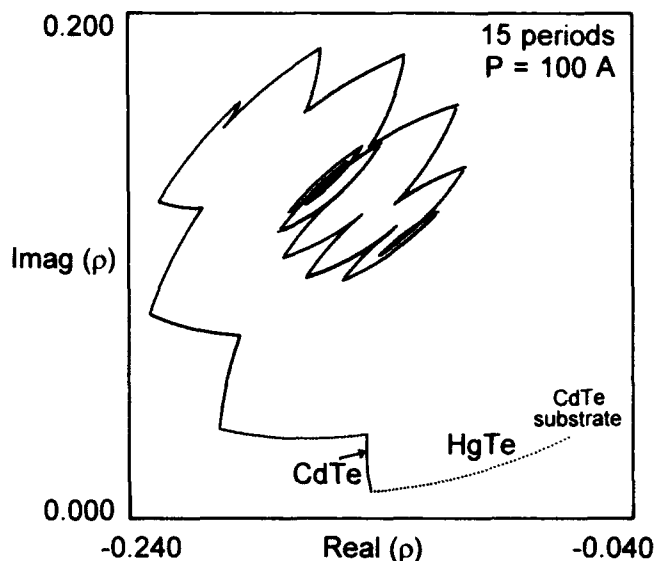


Fig. 9. Result of a thin film multilayer calculation plotted in the  $\rho$ -plane for the first 15 periods of a CdTe(50Å)/HgTe(50Å) superlattice grown on a CdTe substrate. Complex refractive indices at 633 nm for CdTe and HgTe are 3.082–0.182j and 3.92–1.344j, respectively.

2. D.L. Smith, T.C. McGill and J.N. Schulman, *Appl. Phys. Lett.* 43, 180 (1983).
3. J.M. Arias, S.H. Shin, D.E. Cooper, M. Zandian, J.G. Pasko, E.R. Gertner, R.E. DeWames and J. Singh, *J. Vac. Sci. Technol.* A8, 1025 (1990).
4. I. Sugiyama, A. Hobbs, T. Saito, O. Ueda, K. Shinohara and H. Takigawa, *J. Cryst. Growth* 117, 161 (1992).
5. E.R. Youngdale, C.A. Hoffman, J.R. Meyer, F.J. Bartoli, X. Chu, J.P. Faurie, J.W. Han, J.W. Cook and J.F. Schetzina, *J. Vac. Sci. Technol.* A7, 365 (1989).
6. R.H. Hartley, M.A. Folkard, D. Carr, P.J. Orders, D. Rees, I.K. Varga, V. Kumar, G. Shen, T.A. Steele, H. Buskes and J.B. Lee, *J. Cryst. Growth* 117, 166 (1992).
7. R.H. Hartley, M.A. Folkard, D. Carr, P.J. Orders, D. Rees, I.K. Varga, V. Kumar, G. Shen, T.A. Steele, H. Buskes and J.B. Lee, *J. Vac. Sci. Technol.* B10, 1410 (1992).
8. F. Abeles, *Progress in Optics*, Vol. II, E. Wolf, ed. (North Holland, Amsterdam, 1965).
9. J. Reno, R. Sporken, Y.J. Kim, C. Hsu and J.P. Faurie, *Appl. Phys. Lett.* 51, 1545 (1987).
10. C.A. Hoffman, J.R. Meyer, E.R. Youngdale, J.R. Lindle, F.J. Bartoli, J.W. Han, K.A. Harris, J.W. Cook and J.F. Schetzina, *J. Vac. Sci. Technol.* A6, 2785 (1988).
11. O.K. Wu, F.A. Shirland, J.P. Baukus, J.N. Schulman, G.S. Kamath and E.A. Patten, *J. Cryst. Growth* 95, 594 (1989).
12. R.H. Miles, G.Y. Wu, M.B. Johnson, T.C. McGill, J.P. Faurie and S. Sivananthan, *Appl. Phys. Lett.* 48, 1383 (1986).
13. D.E. Aspnes and A.A. Studna, *Phys. Rev. B* 27, 985 (1983).
14. L. Vina, C. Umbach, M. Cardona and L. Vodopyanov, *Phys. Rev. B* 29, 6752 (1984).
15. D.E. Aspnes, S.M. Kelso, R.A. Logan and R. Bhat, *J. Appl. Phys.*, 60, 754 (1986).

# States Confined in the Barriers of Type-III HgTe/CdTe Superlattices

H. LUO,\* L.R. RAM-MOHAN,<sup>†</sup> G.L. YANG,\* Y. XUAN,\* and J.K. FURDYNA\*

\*Department of Physics, University of Notre Dame, Notre Dame, IN 46556

<sup>†</sup>Departments of Physics, Electrical and Computer Engineering Worcester Polytechnic Institute, Worcester, MA 01609 and Naval Research Laboratory 4555 Overlook Drive, Washington, DC 20375-5000

We present a theoretical study of states quasi-localized in CdTe barriers of HgTe/CdTe superlattices. We show that the quasi-localization of both electrons and holes will lead to strong Coulomb interaction, and thus to the formation of excitons. It is further demonstrated that such quasi-localized states, including excitons, exhibit confinement effect similar to those of localized states in quantum wells.

**Key words:** Exciton formation, HgTe/CdTe superlattice, quasi-localized states in CdTe barriers

## INTRODUCTION

Optical transitions in semiconductor superlattices (SLs) have been extensively studied, especially those involving states localized in the quantum wells of the SLs. There have also been observations of optical transitions involving states with energies above the barriers.<sup>1</sup> The behavior of such above-barrier states have been exploited in several experimental and theoretical studies.<sup>1-4</sup>

However, the connection between the quasi-localization of the above-barrier states and its consequences was established only very recently for both type-I and type-II superlattices.<sup>5-8</sup> These studies revealed directly the quasi-localized nature of above-barrier excitons that are responsible for the observed transitions. Such quasi-localization of excitons and their optical properties (e.g. transition probabilities) are direct results of the quasi-localization of the electron and the hole states in the barriers when their energies exceed the respective barriers.

In type-I superlattices, as discussed in Ref. 5, exci-

tons can form between electrons and holes, both of which are quasi-localized in the barriers. Type-I excitons (in which both electrons and holes are localized in the same layer) can also form in type-II superlattices between states localized in the wells of one band (e.g. conduction band), and those quasi-localized in the barrier of another band (e.g. valence band).<sup>6,8</sup> Because of the reported large absorption coefficients, as well as transition energies which are no longer limited by the energy gap of the well materials (because they involve states which exist at energies above the barriers), such transitions present a wide range of possibilities for further experiments and applications, none of which have yet been considered for type-III HgTe/CdTe superlattices.

Because such quasi-localization in the barrier region is an interference effect resulting from the reflection at the barrier-well interface, it is stronger when the band offset is larger (since the conduction and the valence band offsets determine the reflection coefficients for the electron and the hole, respectively).<sup>7</sup> Such a condition is very well satisfied in type-III HgTe/CdTe superlattices because the band offsets for both the  $\Gamma_6$  and the  $\Gamma_8$  are very large, making them

(Received November 4, 1992; revised January 13, 1993)

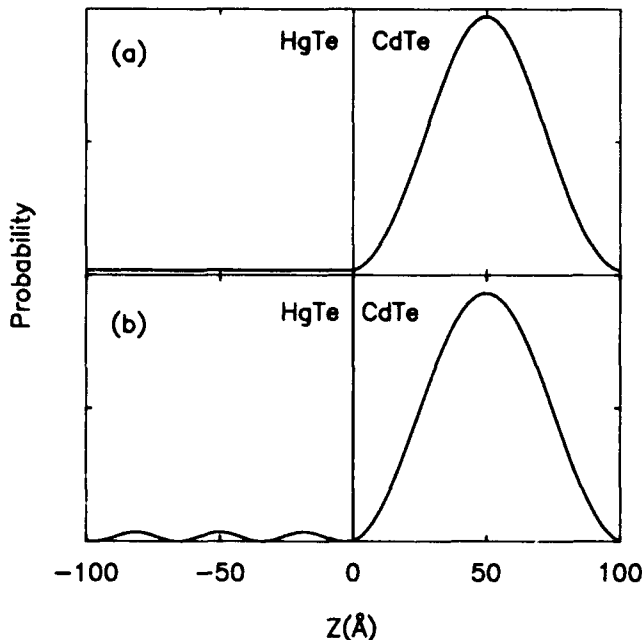


Fig. 1. The probabilities of the first above-barrier conduction subband and heavy-hole subband at the center of the superlattice Brillouin zone are shown in (a) and (b), respectively. Both above-barrier subbands are clearly localized in the CdTe layers. The integrated probability in the CdTe layer is more than 96% in both cases, indicating very strong localization.

particularly well suited for optical studies of the above barrier states.

## RESULTS AND DISCUSSION

In this paper, we examine the properties of above-barrier states in type-III HgTe/CdTe superlattices. To accomplish this, we calculate both the wave functions and the subband energies in the  $k \cdot p$  approximation, taking into account the bulk  $\Gamma_6$  conduction band, and the  $\Gamma_8$  and the  $\Gamma_7$  valence bands. The overall picture of the confinement effect is considerably more complicated for above-barrier states than that for states localized in the wells (i.e. those at energies below the barriers). This is because the description of such states involves running waves in the barrier and the well regions; and, therefore, there is a competition of the interference effects in both regions. Because of the smaller kinetic energy in the barrier region than that in the well, the quantum size effect in the barrier is stronger. Thus, the interference in the barrier region dominates in the competition for localization. Thus, an above-barrier state will be quasi-localized in the barrier region in most of the parameter space, especially when the band offset is large. Such localization is strongest for the lowest above-barrier state (i.e. with the smallest ratio of kinetic energy in the barrier to that in the well) and decreases for higher states, eventually reaching the classical limit. An extended discussion of the general behavior of such states will be given elsewhere. Here we will present calculated results for some specific cases to demonstrate the effect of quasi-localization for the lowest above-barrier states in situations typical for HgTe/CdTe SLs.

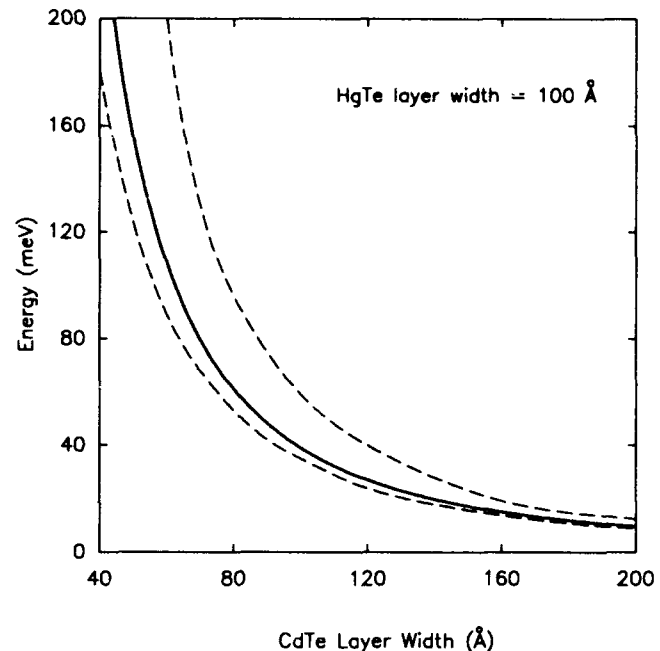


Fig. 2. The area between the dashed lines represents the confinement energy for the first above-barrier conduction subband (measured from the bottom of the CdTe conduction band) as a function of the CdTe layer width, with a fixed HgTe layer width of 100 Å. The solid line is the ground state of a hypothetical CdTe quantum well with infinite barriers.

Our calculations indicate that, because of the large band offsets at the HgTe/CdTe interface, the low-lying above-barrier states can be almost entirely localized in the CdTe layers. We will first discuss the calculated result for a HgTe(100 Å)/CdTe(100 Å) superlattice. The probabilities (i.e.  $|\phi(z)|^2$ ,  $\phi(z)$  being the wave function along the growth direction) of the first above-barrier subbands of the conduction band and of the heavy-hole valence band, calculated at the center of the superlattice Brillouin zone, are shown in Figs. 1a and 1b. The band parameters involved in the calculation are the same as those used in Ref. 9, and a value of 300 meV is used for the valence band offset. The integrated probabilities in the barrier region are more than 96% in both cases! Such degree of localization is comparable to that of the ground state in a typical quantum well; and one can, therefore, expect in the case of above-barrier states in HgTe/CdTe SLs confinement effects (e.g. confinement energy, increased exciton binding energy, and so on) similar to those observed in quantum wells.

One of the consequences of quasi-localization in the barrier region is the dependence of the above-barrier subband energy on barrier width. We illustrate this by calculating confinement energy (measured from the top of the barrier) of the lowest above-barrier conduction subband as a function of barrier width, with the well width fixed at 100 Å. The calculated result for the whole subband is represented by the area between the dashed lines in Fig. 2. It is clear that, as the barrier width decreases, the confinement energy increases, accompanied by an increase of the miniband width (i.e. the vertical distance between the

dashed lines). For comparison, we also plotted the ground state energy (solid line) of a hypothetical CdTe quantum well with infinite barriers (100% confined in the CdTe layer), calculated using the electron mass in CdTe, i.e.  $m^* = 0.0963 m_0$ . As is obvious from Fig. 2, the dependence of the energy of the above-barrier subband on barrier width closely follows the well-known dependence of states localized in a well on the well width.

Since the localization of both electron and hole above-barrier states takes place in the barrier region of a HgTe/CdTe SL, as is shown in Fig. 1, an exciton can naturally form from such a pair of states, and will also be quasi-localized in the CdTe barriers. Such quasi-localization of the free carrier wave functions in the same layer will lead to an increased Coulomb interaction, thus increasing the binding energy of the exciton. A variational technique<sup>10</sup> was used to calculate the exciton binding energy (denoted by  $R_{SL}$ , i.e. the rydberg of the exciton) involving the lowest above-barrier subbands in the conduction band and the heavy-hole valence band as a function of the barrier width. The trial function used in the calculation has the following form

$$\Phi(r_e, r_h) = A \phi_e(z_e) \phi_h(z_h) \exp\left(-\frac{1}{\lambda} \sqrt{(z_e - z_h)^2 + \rho^2}\right) \quad (1)$$

where  $\phi_e(z_e)$  and  $\phi_h(z_h)$  are the free carrier wave functions of the electron and the hole, respectively, along the growth direction, and  $\rho$  is the distance between the electron and the hole perpendicular to the growth direction. The normalization factor of the wave function is represented by  $A$ , and  $\lambda$  is the variational parameter. The free carrier wave functions are obtained by the  $k \cdot p$  method. Since only  $|\Phi(r_e, r_h)|^2$  is involved in the actual calculation, we use the probability obtained from the eight-component free carrier wave functions.

To illustrate the effect of confinement on the exciton binding, we plot the ratio  $R_{SL}/R_{BULK}$  (with  $R_{BULK}$  being the binding energy, or rydberg, of an exciton in bulk CdTe) in Fig. 3 as a function of the barrier (CdTe layer) width. The HgTe width is again fixed at 100 Å. We note again that the effect of confinement on the exciton binding energy is very similar to that characterizing the ground state exciton in a quantum well.<sup>11</sup> The maximum value of the exciton binding energy calculated in this example is 22.4 meV, more than twice that for the bulk. Such an increase of the exciton binding energy is expected to greatly improve the high temperature (e.g. room temperature) exciton absorption. Further study is currently under way to scan the parameter space for even larger binding energy. When the exciton binding energy is larger than the CdTe LO-phonon energy (which is 21 meV), LO-phonon scattering will be significantly reduced, leading to room temperature observation of exciton absorption in HgTe-CdTe superlattices—a feature of considerable importance for device applications. The exciton confinement effect is also expected to lead to

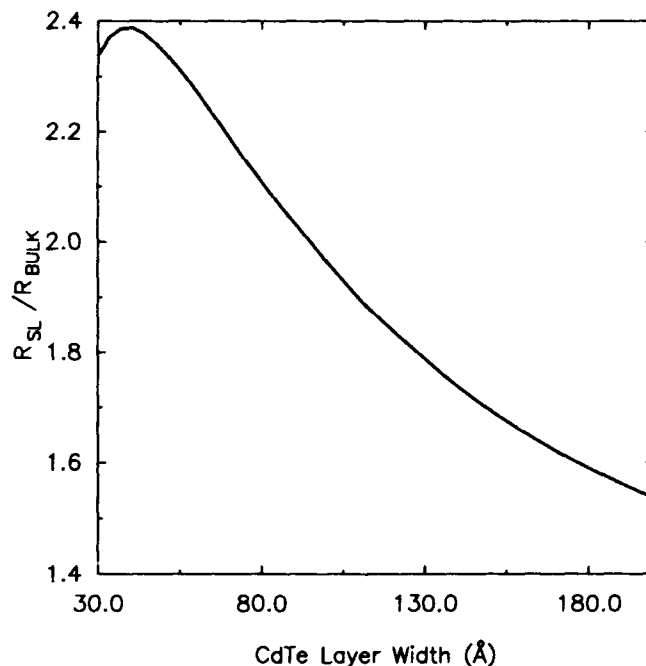


Fig. 3. The ratio  $R_{SL}/R_{BULK}$  (where  $R_{SL}$  and  $R_{BULK}$  are the exciton rydbergs in the superlattice and in the bulk, respectively) plotted as a function of CdTe layer width. Because the exciton in the superlattice is quasi-localized in the CdTe barrier layer, the binding energy shows a confinement behavior very similar to that for excitons localized in

an increase of the absorption coefficient, as has already been observed for exciton absorption involving above-barrier states in the case of CdSe/ZnTe superlattices.<sup>6</sup>

## CONCLUSION

Because of the typically fast relaxation of above-barrier electrons and holes, radiative recombination between these states is not a favorable process. Optical investigation of transitions between above-barrier states should, therefore, involve excitation rather than emission. When HgTe/CdTe superlattices are grown on CdTe substrates, a study of excitation processes will require reflectivity measurements, because the above-barrier transitions occur above the absorption edge of CdTe. On the other hand, in many studies reported in the literature of Hg-based type-III SLs, one actually deals with barriers containing some Hg, introduced intentionally or otherwise. In such HgTe/Cd<sub>1-x</sub>Hg<sub>x</sub>Te SLs, the above-barrier exciton absorption may very well be below the absorption edge of CdTe (depending on the Hg content in Cd<sub>1-x</sub>Hg<sub>x</sub>Te and on the Cd<sub>1-x</sub>Hg<sub>x</sub>Te layer width), so that transmission measurements can also be made. Systematic studies of such transitions involving above-barrier subbands will increase our understanding of HgTe/CdTe as well as HgTe/CdHgTe SLs.

## ACKNOWLEDGMENT

We acknowledge Quantum Semiconductor Algorithms for providing software for some of the calculations presented in this paper. This study was supported by DMR 9204800.



## REFERENCES

1. See for example, G. Bastard, U.O. Ziemelis, C. Delalande, M. Voos, A.C. Gossard and W. Wiegmann, *Solid State Commun.* 49, 671 (1984).
2. J.E. Zucker, A. Pinczuk, D.S. Cnemla, A. Gossard and W. Wiegmann, *Phys. Rev.* B29, 7065 (1984).
3. J.J. Song, Y.S. Yoon, A. Fedotowsky, Y.B. Kim, J.N. Schulman, C.W. Tu, D. Huang and H. Morkoc, *Phys. Rev.* B34, 8958 (1986).
4. M. Jaros and K.B. Wong, *J. Phys. C: Solid State Phys.* 17, L765 (1984).
5. F.C. Zhang, N. Dai, H. Luo, N. Samarth, M. Dobrowolska, J.K. Furdyna and L.R. Ram-Mohan, *Phys. Rev. Lett.* 68, 3220 (1992).
6. H. Luo, W.C. Chou, N. Samarth, A. Petrou and J.K. Furdyna, *Solid State Commun.* 85, 691 (1993).
7. H. Luo and J.K. Furdyna, *Modern Phys. Lett. B* 7, 299 (1993).
8. F.C. Zhang, H. Luo, N. Dai, N. Samarth, M. Dobrowolska, J.K. Furdyna and L.R. Ram-Mohan, *Phys. Rev. B* 47, 3806 (1993).
9. G.Y. Wu and T.C. McGill, *Appl. Phys. Lett.* 47, 634 (1985).
10. G. Bastard, E.E. Mendez, L.L. Chang and L. Esaki, *Phys. Rev.* B26, 1974 (1982).
11. R.L. Greene, K.K. Bajaj and D.E. Phelps, *Phys. Rev.* B29, 1807 (1984).

# Band Gap Uniformity and Layer Stability of HgTe-CdTe Superlattices Grown by Photon-Assisted Molecular Beam Epitaxy

R.W. YANKA, K.A. HARRIS, L.M. MOHNKERN, A.R. REISINGER, and T.H. MYERS\*

Electronics Laboratory, General Electric Co. (now Martin Marietta Corp.), Syracuse, NY 13221

N. OTSUKA

School of Materials Engineering, Purdue University, West Lafayette, IN 47907

Two material properties important to the application of HgTe/CdTe superlattices for device fabrication are band gap uniformity and thermal stability. In this paper, we present the results of an infrared photoluminescence study of (211)B HgTe/CdTe superlattices grown by photon-assisted molecular beam epitaxy which show that cut-off wavelength uniformity can be controlled to a level commensurate with the demands of advanced infrared detector fabrication. Infrared photoluminescence and transmission electron microscopy were also employed to demonstrate that (211)B HgTe/CdTe superlattices are less prone to interdiffusion than previously believed.

**Key words:** HgTe/CdTe superlattice, interdiffusion in superlattices, PAMBE, TEM

## INTRODUCTION

HgTe/CdTe superlattices (SLs) were first proposed more than a decade ago as an alternative to HgCdTe alloy structures for the fabrication of long-wave infrared (LWIR) detectors.<sup>1</sup> Early theoretical work indicated that at a given cut-off wavelength HgTe/CdTe superlattices could offer several advantages over the equivalent alloy, particularly in the very long-wave infrared (VLWIR) regime.<sup>2</sup> The first theoretical band structure calculations for (211)B oriented HgTe/CdTe superlattices were reported in 1990 by Hoffman et al.<sup>3</sup> It has only been recently, however, that superlattices with material properties appropriate for device applications have been demonstrated. In particular, the application of photon-assisted molecular beam epitaxy (PAMBE) to the growth of HgTe/CdTe super-

lattices has resulted in epilayers with excess carrier lifetimes of several hundred nanoseconds<sup>4</sup> as well as the first demonstration of high quantum efficiency superlattice photodiodes.<sup>5</sup>

One important material property required for the practical fabrication of LWIR and VLWIR superlattice detector arrays is that the band gap must not vary significantly across the area of the wafer. This property is essential to insure uniform response. This paper reports the results of infrared photoluminescence (IRPL) mapping measurements made on HgTe/CdTe superlattice epilayers grown by photon-assisted molecular beam epitaxy. Measurements were made at various positions across the SL layer, from which the variation of the band gap across the sample was determined. Our measurements indicate that SL band gaps for material grown in our laboratory (without rotation), exhibit uniformities suitable for array fabrication over areas as large as 2 cm<sup>2</sup>. This result is important because it demonstrates that the PAMBE technique is capable of producing uniform Hg-based

(Received October 12, 1992; revised January 13, 1993)

\*Present address: Department of Physics, West Virginia University, Morgantown, WV 26506, USA

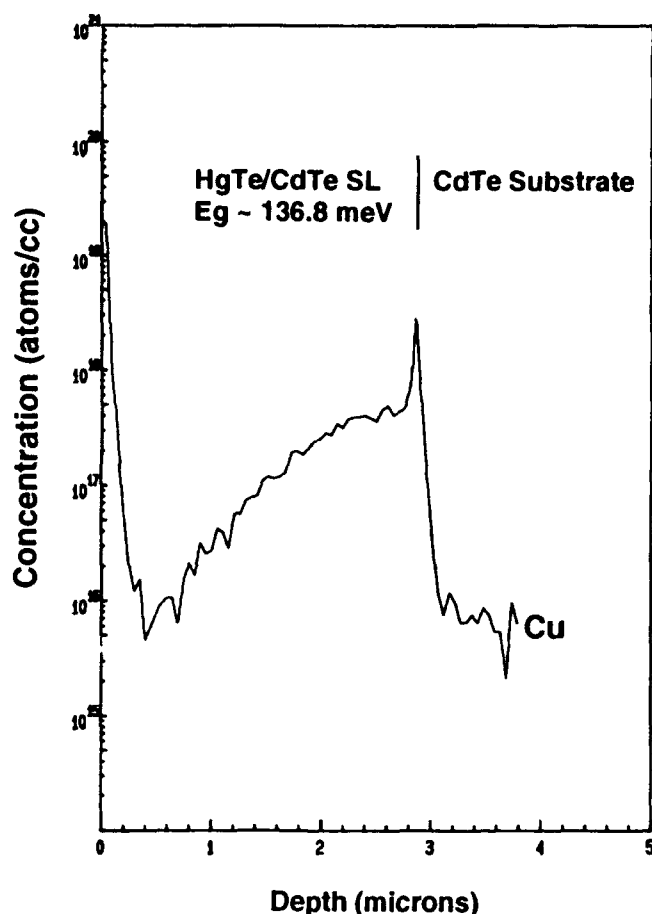


Fig. 1. Secondary ion mass spectroscopy copper profile of an As-doped superlattice grown on a copper contaminated CdTe substrate. Copper levels in the substrate and in the near surface region of the epilayer are at the SIMS detection limit.

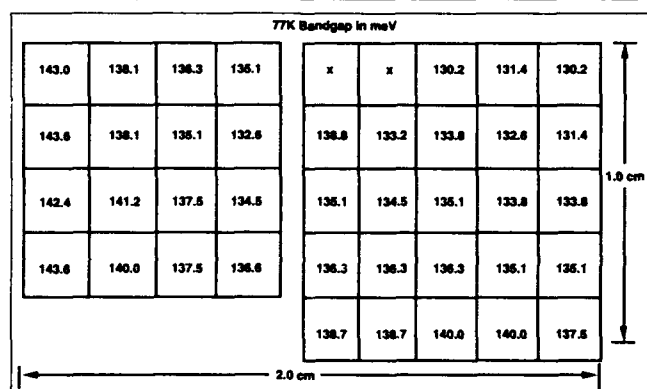


Fig. 2. Infrared photoluminescence band gap map of an LWIR superlattice. The average energy gap is 136.8 meV with  $\sigma = 3.5$  meV, which is equivalent to a cut-off wavelength of 9.09  $\mu\text{m}$  with  $\sigma = 0.23$   $\mu\text{m}$ . The measured uniformity is over a  $2 \times 1$  cm area and is in a range acceptable for the fabrication of detector arrays.

epilayers suitable for IR applications.

Infrared photoluminescence mapping was also used to evaluate the thermal stability of HgTe/CdTe superlattices. This is an important issue since there have been reports of significant interdiffusion of the HgTe and CdTe constituent layers of (111)B oriented superlattices at temperatures as low as 110°C.<sup>6,7</sup> For

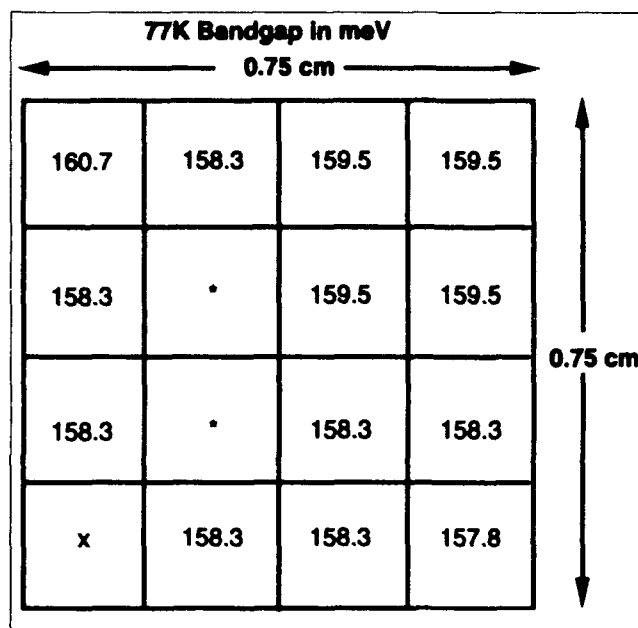


Fig. 3. Infrared photoluminescence band gap map of a superlattice exhibiting an average energy gap of 158.8 meV with  $\sigma = 0.8$  meV. The equivalent  $\lambda_c$  is 7.81  $\mu\text{m}$  with  $\sigma = 0.04$   $\mu\text{m}$  as measured over the 0.5 cm<sup>2</sup> area of the sample.

this study, IRPL measurements were carried out at 77K to determine the SL band gap at various points across the free surface of an epilayer. The sample was then flipped over and corresponding IRPL measurements were made through the transparent substrate. Any variations observed due to layer interdiffusion would be manifested by band gap variations between the corresponding measurements. Preliminary results suggest that SL layer interdiffusion does not occur, to the limit of the measurement, during PAMBE growth. These measurements have also produced evidence of 2-D carrier confinement at the superlattice/substrate interface.

## EXPERIMENTAL DETAILS

HgTe/CdTe superlattice epilayer growth was performed in one of two custom MBE machines modified for PAMBE growth. These systems have been described in an earlier publication.<sup>5</sup> All of the epilayers were grown on (211)B CdTe substrates at a deposition temperature of 170°C.<sup>8</sup> The substrates were prepared using standard wet-etch techniques followed by thermal processing prior to growth.<sup>8,9</sup> Typical beam equivalent pressures used for the source ovens were  $3\text{--}5 \times 10^{-4}$  Torr for Hg,  $1\text{--}3 \times 10^{-6}$  Torr for Te, and  $5\text{--}10 \times 10^{-7}$  Torr for CdTe. Overall growth rates employed were in the range of 0.5 to 1.0  $\mu\text{m/h}$ . The Te and Cd sources were shuttered alternately to produce the superlattice structure. The Hg source was not shuttered, resulting in a constant Hg overpressure throughout the growth. This produced barrier layers consisting of  $\text{Hg}_{1-x}\text{Cd}_x\text{Te}$ , where  $x = 0.85\text{--}0.90$ .

It has recently been reported that the presence of copper in commercially available substrate materials can have a profound effect on the properties of HgCdTe

epilayers grown on these substrates.<sup>10</sup> We have found that this problem extends to HgTe/CdTe superlattices as well, even though they are not exposed to high temperature anneals after growth. Figure 1 shows a secondary ion mass spectroscopy (SIMS) copper profile obtained from an arsenic-doped superlattice grown on a copper contaminated substrate. This superlattice exhibited a band gap of 136.8 meV. A copper diffusion profile is observed emanating from the substrate-epilayer interface and dropping down to SIMS background levels about 1  $\mu\text{m}$  from the film surface. In order to overcome this problem, we have developed a technique for removing copper from commercially available (211)B substrates. This treatment allows the growth and processing of device quality alloy and superlattice epilayers with no apparent copper contamination as measured by SIMS.<sup>11</sup> All epilayer growth at Martin Marietta is currently being carried out on substrates subjected to our copper extraction technique.

Infrared photoluminescence<sup>12</sup> measurements were carried out using a 500 mW CW Nd:YAG laser as the excitation source. The pump beam was focused on a sample mounted in a Janis liquid-helium cryostat equipped with a ZnSe window. A resistive heating element in the cryostat and its associated control circuitry permitted regulation of sample temperature between 10 and 400K. Measurements for this study were carried out at a sample temperature of 77K. The IRPL photon flux was collected and collimated by a set of ZnSe lenses and directed to the input port of a Nicolet 60SX Fourier transform infrared spectrom-

eter (FTIR) equipped with a liquid-nitrogen cooled MCT photovoltaic detector with a nominal cut-off wavelength of 13  $\mu\text{m}$ . Both the cryostat and the input port of the (FTIR) feature ZnSe windows. A Ge filter

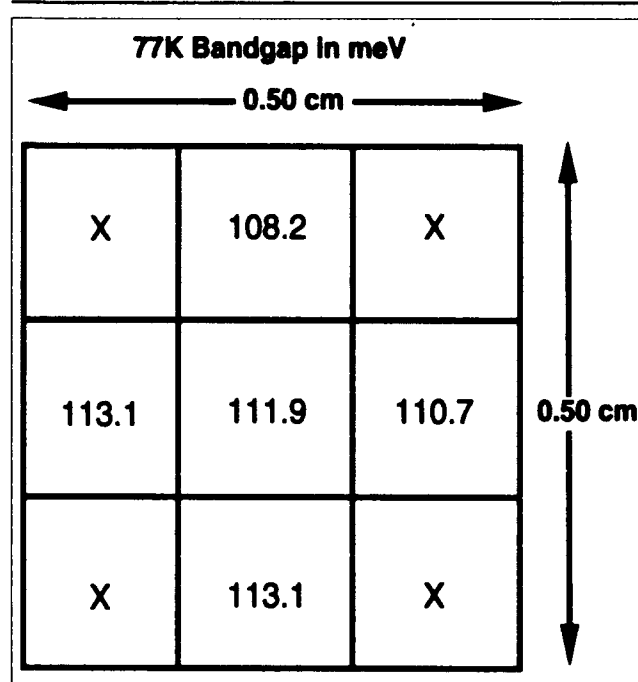


Fig. 4. Infrared photoluminescence cut-off map of a LWIR superlattice. The average band gap of this sample is 111.4 meV with  $\sigma = 2.0$  meV, which is equivalent to  $\lambda_c = 11.13$   $\mu\text{m}$  with  $\sigma = 0.21$   $\mu\text{m}$ . This uniformity is equivalent to the corresponding alloy with  $x = 0.218$  and  $\sigma = 0.0013$ .

| Front-side<br>$E_g \approx 158.8$ , $\sigma = 0.8$ meV<br>PL FWHM $\sim 16$ meV |       |       |       | Substrate-side<br>$E_g \approx 169.1$ , $\sigma = 1.7$ meV<br>PL FWHM $\sim 20$ meV |       |       |       |
|---|-------|-------|-------|---|-------|-------|-------|
| 160.7   | 158.3 | 159.5 | 159.5 | 166.8   | 168.0 | 171.7 | 169.9 |
| 158.3   | *     | 159.5 | 159.5 | 167.4   | 170.5 | 171.7 | 170.5 |
| 158.3   | *     | 158.3 | 158.3 | 166.8   | 167.4 | 169.3 | 170.3 |
| X   | 158.3 | 158.3 | 157.8 | X   | 168.0 | 169.3 | *     |

Fig. 5. Comparison map of frontside vs backside IRPL band gaps. The band gaps agree to within 10 meV, indicating minimal interdiffusion is taking place during film growth. Measurements were made at 77K.

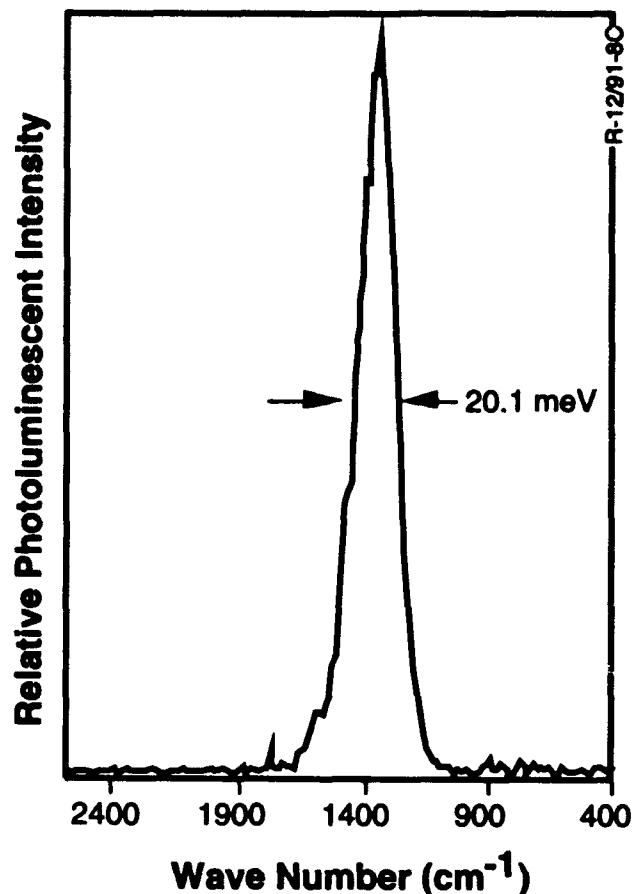


Fig. 6. Representative 77K IRPL peak obtained from the backside of the sample depicted in Fig. 5. The multiple peaks superimposed on the high energy side of the IRPL peak are the signature of quantized transitions.

located before the spectrometer's input port was used to filter out the 1.06  $\mu\text{m}$  pump radiation.

## RESULTS AND DISCUSSION

Infrared photoluminescence provides a direct measurement of the band gap of a superlattice in the near surface region. Since the spot size used is relatively small ( $\sim 400 \mu\text{m}$  diameter in this case), it is possible to probe several areas and produce a band gap energy map for the sample under study. Such a map is shown in Fig. 2 for a  $2 \times 1 \text{ cm}$  SL epilayer. The average energy gap for this sample is 136.8 meV with a standard deviation of  $\sigma = 3.5 \text{ meV}$ . This is equivalent to a cut-off wavelength of  $9.07 \mu\text{m}$  with  $\sigma = 0.23 \mu\text{m}$ , which is suitable for detector array fabrication. A high degree of band gap uniformity can also be seen in the data depicted in Fig. 3 for a  $0.75 \times 0.75 \text{ cm}$  sample. This superlattice exhibits an average energy gap of 158.8 meV with  $\sigma = 0.83 \text{ meV}$ , which corresponds to a cutoff of  $\lambda_c \sim 7.8 \mu\text{m}$  with a  $\sigma$  of  $0.04 \mu\text{m}$ . Finally, Fig. 4 shows a cut-off map for an LWIR superlattice with  $\lambda_c \sim 11.13 \mu\text{m}$  with  $\sigma = 0.21 \mu\text{m}$ . A comparison of this sample with an alloy of comparable band gap shows that the PAMBE grown superlattice exhibits an equivalent alloy x-value variation of  $\sigma = 0.0013$ .

It is important to note that substrate rotation dur-

## Conduction Band Diagram

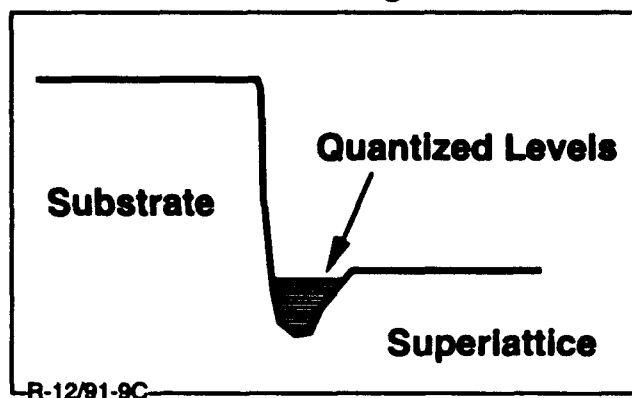


Fig. 7. Schematic representation of the quantum well at the substrate-epilayer interface. Carriers in this quantum well are two-dimensional with quantized energy levels. This model could explain the multiple transitions observed in the IRPL spectrum in Fig. 6.

ing epilayer deposition is not utilized in the MBE system in which the superlattices for this study were grown. Furthermore, these growths employed only one Te source situated  $12^\circ$  off the center growth line. We are currently studying the use of a second Te source placed so as to compensate for the interactions experienced with the high flux from the Hg source. This modification should significantly increase the yield of epilayers exhibiting a high degree of band gap uniformity.

Interdiffusion between superlattice constituent layers was investigated by comparing IRPL band gap maps obtained from the film surface with those obtained at the epilayer/substrate interface (IRPL excitation through the substrate). Figure 5 shows such a comparison obtained from a superlattice grown at Martin Marietta. The band gap variations are within 10 meV, suggesting that minimal interdiffusion takes place during PAMBE growth. This is the first directly measured evidence that the temperatures associated with the PAMBE growth process do not seriously affect the integrity of the superlattice layers.

Figure 6 shows a typical IRPL peak measured at the epilayer/substrate interface of the superlattice depicted in Fig. 5. All of the "backside" spectra exhibited several peaks superimposed on the higher energy side of the main peak. This result may be indicative of 2-D carriers confined at the interface between the substrate and epilayer. Such carriers have been observed in IR magneto-absorption measurements made on this and other superlattices grown at Martin Marietta.<sup>13</sup> Other groups have also reported 2-D carriers in the substrate/epilayer interface region of (211)B HgTe/CdTe superlattices.<sup>3</sup> Two-dimensional carriers confined at the substrate/epilayer interface would exhibit quantized energy levels as shown in Fig. 7. These energy levels could give rise to the additional peaks observed in the IRPL spectrum and tend to broaden and skew the main IRPL peak. This mechanism may be responsible for the 10 meV variation between the front-side and substrate-side IRPL measurements.

To further investigate the integrity of the superlattice layers in the near substrate region, TEM microscopy was performed at Purdue University on the sample depicted in Fig. 5. The constituent layers in the vicinity of the substrate were subjected to a temperature of 170°C for a period of several hours (the growth time of the film). The micrograph in Fig. 8 shows the interface between the superlattice and the (211)B substrate on which it was deposited. The HgTe (dark) and CdTe (light) layers are sharp and well defined all the way down to the substrate with no evidence of interdiffusion. This provides strong evidence that the 10 meV band gap difference seen in Fig. 5 is not due to layer interdiffusion during film growth.

Post-growth anneals have also been used to investigate the thermal stability of HgTe/CdTe superlattices grown at Martin Marietta. Selected epilayers have been subjected to temperatures between 100 and 180°C. Pre- and post-anneal energy gap measurements were then used to determine whether superlattice layer interdiffusion had occurred. Preliminary results indicate that post-growth anneals at temperatures as high as 180°C have little effect on the cut-off wavelength of the HgTe/CdTe superlattices studied. For example, a sample subjected to 180°C for 75 min showed no apparent change in band gap. These initial results suggest that HgTe/CdTe superlattices are more robust than first thought, and bodes well for the development of processes for the fabrication of device structures from this material system.

## SUMMARY

Infrared photoluminescence analysis was used to show that (211)B HgTe/CdTe superlattices can be grown by PAMBE which exhibit uniformities in cut-off wavelength suitable for IR detector array fabrication. We have also demonstrated that these materials are more thermally stable than previously thought in the community. Epilayer growth temperatures of 170°C and exposure to post-growth anneals of up to 180°C were found to have little effect on the cut-off wavelengths of the samples studied. These results represent an important step toward the development of an IR detector array technology based on HgTe/CdTe superlattice materials.

## ACKNOWLEDGMENT

Work supported by the Air Force Wright Laboratory Materials Directorate under contract No. F33615-90-C-5922, contract monitor Ms. L.E. Brown.

## REFERENCES

1. J.B. Schulman and T.C. McGill, *Appl. Phys. Lett.* 34, 663 (1979).
2. D.L. Smith, T.C. McGill and J.N. Schulman, *Appl. Phys. Lett.* 43, 180 (1983).
3. C.A. Hoffman, J.R. Meyer, R.J. Wagner, F.J. Bartoli, X. Chu, J.P. Faurie, L.R. Ram-Mohan and H. Xie, *J. Vac. Sci. Technol. A* 8, 1200 (1990).
4. A.R. Reisinger, K.A. Harris, T.H. Myers, R.W. Yanka and L.M. Mohnkern, *Appl. Phys. Lett.* 61, 699 (1992).
5. K.A. Harris, T.H. Myers, R.W. Yanka, L.M. Mohnkern and N. Otsuka, *J. Vac. Sci. Technol. B* 9, 1752 (1991).
6. D. Arch, J.P. Faurie, J.-L. Staudenmann, M. Hibbs-Brenner

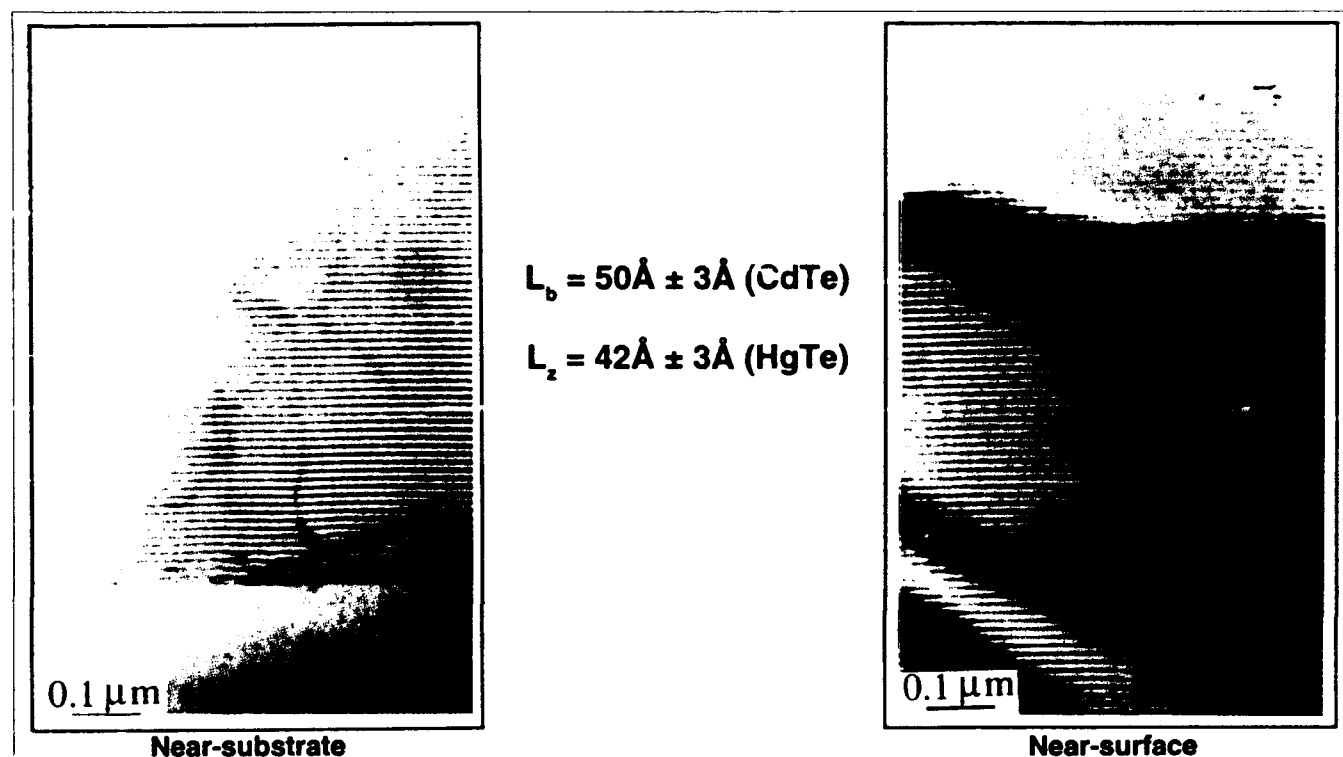


Fig. 8. Cross-sectional TEM micrograph of the substrate-epilayer interface and near-surface region of the superlattice depicted in Fig. 5. The constituent layers are sharply defined all the way down to the substrate. This demonstrates that interdiffusion of superlattice layers during film deposition does not occur to the limit of this measurement technique.

- and P. Chow, *J. Vac. Sci. Technol. A* 4, 2101 (1986).
7. D. Arch, J.-L. Staudenmann and J. P. Faurie, *Appl. Phys. Lett.* 48, 1588 (1986).
8. K.A. Harris, S. Hwang, D.K. Blanks, J.W. Cook, Jr., J.F. Schetzina and N. Otsuka, *J. Vac. Sci. Technol. A* 4, 2061 (1986).
9. T.H. Myers, R.W. Yanka, J.P. Karins, K.A. Harris, J.W. Cook, Jr. and J.F. Schetzina, *Mater. Res. Soc. Symp. Proc.* 90, 295 (1987).
10. T.H. Myers, K.A. Harris, R.W. Yanka, L.M. Mohnkern, R.J. Williams and G.K. Dudoff, *J. Vac. Sci. Technol. B* 10, 1438 (1992).
11. K.A. Harris, R.W. Yanka, L.M. Mohnkern, R.J. Williams, G.K. Dudoff and T.H. Myers, submitted to *Appl. Phys. Lett.*
12. A.R. Reisinger, R.N. Roberts, S.R. Chinn and T.H. Myers, *Rev. Sci. Instrum.* 60, 87 (1989).
13. K.A. Harris, R.W. Yanka, L.M. Mohnkern, A.R. Reisinger, T.H. Myers, J. Lang, Z. Yu, S. Hwang and J.F. Schetzina, *J. Vac. Sci. Technol. B* 10, 1574 (1992).







## AUTHOR INDEX

- Ahlgren, W.L. .... 835  
 Archer, N.A. .... 967  
 Arias, J.M. .... 1039, 1049  
 Austin, J.C. .... 1011  
  
 Baars, J. .... 923  
 Bablet, J. .... 1061  
 Bajaj, J. .... 859, 899, 931  
 Bartholomew, D. .... 1081  
 Beck, J. .... 993  
 Benz, R.G., II .... 815  
 Berding, M.A. .... 1005  
 Bezinger, A. .... 977  
 Bhat, I. .... 873  
 Blanks, D. .... 1081  
 Blazejewski, E.R. .... 931  
 Bouchut, Ph. .... 1061  
 Brink, D. .... 923  
 Bubulac, L.O. .... 859, 923, 1039, 1049  
 Buskes, H. .... 1097  
  
 Carr, D. .... 1097  
 Casagrande, L.G. .... 943  
 Chamonal, J.P. .... 1027  
 Chandra, D. .... 1033  
 Chen, A.-B. .... 843  
 Chen, M.C. .... 1033  
 Chen, Y.P. .... 951  
 Cockrum, C.A. .... 835  
 Colin, T. .... 1061  
 Conte, A. .... 815  
 Cook, J.W., Jr. .... 809, 973  
 Covington, W. .... 1087  
  
 Dean, B. .... 1073  
 Destefanis G. .... 1027, 1061  
 DeWames R.E. .... 931, 1039, 1049  
 DiMarzio, D. .... 943  
 Dobisz, E.Z. .... 1055  
 Dodge, J.A. .... 1033  
 Donnelly, D. .... 1087  
 Dudley, M. .... 943  
 Dura, J.A. .... 1087  
  
 Eddy, C.R., Jr. .... 1055  
 Edwall, D.D. .... 847, 923  
 Ehrenreich, H. .... 1093  
 Ehsani, H. .... 873  
 Ellsworth, J.A. .... 1067, 1073  
  
 Fanning, T. .... 943  
 Faurie, J.P. .... 951  
 Fisher, R.F. .... 1067  
 Foikard, M.A. .... 1097  
 Fueloep, K. .... 1097  
 Furdyna, J.K. .... 1103  
  
 Gal, M. .... 1097  
 Gedridge, R.W., Jr. .... 853, 859  
 Giess, J. .... 915  
 Golding, T.D. .... 1087  
 Goodwin, M.W. .... 1033  
 Gough, J.S. .... 915  
 Grein, C.H. .... 1093  
  
 Hallock, P.H. .... 853  
 Hamilton, W.J. .... 835, 879  
 Harper, V.B. .... 879  
 Harris, K.A. .... 1107  
 Hartley, R.H. .... 1097  
 Helms, C.R. .... 999  
 Higa, K.T. .... 853, 859  
 Hirahara, K. .... 865  
 Hoffman, C.A. .... 1055  
 Hughes, Wm. C. .... 1011  
  
 Irvine, S.J.C. .... 859, 899  
  
 James, J.B. .... 835  
 Johnson, B.A. .... 1097  
 Johnson, C.J. .... 1067, 1073  
 Johnson, S.M. .... 835, 879  
  
 Kalisher, M.H. .... 835  
 Kennedy, J.J. .... 1067, 1073  
 Kestigian, M. .... 907, 959  
 Kinch, M.A. .... 1081  
 Konkel, W.H. .... 835, 879  
 Korenstein, R. .... 853  
 Krueger, E.E. .... 907, 959  
 Kumar, V. .... 1097  
  
 Lansari, Y. .... 809, 973  
 Lee, D.L. .... 853  
 Lee, M.B. .... 943  
 Liao, P.-K. .... 1073  
 Lin, W.P. .... 859  
 List, R.S. .... 1017  
 Littler, C.L. .... 985  
 Liu, H.-Y. .... 821  
 Lorans, D. .... 827  
 Lowney, J.R. .... 985  
 Luo, H. .... 1103  
  
 McGill, T.C. .... 1093  
 Meléndez, J.L. .... 993, 999  
 Meyer, J.R. .... 1055  
 Million, A. .... 1061  
 Mohrkern, L.M. .... 1107  
 Myers, T.H. .... 1107  
 Myrosznyk, J.M. .... 835  
  
 Nakata, F. .... 865  
 Nemirovsky, Y. .... 977  
 Neugebauer, G.T. .... 1067, 1073  
 Nguyen Duy, T. .... 827  
 Norton, P.W. .... 907, 959  
  
 Orders, P.J. .... 1097  
 Otsuka, N. .... 1107  
  
 Palfrey, H.D. .... 967  
 Parkinson, J.B. .... 1073  
 Pasko, J.G. .... 1039, 1049  
 Pultz, G.N. .... 907, 959  
  
 Rajavel, D. .... 803  
 Ram-Mohan, L.R. .... 1103  
 Rees, D. .... 1097  
 Reisinger, A.R. .... 1107  
 Ren, J. .... 973  
 Rhiger D.R. .... 887  
 Risser, R.F. .... 835  
 Ruth, R.P. .... 801  
 Ruzin, A. .... 977  
  
 Sankur, H.O. .... 899  
 Schetzina, J.F. .... 809, 973  
 Schiebel, R.A. .... 1081  
 Seiler, D.G. .... 985  
 Sepich, J. .... 1073  
 Shen, G. .... 1097  
 Sher, A. .... 843, 1005  
 Shigenaka, K. .... 865  
 Shin, S.H. .... 1039, 1049  
 Sivananthan, S. .... 951  
 Song, X.N. .... 985  
 Steele, T.A. .... 1097  
 Sugiura, L. .... 865  
 Sullivan, E. .... 853  
 Summers, C.J. .... 815  
 Svoronos, S.A. .... 899  
 Swanson, M.L. .... 1011  
  
 Tennant W.E. .... 1049  
 Thurber, W.R. .... 985  
 Tobin, S.P. .... 907, 959  
 Tregilgas, J.H. .... 821  
 Triboulet, R. .... 827  
 Tromson-Carli, A. .... 827  
 Tung, T. .... 835  
  
 van Schilfgaarde, M. .... 843, 1005  
 Varga, I.K. .... 1097  
 Vigil, J.A. .... 835, 879  
 Vydyanath, H.R. .... 1067, 1073  
  
 Wagner, B.K. .... 815  
 Wan, C.-F. .... 821  
 Wang, W.-S. .... 873  
 Waterman, J.R. .... 801  
 Williams, G.M. .... 931, 1049  
 Willoughby, A.F.W. .... 967  
 Wong, K.-K. .... 907, 959  
  
 Xuan, Y. .... 1103  
  
 Yang, G.L. .... 1103  
 Yanka, R.W. .... 1107  
 Young, M.L. .... 915  
 Young, P.M. .... 1093  
 Yu, Z. .... 973  
 Yu, Z. .... 985  
  
 Zandian, M. .... 1039, 1049  
 Zborowski, J.T. .... 1087  
 Zinck, J.J. .... 803

GRANT NO: N00014-92-J-2018

ATTACHMENT NUMBER 2

DISTRIBUTION LIST FOR REPORTS

ADDRESSEES

NUMBER OF COPIES

Scientific Officer, Code 6818  
James Waterman  
NAVAL RESEARCH LABORATORY  
4555 Overlook Ave., SW  
Washington, DC 20375-5320

3 copies of proceedings

Grant Administrator

1 copy of proceedings

Defense Technical Information Center  
Building 5, Cameron Station  
Alexandria VA 22314-6145

1 copy of proceedings